ISSN 1816-5230

НАНОСИСТЕМИ, НАНОМАТЕРІАЛИ, НАНОТЕХНОЛОГІЇ

Nanosistemi, Nanomateriali, Nanotehnologii

ЗБІРНИК НАУКОВИХ ПРАЦЬ

ТОМ 23, ВИПУСК 2, 2025

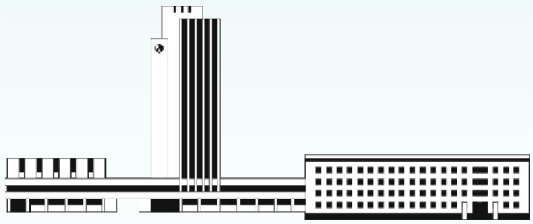

НАЦІОНАЛЬНА АКАДЕМІЯ НАУК УКРАЇНИ

НАНОСИСТЕМИ
НАНОМАТЕРІАЛИ
НАНОТЕХНОЛОГІЇ

NANOSYSTEMS
NANOMATERIALS
NANOTECHNOLOGIES

Засновник: Інститут металофізики ім. Г. В. Курдюмова НАН України
Видавець: Інститут металофізики ім. Г. В. Курдюмова НАН України

«Наносистеми, наноматеріали, нанотехнології» ♦ 'Nanosistemi, Nanomateriali, Nanotehnologii'
Щоквартальний збірник наукових праць ◊ Quarterly Collected Scientific Transactions

РЕДАКЦІЙНА КОЛЕҐІЯ

В. А. Татаренко — ***головний редактор***, акад. НАН України, д.ф.-м.н., проф., Ін-т металофізики ім. Г. В. Курдюмова НАН України

Б. М. Мордюк — ***заступник головного редактора***, д.ф.-м.н., с.н.с., Ін-т металофізики ім. Г. В. Курдюмова НАН України

Т. М. Радченко — ***заступник головного редактора***, д.ф.-м.н., с.н.с., Ін-т металофізики ім. Г. В. Курдюмова НАН України

В. В. Лізунов — ***відповідальний секретар редколегії***, д.ф.-м.н., проф., Ін-т металофізики ім. Г. В. Курдюмова НАН України

С. А. Беспалов — д.т.н., с.н.с., СФТМН НОВ Президії НАН України

М. Я. Валах — чл.-кор. НАН України, д.ф.-м.н., проф., Ін-т фізики напівпровідників ім. В. Є. Лашкарьова НАН України

Р. В. Вовк — акад. НАН України, д.ф.-м.н., проф., Харківський національний ун-т імені В. Н. Каразіна МОН України

І. В. Герасимчук — д.ф.-м.н., с.н.с., Ін-т магнетизму імені В. Г. Барьяхтара НАН України

П. П. Горбик — чл.-кор. НАН України, д.ф.-м.н., проф., Ін-т хімії поверхні ім. О. О. Чуйка НАН України

В. О. Зажигалов — чл.-кор. НАН України, д.х.н., проф., Ін-т сорбції та проблем ендоекології НАН України

В. Л. Карбівський — д.ф.-м.н., проф., Ін-т металофізики ім. Г. В. Курдюмова НАН України

О. А. Кордюк — акад. НАН України, д.ф.-м.н., проф., Київський академічний ун-т

С. О. Котречко — чл.-кор. НАН України, д.ф.-м.н., проф., Ін-т металофізики ім. Г. В. Курдюмова НАН України

М. П. Куліш — чл.-кор. НАН України, д.ф.-м.н., проф., Київський національний ун-т імені Тараса Шевченка МОН України

Б. І. Лев — акад. НАН України, д.ф.-м.н., проф., Ін-т теоретичної фізики ім. М. М. Боголюбова НАН України

Ю. А. Малєтін — чл.-кор. НАН України, д.х.н., с.н.с., Ін-т сорбції та проблем ендоекології НАН України

М. В. Маніло — д.х.н., Ін-т біоколоїдної хімії ім. Ф. Д. Овчаренка НАН України

С. І. Оковитий — чл.-кор. НАН України, д.х.н., проф., Дніпровський національний університет імені Олеся Гончара МОН України

А. В. Панько — д.х.н., Ін-т біоколоїдної хімії ім. Ф. Д. Овчаренка НАН України

Ю. І. Прилуцький — д.ф.-м.н., проф., ННЦ «Ін-т біології та медицини» Київського національного ун-ту імені Тараса Шевченка МОН України

В. А. Прокопенко — д.т.н., проф., Ін-т біоколоїдної хімії ім. Ф. Д. Овчаренка НАН України

О. А. Пуд — д.х.н., проф., Ін-т біоорганічної хімії та нафтохімії ім. В. П. Кухаря НАН України

С. О. Солопан — д.х.н., ст.досл., Ін-т загальної та неорганічної хімії ім. В. І. Вернадського НАН України

П. Є. Стрижак — акад. НАН України, д.х.н., проф., Ін-т фізичної хімії ім. Л. В. Писаржевського НАН України

В. Й. Сугаков — чл.-кор. НАН України, д.ф.-м.н., проф., Ін-т ядерних досліджень НАН України

Л. Ф. Суходуб — чл.-кор. НАН України, д.ф.-м.н., проф., Сумський державний ун-т МОН України

В. М. Уваров — чл.-кор. НАН України, д.ф.-м.н., проф., Ін-т металофізики ім. Г. В. Курдюмова НАН України

О. М. Файнлейб — чл.-кор. НАН України, д.х.н., проф., Ін-т хімії високомолекулярних сполук НАН України

Д. О. Харченко — д.ф.-м.н., проф., Ін-т прикладної фізики НАН України

О. В. Хоменко — д.ф.-м.н., проф., Сумський державний ун-т МОН України

В. О. Шаповалов — чл.-кор. НАН України, д.т.н., проф., Ін-т електрозварювання ім. Є. О. Патона НАН України

EDITORIAL BOARD

V. A. Tatarenko — ***Editor-in-Chief***, Mem. of the N.A.S. of Ukraine, Dr. Sci. (Phys.-Math.), Prof., G. V. Kurdyumov Inst. for Metal Physics of the N.A.S. of Ukraine

B. M. Mordyuk — ***Deputy Editor-in-Chief***, Dr. Sci. (Phys.-Math.), Sr. Researcher, G. V. Kurdyumov Inst. for Metal Physics of the N.A.S. of Ukraine

T. M. Radchenko — ***Deputy Editor-in-Chief***, Dr. Sci. (Phys.-Math.), Sr. Researcher, G. V. Kurdyumov Inst. for Metal Physics of the N.A.S. of Ukraine

V. V. Lizunov — ***Executive Managing Editor***, Dr. Sci. (Phys.-Math.), , Prof., G. V. Kurdyumov Inst. for Metal Physics of the N.A.S. of Ukraine

S. A. Bespalov — Dr. Sci. (Tech.), Sr. Researcher, SPhTMS of Sci.-Org. Dept. of Presidium of the N.A.S. of Ukraine

M. Ya. Valakh — Cor. Mem. of the N.A.S. of Ukraine, Dr. Sci. (Phys.-Math.), Prof., V. Ye. Lashkaryov Inst. of Semiconductor Physics of the N.A.S. of Ukraine

R. V. Vovk — Mem. of the N.A.S. of Ukraine, Dr. Sci. (Phys.-Math.), Prof., V. N. Karazin Kharkiv Natl. Univ. of the Ministry of Education and Science of Ukraine

I. V. Gerasimchuk — Dr. Sci. (Phys.-Math.), Sr. Researcher, V. G. Baryakhtar Inst. of Magnetism of the N.A.S. of Ukraine

P. P. Gorbyk — Cor. Mem. of the N.A.S. of Ukraine, Dr. Sci. (Phys.-Math.), Prof., O. O. Chuiko Inst. of Surface Chemistry of the N.A.S. of Ukraine

V. O. Zazhigalov — Cor. Mem. of the N.A.S. of Ukraine, Dr. Sci. (Chem.), Prof., Inst. of Sorption and Problems of the Endoecology of the N.A.S. of Ukraine

V. L. Karbivskyy — Dr. Sci. (Phys.-Math.), Prof., G. V. Kurdyumov Inst. for Metal Physics of the N.A.S. of Ukraine

O. A. Kordyuk — Mem. of the N.A.S. of Ukraine, Dr. Sci. (Phys.-Math.), Prof., Kyiv Academic Univ.

S. O. Kotrechko — Cor. Mem. of the N.A.S. of Ukraine, Dr. Sci. (Phys.-Math.), Prof., G. V. Kurdyumov Inst. for Metal Physics of the N.A.S. of Ukraine

M. P. Kulish — Cor. Mem. of the N.A.S. of Ukraine, Dr. Sci. (Phys.-Math.), Prof., Taras Shevchenko Nat'l Univ. of Kyiv of the Ministry of Education and Science of Ukraine

B. I. Lev — Mem. of the N.A.S. of Ukraine, Dr. Sci. (Phys.-Math.), Prof., M. M. Bogolyubov Inst. for Theoretical Physics of the N.A.S. of Ukraine

Yu. A. Maletin — Cor. Mem. of the N.A.S. of Ukraine, Dr. Sci. (Chem.), Sr. Researcher, Inst. of Sorption and Problems of Endoecology of the N.A.S. of Ukraine

M. V. Manilo — Dr. Sci. (Chem.), F. D. Ovcharenko Inst. of Biocolloidal Chemistry of the N.A.S. of Ukraine

S. I. Okovytyy — Cor. Mem. of the N.A.S. of Ukraine, Dr. Sci. (Chem.), Prof., Oles Honchar Dnipro Nat'l Univ. of the Ministry of Education and Science of Ukraine

A. V. Panko — Dr. Sci. (Chem.), F. D. Ovcharenko Inst. of Biocolloidal Chemistry of the N.A.S. of Ukraine

Yu. I. Prylutskyy — Dr. Sci. (Phys.-Math.), Prof., NSC 'Inst. of Biology and Medicine' of the Taras Shevchenko Nat'l Univ. of Kyiv of the Ministry of Education and Science of Ukraine

V. A. Prokopenko — Dr. Sci. (Tech.), Prof., F. D. Ovcharenko Inst. of Biocolloidal Chemistry of the N.A.S. of Ukraine

O. A. Pud — Dr. Sci. (Chem.), Prof., V. P. Kukhar Inst. of Bioorganic Chemistry and Petrochemistry of the N.A.S. of Ukraine

S. O. Solopan — Dr. Sci. (Chem.), Sr. Researcher, V. I. Vernadsky Inst. of General and Inorganic Chemistry of the N.A.S. of Ukraine

P. Ye. Strizhak — Mem. of the N.A.S. of Ukraine, Dr. Sci. (Chem.), Prof., L. V. Pisarzhevsky Inst. of Physical Chemistry of the N.A.S. of Ukraine

V. J. Sugakov — Cor. Mem. of the N.A.S. of Ukraine, Dr. Sci. (Phys.-Math.), Prof., Inst. of Nuclear Research of the N.A.S. of Ukraine

L. F. Sukhodub — Cor. Mem. of the N.A.S. of Ukraine, Dr. Sci. (Phys.-Math.), Prof., Sumy State Univ. of the Ministry of Education and Science of Ukraine

V. M. Uvarov — Cor. Mem. of the N.A.S. of Ukraine, Dr. Sci. (Phys.-Math.), Prof., G. V. Kurdyumov Inst. for Metal Physics of the N.A.S. of Ukraine

O. M. Fainleib — Cor. Mem. of the N.A.S. of Ukraine, Dr. Sci. (Chem.), Prof., Inst. of Chemistry of Macromolecular Compounds of the N.A.S. of Ukraine

D. O. Kharchenko — Dr. Sci. (Phys.-Math.), Prof., Inst. of Applied Physics of the N.A.S. of Ukraine

O. V. Khomenko — Dr. Sci. (Phys.-Math.), Prof., Sumy State Univ. of the Ministry of Education and Science of Ukraine

V. O. Shapovalov — Cor. Mem. of the N.A.S. of Ukraine, Dr. Sci. (Chem.), Prof., E. O. Paton Electric Welding Inst. of the N.A.S. of Ukraine

© Інститут металофізики ім. Г. В. Курдюмова НАН України (Київ), 2025

НАЦІОНАЛЬНА АКАДЕМІЯ НАУК УКРАЇНИ
Інститут металофізики ім. Г. В. Курдюмова

НАНОСИСТЕМИ, НАНОМАТЕРІАЛИ, НАНОТЕХНОЛОГІЇ

ЗБІРНИК НАУКОВИХ ПРАЦЬ

ТОМ 23, ВИПУСК 2

РВВ ІМФ
КИЇВ — 2025

УДК 536:669

НАНОСИСТЕМИ, НАНОМАТЕРІАЛИ, НАНОТЕХНОЛОГІЇ / Щоквартальний збірник наукових праць / Том 23, вип. 2. — Київ: РВВ ІМФ, 2025. — XVIII с. + 312 с.

У збірнику наведено оригінальні та оглядові статті за результатами робіт, виконаних у рамках досліджень за напрямом «Перспективні фундаментальні дослідження та інноваційні розробки наноматеріалів і нанотехнологій для потреб промисловості, охорони здоров'я та сільського господарства». Основну увагу приділено розгляду проблемних питань нанофізики, наноелектроніки, особливостей будови наноструктурованих матеріялів, з'ясуванню їхніх електричних, термічних, механічних, реологічних і хемічних властивостей, поверхневих явищ і самоорганізації. Представлено результати фабрикації, оброблення, тестування й аналізування нанорозмірних частинок, наномасштабних структур і багатофункціональних наноматеріялів технічного та біомедичного призначення в умовах впливу зовнішніх чинників. Розглянуто особливості технологій одержання, діягностики та характеризації наносистем.

Статті друкуються мовами оригіналів.

Збірник розраховано на наукових працівників, інженерів, викладачів ЗВО, аспірантів і студентів відповідних спеціяльностей.

РЕДАКЦІЙНА КОЛЕҐІЯ:

*С. А. Беспалов, М. Я. Валах, Р. В. Вовк, І. В. Герасимчук, П. П. Горбик, В. О. Зажигалов, В. Л. Карбівський, О. А. Кордюк, С. О. Котречко, М. П. Куліш, Б. І. Лев, В. В. Лізунов (**відповідальний секретар**), Ю. А. Малєтін, М. В. Маніло, Б. М. Мордюк (**заступник головного редактора**), С. І. Оковитий, А. В. Панько, Ю. І. Прилуцький, В. А. Прокопенко, О. А. Пуд, Т. М. Радченко (**заступник головного редактора**), С. О. Солопан, П. Є. Стрижак, В. Й. Сугаков, Л. Ф. Суходуб, В. А. Татаренко (**головний редактор**), В. М. Уваров, О. М. Файнлейб, Д. О. Харченко, О. В. Хоменко, В. О. Шаповалов*

ISSN 1816-5230

© ІМФ ім. Г. В. Курдюмова НАН України, 2025

НАЦІОНАЛЬНА АКАДЕМІЯ НАУК УКРАЇНИ ● ІНСТИТУТ МЕТАЛОФІЗИКИ ім. Г. В. Курдюмова

НАНОСИСТЕМИ, НАНОМАТЕРІАЛИ, НАНОТЕХНОЛОГІЇ

ЗБІРНИК НАУКОВИХ ПРАЦЬ
ЗАСНОВАНИЙ У ЖОВТНІ 2003 р.

Том 23, вип. 2; 2025 р.

ЗМІСТ

© Інститут металофізики ім. Г. В. Курдюмова НАН України, 2025

Науковий редактор випуску — *В. А. Татаренко*
Відповідальний секретар редакційної колеґії — *В. В. Лізунов*
Редактори-коректори: *І. О. Головашич, Д. С. Леонов, Н. А. Леонова*
Технічні редактори: *Д. С. Леонов, І. М. Заболотний*
Оригінал-макет для прямого репродукування виготовлено комп'ютеризованою групою РВВ Інституту металофізики ім. Г. В. Курдюмова НАН України
Друкується за постановою редакційної колеґії збірника англійською або українською мовами
Затверджено до друку вченою радою ІМФ ім. Г. В. Курдюмова НАН України
Свідоцтво суб'єкта видавничої справи серії ДК № 5875 від 13.12.2017 р.
Рішення Національної ради України з питань телебачення і радіомовлення № 907 від 21.03.2024 р. про суб'єкт у сфері друкованих медіа (ідентифікатор медіа R30-03169)
Підп. до друку 26.06.2025 р. Формат 70×100/16. Гарн. SchoolBookC. Папір офсет. № 1. Друк різограф.
Адреса редакції «ННН»: Інститут металофізики ім. Г. В. Курдюмова НАН України, бульв. Акад. Вернадського, 36, каб. 210; 03142 Київ, Україна
Тел.: +380 44 4241221, +380 44 4249042; факс: +380 44 4242561
Ел. пошта: tatar@imp.kiev.ua, dsleonov@gmail.com
Надруковано в РВВ ІМФ ім. Г. В. Курдюмова НАН України.
бульв. Акад. Вернадського, 36; 03142 Київ, Україна. Тел.: +380 44 4240236
Зав. поліграфічно-розмножувальної групи — *Л. І. Малініна*

NATIONAL ACADEMY OF SCIENCES OF UKRAINE ● G. V. KURDYUMOV INSTITUTE FOR METAL PHYSICS

COLLECTED SCIENTIFIC TRANSACTIONS

NANOSISTEMI, NANOMATERIALI, NANOTEHNOLOGII

FOUNDED IN OCTOBER, 2003

Volume 23, Issue 2 (2025)

CONTENTS

© Інститут металофізики ім. Г. В. Курдюмова НАН України, 2025

Scientific Editor of the Issue—*V. A. Tatarenko*
Executive Managing Editor—*V. V. Lizunov*
Technical Editors—*D. S. Leonov, I. M. Zabolotnyy*
Editorial-Publishing Department, G. V. Kurdyumov Institute for Metal Physics, N.A.S. of Ukraine
State Registration Certificate of the Printed Mass Medium: Media Identifier R30-03169

Editorial Office: 36 Academician Vernadsky Boulevard, UA-03142 Kyyiv, Ukraine
Telephone: +380 44 4241221, +380 44 4249042. Fax: +380 44 4242561
E-mail: tatar@imp.kiev.ua, dsleonov@gmail.com

ІНФОРМАЦІЯ ДЛЯ ПЕРЕДПЛАТНИКІВ

Редакція щоквартального збірника наукових праць
«НАНОСИСТЕМИ, НАНОМАТЕРІАЛИ, НАНОТЕХНОЛОГІЇ»
(CODEN: NNNAAT; ISSN (Print): 1816-5230, ISSN (Online): 2617-3794;
у «Каталозі медіа України «Преса поштою»» передплатний індекс: **94919**)
повідомляє про передплату (починаючи з поточного кварталу випуску).
Рекомендуємо оформити передплату безпосередньо перерахуванням оплати

у гривнях:
«Отримувачу»: Інститут металофізики ім. Г. В. Курдюмова НАН України
на розрахунковий рахунок № UA058201720313291001201001901 в банку ГУДКСУ в м. Києві
код банку 820172
код ЗКПО: 05417331
для «Постачальника» — Інституту металофізики ім. Г. В. Курдюмова НАН України
Свідоцтво платника податку № 36283185
ІПН 054173326066
Код призначення платежу: 25010100
Призначення платежу: за збірник «Наносистеми, наноматеріали, нанотехнології» для РВВ ІМФ НАНУ
Підстава: передоплата 100%

в іноземній валюті (доларах США, євро) через відповідні банки-кореспонденти АТ «Державний експортно-імпортний банк України»:
«Отримувачу»: Філія АТ «Державний експортно-імпортний банк України» в м. Києві (Україна, 04053 Київ, вул. Бульварно-Кудрявська, 11[б])
на розрахунковий рахунок № UA603223130000025308000000067
МФО 322313
для «Постачальника» — Інституту металофізики ім. Г. В. Курдюмова НАН України
Призначення платежу: за збірник «Наносистеми, наноматеріали, нанотехнології» для РВВ ІМФ НАНУ
Підстава: передоплата 100%

За цього способу передплати необхідно сповістити редакцію збірника за поштовою адресою:
РВВ (№ 83) ІМФ НАНУ,
бульв. Акад. Вернадського, 36,
03142 Київ, Україна

e-mail: **tatar@imp.kiev.ua**; факс: +380 44 4242561; телефон: +380 44 4241221, +380 44 4249042

дату сплати, назву установи або найменування передплатника, адресу для поштової доставки, а за потреби — свої реквізити для податкової накладної.

Періодичність — том з 4 випусків у рік.

Із врахуванням поштової пересилки
для передплатників в Україну передплатна ціна: одного примірника випуску — 390 грн., тому — 1560 грн.;
для іноземних передплатників передплатна ціна: одного примірника випуску — 40 US$ (37 EUR), тому — 160 US$ (148 EUR).

✂ *Зразок для оплати річної передплати*

Рахунок-фактура

«Постачальник»: Інститут металофізики ім. Г. В. Курдюмова НАН України
«Отримувач»: Філія АТ «Державний експортно-імпортний банк України» в м. Києві
(Україна, 04053 Київ, вул. Бульварно-Кудрявська, 11[б])
на розрахунковий рахунок № UA603223130000025308000000067, МФО 322313
Призначення платежу: за збірник «Наносистеми, наноматеріали, нанотехнології» для ІМФ НАНУ
«Платник»: .....
.....
Підстава: передоплата 100%

№	Назва	Од. вим.	Кількість	Ціна	Сума
1	збірник «Наносистеми, наноматеріали, нанотехнології» (включаючи доставку поштою)	прим.	4	40 US$	160 US$
	Сума до сплати				160 US$

INFORMATION FOR SUBSCRIBERS

Editorial Board of Quarterly Collected Scientific Transactions
'NANOSISTEMI, NANOMATERIALI, NANOTEHNOLOGII'
(*i.e.* 'NANOSYSTEMS, NANOMATERIALS, NANOTECHNOLOGIES')
(CODEN: NNNAAT; ISSN (Print): 1816-5230, ISSN (Online): 2617-3794)
advertises the subscription on an annual basis for this year.

Orders should be placed through one of the methods described below.

Besides the subscription *via* the Private limited company **'PresCentr Kyiv'** / **«ПресЦентр Київ»** (with address: UA-01019 Kyiv, Ukraine, P.B. 185, tel./fax: +380 44 5361180 / 44 5361175, and e-mails: **podpiska1@prescentr.kiev.ua**, **market7@prescentr.kiev.ua**, **ksl1@prescentr.kiev.ua**) or *via* Internet: **http://www.prescentr.kiev.ua/index.php?route=product/category&path=332_252_266**, as well as besides the subscription *via* **Subscription agency 'Mercury'** / **«Меркурій»** (with juridical address: UA-49000 Dnipro, 10 Slobozhansky Ave., Bldg. 2, apt. 51, postal address in Kyiv: UA-03056 Kyiv, 27 Vadym Hetman Str., tel.: +380 93 3935740 / 44 2210557, e-mails: **podpiska@mercury.net.ua**, **l.podbereznaja.mercury@gmail.com**), the Editorial Board will take orders sent directly to the Editorial Board. To obtain our edition, the persons and institutions, interested in this title, should made the definite payment sent, according to the order, to the account of the Publisher—Institute for Metal Physics of the N.A.S. of Ukraine.

This edition frequency is 4 issues per year. The annual subscription rate for 'Nanosistemi, Nanomateriali, Nanotehnologii' is of 160 US$ (or 148 EUR), including airmail postage, packing and handling charges. All other currency payments should be made using the current conversion rate set by the Publisher (subscribers should contact the Editorial Board).

Subscription is valid after obtaining by the Editorial Board of banker's order. Banker's order should be sent to the address:

G. V. Kurdyumov Institute for Metal Physics, N.A.S. of Ukraine,
currency account No. UA603223130000025308000000067, MFO 322313
in the Kyiv's Branch of JSC 'The State Export-Import Bank of Ukraine'
(Joint Stock Company 'Ukreximbank')
(11[b] Bulvarno-Kudriavska Str., UA-04053 Kyiv, Ukraine)

simultaneously with written notice providing the Editorial Board with a copy of banker's order for subscription and detailed address for mailing.

Address of the Editorial Board Office:

G. V. Kurdyumov Institute for Metal Physics, N.A.S. of Ukraine,
36 Academician Vernadsky Blvd.,
UA-03142 Kyiv, Ukraine.
E-mail: **tatar@imp.kiev.ua** (with subject beginning by word 'nano').
Fax: +380 44 4242561.

After receiving of banker's order, the Editorial Board will send the guarantee letter to the subscriber's address for mailing the collected scientific transactions for a corresponding term.

Editorial Board of this edition hopes for effective co-operation with its present and future readers and asks to promote the maximum information about its contents to persons, institutions and organizations concerned.

ИНФОРМАЦИЯ ДЛЯ АВТОРОВ

Сборник научных трудов «*Наносистеми, наноматеріали, нанотехнології*» (ННН) публикует ещё неопубликованные и не находящиеся на рассмотрении для опубликования в иных изданиях научные обзоры и оригинальные статьи, содержащие и характеризующие результаты экспериментальных и теоретических исследований в области физики, химии, биологии, техники, методов синтеза, обработки и диагностики наноразмерных систем и наномасштабных материалов: кластеров, наночастиц, нанотрубок, нанокристаллов и наноструктур (апатитоподобных и др. биосистем, аморфных и коллоидных наноразмерных систем, наноструктурных плёнок и покрытий, нанопорошков и т.д.).

Сборник ННН не публикует: статьи полемические, классификационные и узкоспециальные, содержащие решения стандартных задач; статьи описательные и методические (если метод не является принципиально новым); статьи, в которых излагаются отдельные этапы исследования или материал, разделённый на несколько последовательных публикаций; статьи о рядовых исследованиях, не представляющих общего интереса и не содержащих значимых выводов.

Статьи публикуются на одном из двух языков: **английском** или **украинском**.

Статьи, в оформлении которых не соблюдены следующие правила для публикации в ННН, возвращаются авторам без рассмотрения по существу. (Датой поступления считается день повторного представления статьи после соблюдения указанных ниже правил.)

1. Статья должна быть подписана всеми авторами (с указанием их адресов электронной почты); **следует указать** фамилию, имя и отчество автора, с которым редакция будет вести переписку, его почтовый адрес, номер телефона (факса), адрес электронной почты.

2. Изложение должно быть ясным, **структурированным** (разделами **«1. Вступ»**, **«2. Експериментальна/Теоретична методика»**, **«3. Результати та їх обговорення»**, **«4. Висновки»**, **«Цитована література»**), сжатым, без длинных введений, отступлений и повторов, дублирования в тексте данных таблиц, рисунков и подписей к ним. Аннотация и раздел **«Висновки»** должны не дублировать друг друга. Числовые данные следует приводить в общепринятых единицах.

3. Объём статьи должен быть не более 5000 слов (с учётом основного текста, таблиц, подписей к рисункам, списка литературы) и 10 рисунков. Вопросы, связанные с публикацией научных обзоров (не более 22000 слов и 60 рисунков), решаются редколлегией ННН на основании предварительно предоставленной авторами расширенной аннотации работы.

4. В редакцию обязательно предоставляется по **e-mail** (или на компакт-диске) файл рукописи статьи (с иллюстративным материалом), набранный в текстовом редакторе Microsoft Word 2003, 2007 или 2010 с названием, состоящим из фамилии первого автора (латиницей), например, Smirnov.doc.

5. Электронная версия рукописи должна содержать **аннотацию** (200–250 слов) статьи (вместе с **5–6 ключевыми словами**) и **5–7 индексов PACS** (в последней редакции 'Physics and Astronomy Classification Scheme 2010'—http://publishing.aip.org/publishing/pacs/pacs-2010-regular-edition; см. **PACS numbers (imp.kiev.ua)**). Тексты украиноязычных статей должны также содержать заглавие статьи (вместе со списком авторов и адресами соответствующих учреждений), расширенную аннотацию (300–350 слов), ключевые слова, заголовки таблиц и подписи к рисункам на **английском языке**. Кроме того, содержания аннотаций на украинском и английском языках должны быть идентичными по смыслу.

7. Рисунки (цветные, черно-белые или полутоновые с градацией серого) должны быть представлены в виде отдельных файлов (предпочтительно в **графических форматах TIFF**, **EPS** или **JPEG**) с названиями, состоящими из фамилии первого автора (латиницей) и номера рисунка, например, Smirnov_fig2a.tiff. Качество **иллюстраций** (в том числе полутоновых) должно обеспечивать их воспроизведение с разрешением 300–600 точек на дюйм. Дополнительно рисунки предоставляются в формате программы, в которой они создавались.

8. Надписи на рисунках (особенно полутоновых) надо по возможности заменить буквенными обозначениями (набранными на контрастном фоне), а кривые обозначить цифрами или различного типа линиями/маркерами, разъясняемыми в подписях к рисункам или в тексте. На графиках все линии/маркёры должны быть чёрного цвета и достаточных толщин/размеров для качественного воспроизведения в уменьшенном в 2–3 раза виде (рекомендуемая ширина рисунка — 12,7 см). Снимки должны быть чёткими и контрастными, а надписи и обозначения должны не закрывать существенные детали (для чего можно использовать стрелки). Вместо указания в подтекстовке увеличения при съёмке желательно проставить масштаб (на контрастном фоне) на одном из идентичных снимков. На графиках подписи к осям, **выполненные на языке статьи**, должны содержать обозначения (или наименования) откладываемых величин и через запятую их единицы измерения.

9. Формулы в текст необходимо вставлять с помощью редактора формул MathType, полностью совместимого с MS Office 2003, 2007, 2010.

10. Рисунки, а также **таблицы** и подстрочные **примечания (сноски)** должны иметь сплошную нумерацию по всей статье.

11. Ссылки на литературные источники следует давать в виде порядкового номера, напечатанного в строку в квадратных скобках. Список литературы составляется в порядке первого упоминания источника. Примеры оформления ссылок приведены ниже; просим обратить внимание на порядок следования инициалов и фамилий авторов, библиографических сведений и на разделительные знаки, а также на необходимость указания **всех** соавторов цитированной работы и (в конце

каждой ссылки) её **цифрового идентификатора DOI**, если таковой имеется у соответствующей публикации (и указан на её интернет-странице издательства):

1. T. M. Radchenko and V. A. Tatarenko, *Usp. Fiz. Met.*, **9**, No. 1: 1 (2008) (in Ukrainian); https://doi.org/10.15407/ufm.09.01.001
2. T. M. Radchenko, A. A. Shylau, and I. V. Zozoulenko, *Phys. Rev. B*, **86**: 035418 (2012); https://doi.org/10.1103/PhysRevB.86.035418
3. A. Meisel, G. Leonhardt, und R. Szargan, *Röntgenspektren und Chemische Bindung* [X-Ray Spectra and Chemical Bond] (Leipzig: Akademische Verlagsgesellschaft Geest & Portig K.-G.: 1977) (in German).
4. J. M. Ziman, *Printsipy Teorii Tvyordogo Tela* [Principles of the Theory of Solids] (Moskva: Mir: 1974) (Russian translation).
5. M. A. Stucke, D. M. Dimiduk, and D. M. Hazzledine, *High Temperature Ordered Intermetallic Alloys. V* (Eds. I. Baker and R. Darolia) (Pittsburgh, PA, USA: MRS: 1993), p. 471.
6. *Handbook of Mathematical Functions with Formulas, Graphs and Mathematical Tables* (Eds. M. Abramowitz and I. A. Stegun), Nat'l Bureau of Standards. Appl. Math. Ser. Vol. **55** (Washington, D.C.: U.S. Govt. Printing Office: 1964).
7. B. B. Karpovych and O. B. Borovkoff, *Proc. of Symp. 'Micromaterials Engineering' (Dec. 25–31, 1999)* (Kyiv: RVV IMF: 2000), vol. **2**, p. 113 (in Ukrainian).
8. T. M. Radchenko, *Vplyv Uporiadkuvannya Defektnoyi Struktury на Transportni Vlastyvosti Zmishanykh Krystaliv* [Influence of Ordering of the Defect Structure on Transport Properties of the Mixed Crystals] (Thesis of Disser. for Dr. Phys.-Math. Sci.) (Kyiv: G. V. Kurdyumov Institute for Metal Physics, N.A.S.U.: 2015) (in Ukrainian).
9. E. M. Gololobov, V. B. Shipilo, N. I. Sedrenok, and A. I. Dudyak, *Sposob Polucheniya Karbonitridov Metallov* [Production Method of Metal Carbonitrides], Authors' Certificate 722341 SSSR (Published November 21, 1979) (in Russian).
10. V. G. Trubachev, K. V. Chuistov, V. N. Gorshkov, and A. E. Perekos, *Sposob Polucheniya Metallicheskikh Poroshkov* [The Technology of Metallic Powder Production]: Patent 1639892 SU. MKI, B22 F9/02, 9/14 (Otkrytiya i Izobreteniya, **34**, No. 13: 11) (1991) (in Russian).
11. Yu. M. Koval' and V. V. Nemoshkalenko, *O Prirode Martensitnykh Prevrashchenij* [On the Nature of Martensitic Transformations] (Kyiv: 1998) (Prepr./N.A.S. of Ukraine. Inst. for Metal Physics. No. 1, 1998) (in Russian).

Следует применять общепринятые сокращения названий журналов и сборников трудов:
http://www.cas.org/content/references/corejournals; http://rmp.aps.org/files/rmpguapb.pdf;
http://images.webofknowledge.com/WOK46P9/help/WOS/A_abrvjt.html;
http://www.ams.org/msnhtml/serials.pdf.

Обязательным требованием является предоставление дополнительного списка цитированной литературы (**References**) в **латинской транслитерации** (система **BGN/PCGN**; рекомендуемые транслитераторы: http://www.slovnyk.ua/services/translit.php; http://ru.translit.net/?account=bgn). После транслитерированных названий книг, диссертаций, патентов и пр. надо приводить в квадратных скобках их англоязычный перевод. При транслитерации статей из ННН надо использовать написание Ф.И.О. авторов, приведённое **только** в англоязычном оглавлении соответствующего выпуска, и **официальное** транслитерированное название сборника (см. также сайт).

12. Корректура авторам может быть выслана электронной почтой в виде pdf-файла. На проверку корректуры авторам отводятся 5 рабочих дней, начиная со дня, следующего за датой отправки корректуры. По истечении указанного срока статья автоматически направляется в печать. Исправления следует отметить и прокомментировать в самом pdf-файле либо оформить в виде перечня исправлений и переслать (от имени уполномоченного представителя коллектива авторов) по электронной почте в адрес редакции.

Рукописи можно направлять непосредственно в редакцию ННН по почтовому адресу: **бульвар Акад. Вернадского, 36, каб. 210; 03142 Киев, Украина** либо члену редакционной коллегии (состав редколлегии указан на 2-й странице обложки). Электронный вариант статьи направляется по e-mail: **tatar@imp.kiev.ua** (с темой, начинающейся словом 'nano').

В соответствии с договорённостью между редакцией ННН и учредителями сборника, редакция считает, что авторы, посылая ей рукопись статьи, передают учредителям и редколлегии право опубликовать эту рукопись на **английском (украинском)** языке, и просит авторов сразу прикладывать к рукописи подписанное авторами «Соглашение о передаче авторского права»:

Угода про передачу авторського права

Ми, що нижче підписалися, автори рукопису « ..... », передаємо засновникам і редколегії збірника наукових праць «*Наносистеми, наноматеріали, нанотехнології*» право опублікувати цей рукопис англійською (чи то українською) мовою. Ми підтверджуємо, що ця публікація **не** порушує авторського права інших осіб, установ або організацій.
Підписи авторів: ..... (ПРІЗВИЩЕ Ім'я, дата, адреса, № телефону, e-mail)

При этом за авторами сохраняются все остальные права как собственников этой рукописи. Авторы могут получить опубликованный выпуск со своей статьёй в редакции сборника по вышеуказанному адресу (тел. №№: **+380 44 4241221**, **+380 44 4249042**), а также загрузить pdf-файл статьи с сайта сборника: http://www.imp.kiev.ua/nanosys/ru/articles/index.html.

INFORMATION FOR CONTRIBUTORS

Submission of Manuscripts: Papers should be sent to the Executive Managing Editor, Editorial Office, Institute for Metal Physics, N.A.S.U., 36 Academician Vernadsky Boulevard, UA-03142 Kyiv, Ukraine. Manuscripts may also be submitted to a member of the Editorial Advisory Board or to the appropriate Editorial Board Member who is familiar with the research presented.

Submission of a paper to '*Nanosistemi, Nanomateriali, Nanotehnologii*' (i.e., 'Nanosystems, Nanomaterials, Nanotechnologies') will be taken to imply that it represents original work not previously published, it is not being considered for publication elsewhere, and if accepted for publication, it will not be published in the same language without the consent of the Editors and Publisher. It is a condition of acceptance by the Editor of a typescript for publication that the Publishers acquire automatically the copyright in the typescript throughout the world.

Scope of the Collected Scientific Transactions: '*Nanosistemi, Nanomateriali, Nanotehnologii*' (i.e., 'Nanosystems, Nanomaterials, Nanotechnologies'—NNN) is the quarterly multidisciplinary peer-reviewed collected scientific transactions, which publish high-quality work on all aspects of nanoscience and nanotechnology. Currently, transactions stand alone in serving the 'nano' community in providing up-to-date information on all developments and progresses being made in nanoscience and nanotechnology and the future predictions for this extraordinary technology. The topics covered by the transactions relate to all 'nano' related areas of the latest research and recent development works including nanomaterials, characterization tools, fabrication methods, numerical simulation, and theory as well as discussions in the field of nanoscience and technology ranging from basic aspects of the science of nanoscale systems and materials to practical applications of such systems and materials ranging from civil engineering to advanced molecular electronics so promising to transform our everyday technology as well as basic economics. The subjects covered include the following: 1. physical sciences; 2. chemical sciences; 3. life sciences; 4. theoretical and computational science and engineering.

The Transactions does not publish: articles, which are polemical and classifying, have a restricted meaning, or contain the solutions of standard problems; descriptive and methodical articles (if the method is not basically new); articles presenting separate stages of studies or the material divided into several parts for subsequent publications; articles with trivial results, which are not of general interest and do not contain significant conclusions.

Language: The language of publication may be English or Ukrainian.

Abstract: Each paper requires an English abstract of 200–250 words summarizing the significant coverage and findings.

Keywords and PACS numbers: Up to six keywords and PACS numbers reflecting the content of the contribution should be supplied (see 'Physics and Astronomy Classification Scheme 2010' at http://publishing.aip.org/publishing/pacs/pacs-2010-regular-edition or **PACS numbers (imp.kiev.ua)**).

Manuscript Preparation: Papers should be typed (in duplicate) with double spacing and wide margins on good quality paper (A4 size). The length of original contributions should not in general exceed 5000 words and 10 figures, and subject review articles should not exceed 22000 words and 60 figures, including tables and diagrams. Authors are urged to arrange the subject matter clearly under headings such as 1. Introduction, 2. Experimental/Theoretical Details, 3. Results, 4. Discussion, 5. Conclusion, References. Subsections should be identified with section and subsection numbers (such as 6.1. Second-Value Subheading).

References and Notes: Notes are indicated in the text by consecutive superior Arabic numbers (without parentheses). References should be numbered consecutively (in square brackets) throughout the text. The full list should be collected and typed at the end of the paper in numerical order. Listed references should be completed in all details including **DOI** (if available) but excluding article titles in journals. All authors' initials should precede their surnames. Examples of references preparation:

1. T. M. Radchenko and V. A. Tatarenko, *Usp. Fiz. Met.*, **9**, No. 1: 1 (2008) (in Ukrainian); https://doi.org/10.15407/ufm.09.01.001
2. T. M. Radchenko, A. A. Shylau, and I. V. Zozoulenko, *Phys. Rev. B*, **86**: 035418 (2012); https://doi.org/10.1103/PhysRevB.86.035418
3. A. Meisel, G. Leonhardt, und R. Szargan, *Röntgenspektren und Chemische Bindung* [X-Ray Spectra and Chemical Bond] (Leipzig: Akademische Verlagsgesellschaft Geest & Portig K.-G.: 1977) (in German).
4. J. M. Ziman, *Printsipy Teorii Tvyordogo Tela* [Principles of the Theory of Solids] (Moskva: Mir: 1974) (Russian translation).
5. M. A. Stucke, D. M. Dimiduk, and D. M. Hazzledine, *High Temperature Ordered Intermetallic Alloys. V* (Eds. I. Baker and R. Darolia) (Pittsburgh, PA, USA: MRS: 1993), p. 471.
6. *Handbook of Mathematical Functions with Formulas, Graphs and Mathematical Tables* (Eds. M. Abramowitz and I. A. Stegun), Nat'l Bureau of Standards. Appl. Math. Ser. Vol. **55** (Washington, D.C.: U.S. Govt. Printing Office: 1964).
7. B. B. Karpovych and O. B. Borovkoff, *Proc. of Symp. 'Micromaterials Engineering' (Dec. 25–31, 1999)* (Kyiv: RVV IMF: 2000), vol. **2**, p. 113 (in Ukrainian).
8. T. M. Radchenko, *Vplyv Uporyadkuvannya Defektnoyi Struktury на Transportni Vlastyvosti Zmis-*

hanykh Krystaliv [Influence of Ordering of the Defect Structure on Transport Properties of the Mixed Crystals] (Thesis of Disser. for Dr. Phys.-Math. Sci.) (Kyiv: G. V. Kurdyumov Institute for Metal Physics, N.A.S.U.: 2015) (in Ukrainian).
9. E. M. Gololobov, V. B. Shipilo, N. I. Sedrenok, and A. I. Dudyak, *Sposob Polucheniya Karbonitridov Metallov* [Production Method of Metal Carbonitrides], Authors' Certificate 722341 SSSR (Published November 21, 1979) (in Russian).
10. V. G. Trubachev, K. V. Chuistov, V. N. Gorshkov, and A. E. Perekos, *Sposob Polucheniya Metallicheskikh Poroshkov* [The Technology of Metallic Powder Production]: Patent 1639892 SU. MKI, B22 F9/02, 9/14 (Otkrytiya i Izobreteniya, **34**, No. 13: 11) (1991) (in Russian).
11. Yu. M. Koval' and V. V. Nemoshkalenko, *O Prirode Martensitnykh Prevrashchenij* [On the Nature of Martensitic Transformations] (Kyiv: 1998) (Prepr./N.A.S. of Ukraine. Inst. for Metal Physics. No. 1, 1998) (in Russian).

Journal title abbreviations should conform to generally accepted styles:
http://www.cas.org/content/references/corejournals; http://rmp.aps.org/files/rmpguapb.pdf;
http://images.webofknowledge.com/WOK46P9/help/WOS/A_abrvjt.html;
http://www.ams.org/msnhtml/serials.pdf.

Equations and Formulae: Formulas in the text should be inserted by MathType, which is fully compatible with MS Office 2003, 2007, 2010.

Tables: Number tables consecutively with Arabic numerals and give a clear descriptive caption at the top.

Figures: All figures should be numbered with consecutive Arabic numerals, have descriptive captions and be mentioned in the text. Keep figures separate at the end of the text and clearly label each figure with author's name and figure number. The labels at axis should contain the designation (or notation) of quantities and their units.

Preparation: Figures submitted (black-and-white or greyscale recommended) must be of a high enough standard for reproduction with 300–600 dpi resolution (including half-tone illustrations). Redrawing or retouching of unusable figures will be charged to the authors.

Colour Plates: Whenever the use of colour is an integral part of the research, or where the work is generated in colour, the Transactions will insert the colour illustrations into the PDF version of the article published on the Editorial Office site. (Reprints in colour will carry a surcharge. Please write to the Publisher for details.)

Submission of Electronic Text with Figures: Authors should submit papers (with figures) by e-mail (**tatar@imp.kiev.ua**) or on a CD. The file should be saved in the native formats of the Microsoft Word 2003, 2007 or 2010 with a name consisting of the name of the first author, for example, Smirnov.doc. The electronic form of figures (graphics files in TIFF, EPS or JPEG formats preferably and with name consisting the name of the first author also, for example, Smirnov_fig2a.tiff) should be planned so that they reduce to 12.7 cm column width (or less), and keep them separate from the text file. It is necessary to submit additionally all the **figures** within the format of the program, in which they were created.

Proofs: In a special emergency, contributors may receive page proofs for correction by e-mail as a PDF document. In that case, these must be returned to Kyiv office (**tatar@imp.kiev.ua**) with subject beginning by word 'nano' within 120 hours of receipt.

Page Charges: There are no page charges to individuals or institutions.

Reprints: Hard-copy reprints provided to the first-named author of each paper may be ordered by completing the appropriate form sent with proofs. Authors can de-archive a PDF version of their published article from the Editorial Office site: http://www.imp.kiev.ua/nanosys/ru/articles/index.html.

Further Information: All questions arising after the acceptance of manuscripts, especially those relating to reprints, should be directed to Executive Managing Editor, Editorial Office, G. V. Kurdyumov Institute for Metal Physics, N.A.S.U., 36 Academician Vernadsky Blvd., UA-03142 Kyiv, Ukraine.
Fax: +380 44 4242561, e-mail: **tatar@imp.kiev.ua** (with subject beginning by word 'nano').
We ask the authors to apply with their manuscript

Copyright Transfer Agreement

We, the undersigned authors of the manuscript '_____', transfer to the founders and the Editorial Board of the Collected Scientific Transactions 'Nanosistemi, Nanomateriali, Nanotehnologii' the right to publish this manuscript in English language (or in the Ukrainian translation). We confirm that publication of this manuscript will not infringe a copyright of other persons, institutions or organizations.

Author(s):_____
(Last Name, First Name, Affiliation)

Correspondence Address:_____
Phone and e-mail: _____

_____ _____
(Signature) *(Date)*

ВИДАВНИЧА ЕТИКА

ТА ЗАПОБІГАННЯ НЕСУМЛІННІЙ ПРАКТИЦІ ПУБЛІКАЦІЙ

Редакційна колеґія збірника наукових праць «Наносистеми, наноматеріали, нанотехнології» дотримується етичних норм, прийнятих міжнародним науковим співтовариством, і робить усе для запобігання будь-яким порушенням їх. У своїй діяльності редакція спирається на рекомендації Комітету з етики наукових публікацій (http://publicationethics.org).

Обов'язки редакції

- Всі представлені статті рецензуються експертами в даній області.
- Під час розгляду статті враховуються її відповідність предметній області, обґрунтованість, значимість, ориґінальність, читабельність і мова (правопис).
- За результатами рецензування стаття може бути прийнята до опублікування без доробки, прийнята з доробкою або відхилена.
- Відхилені статті повторно не рецензуються.
- Статті можуть бути відхилені без рецензії, якщо вони очевидним чином не підходять для публікації.
- Редакція ухвалює рішення щодо публікації, керуючись політикою збірника, з урахуванням діючого законодавства в області авторського права.
- Не допускається до публікації інформація, якщо є достатньо підстав уважати, що вона є плаґіятом.

За наявности яких-небудь конфліктів інтересів (фінансових, академічних, особистих) всі учасники процесу рецензування повинні сповістити про це редколеґії. Всі спірні питання розглядаються на засіданні редколеґії.

Прийняті до опублікування статті розміщаються у відкритому доступі на сайті збірника; авторські права зберігаються за авторами.

Етичні принципи в діяльності рецензентів

- Рецензенти оцінюють статті за їхнім вмістом, безвідносно до національности, статі, сексуальної орієнтації, релігійних переконань, етнічної приналежности або політичних переконань авторів.
- Співробітники редакції не повинні повідомляти яку-небудь інформацію про статті, що надійшли, особам, які не є рецензентами, авторами, співробітниками редакції та видавництва.
- Рецензування повинне бути проведено об'єктивно. Персональна критика автора неприпустима. Рецензенти зобов'язані обґрунтовувати свою точку зору чітко й об'єктивно.
- Рецензування допомагає видавцеві приймати рішення та за допомогою співробітництва з рецензентами й авторами поліпшити статтю.
- Матеріяли, отримані для рецензії, є конфіденційними документами та рецензуються анонімно.
- Рецензент також зобов'язаний звертати увагу редактора на істотну або часткову подібність представленої статті з якою-небудь іншою роботою, з якою рецензент безпосередньо знайомий.

Принципи, якими повинні керуватися автори наукових публікацій

- Автори статей повинні надавати точний звіт про виконану роботу й об'єктивне обговорення її значимости.
- Автори статті повинні надавати достовірні результати проведеного огляду й аналізи досліджень. Свідомо помилкові або сфальсифіковані твердження неприйнятні.
- Стаття повинна містити достатню кількість інформації для перевірки та повторення експериментів або розрахунків іншими дослідниками. Шахрайські або свідомо неправдиві заяви прирівнюються до неетичного поводження і є неприйнятними.
- Автори можуть надавати ориґінальні реґулярні й оглядові роботи. За використання текстової або графічної інформації, отриманої з робіт інших осіб, обов'язково необхідні посилання на відповідні публікації або письмовий дозвіл їхніх авторів.
- Подача статті більш ніж в один журнал розцінюється як неетичне поводження і є неприйнятною.
- Авторство повинне бути обмежене тими, хто зробив значний внесок у концепцію, розробку, виконання або інтерпретацію заявленого дослідження.
- Джерела фінансової підтримки дослідження, що публікується, можуть бути зазначені.

PUBLICATION ETHICS

AND MALPRACTICE STATEMENT

The Editorial Board of the Collected Scientific Transactions '*Nanosistemi, Nanomateriali, Nanotehnologii*' (i.e., 'Nanosystems, Nanomaterials, Nanotechnologies') follows ethics norms accepted by international scientific community and makes every endeavour to prevent any infringements of the norms. The Editorial Board follows the guidelines of the Committee on Publication Ethics (http://publicationethics.org).

Duties of Editors

- All submitted papers are subject to strict peer-review process by reviewers that are experts in the area of the particular paper.
- The factors, which are taken into account in reviewing process, are relevance, soundness, significance, originality, readability, and quality of language.
- The possible decisions include acceptance, acceptance with revisions, or rejection.
- If authors are encouraged to revise and resubmit a submission, there is no guarantee that the revised submission will be accepted.
- Rejected articles will not be re-reviewed.
- Articles may be rejected without review, if they are obviously not suitable for publication.
- The paper acceptance is constrained by such legal requirements as shall then be in force regarding libel, copyright infringement, and plagiarism.

When a conflict of interests arising, all the participants of reviewing process should inform the Editorial Board. All the contentions questions are considered in the Board meeting.

The accepted papers are allocated in open access on the journal site; copyrights reserved.

Duties of Reviewers

- The reviewers evaluate manuscripts for their intellectual content without regard to race, gender, sexual orientation, religious belief, ethnic origin, citizenship, or political philosophy of the authors.
- The staff must not disclose any information about a submitted manuscript to anyone other than the corresponding author, reviewers, other editorial advisers, and the Publisher, as appropriate.
- Reviews should be conducted objectively. Personal criticism of the author is inappropriate. Referees should express their views clearly with supporting arguments.
- Peer review assists the Publisher in making editorial decisions and through the editorial communications with the experts from the scientific board and the author may assist the author in improving the paper.
- Manuscripts received for review are treated as confidential documents and are reviewed by anonymous staff.
- A reviewer should also call to the Publisher's attention any substantial similarity or overlap between the manuscript under consideration and any other published paper of which they have personal knowledge.

Duties of Authors

- Authors of contributions and studies research should present an accurate account of the work performed as well as an objective discussion of its significance.
- A paper should contain sufficient details and references to permit others to replicate the work. Fraudulent or knowingly inaccurate statements constitute unethical behaviour and are unacceptable.
- The authors should ensure that they have written original regular or entirely review works, if the authors have used the work and/or words of others that this has been obligatory and appropriately cited or quoted.
- Submitting the same manuscript to more than one publication concurrently constitutes unethical publishing behaviour and is unacceptable.
- Authorship should be limited to those who have made a significant contribution to the conception, design, execution, or interpretation of the reported study.
- Sources of financial support for the reported results can be specified.

Наносистеми, наноматеріали, нанотехнології
Nanosistemi, Nanomateriali, Nanotehnologii
2025, т. 23, № 2, сс. 307–316
https://doi.org/10.15407/nnn.23.02.0307

© 2025 ІМФ (Інститут металофізики
ім. Г. В. Курдюмова НАН України)
Надруковано в Україні.

PACS numbers: 02.30.Gp, 02.30.Hq, 02.30.Uu, 05.60.Cd, 66.30.Dn, 81.05.Zx

Application of Jumarie's Fractional Derivative to Degassing a Thin Plate

M. E. Mezabia[1], A. Souigat[2], B. Tellab[3], and M. T. Meftah[4]

[1]*Department of Mathematics,*
Kasdi Merbah University,
30000 Ouargla, Algeria
[2]*Ecole Normale Supérieure,*
30000 Ouargla, Algeria
[3]*Department of Process Engineering,*
Kasdi Merbah University,
30000 Ouargla, Algeria
[4]*LRPPS Laboratory,*
Kasdi Merbah University,
30000 Ouargla, Algeria

In this work, we have dealt with a problem encountered in transport phenomena. The equations describing such phenomenon contain fractional derivatives. We use the modified Jumarie's definition of such a derivative to solve the transport equation. In particular, we have treated the space–time fractional diffusion equation (of Fick's law) regarding the process of degassing a thin plate in vacuum.

У цій роботі ми розглядаємо проблему, що виникає в явищах перенесення. Рівняння, що описують таке явище, містять дробові похідні. Ми використовуємо модифіковане визначення за Джумарі такої похідної для розв'язання рівняння перенесення. Зокрема, ми розглядаємо просторово-часове дробове дифузійне рівняння (за Фіковим законом) стосовно процесу дегазації тонкої пластини у вакуумі.

Key words: fractional Jumarie's derivative, Fick's law, Mittag-Leffler functions, Laplace transform.

Ключові слова: дробова похідна за Джумарі, Фіків закон, функції Міттаґ-Леффлера, Ляплясів перетвір.

(Received 12 February, 2024; in revised form, 14 February, 2024)

1. INTRODUCTION

In recent decades, considerable attention has been paid to the fractional derivative by the application of this concept in different areas of physics as quantum physics [1–6], quantum electronics, nanoelectronics, transport in nanostructures [7–10], and in general engineering as: continuum mechanics, viscoelastic and viscoplastic flow, electrical circuits, control theory, image processing, viscoelasticity, biology and hydrodynamics [11–15]. Historically, the fractional calculus has been developed by Riemann and Liouville. Not only does the latter defines a derivative and antiderivative (integral) for an integer order (as usual derivative of order one, two, *etc.*), but to give meaning to the derivative with non-integer order. The fractional calculus was developed recently in Refs. [16–20] and applied successfully for modelling some physical processes [21–29]. One important of such process is the diffusion phenomenon. The associated fractional diffusion equation arises quite naturally in continuous-time random walks. The fractional derivatives may be introduced by different definitions. For example, Jumarie [30] has considered the Riemann–Liouville definition and modified it agreeing with the fractional difference definition and fully consistent with the fractional-difference definition and avoiding any reference to the derivative of order greater than the considered ones.

The purpose of this paper is to study the problems of transport equation as diffusion equation (Fick's equation) in ordinary space. Section 2 starts with defining fractional Jumarie's derivative [30]. We show that this definition is agreed with the standard derivative; as it happens, the fractional derivative of a constant is well zero. Furthermore, when we perform the limit $\alpha = 1$, the standard case is recovered. In Section 3, we treated the Fick's equation, when the derivatives (in time and space) are fractional ($0 \le \alpha \le 1$ and $0 \le \beta \le 2$). The solution of this equation is presented explicitly for a particular case. We end this work with a conclusion in Sec. 4.

2. JUMARIE'S DERIVATIVE

The analytical solutions of the fractional differential equation are emerging branch of applied science also in basic science such as applied mathematics, physics, mathematical biology, and engineering. There are many types of fractional integral and differential operators with the Riemann–Liouville (R–L) definition. Other useful definition includes the Caputo definition of fractional derivative (1967). Riemann–Liouville definition of the fractional derivative of a constant is non-zero that creates a difficulty to relate between the basic calculi. To overcome this difficulty, Jumarie modified the def-

inition of fractional derivative of Riemann–Liouville type as follows [30]:

$$ {}_aD_t^{\alpha} f(t) = \begin{cases} \dfrac{1}{\Gamma(-\alpha)} \int_0^t (t-\xi)^{-\alpha-1} f(\xi) d\xi, \ \alpha < 0, \\ \dfrac{1}{\Gamma(1-\alpha)} \left(\dfrac{d}{dt} \right) \int_0^t (t-\xi)^{-\alpha} \left[f(\xi) - f(0) \right] d\xi, \quad 0 \le \alpha < 1, \\ \left[f^{(\alpha-n)}(t) \right]^n, \ 0 \le \alpha < 1, \ n \ge 1. \end{cases} \quad (1) $$

With this new formulation, we obtain the derivative of a constant as zero. For $\alpha = 1$, we can check that the second definition recovers the standard first derivative of $f(t)$; to be convinced, it easy to see this statement by performing the Laplace transform to both side of the second definition. We must stop here to make an important remark about the second definition of Jumarie ($0 \le \alpha < 1$):

$$ {}_aD_t^{\alpha} f(t) = \frac{1}{\Gamma(1-\alpha)} \left(\frac{d}{dt} \right) \int_0^t (t-\xi)^{-\alpha} \left[f(\xi) - f(0) \right] d\xi = \lambda \frac{d}{dt} g(t) ; \quad (2) $$

we can write it as follows:

$$ \int_0^t (t-\xi)^{-\alpha} \left[f(\xi) - f(0) \right] d\xi = \lambda \Gamma(1-\alpha) g(t) . \quad (3) $$

Recently in Ref. [26], it has developed analytical method for solution of linear fractional differential equations with Jumarie's type derivative in terms of Mittag-Leffler functions and found that the solution of the fractional differential equation ${}^{j}D_t^{\alpha} y = ay$ is $y = E_{\alpha}(ax^{\alpha})$. This new finding has been extended in Ref. [31] to get analytical solution of system of linear fractional differential equations. The main aim of this work is to investigate the possibility of applying these new analytical-solution methods for treatment the space–time fractional diffusion equation with Jumarie's type derivative for degassing a thin plate in vacuum.

3. APPLICATIONS

In this section, we will deal with the Fick's equation describing the diffusion of impurities in a material during the process degassing a thin plate under vacuum, which allows industry of a high-strength component to reduce the impurity (like hydrogen) content within the material by being removed in gas form [32, 33]. The impurity transport in the material during degassing can be modelled by the space–time fractional diffusion equation, which is referred to as

$$D_t^{\alpha} c(x,t) = \mu D_x^{\beta} c(x,t)\,, \tag{4}$$

where μ is the diffusion coefficient of impurity through the material; $0 < \alpha \le 1$ and $0 < \beta \le 2$.

Consider the case of degassing a thin plate of thickness L in vacuum, whose surfaces, $x = 0$, $x = L$, are maintained at zero concentration of impurity. The initial concentration of impurity is a given function $c_0(x)$ defined at all points x on the plate. Therefore, the initial and boundary conditions can be written as the following equations:

$$c(x,0) = c_0(x),\ 0 < x < L;\ c(0,t) = c(L,t) = 0\,. \tag{5}$$

As μ is time-independent, we use the separation of variables technique:

$$c(x,t) = c_1(t)c_2(x)\,, \tag{6}$$

to get the following two equations to solve:

$$^{j}D_t^{\alpha} c_1(t) = -k^2 \mu c_1(t)\,, \tag{7}$$

which is a time-dependent equation, and

$$^{j}D_x^{\beta} c_2(x) = -k^2 c_2(x)\,, \tag{8}$$

which is a space-dependent equation, and k is a positive real constant.

3.1. Time-Dependent Equation

Taking into account the Jumarie's definition (1), we can transform Eq. (7) to the following integral equation:

$$-k^2 \mu c_1(t) = \frac{1}{\Gamma(1-\alpha)} \left(\frac{d}{dt}\right) \int_0^t (t-\xi)^{-\alpha} \left[c_1(\xi) - c_1(0)\right] d\xi\,. \tag{9}$$

By taking Laplace transform in both side, assumed that $C_1(p) = L(c_1(t))$, it is easy to find

$$C_1(p) = \frac{c_1(0)\, p^{\alpha-1}}{k^2 \mu + p^{\alpha}}\,. \tag{10}$$

Then, by taking the inverse of Laplace transform, we find the solution of the time-dependent Eq. (7) as follows:

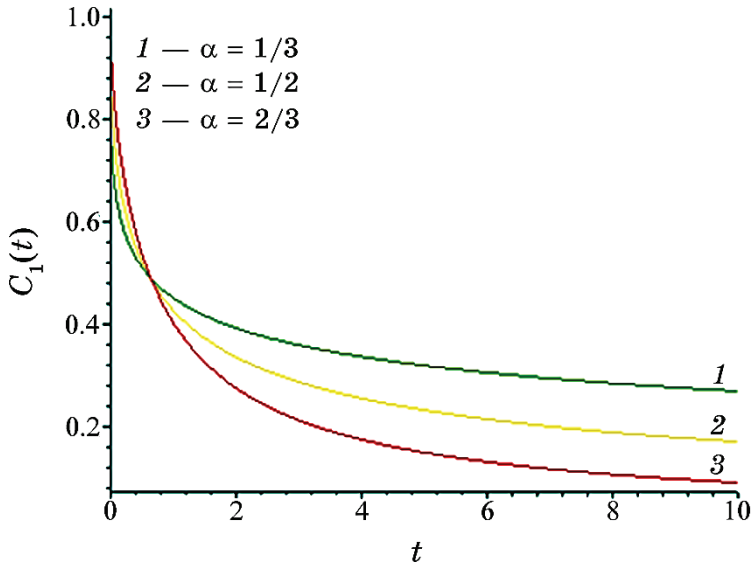

Fig. Time-dependent part of the concentration for different values of α.

$$c_1(t) = \oint_\gamma C_1(p)\exp(pt)dp = c_1(0)\oint_\gamma \frac{p^{\alpha-1}}{k^2\mu + p^\alpha}\exp(pt)dp \equiv E_\alpha(-\mu k^2 t^\alpha)\,, \tag{11}$$

which is shown in Fig. for different values of α.

For example, in case $\alpha = 1/2$, we get:

$$c_1(t) = E_{1/2}(-\mu k^2\sqrt{t}) = \exp(\mu^2 k^4 t)\mathrm{erfc}(\mu k^2\sqrt{t})\,. \tag{12}$$

It is clear that, when we put $\alpha = 1$ in Eq. (11), we retrieve the standard case.

3.2. Space-Dependent Equation

To solve Eq. (8), we put $\beta = 2\gamma$, where $0 < \gamma \le 1$; therefore, Eq. (8) can be written as

$$^{jum}D_x^{2\gamma}c_2(x) = -k^2 c_2(x)\,, \tag{13}$$

From Ref. [26], the solution of the last equation is

$$c_2(x) = A\cos_\gamma(kx^\gamma) + B\sin_\gamma(kx^\gamma)\,, \tag{14}$$

where

$$\cos_\gamma(kx^\gamma) = \sum_{n=0}^{\infty}(-1)^n\,(kx^\gamma)^{2n}/\Gamma(2n\alpha+1)\,, \tag{15}$$

$$\sin_\gamma(kx^\gamma) = \sum_{n=0}^{\infty}(-1)^n\,(kx^\gamma)^{2n+1}/\Gamma(2n\alpha+\alpha+1) \tag{16}$$

are the fractional cosine and sine. Therefore, the solution for the space–time concentration, governed by Eq. (4), can be written as

$$c(x,t) = E_\alpha(-k^2\mu t^\alpha)\left[A\cos_\gamma(kx^\gamma) + B\sin_\gamma(kx^\gamma)\right], \tag{17}$$

where A and B are constants to be determined by using the boundary conditions (5). Using the boundary conditions, we observe that

$$A = 0,\ kL^\gamma = (nM)^\gamma\,, \tag{18}$$

where M is the period [26]. Then, we get

$$c(x,t) = B_{\bullet}E_\alpha\left(-\left(\frac{(nM)^\gamma}{L^\gamma}\right)^2\mu t^\alpha\right)\sin_\gamma\left((nM)^\gamma\,\frac{x^\gamma}{L^\gamma}\right). \tag{19}$$

The general solution is a linear combination

$$c(x,t) = \sum_{n=0}^{\infty}B_nE_\alpha\left(-\mu\left(\frac{(nM)^\gamma}{L^\gamma}\right)^2 t^\alpha\right)\sin_\gamma\left((nM)^\gamma\,\frac{x^\gamma}{L^\gamma}\right). \tag{20}$$

Using the initial conditions (5), we have

$$c(x,0) = c_0(x) = \sum_{n=0}^{\infty}B_n\sin_\gamma\left((nM)^\gamma\,\frac{x^\gamma}{L^\gamma}\right). \tag{21}$$

To determine the coefficients B_n, we multiply the both sides of the last equation by $\sin_\gamma\left((mM)^\gamma\,\dfrac{x^\gamma}{L^\gamma}\right)$, where m is an integer, and integrate both sides of the resulting equation from a zero to L, and we get the following result:

$$\int_0^L c_0(x)\sin_\gamma\left((mM)^\gamma\,\frac{x^\gamma}{L^\gamma}\right)dx = \sum_{n=0}^{\infty}B_n\int_0^L\sin_\gamma\left((mM)^\gamma\,\frac{x^\gamma}{L^\gamma}\right)\sin_\gamma\left((nM)^\gamma\,\frac{x^\gamma}{L^\gamma}\right)dx \equiv$$

$$\equiv B_m\,, \tag{22}$$

or equivalently

$$B_n = \int_0^L c_0(y)\sin_\gamma\left((nM)^\gamma \frac{y^\gamma}{L^\gamma}\right)dy \tag{23}$$

that gives the global solution of the diffusion Eq. (4) as

$$c(x,t) = \\ = \sum_{n=0}^{\infty} E_\alpha\left(-\mu\left(\frac{(nM)^\gamma}{L^\gamma}\right)^2 t^\alpha\right)\sin_\gamma\left((nM)^\gamma \frac{x^\gamma}{L^\gamma}\right)\int_0^L c_0(y)\sin_\gamma\left((nM)^\gamma \frac{y^\gamma}{L^\gamma}\right)dy. \tag{24}$$

As initial function, we take the initial spatial concentration as

$$c_0(y) = c_0 y(L-y)\,. \tag{25}$$

Then, the coefficient B_n (23) becomes as follows:

$$B_n = c_0\int_0^L y(L-y)\sin_\gamma\left((nM)^\gamma \frac{y^\gamma}{L^\gamma}\right)dy\,. \tag{26}$$

By replacing the fractional sine and making the change $y = Lh$, we find

$$B_n = c_0 L^3\int_0^1 h(1-h)\sum_{k=0}^{\infty}(-1)^k \frac{\left((nM)^\gamma h^\gamma\right)^{2k+1}}{\Gamma(2k\alpha+\alpha+1)}dh \tag{27}$$

or equivalently

$$B_n = c_0 L^3\sum_{k=0}^{\infty}(-1)^k \frac{(2k+1)\gamma+1}{\Gamma\left((2k+1)\gamma+4\right)}\left((nM)^\gamma\right)^{2k+1}. \tag{28}$$

The last expression can be seen to be replaced by

$$B_n = c_0 L^3 (nM)^\gamma\left[\sum_{k=0}^{\infty}\frac{(-\lambda_n)^k}{\Gamma\left((2k+1)\gamma+3\right)} - 2\sum_{k=0}^{\infty}\frac{(-\lambda_n)^k}{\Gamma\left((2k+1)\gamma+4\right)}\right] \tag{29}$$

or equivalently

$$B_n = c_0 L^3 (nM)^\gamma\left[E_{2\gamma,\gamma+3}(-\lambda_n) - 2E_{2\gamma,\gamma+4}(-\lambda_n)\right], \tag{30}$$

such that $E_{\mu,\nu}(x)$ is the Mittag-Leffler function of the second kind, and

$$\lambda_n = (nM)^{2\gamma}\,, \tag{31}$$

leading to the following final closed result ($\gamma = \beta/2$):

$$c(x,t)=\sum_{n=0}^{\infty}E_{\alpha}\left(-\mu\left(\frac{\sqrt{\lambda_n}}{L^{\gamma}}\right)^{2}t^{\alpha}\right)B_n\sin_{\gamma}\left(\sqrt{\lambda_n}\,\frac{x^{\gamma}}{L^{\gamma}}\right), \tag{32}$$

$$c_0L^3\sum_{n=0}^{\infty}E_{\alpha}\left(-\mu\left(\frac{\sqrt{\lambda_n}}{L^{\gamma}}\right)^{2}t^{\alpha}\right)\sqrt{\lambda_n}E_{2\gamma,\gamma+3}\left(-\lambda_n\right)\sin_{\gamma}\left(\sqrt{\lambda_n}\,\frac{x^{\gamma}}{L^{\gamma}}\right)=$$

$$=-2c_0L^3\sum_{n=0}^{\infty}E_{\alpha}\left(-\mu\left(\frac{\sqrt{\lambda_n}}{L^{\gamma}}\right)^{2}t^{\alpha}\right)\sqrt{\lambda_n}E_{2\gamma,\gamma+4}\left(-\lambda_n\right)\sin_{\gamma}\left(\sqrt{\lambda_n}\,\frac{x^{\gamma}}{L^{\gamma}}\right). \tag{33}$$

4. CONCLUSION

In this work, we have treated some problems, which encountered in transport phenomena. The equations describing these phenomena have fractional derivatives. At first, we have presented the modified Jumarie's definition of such derivatives. After what, we have, as application, solved the fractional diffusion equation (Fick's law) that presents a partial fractional differential on the time t and a partial fractional differential on the spatial co-ordinate x. The order of the fractionality in the time is α $(0 \le \alpha < 1)$ and in the space is β $(0 \le \beta < 2)$. The solution of the time fractional equation is expressed in term of Mittag-Leffler function of the first kind, whereas the solution of the spatial fractional equation is expressed in term of Mittag-Leffler function of the second kind (see Eq. (33)). This treatment can be useful to describe the transport phenomena in nanomaterials and nanostructures.

ACKNOWLEDGMENTS

The first author acknowledges the support by the University of Kasdi Merbah and the High Ministry of Education and Research at Alger.

REFERENCES

1. N. Laskin, *Phys. Lett. A*, **268**, Iss. 4–6: 298 (2000); https://doi:10.1016/S0375-9601(00)00201-2
2. X. Guo and M. Xu, *J.M.P.*, **47**, Iss. 8: 082104 (2006); https://doi:10.1063/1.2235026
3. J. Dong and M. Xu, *J.M.P.*, **48**, Iss. 7: 072105 (2007); https://doi:10.1063/1.2749172.135
4. R. Herrmann, *The Fractional Schroedinger Equation and the Infinite Poten-*

tial Well-Numerical Results Using the Riesz Derivative, arXiv e-prints (2012) arXiv:1210.4410[math-Ph].
5. Z. K. F. E. Bouzenna and M. Meftah, *Rep. Math. Phys.*, **85**, Iss. 1: 57 (2020); https://doi:10.1016/S0034-4877(20)30010-0
6. J. Swift and P. C. Hohenberg, *Phys. Rev. A*, **15**, Iss. 1: 319 (1977); https://doi:10.1103/PhysRevA.15.319
7. Ahmed Hashim, Aseel Hadi, and Noor Al-Huda Al-Aaraji, *Nanosistemi, Nanomateriali, Nanotehnologii*, **21**, Iss. 3: 553 (2023); https://doi.org/10.15407/nnn.21.03.553
8. Ugo Otuonye, Hee Woo Kim, and Wei D. Lu, *Appl. Phys. Lett.*, **110**: 173104 (2017); https://doi.org/10.1063/1.4982648
9. Yana Hlek, Olga Khliyeva, Dmytro Ivchenko, Nikolay Lapardin, Viacheslav Khalak, and Vitaly Zhelezny, *Nanosistemi, Nanomateriali, Nanotehnologii*, **20**, Iss. 3: 0745 (2022); https://doi.org/10.15407/nnn.20.03.745
10. B. Kramer, T. Brandes, W. Hausler, K. Jauregul, W. Pfaff, and D. Weinmann, *Semicond. Sci. Technol.*, **9**, Iss. 115: 1871 (1994); https://doi:10.1088/0268-1242/9/11S/004
11. J. M. J. Lega and A. C. Newell, *Phys. Rev. Lett.*, **73**, Iss. 22: 2978 (1994); https://doi:10.1103/PhysRevLett.73.2978
12. D. H. J. M. I. Aranson, *Phys. Rev. A*, **55**, Iss. 4: 3173 (1997); https://doi:10.1103/PhysRevA.55.3173
13. H. Sakaguchi and H. R. Brand, *Physica D*, **117**, Iss. 1–4: 95 (1998); https://doi:10.1016/S0167-2789(97)00310-2.9
14. M. Bartuccelli, *Mathematical Methods in the Applied Sciences*, **25**, Iss. 8: 701 (2002); https://doi:10.1002/mma.309
15. X-Jun Yang, *Local Fractional Functional Analysis & Its Applications. Nonlinear Sciences Series* (Asian Academic Publisher Limited: 2011).
16. X. J. Yang, *Advanced Local Fractional Calculus and Its Applications* (New York: World Science Publisher: 2012).
17. K. S. M. B. Ross, *An Introduction to the Fractional Calculus and Fractional Differential Equations* (Wiley: 1993).
18. S. Das, *Functional Fractional Calculus* (Springer: 2011), vol. **1**.
19. I. Podlubny, *Fractional Differential Equations. Mathematics in Science and Engineering* (Elsevier: 1999), vol. **198**.
20. V. V. Anh and N. N. Leonenko, *Stochastic Processes and Their Applications*, **84**, Iss. 1: 91 (1999); https://doi:10.1016/S0304-4149(99)00053-8
21. V. V. Anh and N. N. Leonenko, *Statistics & Probability Letters*, **48**, Iss. 3: 239 (2000); https://doi:10.1016/S0167-7152(00)00003-1
22. Y. Povstenko and J. Klekot, *Journal of Applied Mathematics and Computational Mechanics*, **13**, Iss. 1: 95 (2014); https://doi:10.17512/jamcm.2014.1.10
23. U. Siedlecka and S. Kukla, *Journal of Applied Mathematics and Computational Mechanics*, **14**, Iss. 3: 95 (2015); https://doi:10.17512/jamcm.2015.3.10
24. S. Kukla and U. Siedlecka, *Journal of Applied Mathematics and Computational Mechanics*, **14**, Iss. 4: 105 (2015); https://doi:10.17512/jamcm.2015.4.10
25. M. Basu and D. P. Acharya, *Journal of Applied Mathematics and Computing*, **10**, Iss. 1: 131 (2002); https://doi:10.1007/BF02936212

26. M. Caputo, *Geophysical Journal International*, **13**, Iss. 5: 529 (1967); https://doi:10.1111/j.1365-246X.1967.tb02303.x
27. M. Caputo, *Rendiconti Lincei*, **7**, Iss. 4: 243 (1996); https://doi:10.1007/BF03002242
28. R. Goreno and F. Mainardi, *Problems and Methods in Mathematical Physics. Conference Proceeding* (Springer: 2001), p. 120–145.
29. G. Jumarie, *Computers & Mathematics with Applications*, **51**, Iss. 9–10: 1367 (2006); https://doi:10.1016/j.camwa.2006.02.001
30. S. S. U. Ghosh, S. Sengupta, and S. Das, *American Journal of Mathematical Analysis*, **3**, Iss. 2: 32 (2015); https://doi:10.12691/ajma-3-2-2
31. U. Ghosh, S. Sarkar, and S. Das, *American Journal of Mathematical Analysis*, **3**, Iss. 3: 72 (2015); https://doi:10.12691/ajma-3-3-3
32. C. J. Carneiro Filho, M. B. Mansur, P. J. Mondenesi, and B. M. Gonzalez, *Materials Science and Engineering A*, **527**, Iss. 18–19: 4947 (2010); https://doi:10.1016/j.msea.2010.04.042
33. E. I. Galindo-Nava, B. I. Y. Basha, and P. E. J. Rivera-Díaz-del-Castillo, *Journal of Materials Science & Technology*, **33**, Iss. 12: 1433 (2017); https://doi:10.1016/j.jmst.2017.09.011

Наносистеми, наноматеріали, нанотехнології
Nanosistemi, Nanomateriali, Nanotehnologii
2025, т. 23, № 2, сс. 317–332
https://doi.org/10.15407/nnn.23.02.0317

© 2025 ІМФ (Інститут металофізики
ім. Г. В. Курдюмова НАН України)
Надруковано в Україні.

PACS numbers: 47.20.Ib, 47.61.-k, 68.08.-p, 68.15.+e, 81.15.Rs, 82.70.Rr, 83.60.Wc

Дисперґування рідин розпорошувачами, що обертаються

П. Є. Трофименко[1], М. В. Найда[1], О. В. Хоменко[1], М. М. Ляпа[1], Д. О. Сушинський[2]

[1]*Сумський державний університет,*
вул. Харківська, 116,
40007 Суми, Україна
[2]*Науково-дослідницький центр ракетних військ і артилерії,*
вул. Герасима Кондратьєва, 165,
40021 Суми, Україна

Дисперґування рідин розпорошувачами, що обертаються, є однією з найефективніших технік одержання дисперсних систем з наночастинками. Основне призначення дисперґувальних пристроїв — це перетворення суцільного потоку рідини на дисперсну систему, що складається з однорідних крапель рідини. Є два способи перетворення струменів рідини в тонкі плівки: гідростатичний (на похилій пластині) і відцентровий (на плівкоутворювачі — лопаті). Дисперґування рідин — це важлива технологія, яка застосовується в різних промислових галузях, таких як нафтогазова, фармацевтична, харчова та інші. У цій статті ми розглянемо дисперґування рідин розпорошувачами, що обертаються. Цей метод уможливлює одержати дрібнодисперсні системи з пониженим розміром частинок, що відкриває широкі можливості для поліпшення якости кінцевого продукту. Потрібно знаходити нові підходи до конструювання розпорошувачів великої одиничної потужности. Для обґрунтування їх слід проводити принципові теоретичні дослідження, а з метою корекції результатів теоретичну аналізу необхідно ретельно перевіряти та кориґувати лабораторними та промисловими дослідженнями. В статті показано основні принципові схеми розпорошувачів рідини, що обертаються (сопловий відцентровий розпорошувач, лопатковий відцентровий розпорошувач, віяловий розпорошувач), і проаналізовано, не вдаючись у технічні подробиці, їхні принципові недоліки, а також можливі напрями пошуків способів зменшення енергоспоживання на дисперґування та поліпшення дисперсного складу крапель розпорошеної рідини та, зокрема, одержання складу крапель, однорідного за розмірами. Розглянуто важливі питання поведінки рідини всередині циліндричних оболонок, що обертаються, а також показано особливості руху рідини під час виходу її з розпорошувача.

Dispersing liquids with rotating atomizers is one of the most effective techniques for obtaining dispersion systems with nanoparticles. The main purpose of dispersing devices is to transform a continuous flow of liquid into a dispersed system consisting of liquid droplets. There are two methods of converting liquid jets into thin films: hydrostatic (on an inclined plate) and centrifugal (on a film-forming blade). Liquid dispersion is an important technology that is used in various industries such as oil and gas industries, pharmaceutical, food, and other ones. Dispersing liquids with rotary atomizers has its advantages and disadvantages. On the one hand, this method is very effective, as it allows obtaining a homogeneous dispersion system with nanoparticles. On the other hand, the dispersion process can be quite complex, as its success depends on many factors, such as atomizer-rotation speed, droplet size, liquid properties, *etc*. In this article, we will look at the dispersion of liquids by rotating atomizers. This method makes it possible to obtain finely dispersed systems with a reduced particle size that opens up wide opportunities for improving the quality of the product. It is necessary to find new approaches to the design of atomizers with a large unit capacity. For their substantiation, fundamental theoretical studies should be conducted, and in order to correct the results, the theoretical analysis should be carefully checked and corrected by laboratory and industrial studies. The article shows the main principle schemes for rotating liquid atomizers (nozzle centrifugal atomizer, vane centrifugal atomizer, fan atomizer), and we will analyse, without going into technical details, their fundamental shortcomings, as well as possible directions of searching for ways to reduce energy consumption for dispersion and improve dispersed composition of droplets of sprayed liquid, and, in particular, obtaining a composition of droplets that is uniform in size. Important issues of fluid behaviour inside rotating cylindrical shells are considered. In addition, the features of the movement of the liquid, when it leaves the atomizer, are shown too.

Ключові слова: рідина, крапля, дисперґування, плівкоутворювач, відцентровий розпорошувач.

Key words: liquid, droplet, dispersion, film former, centrifugal atomizer.

(Отримано 29 травня 2024 р.)

1. ВСТУП

Дисперґування рідин розпорошувачами, що обертаються, є однією з найефективніших технік одержання дисперсійних систем з наночастинками. Цей метод полягає в тому, що рідина подається на розпорошувач, який випускає її у вигляді мікроскопічних крапель. Розпорошувачі, що обертаються, характеризуються великою швидкістю обертання, що допомагає подрібнювати рідину на дрібніші крапельки [1–4].

Застосування розпорошувачів, що обертаються, для дисперґу-

вання рідин знайшло широке застосування у різних галузях науки та техніки. Наприклад, вони використовуються у фармацевтиці для одержання лікарських засобів, в харчовій промисловості для виробництва напоїв і продуктів харчування, у косметичній промисловості для одержання косметичних засобів, а також у нафтогазовій галузі для розчинення інгібіторів корозії й інших речовин.

Дисперґування рідин розпорошувачами, що обертаються, має свої переваги та недоліки. З одного боку, цей метод є дуже ефективним, оскільки уможливлює одержати гомогенну дисперсну систему з наночастинками. З іншого боку, процес дисперґування може бути достатньо складним, оскільки успішність його залежить від багатьох чинників, таких як обертова швидкість розпорошувача, розмір краплин, властивості рідини тощо. Для досягнення бажаного результату необхідно правильно підібрати розпорошувач, враховуючи потреби конкретного застосування [5–11].

Отже, дисперґування рідин розпорошувачами, що обертаються, є важливим технологічним процесом, який використовується у багатьох галузях промисловости та науки. За правильного застосування цей метод дає змогу одержати високоякісні дисперсні системи з наночастинками [12–18]. Однак перед застосуванням розпорошувачів, що обертаються, потрібно ретельно проаналізувати умови процесу та правильно підібрати розпорошувач, щоб забезпечити його ефективність й успішність. Метою даної статті є показати основні схеми розпорошувачів рідини, що обертаються, а також проаналізувати їхні принципові недоліки та можливі напрями пошуків способів зменшення енергоспоживання та поліпшення дисперсного складу крапель розпорошеної рідини.

2. ЗАГАЛЬНІ ПИТАННЯ СТОСОВНО ДЕСПЕРҐУВАННЯ РІДИН ОБЕРТОВИМИ РОЗПОРОШУВАЧАМИ

Найбільш потужні дисперґатори одиничної продуктивности за рідиною, яку розпорошують, за достатньо дрібнодисперсного складу розпорошення — розпорошувачі, що обертаються. Розглянемо основні принципові схеми розпорошувачів рідини, що обертаються, та проаналізуємо, не вдаючись у технічні подробиці, принципові недоліки їх, а також можливі напрями пошуків способів зменшення енергоспоживання на дисперґування та поліпшення дисперсного складу крапель розпорошеної рідини і, зокрема, одержання складу крапель, однорідного за розмірами.

На рисунку 1 наведено принципову схему конструкції соплового (дюзового) відцентрового розпорошувача [1, 2]. Сопловий відцентровий розпорошувач (сопловий диск) складається з обертового корпусу *1* (наприклад, циліндричної обичайки), що розташо-

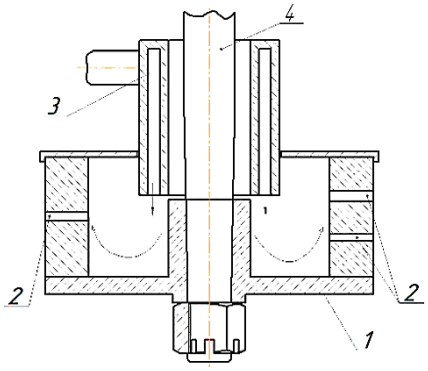

Рис. 1. Принципова схема соплового (дюзового) відцентрового розпорошувача.[1]

ваний на валу *4*, сопла (дюзи) *2*, пристрою *3* для підведення та рівномірного розподілу всередині корпусу рідини, яка під дією відцентрової сили утворює по внутрішній поверхні стінок обичайки кільце.

В разі постійної частоти обертання диска витрата рідини визначається умовами входу рідини на диск, товщиною рідкого кільцевого шару, кількістю та діяметром сопел. Для збільшення продуктивности соплового розпорошувача його виготовляють багаторядним (що складається з кількох рядів сопел). Рідина, надходячи у сопло, притискається до задньої по ходу обертання розпорошувача стінки, і тому окружні швидкості сопла та рідини є однаковими. Із виходом у газове (повітряне) середовище швидкість рідини складається з окружної складової швидкости та складової відносного руху рідини по соплу, яку для низьков'язких рідин можна обрати рівною радіяльній.

Соплові диски є простими за конструкцією, мають високу одиничну продуктивність і в багатьох випадках дають змогу одержати характеристики розпорошення, що задовольняють промисловість. Однак дрібнодисперсне розпорошення з соплового диска можна одержати тільки за значних окружних швидкостей (у 120 м/с і вище). Це відбувається з наступної причини. На виході із сопла струмінь рідини (порівняно великого діяметра) взаємодіє з навколишнім середовищем (повітрям, газом). Спочатку він розривається на окремі великі фраґменти, а після повторних роздрібнювань перетворюється на дедалі дрібніші краплі.

Сила взаємодії струменя, що виходить із сопел у газову фазу, прямо пропорційна швидкості зміни імпульсу струменя та лобового перерізу струменя. Ця величина у свою чергу пропорційна діяметру сопла (10 мм). Тому для дрібнодисперсного дроблення струменя такого перерізу струмінь розганяють до швидкостей у

120–150 м/с і вище. З цієї причини недоліком соплових розпорошувачів є велике питоме споживання енергії у 4–6 кВт·год на тонну рідини, що розпорошується [3].

Є й другий важливий недолік розпорошувачів соплового типу. Діяметри крапель за розпорошування розпорошувачами, що обертаються, пропорційні характерному розміру, зокрема, товщині струменя рідини. Із виходом струменя рідини із сопла його переріз у площині, перпендикулярній до радіяльного напряму, має вигляд сеґмента. Тому після виходу струменя в газове середовище спочатку руйнуються його найтонші ділянки, а потім — дедалі товстіші. Через такі особливості дисперсний склад крапель, що утворюються сопловими розпорошувачами, знаходиться в достатньо широкому інтервалі розмірів, що для більшости промислових технологій є неґативним чинником.

За аналізи роботи соплових дисків можна виокремити дві особливості (проблеми). Для дрібного дисперґування сопловими розпорошувачами необхідно застосовувати великі швидкості обертання через велику товщину струменя рідини, що виходить із сопла, і, отже, споживати водночас значну кількість енергії, а з іншого боку розпорошення рідини є принципово полідисперсним. Основне завдання — пониження потужности, що витрачається на дисперґування великої кількости рідини за оптимальних розмірів крапель, — може бути вирішене лише з вирішенням питання про істотне зменшення товщини струменів, що виходять у газове середовище в момент розпорошування їх. Цією проблемою займалося багато дослідників і теоретиків. Для розрахунку середнього діяметра крапель відцентрових розпорошувачів запропоновано багато залежностей. Однією з таких формул, яка заслуговує на увагу — формула Маршалла [4]. Її було істотно модернізовано Пітерським [2, 5], і застосовується вона за продуктивности відцентрового розпорошувача за рідиною у понад 30 т/год.:

$$d_{32} = 0{,}1\, q^{3/2} \left(\omega^2 r\right)^{1/3}, \qquad (1)$$

де $q = Q/l$ — лінійна густина об'ємної витрати рідини, м^3/(с·м); l — довжина змоченого периметра кромок розпорошувача (сумарна ширина плівок, що розпорошуються), м; ω — кутова швидкість обертання диска, с$^{-1}$; r — радіюс обертання розпорошувальних кромок розпорошувача, м. Аналізуючи (1), можна переконатися, що для постійного діяметра крапель d_{32} для різних розпорошувачів добуток ωl має бути постійним (за однакової витрати Q).

Показано [6], що формула (1) застосовна й у дещо ширшому діяпазоні продуктивностей соплових дисків. Звідси напрошується висновок: істотного пониження споживаної потужности можна досягти шляхом пониження обертів диска, що розпорошує, за

відповідного збільшення довжини змоченого периметра. Для вирішення цієї проблеми необхідно струмінь рідини будь-якої первинної форми перетворити на плівку за можливости більшої ширини. З вирішенням проблеми низькоенергетичного одержання однорідної рідкої плівки на розпорошувачах, що обертаються, автоматично вирішиться друга проблема відцентрових розпорошувачів — одержання якісного розпорошення, тобто одержання більш монодисперсних крапель. Обговоримо з цієї точки зору більш придатні конструкції розпорошувачів, що обертаються, для вирішення поставленої проблеми — лопатеві (щілинні) розпорошувачі [3].

Принципову схему конструкції лопатевого відцентрового розпорошувача показано на рис. 2. Лопатевий розпорошувач включає в себе циліндричний корпус *1* — власне диск, який кріпиться на валу *4*. На периферії диска розташовані пласкі лопаті *2*. На певній віддалі від осі обертання розташовуються канали або інші елементи ввідного пристрою *3*. Через ввідний пристрій *3* рідина надходить всередину корпусу *1* і більш-менш рівномірно розподіляється перед надходженням на лопаті *2*.

На початку руху рідини, яка надходить у диск, що обертається, діє, крім ґравітаційної сили, сила в'язкого тертя, за допомогою якої вона розкручується, розганяється та переміщається в напрямку лопаті. На лопаті рідина перебуває під дією відцентрової та Коріолісової сил. Поздовжня складова відцентрової сили розганяє струмінь рідини вздовж лопаті. Поздовжня складова швидкости елементів рідини (типу води) вздовж лопаті наближається до окружної швидкости відповідних точок лопаті.

Коріолісова сила та нормальна складова відцентрової сили спричиняють появу осьової складової швидкости елементів рідкої

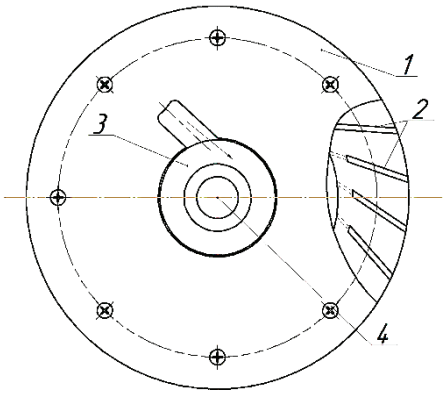

Рис. 2. Принципова схема конструкції лопатевого відцентрового розпорошувача.[2]

плівки, що приводить до розтікання плівки в осьовому напрямку. Сумарна дія цих сил перетворює струмінь рідини на лопаті, що обертається, в тонку плівку. Для зменшення гідравлічного удару та додаткового поліпшення розподілу рідини в місцях входу рідини на лопаті встановлюють напрямні елементи.

З метою збільшення одиничної продуктивности лопатевого диска без зміни якости розпорошення та діяметра диска запропоновано конструкції багатоярусних дисків. Всі ці й інші «хитрощі», на жаль, не дають помітного ефекту. І все це — через велику турбулентність потоку рідини в момент її входу на лопать, особливо в багатоярусних дисках. Тому, здавалося б, що, згідно з (1), досягнуто велику довжину змоченого периметра, що теоретично уможливлює одержати дрібнодисперсне розпорошення, але побічні ефекти зводять результат нанівець.

3. ОСОБЛИВОСТІ РУХУ РІДИНИ ІЗ ВИХОДОМ ЇЇ З РОЗПОРОШУВАЧА

Розглянемо деякі важливі питання поведінки рідини всередині циліндричних оболонок, що обертаються, якщо їхні осі симетрії збігаються з нерухомою у просторі вертикальною віссю обертання. Нехай нерухома рідина знаходиться у нерухомій вертикально встановленій оболонці або обичайці та надходить у бічний отвір (сопло, круглий або іншої форми отвір). Об'ємна витрата Q рідини через отвір визначається за відомим з гідродинаміки рівнянням [7, 8]:

$$Q = \varepsilon \phi S \sqrt{\frac{2P}{\rho}}, \tag{2}$$

де S — переріз отвору в площині, перпендикулярній напрямку швидкости витоку; P — тиск перед отвором витоку; ε і φ — коефіцієнти витрати.

Коефіцієнти витрати визначаються формою, розмірами отвору входу рідини, напором і фізичними властивостями самої рідини (в'язкістю, поверхневим натягом), а також, що важливо, гідродинамічною обстановкою в момент надходження рідини в боковий отвір у циліндричній обичайці. Коефіцієнт φ — це так званий коефіцієнт швидкости, який враховує розподіл швидкостей по перерізу струменя, ε — коефіцієнт стиснення, що визначається відношенням нормального перерізу струменя S_0, що витікає з отвору, до нормального перерізу S отвору витікання:

$$\varepsilon = \frac{S_0}{S}. \tag{3}$$

Для нерухомих обичайок коефіцієнти витрати визначаються напором рідини, положенням плівкоутворювача та турбулентністю потоку (Рейнольдсовим числом *Re*). За обертання оболонки відносно рідини, що знаходиться всередині цієї оболонки, картина витікання через бічний отвір у самій оболонці істотно змінюється. Вперше таке завдання розглядалося у застосуванні центрифуг Б. Г. Холіним і О. І. Іноземцевим. Для аналітичного визначення коефіцієнтів витрати у разі обертової обичайки розпорошувача використовується рівняння Нав'є–Стокса в циліндричній системі координат, жорстко пов'язаній з обичайкою, що обертається, і рівняння нерозривности струменя [9]:

$$u_r \frac{\partial u_r}{\partial r} - \frac{u_\tau^2}{r} = -\frac{1}{\rho}\frac{\partial P}{\partial r} + \nu\left(\frac{\partial^2 u_r}{\partial r^2} + \frac{\partial u_r}{r\,\partial r} - \frac{u_r}{r^2}\right),$$

$$u_r \frac{\partial u_\tau}{\partial r} - \frac{u_r u_\tau}{r} = \nu\left(\frac{\partial^2 u_\tau}{\partial r^2} + \frac{\partial u_\tau}{r\,\partial r} - \frac{u_\tau}{r^2}\right),$$

$$g + \frac{1}{\rho}\frac{\partial P}{\partial z} = 0, \quad \frac{\partial u_r}{\partial r} - \frac{u_r}{r} = 0. \qquad (4)$$

Тут u_r — радіяльна складова швидкости рідини, а u_τ — танґенційна (окружна) складова швидкости рідини; ρ, ν — густина та кінематична в'язкість рідини. Координату z спрямовано вздовж осі обертання.

Для складової коефіцієнта витрати φ розв'язання даної системи нічого нового не дає. Та це й зрозуміло з суто фізичних міркувань, тому що φ визначається лише станом руху рідини, тобто числом *Re* і, отже, за $Re = \text{const}$ однакове для всіх рідин. Інша ситуація — з коефіцієнтом стиснення струменя ε (3). У даному випадку він визначається в обичайці, що обертається з деякою не рівною нулю відносною швидкістю, за відношенням до кутової швидкости обертання суцільної рідини.

Нехай циліндрична обичайка та рідина мають загальну вісь обертання, що збігається з віссю координат *Oz*. Якщо окружна швидкість обертання оболонки й окружна швидкість рідини у місцях закінчення останньої дорівнюють одна одній, їхня відносна швидкість дорівнює нулю. За такої ситуації рідина надходить в отвори з таким самим значенням ε, як і у випадку абсолютно нерухомих рідини й обичайки.

Нехай у обичайку з гладкими внутрішніми стінками радіюса R_1, що обертається з кутовою швидкістю Ω_1, надходить на радіюсі R_0 рідина, що не обертається. Рідина через сили в'язкости починає закручуватися, обертатися. Максимальна кутова швидкість обертання рідини ω залежить [9] від відносної віддалі від осі обе-

ртання та Re, обчисленого за відносною швидкістю між швидкістю обичайки та швидкістю шарів рідини, що знаходяться в безпосередній близькості від поверхні обичайки. За радіюса надходження рідини $R_0 \to 0$ кутова швидкість ω рідини на віддалі r від осі обертання, як показано в зазначеній роботі, дорівнює

$$\omega = \Omega_1 \left(\frac{r}{R_1} \right)^{Re},$$

а відповідна окружна швидкість цих елементів рідини дорівнює

$$u_\tau = \omega r = \Omega_1 r \left(\frac{r}{R_1} \right)^{Re}, \qquad (5)$$

де r — поточна циліндрична координата елементу рідини; R_1 — радіюс внутрішньої поверхні циліндра обичайки; комплекс $Re = QR_1/\nu$ — Рейнольдсове число в радіяльному напрямку руху рідини в момент входу її в отвір обичайки.

Як показано в [9], за всіх $R_0 > 0$ кутова швидкість ω і, відповідно, u_τ менша, ніж за (5), тобто обертання рідини в реальних умовах відстає від швидкости обертання циліндричної обичайки, для якої окружна швидкість u внутрішньої поверхні обичайки завжди дорівнює $u = \Omega_1 R_1$. З цього випливає, що, якщо рідина всередині обертової гладкої обичайки має кутову швидкість обертання іншу, ніж кутова швидкість внутрішніх стінок обичайки, в цих умовах коефіцієнт стиснення струменя, що витікає з бокового отвору та, відповідно, об'ємна витрата Q дорівнюють

$$\varepsilon = \frac{S_0}{S} = \frac{P\left(\alpha_2 + \xi\right)}{\rho\left(\left(\Omega_1 R_1\right)^2 \alpha_1 + 2P/\rho\right)} \text{ і } Q = \frac{SP}{\rho}\sqrt{\frac{\alpha_2 + \xi}{\left(\Omega_1 R_1\right)^2 \alpha_1 + 2P/\rho}}, \qquad (6)$$

де S — переріз бічного отвору для витікання рідини, P — повний тиск рідини перед отвором витікання, α_1 і α_2 — коефіцієнти кінетичної енергії за Коріолісом для рідин типу води (≈ 1), ξ — коефіцієнт місцевого опору в точках витікання для рідин типу води (≈ 0). Якщо рідина є нерухомою щодо лабораторної системи відліку, то об'ємна витрата рідини через бічний отвір у обичайці, що обертається, згідно з (6), дорівнює

$$Q = \frac{SP}{\rho\Omega_1 R_1}, \qquad (7)$$

оскільки повний тиск P є незначним у порівнянні з $(\Omega_1 R_1)^2$, і ним під коренем у знаменнику виразу (6) можна нехтувати.

Відносна швидкість u_τ (швидкість обичайки щодо рідини) за

виконання цієї умови згідно з (5) наближається до лінійної тангенційної (окружної) швидкости внутрішньої поверхні обичайки, що обертається: $u_\tau \to u = \Omega_1 R_1$. Відповідно до (6), коефіцієнт витрати ε рідини зі збільшенням відносної швидкости між шарами рідини та внутрішньою поверхнею обичайки зменшується. Звідси випливає, що, чим швидше обертається обичайка ($\Omega_1 \to \infty$) з рідиною, що не обертається всередині, тим, відповідно до (6) і (7), меншою є витрата її через бічний отвір в обичайці. Оскільки реальна рідина все-таки обертається, то відносна швидкість між шарами рідини та поверхнею обичайки, що обертається, зменшується, а коефіцієнт стиснення ε рідини стає іншим. Тому можна стверджувати, що величина загального коефіцієнта витрати за витікання рідини з бокового отвору в обичайці, що обертається, є іншою в порівнянні з величиною коефіцієнта витрати за витікання нерухомої рідини з нерухомої обичайки.

У роботі [9] показано, що зі зменшенням відносної швидкости обичайки та рідини коефіцієнт ε проходить через мінімум, а це означає, що площа перерізу струменя, що виходить з отвору обичайки, може бути значно меншою, ніж площа перерізу отвору. Відповідно, об'ємна витрата рідини Q за перерахованих умов через сопло або іншу насадку в бічному отворі обичайки може мати значно меншу величину, ніж у разі відносних швидкостей, що наближаються до нуля. І що особливо дивно: відносне зменшення витрати спостерігається більшою мірою за великих діяметрів отворів витікання, ніж за малих. Такий теоретичний висновок зареєстрований прямими спостереженнями (рис. 3).

На рисунку 3 зареєстровано стиск струменя рідини типу води, що виходить з циліндричної обичайки, яка обертається, через лопатеві канали на плаский плівкоутворювач (диск діяметром у

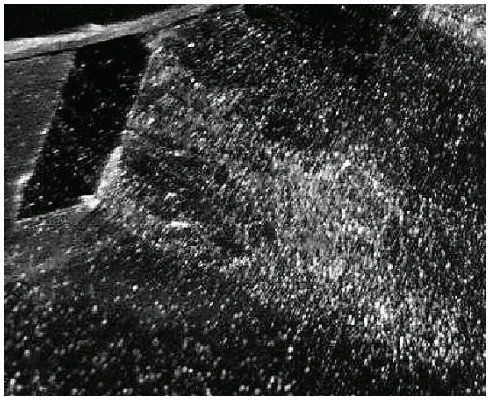

Рис. 3. Стиснення струменя, що витікає з каналів лопатевого розпорошувача.[3]

270 мм, обороти диска — 2800 об/хв). На фото видно, що рідина, яка витікає з каналу в обичайці, лише частково заповнює його. Це свідчить про те, що коефіцієнт стиснення ε в цьому випадку є меншим за одиницю.

Наведені фотографії є експериментальним підтвердженням стиснення струменя під час роботи будь-якого відцентрового розпорошувача. Реальний стиск струменів рідини потрібно враховувати та використовувати. Він знайшов інженерне застосування для конструювання розпорошувачів.

На рисунку 4 показано розподіл середньої товщини плівки по висоті каналу за різних частот обертання диску та постійної витрати рідини. Експеримент проводили з диском, що має діяметер d 270 мм, кількість каналів — 16, висоту каналів — $H = 25$ мм, ширину каналів — $b = 25$ мм. Характеристика рідини, що розпорошується: технічна вода кімнатної температури, витрата рідини — $Q = 0{,}4$ м^3/год.

Аналізуючи одержані результати, робимо висновки, що зі збільшенням частоти обертання товщина плівки на виході з каналів диску стає меншою. Також з рисунків помітно, що рідина заповнює канал по висоті нерівномірно, а пік товщини плівки зміщується зі зміною частоти обертання. Така нерівномірність істотно впливає на дисперсність розпорошення. Для досягнення більш якісного розпорошення рідини потрібно прагнути одержати результат, за якого товщина плівки буде однаковою по всій висоті каналу.

Якщо витрату рідини змінити, то характер середньої товщини плівки також зміниться. На рисунку 5 показано розподіл середньої товщини плівки по висоті каналу за частоти обертання диску у 3000 об/хв і витрати рідини $Q = 1$ м^3/год. Зі збільшенням витрати рідини товщина плівки стає більш рівномірною по висоті каналу, але все ще недосконалою, хоча і поліпшує дисперсність розпорошення.

Під час проєктування конструкції розпорошувача треба зважати на багато чинників, щоб досягти оптимального результату дисперсности розпорошення. На це впливає не тільки конструкція самого розпорошувального диску, а й частота обертання, умови роботи, характеристика рідини, що розпорошується, та інше.

На рисунку 6 показано схему однієї з найпростіших конструкцій віялового розпорошувача, що добре працює в промисловості. Віяловий розпорошувач складається з обичайки, що обертається, — корпусу *1*, з'єднаного з валом *2*. В обичайці *1* передбачено отвори *3* для витоку рідини, поруч з якими прикріплено пласкі пластини-плівкоутворювачі *4*, розташовані віялом (звідси й назва типу розпорошувачів — віяло). Рідина через заливну трубу *5* або інший пристрій подається в обичайку *1*, в якій вона закручуєть-

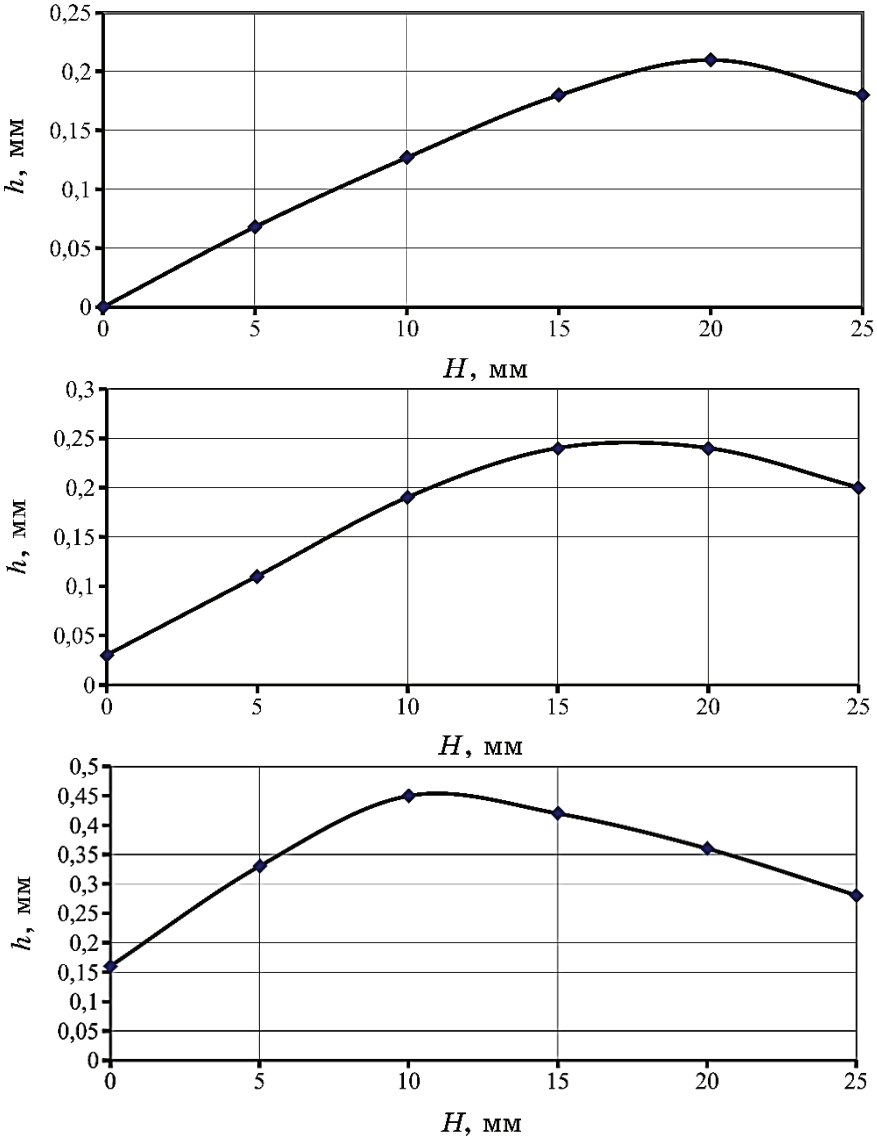

Рис. 4. Розподіл середньої товщини плівки по висоті каналу за $Q = 0{,}4$ м^3/год і $n = 2000$ об/хв, $n = 3000$ об/хв, $n = 3600$ об/хв (відповідні рисунки розташовано згори униз).[4]

ся під дією сил в'язкого тертя та піднімається до отворів *3* в обичайці *1* і через них виходить на віялові пластинки.

Віяловий розпорошувач працює так. Кожен струмінь рідини, що витікає з отвору *3*, розтікається по віялових пластинах, перетворюючись на одиночну плівку рідини. Отвори *3* по висоті роз-

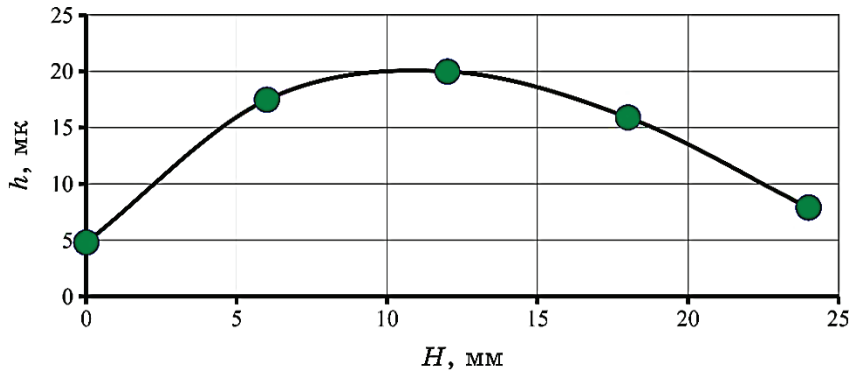

Рис. 5. Розподіл середньої товщини плівки по висоті каналу ($Q = 1$ м^3/год і $n = 3000$ об/хв).[5]

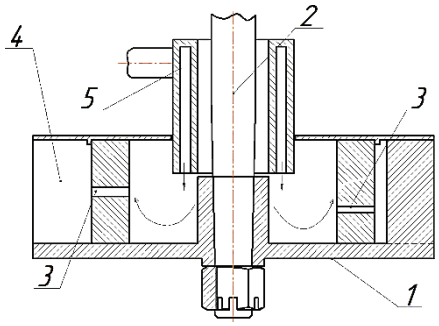

Рис. 6. Принципова схема віялового розпорошувача.[6]

ташовують так, щоб окремі плівки рідини на віяловій пластині-плівкоутворювачі встигли злитися (об'єднатися) у суцільну тонку неперервну плівку великої сумарної довжини. Плівка рідини, зриваючись із віялових пластин і потрапляючи в газове середовище, інтенсивно розпорошується. Саме утворення тонкої плівки великої ширини забезпечує високий енергетичний коефіцієнт корисної дії дисперґування рідин віяловими розпорошувачами.

Віялові розпорошувачі успішно працюють, наприклад, у пиловловлювальних установках у хемічній і харчовій промисловостях, чорній металурґії, в абсорбційних скруберах для проведення хемічних реакцій і в установках для інших цілей. Перевагою віялових розпорошувачів є те, що їхні отвори витікання є порівняно великими, наприклад, у 10 мм і більше, та дають можливість використовувати для розпорошення забруднені рідини. Крім того, за допомогою віялових розпорошувачів є можливість одержати розпорошення, близьке до монодисперсного (за рахунок перетворення струменів рідини на плівки великої ширини та майже

постійної товщини).

4. ВИСНОВКИ

Дисперґування рідин розпорошувачами, що обертаються, є одним з найефективніших методів одержання гомогенної дисперсної системи. У цій статті розглянуто принцип роботи таких розпорошувачів і застосування їх для дисперґування рідин у різних галузях науки та техніки. Ми також проаналізували переваги та недоліки цього методу, а також його можливості для вирішення практичних завдань. Дізналися, які параметри розпорошувачів впливають на якість дисперґування, і як правильно підібрати розпорошувач для досягнення потрібного результату.

Показано, що потрібні нові підходи до конструювання розпорошувачів великої одиничної потужности. Для обґрунтування їх слід проводити принципові теоретичні дослідження, а з метою корекції результатів теоретичну аналізу необхідно ретельно перевіряти та кориґувати лабораторними та промисловими дослідженнями. Серед них першочерговими та важливими для розпорошувачів, що обертаються, є:

— по-перше, з'ясування та вивчення умов входу рідини на лопать і вплив цих процесів на продуктивність та інші характеристики розпорошувачів;

— по-друге, всебічні теоретичні й експериментальні дослідження формування рідини на лопаті, що обертається, тобто перетворення неорганізованого потоку рідини в упорядкований однорідний плівковий рух з найменшими витратами енергії, та, в першу чергу, вивчення впливу форми та швидкостей руху лопаті на параметри перетворення рідини у добре організований тонкоплівковий рух з прогнозованими параметрами;

— по-третє, експериментальне вивчення інших можливих способів дисперґування рідин, виходячи з молекулярно-кінетичних особливостей їхньої будови.

Автори висловлюють подяку МОН України за фінансову підтримку проєкту «Механізми формування та моделювання структурного стану плівок тугоплавких сполук с прогнозованими механічними характеристиками» (№ 0122U000776) та пріоритетних напрямів наукових досліджень і науково-технічних (експериментальних) розробок (додаткова угода № БФ/25-2021).

ЦИТОВАНА ЛІТЕРАТУРА

1. В. А. Бородин, Ю. Ф. Дитяткин, Л. А. Клячко, В. И. Ягодкин, *Распыливание жидкостей* (Москва: Машиностроение: 1967).
2. Д. Г. Пажи, В. С. Галустов, *Основы техники распыливания жидкостей*

(Москва: Химия: 1984).
3. Д. Г. Пажи, А. А. Корягин, Э. Л. Ламм, *Распыливающие устройства в химической промышленности* (Москва: Химия: 1975).
4. W. R. Marshal and C. R. Adler, *Chem. Eng. Prog.*, **47**, No. 10: 52 (1951).
5. Г. П. Питерских, *TOXT*, **2**: 745 (1981).
6. P. Trofimenko and M. Naida, *Int. Appl. Mech.*, **53**, No. 1: 116 (2017); https://doi.org/10.1007/s1077
7. Б. Т. Емцев, *Техническая гидромеханика* (Москва: Машиностроение: 1978).
8. А. Г. Касаткин, *Основные процессы и аппараты химической технологии* (Москва: Химия: 1972).
9. Б. Г. Холин, *Центробежные и вибрационные грануляторы плавов и распылители жидкости* (Москва: Машиностроение: 1977).
10. P. E. Trofimenko, M. V. Naida, and A. V. Khomenko, *Nanosistemi, Nanomateriali, Nanotehnologii*, **18**, Iss. 3: 565 (2020) (in Ukrainian); https://doi.org/10.15407/nnn.18.03.565
11. P. E. Trofimenko, M. V. Naida, A. V. Khomenko, and Yu. I. Pushkarov, *Nanosistemi, Nanomateriali, Nanotehnologii*, **20**, Iss. 3: 657 (2022); https://doi.org/10.15407/nnn.20.03.657
12. A. D. Pogrebnjak, M. A. Lisovenko, A. Turlybekuly, and V. V. Buranich, *Phys.-Usp.*, **64**, No. 3: 253 (2020); https://doi.org/10.3367/UFNe.2020.08.038823
13. O. V. Khomenko, A. A. Biesiedina, K. P. Khomenko, and R. R. Chernushchenko, *Prog. Phys. Met.*, **23**, No. 2: 239 (2022); https://doi.org/10.15407/ufm.23.02.239
14. O. A. Goncharov, D. A. Belous, A. N. Yunda, A. V. Khomenko, E. V. Mironenko, L. V. Vasilyeva, and C. A. Goncharova, *Nanosistemi, Nanomateriali, Nanotehnologii*, **20**, Iss. 2: 385 (2022);https://doi.org/10.15407/nnn.20.02.385
15. O. Mazur, K. Tozaki, and L. Stefanovich, *Solid State Commun.*, **361**: 115072 (2023); https://doi.org/10.1016/j.ssc.2023.115072
16. A. Khomenko, D. Boyko, and K. Khomenko, *Mol. Cryst. Liq. Cryst.*, **719**, Iss. 1: (2021); https://doi.org/10.1080/15421406.2020.1860531
17. A. V. Khomenko, I. A. Lyashenko, and L. S. Metlov, *Metallofiz. Noveishie Tekhnol.*, **30**: 859 (2008).
18. A. Khomenko, D. Troshchenko, and L. Metlov, *Phys. Rev. E*, **100**: 022110 (2019); https://doi.org/10.1103/PhysRevE.100.022110

REFERENCES

1. V. A. Borodin, Yu. F. Dytiatkyn, L. A. Klyachko, and V. I. Yagodkyn, *Raspylivanie Zhydkostei* [Dispersing of Liquids] (Moskva: Mashinostroyenie, 1967) (in Russian).
2. D. H. Pazhy, V. S. Halustov, *Osnovy Tekhnyky Raspylivaniya Zhydkostei* [Basics of Techniques for Dispersing of Liquids] (Moskva: Khimiya: 1984) (in Russian).
3. D. H. Pazhy, A. A. Koriahyn, and E. L. Lamm, *Raspylivayushchie Ustroistva v Khimicheskoi Promyshlennosti* [Dispersing Devices in Chemical Industry] (Moskva: Khimiya: 1975) (in Russian).
4. W. R. Marshal and C. R. Adler, *Chem. Eng. Prog.*, **47**, No. 10: 52 (1951).

5. H. P. Pyterskykh, *TOKhT*, **2**: 745 (1981) (in Russian).
6. P. Trofimenko and M. Naida, *Int. Appl. Mech.*, **53**, No. 1: 116 (2017); https://doi.org/10.1007/s1077
7. B. T. Emtsev, *Tekhnicheskaya Hidromekhanika* [Technical Hydrodynamics] (Moskva: Mashinostroyenie: 1978) (in Russian).
8. A. G. Kasatkin, *Osnovnyye Protsessy i Apparaty Khimicheskoy Tekhnologii* [Basic Processes and Apparatuses of Chemical Engineering] (Moskva: Khimiya: 1975) (in Russian).
9. B. G. Kholin, *Tsentrobezhnyye i Vibratsionnyye Granulyatory Plavov i Raspyliteli Zhidkosti* [Centrifugal and Vibration Granulators of Melts and Liquid Sprayers] (Moskva: Mashinostroyenie: 1977) (in Russian).
10. P. E. Trofimenko, M. V. Naida, and A. V. Khomenko, *Nanosistemi, Nanomateriali, Nanotehnologii*, **18**, Iss. 3: 565 (2020) (in Ukrainian); https://doi.org/10.15407/nnn.18.03.565
11. P. E. Trofimenko, M. V. Naida, A. V. Khomenko, and Yu. I. Pushkarov, *Nanosistemi, Nanomateriali, Nanotehnologii*, **20**, Iss. 3: 657 (2022); https://doi.org/10.15407/nnn.20.03.657
12. A. D. Pogrebnjak, M. A. Lisovenko, A. Turlybekuly, and V. V. Buranich, *Phys.-Usp.*, **64**, No. 3: 253 (2020); https://doi.org/10.3367/UFNe.2020.08.038823
13. O. V. Khomenko, A. A. Biesiedina, K. P. Khomenko, and R. R. Chernushchenko, *Prog. Phys. Met.*, **23**, No. 2: 239 (2022); https://doi.org/10.15407/ufm.23.02.239
14. O. A. Goncharov, D. A. Belous, A. N. Yunda, A. V. Khomenko, E. V. Mironenko, L. V. Vasilyeva, and C. A. Goncharova, *Nanosistemi, Nanomateriali, Nanotehnologii*, **20**, Iss. 2: 385 (2022); https://doi.org/10.15407/nnn.20.02.385
15. O. Mazur, K. Tozaki, and L. Stefanovich, *Solid State Commun.*, **361**: 115072 (2023); https://doi.org/10.1016/j.ssc.2023.115072
16. A. Khomenko, D. Boyko, and K. Khomenko, *Mol. Cryst. Liq. Cryst.*, **719**, Iss. 1: (2021); https://doi.org/10.1080/15421406.2020.1860531
17. A. V. Khomenko, I. A. Lyashenko, and L. S. Metlov, *Metallofiz. Noveishie Tekhnol.*, **30**: 859 (2008).
18. A. Khomenko, D. Troshchenko, and L. Metlov, *Phys. Rev. E*, **100**: 022110 (2019); https://doi.org/10.1103/PhysRevE.100.022110

[1]*Sumy State University,*
116, Kharkivska Str.,
UA-40007 Sumy, Ukraine
[2]*Research Centre of Missile Troops and Artillery,*
165, Herasym Kondratiev Str.,
UA-40021 Sumy, Ukraine

[1] **Fig. 1.** Schematic diagram of a nozzle (nozzle) centrifugal sprayer.
[2] **Fig. 2.** Schematic diagram of the design of a bladed centrifugal sprayer.
[3] **Fig. 3.** Compression of the jet flowing from the channels of the blade sprayer.
[4] **Fig. 4.** Distribution of the average thickness of the film along the height of the channel at $Q = 0.4$ m^3/h and $n = 2000$ rpm, $n = 3000$ rpm, $n = 3600$ rpm (corresponding figures are located from top to bottom).
[5] **Fig. 5.** Distribution of the average thickness of the film along the height of the channel ($Q = 1$ m^3/h and $n = 3000$ rpm).
[6] **Fig. 6.** Schematic diagram of a fan sprayer.

Наносистеми, наноматеріали, нанотехнології
Nanosistemi, Nanomateriali, Nanotehnologii
2025, т. 23, № 2, сс. 333–348
https://doi.org/10.15407/nnn.23.02.0333

© 2025 ІМФ (Інститут металофізики
ім. Г. В. Курдюмова НАН України)
Надруковано в Україні.

PACSnumbers: 03.67.Dd, 68.65.Hb, 68.65.La, 73.21.Hb, 73.21.La, 73.63.Kv, 73.63.Nm, 85.35.Be

QCA Nanoarchitecture for Morphological Processes on Binary Images

Nasima Akter[1], Md. Abdullah-Al-Shafi[2], and Md. Nasim Akhtar[1]

[1]*Dhaka University of Engineering & Technology, Gazipur, Bangladesh*
[2]*University of Development Alternative (UODA), Dhanmondi, Dhaka, Bangladesh*

A prospective nanoarchitecture, quantum-dot cellular automata (QCA), provides a novel technique for plotting digital architectures at a minimal scale with substantial advances. It is a promising nanoarchetype with outstanding achievement to challenge the deficiencies of complementary metal–oxide–semiconductor (CMOS) based architecture just as switching speed, design, and fabrication sizes. QCA relies on the manipulation of quantum dots (nanoscale semiconductor particles) to perform computation and store information. Complex image processing approaches take in a number of cases that identified binary median filter and mathematical morphological (MM) procedures, for instance, erosion and dilation. When it comes to MM on binary images, QCA can be used to implement digital image-processing operations. Morphological operations are fundamental in image processing and computer vision for tasks such as noise reduction, object detection, and image enhancement. QCA can provide a platform for designing and implementing efficient morphological operators for binary images. Erosion and dilation are substantial approaches in frequent real-life image appliance. In this research, optimized nanostructures in QCA are outlined for MM applications that function dilation and erosion. The proposed nanoarchitecture is compared with the best counterpart that reveals a substantial advancement with regard to cell operation, extent, and delay. The proposed configurable design achieved 42.20%, 41.18%, 50.00% and 60.84% improvement, and the non-configurable design achieved 12.42%, 31.24%, 34.36% and 12.45% improvement in terms of employed cell, enclosed extent, clock and cell extent, correspondingly. Further, the energy consumption through the structures is assessed at distinct temperatures' level of 2 K.

Перспективна наноархітектура, — квантово-точкові клітинні автомати (КТА), — пропонує новий метод побудови цифрових архітектур у мінімальному масштабі зі значними досягненнями. Це — перспективний

наноархітип з видатними досягненнями у подоланні недоліків комплементарної архітектури на основі метал-оксид-напівпровідників (КМОП), а також у швидкості перемикання, дизайні та розмірах виготовлення. КТА спирається на маніпулювання квантовими точками (нанорозмірними напівпровідниковими частинками) для виконання обчислень і зберігання інформації. Складні підходи до обробки зображень враховують низку випадків, які ідентифікують бінарний медіянний фільтр і математичні морфологічні (ММ) процедури, наприклад, ерозію та дилятацію. Коли справа доходить до ММ на бінарних зображеннях, КТА може бути використана для реалізації операцій цифрової обробки зображень. Морфологічні операції є фундаментальними в обробці зображень і комп'ютерному зорі для таких завдань, як зменшення шуму, виявлення об'єктів і поліпшення зображення. КТА може забезпечити платформу для проєктування та впровадження ефективних морфологічних операторів для бінарних зображень. Ерозія та дилятація є важливими підходами в частому застосуванні реальних зображень. У цьому дослідженні описано оптимізовані наноструктури в КТА для застосувань ММ, що функціонують як дилятація й ерозія. Запропонована наноархітектура порівнюється з найліпшим аналогом, що демонструє істотний проґрес щодо роботи комірки, обсягу та затримки. Запропонована конфіґурована конструкція досягла поліпшення на 42,20%, 41,18%, 50,00% і 60,84%, а неконфіґурована конструкція досягла поліпшення на 12,42%, 31,24%, 34,36% і 12,45% з точки зору використовуваної комірки, обсягу замкнутого простору, тактової частоти та обсягу комірки відповідно. Крім того, споживання енергії структурами оцінюється на різних температурних рівнях у 2 К.

Key words: quantum-dot cellular automata, morphology, erosion, dilation.

Ключові слова: квантово-точкові клітинні автомати, морфологія, ерозія, дилятація.

(Received 18 December, 2023; in revised form, 27 January, 2024)

1. INTRODUCTION

QCA are imminent nanoarchitecture beyond existing changes to encode binary information [1–3]. In CMOS architecture, the computing supremacy has improved drastically throughout the previous 10 years and has been reliant on transistor decline [4–6], and so, improved configurability of CMOS architecture effects the execution of several aspects such as heat depletion and outflow currents [7–9].

Many studies are accepted by researchers to annihilate the limitations of transistor-based architecture. QCA, as one of the resolutions, is an innovative transistor less quantum model with extreme low power dissipation and decidedly small extent [10–13]. The logic statuses of QCA are presented by a cell that is operated to encode and transmit da-

ta through the two state electron arrangements [14–17].

The QCA cell group can be combined and ordered specifically to manage computation functions [18–20]. Image operations is a particularly investigating area in very large-scale integration (VLSI) archetype by reason of its several restrictions in processing power and as yet, this archetype is extensively operated to design the distinction of image operations. In real life image operations, it is recurrently vital to lessen noise level through specific substances of the image need to be sustained to expand the complete effect. A nonlinear filtering approach such as median is adept to exclude coercion noise although alleviating the image thresholds [3].

A familiar nonlinear image operation process is morphology [4] that is placed on the figure of an individual embedded in an image and profoundly linked with the set theory [5] and Minkowski algebra [6]. In the early, MM process was functioned on binary images later, several deviations and generalizations processes have been defined to be practicable on monochrome or pigmented images [7]. Through the usage of complex coding and scripting, there are provisional consequences where binary images emerge. Digital image operation is continuously emergent research part with huge applications spreading out into our life and such utilization embrace several techniques like object realization and image improvement. Recognizing such complex presentations on everyday computer can be adequate, but not decisive due to restrictions on computational memory and peripheral machines [8]. Operating complex computational functions on hardware through pipelining and parallelism in algorithms, return significant falling in execution phases [9].

Emerging nanoarchetypes have been the consideration of comprehensive investigation whereas traditional VLSI archetypes are getting their substantial ceiling. QCA shows a state-of-the-art information presentation system that proposed a systematic digital logic presence and points to the expansion of different design methods [10]. Numerous logic designs and devices are proposed through QCAs, *e.g.*, QCA wire [11], 3-input and 5-input majority logic, XOR circuit [12], several and flip-flops [13–19], several sequential and combinational logic architectures [20–26], and reversible architectures [27, 28].

Now, a number of operations are identified for scientific MM methods with nonlinear filters. A marginal median filter was designed without QCA structure in [29]. This work, two MM filters are outlined focused on circuit functionality where the designed circuits present parallel processing, intense functioning, and minimal energy depletion. Moreover, the designs are developed in reference to cell intricacy, dimension, and latency as associated with the existing layout [30, 33].

The preeminent purpose of this research is described below:
— designing optimal layouts of single layer QCA configurable and non- configurable MM filters to decrease cell complexities and covered area;
— comparing and assessing the presented schematization with existing schematizations;
— investigating and demonstrating the effectiveness of the proposed layouts with the usage of the QCADesigner and QCAPro simulation engine.

In the following Section, a detailed summary of MM operation is systematized. Section 3 provides the relative study of QCA nanoarchetypes, and Sec. 4 presents the performance of the proposed circuits. Energy depletion and output emission by the designed circuits are provided in Sec. 5 and consequently conclusion in Sec. 6.

2. MORPHOLOGICAL TECHNIQUES IN IMAGE OPERATION

A number of shortcomings may enclose in binary images and, in certain contexts, the binary spaces assembled by plain thresholding are distorted by textures. MM process is a substantial choice of image applications that adjusts the binary images based on contours. This operation is measured to be particular data processing techniques convenient in image practices *e.g.*, noise abolition, boundary removal, texture evaluation and more [5]. MM image operations stick to the aim of abolishing the shortcomings and preserving the formation of binary image. The procedures are certain basically on the correlated classifying of pixel values, instead of the statistical values, thus the process realized more on images, nevertheless this process can also be practical to monochrome images where the light transmission is unidentified and therefore the outright picture element are not received in concern [6]. MM procedures substantiate the image through a small prototype called configuring module and this module is practical to all potential settings of the feedback image and produces the similar dimension's output. Within this operation, the producing image picture element values are formed on same picture elements of feedback image through is neighbours. This process shows a new image where if the assessment is positive, it will perform non-null picture elements at that setting in the feedback image. The basis of the MM process is opening, closing, erosion, dilation specified in logical AND, OR representation and defined by set evaluation [6]. The exclusion or addition of picture elements rests on the configuring module that utilized for operating the image.

Erosion is a particular and essential operator in MM and it is the reasons of image lessening or become narrow in dimension. Erosion

is mostly dwindling with the margins of the forefront that outcomes in spaces of those picture elements shorten in dimension and voids of those dimensions converted higher [7]. Thus, after thinning and loading the voids of images, the margins become occupied, hence, to some extent isolated; the margins erosion is practical so as to create the margins of the images narrower for enhanced output [8]. In this process, two elements work as data. The initial one is the feedback image to be eroded and next is the configuring module. Let M be a complete grid and B is an image in M. The mathematical characterization of erosion of B by the configuring module C is recognized by

$$B \ominus C = \{z \in M | \, C_z \subseteq B\}. \tag{1}$$

In this equation, C_z is the conversion of C through the direction z.

Dilation is another essential process in MM where it is practical not only to binary image but also practical to monochrome image. This operation reasons the image objects to rise in dimensions. The outcome of this process will steadily rise the margins of forefront pixels; hence, spaces rise in dimensions and voids in that dimensions convert smaller [7, 38]. Unlike erosion, the dilation takes has two elements that works as data. The initial one is the feedback image that needs to be dilated and next one is the configuring module also recognized as kernel. The mathematical characterization of dilation of B by C is recognized by

$$B \oplus C = \bigcup_{c \in C} B_c \, . \tag{2}$$

This operation can also be achieved as follows:

$$B \oplus C = \left\{ z \in M \mid \left(C^z \right)_z \cap B \neq \varnothing \right\}. \tag{3}$$

In this equation, C^s indicates the proportionate of C.

It can be perceived from Fig. 1 that the dilation and erosion model can be noted the previous formation of the image and precisely in what way the procedures of configuring module alter the initial image. During the dilation procedure if the origin of the configuring module overlays through a dark picture element, then spot dark all picture elements from the image surrounded through the module. Wherever the origin of the module overlays with a white one, then adjusts to the subsequent picture element.

Through the erosion operation if the origin of the configuring module overlays through a dark picture element and as a least one of the dark picture elements in the module drops over a white one, then change the dark element in the binary image from dark to

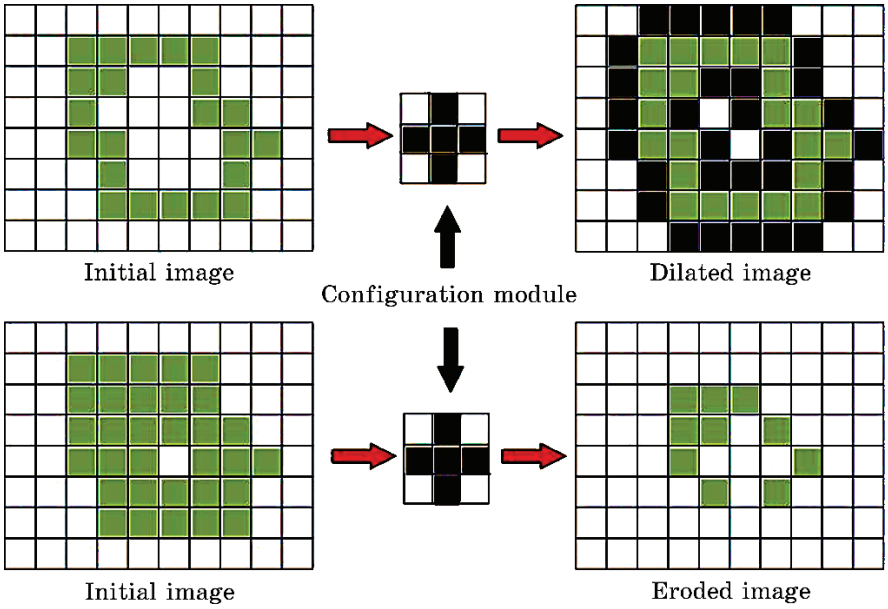

Fig. 1. Dilation and erosion operations by configuring module.

white. Wherever the origin of the module overlays with a white one in the image, then no adjustment is needed, directly adjust to the subsequent picture element.

3. QCA SUMMARY

QCA is a prospective generation nanoarchetype, which signifies logic conditions not as voltage state but relatively as the form of a couple of electrons in a square cell. The square cell is consisting of four dots known as quantum-dots that are employed in the edges of each cell, and two additional movable electrons. The electrons can channel concerning the quantum dots in the square cell, however cannot skip the cell. Then electrons continuously employ the dots at the transversely contrasting edges, because of the coulomb revulsion within the electrons. Therefore, two firm statuses can be shaped in the quantum cell, as indicated in Fig. 2, *a*, logic '0' and logic '1' or polarization −1 and polarization +1, respectively. Information in binary format can be conducted by adjoining cell interfaces along a route of cells that is termed as QCA wire. Another revolved (45°) cells, as exposed in Fig. 2, *b*, for realizing a QCA inverter chain also for crossing resolutions in QCA [9]. In this archetype, almost all designs are executed with inverter gate and majority voters as directed in Fig. 2, *c* and Fig. 2, *d*, correspondingly.

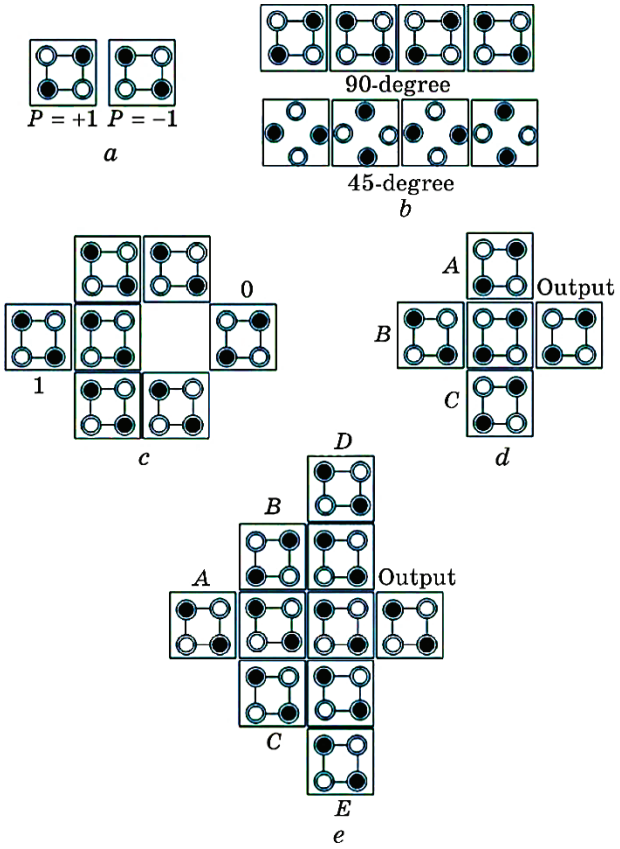

Fig. 2. QCA logical designs: *a*—plain cell; *b*—wires; *c*—potent inverter; *d*—3-input majority gate; *e*—5-input majority gate.

Placing the QCA cells transversely enables the inversion process. A basic majority voter can be executed with five QCA cells. Logical AND or OR designs are arranged by changing particular fixed feedbacks of the gate to logic '0' or logic '1', correspondingly. The settled feedback in the input defines the statues of the others two inputs and it is a condition of the conservative three-input majority voter. A different sort of QCA five-input majority voters is presented in [13–15, 19, 21–23, 37] but the most common is presented in Fig. 2, *e*.

Like the archetypal CMOS layout, the clocking mechanism is a decisive element in all combinational and sequential QCA architectures. The foremost assistance of clocking keeps in the circumstance that information forfeiture and lessening can be re-established. An electric mechanism assists to generate the QCA clocking field [12]. The substantial states specify a benefit to QCA architecture [17];

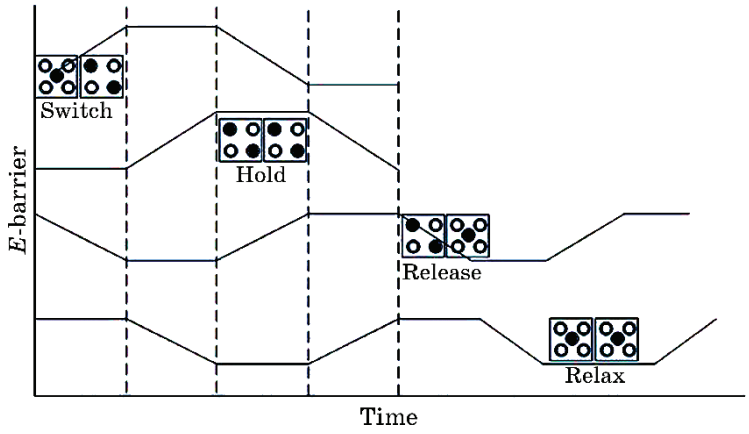

Fig. 3. QCA clocking procedures.

however, it is essential to plot with the consistent clarification of the challenge for which the architecture is intended to resolve. QCA architecture can be in several excited statuses if the feedback of the architecture is moved unexpectedly which directs to a meta-steady situation, and it can initiate interval to attain at its steady ground situation [31]. Accordingly, to evade such complications, adiabatic switching gains the attention. As per the research in Ref. [12], a clock requisite four levels specifically switch, hold, release, and relax as presented in Fig. 3 for an adiabatic sequence. In the initial level, the inter-dot impediments are composed that polarizes the cell. After that in the hold level, the impediments are so elevated that the emission of the cells cannot be altered from an outside origin; therefore, it holds its emission status [31]. The impediments are dropped and the polarization are declines in the release level and in time, the cells turn into un-polarized in the relax level. In every rotation, the neutralized cells are revitalized [17]. The energy depletion is minimal since only two additional electrons are affecting [31, 37].

4. OUTLINED QCA CIRCUIT ARCHITECTURES

It is quite necessary in nanoscale design to propose a structure that can perform with advanced reliability [33]. It has been investigated that easy QCA outlines perform in computer simulation though, break down once it is set to perform as a part of a complex architectures. In other illustrations, the circuit architects that take about their projects to run it in computer simulation, they simply regulate simulation constraints. Hence, a number of circuits are not

practical. This part the designed architectures are provided with applicable outcome. For erosion process, configuring module need to be kept in the feedback image and for dilation process, it needs to be temperately narrowed. At this time, all five-pixel valuation of the image, which drops under the distinct picture element of 3×3 configuring module, is detached. Wherever the full dark picture elements of the configuring module overlay with picture element on the feedback binary image validate dark the pixel of the subsequent object that relays to the configuring module. The resulting binary image is dilated, if OR calculation of these picture elements is certain, and the resulting binary image is eroded, if AND calculation of these picture elements is occupied.

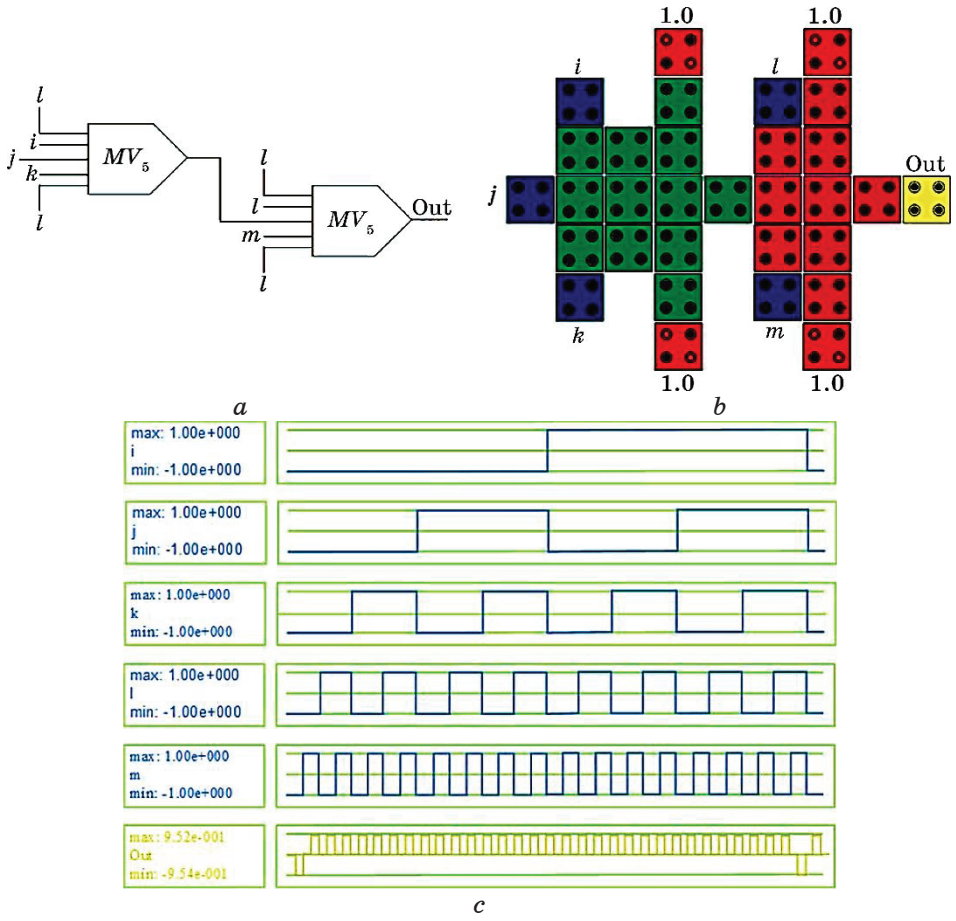

Fig. 4. QCA formation of designed non-configurable circuit: *a*—QCA schematic; *b*—QCA representation; *c*—outcome.

The designed architecture is drawn in Fig. 4, *a* and *b*, separately and the consistent outcome is given in Fig. 4, *c* where, it is coherent that the outlined process operates applicably. The outcome square is 1 (elevate), if each feedback is elevated excluding input *i*.

An innovative configurable design is also projected which contains 5 inputs as drawn in Fig. 5, *a* and *b*, separately. The computer simulation outcome is presented in Fig. 5, *c*, which authorizes the precision of the designed nanoarchitecture. As of the simulation process, it can be perceived that the outcome square is 0 (drop), if each feedback is elevated excluding input *i*.

A systematic calculation in state-of-the art and the designed architectures is provided in Table 1 and the productivity of the de-

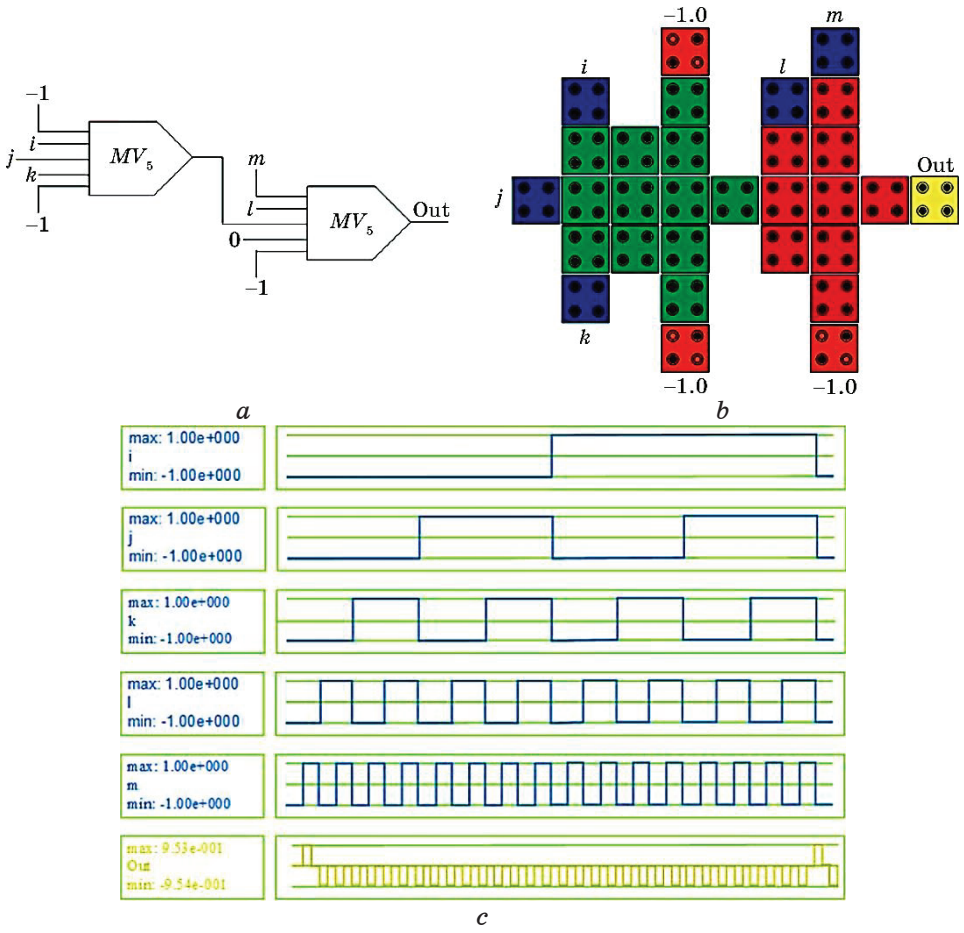

Fig. 5. QCA formation of designed configurable circuit: *a*—QCA schematic; *b*—QCA representation; *c*—outcome.

TABLE 1. Valuation of designed QCA nanoarchitectures.

Architecture	Employed cell	Extent in, μm^2	Clock cycle	Cell extent in, μm^2
Non-configure in [33]	35	0.044	3	0.01136
This paper	31	0.031	2	0.01007
Configure in [30]	51	0.051	4	0.01654
This paper	30	0.031	2	0.00976

signed architectures is certain from assessment. The outlined non-configurable nanoarchitecture achieved 12.42, 31.24, 34.36 and 12.45% improvement in terms of employed cell, enclosed extent, clock, and cell extent, respectively. Likewise, the configurable nanoarchitecture achieved 42.20, 41.18, 50.00 and 60.84% enhancement in terms of employed cell, enclosed extent, clock and cell extent, correspondingly.

5. ENERGY DISSIPATION OF THE DESIGNED NANOCIRCUITS

Designing QCA nanoarchetype circuits, the comprehensive energy of a cell is measured through Hamiltonian matrix [34, 35]. Used for a group of cells, the matrix and Hartree–Fock assessment with the columbic interaction regarding cells by a matrix explanation are stated in Refs. [36, 37]. Now from Eq. (4), M_i directs the overall emission f the i^{th} adjoining cell, $h_{i,j}$ is the numerical phase defining electrostatic control inside m and n cells reliable with the numerical plot, γ is the channelling energy concerning two logic phases of a QCA cell in addition Σ_i is the comprehensive amount adjoining the cells;

$$H = \begin{bmatrix} \dfrac{-E_k}{2}\sum_i M_i h_{m,n} & -\gamma \\ -\gamma & \dfrac{E_k}{2}\sum_i M_i h_{m,n} \end{bmatrix}. \tag{4}$$

The energy consumption can be nominal by calculating and completely;

$$P_{diss} = \frac{E_{diss}}{T_{cc}} \left\langle \frac{\hbar}{2T_{cc}} \Gamma_+ \left[\frac{\Gamma_-}{|\Gamma_-|} \tanh\left(\frac{\hbar|\Gamma_-|}{K_c T} \right) - \frac{\Gamma_+}{|\Gamma_+|} \tanh\left(\frac{\hbar|\Gamma_+|}{K_c T} \right) \right] \right\rangle. \tag{5}$$

TABLE 2. Inclusive energy consumed through the designed nanocircuits at specific energy phase.

Outlined nanoarchitectures	Average energy consumed in, meV	Energy consumption at $T = 2$ K		
		$0.50E_k$	$1.0E_k$	$1.5E_k$
Non-configurable	Leakage energy	0.00828	0.02317	0.04096
	Switching energy	0.05448	0.05200	0.04524
	Energy consumption	0.06276	0.07517	0.08620
Configurable	Leakage energy	0.00836	0.02304	0.04027
	Switching energy	0.05148	0.04716	0.04261
	Energy consumption	0.05984	0.07020	0.08288

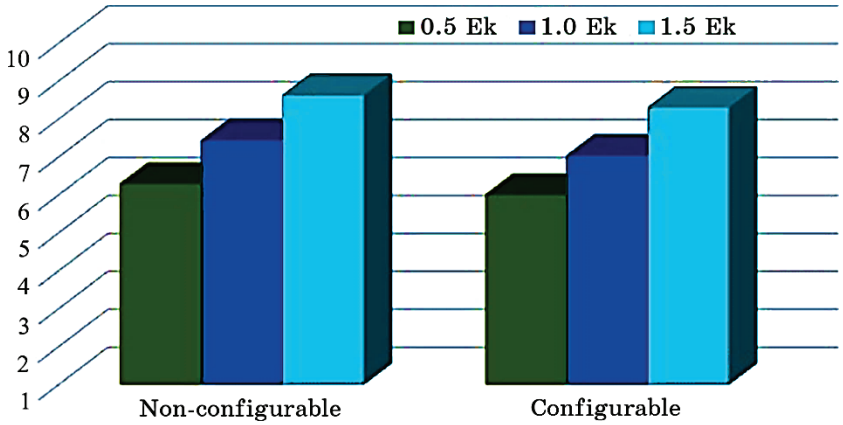

Fig. 6. Inclusive energy consumption at three different tunnelling phase where $T = 2$ K.

In Equation (5), Γ_+ and Γ_- defines the Hamiltonian values earlier and afterward the adjustment, T denotes the temperature, and K_c is the Boltzmann element. Overall energy consumption of the outlined nanoarchitectures is estimated through QCAPro simulation engine [35, 36]. The simulation engine evaluates the depleted energy of inclusive layout all design in a number of energy levels under non-adiabatic converting [37]. Total energy consumption is estimated at three specific channelling points is provided in Table 2 at a firm temperature of 2 K.

Figure 6 shows overall energy consumption for several tunnelling

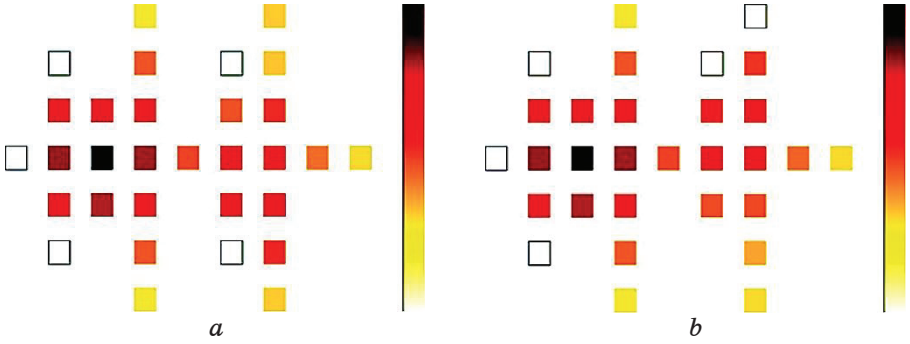

Fig. 7. The energy emission plots of designed (*a*) non-configurable and (*b*) configurable nanoarchitectures with $1.0E_k$ tunnelling energy at $T = 2$ K.

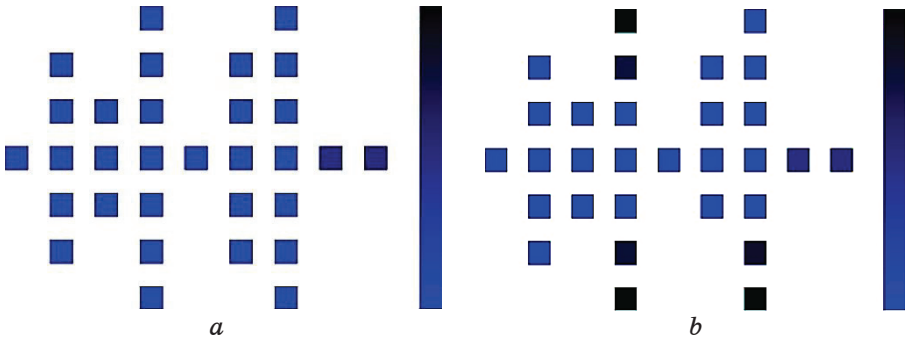

Fig. 8. The emission plots of designed (*a*) non-configurable and (*b*) configurable nanoarchitectures with $1.0E_k$ tunnelling energy at $T = 2$ K.

phase at a firm temperature of 2 K. The diagram shows that the inclusive energy consumption growths steadily for practical tunnelling level in the proposed nanoarchitectures.

The energy consumption map with $1.0E_k$ tunnelling energy at temperature of 2 K is provided in Fig. 7 mutually considering configurable and non-configurable nanocircuits.

Besides, Figure 8 presents the emission plots for both nanoarchitectures.

The temperature level effect on the output emission of proposed nanoarchitectures is achieved in this study. The output emission is occupied at several temperatures with QCADesigner engine. The average emission for every QCA cell is analysed from [14, 18] and systematized in Fig. 9. The structures perform proficiently in a temperature level of 1–11 K, and the emission for QCA cell is altered slightly in this level.

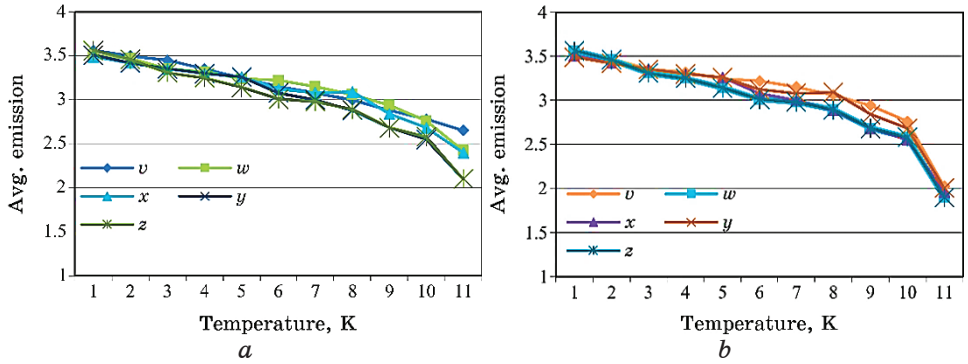

Fig. 9. Temperature *vs.* output emission; (*a*) non-configurable and (*b*) configurable nanoarchitectures.

6. CONCLUSION

In this research, the design and computer simulation of the MM configurable and non-configurable nanoarchitectures of dilation and erosion on digital binary images are analysed. The designed nanocircuits provide enhanced design achievement, comparable dispensation with minimal energy consumption related to state-of-the art nanoarchitectures. The simulation outcomes confirm the precise performance of the designed layouts. Moreover, the energy consumption by the architectures indicates that depleted energy level is rather minimal. This assists to form the proposed nanoarchitectures appropriating image processing operations practical on independent or cellular appliances.

REFERENCES

1. J. A. Carballo, W. T. J. Chan, P. A. Gargini, A. B. Kahng, and S. Nath, *32nd International Conference on Computer Design (ICCD) (19 October, 2014)*, p. 139; https://doi.org/10.1109/ICCD.2014.6974673
2. C. S. Lent, P. D. Tougaw, W. Porod, and G. H. Bernstein, *Nanotechnology*, **4**, Iss. 1: 49 (1993); https://doi.org/10.1088/0957-4484/4/1/004
3. N. Gallagher and G. Wise, *IEEE Trans. Acoust., Speech, Signal Process*, **29**, Iss. 6: 1136 (1981); https://doi.org/10.1109/TASSP.1981.1163708
4. E. Aptoula and S. Lefиvre, *Pattern Recognit*, **40**, Iss. 11: 2914 (2007); https://doi.org/10.1016/j.patcog.2007.02.004
5. I. Grattan-Guinness, *Hist. Math*, **31**, Iss. 2: 163 (2004); https://doi.org/10.1016/S0315-0860(03)00032-6
6. K. Michielsen and H. De Raedt, *Phys. Rep.*, **347**, Iss. 6: 461 (2001); https://doi.org/ 10.1016/S0370-1573(00)00106-X
7. V. Chatzis and I. Pitas, *IEEE Trans Image Process*, **19**, Iss. 7: 699 (2000);

https://doi.org/10.1109/42.875192
8. K. Benkrid, A. Benkrid, and S. Belkacemi, *J. Syst. Archit.*, **53**, Iss. 4: 184 (2007); https://doi.org/10.1016/j.sysarc.2006.09.010
9. K. Konstantinidis, G. C. Sirakoulis, and I. Andreadis, *IEEE Trans. Syst. Man Cybern, Pt. C*, **39**, Iss. 5: 520 (2009); https://doi.org/10.1109/TSMCC.2009.2020511
10. T. Cole and J. C. Lusth, *Prog. Quantum. Electron*, **25**, Iss. 4: 165 (2001); https://doi.org/10.1016/S0079-6727(01)00007-6
11. M. Abdullah-Al-Shafi and A. N. Bahar, *5th Intl. Conf. on Informatics, Electronics & Vision (May 13, 2016)*, p. 620; https://doi.org/10.1109/ICIEV.2016.7760076
12. P. D. Tougaw and C. S. Lent, *J. Appl. Phys.*, **75**, Iss. 3: 1818 (1994); https://doi.org/10.1063/1.356375
13. M. Abdullah-Al-Shafi and A. N. Bahar, *Cogent. Eng.*, **3**, Iss. 1: 1237864 (2016); https://doi.org/10.1080/23311916.2016.1237864
14. M. Abdullah-Al-Shafi, *Nanosistemi, Nanomateriali, Nanotehnologii*, **16**, Iss. 2: 289 (2018); http://dx.doi.org/10.15407/nnn.16.02.289
15 M. Abdullah-Al-Shafi, M. S. Islam, and A. N. Bahar, *Int. J. Comput. Appl.*, **128**, Iss. 2: 27 (2015); https://doi.org/10.5120/ijca2015906434
16. M. Abdullah-Al-Shafi, A. N. Bahar, F.Ahmad, and K. Ahmed, *Cogent. Eng.*, **4**, Iss. 1: 1349539 (2017); https://doi.org/10.1080/23311916.2017.1349539
17. M. Abdullah-Al-Shafi and A. N. Bahar, *Cogent. Eng.*, **4**, Iss. 1: 1391060 (2017); https://doi.org/10.1080/23311916.2017.1391060
18. M. Abdullah-Al-Shafi and A. N. Bahar, *J. Nanoelectron. Optoelectron.*, **13**, Iss. 6: 856 (2018); https://doi.org/10.1166/jno.2018.2302
19. M. Abdullah-Al-Shafi and A. N. Bahar, *Int. Nano Lett.*, **9**, Iss. 3: 265 (2019); https://doi.org/10.1007/s40089-019-0279-1
20. M. Abdullah-Al-Shafi and A. N. Bahar, *J. Comput. Theor. Nanosci.*, **14**, Iss. 5: 2416 (2017); https://doi.org/10.1166/jctn.2017.6842
21. M. Abdullah-Al-Shafi and A. N. Bahar, *Sens. Lett.*, **17**, Iss. 7: 595 (2019); https://doi.org/10.1166/sl.2019.4117
22. M. Abdullah-Al-Shafi and A. N. Bahar, *J. Nanoelectron. Optoelectron.*, **14**: Iss. 9: 1275 (2019); https://doi.org/10.1166/jno.2019.2630
23. M. Abdullah-Al-Shafi and Z. Rahman, *Solid State Electron. Lett.*, **1**, Iss. 2: 73 (2019); https://doi.org/10.1016/j.ssel.2019.11.004
24. M. Abdullah-Al-Shafi, A. N. Bahar, M. A. Habib, M. M. R. Bhuiyan, F. Ahmad, P. Z. Ahmad, and K. Ahmed, *Ain Shams Eng. J.*, **9**, Iss. 4: 2641 (2018); https://doi.org/10.1016/j.asej.2017.05.010
25. M. T. Niemier, M. J. Kontz, and P. M. Kogge, *Proc. 37th Annual Design Automation Conference (2000)*, p. 227; https://doi.org/10.1145/337292.337398
26. M. Crocker, X. S. Hu, M. Niemier, M. Yan, and G. Bernstein, *IEEE Trans. Nanotechnol.*, **7**, Iss. 3: 376 (2008); https://doi.org/10.1109/TNANO.2007.915022
27. M. Abdullah-Al-Shafi and A. N. Bahar, *Int. J. Inf. Technol. Comput. Sci.*, **10**, Iss. 10: 38 (2018); https://doi.org/10.5815/ijitcs.2018.10.05
28. Md. Abdullah-Al-Shafi, *Commun. Appl. Electron.*, **4**, Iss. 1: 20 (2016); http://dx.doi.org/ 10.5120/cae2016652004
29. J. L. Cardenas-Barrera, K. N. Plataniotis, and A. N. Venetsanopoulos,

Math. Probl. Eng., **8**, Iss. 1: 87 (2002); https://doi.org/10.1080/10241230211381
30. V. Mardiris and V. Chatzis, *J. Eng. Sci. Technol. Rev.*, **9**, Iss. 2: 25 (2016); https://doi.org/10.25103/jestr.092.05
33. R. Zhang, K. Walus, W. Wang, and G. A. Jullien, *IEEE Trans. Nanotechnol.*, **3**, Iss: 4: 443 (2004); https://doi.org/10.1109/TNANO.2004.834177
34. I. Amlani, A. O. Orlov, R. K. Kummamuru, G. H. Bernstein, C. S. Lent, and G. L. Snider, *Appl. Phys. Lett.*, **77**, Iss. 5: 738 (2000); https://doi.org/10.1063/1.127103
35. S. B. Tripathi, A. Narzary, R. Toppo, M. Goswami, and B. Sen, *J. Phys. Conf. Ser.*, **1039**, Iss. 1: 012028 (2018); https://doi.org/10.1088/1742-6596/1039/1/012028
36. M. Abdullah-Al-Shafi and R. Ziaur, *Solid State Electron. Lett.*, **1**, Iss. 2: 73 (2019); https://doi.org/10.1016/j.ssel.2019.11.004
37. S. Sheikhfaal, S. Angizi, S. Sarmadi, M. H. Moaiyeri, and S. Sayedsalehi, *Microelectron. J.*, **46**, Iss.6: 462 (2015); https://doi.org/10.1016/j.mejo.2015.03.016
38. S. S. Ahmadpour, M. Mosleh, and S. Rasouli Heikalabad, *J. Supercomput.*, **76**, Iss. 12: 10155 (2020); https://doi.org/10.1007/s11227-020-03249-3
39. M. Abdullah-Al-Shafi, M. S. Islam, and A. N. Bahar, *Int. Nano Lett.*, **10**, Iss. 3: 177 (2020); https://doi.org/10.1007/s40089-020-00304-y
40. M. R. Hasan, R. Guest, and F. Deravi, *ACM Comput. Surv.*, **55**, Iss. 13: 1 (2023); https://doi.org/10.1145/3583135

Наносистеми, наноматеріали, нанотехнології
Nanosistemi, Nanomateriali, Nanotehnologii
2025, т. 23, № 2, сс. 349–362
https://doi.org/10.15407/nnn.23.02.0349

© 2025 ІМФ (Інститут металофізики
ім. Г. В. Курдюмова НАН України)
Надруковано в Україні.

PACS numbers: 07.07.Df, 07.07.Vx, 87.85.Rs, 89.20.Hh, 89.60.Fe, 92.60.Jq, 92.60.jk

Application-Driven IoT-Based Home-Gardening System

P. Vivekanandan, P. Radhika, S. Bharathi, S. Gowtham, Pandey Om, and V. Paul Japez

SNS College of Technology,
Department of Mechatronics Engineering,
Coimbatore, Tamilnadu, India

The ‘internet of things’ is a computer-science branch that offers concepts as well as methods for connecting a broad variety of digital gadgets in order to speed up mechanical operations. People living in cities, who struggle to maintain their own gardens, find expert gardeners. This study presents a NodeMCU or Arduino-based microcontroller-based Internet of Things (IoT) method for monitoring smart gardens, enabling users to check critical temperature, moisture, and humidity characteristics of their indoor plants and gardens. A prototype is developed to show how the recommended technique may be used in practise. An Android smartphone application is made to display the real-time profiles of environmental factors such as temperature, wetness, and humidity. With the use of this technology, users will be able to better take care of the development and health of their plants in their gardens. This scientific endeavour takes the place of the need for gardeners and the challenges associated with maintaining gardens in major cities. The purpose of this study is to advance IoT innovation for smart cities in our culture.

«Інтернет речей» — це галузь інформатики, яка пропонує концепції, а також методи підключення широкого спектру цифрових ґаджітів для пришвидшення механічних операцій. Люди, які живуть у містах і яким важко доглядати за власними садами, знаходять досвідчених садівників. У цьому дослідженні представлено метод Інтернету речей (IoT) на базі мікроконтролера NodeMCU або Arduino для моніторинґу розумних садів, що дає змогу користувачам перевіряти критичні характеристики температури, сирости та вологости своїх кімнатних рослин і садів. Було розроблено прототип, щоб показати, як рекомендований метод можна використовувати на практиці. Було створено застосунок для смартфонів Android, який відображатиме профілі факторів навколишнього середовища в режимі реального часу, таких як температура, сирість та вологість. Завдяки використанню цієї технології користувачі зможуть ліпше піклуватися про розвиток і здоров’я своїх рослин у са-

дах. Це наукове зусилля замінює потребу у садівниках і проблеми, пов'язані з доглядом за садами у великих містах. Метою цього дослідження є просування інновацій IoT для розумних міст у нашій культурі.

Key words: internet of things (IOT), fertilization, humidity, water level sensor.

Ключові слова: інтернет речей (IoT), удобрювання, вологість, давач рівня води.

(Received 25 August, 2023)

1. INTRODUCTION

Agriculture is considered the primary sector of the Indian economy, and its growth plays a crucial role in achieving sustainable economic development on a global scale. The tropical climate of India provides an excellent environment for cultivating diverse crops that can be used for consumption. However, the availability of freshwater and fertile land is even more critical for the success of agriculture in India. These natural resources are the backbone of the country's agricultural production and must be managed effectively to ensure sustained growth in the sector. As such, it is essential to focus on preserving and efficiently utilizing these resources to maximize the potential of agriculture in India. Water scarcity is a major issue in India, a country that heavily relies on agriculture as a key driver of its economy. Insufficient water supply has a significant impact on crop yields and agricultural output, which in turn affects food production. Farmers face numerous challenges in producing crops due to a lack of water, making it increasingly difficult to meet the growing demand for food in the world. As a result, addressing water scarcity has become a critical concern for policymakers, stakeholders, and communities involved in the agricultural sector in India. It is essential to implement effective measures to manage and conserve water resources to ensure sustainable agricultural practices and food security in the country.

According to the International Water Management Institute (IWMI), around 70% of land-based water consumption is used for domestic, industrial, and environmental purposes, exacerbating the issue of water scarcity. This makes it necessary to explore better ways of managing water resources, especially in agriculture, where water usage can be minimized. Irrigation is a technique used to water food or cash crops, and it has been shown to increase agricultural production. However, traditional irrigation methods can be wasteful, leading to an overuse of water. To address this issue, irrigation management techniques based on the World Bank have been developed to enhance irrigated regions and increase earnings.

The use of water-efficient agricultural systems has been shown to boost economic development. Robotic equipment has largely replaced traditional watering methods, but it may not be suitable for areas with water scarcity. Therefore, before implementing automatic irrigation, factors like soil and plant moisture conditions, water availability, and operational relevance of irrigation systems must be considered. A smart watering system, which can automate the entire watering process, could be a better alternative to traditional irrigation methods.

The proposed project aims to monitor the irrigation network automatically, without requiring human intervention. This is particularly useful for farmers who may have fields located far away from their place of residence, making it difficult for them to visit and inspect their crops regularly. With the implementation of an IoT system, farmers can manage their plants remotely. The system works by using a Node-MCU microcontroller to detect the present temperature, moisture, and dampness parameters of the plants and gardens. The data collected is then displayed in real-time on a mobile application for smartphones, which also provides information on external elements such as temperature, humidity, and wetness. This approach allows farmers to modify the amount of water flowing from the pump and adjust the intervals between watering cycles as needed, providing greater control over the irrigation process. Overall, this IoT-based technique offers a smarter way to monitor gardens and crops, enabling farmers to make informed decisions regarding irrigation management. This research project aims to provide garden owners with the tools to have better manage their gardens in terms of plant growth and health, particularly in urban areas where space is limited. The use of IoT technology can help address the challenges faced by gardeners in urban settings. The primary objective of this research is to implement and develop IoT systems for smart cities, focusing on the specific application of smart gardening. By utilizing IoT sensors and devices, gardeners can monitor key parameters such as temperature, humidity, and moisture levels, and adjust irrigation and other gardening practices accordingly. This approach can lead to more efficient use of resources, reduced wastage, and improved overall garden health. Ultimately, this research aims to promote the use of IoT technology in urban gardening to create sustainable and thriving green spaces in smart cities.

2. LITERATURE SURVEY

The research conducted by Jinling *et al.* proposed a remote-control system for greenhouses, which is based on the Global System for

Mobile GSM-SMS. This system is capable of sending temperature, ambient temperature, and humidity status *via* SMS, as well as controlling watering equipment through remote machines. Additionally, factories utilize sensors and automation devices to improve their operations and efficiency [1]. Gautam and Reddy suggested a novel on-board irrigation system that can be controlled remotely using GSM and Bluetooth technology [2].

Suresh and colleagues presented a framework based on the functionalities of present and future microcontrollers, as well as their usage demands [3]. Kansara *et al.* introduced an IoT-based smart irrigation system that reduces the need for human intervention. This system uses sensors to detect changes in temperature and humidity in the bypass region, and then sends a signal to the microcontroller to enable or disable the irrigation setting. The microcontroller in this system is designed to minimize power usage and extend the system's lifespan by reducing power consumption [4].

Archana and Priya have proposed a system based on a microcontroller that monitors the water level and irrigated area. This system includes sensors that detect the presence of water in the fields. Anitha proposed an IoT-based waste monitoring system that employs sensors on the lid of the waste container to detect the level of waste based on the height of the container. This system provides real-time information on the waste level, allowing for efficient and timely waste management. Uddin *et al.* proposed an automatic microcontroller-based variable irrigation system model that solely uses solar energy as a power source to control the entire system [7].

Sensors are installed in rice fields to constantly detect water levels and transmit the information to farmers to keep them informed about the water level. Farmers can remotely monitor and control various environmental factors using transparent wireless sensor networks (WSN) developed by Chavan and Karande. These networks are designed to monitor soil moisture, temperature, humidity, and other factors in agricultural environments, which can be crucial for efficient crop management. Anitha proposed an IoT-based home security system that includes motion sensors and a camera to detect any suspicious activities in the home. The system also includes an alarm that is triggered, when a potential threat is detected, and notifications are sent to the homeowner’s mobile phone. The system can be remotely controlled through a mobile application, allowing the homeowner to monitor their home from anywhere. Additionally, the system includes a smoke sensor to detect any fire hazards and alert the homeowner [9]. Parameswaran *et al.* proposed an irrigation system that utilizes soil moisture sensors and solenoid valves to regulate water flow in crops [10].

The system takes into account not only the climatic conditions

but also the pH levels of water and soil, as they are important factors in crop production. Monitors are used to display information on pH, moisture content, and temperature, thus improving the agricultural system and increasing productivity. The system can also provide remote monitoring and control, allowing farmers to adjust irrigation levels and pH values from a distance. This technology can be very useful in areas where water resources are scarce or in instances where manual monitoring and adjustment of irrigation systems are not feasible.

3. MATERIALS AND METHODOLOGY

The research paper lists the necessary components for the system, which includes Arduino Uno, fertilizer sensor, moisture sensor, relay, pump. The software requirements are Arduino IDE, MIT App Inventor.

3.1. Arduino Uno

Arduino Uno is a type of open-source computer hardware that is designed to simplify the creation of microcontroller-based projects by providing a user-friendly programming environment and a community of users who can share resources and knowledge. A microcontroller board can be used to sense and control various inputs and outputs. The Arduino Uno is a popular board in the Arduino family due to its affordability, ease of use, and compatibility with a wide range of operating systems. It can be programmed using various programming languages, including C++ and JAVA. A visual representation of an Arduino Uno is displayed in Fig. 1.

3.2. Fertilizer Sensor

The sensor used for fertiliser monitoring is illustrated in Fig. 2. Its

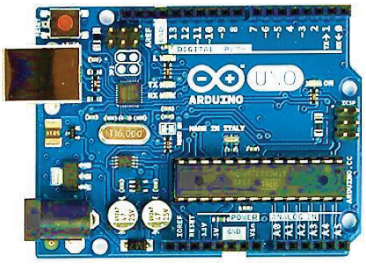

Fig. 1. Arduino Uno board.

Fig. 2. Fertilizer sensor.

function is to measure the concentration of ammonium in the soil, which is utilized by soil bacteria to produce nitrites and nitrates. In conjunction with meteorological data, pH readings, and soil conductivity measurements, the sensor employs machine learning to calculate the optimal timing for fertilisation. Based on this information, it predicts the total nitrogen present in the soil currently and in the next 12 days.

4. MOISTURE SENSOR

Soil moisture sensors (Fig. 3) are widely used for measuring the water content in soil. Traditional methods for measuring soil moisture require drying and weighing samples, which can be time-consuming and labour-intensive. However, modern soil moisture sensors utilize various indirect methods such as dielectric constant, electrical resistance, or neutron interaction to estimate soil moisture. These factors can be affected by factors like temperature, soil type, and electrical conductivity, which, in turn, influence the accuracy of the measurement.

The dielectric constant of soil is related to its water content, and soil moisture sensors utilize capacitance to measure the dielectric permittivity of the soil and determine its water content. These sensors are inserted into the soil and provide the water content status as a percentage. The data collected from these sensors can be used for a variety of applications in hydrology, agriculture, soil science, and environmental science. These sensors are also helpful in teaching concepts related to horticulture, biology, and agriculture.

5. WATER PUMP

Figure 4 illustrates a water pump, which is a mechanical device that increases water pressure for conveying it from one place to another. These pumps are utilized worldwide to provide water for domestic, agricultural, industrial, and municipal purposes. By guaranteeing that the correct amount of water is supplied to every section of a field, water pumps enhance irrigation efficiency and speed up crop growth. These pumps are easier to maintain due to their less complicated design and fewer moving components, which results in less maintenance work.

6. RELAY

A relay is a switch that operates using electricity. It consists of a set of input terminals for one or more control signals and a set of

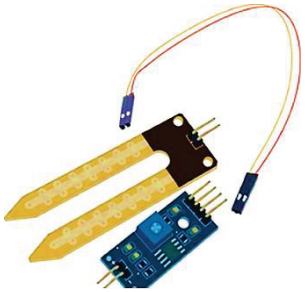

Fig. 3. Soil moisture sensor.

Fig. 4. Water pump.

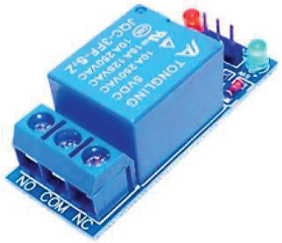

Fig. 5. Relay.

functional contact terminals. Relays use electromagnetism to convert weak electrical inputs into stronger currents, where the electromagnets break or create circuits in response to these inputs. The device is designed for simple updates to contacts and isolates the activation component of the actuating part. It can operate at high temperatures and requires little current to function, yet it can power large machinery. Figure 5 shows a general image of a 5-V relay.

7. PROPOSED METHODOLOGY

The purpose of this study is to develop a system that can remotely monitor soil moisture levels in agricultural fields to maintain optimal moisture levels for crop growth. This IoT-based system is designed to accomplish this task. The prototype developed in this study allows for monitoring and maintenance of soil moisture levels in any agricultural field. This framework is expected to operate and generate reports in real-time. Although adjustments in sensing components, technologies, and source code may be necessary for actual implementation, the proposed approach and control remain consistent. The proposed system was demonstrated using ThingSpeak cloud, an IoT analytics platform that allows for real-time da-

ta stream aggregation, visualization, and analysis. ThingSpeak also allows for the execution of MATLAB code and can be used for prototyping and proof of concept IoT systems that require analytics. This system has the potential to promote sustainable agriculture practices in any country.

7.1. PROPOSED SYSTEM

According to the presented methodology, data is gathered from various sensors including soil moisture level, temperature of the area, air moisture, and water level. These sensors are connected to a breadboard, which is further connected to an Arduino board. The collected data is then transferred to the Arduino IDE for processing. The programming language utilized in the system runs instructions to extract and display the data. If the data is found to be invalid, the process is terminated, as illustrated in Figs. 6 and 7.

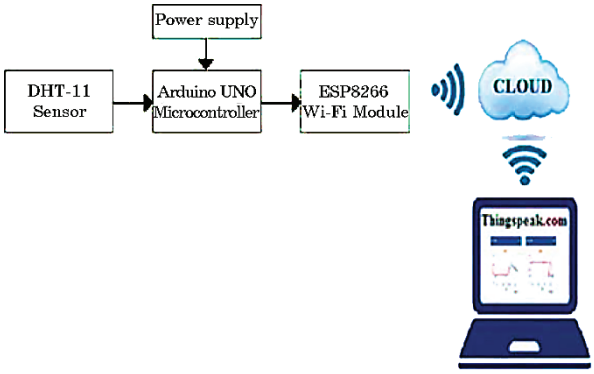

Fig. 6. Proposed system.

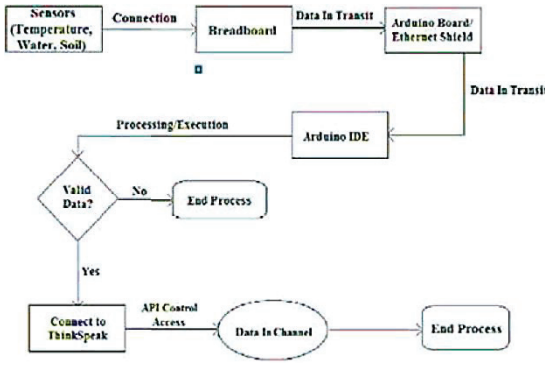

Fig. 7. Data flow diagram of the proposed system.

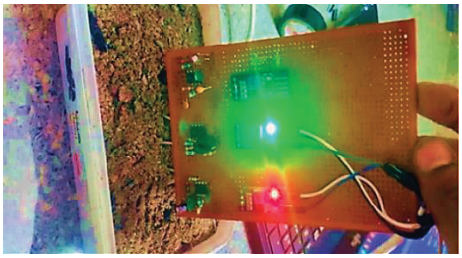

Fig. 8. Working model of the proposed system.

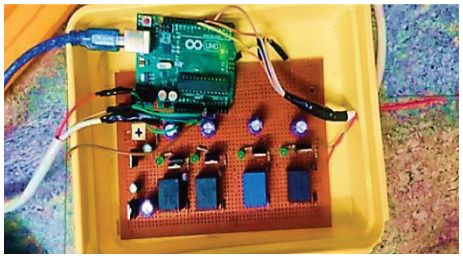

Fig. 9. Complete connection of the system.

8. IMPLEMENTATION OF THE PROPOSED SYSTEM

The proposed system aims to automate and regulate the irrigation process by monitoring the moisture level of the field. This smart irrigation device is designed to be a useful tool for farmers and gardeners who have limited time to water their plants. Moisture sensors and temperature sensors are used to measure the water content and temperature of the plants. If the moisture level is found to be below the desired level, the moisture sensor sends a signal to the Arduino board, which activates the Water Pump to supply water to the specific plant. The system can also be extended for outdoor use. The operational model of the proposed system is illustrated in Figs. 8 and 9.

9. EXPERIMENTAL ANALYSIS

The DHT11 sensor was chosen due to its high sensitivity and accuracy in measuring temperature and humidity. A digital sensor communicates with the ESP8266 NodeMCU *via* a single-wire serial interface. The NodeMCU's analogue pin A0 was utilised to read the analogue output from the moisture sensor, which is a variable resistor that changes its resistance based on the moisture content in the soil. The analogue value read by the NodeMCU is then converted to a digital value using the built-in ADC (analogue-to-digital converter). To control the water pump, a relay module was used to switch the higher voltage required by the motor pump. The NodeMCU's GPIO pins can only supply up to 3.3 V, which is not sufficient to operate the motor pump. The relay module acts as a switch that can handle higher voltage and current, allowing the NodeMCU to control the pump. An external 5-V power supply was also used to power the DHT11 and moisture sensors, as they require more power than what the NodeMCU can provide. Overall, the selection of these components and their integration into the system design is crucial in ensuring the accuracy, reliability, and efficiency of the automated irrigation system.

The table below lists the information gathered from various sensors.

TABLE. Sample dataset.

Created at Date	Created Time	Entry Id	A1	A2	A3	A4
09 March 2019	07:22:24	113	35	51	49	106
23 March 2019	07:28:31	191	40	72	48	547
17 March 2019	06:18:24	138	37	71	44	589
22 March 2019	07:19:52	118	29	68	40	132
13 March 2019	07:27:16	132	32	51	49	562
23 March 2019	08:05:10	174	37	61	33	112
09 March 2019	07:21:28	165	36	61	45	703
19 March 2019	06:01:54	172	33	77	45	674
21 March 2019	08:36:26	180	38	53	34	137
20 March 2019	07:37:26	180	26	78	32	123
08 March 2019	08:49:11	176	28	50	28	138
14 March 2019	07:48:11	113	36	70	25	421
20 March 2019	08:08:36	105	38	57	35	140
10 March 2019	06:59:37	108	29	71	46	136
11 March 2019	06:30:22	159	40	78	27	304
14 March 2019	07:46:55	105	32	71	37	124
23 March 2019	07:03:52	130	36	61	33	948
16 March 2019	07:50:15	148	39	79	39	356

Continuation **TABLE.**

Created at Date	Created Time	Entry Id	A1	A2	A3	A4
08 March 2019	06:10:09	128	30	80	31	625
05 March 2019	06:09:10	107	26	67	35	729
20 March 2019	08:58:26	175	36	71	31	659
23 March 2019	06:33:05	159	38	64	43	986
26 March 2019	07:02:14	108	34	55	25	368
19 March 2019	06:21:19	146	34	57	43	1388
28 March 2019	08:11:07	161	25	65	41	589
19 March 2019	08:14:18	146	34	66	39	804
29 March 2019	07:02:34	186	33	56	34	827
11 March 2019	08:40:52	158	28	65	50	545
07 March 2019	07:10:18	163	32	72	34	785
04 March 2019	07:26:47	129	33	58	33	1262
19 March 2019	08:12:42	136	32	67	27	680
27 March 2019	06:31:06	103	37	69	45	1111
16 March 2019	07:25:23	199	31	73	47	1469
08 March 2019	06:42:43	190	37	76	29	428
10 March 2019	06:49:04	189	40	65	30	916

The data from the sensors for temperature, humidity, soil moisture, and water level are shown in Table under the characteristics A1, A2, A3, and A4, correspondingly.

The temperature measured by the DTH11sensor at various times and dates at various locations in Vellore is depicted in Fig. 10 below.

Similar to that, Fig. 11 of the graph below shows the humidity measured by the DHT11 Sensor at various locations.

The soil moisture level recorded by the soil moister sensors is depicted graphically in Fig. 12.

The water level sensor is used to track the water level in different fields throughout the Vellore districts. The following Fig. 13 makes this very evident.

The ThingSpeak cloud receives this data for visualisation, and a connection between temperature and humidity is computed. When watering plants, the relationship between temperature and humidity is crucial. Therefore, we can turn on or off the irrigation system depending on the correlation. The association is displayed in the following Fig. 14 using ThingSpeak to visualise data from the Matlab.

The working space of Arduino was depicted in Fig. 15.

The proposed work is new since, up until now, the majority of

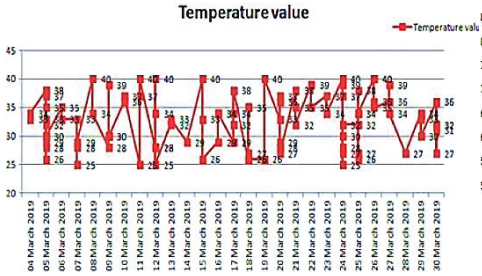

Fig. 10. Temperature recorded by DTH-11 sensor.

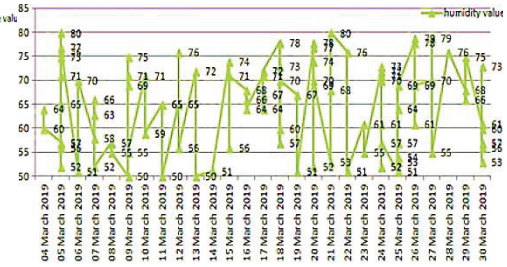

Fig. 11. Humidity recorded by DTH-11 sensor.

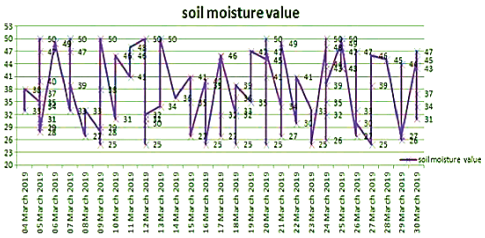

Fig. 12. Soil moisture recorded by soil moisture sensor.

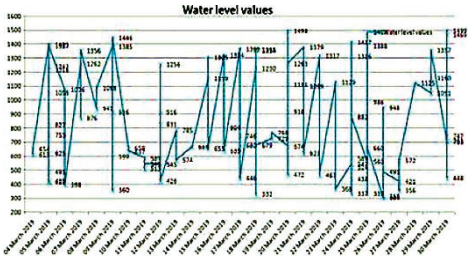

Fig. 13. Water level recorded by water level sensor.

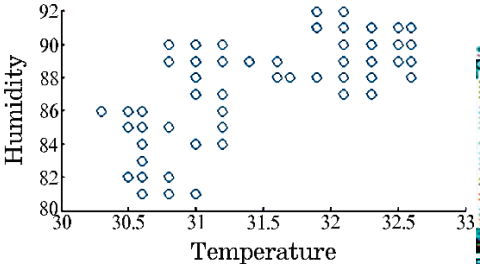

Fig. 14. Correlation map between temperature and humidity.

Fig. 15. Arduino workspace.

research on irrigation systems has typically recorded data and sent SMSs or alarms to the owners to let them know when to water or turn off the water supply. However, the suggested approach uses data gathered from numerous sensors to turn autonomously on and off. Additionally, the captured data is kept in the cloud for later use.

10. CONCLUSION AND FUTURE WORK

In addition to automating the data collection process for soil and plant nutrition requirements, future advancements in intelligent irrigation systems may also involve the use of advanced algorithms to predict soil moisture levels based on collected data. This could result in even greater efficiency and cost-effectiveness in the long run.

Furthermore, the use of sensors to monitor and regulate other important factors such as water level and sand content in soil can also be incorporated into the intelligent irrigation system. By incorporating additional variables, the system can become more precise and effective in delivering the correct amount of water to the plants.

The system described in this study is just the beginning of what is possible with smart agriculture. As more data is collected and analysed, the system can be further tailored for specific applications and scenarios. Ultimately, the objective is to not only save water but also reduce system costs, making it a more sustainable and profitable solution for farmers and agriculturalists.

REFERENCES

1. G. S. Jin, S. Jingling, H. Qiuyan, W. Shengde, and Y. Yan, *2007 8th International Conference on Electronic Measurement and Instruments IEEE*

(16–18 August, 2007, Xian, China), p. 2–82.
2. Indu Gautam and S. R. N. Reddy, *International Journal of Computer Applications*, **47**, No. 13: 1 (2012); https://doi.org/10.5120/7245-0043
3. R. Suresh, S. Gopinath, K. Govindaraju, T. Devika, and N. S. Vanitha, *International Journal of Advanced Research in Computer and Communication Engineering*, **3**: 5654 (2014); https://www.researchgate.net/publication/381583052_Smart_Irrigation_system_using_Internet_of_Things
4. K. Kansara, V. Zaveri, S. Shah, S. Delwadkar, and K. Jani, *International Journal of Computer Science and Information Technologies*, **6**: 5331 (2015).
5. P. Archana and R. Priya, *International Journal of Advanced Engineering and Global Technology*, **4**: 1567 (2016).
6. A. Anitha, 'Garbage Monitoring System Using IoT'. *IOP Conference Series. Materials Science and Engineering* (2017), p. 420–427.
7. M. Uddin, *Measurements of Evaporation During Sprinkler Irrigation* [Doctoral dissertation] (University of Southern Queensland: 2012).
8. C. H. Chavan and P. V. Karande, *Int. J. Eng. Trends Technol. (IJETT)*, **11**, No. 10: 493 (2014); doi:10.14445/22315381/IJETT-V11P296
9. A. Anitha, *Materials Science and Engineering Conference Series*, **263**, Iss. 4: 042027 (2017); doi:10.1088/1757-899X/263/4/042027
10. G. Parameswaran and K. Sivaprasath, *Int. J. Eng. Sci.*, **6**, Iss. 5: 5518: (2016).
11. L. Savadamuthu, S. Muthu, and P. Vivekanandan, *European Journal of Scientific Research*, **69**, No. 1: 64 (2012).
12. L. Savadamuthu, S. Muthu, and P. Vivekanandan, *International Journal of Soft Computing and Engineering*, **1**, No. 4: 2231 (2011).
13. P. Vivekanandan and V. P. Arunachalam, *International Review of Mechanical Engineering (IREME)*, **8**, No. 1: 75 (2014).
14. T. Prakash, Arun G, Arun Kumar B, Deepan. S, and Kalyana Venkata Ramanan, *International Research Journal on Advanced Science Hub (IRJASH)*, **02**, Iss. 04: 7 (2020); https://doi.org/10.47392/irjash.2020.20

Наносистеми, наноматеріали, нанотехнології
Nanosistemi, Nanomateriali, Nanotehnologii
2025, т. 23, № 2, сс. 363–377
https://doi.org/10.15407/nnn.23.02.0363

© 2025 ІМФ (Інститут металофізики
ім. Г. В. Курдюмова НАН України)
Надруковано в Україні.

PACS numbers: 81.16.Hc, 81.20.Ym, 87.50.-a, 87.85.Rs, 89.60.Ec, 92.20.jb, 92.40.kc

Driving Potential of Nanotechnological 'Softening' Approaches for the Maritime Industry: Application, Preference, and Prospects

Nataliia Tiron-Vorobiova[1], Emrah Şik[2], Anatoliy Danylyan[1], Olha Romanovska[1], Valentyn Chymshyr[1], Ihor Maslov[1], Vitalii Zalozh[1], and Andrii Naydyonov[1]

[1]*Danube Institute of National University 'Odesa Maritime Academy',*
9, Fanahoriyska Str.,
UA-68607 Izmail, Odesa Region, Ukraine
[2]*Istanbul Technical University,*
Faculty of Maritime, Tuzla Campus,
TR-34940 Tuzla/Istanbul, Türkiye

The article discusses certain nanotechnologies' key aspects: their rapid development, purposes, and uses. The types of certain nanotechnology generation are explained. Emphasis on the use is given to the cleaning of drinking water, in particular, sewage and ballast water. The latter is discussed at the level of the publisher and organizer of the international water industry—Global Water Intelligence. The variety of ways of applying nanotechnologies to reduce pollution of aquatic environments is presented, and the disadvantages are emphasized. The article is descriptive and applied to help the reader understand the essence of the growth of the nanotechnology boom in several different technologies, ways, and distribution methods. A comparison of nanofiltration membranes with reverse osmosis (SWRO) systems is provided, concerning to processes at the nanoscale level, namely, the use of semi-permeable membranes, which allow only molecules of a certain size to pass through; the pore size in such membranes is measured in nanometers. Therefore, reverse osmosis is an example of a nanoscale technology that is widely used for water purification. The article contains, as a research part, an illustrative example of the application of the nanotechnological principle of the self-discharge filter in the innovative process of disinfection/purification of ballast water according to the quality standard D-2 of the IMO Convention, based on an experimental level by the developers of the Danube Institute of the National University 'Odessa Maritime Academy' (DI NU 'OMA'; Izmail, Ukraine). It is shown how, with the help of its effective application process, the level of final destruction of invasive foreign organisms in ballast water increases. In the discussion of the article, it is stated that this filter will significantly reduce the labour costs of the marine ships' engine crew for the produc-

tion of high-quality distillate and will allow to improve the cleaning and washing of the filter working elements of the modernized ships' SWRO. In particular, shortly, these are ceramic membranes, which will be commercialized and industrialized in the areas of water purification and desalination, as opposed to the use of the SWRO and nanofiltration membranes. The application No. 1059B162300675 submitted by the applicant, Candidate of technical sciences, Docent of the Department of Management in the Transport Industry of the DI NU 'OMA' of the Ministry of Education and Science of Ukraine Nataliia Tiron-Vorobiova (2216B—TÜBITAK-TWAS Postgraduate and Postdoctoral Fellowship Programs 2024–2027), refers to the use of ceramic membranes: Ballast Water Treatment System (BWTS) using Ceramic Membrane Filtration Method, Electrooxidation (EOx) Development and Ecological Assessment. The application provides a key decision (quotation): 'Recently, research has mainly focused on improving adequate, cheap, and aquatic-safe ballast water management systems (BWTS). However, most of these treatment processes alone do not meet all the required discharge quality indicators; they require modification. Thus, there is a significant need for innovative environmental technologies and clean, cost-effective, sustainable maintenance of safe seawater sources. Recently, the integration of electrochemical (EOx) processes with improved membrane filtration processes has been considered as a means to overcome this barrier. The main idea is aimed at creating modern BWTS that meet the requirements of the quality standard D-2 of the IMO Convention. BWTS developed based on experimental research within the bilateral project Ukraine–Türkiye ('2514 TÜBİTAK ve MESU İkili İşbirliği Programı', 2021), is innovative, multifunctional, based on high nanotechnological principles.'. Against the background of the driving advantage of the use of nanofiltration, reverse osmosis, special attention is be paid to the acceptance of 'nanotechnology: the environment' (because the latter remains under threat) with the participation of the increasingly widespread use of nanotechnological approaches.

У статті розглядаються ключові аспекти певних нанотехнологій: їхній стрімкий розвиток, призначення та використання. Пояснюється певні типи ґенерації нанотехнологій. Акцент робиться на використанні для очищення питної води, зокрема, стічних вод і баластних вод. Останнє обговорювалося на рівні видавця й організатора міжнародної водної галузі Global Water Intelligence. Представлено різноманітні способи застосування нанотехнологій для зменшення забруднення водного середовища та зазначено недоліки. Стаття має описовий і прикладний характер, щоб допомогти читачеві зрозуміти суть зростання буму нанотехнологій у кількох певних різних технологіях, шляхах і методах поширення. Наведено порівняння нанофільтраційних мембран із системами зворотньої осмози (SWRO) щодо процесів на нанорівні з використанням напівпроникних мембран, які пропускають лише молекули певного розміру; розмір пор у таких мембранах вимірюється в нанометрах. Отже, зворотня осмоза є прикладом наномасштабної технології, яка широко використовується для очищення води. Стаття містить як дослідницьку частину ілюстративний приклад застосування нанотехнологічного принципу саморозрядного фільтра в інноваційному процесі

дезінфікування/очищення баластних вод відповідно до стандарту якості D-2 Конвенції ІМО, заснованому на експериментальному рівні розробниками Дунайського інституту Національного університету «Одеська морська академія» (ДІ НУ «ОМА»; Ізмаїл, Україна). Показано, як за допомогою ефективного процесу його застосування підвищується рівень остаточного знищення інвазійних сторонніх організмів у баластних водах. В обговоренні статті зазначено, що цей фільтр значно понизить витрати праці машинного екіпажу морського судна на виробництво високоякісного дистиляту та дасть змогу поліпшити очищення та промивання робочих елементів фільтра модернізованого суднового СООП. Зокрема, найближчим часом саме керамічні мембрани будуть комерціялізовані та промислово впроваджені в сферах очищення та опріснення води, на відміну від використання СООП і нанофільтраційних мембран. Заявка № 1059B162300675, подана заявником — к.т.н., доцентом кафедри менеджменту в транспортній галузі ДІ НУ «ОМА» Міністерства освіти і науки України Тірон-Воробйовою Наталією (2216B за Програмою стипендій для аспірантів та постдокторантів TÜBITAK-TWAS 2024–2027 років), стосується використання керамічних мембран: системи очищення баластних вод (СОБВ) з використанням методу фільтрації через керамічні мембрани, розробки електроокиснення (ЕОх) та екологічної оцінки. Заявка містить ключове рішення (цитата): «Останнім часом дослідження в основному зосереджені на вдосконаленні адекватних, дешевих та безпечних для водного середовища систем управління баластними водами (СОБВ). Однак більшість цих процесів очищення самі по собі не відповідають усім необхідним показникам якості скидів; вони потребують модифікації.». Таким чином, є значна потреба в інноваційних екологічних технологіях і чистому, економічно ефективному, сталому обслуговуванні безпечних джерел морської води. Останнім часом інтеґрація електрохемічних (ЕОх) процесів з удосконаленими процесами мембранної фільтрації розглядається як засіб подолання цього бар'єру. Основну ідею спрямовано на створення сучасних СОБВ, що відповідають вимогам стандарту якости D-2 Конвенції ІМО. СОБВ, розроблена на основі експериментальних досліджень у рамках двостороннього проєкту Україна–Туреччина («2514 TÜBİTAK ve MESU İkili İşbirliği Programı», 2021), є інноваційною, багатофункціональною, заснованою на високих нанотехнологічних принципах. На тлі рушійної переваги застосування нанофільтрації, зворотньої осмози, особливу увагу буде приділено прийняттю «нанотехнології: довкілля» (оскільки останнє залишається під загрозою) завдяки все більш широкому використанню нанотехнологічних підходів.

Key words: nanofiltration, nanofiltration materials, reverse osmosis, marine environment, 'softening' membranes, self-discharging nanofilter.

Ключові слова: нанофільтрація, нанофільтраційні матеріяли, зворотня осмоза, морське середовище, «пом'якшувальні» мембрани, саморозрядний нанофільтер.

(Received 31 March, 2024; in revised form, 29 May, 2024)

1. INTRODUCTION

Water is a rich source of valuable resources, whether it is chemicals in industrial wastewater, minerals in geothermal brines, or water itself. Interest in efficiently capturing and reusing products from the aquatic environment is growing, creating opportunities for technologies such as nanofiltration. Global Water Intelligence (GWI), a leading publisher and event organizer serving the international water industry, provides an essential guide to exploring this key technology for resource recovery.

Stricter water quality standards have led to increased demand for efficient membrane filtration technologies such as nanofiltration.

1.1. Nanofiltration as a Circular Economy

Nanofiltration (NF) (Fig. 1) is a type of semipermeable membrane, a thin selective barrier used to filter liquids in many industries. Positioned between reverse osmosis and ultrafiltration, nanofiltration is the second densest membrane with a pore size ranging between 1–10 nanometers. Nanofiltration membranes are available in various configurations, with the most common being spiral membranes; however, hollow fibre membranes have gained popularity since Pentair X-Flow introduced them in 2013. While polymeric NF materials dominate the market, other options include ceramics and cellulose.

Pressure is required to push the liquid through the membrane, with the permeate passing through while the concentrate is rejected. Particles can be rejected not only by size exclusion, but also by the chemistry of the membrane surface, selectively attracting or repelling certain contaminants based on their charge or chemical affinity.

Nanofiltration can purify high-quality water with less energy consumption than reverse osmosis (RO). For applications that do not require the removal of high levels of dissolved salts, nanofiltration membranes can be a useful alternative to RO, capable of removing bacteria, viruses, organics, and divalent ions.

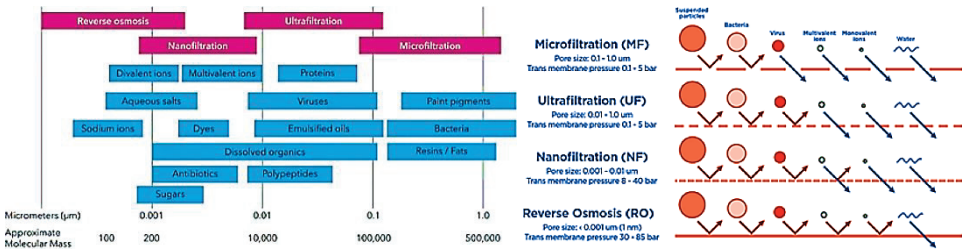

Fig. 1. Nanofiltration [1].

Nanofiltration was initially used for sulphate removal in the oil and gas sector, but now, it is applied for various purposes such as water softening, drinking water treatment, and purification of many industrial wastewater and brines. Recently, NF has also been employed for removing emerging contaminants from drinking water.

Nanofiltration aligns with the principles of the circular economy, primarily by reclaiming high-quality water suitable for reuse, but the recovery of other commodities such as biomass, minerals, and chemicals is gaining momentum in the market [1].

Nanofiltration should be used with fresh water and low-salinity brackish water if it contains heavy metals or microbiological contamination. In such situations, reverse osmosis will produce overly pure water that will need to be demineralized, increasing the cost and complexity of the purification system.

2. MAIN PROBLEMS: GOALS AND SOLUTIONS

2.1. Water Pollution and Nanotechnology [2]

How can nanotechnology be used to reduce water pollution?

Nanotechnology is utilized to address three very distinct water quality issues.

One problem involves removing industrial water contaminants from groundwater, such as a solvent used in cleaning called TCE (trichloroethylene). Nanoparticles can be employed to transform the contaminant through a chemical reaction to render it harmless. Research has shown that this method can effectively capture contaminants dispersed in underground aquifers at significantly lower costs than methods requiring pumping water from the ground for purification.

Another complex issue is the removal of salt or metals from water. The deionization method using electrodes made of nanofibers shows promise in reducing costs and energy requirements for converting saline water into potable water.

The third problem lies in standard filters being ineffective against viral cells. Currently, a filter with a diameter of just a few nanometers is being developed to be capable of removing viral cells from water.

3. MAIN TEXT. WATER POLLUTION: APPLICATION OF NANOTECHNOLOGY IN DEVELOPMENT

3.1. Research

Researchers at the University of Tokyo demonstrated the use of

fluorine nanochannels for salt removal from water.

Researchers at EPFL demonstrated a water filter powered by solar panels, which utilizes nanowires of titanium dioxide (TiO_2) and carbon nanotubes for water purification.

Researchers at Brown University demonstrated the creation of water filters using short channels between graphene sheets, allowing water to pass through but blocking larger contaminants.

Researchers at North-Western University developed a nanocomposite coating that can be applied to a sponge to absorb oil but repel water.

Researchers at Nagoya University demonstrated the use of amino-modified nanocarbons for removing heavy metal ions from water.

Researchers at RMIT University and the University of New South Wales demonstrated a filter made of nanosheets of aluminium oxide, which can filter water for both heavy metals and oils.

Researchers at the University of Cincinnati demonstrated a method for removing antibiotics contaminating waterways. The method utilizes vesicle nanoparticles that absorb antibiotics.

Researchers at the Pacific Northwest National Laboratory developed a material for removing mercury from groundwater. The material is called SAMMS, which stands for Self-Assembled Monolayers on Mesoporous Supports. This involves taking a ceramic particle with many nanosize pores on its surface and lining the nanopores with molecules containing sulphur atoms on one end, leaving a hole in the centre lined with sulphur atoms, as shown in the SAMMS figure. They line the nanopores with sulphur-containing molecules as sulphur binds to mercury, trapping mercury atoms inside the nanopores.

3.2. Usage

–Nanosponges with a reactive nanoparticle layer covering a synthetic core that easily magnetizes. For example, silver nanoparticles, if bacteria are a problem, attach to pollutants or kill them. Then, when a magnetic field is applied, the nanosponges are removed from the water.

–Pellets containing nanostructured palladium and gold as catalysts for breaking down chlorinated compounds polluting groundwater. Since palladium is very expensive, researchers formed pellets of nanoparticles that allow nearly every palladium atom to react with chlorinated compounds, reducing processing costs.

–Enzyme-functionalized micromotors for removing carbon dioxide from water.

–Graphene oxide for removing radioactive material from water. Re-

searchers found that graphene oxide patches absorb radioactive ions in water. Then, graphene oxide forms clumps that can be removed from water for disposal.
–Graphene as membranes for inexpensive water desalination. Researchers have found that graphene with nanopores a nanometer or less in size can be used to remove ions from water. They believe this can be used for desalinating seawater at a lower cost than reverse osmosis methods currently used.
–Carbon nanotubes as pores in reverse osmosis membranes. This can reduce the power required to operate reverse osmosis desalination plants as water molecules pass through carbon nanotubes more easily than through other types of pores. Other researchers are using carbon nanotubes to develop small inexpensive water purification devices needed in developing countries.
–Carbon nanotubes for oil spill clean up. Researchers found that adding boron atoms during carbon nanotube growth results in the nanotubes growing into a sponge-like structure that can absorb oil many times its weight.
–Nanoparticle-like hairs (nanohairs) for capturing and measuring mercury contamination levels in water.
–Integration of nanomembranes with solar energy to reduce the cost of seawater desalination.
–Iron nanoparticles for cleaning groundwater from tetrachloroethylene contamination.
–Addition of graphene oxide to sand filters to enhance their ability to remove pollutants from water.
–Silver chloride nanowires as photocatalysts for decomposing organic molecules in polluted water.
–Electrified filter consisting of silver nanowires, carbon nanotubes, and cotton for bacteria eradication in water.
–Nanoparticles capable of absorbing radioactive particles polluting groundwater.
–Iron nanoparticle coatings allowing them to neutralize dense hydrophobic solvents polluting groundwater.
–Nanodroplet mats for absorbing oil spills.
–Iron oxide nanoparticles for arsenic removal from water wells.
–Carbon nanotubes with a gold tip for capturing oil droplets polluting water.

Antimicrobial nanofibers and activated carbon in a disposable filter as an inexpensive means of purifying contaminated water.

3.3. Nanofiltration is Sometimes Used for Wastewater Treatment

It provides higher flow rates and consumes less energy than reverse osmosis systems. The design and operation of nanofiltration are

very similar to 'nanofiltration, considerably similar to reverse osmosis', with some differences.

The main difference is that the nanomembrane is not as 'tight' as the reverse osmosis membrane. It operates at a lower feed water pressure and does not remove monovalent (*i.e.*, those with one charge or valence) ions from water as effectively as the RO membrane.

While an RO membrane typically removes 98–99% of monovalent ions such as chlorides or sodium, a nanofiltration membrane typically removes 50% to 90%, depending on the membrane material and manufacturing. Due to its ability to remove effectively divalent and trivalent ions, nanofiltration is often used for water softening, leaving a smaller impact on the overall content of dissolved solids than RO. For this reason, it is called a 'softening membrane'. Nanofiltration is often used to filter water with low levels of dissolved solids, remove organic matter, and soften water.

As it is a 'looser membrane', nanofiltration membranes are less likely to foul or scale and require less pretreatment than reverse osmosis systems. Sometimes it is even used as pretreatment for reverse osmosis.

Nanofiltration can be used in various water and wastewater treatment applications for economically efficient removal of ions and organic matter.

In addition to water purification, nanofiltration is often used in the manufacturing process for pharmaceuticals, dairy products, textiles, and bakeries.

In particular, WaterProfessionals® have extensive experience in

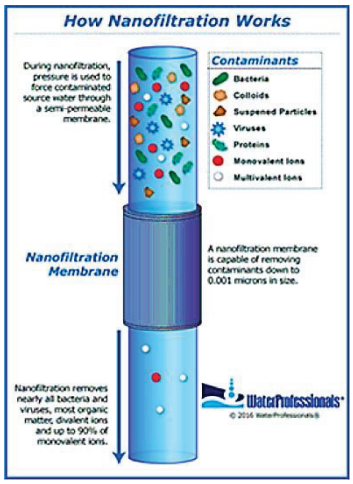

Fig. 2. How nanofiltration works [3].

applying nanofiltration systems to address water purification challenges (Fig. 2).

3.4. Sea Water Reverse Osmosis (SWRO) Systems on Maritime Vessels

Steam vacuum systems from leading manufacturers such as Alfa Laval, Mitsubishi, and others, according to design documentation, are expected to produce high-quality distillate on-board maritime vessels. However, in practice, due to changes in the operation modes of the main engine, the temperature of the water in the internal circuit of the engine, which serves as the heat carrier of the ship's desalination plant, may vary. As a result, the obtained distillate may not always meet the 1.5-ppm standard after desalination. The obtained permeate does not meet the quality standard, leading to fouling of the internal circuit of the main engine's diesel generators. This increases the deposition of solid scale and loose sludge in the engine rooms of internal combustion maritime diesel engines (ICME) and boiler drums, requiring additional use of expensive reagents for water treatment.

Currently, on new vessels, Sea Water Reverse Osmosis Systems (SWRO) are being additionally installed alongside existing steam vacuum systems, reducing energy costs for desalinating seawater.

Energy costs can be analysed using reversible thermodynamic processes. From thermodynamic principles, it follows that any water desalination method will be most efficient if it includes a thermodynamically reversible process. Energy calculation to determine a reversible system serves as the lower bound of energy for any other process [4].

To obtain large volumes of freshwater, a significant amount of seawater must be used, where, as a result of desalination, we obtain pure permeate and highly concentrated NaCl brine, which is completely drained overboard.

The ratio of produced freshwater to the volume of seawater required to obtain freshwater is called the water recovery coefficient—a.

In practice, a reverse osmosis desalination system cannot be a reversible process; there will always be losses depending on the coefficient.

$$a = \frac{V}{V + V_0}, \tag{1}$$

where V is the volume of fresh water ('sweet-water') produced; V_0 is the volume of water remaining after the desalination process has not been converted into fresh water ('sweet-water'). It is usually

called brine or concentrate.

For example, if the system processes 1000 L of seawater: $V + V_0 = 1000$ L and, at the same time, receives 400 L of fresh water: $V = 400$ L, and 600 L remain as brine, then, the water recovery coefficient will be:

$$a = 400/(400 + 600) = 400/1000 = 0.4.$$

This means that 40% of the original seawater was converted into fresh water.

Actual work considering losses are in a formula, more specifically taking into account osmotic pressure and water volume. This formula takes into account that the volume of seawater exceeds the volume of fresh water ('sweet-water') by the water recovery coefficient:

$$W = PV\left(\frac{1}{a} - 1\right), \tag{2}$$

where P is the osmotic pressure, V is the volume of pumped water.

For most engineering calculations, this simplified version of this formula is used, which directly relates the volume of fresh water to osmotic pressure and water recovery coefficient.

Another example. Let us say we need to get 100 L of fresh water. Osmotic pressure P is of 5 bar (this is approximately of 0.5 MPa). The water recovery coefficient a is of 0.4 (40% of the original seawater is converted into fresh water).

The actual work done by W is of 0.075 MJ (megajoules).

To convert into more convenient units, for example, kWh, you can use the following conversion:

$$1 \text{ MJ} = 0.27778 \text{ kWh}.$$

So, to obtain 100 L of fresh water under these conditions, it is necessary to expend approximately 0.0208 kWh of energy.

It is sufficient to provide an example by comparing the Alfa Laval VSP-36-C-125 steam vacuum unit, which has a capacity of 36 m^3/day, with a permeate quality of 1.5 ppm and consumes 52 kWh/m^3 [5]. In reverse osmosis units, energy consumption will be five to ten times lower depending on the membranes used [6].

In recent years, reverse osmosis systems have gained widespread popularity for water purification and desalination, with the use of nanotechnology.

The FiiZK Aqua membrane filtration technology (see, for instance, https://fiizk.com/en/news-from-fiizk/water-purification-and-desalination-solutions-for-land-based-farming-and-parasite-control/)

Applications

Membrane Filtration	Pore Size (µm)	Raw Water Source	Desalinated	Application
Ultrafiltration (UF)	0.01 – 1.0	Sea water	No	Intake water for land-based facilities
Nanofiltration (NF)	0.001 – 0.01	Sea Water Brackish water Salty groundwater	Partially (3-22 ‰)	Prevention & treatment of parasitesIntake water for land-based facilities
Reverse Osmosis (RO)	< 0.001	Sea water	Yes (0.3 ‰)	Intake water for land-based facilities

Fig. 3. Applications (MF)/Seawater [3].

utilizes membrane filtration to stop unwanted substances. The use of membranes is intended to prevent contamination by organic and biological contaminants (parasites, bacteria, and viruses).

The membrane pore size determines the fraction that can be retained through filtration and our installations offer means for (Fig. 3):

–ultrafiltration (UF; pore size of 0.01–1.0 µm),
–nanofiltration (NF; pore size of 0.001–0.01 µm),
–reverse osmosis (RO; pore size < 0.001 µm).

A significant drawback of using SWRO systems in the maritime fleet is the high operating pressure of up to 100 bar required to achieve the quality standards of the obtained permeate. All types of installations are compelled to flush the working membranes from heavy metals, salts, and other inclusions, and discharge them overboard along with the brine, causing significant harm to the marine environment and biodiversity.

4. DISCUSSION

In earlier works, the authors proposed a catalyst capable of obtaining crystalline salt from the brine obtained during seawater desalination with minimal costs, using modern crystallizers to produce technical-grade salt in maritime conditions.

The scientific breakthrough in creating nanotubes, which subsequently found application in the production of nanomembranes for seawater desalination in SWRO installations, provided enormous potential for reducing energy consumption and operating pressure from 80 bars to 3 bars. The material used to produce nanotubes consists of sheets of carbon atoms. Their density is so high that only seven water molecules can pass through their cells, and the rate

of seawater passage through nanotubes is 5000 times higher than in synthetic membranes. This effect has not found a complete explanation in science and requires further study. The quality of the obtained fresh water is 0.5 ppm, and energy consumption does not exceed 2 kWh/m^3 [7, 8].

According to the authors of the article, a decision has been made to propose the creation of a nanodischarge automated filter with disks made of nanocarbon tubes in the development and testing of a ballast water treatment/disinfection system created at the Danube Institute of the National University 'Odesa Maritime Academy' (Izmail, Odesa region, Ukraine) in accordance with the IMO Convention D-2 quality standard (Fig. 4).

Such a filter will significantly reduce the labour costs of the ship's crew for the production of high-quality distillate and improve the cleaning and flushing of the filtering elements of the modern SWRO ship system.

The advantage of the self-cleaning filter lies in providing the installation with a high level of invasive species destruction in ballast water treatment. The disc filter is used for filtering fine-dispersed suspensions; it consists of a housing in which a hollow shaft with perforated discs mounted on bearings is connected to the shaft cavity (Fig. 4).

Filtration cloth is fastened to the surface of the discs using clamps. During filtration, the shaft with the discs remains stationary, and the filtrate passes through the filtering partition inside the discs, then into the hollow shaft, and is discharged from the top. A sediment layer forms on the upper and lower surfaces of the

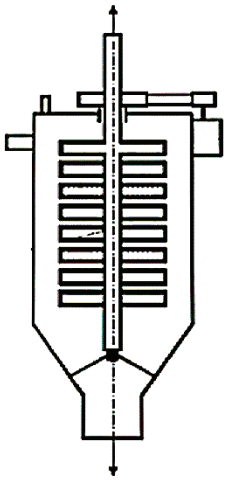

Fig. 4. View of the disc self-cleaning filter [4].

discs. After filtration is completed, the suspension is drained, and flushing liquid is supplied inside the shaft and discs, while the shaft with the discs is rotated by an electric drive.

Due to centrifugal forces, sediment is removed from the discs and discharged from the bottom of the filter. Then the filtration and flushing cycles are repeated. The positive quality of the filter is automatic sediment discharge.

The application of existing technologies from such company as CJC™ for purifying circulating lubricants and heavy fuel for ship engines provides the authors with practical experience and acquired expertise. Regarding ballast water treatment, proposed fine purification filters can be successfully applied since the density of oil is significantly higher than the density of ballast water, which increases the fluid's permeability.

5. CONCLUSION

According to experts, nanotechnologies will become a driving force of the industrial revolution and will change our way of life. Research and development in nanotechnologies are on the rise in the pursuit of original and useful things, and while there is a boom in factory production, little is being done to ensure the safety of society and the environment.

According to the National Science Foundation of the U.S.A., over the next decade, nanotechnologies are expected to 'capture' 1 trillion dollars of the world market. Nanotechnologies promise enormous potential benefits in improving almost all types of industrial products. However, on the other hand, the question arises: are they safe? The increasing number of scientific studies and government reports warns that created nanoparticles may pose a danger to human health and the environment, although there have been few studies on their toxicity.

Considerable efforts have been made to overcome the shortage of clean water, and nanotechnologies are a strong candidate for rapid development. Research and commercialization of polymer RO and NF membranes began in the early 1960s. So far, two types of membranes dominate the water desalination market: cellulose-based membranes (CA) and thin-film composite membranes (TFC). The most representative products, such as TS40, TS80, and AD-90, were developed over 30 years ago, and since then, there have been no significant changes due to low production costs and a high level of salt rejection. New research directions in barrier layers of TFC membranes include improving resistance to contamination, as well as chemical and thermal stability. Meanwhile, microporous supports can be optimized to increase mechanical strength and permeability.

Inorganic RO and NF membranes have been studied on a laboratory scale for water purification since the 1980s. The most typical ceramic membranes are metal-oxide membranes and carbon-based membranes. The main method for synthesizing metal oxide membranes is the sol–gel technique, which requires further optimization for particle size and distribution control. The efficiency of mixed matrix membranes (MMMs), made from both organic and inorganic nanomaterials, is excellent, but they are too expensive compared to other membranes. Therefore, it is important to understand the economic competitiveness of MMMs, as well as their potential application.

Although nanotechnologies are leading the way in the development of RO and NF membranes for water purification, there are still technical and scientific problems that need to be addressed before more advantages can be gained. Despite the difficulties that need to be overcome, it is very likely that ceramic membranes will be commercialized and industrialized in water purification and desalination in the near future [9].

Thus, nanotechnologies encompass a wide range of technologies for controlling the structure of matter at the atomic and molecular levels. A nanometer is one billionth of a meter, the length of a chain of 10 adjacent hydrogen atoms; the thickness of a human hair is approximately 80.000 nanometers. It is difficult to imagine something so small, let alone believe that it can be used in manufacturing processes [10].

At such a microscopic level, matter behaves differently than in our everyday life in this world dominated by 'classical Newtonian physics'. In the nanoworld, 'the properties of matter are determined by a complex and rich combination of classical physics and quantum mechanics', as stated in an exclusive online issue of Scientific American in January 2006. Moreover, in larger quantities, miniature nanomaterials can have enormous power due to their significantly higher surface area to volume ratio. As the particle size decreases and its reactivity increases, a substance that may be inert on a micro or macroscale can acquire hazardous properties on a nanoscale [11].

Regarding social and ethical issues, according to Vital Signs 2006–2007, serious concerns are not limited to safety and health impact; broader social and ethical implications need to be studied.

As with other forms of black carbon, such as carbon nanotubes, there is an increasing risk to the environment and/or public concern that graphene-based/(restored) *r*GO (GO—graphene oxide) nanomaterials will be found in natural water bodies due to their diverse applications. In addition, these nanomaterials may play an important role in biogeochemical activity due to their high mobility in

the environment. These nanoadsorbents may also contain various toxic chemicals due to potential impurities.

Therefore, comprehensive research is needed to develop environmentally friendly methods for producing clean nanomaterials based on graphene/(restored) *r*GO and to assess the toxicity and biocompatibility of these nanomaterials.

'The nanotechnological revolution is driven by profit—it is not a necessity for human development; as long as poverty and social injustice are fundamental problems, new technologies will never be a universal solution to them', as stated in the Vital Signs report.

REFERENCES

1. *Wastewater*; https://www.aquatechtrade.com/news/wastewater/emerging-resource-recovery-opportunities-nanofiltration
2. *Nano. Understanding*; https://www.understandingnano.com/water.html
3. *Waterprofessionals*; https://www.waterprofessionals.com/learning-center/nanofiltration/#:~:text=Nanofiltration%20is%20often%20used%20to,pretreatment%20than%20reverse%20osmosis%20systems
4. Uri Lachish, *Osmos Reverse Osmosis and Osmotic Pressure What They Are*, (*guma science*); https://urila.tripod.com/
5. J. Kucera, *Reverse Osmosis—Industrial Applications and Processes* (Wiley–Scrivener Publishing LLC: 2010).
6. A. G. Danylyan, *Automation of Ship Technical Equipment*, **17**: 24 (2011); http://mail.onma.edu.ua/index.php?nauka-asts_ru
7. Aditi Risbud, *Cheap Drinking Water from the Ocean. Carbon Nanotube-Based Membranes Will Dramatically Cut the Cost of Desalination*; https://www.technologyreview.com/2006/06/12/228982/cheap-drinking-water-from-the-ocean/
8. Kevin Bullis, *A Cheaper Way to Clean Water. Oasys Water Says It Will Test Complete, Large-Scale Systems Using Forward Osmosis Early Next Year* (December 16: 2010); https://www.technologyreview.com/2010/12/16/89485/a-cheaper-way-to-clean-water/
9. *A Review on Reverse Osmosis and Nanofiltration Membranes for Water Purification*; https://www.ncbi.nlm.nih.gov/pmc/articles/PMC6723865/
10. F. Rahman, *Nanostruktury v Ehlektronike i Fotonike* [Nanostructures in Electronics and Photonics] (Moskva: Tekhnosfera: 2010) (in Russian).
11. Yu. I. Golovin, *Nanotekhnologicheskaya Revolyutsiya Startovala!* [Nanotechnology Revolution Has Started!] (in Russian); http://www.abitura.com/modern_physics/nano/nano2.html

Наносистеми, наноматеріали, нанотехнології
Nanosistemi, Nanomateriali, Nanotehnologii
2025, т. 23, № 2, сс. 379–392
https://doi.org/10.15407/nnn.23.02.0379

© 2025 ІМФ (Інститут металофізики
ім. Г. В. Курдюмова НАН України)
Надруковано в Україні.

PACS numbers: 61.46.-w, 61.48.De, 65.80.-g, 66.20.Ej, 83.80.Hj, 83.80.Nb, 91.60.-x

Research on the Influence of Nanoadditives on the Thermodynamic and Hydrodynamic Stability of the Solidification Structure of the Ettringite Phase and Its Composition with Calcium Sulphates

H. M. Hryshko, Yu. L. Savin, D. O. Smolin, O. W. Vatazhyshyn, and V. I. Mospan

Ukrainian State University of Science and Technologies,
Educational and Scientific Institute
'Prydniprovs'ka State Academy of Civil Engineering and Architecture',
24[a], Architect Oleh Petrov Str.,
UA-49005 Dnipro, Ukraine

The paper considers influence of various factors on the stability of the ettringite structure of two forms of formation: *a*—on the base of pure minerals $C_3A + C\dot{S}H_2$, *b*—a mixture of alumina cement (AC-400) and gypsum plaster (G5); besides, a model of hydration process using the example of calcium sulphate hemihydrate is presented. Factors affecting stability of ettringite depending on changes in humidity and pH of the environment, temperature, and operating conditions are established. It is confirmed the hypothesis of the effect caused by the ratio $G = f(CaO/Al_2O_3)$ in the minerals of the $CaO–Al_2O_3–H_2O$ system on the Gibbs surface energy: for $CA_2 = 0.27$, $\Delta G = 24.70$; for $CA = 0.54$, $\Delta G = 51.86$; for $C_{12}A_7 = 0.8$, $\Delta G = 141.00$, for $C_3A = 1.63$, $\Delta G = 145$. It is also determined the dependence of the order of formation of hydrate compounds during hydration of aluminate and sulphoaluminate cements on the Gibbs surface energy $\Delta G = f(Da)$ and the ratio $\Delta G = f(CaO/Al_2O_3)$ for the minerals of the system by means of the average Gibbs energy (for CA_2, 24.70; for CA, 51.86; for $C_{12}A_7$, 141.00; for C_3A, 145) of the system $CaO–Al_2O_3–H_2O$: C_2AH_8, C_4AH_{13}, C_4AH_{10}, CAH_{10}, $Al(OH)_3$. Change in the heat of hydration of pure clinker minerals over time and change in their degree of hydration depend on the value of the coefficients. For example, the coefficient K ($mCaO/nAl_2O_3$ ratio) is the largest for C_3A mineral, *i.e.*, 1.63, and the heat of hydration is correspondingly the highest for C_3A mineral and is of 873 J/g on the 28th day; therefore, accordingly, C_3A mineral will enter the hydration reaction as the fastest. An increase in temperature is detected for artificially formed ettringite in the $C_3A + C\dot{S}H_2$ system followed by $CA + C\dot{S}H_2$ and $CA_2 + C\dot{S}H_2$ that confirms the main idea of the experiments.

Stabilization of the ettringite phase is carried out by means of the nanomodification with carbon nanotubes (CNTs), taurite, and silicon dioxide. Results of investigations performed confirm a 4–5-fold increase in strength indicators, a change in the softening factor depending on the type of nanomodifier and systems with different plasticizers and nanotubes.

В роботі розглянуто вплив різних чинників на стабільність структури еттрингіту двох форм утворення: *а*) на основі чистих мінералів $C_3A + C\dot{S}H_2$, *б*) суміші глиноземистого цементу (ГЦ-400) і гіпсу будівельного (Г5); також представлено модель процесу гідратації на прикладі напівводяного сульфату Кальцію. Встановлено чинники впливу на стабільність еттрингіту від зміни вологости та pH середовища, температури, умов експлуатації. Підтверджено гіпотезу впливу співвідношення $G = f(CaO/Al_2O_3)$ в мінералах системи $CaO–Al_2O_3$ на Ґіббсову поверхневу енергію: $CA_2 = 0{,}27$ — $\Delta G = 24{,}70$, $CA = 0{,}54$ — $\Delta G = 51{,}86$, $C_{12}A_7 = 0{,}8$ — $\Delta G = 141{,}00$, $C_3A = 1{,}63$ — $\Delta G = 145$; визначено залежність порядку формування гідратних сполук за гідратації алюмінатних і сульфоалюмінатних цементів від Ґіббсової поверхневої енергії $\Delta G = f$(а.о.м.) і співвідношення $\Delta G = f(CaO/Al_2O_3)$ для мінералів системи за середньою Ґіббсовою енергією: CA_2 — 24,70, CA — 51,86, $C_{12}A_7$ — 141,00, C_3A — 145 системи $CaO–Al_2O_3–H_2O$: C_2AH_8, C_4AH_{13}, C_4AH_{10}, CAH_{10}, $Al(OH)_3$. Зміна теплоти гідратації чистих клінкерних мінералів у часі та зміна їхнього ступеня гідратації залежать від величини коефіцієнтів. Наприклад, коефіцієнт K (співвідношення $mCaO/nAl_2O_3$) є найбільшим для мінералу C_3A — 1,63, а теплота гідратації, відповідно, найвища у мінералу C_3A і становить на 28 добу 873 Дж/г; тому, відповідно, мінерал C_3A буде найшвидше вступати в реакцію гідратації. Виявлено підвищення температури для штучно утвореного еттрингіту в системі $C_3A + C\dot{S}H_2$, далі $CA + C\dot{S}H_2$ і $CA_2 + C\dot{S}H_2$, що підтверджує основну ідею дослідів. Проведено стабілізацію еттрингітової фази за рахунок наномодифікування вуглецевими нанотрубками (ВНТ), тауритом, діоксидом Силіцію. Наведені результати досліджень підтверджують збільшення в 4–5 разів міцнісних показників, зміну коефіцієнта розм'якшення в залежності від виду наномодифікатора та систем з різними пластифікаторами і нанотрубками.

Key words: nanomodifying, alumina cement, carbon nanotubes, hydration, nanosystem, solidified structure.

Ключові слова: наномодифікування, глиноземистий цемент, вуглецеві нанотрубки, гідратація, наносистема, затвердла структура.

(Received 20 June, 2024; in revised form, 26 June, 2025)

1. PROBLEM STATEMENT

The need for the production of the latest building materials for the

repair and construction of high-quality buildings is constantly increasing and requires a solution [1–4].

The rapid pace of construction of buildings and structures requires rapid dismantling of monolithic structures, increasing the reversibility of forms during the factory production of building structures. In monolithic construction, such technologies are possible when using fast-hardening binders, which can gain up to 90–100% strength after 1–3 days. This also applies to the emergence of 3*D*-construction technologies.

In addition, during the war and post-war years, the restoration of construction objects, thermal units of metallurgical plants as well as production of building materials and reconstruction of existing objects are possible only within short periods of time, and such processes may include the use of composites based on alumina cement and gypsum, which, in the early hardening periods, have high indicators of strength properties.

In this regard, a particular attention should be paid to aluminate, sulphate and sulphoaluminate binders [3–6].

One of the problems of their use consists in recrystallization of sulphoaluminates during hardening and insufficient stabilization of the ettringite phase during operation [3, 5].

Therefore, studies of the structure and durability of the ettringite phase and its composition with calcium sulphates are relevant.

2. RESULTS AND DISCUSSION

Based on the analysis of literary sources of Ukrainian and foreign scientists [1–3], it was concluded that there is a need to solve the problem of developing compositions of composite binders based on the $CaO–Al_2O_3–SO_3$ system, surfactants with high structure density and strength indicators by means of stabilizing the state of the ettringite component. This will contribute to the intensification of the construction period and to the formation of a durable concrete strong structure.

After conducting an analysis of possible directions for formation of the concrete structure, a hypothesis was proposed about the possibility of:

– stabilization of the ettringite phase by means of modification with nanoadditives; in order to solve this problem, it is necessary to determine the conditions under which the ettringite phase goes into an unstable state;

– the technology of introducing nanoadditives and studying solutions with the maximum amount of ettringite for the stability of their structure and mineral composition of the $CaO–Al_2O_3–SO_3–H_2O$ system.

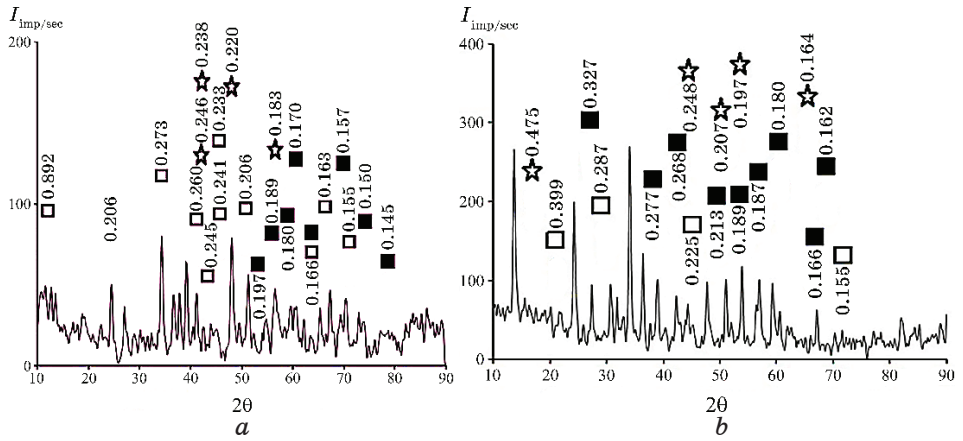

Fig. 1. X-ray diffractograms of samples made of the composition $C_3A–C\dot{S}H_2$ on the 3rd day of hardening (*a*) and on the 28th day of hardening (*b*); ■—ettringite $3CaO·Al_2O_3·3CaSO_4·31H_2O$; □—ettringite $3CaO·Al_2O_3·3CaSO_4·12H_2O$; ★—tetracalcium nineteen-hydroaluminate $3CaO·Al_2O_3·19H_2O$.

The cited results of research into the hydration processes of the pure $C_3A–C\dot{S}H_2$ system showed that three periods of formation are visible in the life cycle of ettringite: primary ettringite (hardening, Fig. 1, *a*), secondary ettringite (Fig. 1, *b*), and recrystallization during operation.

Thus, in the $C_3A–C\dot{S}H_2$ system (Fig. 1, *a*), after 3 days of hardening, the main lines of hydrated ettringite phases appear (d/n = 0.892, 0.273, 0.260, 0.245, 0.241, 0.233, 0.197, 0.189, 0.180, 0.170, 0.166, 0.163, 0.150, 0.145 nm), $4CaO·13H_2O$ (d/n = 0.246, 0.220, 0.183 nm) (Fig. 1).

After 28 days of hardening, there is an increase in the intensity of the main interplanar distances and hydrated phases $C_3AC_3H_{32}$ (d/n = 0.475, 0.399, 0.327, 0.2773, 0.2680, 0.225, 0.2130, 0.189, 0.187, 0.180, 0.166, 0,162, 0.155 nm) (Fig. 6, *b*). $4CaO·Al_2O_3·13H_2O$ lines (d/n = 0.475, 0.248, 0.207, 0.197, 0.164 nm) are observed (Fig. 1, *b*).

Further, to determine the factors and conditions of stability of the ettringite phase for compositions based on aluminate and sulphate components and sulphoaluminate cements, studies of the stability of the ettringite phase with changes in humidity and pH of the environment, temperature, and operating conditions were conducted (Figs. 2–4).

The rate of heat release, total heat release, temperature and intensity of reactions of the hydration process depend on the ratio $\Delta G = f(CaO/Al_2O_3)$ of CaO, Al_2O_3 molecular weights. As is customary in the work, this ratio is defined as the coefficient of dependence of

the Gibbs surface energy on the molar mass ratio. The higher the mineral coefficient and the Gibbs surface energy, the higher the exothermic rate of hydration and the total heat release (Fig. 2) [18].

The composition with a C_3A mineral content of 70%, 150–200 J/g C_3A has the highest exothermic rate during C_3A hydration in the C_3A–$C\dot{S}H_2$ system with different $C\dot{S}H_2$ content (Fig. 2, *b*). Because its surface energy is 2.8-times higher than that of C*A* and 5.8-times higher than that of CA_2. Thermodynamic curves characterize the rate of the hydration process and the influence caused by the ettringite formation phase on the structure of the mixture and, accordingly, on its properties.

In addition, the surface energy and specific surface area affect the formation of ettringite crystals, which subsequently creates

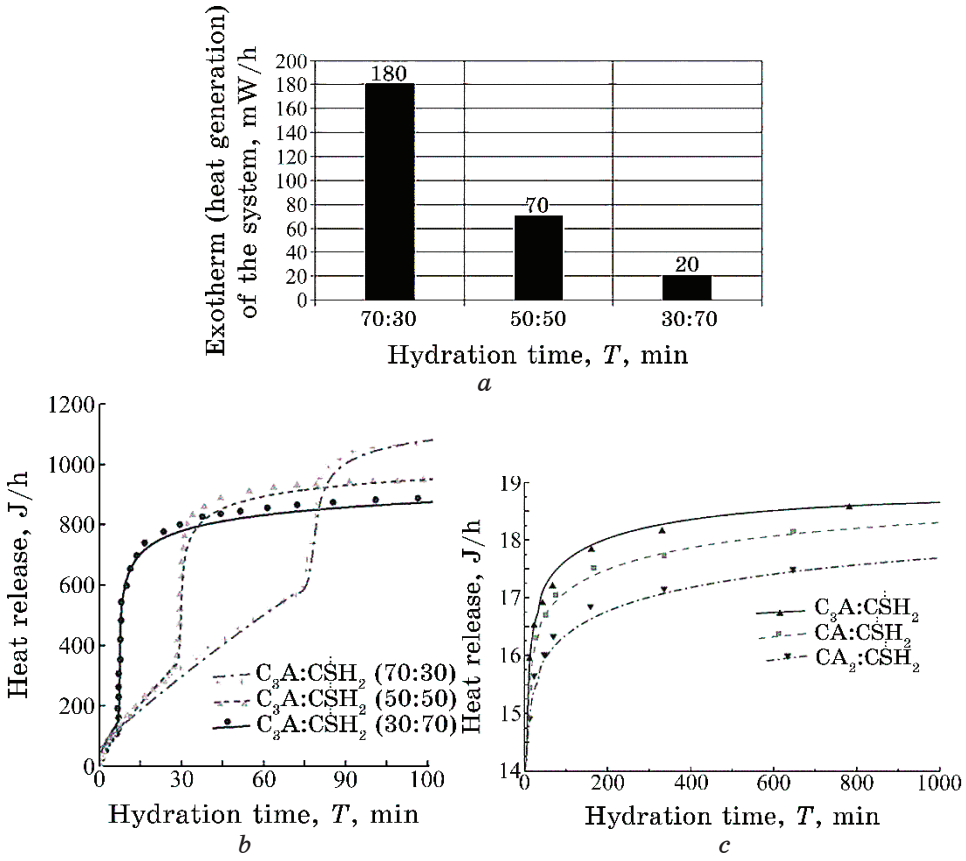

Fig. 2. Thermodynamic characteristics of the $C_3A + C\dot{S}H_2$ system: (*a*) exothermic histograms (mW/h); (*b*) heat release (J/g) [18]; (*c*) hydration temperature of $CA + C\dot{S}H_2$, $CA_2 + C\dot{S}H_2$, $C_3A + C\dot{S}H_2$ systems [18].

prerequisites for recrystallization in the process of system hardening (Fig. 3) [18].

The study of the influence of external factors was carried out,

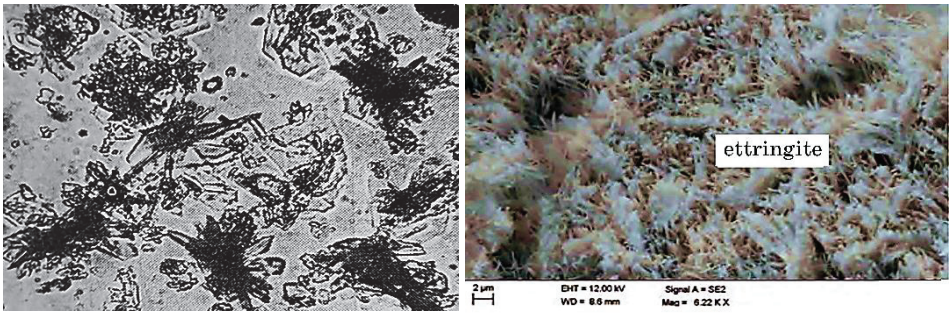

a *b*

Fig. 3. Photomicrographs of the $C_3A + C\dot{S}H_2$ structure depending on the heat release of the system: *a*—$C_3A + C\dot{S}H_2$ (70:30); *b*—*AC* + Gypsum (30:70) [18].

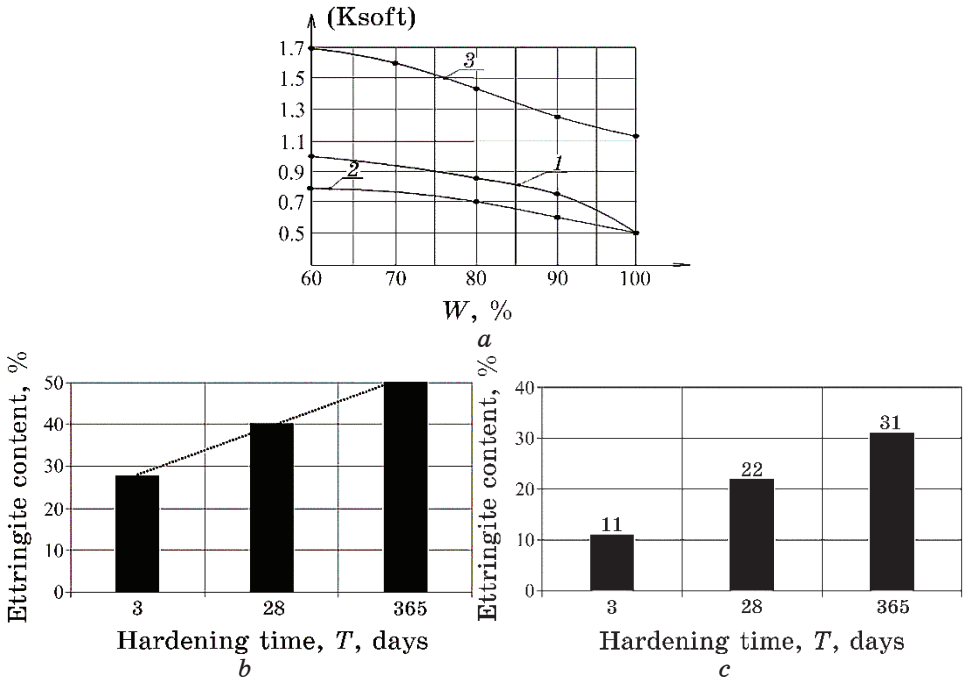

a *b* *c*

Fig. 4. Graphs of dependence [18]: coefficient of softening K_{soft} (*a*) on the medium with variable humidity of samples containing: *1*—C_3AH_6 hydrate, *2*—$C_3AC_3H_{32}$ mineral, *3*—*AC*:G; change in ettringite content over time: *b*—$C_3A + C\dot{S}H_2$, *c*—*AC* + Gypsum [18].

e.g., humidity for 3 days (Fig. 4, *a*). Change of the ettringite phase over time of nanomodified samples under normal conditions (Fig. 4, *b*, *c*).

Due to the high cost of pure minerals, it was decided to conduct further studies of the ettringite phase formed on the basis of the *A*C + G composition (intended to replace alumina cement 70:30 and modify gypsum binders with the *A*C:G composition (30:70)).

Stability of ettringite crystals depends on the morphology of the crystals formed under different conditions, for example, on the pH value. The pH range of 11–12 provides a needle-like form of ettringite [7–10]. As the pH value increases, the length and thickness of needle fibres of ettringite decreases. At a pH greater than 13, ettringite has an x-ray amorphous gel-like structure (Fig. 5) [18].

Study of the stability of the ettringite phase of the *A*C:G (70:30) system. Stabilization was carried out with nanomodifiers—taurite, silicon dioxide, nanotubes, SiC after determining the effect of surfactants. The following additives were used as plasticizers: Sika Viscocrete G, MC Bauhemi 2695, and Stachema STP 156. The smallest reduction in W/T and the best indicators of the main physicomechanical and technological properties are achieved using the Sika Viscocrete G additive: W/T for the *A*C:G composition (70:30) is of 0.27 compared to 0.32 without plasticizer, compressive and flexural strength is of 19 MPa and 14 MPa, respectively [1].

In the compositions after three days of hardening, in the compositions of alumina cement *A*C-40 gypsum grade G-5, after 3 days of hardening, the main interplanar distances and intensities of hydrated phases $C_3AC_3H_{32}$ ($d/n = 0.973$, 0.561, 0.388, 0.348, 0.256 nm) appear

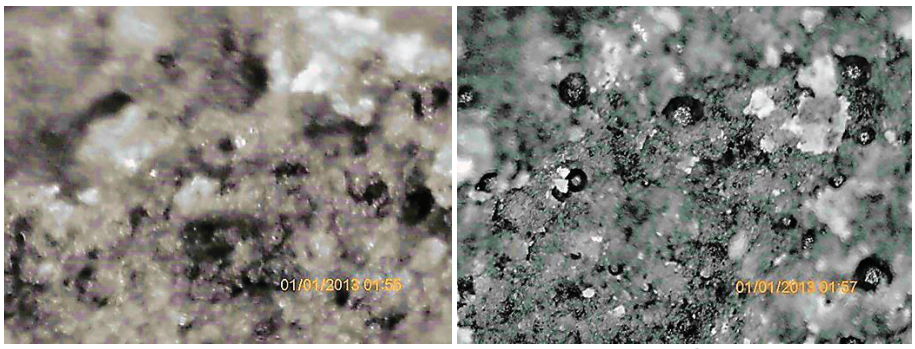

a *b*

Fig. 5. The influence of the environment temperature on the structure and morphology of samples made of the composition of *A*C:G (70:30) on the 3rd day of hardening under normal conditions in running water (*a*) and on the 3rd day of hardening at an elevated temperature of 40–50°C (*b*) [18].

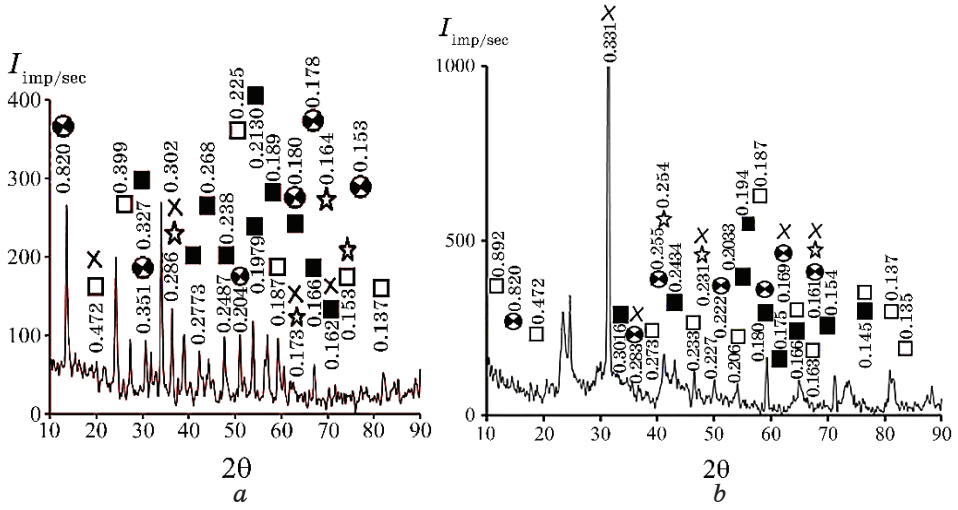

Fig. 6. X-ray diffractograms of samples made of the composition *A*C:G (70:30) on the 3rd day of hardening (*a*) and on the 28th day of hardening (*b*); ■—ettringite $3CaO{\cdot}Al_2O_3{\cdot}3CaSO_4{\cdot}31H_2O$; □—ettringite $3CaO{\cdot}Al_2O_3{\cdot}3CaSO_4{\cdot}12H_2O$; ⊗—hydroaluminate $Ca_4O{\cdot}Al_2(OH)_{14}{\cdot}6H_2O$; ★—tetracalcium nineteen-hydroaluminate $4CaO{\cdot}Al_2O_3{\cdot}19H_2O$; —tetracalcium thirteen-hydroaluminate $4CaO{\cdot}Al_2O_3{\cdot}13H_2O$.

(Fig. 10). The observed lines are as follow: $4CaO{\cdot}Al_2O_3{\cdot}13H_2O$ (d/n = 0.423, 0.266, 0.246, 0.238, 0.212, 0.168 nm), $4CaO{\cdot}Al_2O_3{\cdot}19H_2O$ (d/n = 0.331, 0.238, 0.151 nm), $Ca_4Al_2(OH)_{14}{\cdot}6H_2O$ (d/n = 0.463, 0.255, 0.176, 0.151 nm) (Fig. 6).

In the process of hardening, after 3 days, intensity of ettringite and calcium hydroxide lines appears and increases, which confirms the fact of the intensified hydration process (Fig. 6, *b*).

When modified with nanoadditives, the structure of samples with increased surface energy of the solid phase is formed as a result of an increase in the number of crystallization centres, and as a result, the structure is formed more quickly.

During the hardening process, the structure will have the property to deform [10–17]. At the same time, the tubes play a reinforcing role between the blocks [6].

Nanotubes and nanoadditives are entered into the crystal structure and alloying it.

As a result of modification with nanoadditives, an increase in the strength indicators of composite materials was achieved: for *A*C:G (70:30)% + 0.18% nanotubes + 0.4% Sika, up to 70.2 MPa compared to 14.67 MPa of the reference composition *A*C:G (70:30)%; for *A*C:G (70:30)% + 0.75% taurite + 0.4% Sika, up to 66.40 MPa; for *A*C:G (70:30)% + 1.0% silicon dioxide + 0.4% Sika, up to 60.73 MPa.

The softening coefficients increase accordingly: when *A*C:G (70:30)% is modified with nanotubes, up to 1.16; when it is modified with taurite, up to 1.02; when it is modified with silicon dioxide, up to 1.07 (Fig. 7).

Research on the compressive strength limit of samples modified with nanotubes over time showed that the composition with the optimal content of ettringite *A*C:G (70:30) at the age of three days has a compressive strength of 70.2 MPa, while, for the base composition, it is 14.7 MPa (Fig. 8).

The issue of the proposed hypothesis of increasing the stability of the ettringite phase due to modification with nanoadditives was considered.

The developed model of the hydration processes of mineral binders (on the example of gypsum binders) is presented in the form of

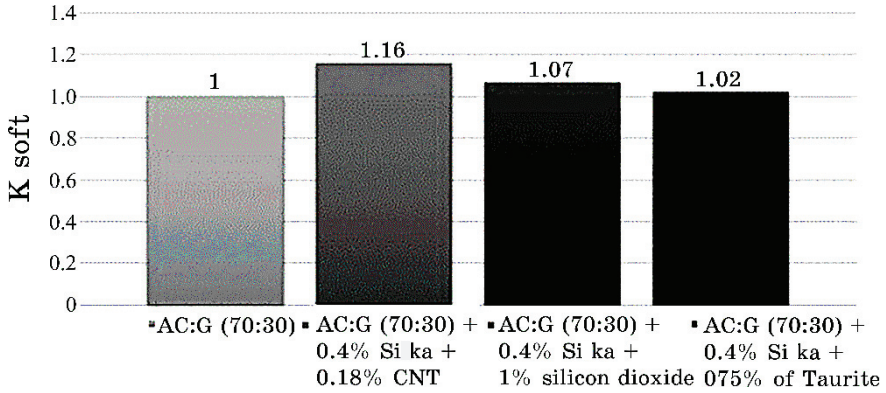

Fig. 7. Dependence of the softening coefficient for the *A*C:G (70:30) + Sika system on the type of nanomodifier.

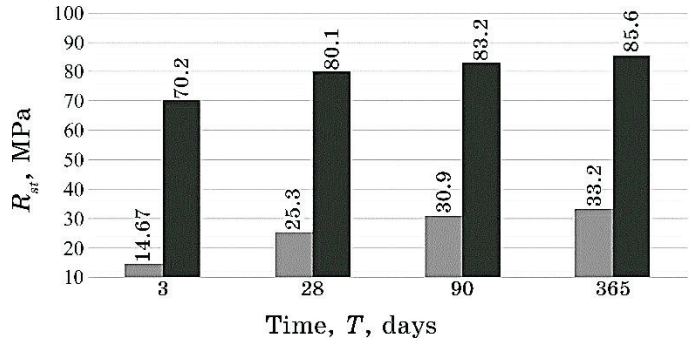

Fig. 8. Change in the compressive strength limit for the composition *A*C:G (70:30)% + 0.4% Sika + 0.18% CNT.

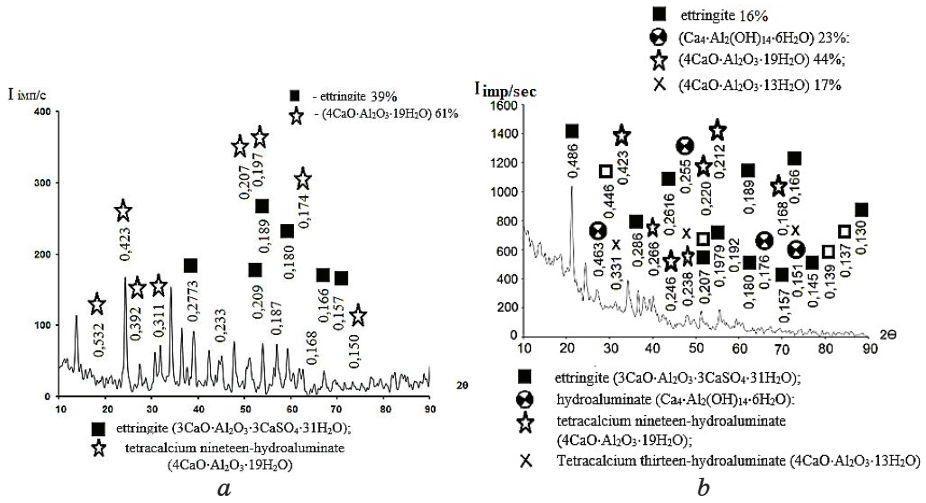

Fig. 9. The amount of the formed ettringite phase for the composition $C_3A + C\dot{S}H_2$ (*a*) (■—ettringite 28%, □—ettringite 11%, ★—tetracalcium nineteen-hydroaluminate $3CaO{\cdot}Al_2O_3{\cdot}19H_2O$) and *AC*:G (70:30)% (*b*) (■—ettringite 11%, □—ettringite 5%, ⊗—hydroaluminate $Ca_4O{\cdot}Al_2(OH)_{14}{\cdot}6H_2O$ 23%, ★—tetracalcium nineteen-hydroaluminate $4CaO{\cdot}Al_2O_3{\cdot}19H_2O$, — tetracalcium thirteen-hydroaluminate $4CaO{\cdot}Al_2O_3{\cdot}13H_2O$) for 3 days during hardening under normal conditions.

a system that changes over time and passes through the stages of the physical state of macro–micro–nano–micro–macro. The transition from macro-/micro- to nanosystem with formation of a dispersed medium is presented in the form of a surface (Fig. 10), consisting of nanoparticles in a multidimensional phase space [3].

The model represents a three-phase medium binder → solution → → stone and is separated with two surfaces. The surface is the in-

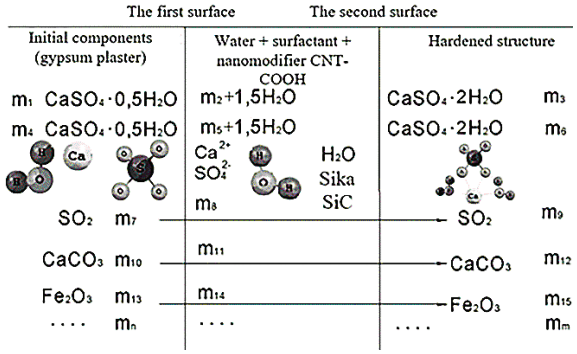

Fig. 10. Model of the hydration process on the example of hemihydrate.

terface between structural elements and the dispersed medium. The second surface is the interface between the dispersed medium and the solidified structure. At the interface, there is a partial transition of the macro- and microsystem into a nanosystem, as well as topochemical reactions of the transition of hemihydrate of calcium sulphate into calcium sulphate dihydrate.

The measure of the change in the characteristic function at constant parameters and masses (concentrations) of all substances (except for the mass (concentration) of the component with a changing amount in the system) is presented as the chemical potential, which allows creating a structure and framework of the highest strength by adjusting the dimensions of the solid surface and the number of crystallization centres. Creation of a frame with the highest strength can be achieved by adjusting the size of the solid surface and centres of crystallization, which affect the primary spatial structure.

The idea is that a frame of the highest strength can be created by adjusting the dimensions of the solid surface and the number of crystallization centres that affect formation of the spatial structure. Internal stresses, which lead to the weakening of the not yet formed structure, do not arise as a result of the fact that the joining of blocks takes place in free space.

The entire transformation of the system is reduced to obtaining a solidified structure with certain properties.

In the system of macro-/micro- and nanoevolution, each of its elements passes from one permitted state to another.

Calculation of the state of the nanosystem consists in the calculation of the external and internal components and means $\psi(\bar{\xi}, \tau)Z_i(m, \bar{\xi}_i)$ introduction of the elementary density, which can be calculated by solving the Schrödinger equation.

According to the proposed model at the starting point, the specific surface of solid components consists of particles in contact with the solution:

$$\sum M_{вих} = m_1 + m_4 + m_7 + m_{10} + m_{13} + \ldots;$$

m_1 $CaSO_4 \cdot 0.5H_2O$ (mass of hemihydrate conversion to dihydrate due to dissolution); m_4 $CaSO_4 \cdot 0.5H_2O$ (topochemical reaction); m_7, m_{10}, m_{13}, $mn-2$ $CaCO_3$, Fe_2O_3, and other, respectively.

Taking the structure of hardened binder or materials based on it as the final criterion (initial factor), it is necessary to determine the main parameters. Such parameters include the spatial framework, shape of the blocks, and morphology of the crystals.

A decisive role for formation of these parameters belongs to solutions of a certain concentration, presence of a solid surface of the

site (crystallization of centres), (water), temperature, pressure, and the mechanism of transition of calcium sulphate hemihydrate to calcium sulphate dihydrate.

The sequence of changes in the concentration of the solution determines the moving force of the interaction, which varies from 0 to 1. The maximum concentration of $C_2 = 0.008$ g/l contributes to creation of crystallization centres, growth and formation of blocks, as well as to filling of voids.

Therefore, by means of changing conditions for introduction of various additives into the solution system, it is possible to influence the shape, size, number of crystals, and, accordingly, formation of a spatial structure for the purpose of obtaining a product with certain properties.

4. CONCLUSIONS

Studies of the structure and durability of the ettringite phase and its composition with calcium sulphates were carried out. Raw material compositions based on fast-hardening binder systems $CaO–Al_2O_3–SO_3–H_2O$ *A*C:G (70:30) for obtaining concrete grades 300–400 were developed, which makes it possible to obtain fast-hardening binders in monolithic construction that are capable to gain up to 90–100% of their strength within 1–3 days and increase the reversibility of forms in case of factory production of building structures.

The influence of the Gibbs surface energy on the order of formation of hydrated compounds during the hydration of minerals of alumina cements was established theoretically and confirmed experimentally: for CA_2, 24.70; for C*A*, 51.86; for $C_{12}A_7$, 141.00; for C_3A, 145 of the system $CaO–Al_2O_3–H_2O$: C_2AH_8, C_4AH_{13}, C_4AH_{10}, CAH_{10}, $Al(OH)_3$, which makes it possible to determine the list of stable hydrate compounds and structures, which affect recrystallization in multicomponent systems.

The theoretical position of influence of ΔG during hydration of aluminate cements in the presence of gypsum received further development; the frequencies of chemical reactions $CaO–Al_2O_3–SO_3–H_2O$ can be divided into two parts: *a*) $CaO–Al_2O_3–H_2O$; *b*) $CaO–Al_2O_3–SO_3–H_2O$, and, as a result, C_3AH_6, CAH_{10}, C_2AH_8, C_4AH_{13}, $Ca_2(OH)_2$ are formed in the first one, and trisulphate C–*A*–S–H and monosulphate C–*A*–S–H are formed in the second one. As a result, it is possible to determine the tendency of hydrate compounds to interact with other components and creates conditions for recrystallization of hardened stone.

It was theoretically established and experimentally confirmed that the optimal content of calcium sulphate in *A*C + G5 compositions is, according to the calculation, in the range from 28% to

38% of the mass of the aluminate binder and contributes to the increase in the formation of ettringite and allows obtaining the structure of cement stone with special characteristics.

Formulations of special solutions for the production of prestressed products (road, airfield slabs, expanding, waterproofing concrete) were developed that makes it possible to satisfy the need for the production of the latest building materials for the repair and construction of high-quality structures.

For the first time, a theoretical model of the hydration process of mineral binders using ultra- and nanoadditives, surfactants was proposed. The developed model of the hydration process can be used in various systems, including those presented earlier.

REFERENCES

1. V. M. Derevianko, H. M. Hryshko, and O. V. Vatazhishin, *Ukrainian Journal of Civil Engineering and Architecture*, **4**, No. 016: 71 (2023); https://doi.org/10.30838/J.BPSACEA.2312.290823.71.972
2. K. Pushkarova, M. Sukhanevych, and A. Marsikh, *Materials Science Forum (Brno, Czech Republic, 2016)*, vol. **865**, p. 6.
3. V. N. Derevianko, N. V. Kondratieva, H. M. Hryshko, and M. A. Sanytsky, *Nanosistemi, Nanomateriali, Nanotehnologii*, **18**, Iss. 1: 107 (2020); https://doi.org/10.15407/nnn.18.01.107
4. Vinay Deep Punetha, Sravendra Rana, Hye Jin Yoo, Alok Chaurasia, James T. McLeskey Jr., Madeshwaran Sekkarapatti Ramasamy, Nanda Gopal Sahoo, and Jae Whan Cho, *Progress in Polymer Science*, **67**: 1 (2017); https://doi.org/10.1016/j.progpolymsci.2016.12.010
5. V. Derevianko, N. Kondratieva, V. Volkova, and H. Hryshko, *IOP Conference Series: Materials Science and Engineering*, **1162**, No. 1: 012001 (2021); https://doi.org/10.1088/1757-899X/1162/1/012001
6. M. A. Sanytsky, H.-B. Fischer, R. A. Soltysik, und S. W. Korolko, *Internationale Baustofftagung 'Ibausil', Tagungsband*, **1**: 0211 (in German).
7. A. Ye. Kononiuk, *Obobshchyonnaya Teoriya Modelirovaniya. Nachala* [Generalized Modelling Theory: Principles] (Kyiv: Osvita Ukraiiny: 2012), Book 1 (in Russian).
8. P. V. Kryvenko, K. K. Pushkariova, V. B. Baranovskyi, M. O. Kochevyh, Ye. G. Hasan, B. Ya. Konstantynivskyi, and V. O. Raksha, *Budivel'ne Materialoznavstvo: Pidruchnik* [Materials Science in Construction: Textbook] (Ed. P. V. Kryvenko) (Kyiv: Lira-K: 2015) (in Ukrainian).
9. A. A. Pashchenko, V. P. Serbin, and Ye. A. Starchevskaya, *Vyazhushchie Materialy* [Binding Materials] (Kiev: Vysshaya Shkola: 1985) (in Russian).
10. K. K. Pushkariova and M. O. Kochevykh *Materialoznavstvo dlya Arkhitektoriv ta Dyzayneriv: Navchal'nyy Posibnyk* [Materials Science for Architects and Designers: Textbook] (Kyiv: Lira-K: 2018) (in Ukrainian).
11. W. M. M. Heijnen and P. Hartman, *Journal of Crystal Growth*, **108**, Iss. 1–2: 290 (1991); https://doi.org/10.1016/0022-0248(91)90376-G
12. S. Y. Petrunin, L. V. Zakrevska, and V. Ye. Vaganov, *XXII International*

Science and Technology Conference Proceedings 'Starodubov Readings. Construction, Materials Science, and Engineering' (April 19–21, 2012, Dnipro), vol. **64**, p. 74 (in Ukrainian).

13. V. Derevianko, N. Kondratieva, N. Sanitskiy, and H. Hryshko, *Journal of Engineering Science*, **XXV**, No. 3: 74 (2018); http://doi.org/10.5281/zenodo.2557324
14. Victor Derevianko, Natalia Kondratieva, and Hanna Hryshko, *French–Ukrainian Journal of Chemistry*, **6**, No. 1: 92 (2018) (in Ukrainian); https://doi.org/10.17721/fujcV6I1P92-100
15. L. Kondofesky-Mintova and J. Plank, *Superplasticizers and Other Chemical Admixtures in Concrete: Proceedings of Tenth International Conference (October 2012, Prague, Czech Republic)*, p. 423.
16. M. A. Sanytskyi and N. V. Kondratieva, *III All-Ukrainian Science and Technology Conference 'Modern Trends in the Development and Production of Silicate Materials' (September 5–8, 2016, Lviv)* (in Ukrainian), p. 93.
17. *Fizika i Khimiya Poverkhnosti. Kniga I. Fizika Poverkhnosti* [Surface Physics and Chemistry. Book I. Surface Physics] (Eds. M. T. Kartel and V. V. Lobanov) (Kyiv: O. O. Chuiko Institute of Surface Chemistry of the NA.S. of Ukraine–Interservis LLC: 2015) (in Ukrainian).
18. V. Derevianko, H. Hryshko, Y. Zaiats, and A. Drozd, *Eastern-European Journal of Enterprise Technologies*, **1**, No. 6 (133): 42–52 (2025) (in Ukrainian); https://doi.org/10.15587/1729-4061.2025.323295

Наносистеми, наноматеріали, нанотехнології
Nanosistemi, Nanomateriali, Nanotehnologii
2025, т. 23, № 2, сс. 393–405
https://doi.org/10.15407/nnn.23.02.0393

© 2025 ІМФ (Інститут металофізики
ім. Г. В. Курдюмова НАН України)
Надруковано в Україні.

PACS numbers: 61.66.Fn, 61.68.+n, 64.70.dg, 81.10.Dn, 82.45.Gj, 82.45.Yz, 83.60.Np

Вплив магнетного поля на утворення нанорозмірних кристалітів за кристалізації карбонату Кальцію з гідрокарбонатних розчинів

В. Р. Гаєвський[1], В. З. Кочмарський[1], Б. Д. Нечипорук[2], С. Г. Гаєвська[3], О. В. Гаращенко[1]

[1]*Національний університет водного господарства та природокористування, вул. Соборна, 11, 33028 Рівне, Україна*
[2]*Рівненський державний гуманітарний університет, вул. Степана Бандери, 12, 33028 Рівне, Україна*
[3]*Рівненський науково-дослідний експертно-криміналістичний центр Міністерства внутрішніх справ України, вул. Василя Червонія, 39, 33003 Рівне, Україна*

Досліджено утворення нанорозмірних кристалітів за кристалізації карбонату Кальцію з гідрокарбонатних водних розчинів під впливом постійного магнетного поля. Кристалізація відбувалась у гідрокарбонатних водних розчинах шляхом змішування водних розчинів $CaCl_2$ і $NaHCO_3$. Концентрації початкових компонентів досліджуваної системи розраховувалися на основі термодинамічних констант дисоціяції вугільної кислоти по першому та другому ступеням, концентраційних констант стійкости комплексів $NaCO_3^-$ і $NaHCO_3^0$, рівняння електронейтральности та рівняння балансу мас, а також експериментального міряння показника активности йонів Гідроґену. Для розрахунку йонної сили розчину за теорією Дебая–Гюккеля використовували метод ітерацій, у якому для першої ітерації брали початкові модельні концентрації. В результаті розрахунків встановлено, що основним компонентом карбонатної підсистеми в даних умовах є HCO_3^-, відношення концентрацій гідрокарбонат-йонів до карбонат-йонів перевищувало 18, а тому процес кристалізації карбонату Кальцію відбувався через проміжну реакцію дисоціяції гідрокарбонат-йонів, що є особливістю досліджуваного процесу. Рентґеноструктурні дослідження показали, що за даних умов експерименту утворюються дві модифікації карбонату Кальцію: кальцит і ватерит, але малоймовірно, що буде утворюватись араґоніт. Розрахунок розмірів кристалітів методом Дебая–Шеррера показав, що в результаті синтези утворюються нанокристали, розміри яких для кальциту становлять 110 нм, а для вателиту — 23 нм. Встановлено, що за даних умов

синтези магнетне поле індукцією у 125–250 мТл практично не впливає на розміри нанокристалів кальциту та ватериту.

The formation of nanosize crystallites during the crystallization of calcium carbonate from aqueous bicarbonate solutions under the influence of a permanent magnetic field is studied. Crystallization took place in aqueous hydrocarbon solutions by mixing aqueous solutions of $CaCl_2$ and $NaHCO_3$. The concentrations of the initial components of the studied system are calculated on the basis of the thermodynamic constants of the first- and second-order dissociations of carbonic acid, the concentration constants of stability of the $NaCO_3^-$ and $NaHCO_3^0$ complexes, the electroneutrality equation and the mass-balance equation, as well as the experimental measurement of the activity index of hydrogen ions. To calculate the ionic strength of the solution according to the Debye–Hückel theory, the method of iterations is used, in which the initial model concentrations are taken for the first iteration. As a result of the calculations, it is established that the main component of the carbonate subsystem under these conditions is HCO_3^-, the ratio of concentrations of hydrocarbonate ions to carbonate ions exceeds 18, and therefore, the process of crystallization of calcium carbonate occurs through the intermediate reaction of dissociation of hydrocarbonate ions that is a feature of the investigated process. XRD studies show that under the given conditions of the experiment, two modifications of calcium carbonate are formed: calcite and vaterite; but aragonite is unlikely to be formed. Calculation of crystallite sizes using the Debye–Scherrer method shows that, as a result of synthesis, nanocrystals are formed, the sizes of which are of 110 nm for calcite and of 23 nm for vaterite. As established, under the given conditions of synthesis, the magnetic field with an induction of 125–250 mT practically does not affect the sizes of the calcite and vaterite nanocrystals.

Ключові слова: магнетне оброблення, кристалізація карбонату Кальцію, гідрокарбонатна водна система, розчини електролітів, теорія Дебая–Гюккеля, метод ітерацій, рентґеноструктурна аналіза, метод Дебая–Шеррера.

Key words: magnetic treatment, crystallization of calcium carbonate, carbonate aqueous system, electrolyte solutions, Debye–Hückel theory, iteration method, XRD analysis, Debye–Scherrer method.

(Отримано 28 квітня 2024 р.; після доопрацювання — 16 січня 2025 р.)

1. ВСТУП

Дослідження кристалізації карбонату Кальцію за утворення полікристалів, які являють собою аґльомерацію нанорозмірних кристалітів, за наявности магнетного поля виконуються понад 60 років [1]. За цей період велика кількість експериментальних даних показала, що вплив магнетного поля на кристалізацію $CaCO_3$ не є повністю й однозначно встановленим [2, 3]. Така не-

однозначність, очевидно, пов'язана зі складністю досліджуваної системи, у якій під час кристалізації відбувається ряд послідовно-паралельних хемічних реакцій [2–4], які в кінці приводять також до складних фазових перетворень і поверхневих процесів, відповідальних за кінцеве утворення поліморфного карбонату Кальцію [5]. Складність досліджуваної системи також полягає у її нестабільності по відношенню до рівноважного цій системі CO_2 [6], що може змінюватися за різних умов експерименту.

Таким чином, встановлення умов, за яких чітко фіксувалися б ефект впливу магнетного поля або відсутність такого ефекту на кристалізацію карбонату Кальцію, є важливою науковою задачею з точки зору як прикладних технологічних процесів [7, 8], так і з точки зору фундаментальних питань стосовно процесів кристалізації [4, 9, 10].

2. ЕКСПЕРИМЕНТАЛЬНА МЕТОДИКА

Ініціювання кристалізації карбонату Кальцію виконували шляхом змішування 50 мл водного розчину $CaCl_2$ концентрацією у 20,0 ммоль/дм^3 і 50 мл розчину $NaHCO_3$ з концентрацією у 20,0 ммоль/дм^3. Експерименти виконували паралельно у двох однакових хемічних стаканах ємністю по 100 мл. Після того, як розчини змішувались, один хемічний стакан поміщали у контейнер з магнетами. Упродовж експерименту розчини перемішували скляними паличками впродовж однієї хвилини. Усі розчини готували з хемічно чистих реаґентів. Реаґенти готували на дистильованій воді з питомою електропровідністю у 3–4 мкСм/см. Концентрації приготовлених розчинів перевірялися шляхом міряння йонів Na^+ полум'яним аналізатором рідин ПАЖ-2 з відносною похибкою міряння у 1% і йонів Cl^- — аналізатором йонів АІ-123 (Cl^--йон-селективна електрода) з похибкою у 0,015 од. Показник pH розчину $NaHCO_3$ перевірявся аналізатором йонів АІ-123 (pH-електрода) з похибкою у 0,01 од. Магнетне поле створювалося за допомогою контейнера з двома пласкими самарій-кобальтовими магнетами (рис. 1, *а*). Температура у всіх дослідах була у межах 18–20°C. На рисунку 1, *б* показано розподіл магнетного поля у хемічному стакані. Індукція магнетного поля міряла магнетометром МТ-1 з похибкою, що не перевищувала 5%.

3. РЕЗУЛЬТАТИ Й ЇХ ОБГОВОРЕННЯ

3.1. Визначення компонентного складу гідрокарбонатної підсистеми

Для умов експерименту запишемо рівняння балансу мас:

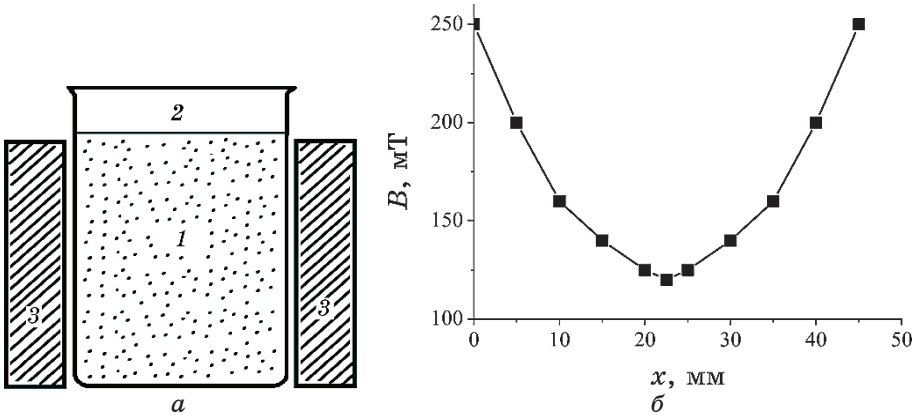

Рис. 1. Схема експериментального устаткування для дослідження кристалізації $CaCO_3$ в магнетному полі (*а*): *1* — суспензія $CaCO_3$, *2* — хемічний стакан, *3* — постійні магнети. Розподіл магнетного поля в стакані (*б*).[1]

$$\left(C_{Na^+}\right)_0 + \left(C_{HCO_3^-}\right)_0 = C_{Na^+} + C_{HCO_3^-} + C_{CO_3^{2-}} + C_{CO_2} + C_{NaCO_3^-} + C_{NaHCO_3^0}, \quad (1)$$

а також рівняння електронейтральности:

$$C_{Na^+} + C_{H^+} = 2C_{CO_3^{2-}} + C_{HCO_3^-} + C_{NaCO_3^-} + C_{OH^-}, \quad (2)$$

де C_x — концентрація відповідного компонента x. Для встановлення кількісних співвідношень між компонентами карбонатної підсистеми (CO_3^{2-}, HCO_3^-, CO_2) запишемо хемічні реакції, що відбуваються у даній системі з утворенням водного розчину $NaHCO_3$, а саме: реакції дисоціяції вугільної кислоти по першому та другому ступенях (1), (2):

$$HCO_3^- + H^+ \leftrightarrow H_2O + CO_2, \quad (3)$$

$$CO_3^{2-} + H^+ \leftrightarrow HCO_3^- \quad (4)$$

відповідно; реакції дисоціяції води:

$$H_2O \leftrightarrow H^+ + OH^-; \quad (5)$$

реакції утворення комплексів $NaHCO_3^0$ і $NaCO_3^-$:

$$HCO_3^- + Na^+ \leftrightarrow NaHCO^0, \quad (6)$$

$$CO_3^{2-} + Na^+ \leftrightarrow NaCO^- \quad (7)$$

відповідно.

На основі реакцій (3)–(7) запишемо термодинамічні константи дисоціяції вугільної кислоти по першому і другому ступенях:

$$K_1 = \frac{a_{\mathrm{H}^+} a_{\mathrm{HCO}_3^-}}{a_{\mathrm{CO}_2}}, \tag{8}$$

$$K_2 = \frac{a_{\mathrm{H}^+} a_{\mathrm{CO}_3^{2-}}}{a_{\mathrm{HCO}_3^-}} \tag{9}$$

відповідно, а також термодинамічну константу дисоціяції води K_w:

$$K_w = a_{\mathrm{H}^+} a_{\mathrm{OH}^-}. \tag{10}$$

Концентраційні константи стійкости комплексів NaCO_3^- і NaHCO_3^0 матимуть вирази:

$$K_3 = \frac{C_{\mathrm{NaCO}_3^-}}{C_{\mathrm{Na}^+} C_{\mathrm{CO}_3^{2-}}}, \tag{11}$$

$$K_4 = \frac{C_{\mathrm{NaHCO}_3^0}}{C_{\mathrm{Na}^+} C_{\mathrm{HCO}_3^-}} \tag{12}$$

відповідно.

Також необхідно враховувати рівняння балансу мас і рівняння електронейтральности:

$$\left(C_{\mathrm{Na}^+}\right)_0 + \left(C_{\mathrm{CO}_3^{2-}}\right)_0 = C_{\mathrm{Na}^+} + C_{\mathrm{CO}_3^{2-}} + C_{\mathrm{HCO}_3^-} + C_{\mathrm{CO}_2} + C_{\mathrm{NaCO}_3^-} + C_{\mathrm{NaHCO}_3^0}, \tag{13}$$

$$C_{\mathrm{Na}^+} + C_{\mathrm{H}^+} = 2C_{\mathrm{CO}_3^{2-}} + C_{\mathrm{HCO}_3^-} + C_{\mathrm{NaCO}_3^-} + C_{\mathrm{OH}^-} \tag{14}$$

відповідно.

Значення констант: K_1 $1{,}72 \cdot 10^{-4}$, $K_2 = 4{,}40 \cdot 10^{-11}$, K_w $1{,}00 \cdot 10^{-14}$.

Із (1)–(14) одержуємо залежність CO_3^{2-} від H^+ у вигляді:

$$\left(\mathrm{Na}^+\right)_0 \frac{1 - K_3 C_{\mathrm{CO}_3^{2-}}}{1 + A\left(\mathrm{H}^+\right) C_{\mathrm{CO}_3^{2-}}} = B\left(\mathrm{H}^+\right) - C\left(\mathrm{H}^+\right), \tag{15}$$

де

$$A\left(\mathrm{H}^+\right) = \frac{K_4 \gamma_{\mathrm{CO}_3^{2-}}}{K_4 \gamma_{\mathrm{HCO}_3^{2-}}} \mathrm{H}^+ + K_3, \quad B\left(\mathrm{H}^+\right) = \frac{\gamma_{\mathrm{CO}_3^{2-}}}{K_2 \gamma_{\mathrm{HCO}_3^{2-}}} \mathrm{H}^+ + 2,$$

$$C\left(\mathrm{H}^+\right) = \frac{K_w}{\gamma_{\mathrm{HCO}_3^{2-}} \mathrm{H}^+} - \frac{\mathrm{H}^+}{\gamma_{\mathrm{H}^+}}.$$

Коефіцієнти активностей γ визначали за другим наближенням теорії Дебая–Гюккеля [11]:

$$\log(\gamma) = -\frac{0,512Z^2\sqrt{I}}{1+0,328a\sqrt{I}}, \qquad (16)$$

де Z — йонний заряд, b — віддаль найменшого зближення йонів, I — йонна сила розчину, що визначається як

$$I = 0,5\sum_{i=1}^{N} C_i Z_i^2; \qquad (17)$$

ефективні розміри йонів [12]: $a_{\text{H}^+} = 9$, $a_{\text{Na}^+} = 4$, $a_{\text{CO}_3^{2-}} = 5$, $a_{\text{HCO}_3^-} = 4$, $a_{\text{OH}^-} = 3$ (у [Å]). Йонну силу I визначали ітераційним методом, перше наближення якого відповідало початковим значенням концентрацій: $\left(\text{Na}^+\right)_0 = 40$ ммоль/дм^3 та $\left(C_{\text{CO}_3^{2-}}\right)_0 = 20,0$ ммоль/дм^3. У даному випадку достатньо було трьох ітерацій (рис. 2). Оскільки розв'язок (15) є громіздким, то введемо додаткові позначення:

$$D = \frac{1}{2AB}, \quad E = -\left(\text{Na}^+\right)_0 K_з - AC - B,$$

$$F = \left(\text{Na}^+\right)_0 K_з\left(\left(\text{Na}^+\right)_0 K_з + 2B + 2AC + \frac{4AB}{K_з}\right), \quad G = (B - AC)^2. \qquad (18)$$

У термінах позначень (18) розв'язок (15) буде мати вигляд:

$$C_{\text{CO}_3^{2-}} = D\left[E + (F+G)^{1/2}\right]. \qquad (19)$$

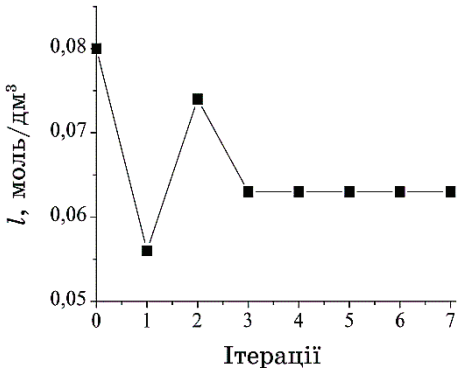

Рис. 2. Залежність йонної сили від кількости ітерацій.[2]

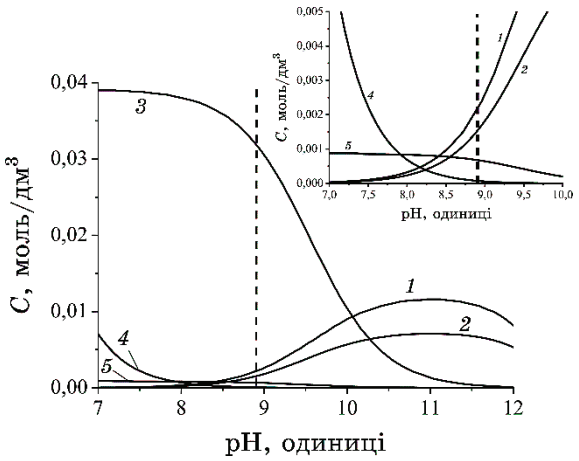

Рис. 3. Концентрації компонентів водного розчину 0,02 моль/дм^3 Na_2CO_3 в залежності від pH розчину: *1* — CO_3^{2-}, *2* — $NaCO_3^-$, *3* — HCO_3^-, *4* — CO_2, *5* — $NaHCO_3^0$.[3]

За (15)–(19) обрахували $C_{CO_3^{2-}}$, $C_{HCO_3^-}$, $C_{NaCO_3^-}$, $C_{NaHCO_3^0}$ і C_{CO_2} (рис. 3) та співвідношення між компонентами карбонатної підсистеми $C_{CO_3^{2-}}$, $C_{HCO_3^-}$ і C_{CO_2}. Із рисунку 3 видно, що за pH дозованого розчину $NaHCO_3$, що дорівнює 8,9, молярні концентрації компонентів мають наступні значення:

$$C_{CO_3^{2-}} = 1,78\,\frac{\text{ммоль}}{\text{дм}^3},\ C_{HCO_3^-} = 33,18\,\frac{\text{ммоль}}{\text{дм}^3},\ C_{NaCO_3^-} = 1,26\,\frac{\text{ммоль}}{\text{дм}^3},$$

$$C_{NaHCO_3^0} = 0,71\,\frac{\text{ммоль}}{\text{дм}^3}\ \text{і}\ C_{CO_2} = 0,095\cdot 10^{-3}\,\frac{\text{ммоль}}{\text{дм}^3}.$$

Із рисунку 4 видно, що за pH дозованого розчину Na_2CO_3, що дорівнює 8,9, основним компонентом є HCO_3^-. Розраховані співвідношення між компонентами карбонатної підсистеми в даних умовах будуть такими: $\varepsilon_{HCO_3^-} = 94,6\%$, $\varepsilon_{CO_3^{2-}} = 5,1\%$ і $\varepsilon_{CO_2} = 0,3\%$.

3.2. Рентґеноструктурні дослідження

Рентґеноструктурну аналізу досліджуваних зразків було проведено з використанням рентґенівського дифрактометра ДРОН-4 за кімнатної температури. В якості джерела рентґенівського випромінення використано рентґенівську трубку з мідною анодою. Для вбирання K_β-випромінення використовували ніклевий фільтр.

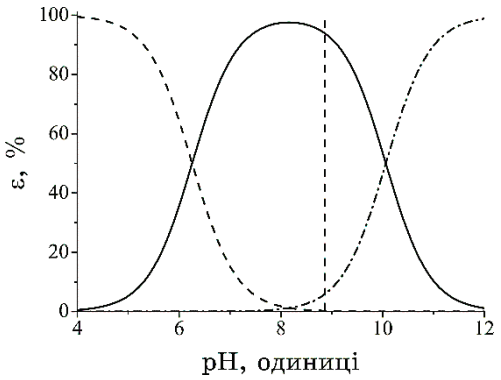

Рис. 4. Співвідношення ε (у відсотках) між компонентами карбонатної підсистеми водного розчину 0,02 моль/дм^3 $NaHCO_3$ в залежності від pH розчину. — —HCO_3^-, ---- —CO_2, - - —CO_3^{2-}.[4]

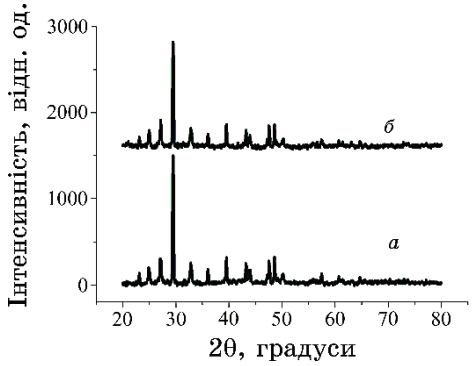

Рис. 5. Рентґенівські дифрактограми зразків, синтезованих без дії магнетного поля (*а*) і під дією магнетного поля (*б*).[5]

Режим роботи рентґенівської трубки: анодна напруга — 41 кВ, сила струму — 21 мА. Крок сканування дифрактограми — 0,05°, а час експозиції — 5 с.

В процесі обробки експериментальних дифрактограм кожний рефлекс описували Ґауссовою функцією, в результаті чого були одержані такі параметри рефлексів: кутове положення 2θ, півширина (ширина на половині висоти) β, інтеґральна інтенсивність *I*. Одержані результати використовувалися для інтерпретації експериментальних дифрактограм і розрахунку розмірів нанокристалів.

На рисунку 5 показано рентґенівські дифрактограми двох зразків, яких було одержано без впливу і під дією постійного магнетного поля за однакових інших умов. З дифрактограм видно, що

вони достатньо подібні. Було висловлено припущення, що рефлекси дифрактограм належать карбонату Кальцію. Відомо, що карбонат Кальцію кристалізується в трьох модифікаціях: кальцит, ватерит і араґоніт [13]. З використанням відомих міжплощинних віддалей [14] і формули Вульфа–Бреґґа [15]

$$2d \sin \vartheta = k\lambda , \qquad (20)$$

де d — міжплощинна віддаль, θ — кут дифракції, k — порядок дифракційного максимуму, λ — довжина хвилі рентґенівського випромінення, було розраховані кутові положення рефлексів 2θ для різних модифікацій карбонату Кальцію. В таблиці наведено порівняння результатів розрахунку та літературних даних з експериментальними даними для двох модифікацій карбонату Кальцію (кутові положення наведено в ґрадусах, інтенсивності — у відсотках). Експериментальні кутові положення 2θ в таблиці наведено лише для зразка, синтезованого без впливу магнетного поля, оскільки для зразка, синтезованого в магнетному полі, відповідні значення дуже близькі.

З таблиці видно, що на дифрактограмах присутні лише рефлекси, характерні для кальциту та вателиту. Рефлексів ще однієї модифікації, а саме, араґоніту, не було зафіксовано. Розраховані й експериментальні значення кутових положень рефлексів добре збігаються між собою. Відмінності відносних інтенсивностей зумовлено тим, що літературні дані наведено для пікових інтенсивностей, а нами використано інтеґральні інтенсивності. Крім того, дифрактограми було одержано з використанням рентґенівського випромінення різних довжин хвиль в обох випадках.

ТАБЛИЦЯ. Експериментальні та літературні дані для кальциту й вателиту.[6]

Кальцит				Ватерит			
Розрахунок		Експеримент		Розрахунок		Експеримент	
2θ	I	2θ	I	2θ	I	2θ	I
23,0	12%	23,1	11%	24,9	63%	24,9	66%
29,4	100%	29,5	100%	27,1	75%	27,1	100%
36,0	14%	36,0	10%	32,8	100%	32,8	72%
39,4	18%	39,5	17%	44,0	63%	43,9	46%
43,2%	18%	43,2%	15%	48,8	15%	49,2	50%
47,2	5%	47,2	6%	49,9	63%	50,1	42%
47,5	17%	47,6	19%				
48,6	17%	48,6	22%				
57,5	8%	57,5	8%				

Для індексації рефлексів наших дифрактограм було використано формулу Вульфа–Бреґґа та квадратичну форму для гексагональної синґонії [15]:

$$\frac{1}{a^2} = \frac{4}{3}\frac{h^2 + hk + k^2}{a^2} + \frac{l^2}{c^2}, \qquad (21)$$

де a і c — параметри елементарної комірки, ($h\,k\,l$) — Міллерові індекси рефлексу. В результаті було встановлено, що рефлекси з кутовими положеннями 23,1°, 29,5°, 36,0°, 39,5°, 43,2°, 47,2°, 47,6°, 48,6° і 57,4° належать кальциту та мають Міллерові індекси (102), (104), (110), (113), (202), (204), (108), (116) і (212) відповідно. Рефлекси ватериту мають Міллерові індекси (100), (101), (102), (110), (112), (104) та (202), яким відповідають кутові положення 24,9°, 27,1°, 32,8°, 43,9°, 49,2° та 50,1° відповідно. Наші рентґеноструктурні дослідження добре корелюють з результатами робіт [16–18], в яких автори досліджували синтетичні модифікації карбонату Кальцію.

Для розрахунку розмірів наночастинок використали формулу Дебая–Шеррера [19, 20]

$$D = \frac{0,89\lambda}{\beta\cos\theta}, \qquad (22)$$

де λ — довжина хвилі рентґенівського випромінення, β — півширина рефлексу, θ — кут дифракції. Фізичне значення півширини обчислено за формулою

$$\beta = (\beta_1^2 - \beta_2^2)^{1/2}, \qquad (23)$$

де β_1 — експериментальне значення півширини рентґенівського рефлексу, β_2 — інструментальне значення півширини рентґенівського рефлексу. Інструментальне значення півширини рентґенівських рефлексів визначалося на основі аналізи рентґенівських дифрактограм еталонних порошків кремнію й Al_2O_3, яких було одержано за таких самих умов.

За допомогою формули Дебая–Шеррера визначали розміри для всіх рефлексів двох модифікацій карбонату Кальцію та знаходили середнє арифметичне значення одержаних результатів для кожної модифікації. Внаслідок цього було встановлено, що для зразка, синтезованого без впливу магнетного поля, розміри наночастинок кальциту складають 110 нм, ватериту — 23 нм. А для зразка, одержаного в постійному магнетному полі розміри складають 115 нм і 25 нм відповідно. Таким чином, постійне магнетне поле не впливає на розміри нанокристалів кальциту та ватериту за кристалізації кальцій-гідрокарбонатної системи чи то цей

вплив не є істотним.

В попередній нашій роботі [3] ми досліджували кристалізацію карбонату Кальцію з кальцій-карбонатної водної системи та встановили, що за кристалізації у магнетному полі розміри ватериту зростають від 24 нм до 31 нм, а кальциту — від 100 нм до мікронних розмірів, які неможливо визначити методом Дебая–Шеррера. Крім того, інтеґральні інтенсивності рефлексів кальциту та ватериту приблизно співмірні. У даній роботі інтеґральні інтенсивності рефлексів кальциту істотно перевищують інтенсивності рефлексів ватериту (рис. 5). Оскільки інтеґральні інтенсивності прямо пропорційні об'ємному вмісту компонентів суміші, за кристалізації з різних систем (кальцій-карбонатної та кальцій-гідрокарбонатної) утворюються різні об'ємні співвідношення кальциту та ватериту. Для кількісної оцінки цих співвідношень необхідні додаткові дослідження.

З точки зору фізико-хемічних процесів, що відбуваються в кальцій-карбонатній і кальцій-гідрокарбонатній водних системах, у цих системах діє принципіяльно різні механізми утворення $CaCO_3$. За кристалізації карбонату Кальцію з кальцій-гідрокарбонатних водних розчинів, утворення $CaCO_3$ відбувається в результаті депротонізації гідрокарбонату в полі йона Кальцію за реакцією

$$Ca^{2+} + 2HCO_3^- = CaCO_3 + CO_2 + H_2O\,. \qquad (24)$$

За кристалізації ж $CaCO_3$ з кальцій-карбонатних водних розчинів відбувається пряма реакція синтези

$$Ca^{2+} + CO_3^{2-} = CaCO_3\,. \qquad (25)$$

На думку авторів, вказана ріжниця в механізмі утворення $CaCO_3$ може бути причиною різного впливу магнетного поля на кристалізацію карбонату Кальцію з кальцій-гідрокарбонатних і кальцій-карбонатних водних розчинів, що потребує спеціяльних цільових досліджень.

4. ВИСНОВКИ

Дослідження показали, що за значного перевищення у розчині йонів HCO_3^- над йонами CO_3^{2-} (у даній роботі — в 18,6 разів) за температур у 18–20°C з найбільшою ймовірністю утворюються кальцит і ватерит, та малоймовірно, що буде утворюватися арагоніт.

В процесі кристалізації з гідрокарбонатного водного розчину утворюються нанокристали кальциту та ватериту з розмірами у

110 нм і 23 нм відповідно.

Проведення кристалізації $CaCO_3$ гідрокарбонатного водного розчину в постійному магнетному полі у 125–250 мТл практично не впливає на розміри нанорозмірних кристалітів кальциту та ватериту.

ЦИТОВАНА ЛІТЕРАТУРА–REFERENCES

1. T. Vermeiren, *Anti-Corrosion Methods and Materials*, **5**, No. 7: 215 (1958); https://doi.org/10.1108/eb019464
2. V. Z. Kochmarskii, V. R. Gayevskii, O. V. Kochmarskii, and S. G. Nechyporuk, *Visnyk NUWEE*, **2**, No. 46: 234 (2009) (in Ukraine).
3. V. R. Gayevskii, B. D. Nechyporuk, and S. G. Gayevska, *Physics and Chemistry of Solid State*, **24**, No. 4: 616 (2023); https://doi.org/10.15330/pcss.24.4.616-622
4. V. R. Gayevskii, V. Z. Kochmarskii, and S. G. Gayevska, *Journal of Crystal Growth*, **548**: 125844 (2020); https://doi.org/10.1016/j.jcrysgro.2020.125844
5. *CRC Handbook of Chemistry and Physics. 90th Edition (CD-ROM Version 2010)* (Ed. D. R. Lide) (Boca Raton, FL: CRC Press–Taylor and Francis: 2010).
6. V. R. Gajevskiy, *Ukrainian Journal of Physics*, **60**: 258 (2015); https://doi.org/10.15407/ujpe60.03.0258
7. V. R. Gayevskii and V. Z. Kochmarskii, *Pidvyshchennya Ehfektyvnosti Oborotnykh System Okholodzhennya Minimizatsiyeyu Kaltsiy-Karbonatnykh Vidkladen'* [Increasing the Efficiency of Reversible Cooling Systems by Minimizing Calcium Carbonate Deposits] (Rivne: NUWEE: 2018) (in Ukrainian); http://ep3.nuwm.edu.ua/id/eprint/15612
8. V. R. Gayevskii, V. L. Fylypchuk, and O. U. Deyneka, *Ukrainian Journal of Construction and Architecture*, No. **5** (011): 27 (2022) (in Ukrainian); https://doi.org/10.30838/J.BPSACEA.2312.251022.27.888
9. V. Z. Kochmarskii, V. R. Gayevskii, and N. L. Tyshko, *Ukrainian Journal of Physics*, **62**, No. 5: 382 (2017); https://doi.org/10.15407/ujpe62.05.0382
10. V. R. Gayevskii, V. Z. Kochmarskii, and S. H. Gayevska, *Ukrainian Journal of Physics*, **66**, No. 8: 708 (2021); https://doi.org/10.15407/ujpe66.8.708
11. H. S. Harned and B. B. Owen, *The Physical Chemistry of Electrolytic Solutions* (New York: Reinhold: 1967).
12. D. G. Peters, J. M. Hayes, and G. M. Hieftje, *Chemical Separations and Measurements. Theory and Practice of Analytical Chemistry* (W. B. Saunders Co.: 1974).
13. Ye. O. Mykhailova, M. O. Moroz, and O. L. Sincheskul, *Herald NTU 'KhPI'. Series: Chemistry, Chemical Technology and Ecology*, No. 48 (1269): 68 (2017) (in Ukrainian).
14. L. Y. Mirkin, *Spravochnik po Rentgenostrukturnomu Analizu Polikristallov* [Handbook of X-Ray Diffraction Analysis of Polycrystals] (Ed. Ya. S. Umanskiy) (Moskva: 1961) (in Russian).
15. V. Y. Lysoivan, *Izmerenie Parametrov Ehlementarnoy Yacheiki na Odnokristal'nom Spektrometre* [Measurement of Unit Cell Parameters on a Single-

Crystal Spectrometer] (Novosibirsk: Nauka, Sib. Otd.: 1982) (in Russia).
16. A. Achour, A. Arman, M. Islam, A. A. Zavarian, A. Basim Al-Zubaidi, and J. Szade, *Eur. Phys. J. Plus*, **132**: 267 (2017); https://doi.org/10.1140/epjp/i2017-11531-8
17. Gen-Tao Zhou, Jimmy C. Yu, Xin-Chen Wang, and Li-Zhi Zhang, *New. J. Chem.*, **28**: 1027 (2004); https://doi.org/10.1039/B315198K
18. Mehrdad Khatami, Hajar Q. Alijani, Farideh Mousazadeh, Nooshin Hashemi, Zahra Mahmoudi, Samaneh Darijani, Mehdi Bamorovat, Alireza Keyhani, Meghdad Abdollahpour-Alitappeh, and Fariba Borhani, *Royal Society of Chemistry Advances*, **10**, Iss. 62: 38063 (2020); https://doi.org/10.1039/D0RA04503A
19. V. R. Gaevs'kyi, B. D. Nechyporuk, N. Yu. Novoselets'kyi, and B. P. Rudyk, *Ukrainian Journal of Physics*, **58**, No. 4: 385 (2013); https://doi.org/10.15407/ujpe58.04.0385
20. N. B. Danilevska, M. V. Moroz, M. Yu. Novoseletskyi, B. D. Nechyporuk, and B. P. Rudyk, *Journal of Physical Studies*, **20**, No. 3: Article 3601 (2016); https://doi.org/10.30970/jps.20.3601

[1]*National University of Water Governance and Nature Conservation,*
11, Soborna Str.,
UA-33028 Rivne, Ukraine
[2]*Rivne State Humanitarian University,*
12, Stepana Bandery Str.,
UA-33028 Rivne, Ukraine
[3]*Rivne Research and Forensic Science Centre,*
Ministry of Internal Affairs of Ukraine,
39, Vasyl Chervoniy Str.,
UA-33003 Rivne, Ukraine

[1] **Fig. 1.** Scheme of the experimental setup for studying the crystallization of $CaCO_3$ in a magnetic field (*а*): *1*—suspension of $CaCO_3$, *2*—chemical beaker, *3*—permanent magnets. Distribution of the magnetic field in the glass (*б*).
[2] **Fig. 2.** Dependence of the ionic strength on the number of iterations.
[3] **Fig. 3.** Concentrations of the components of an aqueous solution of 0.02 mole/dm^3 Na_2CO_3 depending on the pH of the solution. *1*—CO_3^{2-}, *2*—$NaCO_3^-$, *3*—HCO_3^-, *4*—CO_2, *5*—$NaHCO_3^0$.
[4] **Fig. 4.** The ratio ε (in percent) between the components of the carbonate subsystem of an aqueous solution of 0.02 mole/dm^3 $NaHCO_3$ depending on the pH of the solution. — —HCO_3^-, ---—CO_2, - - - —CO_3^{2-}.
[5] **Fig. 5.** XRD-patterns of samples synthesized without the action of a magnetic field (*а*) and with the action of a magnetic field (*б*).
[6] **TABLE.** Experimental and literary data for calcite and vaterite.

Наносистеми, наноматеріали, нанотехнології
Nanosistemi, Nanomateriali, Nanotehnologii
2025, т. 23, № 2, сс. 407–422
https://doi.org/10.15407/nnn.23.02.0407

© 2025 ІМФ (Інститут металофізики
ім. Г. В. Курдюмова НАН України)
Надруковано в Україні.

PACS numbers: 64.75.Nx, 65.40.Ba, 65.40.gd, 81.30.Dz, 81.30.Mh, 82.33.Pt, 82.60.Lf

Isomorphous Substitutions of Calcium with Rare-Earth Elements and Lithium in Scheelite-Structured Molybdates for Actinoid Simulation

E. I. Get'man and S. V. Radio

Vasyl' Stus Donetsk National University,
21, 600-Richchia Str.,
UA-21027 Vinnytsia, Ukraine

Using V. S. Urusov's crystal-energy theory of isomorphous miscibility, the mixing energies, critical decomposition temperatures, and limits of isomorphous substitutions are calculated, and the regions of thermodynamic stability of $Ca_{1-x}(Li_{0.5}Ln_{0.5})_xMoO_4$ solid solutions, where Ln are rare-earth elements (REE), are determined. As shown, the critical decomposition temperatures decrease symbately with the mixing energy as the REE number increases in the La–Sm series within the temperature range of 162–16 K, and it increases in the Eu–Lu series within the temperature range of 30–294 K. The thermodynamic stability diagram and the decomposition domes of solid solutions in the concentration range from $x = 0$ to $x = 1.0$ through $x = 0.05$ are presented. These allow for the determination of equilibrium substitution limits by temperature, temperature by a given substitution limit, or ranges of thermodynamic stability of solid solutions. The results may be useful for the storage and disposal of actinoides, radioactive REE isotopes, and molybdenum in the field of ultra-low temperatures.

З використанням кристалоенергетичної теорії ізоморфної змішуваности В. С. Урусова розраховано енергії змішання, критичні температури розпаду, межі ізоморфних заміщень, а також визначено області термодинамічної стабільности твердих розчинів $Ca_{1-x}(Li_{0,5}Ln_{0,5})_xMoO_4$, де Ln — рідкісноземельні елементи (РЗЕ). Показано, що критичні температури розпаду зі збільшенням номера РЗЕ в ряду La–Sm симбатно з енергією змішання зменшуються в інтервалі температур 162–16 К, а в ряду Eu–Lu зростають в інтервалі температур 30–294 К. Представлено діяграму термодинамічної стабільности, а також бані розпаду твердих розчинів у діяпазоні концентрацій від $x = 0$ до $x = 1{,}0$ через $x = 0{,}05$. Вони дають змогу визначати рівноважні межі заміщень за температурою, або температуру за заданою межею заміщення, чи то області термодинамічної стабільности твердих розчинів. Результати роботи можуть бути корис-

ними для зберігання та захоронення актиноїдів, радіоактивних ізотопів РЗЕ та Молібдену в області наднизьких температур.

Key words: solid solution, mixing energy, molybdates, lanthanides, actinoides, calcium, lithium, scheelite structure, isomorphous substitutions, thermodynamic stability.

Ключові слова: твердий розчин, енергія змішання, молібдати, лантаноїди, актиноїди, Кальцій, Літій, структура шеєліту, ізоморфні заміщення, термодинамічна стабільність.

(Received 30 July, 2024)

1. INTRODUCTION

Materials with scheelite mineral structure (calcium tungstate, $CaWO_4$), based on individual molybdates and tungstates or solid solutions, which are considered as matrices for immobilizing radioactive isotopes, can contain elements in oxidation states from +1 to +7 (in the Ca positions: Li, Na, K, Rb, Cs, and Tl; Ca, Sr, Ba, Mn, and Cu; Fe, La–Lu, and Y; Th, U, Np, and Pu; in the W positions: Nb, Ta, Mo, W, Re, I, V, and Ge [1]. Normal salts of tungstates and molybdates of alkaline earth elements of the composition $M^{II}XO_4$ and double molybdates and tungstates of alkali and rare-earth elements (REE) of the composition $Na_{0.5}Ln_{0.5}XO_4$ (where M^{II} is an alkaline earth metal, Ln is a rare-earth element, and X = Mo or W) with a scheelite structure are of interest due to their potential practical applications as ion conductors, microwave dielectrics [2], luminophores [3], scintillators [4], LEDs, optical fibres, photocatalysts for wastewater treatment [5], high-performance electrochemical supercapacitors for energy storage and conversion [6], lasers [7], and in many other cases.

Of particular interest is the recent trend of using molybdates and tungstates of alkaline earth elements doped with double molybdates and tungstates of alkali metals and REEs with a scheelite structure for the storage and disposal of high-level radioactive waste with long-lived radioactivity [8–13]. Previously, alumophosphate or borosilicate glasses, which have a lifetime of no more than 30–40 years, were used as matrices for radioactive waste disposal [14]. According to [8, 15], under conditions typical for deep geological repositories, borosilicate glass may dissolve upon contact with groundwater over geological timescales. Meanwhile, according to current regulations, the matrix material must ensure environmental safety for more than 10^5 years [16]. Such a long time can be provided by ceramic matrices of minerals that can persist in natural conditions for at least the above-mentioned number of years, in partic-

ular, molybdates and tungstates of alkaline-earth elements with a scheelite-type structure, which can isomorphously incorporate radioactive isotopes of actinoides and lanthanides close to them in size and charge (the amount of the latter, according to [17], is up to 35 wt.% of nuclear reactor waste), as well as radioactive isotopes of molybdenum.

However, most publications focus on studying synthesis conditions and properties of the corresponding solid solutions but do not predict their behaviour during storage and disposal. As known [18], solid solutions tend to decompose upon cooling, which can lead to the degradation of materials based on them, as well as changes and non-reproducibility of their properties. The insufficient information on the substitution limits and thermodynamic stability areas of solid solutions forces researchers to choose material compositions and synthesis conditions either by analogy with related systems or by the 'trial and error' method, which can lead to excessive consumption of expensive reagents and increase the duration of research. Therefore, it is rational to apply not only experimental but also computational methods, free from the drawbacks. An example of such an approach can be found in the works [19, 20], where the results of calculations from the study [21] were used to select synthesis conditions for solid solution samples of the $Y_{1-x}Sc_xPO_4$ system.

At the same time, to date, studies have mainly focused on systems in which larger REE ions were used as simulators for large triple-charged actinoides, such as U or Pu, in matrices containing strontium and sodium [9–13]. At the same time, to the best of our knowledge, only in the $Ca_{1-x}Li_{x/2}Gd_{x/2}MoO_4$ system [8] was Gd^{3+} used as a simulator for minor actinoide Cm^{3+}, involving, according to the requirements of isomorphous substitutions [18], smaller calcium and lithium cations compared to strontium and sodium. As noted in Ref. [8], the study of the structure and chemical stability of $Ca_{1-x}Li_{x/2}Gd_{x/2}MoO_4$ yields promising results in the development of new single- or multicomponent systems for immobilizing high-level nuclear waste with high molybdenum content.

Therefore, the present work aimed to predict the limits of isomorphous substitutions and the thermodynamic stability of $Ca_{1-x}(Li_{0.5}Ln_{0.5})_xMoO_4$ solid solutions with a scheelite structure containing REE cations as actinoide simulators for the disposal of high-level radioactive waste.

2. INITIAL DATA AND CALCULATION METHODOLOGY

In V. S. Urusov's crystal-energy theory of isomorphous miscibility, the main problem in determining the limits of isomorphous substitutions is finding the mixing energy (Q_{mix}) [18]. Since both compo-

nents of the $Ca_{1-x}(Li_{0.5}Ln_{0.5})_xMoO_4$ systems are isostructural with scheelite, the mixing energy can be calculated as the sum of only two contributions, resulting from the differences in the degrees of ionicity of the chemical bonds in the system components (Q_ε) and the sizes of the substituting structural units (Q_R) [18]:

$$Q_{\text{mix}} = Q_\varepsilon + Q_R = \frac{1390 m z_m z_x \alpha(\Delta\varepsilon)^2}{2R} + C m n z_m z_x \left(\frac{\Delta R}{R_1}\right)^2 \text{ [kJ/mol]}, (1)$$

where $m = 2$ is the number of different structural units in the components of the systems in the pseudobinary approximation of the scheelite structure (lithium and lanthanides, statistically located at the cation sites in the $Li_{0.5}Ln_{0.5}MoO_4$ scheelite structure, are considered as one structural unit, and the molybdate anion is considered as the second one); $z_m = z_x = 2$—the formal (integer) charges of the substituting (z_m) and common (z_x) structural units of the components; $\alpha = 1.723$ is the reduced Madelung constant, calculated using the Templeton formula [22]; $C = 20(2\Delta\chi + 1)$ is a constant depending on the properties of the components, where $\Delta\chi$ is the difference in electronegativity (χ) values of the cations taken from Ref. [23], and the anion MoO_4^{2-} taken, according to the recommendation [24], as equal to the χ of the oxide anion O^{2-} (3.758). The choice of the χ scale [23], as opposed to the scales of other authors, was because the χ values change in it with a regular periodicity, increasing in the series La^{3+}–Eu^{3+} from 1.327 to 1.433 and Gd^{3+}–Yb^{3+} from 1.386 to 1.479, with a sharp drop during the transitions Eu^{3+}–Gd^{3+} from 1.433 to 1.386 and Yb^{3+}–Lu^{3+} from 1.479 to 1.431, which is due to the structure of the electronic shells of the REEs. Europium and gadolinium have a half-filled 4*f*-shell (7 electrons), and ytterbium and lutetium have a filled shell (14 electrons). When transitioning from europium to gadolinium and from ytterbium to lutetium, the first electron appears in the 5*d*-sublevel; $n = 8$ is co-ordination number of the substituting structural unit in the pseudobinary representation of the scheelite structure; $R_{\text{Li, Ln}-M}$ is interatomic distance 'cation–tetrahedral anion' in $Li_{0.5}Ln_{0.5}MoO_4$ calculated from the unit cell parameters taken from Ref. [25]; ΔR is the difference in the interatomic distances 'cation–tetrahedral anion' in $CaMoO_4$ and $Li_{0.5}Ln_{0.5}MoO_4$; $\Delta R/R_1$ is relative difference in the interatomic distances 'cation–tetrahedral anion' in the system components (dimensional parameter); R_1 is interatomic distance 'cation–tetrahedral anion' in the system component with the smaller cation radius; $\Delta\varepsilon$ is the difference in the degrees of ionicity of the chemical bonds in the system components in the pseudobinary approximation of the structure. The degree of ionicity of the chemical bond ε in the crystals was determined by the difference in χ between the tetrahedral

TABLE 1. Some initial data*, calculated mixing energies, and critical decomposition temperatures of the solid solutions in the $Ca_{1-x}(Li_{0.5}Ln_{0.5})_xMoO_4$ systems.

Ln	$R(LiLn(MoO_4)_2)$, Å	χ_{Ln}	$\Delta\chi$	$C = 20\cdot(2\Delta\chi + 1)$	$\Delta R/R_1$	Q_R, kJ/mole	Q_{mix}, kJ/mole	T_{cr}, K
La	3.851	1.327	2.594	123.76	0.0185	2.710	2.720	162
Ce	3.837	1.348	2.589	123.56	0.0148	1.732	1.772	105
Pr	3.812	1.374	2.582	123.28	0.0081	0.518	0.609	36
Nd	3.798	1.382	2.580	123.2	0.0044	0.153	0.314	19
Sm	3.775	1.410	2.573	122.92	0.0016	0.020	0.274	16
Eu	3.765	1.433	2.567	122.68	0.0043	0.145	0.511	30
Gd	3.756	1.386	2.579	123.16	0.0067	0.359	0.522	31
Tb	3.744	1.410	2.573	122.92	0.0099	0.771	1.027	61
Dy	3.734	1.426	2.569	122.76	0.0126	1.249	1.618	96
Ho	3.727	1.433	2.567	122.68	0.0145	1.651	2.021	120
Er	3.714	1.438	2.566	122.64	0.0181	2.571	3.077	183
Tm	3.707	1.455	2.562	122.48	0.0200	3.135	3.642	217
Yb	3.698	1.479	2.556	122.24	0.0225	3.961	4.800	286
Lu	3.692	1.431	2.568	122.72	0.0241	4.562	4.936	294

*_Note:_ The unit cell parameters of $CaMoO_4$ for calculating the distance $R(CaMoO_4) = 3.7812$ Å are taken from Ref. [30], and the distances $R(LiLn(MoO_4)_2)$ are taken from Ref. [31]. $\chi_{Li} = 1.009$; $\chi_{Ca} = 1.160$; $\chi(Ca_{1-x}(Li_{0.5}Ln_{0.5})_x) = ((\chi_{Li} + \chi_{Ln})/2 + \chi_{Ca})/2$; $\Delta\chi = 3.758 - ((\chi_{Li} + \chi_{Ln})/2 + \chi_{Ca})/2$.

anion and the cations according to the tabulated data provided by S. Batsanov [26].

Since the size parameter, $\Delta R/R_1$, was significantly less than 0.1 (Table 1), according to Ref. [18], the calculation of the equilibrium substitution limits as a function of temperature was carried out in the approximation of regular solid solutions using Becker's equation [27]

$$\frac{-(1-2x)}{\ln[x/(1-x)]} = \frac{R_g T_d}{Q_{mix}}, \qquad (2)$$

where x is the mole fraction of the dissolved component, R_g is the universal gas constant, T_d is the decomposition temperature of the

solid solution. The values of R_g and Q_{mix} in both latter cases were expressed in calories [18].

The critical decomposition temperatures, T_{cr}, were calculated according to Ref. [18] in the approximation of regular solid solutions using equation

$$T_{cr} = \frac{Q_{mix}}{2kN}, \quad (3)$$

where k is the Boltzmann constant, and N is the Avogadro number.

The error in calculating the critical (maximum) decomposition temperature of solid solutions was ±100 K, and the mixing energy Q_R, considering the error of the initial data, was up to ±13% [18].

3. RESULTS OF CALCULATIONS AND THEIR DISCUSSION

3.1. Mixing Energies of Solid Solutions

Some initial data and calculation results of mixing energies are summarized in Tables 1 and 2 and presented in Fig. 1. As can be

TABLE 2. Data for calculating the mixing energy for solid solutions in the $Ca_{1-x}(Li_{0.5}Ln_{0.5})_xMoO_4$ systems.

Ln	$\chi(MoO_4) - \chi(Li_{0.5}Ln_{0.5})$	$\varepsilon(Li_{0.5}Ln_{0.5})MoO_4$	$\Delta\varepsilon^*$	Q_ε, kJ/mole
La	2.590	0.768	0.002	0.010
Ce	2.579	0.766	0.004	0.040
Pr	2.566	0.764	0.006	0.091
Nd	2.562	0.762	0.008	0.161
Sm	2.548	0.760	0.010	0.254
Eu	2.537	0.758	0.012	0.366
Gd	2.560	0.762	0.008	0.163
Tb	2.548	0.760	0.010	0.256
Dy	2.540	0.758	0.012	0.369
Ho	2.537	0.758	0.012	0.370
Er	2.534	0.756	0.014	0.506
Tm	2.526	0.756	0.014	0.507
Yb	2.514	0.752	0.018	0.839
Lu	2.538	0.758	0.012	0.374

**Note:* $\Delta\varepsilon = \varepsilon(CaMoO_4) - \varepsilon(Li_{0.5}Ln_{0.5})MoO_4$; the value of $\varepsilon(CaMoO_4) = 0.77$ was determined according to the tabular data of S. Batsanov [26], based on $\chi(MoO_4) = 3.758$ and $\chi(Ca) = 1.160$.

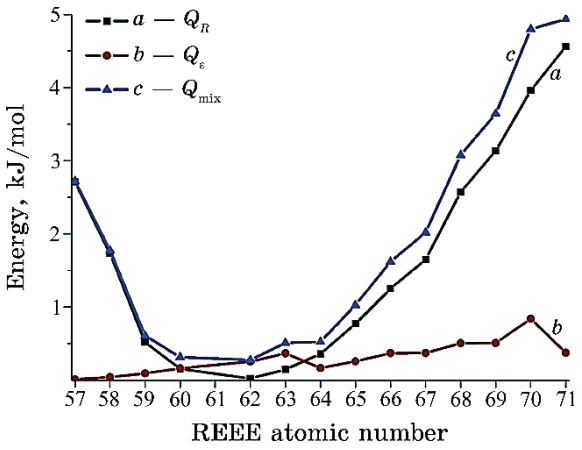

Fig. 1. Dependences of the calculated contributions to the mixing energy Q_R (*a*), Q_ε (*b*), and the total mixing energy Q_{mix} (*c*) of the $Ca_{1-x}(Li_{0.5}Ln_{0.5})_xMoO_4$ systems on REE atomic number.

seen from the data provided, with an increase in the atomic number of REEs, the contributions to the total mixing energy due to differences in the sizes of the substituting structural units, Q_R, initially decrease significantly and smoothly from 2.71 to 0.02 kJ/mole in the REEs series from La to Sm, then increase from 0.02 to 4.56 kJ/mole in the REEs series from Sm to Lu (Table 1, Fig. 1 *a*). This is related to a similar change in the size parameter $\Delta R/R_1$, which first decreases from 0.0185 to 0.0044 and then increases to 0.0241. Such a change in $\Delta R/R_1$ is because the crystal ionic radius of the substituted double-charged calcium cation, which mainly determines the value of $\Delta R/R_1$, lies within the range of ionic radii of the substituting REEs from lanthanum to lutetium and is close to the ionic radius of samarium [28].

The dependences of the contributions to the total mixing energy due to differences in the degrees of ionicity of the chemical bonds of the components, Q_ε, for the cerium and yttrium subgroups are identical (Fig. 1, *b*). They systematically increase in the groups of systems containing REEs of the La–Eu series from 0.010 to 0.366 kJ/mole and REEs of the Tb–Yb series from 0.256 to 0.839 kJ/mole, followed by a sharp decrease when transitioning from the system containing Eu to the system containing Gd, from 0.366 to 0.163 kJ/mole, and from the system containing Yb to the system containing Lu, from 0.839 to 0.374 kJ/mol. This is due to the aforementioned structure of the electron shells of the REEs.

According to Ref. [18], in general case, if the differences in the degrees of ionicity of the chemical bonds in the system components

are less than 0.05, the value of Q_ε will be insignificant and can be neglected. This is also because the errors in the values of electronegativity, which served as the basis for calculating Q_ε, are on the order of 0.05 [29], which is much larger than the inaccuracies in determining the parameters of the unit cells, which are mainly used to determine the Q_R energy.

In this case, $\Delta\varepsilon$ varies from 0.002 to 0.018 (Table 2), and most of the Q_ε values are significantly smaller than Q_R (Fig. 1, *a*, *b*). However, in the case of systems with samarium and europium compounds, the Q_ε values, on the contrary, exceed Q_R values. Therefore, the contributions of Q_ε to the mixing energies were considered in all systems.

3.2. Decomposition Temperatures of Solid Solutions

The calculated critical decomposition temperatures T_{cr} of the unlimited series of solid solutions in the $Ca_{1-x}(Li_{0.5}Ln_{0.5})_xMoO_4$ systems (Table 1, Fig. 2, *e* for $x = 0.5$) decrease in the range of 162–16 K with an increasing of REEs atomic number in the La–Sm series, in correlation with the mixing energy. In the Eu–Lu series, the values of T_{cr} increase in the range of 30–294 K. It should be noted that the $Ca_{1-x}(Li_{0.5}Ln_{0.5})_xMoO_4$ systems are characterized by very low critical decomposition temperatures for solid solutions (for 12 out of 14 systems, they are below room temperature), and only for two of

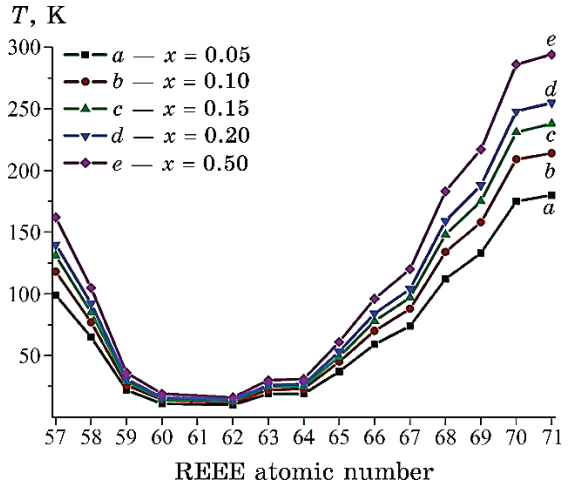

Fig. 2. Dependences of decomposition temperatures for solid solutions in the $Ca_{1-x}(Li_{0.5}Ln_{0.5})_xMoO_4$ systems on the REEs' atomic numbers (thermodynamic-stability diagram) for substitution limits of $x = 0.05$ (*a*), 0.10 (*b*), 0.15 (*c*), 0.20 (*d*), and 0.50 (*e*).

TABLE 3. Calculated thermodynamically possible decomposition temperatures (T_d [K]) for solid solutions in the $Ca_{1-x}(Li_{0.5}Ln_{0.5})_xMoO_4$ systems at $x = 0.05$, 0.10, 0.15, and 0.20.

Ln	Values of T_d [K] at corresponding x			
	0.05	0.10	0.15	0.20
La	99	118	131	140
Ce	65	77	85	92
Pr	22	26	29	31
Nd	11	14	15	16
Sm	10	12	13	14
Eu	19	22	25	26
Gd	19	23	25	27
Tb	37	45	49	53
Dy	59	70	78	84
Ho	74	88	97	104
Er	112	134	148	159
Tm	133	158	175	188
Yb	175	209	231	248
Lu	180	214	238	255

them, $Ca_{1-x}(Li_{0.5}Yb_{0.5})_xMoO_4$ and $Ca_{1-x}(Li_{0.5}Lu_{0.5})_xMoO_4$, they are close to room temperature.

For all systems, based on the critical decomposition temperatures T_{cr} (at $x = 0.5$, Table 1) and the decomposition temperatures (T_d for substitution limits $x = 0.05$, 0.10, 0.15, and 0.20, Table 3) of the limited series of $Ca_{1-x}(Li_{0.5}Ln_{0.5})_xMoO_4$ solid solutions, thermodynamic-stability diagrams, *i.e.*, dependences of decomposition temperatures on the REEs' atomic numbers, have been plotted (Fig. 2).

These dependences can be used to determine graphically the equilibrium substitution limits x at given decomposition temperatures T_d or the decomposition temperatures at given substitution limits [32]. The intersection points of an isotherm, drawn from a given decomposition temperature, with a vertical line drawn from the REE atomic number, make it possible to determine the composition range in which the substitution limit is located. Interpolating the segment of this vertical line between the two nearest curves provides the possible substitution limit.

3.3. Areas of Thermodynamic Stability

From the thermodynamic stability diagram, it follows that the unlimited solid solutions of the $Ca_{1-x}(Li_{0.5}Ln_{0.5})_xMoO_4$ systems, which are

stable at temperatures above the critical (Fig. 2, above curve *e*), should decompose when the temperature is lowered below the critical, forming limited areas. This would occur if the diffusion rate and time were sufficiently large to allow stable nuclei of the new phase to form and begin to grow.

For each of the $Ca_{1-x}(Li_{0.5}Ln_{0.5})_xMoO_4$ systems, the decomposition temperatures of the solid solutions were calculated in the composition range of $1.0 > x > 0$ with a step of $x = 0.05$ and decomposition domes were plotted (Fig. 3). According to them with greater accuracy than in Fig. 2, it is possible to determine graphically for each system the decomposition temperature at a given substitution limit or the equilibrium substitution limit at a given temperature, as well as the regions of thermodynamic stability. Above the peaks of the decomposition domes, a continuous series of stable solid solutions will exist; below the peaks but above the dome lines, there will be

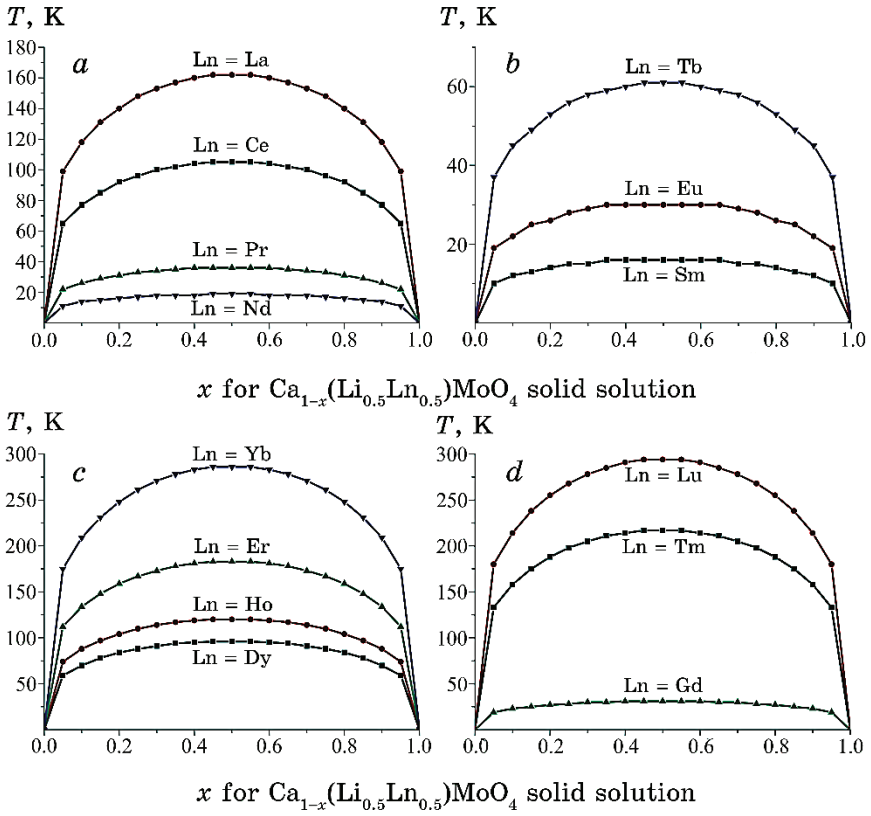

Fig. 3. Decomposition domes for solid solutions in the $Ca_{1-x}(Li_{0.5}Ln_{0.5})_xMoO_4$ ($1.0 > x > 0$) systems: (*a*) Ln = La, Ce, Pr, and Nd; (*b*) Ln = Sm, Eu, and Tb; (*c*) Ln = Dy, Ho, Er, and Yb; (*d*) Ln = Gd, Tm, and Lu.

two limited solubility regions; and below the dome lines, there will be two limited solubility regions and mixtures of two solid solutions based on each of the system components.

3.4. Comparison of Calculation Results with Literature Data

As far as we know, there is no literature data on the critical decomposition temperatures, limits of isomorphous substitutions in the case of limited solubility of components, and thermodynamic stability of solid solutions in the $Ca_{1-x}(Li_{0.5}Ln_{0.5})_xMoO_4$ systems.

Previously (see Table 3), the synthesis conditions and some properties of solid solutions in systems with wide areas of solid solutions, such as $[(Li_{0.5}Nd_{0.5})_{1-x}Ca_x]MoO_4$ and $[(Li_{0.5}Sm_{0.5})_{1-x}Ca_x]MoO_4$ ($x = 0.2–0.9$) [33], the unlimited solubility of components in $Ca_{1-2x}Eu_xLi_xMoO_4$ [34] and $[(Li_{0.5}Gd_{0.5})_{1-x}Ca_x]MoO_4$ [8], as well as one solid solution composition $Ca_{0.9}MoO_4$:$0.05Eu^{3+}$, $0.05Li^+$ [35], have been studied. Additionally, the literature presents results on the study of solid solutions in the systems $CaMoO_4$:Eu^{3+}, Li^+ [36] and $CaMoO_4$:Eu^{3+}, M^+ (M = Li, Na, K) [37] without specifying the component ratios.

The results obtained in this study are consistent with the data [8, 33–37] in the sense that the synthesis temperature ranges for the samples of these systems (673–1223 K, Table 3) fall within the predicted areas of thermodynamic stability of the solid solutions, *i.e.*, well above the decomposition domes presented in Fig. 3, *a*, *b*, and *d*.

It is known [38] that, for radioactive waste disposal, its components are included in chemically and mechanically stable matrices, with subsequent placement in underground storage until the complete decay of radionuclides or until their activity approaches the level of the surrounding natural background. In this process, the oxides of fission products are incorporated into a glassy matrix, since glass, being a non-stoichiometric compound, can dissolve a complex mixture of fission products in its liquid state and subsequently retain it firmly upon cooling (and solidification). The resulting product has relatively high chemical and radiation resistance. Most commonly, two types of glass are widely used for immobilizing radioactive waste: aluminophosphate glass and borosilicate glass. However, the main problem of glass remains unresolved, *i.e.*, its thermodynamic instability, which manifests as glass crystallization (devitrification) under the influence of increased temperatures caused by radioactive decay. Devitrification phenomena degrade the initial properties of the product, particularly increasing its leaching rate, resulting in the release of radioactive waste elements into the solution over a relatively short period. In addition, due to the formation of crystalline phases with a total lower iso-

morphous capacity than that of glass, some radionuclides may leach into aqueous solutions, posing a threat to the biosphere. It is noted [39] that glass and ceramics are among the most reliable materials for immobilizing radioactive waste. Ceramic matrices have the greatest potential for practical use due to their high chemical stability and thermal stability. Ceramics based on natural and artificially synthesized mineral additives can incorporate a significantly larger volume of radioactive waste than glass. Furthermore, it has been noted [40] that the immobilization of certain radioactive isotopes proves to be a more complex process for molybdenum-rich waste generated during the reprocessing of used nuclear fuel, such as UMo–MoSnAl fuel from gas-graphite reactors, or mixed waste containing lanthanides and transition metals proposed for nuclear fuel reprocessing in the United States. In both cases, immobilization in glass is found to be impossible, as the waste contains substantial amounts of highly radioactive isotopes that release heat during decay, as well as a large quantity of molybdenum that exceeds the solubility limits in borosilicate glasses. Currently, it is planned to mix such waste with aluminoborosilicate, during which separation into two liquid phases occurs upon cooling, followed by the crystallization of molybdate phases and further additional separation into two liquid phases. It has been noted [40] that a detailed understanding of the thermochemistry of vitrification and phase formation processes is required to ensure the formation of the desired crystalline phase.

As the further development of nuclear power engineering could lead to unacceptable radioactive contamination of the Earth's biosphere, one direction for preventing this situation could be the disposal of radioactive waste in space [41]. If it becomes necessary to dispose of radioactive waste not only within the Earth's crust but also at ultra-low temperatures in space, materials based on solid solutions of $Ca_{1-x}(Li_{0.5}Ln_{0.5})_xMoO_4$ may be used, particularly those containing Nd, Sm, Eu, Gd, and actinoides close to them in size. Such materials have lower critical decomposition temperatures (16–31 K) compared to previously recommended materials based on solid solutions of other compositions: phosphates $La_{1-x}Ln_xPO_4$, fluorides $La_{1-x}Ln_xF_3$, and arsenates $Lu_{1-x}Ln_xAsO_4$. The critical decomposition temperatures of the latter are in the intervals of 150–830 K [42], 522–1811 K [43], and 186–624 K [44], respectively.

4. CONCLUSIONS

1. Within the framework of V. S. Urusov's crystal-energy theory of isomorphous substitutions, the mixing energies (interaction parameters), critical decomposition (stability) temperatures, and the lim-

its of isomorphous substitutions have been calculated, and the thermodynamic stability of the solid solutions in the $Ca_{1-x}(Li_{0.5}Ln_{0.5})_xMoO_4$ systems, where Ln are rare earth elements, has been assessed.

2. It has been shown that with the increase in the REE number, the contributions to the total mixing energy due to differences in the sizes of the substituting structural units, Q_R, initially decrease significantly from 2.71 to 0.02 kJ/mole in the REEs series from La to Sm, and then increase from 0.02 to 4.56 kJ/mole in the REEs' series from Sm to Lu.

3. The contributions to the total mixing energy Q_{mix} due to differences in the sizes of the substituting structural units Q_R significantly exceed the contributions due to differences in the degrees of ionicity of the components Q_ε. However, in the case of systems with samarium and europium compounds, the Q_ε values exceed the Q_R values.

4. The calculated critical decomposition temperatures T_{cr} of the unlimited series of solid solutions in the studied systems decrease along with the mixing energy as the REEs' numbers increase in the La–Sm series, ranging from 162 to 16 K, and increase in the Eu–Lu series, ranging from 30 to 294 K.

5. A thermodynamic stability diagram and decomposition domes for each solid solution system are presented in the concentration range from $x = 0$ to $x = 1.0$ through $x = 0.05$. These allow for the graphical determination of the decomposition temperature of solid solutions for a given composition x, the equilibrium substitution limit for a given decomposition temperature, and the assessment of thermodynamic stability regions over a wide range of compositions and temperatures.

6. The calculated results do not contradict the literature data, in the sense that the temperature range for obtaining samples of previously synthesized systems falls within the thermodynamic stability regions of solid solutions as predicted by modelling.

7. For the disposal of radioactive waste at extremely low temperatures (*e.g.*, in space), materials based on solid solutions of $Ca_{1-x}(Li_{0.5}Ln_{0.5})_xMoO_4$, particularly those containing Nd, Sm, Eu, Gd, and actinoides of similar size, may be used. These materials have significantly lower critical decomposition temperatures (16–31 K) compared to previously recommended materials based on solid solutions of other compositions such as $La_{1-x}Ln_xPO_4$ phosphates, $La_{1-x}Ln_xF_3$ fluorides, and $Lu_{1-x}Ln_xAsO_4$ arsenates.

ACKNOWLEDGMENTS

The study was carried out within the framework of the Programme

of Fundamental Research funded by the Ministry of Education and Science of Ukraine (grant ID 0122U000762).

REFERENCES

1. A. I. Orlova and M. I. Ojovan, *Materials*, **12**: 2638 (2019); https://doi.org/10.3390/ma12162638
2. A. A. Nikitina, Z. A. Mikhaylovskaya, N. S. Knyazev, A. I. Malkin, and A. N. Korotkov, *Fizika. Tekhnologii. Innovatsii: Sbornik Statey VII Mezhdunarodnoy Molodezhnoy Nauchnoy Konferentsii* (Yekaterinburg: Ur-FU: 2020) (in Russian); http://elar.urfu.ru/handle/10995/91850
3. I. C. Nogueira, L. S. Cavalcante, P. F. S. Pereira, M. M. de Jesus, J. M. Rivas Mercury, N. C. Batista, M. Siu Li, and E. Longo, *J. Appl. Cryst.*, **46**, No. 5: 1434 (2013); https://doi.org/10.1107/S0021889813020335
4. A. Priya, E. Sinha, and S. K. Rout, *Solid State Sci.*, **20**: 40 (2013); https://doi.org/10.1016/j.solidstatesciences.2013.03.002
5. B. Bakiz, A. Hallaoui, A. Taoufyq, A. Benlhachemi, F. Guinneton, S. Villain, M. Ezahri, J.-C. Valmalette, M. Arab, and J.-R. Gavarri, *J. Solid State Chem.*, **258**: 146 (2018); https://doi.org/10.1016/j.jssc.2017.10.014
6. T. Anitha, A. E. Reddy, Y. A. Kumar, Y.-R. Cho, and H.-J. Kim, *Dalton Trans.*, **48**, No. 28: 10652 (2019); https://doi.org/10.1039/C9DT01931F
7. O. A. Buryi, D. M. Vynnyk, T. I. Voroniak, I. V. Stasyshyn, A. T. Ratych, and A. S. Andrushchak, *Ukrainian Journal of Physics*, **68**, No. 2: 92 (2023); https://doi.org/10.15407/ujpe68.2.92
8. Ch. Meng, W. Li, Ch. Ren, and J. Zhao, *J. Mater. Sci.*, **55**: 2741 (2020); https://doi.org/10.1007/s10853-019-04223-y
9. M. G. Tokarev, E. A. Potanina, A. I. Orlova, S. A. Khainakov, M. S. Boldin, E. A. Lantsev, N. V. Sakharov, A. A. Murashov, S. Garcia-Granda, A. V. Nokhrin, and V. N. Chuvil'deev, *Inorg. Mater.*, **55**, No. 7: 730 (2019); https://doi.org/10.1134/S0020168519070203
10. A. I. Orlova, Ye. A. Potanina, M. G. Tokarev, M. S. Boldin, and Ye. A. Lantsev, *Voprosy Radiatsionnoy Bezopasnosti*, **2**, No. 86: 2 (2017) (in Russian).
11. E. A. Potanina, A. I. Orlova, D. A. Mikhailov, A. V. Nokhrin, V. N. Chuvil'deev, M. S. Boldin, N. V. Sakharov, E. A. Lantcev, M. G. Tokarev, and A. A. Murashov, *J. Alloy Compd.*, **774**: 182 (2019); https://doi.org/10.1016/j.jallcom.2018.09.348
12. E. A. Potanina, A. I. Orlova, A. V. Nokhrin, M. S. Boldin, N. V. Sakharov, O. A. Belkin, V. N. Chuvil'deev, M. G. Tokarev, S. V. Shotin, and A. Yu. Zelenov, *Ceram. Int.*, **44**, No. 4: 4033 (2018); https://doi.org/10.1016/j.ceramint.2017.11.199
13. A. A. Belov, O. O. Shichalin, E. K. Papynov, I. Y. Buravlev, A. S. Portnyagin, S. A. Azon, A. N. Fedorets, A. A. Vornovskikh, E. S. Kolodeznikov, E. A. Gridasova, A. Pogodaev, N. B. Kondrikov, Y. Shi, and I. G. Tananaev, *Materials*, **16**, No. 17: 5838 (2023); https://doi.org/10.3390/ma16175838
14. A. E. Grechanovsky, N. N. Eremin, and V. S. Urusov, *Phys. Solid State*, **55**, No. 9: 1929 (2013); https://doi.org/10.1134/S1063783413090138

15. D. Bosbach, T. Rabung, F. Brandt, and T. Fanghänel, *Radiochim. Acta*, **92**, Nos. 9–11: 639 (2004); https://doi.org/10.1524/ract.92.9.639.54976
16. I. S. Skiter and Ye. Ye. Vtornikova, *Yaderna ta Radiatsiyna Bezpeka* [Nuclear and Radiation Safety], **2**, No. 78: 36 (2018) (in Ukrainian); https://doi.org/10.32918/nrs.2018.2(78).06
17. L. A. Boatner, *Rev. Mineral. Geochem.*, **48**, No. 1: 87 (2002); https://doi.org/10.2138/rmg.2002.48.4
18. V. S. Urusov, *Teoriia Izomorfnoi Smesimosti* [The Theory of Isomorphous Miscibility] (Moskva: Nauka: 1977) (in Russian).
19. D. Spassky, A. Vasil'ev, V. Nagirnyi, I. Kudryavtseva, D. Deyneko, I. Nikiforov, I. Kondratyev, and B. Zadneprovski, *Materials*, **15**, No. 19: 6844 (2022); https://doi.org/10.3390/ma15196844
20. V. S. Voznyak-Levushkina, A. A. Arapova, D. A. Spassky, I. V. Nikiforov, and B. I. Zadneprovski, *Phys. Solid State*, **64**, No. 11: 567 (2022); https://doi.org/10.1134/S1063783422110130
21. E. I. Get'man, S. V. Radio, and L. I. Ardanova, *Inorg. Mater.*, **54**, No. 6: 596 (2018); https://doi.org/10.1134/S0020168518060031
22. D. H. Templeton, *J. Chem. Phys.*, **21**, No. 11: 2097 (1953); https://doi.org/10.1063/1.1698788
23. K. Li and D. Xue, *J. Phys. Chem. A*, **110**, No. 39: 11332 (2006); https://doi.org/10.1021/jp062886k
24. S. S. Batsanov, *Russ. Chem. Rev.*, **37**, No. 5: 332 (1968); https://doi.org/10.1070/RC1968v037n05ABEH001639
25. A. A. Yevdokimov, V. A. Yefremov, V. K. Trunov, I. A. Kleyman, and B. F. Dzhurinskiy, *Soyedineniya Redkozemel'nykh Ehlementov. Molibdaty, Vol'framaty* [Compounds of Rare-Earth Elements. Molybdates, Tungstates] (Moskva: Nauka: 1991) (in Russian).
26. S. S. Batsanov, *Strukturnaya Khimiya. Fakty i Zavisimosti* [Structural Chemistry. Facts and Dependences] (Moskva: Dialog-MGU: 2000) (in Russian).
27. R. Becker, *Z. Metallkd.*, **29**: 245 (1937).
28. R. D. Shannon, *Acta Crystallogr., Sect. A*, **32**, No. 5: 751 (1976); https://doi.org/10.1107/S0567739476001551
29. L. Pauling, *General Chemistry* (San-Francisco: W. H. Freeman and Co.: 1970).
30. E. Gürmen, E. Daniels, and J. S. King, *J. Chem. Phys.*, **55**, No. 3: 1093 (1971); https://doi.org/10.1063/1.1676191
31. E. I. Get'man, *Izomorfnyye Zameshcheniya v Vol'framatnykh i Molibdatnykh Sistemakh* [Isomorphous Substitutions in Tungstate and Molybdate Systems] (Novosibirsk: Nauka: 1985) (in Russian).
32. E. I. Get'man, S. V. Radio, L. B. Ignatova, and L. I. Ardanova, *Russ. J. Inorg. Chem.*, **64**, No. 1: 118 (2019); https://doi.org/10.1134/S0036023619010091
33. H.-H. Xi, D. Zhou, H.-D. Xie, B. He, and Q.-P. Wang, *J. Am. Ceram. Soc.*, **98**, No. 2: 587 (2015); https://doi.org/10.1111/jace.13332
34. J. Wang, X. Jing, Ch. Yan, and J. Li, *J. Electrochem. Soc.*, **152**, No. 3: G186 (2005); https://doi.org/10.1149/1.1856924
35. Q. Zhang and Zh. Xia, *RSC Adv.*, **4**, No. 95: 53237 (2014); https://doi.org/10.1039/C4RA09136A

36. X. Wang, Y. He, G. Peng, Zh. Liang, and J. Wu, *Chinese Journal of Materials Research*, **26**, No. 6: 615 (2012); https://www.cjmr.org/EN/Y2012/V26/I6/615
37. X. Liu, L. Li, H. M. Noh, J. H. Jeong, K. Jang, and D. S. Shin, *RSC Adv.*, **5**, No. 13: 9441 (2015); https://doi.org/10.1039/C4RA12183J
38. A. R. Kotelnikov, G. M. Akhmedzhanova, N. I. Suk, K. V. Martynov, O. T. Gavlina, and V. A. Suvorova, *Geochem. Int.*, **57**, No. 10: 1066 (2019); https://doi.org/10.1134/S0016702919100057
39. O. E. Shubabko, G. Ye. Ovsyannikova, Min Kheyn Tkhet, and M. A. Vartanyan, *Uspekhi v Khimii i Khimicheskoy Tekhnologii*, **32**, No. 2: 188 (2017) (in Russian).
40. J. S. McCloy and A. Goel, *MRS Bulletin*, **42**: 233 (2017); https://doi.org/10.1557/mrs.2017.8
41. A. V. Degtyarev, *Kosmichna Nauka i Tekhnologiya*, **20**, No. 1: 58 (2014); https://www.mao.kiev.ua/biblio/jscans/knit/2014-20/knit-2014-20-1-07-degtyarev.pdf
42. E. I. Get'man and S. V. Radio, *Inorg. Mater.*, **53**, No. 7: 718 (2017); https://doi.org/10.1134/S0020168517070044
43. Y. A. Oleksii, E. I. Get'man, S. V. Radio, L. I. Ardanova, and E. E. Zubov, *2021 IEEE 11th International Conference 'Nanomaterials: Applications & Properties' (NAP) (Odesa, Ukraine, 2021)*, p. 1–5; https://doi.org/10.1109/NAP51885.2021.9568596
44. E. I. Get'man, Y. A. Oleksii, O. V. Kudryk, S. V. Radio, and L. I. Ardanova, *Nanomaterials and Nanocomposites, Nanostructure Surfaces, and Their Applications. Springer Proceedings in Physics* (Eds. O. Fesenko and L. Yatsenko) (Cham: Springer: 2021), vol. **263**, p. 3; https://doi.org/10.1007/978-3-030-74741-1_1

Наносистеми, наноматеріали, нанотехнології
Nanosistemi, Nanomateriali, Nanotehnologii
2025, т. 23, № 2, сс. 423–435
https://doi.org/10.15407/nnn.23.02.0423

© 2025 ІМФ (Інститут металофізики
ім. Г. В. Курдюмова НАН України)
Надруковано в Україні.

PACS numbers: 73.63.Nm, 74.78.Na, 75.30.Fv, 75.47.Lx, 75.60.Ej, 81.07.Vb, 85.35.Be

Creating of Bounded Majorana Pairs in Superconducting Net of Quantum Nanowires in $SmMnO_{3+\delta}$

F. M. Bukhanko

Donetsk Institute for Physics and Engineering named after O. O. Galkin, N.A.S. Ukraine,
46, Nauky Ave.,
03028 Kyiv, Ukraine

In this work, the formation of a superconducting network of quantum nanowires in $SmMnO_{3+\delta}$ manganites in two hidden topological states CSL1 and CSL2 of a chiral quantum spin liquid is experimentally studied. As believed, the states of bound pairs of Majorana fermions are trapped at the two ends of the quantum nanowire. The formation of nanofragments of 1*D* coupled charge and spin densities' waves with wave vectors $\mathbf{q}_1 \| \mathbf{a}$ and $\mathbf{q}_2 \| \mathbf{b}$ as regards directions in the crystal lattice within the magnetic fields $H \geq 100$ Oe indicates formation in *ab* planes of 2*D* quantum-nanowires' net. Within the weak magnetic fields $H = 100$ Oe, 350 Oe and 1 kOe, the continuous spectrum of the thermal excitations of bounded Majorana pairs in $SmMnO_{3+\delta}$ in temperature interval of 4.2–12 K is divided into two low-energy Landau zones with numbers $n = 1$ and $n = 2$ with two specific features of magnetization $M(T)$ in the shape of alternating double peaks and truncated Dirac cones.

У цій роботі експериментально вивчено утворення надпровідної сітки квантових нанопроводів у манґанітах $SmMnO_{3+\delta}$ у двох прихованих топологічних станах CSL1 і CSL2 кіральної квантової спінової рідини. Вважається, що стани пов'язаних пар Майоранових ферміонів захоплюються на двох кінцях квантового нанопроводу. Утворення нанофраґментів 1*D*-зв'язаних хвиль зарядової та спінової густин з хвильовими векторами $\mathbf{q}_1 \| \mathbf{a}$ й $\mathbf{q}_2 \| \mathbf{b}$ щодо напрямків кристалічної ґратниці у магнетних полях $H \geq 100$ Е вказує на утворення в площинах *ab* 2*D*-сітки квантових нанопроводів. У слабких магнетних полях $H = 100$ Е, 350 Е і 1 кЕ безперервний спектер теплових збуджень пов'язаних Майоранових пар у $SmMnO_{3+\delta}$ в інтервалі температур 4,2–12 К розбивається на дві низькоенергетичні зони Ландау з номерами $n = 1$ і $n = 2$ із двома особливостями намагнетованости $M(T)$ у формі подвійних піків і зрізаних Діракових конусів, що чергуються.

Key words: Majorana and Dirac fermions, alternating double peaks and

truncated Dirac cones, chiral quantum spin liquid.

Ключові слова: Майоранові та Діракові ферміони, чергування подвійних піків і зрізаних Діракових конусів, кіральна квантова спінова рідина.

(Received 24 September, 2024)

1. INTRODUCTION

Topological superconductors (TS) in dimensions $D = 1, 2$, with broken time-reversal (TR) symmetry have recently attracted a lot of attention [1–10]. These systems support Majorana fermion excitations at order-parameter defects such as vortices and sample edges. Majorana fermion excitations, with second quantized operators γ satisfying the self-Hermitian condition $\gamma^{\dagger} = \gamma$, can be construed as quantum particles, which are their own antiparticles [11]. The self-Hermitian character of Majorana fermions (MFs) leads to a $2D$ quasi-particle exchange statistics, which is non-Abelian [1, 12]. The non-Abelian statistics of MFs can be used as a robust quantum mechanical resource to implement fault-tolerant topological quantum computation (TQC) [13, 14]. In $1D$ TS with broken TR symmetry, Majorana fermion modes are supposed to be trapped at the two ends of a quantum wire [13–15], which, in a $2D$ quantum wire network [15], can potentially lead to successful demonstration of non-Abelian statistics as well as TQC [15–17]. According to Ref. [18], in flat-band superconductors, the group velocity v_F of charge carriers is extremely small, which leads to freezing of the kinetic energy. Superconductivity in this case seems impossible, since within the framework of the BCS theory this means the disappearance of such microproperties as the coherence length of Cooper pairs, their superfluidity rigidity, and the critical current. The authors report the existence of a group velocity of free charge carriers in the two-layer graphene studied by them, which is characteristic of a graphene superlattice with a Dirac superconducting flat zone [19–23]. For the filling factor of the moiré superlattice in superconducting graphene $1/2 < \nu < 3/4$, a very small value of the group velocity $v_F \cong 1000$ m/sec was found. It is important to note that the measurement of superfluidity, which controls the electrodynamic response of a superconductor, shows that it is dominated not by kinetic energy, but by an interaction-controlled superconducting gap, which is consistent with the theories of the quantum geometric contribution [19–23]. Evidence has been found for the crossover of electron-pairs characteristic of BCS and Bose–Einstein condensation [24–27]. The superconducting properties of a deformed graphene, which in normal state has a spectrum of free charge carriers with a flat energy

band, were studied in Ref. [28].

According to Ref. [29], in systems with a condensed state, when a quasi-particle is a superposition of electron and hole excitations and its production operator $\gamma^{\dagger}$ becomes identical to the annihilation operator γ, such a particle can be identified as a Majorana fermion. In the Reed–Green model, the Bogolyubov quasi-particles in the volume become dispersive Majorana fermions, and the bound state formed in the core of the vortex becomes the Majorana zero mode. The former is interesting as a new type of wandering quasi-particles, while the latter is useful as a qubit for topological quantum computing. In condensed matter, the constituent fermions are electrons. Because the electron has a negative charge, it cannot be a Majorana fermion. Nevertheless, Majorana fermions can exist as collective excitations of electrons. The resulting Majorana fermions do not retain the true Lorentz invariance of the Dirac equation, since they do not move at the speed of light. However, with proper length and time scaling, the resulting Majorana fermions also obey the Dirac equation. Such Majorana fermions appear within the boundaries of topological superconductors or in the class of spin-liquid systems [29].

The condensation of bosons in the form of a bound state of Majorana fermions was previously studied in topological superconductors by tunnelling spectroscopy [30–32]. The tunnelling conductivity spectra of topological superconductors depend on their size and symmetry. In one-dimensional topological superconductors with time reversal violation, there is an isolated single Majorana zero mode at each end. Tunnelling conductance due to the isolated zero mode shows a differential conductance peak dI/dV with zero offset height $2e^2/h$ [30–32]. If one Majorana zero mode is coupled to another Majorana zero mode at the other end of the superconductor, the tunnelling conductance is highly dependent on the coupling t between the Majorana modes at the different ends. When the ratio t/Γ of the coupling between modes to the width of the fermion spectrum Γ is very small, the peak shape dI/dV is realized [32]. However, in the case of significant mixing of the two Majorana modes, the differential conductivity has the form of a trough. In this case, the zero-bias conductance vanishes. The cause of the coexistence of superconductivity and strong correlations in electron systems with flat bands was studied in Ref. [33]. Flat band systems with a low density of charge carrier states play an important role because the flat band energy range is so narrow that the Coulomb interactions between free carriers $E_C \propto e^2/a$ dominate over the kinetic energy, which puts these materials in a regime with strong correlations. If the flat band is narrow in both energy and momentum, its occupation can be easily changed in a wide range from zero to full.

It is well known that Landau levels are a striking example of two-dimensional flat bands. They occur when a strong magnetic field acts on a 2*D* electron system. In this case, the electron motion is reduced by the Lorentz force to quantized cyclotron orbits. In this case, the translational degeneracy leads to completely flat zones, the width of which is completely determined by the degree of disorder. Partially filled Landau levels, first studied in semiconductor heterostructures, contain a rich set of competing orders, including ferromagnetism, charge-ordered band and bubble phases, and the best-known fractional quantum Hall liquids. The essential feature of these states is their intrinsic Berry curvature, which underlies their topological character and leads to integer and fractional quantum Hall effects. Twisted bilayer graphene has recently been found to exhibit highly correlated states and superconductivity. Thus, the formation of flat bands of Majorana fermions is a characteristic mechanism of topological superconductivity, BCS and Bose–Einstein condensation of bosons in the form of a bound state of 2*D* Majorana fermions and Dirac superconducting flat zone. The crossover of electron pairs characteristic of BCS and Bose–Einstein condensation of bosons in the form of a bound state of Majorana fermions (Majorana zero mode) was also studied in topological superconductors.

The phase transition of a quantum spin liquid (QSL) to a chiral state in 2*D* frustrated AFMs with different types of crystal lattice, caused by an external magnetic field close to $H = 0$ Oe, has attracted great interest among theoreticians and experimenters [34, 35]. It was shown that the transition of the QSL to the chiral state induced by an external magnetic field is accompanied by a phase transition into a phase with a topological order and excitation of fractional fermions (Majorana fermions). Kitaev was the first to construct a quantitative model of the so-called Z_2 quantum spin liquid (a spin liquid with a local Z_2 magnetic flux in the unit cell) for spins $S = 1/2$ located at the nodes of a quasi-two-dimensional hexagonal lattice [34]. As shown in work [35], the chiral spin liquid state spontaneously breaks time-reversal symmetry (TRS), but retains other symmetries. There are two topologically different CSL1 and CSL2 states of the chiral spin liquid separated by a quantum critical point. In this work, the formation of quantum nanowires-like net bounded Majorana pairs in $SmMnO_{3+\delta}$ manganites was first experimentally studied in two hidden topological states CSL1 and CSL2 of chiral quantum spin liquid.

2. MATERIAL AND METHODS

Samples of self-doped manganites $SmMnO_{3+\delta}$ ($\delta \cong 0.1$) were obtained

from high-purity oxides of samarium and electrolytic manganese, taken in a stoichiometric ratio. The synthesized powder was pressed under pressure of 10 kbar into discs of 6 mm in diameter, 1.2 mm thick and sintered in air at a temperature of 1170°C for 20 h followed by cooling at a rate of 70°C/h. The resulting tablets were a single-phase ceramic according to x-ray data. X-ray studies were carried out with 300 K on DRON-1.5 diffractometer in radiation Ni$K_{\alpha_1+\alpha_2}$. Symmetry and crystal lattice parameters were determined by the position and character splitting reflections of the pseudocubic perovskite-type lattice. Temperature dependences of *dc* magnetization were measured using a VSM EGG (Princeton Applied Research) vibrating magnetometer and a nonindustrial magnetometer in ZFC and FC modes.

3. RESULTS AND DISCUSSION

According to our previous work [36], the temperature dependences of the magnetization of frustrated manganites $La_{1-y}Sm_yMnO_{3+\delta}$ ($\delta \cong 0.1$, $y = 0.85$, 1.0) contain two sharp peaks $M(T)$ of different intensity at close temperatures T_1 and T_2 slightly above the critical temperature T_c of the phase transition of the samples to the coherent superconducting state. It was shown that these features correspond to the Lindhard divergence $\chi_L(\mathbf{q}_{nest})$ of the temperature dependence of the paramagnetic susceptibility of stripe-like 1*D* electron/spin correlations modulated with the wave vectors $\mathbf{q}_{nest1} = 2\mathbf{k}_{F1}$ and $\mathbf{q}_{nest2} = 2\mathbf{k}_{F2}$. The appearance and evolution of the magnetization features with increasing field are explained by the formation in *ab* planes with complete nesting of the electron–hole regions of the Fermi surface of a spatial modulation of the electronic and magnetic properties in the form of fragments of two fluctuating quasi-one-dimensional waves of the charge/spin density (CDW/CDW) incommensurate with the crystal lattice with the wave vectors $\mathbf{q}_1 \| \mathbf{a}$ and $\mathbf{q}_2 \| \mathbf{b}$ directions. As can be seen in Fig. 1, the peak features of the magnetization $M(T)$ in $SmMnO_{3+\delta}$ arise at temperatures $T_1 = 20$ K and $T_2 = 50$ K slightly above $T_c = 12$ K. In contrast to the sample with $y = 0.85$, the intensity of the peak feature near the temperature T_1 in $SmMnO_{3+\delta}$ is negligible but finite. A small Curie-like increase in magnetization at $T \to 0$ K should also be noted. An increase in the measuring field strength to 350 Oe did not lead to a qualitative change in the temperature dependence of magnetization.

Cardinal changes in the magnetization $M(T)$ were detected during measurements in a magnetic field of $H = 1$ kOe. An increase in the magnetic field led to a decrease in the Kosterlitz–Thouless jump in the magnetization of the sample near the temperature $T_c = 12$ K of its transition to the coherent SC state, complete suppression of the

magnetization peak near T_1 and significant broadening of the $M(T)$ peak near T_2.

The final stage of the evolution of the temperature dependences of magnetization $M(T)$ in $SmMnO_{3+\delta}$ with increasing external magnetic field strength can be considered the results of measurements in a field of $H = 3.5$ kOe, shown in Fig. 2.

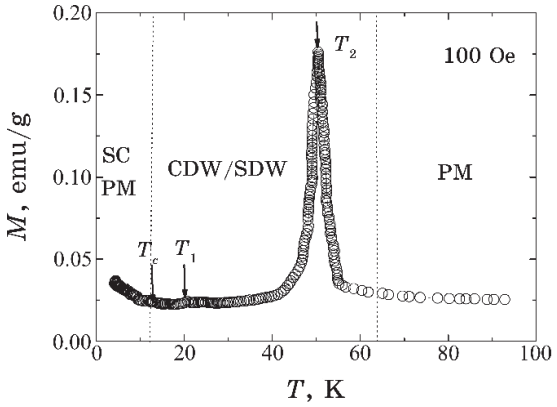

Fig. 1. Temperature dependence of magnetization $M(T)$ in a field $H = 100$ Oe in the ZFC-measurement mode. In the ZFC mode of magnetization measuring in the temperature range $4.2 \le T \le 100$ K, a coherent superconducting state with a critical temperature $T_c = 12$ K is observed. In the temperature range 12–60 K, the charge/spin density wave state is realized in the form of a two-peak magnetization feature $M(T)$.

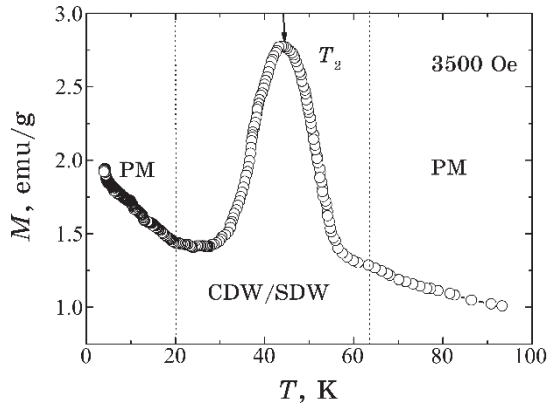

Fig. 2. Temperature dependence of magnetization $M(T)$ in a field $H = 3500$ Oe in the ZFC-measurement mode in the temperature range $4.2 \le T \le 100$ K. A coherent superconducting state with a critical temperature $T_c = 12$ K is absent. In the temperature range 20–70 K, the spin-density wave state is realized in the form of a wide-peak magnetization feature M (T).

At temperatures below 60 K of the transition of the sample from the paramagnetic phase to the phase with periodic nanoscale ordering of quasi-particles in the form of fluctuating CDW/CDW fragments, only a wide peak of magnetization near the temperature $T_2 \approx 42$ K is preserved. As a result of the increase in the external magnetic field strength in the range of fields of 100 Oe $\leq H \leq$ 3500 Oe, a 'metallic' state of the SDW type with a fairly high density of free quasi-particles at the Fermi level was formed in the $SmMnO_{3+\delta}$ sample at temperatures below 60 K. This indicates a small value (absence) of the charge pseudogap in the electron spectrum of charge/spin carriers in $SmMnO_{3+\delta}$ at EF in a magnetic field of $H = 3.5$ kOe.

Thus, an increase in the field strength to $H = 3.5$ kOe led to the suppression of the charge pseudogap in the quasi-particle spectrum, to a decrease in the 1D CDW amplitude and, accordingly, to an increase in the amplitude of the fluctuating 1D SDW incommensurate with the crystal lattice. With increasing H, we have a transformation of the mixed state of nanofragments of charge-spin density waves into a 1D spin-density wave. The increase in the width of the $M(T)$ peak near T_2 with increasing H is apparently caused by the renormalization of the spectrum by coupling with magnons. Thus, we associate the appearance of the two peak features of magnetization at temperatures slightly above T_c with the formation in $SmMnO_{3+\delta}$ in weak fields $H \geq 100$ Oe of nanofragments of 1D coupled charge and spin density waves incommensurate with the crystal lattice in two spatially separated regions of the sample (conventionally 'metallic' and 'dielectric' nanophases) with high and low densities of states free carriers at the Fermi level $N_1(E_F) \ll N_2(E_F)$. With an increase in the external magnetic field strength H, 'metallization' of the spectrum of free charge carriers in $SmMnO_{3+\delta}$ occurs.

Previously, the formation of a broad continuum of spinon pair excitations in $SmMnO_{3+\delta}$ in the 'weak magnetic field' regime $H = 100$ Oe, 1 kOe in the FC mode is explained in the framework of the Landau quantization models of the compressible spinon gas with fractional values of the factor ν of filling three overlapping bands with quantum numbers $n = 1$, 2, and 3 [37]. In the regime of 'strong magnetic field' $H = 3.5$ kOe, the new step-like quantum oscillations of temperature dependences of supermagnetization of incompressible spinon liquid were found. According to the experimental results obtained in this work, in low-energy Landau zones with numbers $n = 1$, 2, with an increase in the strength of the measuring field H, two alternating supermagnetization features are formed, which are characteristic of the excitation of 2D Majorana and Dirac fermions.

A singularity of supermagnetization $M(T)$ in Landau band with number $n = 1$ in a magnetic field $H = 100$ Oe has a double-peaks' shape with a strong dip near the average temperature $T \cong 4.65$ K (Fig. 3).

However, in the zone with $n = 2$, the singularity has a distinct shape: a truncated Dirac cone with a flat top in an ultra-narrow energy range $\Delta E \cong 0.01$ meV with a weak dip in its top near the average excitation temperature of massless Dirac quasi-particles, $T \cong 5.41$ K (Fig. 4).

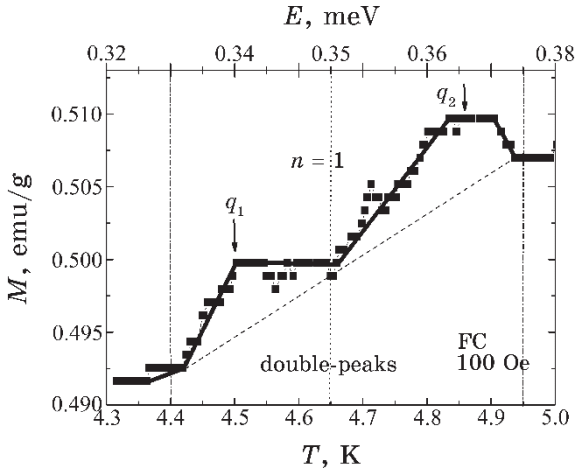

Fig. 3. An alternate excitation in the FC-measurement mode of a double-peaks' feature in the magnetic response arise from excitation of bounded Majorana pairs in Landau zone with $n = 1$ near average temperature $T \cong 4.65$ K in external magnetic field $H = 100$ Oe (CSL1 state).

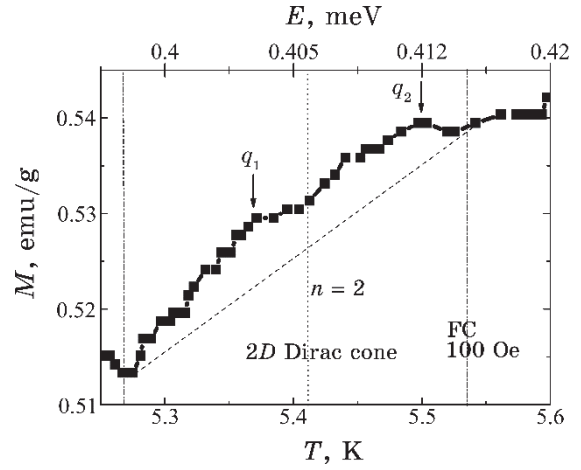

Fig. 4. An alternate excitation in the FC-measurement mode of a 2*D* Dirac cones-like feature in the magnetic response arise from excitation of bounded Majorana zero modes with energy $E_{MZM} \cong 0.4$ meV in Landau zone with $n = 2$ in external magnetic field $H = 100$ Oe (CSL2 state).

In a magnetic field $H = 350$ Oe, the alternation of magnetization features $M(T)$ in the zones with number $n = 1$ and 2 changed to the opposite. In the zone with number $n = 1$, a singularity $M(T)$ in Landau band has a shape a truncated Dirac cone with a flat top in a wider energy range $\Delta E \cong 0.05$ meV with a weak dip in its top near the average excitation temperature of massless Dirac quasi-particles $T \cong 4.6$ K. At the same time, in the zone $n = 2$, the supermagnetization feature has the form of two broad weak peaks $M(T)$ with a strong dip near the average temperature of the excitation of Majorana fermions near $T \cong 5.5$ K. As can be seen in Figs. 5, 6, this regularity in the alternation of features $M(T)$ in low-energy Landau bands with number $n = 1$ and 2 is also preserved in the measuring field $H = 1$ kOe despite a significant expansion of features $M(T)$ caused by the appearance of strong fluctuations of the topological order in spin system.

In the $n = 1$ zone, a two-peak super magnetization feature forms near the average temperature $T \cong 4.6$ K, while in the $n = 2$ zone, with increasing temperature near the average excitation temperature $T \cong 5.5$ K, a cone-like feature $M(T)$ with a flat top appears in a wide energy range $\Delta E \cong 0.05$ meV. Thus, an increase in the magnetic field strength in $SmMnO_{3+\delta}$ in the 'weak magnetic fields' mode is accompanied by a rearrangement of singularities of super magnetization in low-energy Landau bands with number $n = 1$ and 2. As shown in Fig. 7, new step-like features of super magnetization form in 'strong magnetic fields' regime. An alternate permutation of the

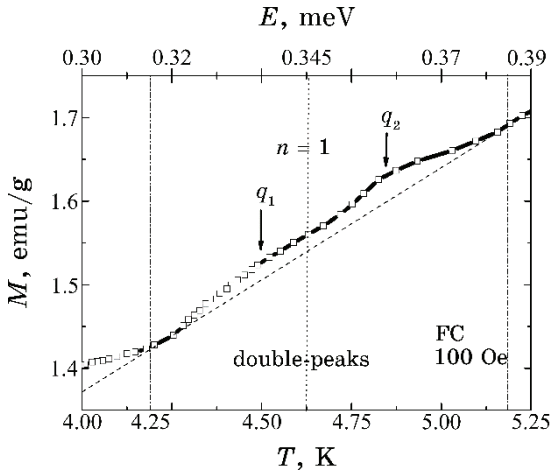

Fig. 5. An alternate excitation in the FC-measurement mode of a double-peaks' feature in the magnetic response arise from excitation of bounded Majorana pairs in Landau zone with $n = 1$ near average temperature $T \cong 4.65$ K in external magnetic field $H = 1$ kOe (CSL1 state).

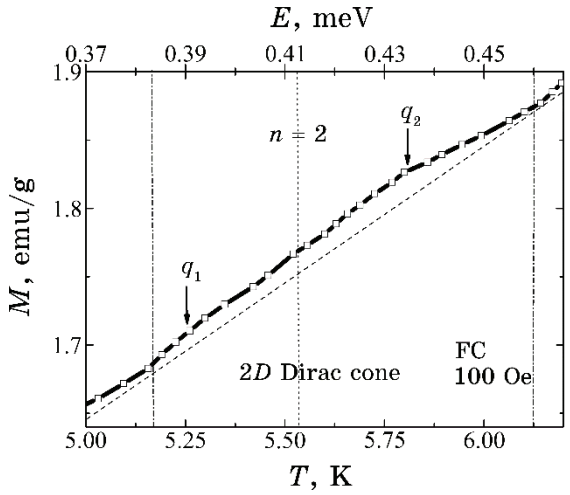

Fig. 6. An alternate excitation in the FC-measurement mode of a Dirac cones-like feature in the magnetic response arise from excitation of bounded Majorana modes with energy $E_{MZM} \cong 0.41$ meV in Landau zone with $n = 2$ near average temperature $T \cong 5.5$ K in external magnetic field $H = 1$ kOe (CSL2 state).

double-peaks' and truncated-Dirac-cones' features of the magnetization $M(T)$ in two Landau bands with number $n = 1, 2$ during the Landau quantization of the fermion pairs spectrum in $SmMnO_{3+\delta}$ in 'weak magnetic fields' regime may be explained by the existence in this material of two well-known in the literature hidden states CSL1 and CSL2 of the chiral spin liquid.

4. CONCLUSIONS

According to the experimental results of this work, the temperature dependences of the magnetization of $SmMnO_{3+\delta}$ in ZFC-measurement mode contain two sharp peaks of different intensity at close temperatures T_1 and T_2 slightly above the critical temperature T_c of the phase transition of the samples to the coherent superconducting state.

It was shown that these features correspond to the Lindhard divergence $\chi_L(\mathbf{q}_{nest})$ of the temperature dependence of the paramagnetic susceptibility of stripe-like $1D$ electron/spin correlations modulated with the wave vectors $\mathbf{q}_{nest1} = 2\mathbf{k}_{F1}$, $\mathbf{q}_{nest2} = 2\mathbf{k}_{F2}$. We associate the appearance of the two-peak features of magnetization with the formation in $SmMnO_{3+\delta}$ in weak fields $H \geq 100$ Oe of nanofragments of $1D$ coupled charge and spin density waves incommensurate with the crystal lattice in two spatially separated regions of the

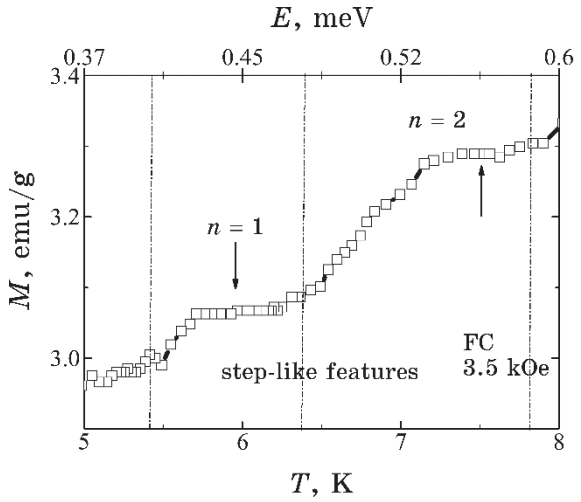

Fig. 7. The thermal excitation in the FC-measurement mode of a step-like features of temperature dependence of supermagnetization in interval temperature 5–8 K of incompressible quantum spin liquid in Landau zones with $n = 1$ and 2 in external magnetic field $H = 3.5$ kOe.

sample (conventionally 'metallic' and 'dielectric' nanophases) with high and low densities of states free carriers at the Fermi level $N_1(E_F) \ll N_2(E_F)$. An increase in the field strength to $H = 3.5$ kOe led to: 1) the suppression of the charge pseudogap in the quasiparticle spectrum; 2) a decrease in the 1*D* CDW amplitude; 3) an increase in the amplitude of the fluctuating 1*D* SDW incommensurate with the crystal lattice. With increasing H, we have a transformation of the mixed state of nanofragments of 1*D* CDW/SDW into a 1*D* SDW.

In the weak magnetic fields $H = 100$ Oe, 350 Oe and 1 kOe, the continuous spectrum of the thermal excitations of bounded Majorana pairs in $SmMnO_{3+\delta}$ in interval temperature 4.2–12 K in FC mode is divided into two low-energy Landau zones with numbers $n = 1$, $n = 2$, with two specific features of magnetization $M(T)$ in the shape of alternating double peaks and truncated Dirac cones. An increase in the magnetic field strength in $SmMnO_{3+\delta}$ to $H = 3.5$ kOe is accompanied by a rearrangement of singularities of super magnetization in low-energy Landau bands with number $n = 1$ and 2: new step-like features of super magnetization form in 'strong magnetic fields' regime. An alternate permutation of the double-peaks' and truncated-Dirac-cones' features of the magnetization $M(T)$ in two Landau bands with number $n = 1$, 2 during the Landau quantization of the bounded Majorana pairs spectrum in $SmMnO_{3+\delta}$ in 'weak magnetic fields' regime may be explained by the existence in

this material of two well-known in the literature hidden states CSL1 and CSL2 of the chiral spin liquid.

REFERENCES

1. N. Read and D. Green, *Phys. Rev. B*, **61**, Iss. 15: 10267 (2000); https://doi.org/10.1103/PhysRevB.61.10267
2. J. D. Sau, R. M. Lutchyn, S. Tewari, and S. Das Sarma, *Phys. Rev. Lett.*, **104**, Iss. 4: 040502 (2010); https://doi.org/10.1103/PhysRevLett.104.040502
3. J. D. Sau, S. R. Tewari, R. M. Lutchyn, T. D. Stanescu, and S. Das Sarma, *Phys. Rev. B*, **82**, Iss. 21: 214509 (2010); https://doi.org/10.1103/PhysRevB.82.214509
4. M. Leijnse and K. Flensberg, *arXiv:1107.5703v2* [cond-mat.supr-con] 30 Nov 2011.
5. Y. Oreg, G. Refael, and F. V. Oppen, *Phys. Rev. Lett.*, **105**, Iss. 17: 177002 (2010); https://doi.org/10.1103/PhysRevLett.105.177002
6. S. Tewari and J. D. Sau, *Phys. Rev. Lett.*, **109**, Iss. 15: 150408 (2012); https://doi.org/10.1103/PhysRevLett.109.150408
7. J. D. Sau, S. Tewari, and S. Das Sarma, *arXiv:1111.2054v3* [cond-mat.supr-con] 27 Feb 2012.
8. T. P. Choy, J. M. Edge, J. M. Akhmerov, and C. W. J. Beenakker, *arXiv:1108.0419v1* [cond-mat.mes-hall] 1 Aug 2011.
9. I. Martin and A. F. Morpurgo, *arXiv:1110.5637v2* [cond-mat.mes-hall] 29 Mar 2012.
10. W. DeGottardi and D. Sen, *arXiv:1208.0015v1* [cond-mat.str-el] 31 Jul 2012.
11. F. Wilczek, *Nature Phys.*, **5**, Iss. 5: 614 (2009); https://doi.org/10.1038/nphys1380
12. K. Pakrouski, M. R. Peterson, T. Jolicoeur, V. W. Scarola, C. Nayak, and M. Troyer, *Phys. Rev. X*, **5**, Iss. 4: 021004 (2015); doi:10.1103/PhysRevX.5.021004
13. A. Kitaev, *Ann. Phys.*, **303**, Iss. 1: 2 (2003); https://doi.org/10.1016/S0003-4916(02)00018-0
14. C. Nayak, S. H. Simon, A. Stern, M. Freedman, and S. Das Sarma, *Rev. Mod. Phys.*, **80**, Iss. 3: 1083 (2008); https://doi.org/10.1103/RevModPhys.80.1083
15. J. Alicea, Y. Oreg, G. Refael, F. von Oppen, and M. P. A. Fisher, *Nature Physics*, **7**, Iss. 2: 412 (2011); http://dx.doi.org/10.1038/nphys1915
16. J. D. Sau, S. Tewari, R. Lutchyn, T. Stanescu, and S. Das Sarma, *arXiv:1006.2829v2* [cond-mat.supr-con] 30 Jun 2010.
17. R. M. Lutchyn, T. D. Stanescu, and S. Das Sarm, *Phys. Rev. Lett.*, **106**, Iss. 12: 127001 (2011); https://doi.org/10.1103/PhysRevLett.106.127001
18. H. Tian, S. Che, T. Xu, P. Cheung, K. Watanabe, T. Taniguchi, M. Randeria, F. Zhang, C. N. Lau, and M. W. Bockrath, *arXiv 2112 13401* [cond-mat.supr-cond] 2021.
19. S. Peotta and P. Törmä, *arXiv:1506.02815v3* [cond-mat.supr-con] 2 Dec 2015.

20. X. Hu, T. Hyart, D. I. Pikulin, and E. Rossi, *Phys. Rev. Lett.*, **123**, Iss. 23: 237002 (2019); https://doi.org/10.1103/PhysRevLett.123.237002
21. F. Xie, Z. Song, B. Lian, and B. A. Bernevig, *Phys. Rev. Lett.*, **124**, Iss. 16: 167002 (2020); https://doi.org/10.1103/PhysRevLett.124.167002
22. A. Julku, T. J. Peltonen, L. Liang, T. T. Heikkilä, and P. Törmä, *Phys. Rev. B*, **101**, Iss. 6: 060505 (2020); https://doi.org/10.1103/PhysRevB.101.060505
23. N. Verma, T. Hazra, and M. Randeria, *Proc. Nat. Acad. Sci.*, **118**, Iss. 8: e2106744118 (2021); https://doi.org/10.1073/pnas.2106744118
24. Q. Chen, J. Stajic, S. Tan, and K. Levin, *Physics Reports*, **412**, Iss. 1: 1 (2005); https://doi.org/10.1016/j.physrep.2005.02.005
25. M. Randeria and E. Taylor, *Annual Reviews of Condensed Matter Physics*, **5**, Iss. 3: 209 (2014); https://doi.org/10.1146/annurev-conmatphys-031113-1338299
26. Y. Nakagawa, Y. Kasahara, T. Nomoto, R. Arita, T. Nojima, and Y. Iwasa, *Science*, **372**, Iss. 4: 190 (2021); doi:10.1126/science.abb9860
27. T. T. Heikkilä and G. E. Volovik, *Basic Physics of Functionalized Graphite*, **123**, Iss. 7: 123 (2016); https://doi.org/10.1007/978-3-319-39355-1_6
28. V. J. Kauppila, F. Aikebaier, and T. T. Heikkilä, *Phys. Rev. B*, **93**, Iss. 6: 214505 (2016); https://doi.org/10.1103/PhysRevB.93.214505
29. M. Sato and Y. Ando, *Rep. Prog. Phys.*, **80**, Iss. 7: 076501 (2017); https://doi.org/10.1088/1361-6633/aa6ac7
30. K. T. Law, P. A. Lee, and T. K. Ng, *Phys. Rev. Lett.*, **103**, Iss. 23: 237001 (2009); https://doi.org/10.1103/PhysRevLett.103.237001
31. K. Flensberg, *Phys. Rev. B*, **82**, Iss. 18: 180516 (2010); https://doi.org/10.1103/PhysRevB.82.180516
32. P. A. Ioselevich and M. V. Feigel'man, *New J. Phys.*, **15**, Iss. 5: 055011 (2013); https://doi.org/10.1088/1367-2630/15/5/055011
33. L. Balents, C. R. Dean, D. K. Efetov, and A. F. Young, *Nature Physics*, **16**, Iss. 5: 725 (2020); https://doi.org/10.1038/s41567-020-0906-9
34. A. Kitaev, *Annals of Physics*, **321**, Iss. 6: 2 (2006); https://doi.org/10.1016/j.aop.2005.10.005
35. H. Yao and S. A. Kivelson, *Phys. Rev. Lett.*, **99**, Iss. 24: 247203 (2007); https://doi.org/10.1103/PhysRevLett.99.247203
36. F. N. Bukhanko and A. F. Bukhanko, *Physics of the Solid State*, **61**, Iss. 12: 2525 (2019); doi:10.1134/S1063783419120084
37. F. N. Bukhanko and A. F. Bukhanko, *Fiz. Nizk. Temp.*, **47**, Iss. 11: 1021 (2021); doi:10.1063/10.0006569

Наносистеми, наноматеріали, нанотехнології
Nanosistemi, Nanomateriali, Nanotehnologii
2025, т. 23, № 2, сс. 437–448
https://doi.org/10.15407/nnn.23.02.0437

© 2025 ІМФ (Інститут металофізики
ім. Г. В. Курдюмова НАН України)
Надруковано в Україні.

PACS numbers: 61.72.Mm, 68.37.Ps, 68.55.J-, 78.55.Hx, 78.60.Lc, 81.15.Cd, 81.40.Tv

Surface Morphology and Low-Temperature Luminescence of Thin $(Y_{0.06}Ga_{0.94})_2O_3:Cr^{3+}$ Films

O. M. Bordun[1], I. O. Bordun[1], I. I. Medvid[1], D. M. Maksymchuk[1], I. Yo. Kucharskyy[1], I. M. Kofliuk[1], and D. S Leonov[2]

[1]*Ivan Franko National University of Lviv,*
50, Drahomanov Str.,
UA-79005 Lviv, Ukraine
[2]*Technical Centre, N.A.S. of Ukraine,*
13, Pokrovska Str.,
UA-04070 Kyiv, Ukraine

Thin films of $(Y_{0.06}Ga_{0.94})_2O_3$:Cr are obtained by radio-frequency (RF) ion-plasma sputtering in an argon atmosphere on amorphous υ-SiO_2 substrates. The surface morphology of the obtained films is studied by means of AFM. The low-temperature (8.6 K) luminescence of the thin films of $(Y_{0.06}Ga_{0.94})_2O_3:Cr^{3+}$ under excitation by synchrotron radiation (22.14 eV and 7.75 eV) is studied. The obtained luminescence spectra are analysed according to excitation energy. A high-energy shift of the R_1-line in the spectra of the activator luminescence of the Cr^{3+} ion in the thin films of $(Y_{0.06}Ga_{0.94})_2O_3:Cr^{3+}$ is found relative to the same for single crystal samples. This shift is analysed in the form of a nephelauxetic effect.

Методом високочастотного (ВЧ) йонно-плазмового розпорошення в атмосфері арґону на аморфних підкладинках υ-SiO_2 одержано тонкі плівки $(Y_{0,06}Ga_{0,94})_2O_3$:Cr. Методом АСМ досліджено морфологію поверхні одержаних плівок. Проведено дослідження низькотемпературної (8,6 К) люмінесценції тонких плівок $(Y_{0,06}Ga_{0,94})_2O_3:Cr^{3+}$ через збудження синхротронним випромінюванням (22,14 еВ і 7,75 еВ). Проаналізовано одержані спектри люмінесценції залежно від енергії збудження. Встановлено високоенергетичне зміщення R_1-лінії у спектрах активаторного свічення йона Cr^{3+} у тонких плівках $(Y_{0,06}Ga_{0,94})_2O_3$:Cr відносно такої для монокристалічних зразків. Дане зміщення проаналізовано у формі нефелоксетичного ефекту.

Key words: gallium oxide, yttrium oxide, chromium activator, thin films, nanocrystals, photoluminescence, synchrotron radiation.

Ключові слова: оксид Ґалію, оксид Ітрію, активаторний Хром, тонкі плі-

вки, нанокристаліти, фотолюмінесценція, синхротронне випромінення.

(Received 16 April, 2025)

1. INTRODUCTION

In recent years, oxide nanostructures based on β-Ga_2O_3 have been extensively studied. This material, which belongs to wide bandgap semiconductors, is widely used in ultraviolet photodetectors, gas sensors, solar cells, luminescent devices, and high-power Schottky diodes [1–8]. Due to their operational and chemical properties, pure and activated nanometre thin films of β-Ga_2O_3 obtained by various methods are widely used in luminescent devices. Among them, an important place is occupied by β-Ga_2O_3:Cr^{3+} as a red phosphor for multiple types of luminescent screens, including flat panel PDP (plasma, display, panel) screens [9–13].

In general, the optical and luminescent properties of thin oxide films, including β-Ga_2O_3:Cr^{3+}, are determined by the methods of preparation, deposition modes, processing technology, and the introduction of special impurities that can purposefully change the spectral and luminescent properties of the films. Given that the luminescence of β-Ga_2O_3 depends significantly on structural defects [14–16], in this work, some Ga^{3+} ions were replaced by isovalent Y^{3+} ions, which did not require local compensation of the electric charge. At the same time, it was taken into account that Y_2O_3 thin films are quite promising when used in optoelectronics and luminescent technology [17–20]. This led to the study of thin films with the chemical composition $(Y_{0.06}Ga_{0.94})_2O_3$:Cr^{3+} in this work.

Taking into account that the physical properties of thin films are determined by the size of the nanocrystalline grains from which they are formed and the presence of intergranular boundaries, the surface morphology of thin $(Y_{0.06}Ga_{0.94})_2O_3$:Cr^{3+} films was studied by atomic force microscopy (AFM). In order to study in detail the luminescence in these films, the luminescence spectra were studied under excitation by synchrotron radiation at low temperatures $T = 8.6$ K. The films were obtained by the method of RF ion-plasma sputtering, which is considered optimal for depositing homogeneous multicomponent semiconductor and dielectric films [21].

2. EXPERIMENTAL TECHNIQUE

Thin films of $(Y_{0.06}Ga_{0.94})_2O_3$:Cr with a thickness of 0.3–1.0 μm were obtained by RF ion-plasma sputtering in an argon atmosphere on amorphous substrates of fused quartz υ-SiO_2. The feedstock was a

mixture of Y_2O_3 and Ga_2O_3 oxides of the stoichiometric composition of the 'ОСЧ' (especially pure) grade. The concentration of the activator ion Cr^{3+} was 0.5 mol.%. After the films were deposited, they were heat treated in argon at 1000–1100°C.

The structure and phase composition of the obtained films were studied by x-ray diffraction analysis (Shimadzu XDR-600). X-ray diffraction studies have shown the presence of a polycrystalline structure with a predominant orientation in the (002), (111), (110), and (512) planes. The analysis of the obtained diffractograms shows that the structure of the films corresponds to the monoclinic crystal structure of β-Ga_2O_3.

At the same time, the obtained diffractograms practically coincide with the diffractograms of unalloyed films of $(Y_{0.06}Ga_{0.94})_2O_3$, which were presented earlier in our work [22].

Using an OXFORD INCA Energy 350 energy dispersive spectrometer, elemental analysis of the samples was carried out at several points on the surface of the films. The calculations showed that the percentage of components in the obtained films corresponded to their percentage in the $(Y_{0.06}Ga_{0.94})_2O_3$:Cr compound.

The surface morphology of the thin films was studied using an INTEGRA TS-150 atomic force microscope (AFM). The image of the thin film surface was obtained in the semi-contact mode.

The luminescence spectra at $T = 8.6$ K were studied using synchrotron radiation at the Superlumi facility (DESY, Hamburg, Germany) [23]. A primary monochromator with a spectral resolution of 4 Å was used to select the spectral range of synchrotron radiation for luminescence excitation. The luminescence spectra were recorded and analysed using an ANDOR Kymera monochromator with a spectral resolution of 2 Å, a Newton 920 CCD camera, and a Hamamatsu R6358 photoelectronic multiplier.

3. RESULTS AND DISCUSSION

Microphotographs of the surface of thin $(Y_{0.06}Ga_{0.94})_2O_3$:Cr films are shown in Fig. 1.

The topography of the samples was quantitatively characterized by standard parameters: root mean square roughness, maximum grain height, and average grain diameter, which were calculated from AFM data using Image Analysis 3.5 image processing software for a 5000×5000 nm area.

Based on the analysis of the surface morphology images, it was found that thin films of $(Y_{0.06}Ga_{0.94})_2O_3$:Cr after argon heat treatment have an average square surface roughness of 2.9 nm with a maximum grain height of 33 nm. The average grain diameter is of 123 nm.

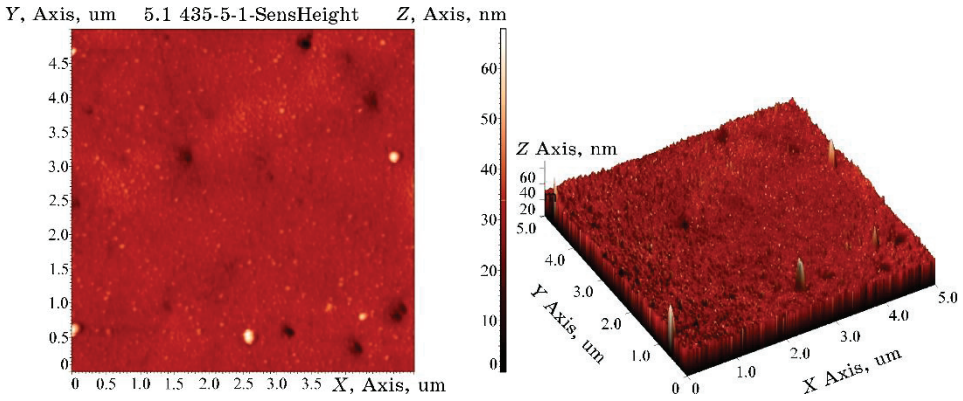

Fig. 1. Images of the surface morphology of thin $(Y_{0.06}Ga_{0.94})_2O_3$:Cr films after heat treatment in an argon atmosphere on υ-SiO_2 substrates. *a*—two-dimensional image; *b*—three-dimensional image.

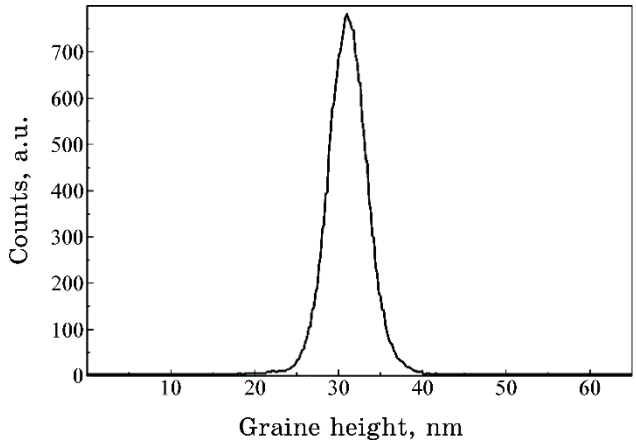

Fig. 2. Grain height distribution for AFM images of the surface of thin $(Y_{0.06}Ga_{0.94})_2O_3$:Cr films after heat treatment in an argon atmosphere.

The histogram of grain height distribution for the obtained films is shown in Fig. 2.

The characteristic distribution of grain diameter sizes in thin $(Y_{0.06}Ga_{0.94})_2O_3$:Cr films is shown in Fig. 3.

As can be seen in Fig. 3, the distribution of grain diameters in the obtained thin films has the form of a bimodal distribution. The growth of crystalline grains and the evolution of crystal structures were analysed in a thorough review [24], and it was shown that polycrystalline thin films with a thickness of up to 1 μm, which is typical for our $(Y_{0.06}Ga_{0.94})_2O_3$:Cr films, often have 2*D*-like struc-

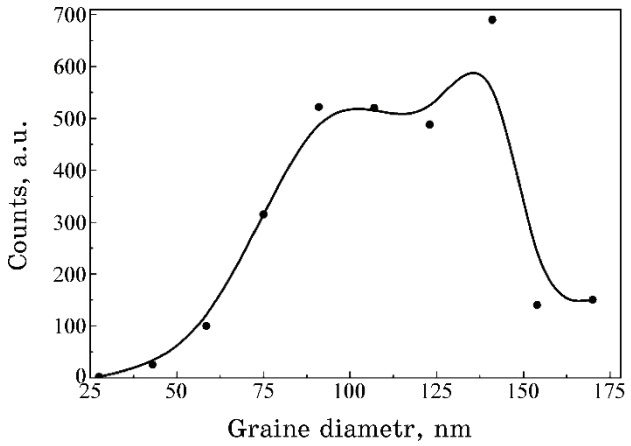

Fig. 3. Distribution of grain diameter sizes and calculated approximate diameter distribution on AFM images of thin $(Y_{0.06}Ga_{0.94})_2O_3$:Cr films after heat treatment in argon atmosphere.

tures. Most of the materials analysed in Ref. [24] form thin films of nonequilibrium grains, whose dimensions are smaller than the film thickness, and they form two-dimensional structures only after annealing. In some cases, further grain growth is observed due to 'anomalous' growth or preferential coalescence of several grains, which usually have specific crystallographic orientations and ratios relative to the substrate surface plane. Our results show that such a situation is most likely characteristic of the $(Y_{0.06}Ga_{0.94})_2O_3$:Cr films we obtained. In particular, according to Ref. [25], when the number of growing grains leads to a 'matrix' of grains beyond statistical limits, a bimodal grain size distribution develops, which is called secondary grain growth. Grains that grow abnormally often have a limited or homogeneous texture.

Our results (Fig. 3) show that the distribution of grain diameters on the surface of the $(Y_{0.06}Ga_{0.94})_2O_3$:Cr film after argon heat treatment is described by a two-modal distribution with maxima in the region of 100 and 135 nm. This situation may indicate that grain growth occurred during the heat treatment due to growth and sintering processes. It should be noted that a similar situation is observed during RF deposition on similar υ-SiO_2 substrates and pure thin β-Ga_2O_3 films, where the growth of secondary and even tertiary grains is observed [26].

The luminescence spectra of the obtained thin $(Y_{0.06}Ga_{0.94})_2O_3$:Cr films under excitation by synchrotron radiation at 56 nm (22.14 eV) and 160 nm (7.75 eV) are shown in Fig. 4.

As can be seen from the results shown in Fig. 4, the spectra ob-

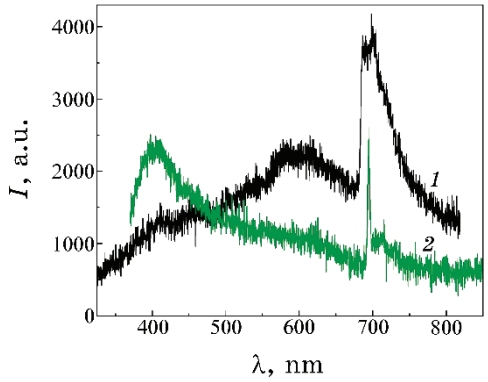

Fig. 4. The emission spectra of thin $(Y_{0.06}Ga_{0.94})_2O_3$:Cr films at $\lambda_{exc} = 56$ nm (*1*) and $\lambda_{exc} = 160$ nm (*2*) at 8.6 K.

tained at different excitation energies differ slightly. The luminescent luminescence spectrum under 56 nm excitation is characterised by intense luminescence in the 690–750 nm region with a maximum at 700 nm (1.77 eV) and a less intense band with a maximum at 600 nm (2.07 eV) and a local maximum in the luminescence spectrum at 400 nm (3.10 eV). When excited at 160 nm, a broad intense luminescence with a maximum in the 400 nm region, a local maximum in the 600 nm region, and a slight luminescence in the 690–750 nm region, which shows a narrow band with a maximum at 693.5 nm (1.788 eV), are observed.

The luminescent band with a maximum around 400 nm is a typical luminescence of the $(Y_{0.06}Ga_{0.94})_2O_3$ substrate, which was discussed in detail in Ref. [27]. This luminescence is also characteristic of pure β-Ga_2O_3 crystals [28, 29] and thin β-Ga_2O_3 films [30]. The luminescent band with a maximum in the region around 600 nm most likely corresponds to the luminescence of defects, primarily due to a disturbance in stoichiometry. This luminescence has not been reported in studies of nominally pure β-Ga_2O_3 crystals [28, 29] or the β-Ga_2O_3 and $(Y_{0.06}Ga_{0.94})_2O_3$ films [30], but it has been observed in thin $ZnGa_2O_4$:Cr films [31] and Y_2O_3:Cr^{3+} nanophosphors [32]. At the same time, as can be seen in Fig. 4, the luminescence intensity of luminescence and such defects depends on the energy of the excitation quanta. A similar situation is observed in the photoluminescence of $ZnGa_2O_4$:Cr [31].

The wide luminescence band in the 690–750 nm region is due to the intracentre luminescence of the Cr^{3+} impurity [33]. Gallium oxide has a monoclinic structure, and Cr^{3+} ions in the structure of β-Ga_2O_3 are in an octahedral oxygen environment [33]. In such an environment with an inversion centre, electrodipole transitions are

prohibited by parity. Therefore, the luminescent spectrum can be caused either by the displacement of chromium ions from the inversion centre or by interaction with crystal lattice vibrations. The indicated broad band of luminescence arises from the radiative transition $^4T_2 \rightarrow {}^4A_2$ [33] in Cr^{3+} ions. Against the background of this band, two narrow R-lines (R_1 and R_2), characteristic of Cr^{3+} ions in an octahedral environment, are distinguished in the short-wave region. The spectral position of these lines depends significantly on the temperature and the perfection of the samples obtained. In particular, with a decrease in temperature, the maxima of the R_1- and R_2-lines shift to the short-wave (high-energy) region [36–39]. In addition, our studies show that the cooling of β-Ga_2O_3:Cr^{3+} crystals to lower liquid nitrogen temperatures leads to a sharp decrease in the luminescence yield of the $^4T_2 \rightarrow {}^4A_2$ transition, quenching of the R_2 line, and a strong increase in the intensity of the R_1 line [36–39]. Our results are in good agreement with the above results and show that the intensity of the $^4T_2 \rightarrow {}^4A_2$ transition is determined not only by the temperature but also by the excitation energy.

A characteristic feature of the results of the study of the luminescence of β-Ga_2O_3:Cr^{3+} crystals at temperatures of 20 K and lower [36–39] is the presence of an intense luminescence of the R_1 line, the spectral position of which differs slightly from one author to another. In particular, in Ref. [36], the spectral position of the R_1 band is of 695.3 nm; in Ref. [37], it is of 695.6 nm; in Ref. [38], it is of 694.5 nm; and in Ref. [39], it is of 696.1 nm. Most likely, this situation is due to the structural perfection of the studied samples in different works. At the same time, in the obtained luminescence spectra of thin $(Y_{0.06}Ga_{0.94})_2O_3$:Cr^{3+} films, the spectral position of the R_1 band is even more energetic, *i.e.*, of 693.5 nm. Such a shift could be explained by the addition of Y^{3+} ions to the structure of β-Ga_2O_3 instead of some Ga^{3+} ions. However, this situation seems unlikely. Unfortunately, we have not found any scientific publications devoted to the low-temperature luminescence of Y_2O_3:Cr^{3+}. However, studies of such luminescence at room temperature [32] show that the spectral position of the R_1 line in the luminescence spectra of Y_2O_3:Cr^{3+} is more than 700 nm. At the same time, at room temperature, the position of the R_1-line varies from 695.6 nm [38] to 694.5 nm [39] depending on the perfection of the β-Ga_2O_3:Cr^{3+} samples. Therefore, the replacement of some Ga^{3+} ions with Y^{3+} ions should shift the R_1-band to a longer wavelength region, but the opposite situation is observed.

To analyse the observed high-energy shift in the spectral position of the R_1 band in the low-temperature luminescence spectra of thin $(Y_{0.06}Ga_{0.94})_2O_3$:Cr^{3+} films, we assume that they consist of nanocrystalline grains, for which a size effect is possible. The main reason

for such effects is the influence of surface energy. In a review article [40], the authors point out that the source of the change in surface energy is a large number of incomplete broken bonds. In this case, the smaller the size of the nanoparticle, the more such bonds account for the total number of bonds in the nanocrystal. That is, as the particle diameter decreases, the surface energy also decreases.

According to Ref. [41], a decrease in surface energy increases the volume of a unit cell. Therefore, in thin films consisting of nanocrystalline grains, the metal–ligand (Cr–O) distance increases and, as a result, the crystal field strength decreases, and the position of the emission bands is shifted. This situation, in particular, is observed in thin films of β-Ga_2O_3:Cr, where the crystal field strength is $D_q = 1667$ cm^{-1} [31]. The calculations of D_q in single-crystal samples of β-Ga_2O_3:Cr^{3+} [42] give the value of $D_q = 1680.7$ cm^{-1}.

An increase in the metal–ligand (Cr–O) distance leads to a change in the Raká parameters, which may result in a nephelauxetic effect. The term 'nephelauxetic' was introduced by Jørgensen in Ref. [43] to describe the expansion of the 3*d*-electron cloud, when a metal ion is in a crystal lattice. For a metal ion in a crystal lattice, the electrostatic repulsion between these electrons is weaker, and the electron-to-electron repulsion parameter Raká B decreases. A simple phenomenological description of this effect was proposed in Ref. [43]:

$$B = \beta B_0, \tag{1}$$

where B_0 is the Raká's parameter of the free ion and β is the proportionality coefficient, called the nephelauxetic parameter. In Ref. [44], certain limitations of the relation (1) were noted, and an extended form of the nephelauxetic parameter was proposed, which takes into account both the Raká's parameters B and C, in particular,

$$\beta_1 = \sqrt{\frac{B}{B_0} + \frac{C}{C_0}}, \tag{2}$$

where C_0 is the Raká's parameter of the free ion.

When the Cr^{3+} ion is in the $^4A_2$ ground state, three 3*d*-electrons occupy orbitals stretched in the directions between the ligands. As the ligands approach the metal ion (Cr–O), the bonds become more covalent, the 3*d*-electrons move further away, and the B parameter decreases. This leads to an increase in the distance between the $^4A_2$ ground state and the excited ^2E state. Given that, the excited ^2E

state splits in the crystal field into two sublevels, $\bar{E}$ and $2\bar{A}$, we observe two R-lines in the luminescence spectra.

Since, by definition, the nephelauxetic effect is manifested in a decrease in the Raká's B parameter and an increase in the C parameter with a decrease in the metal–ligand distance, *i.e.*, with an increase in the size of crystallites, we observe the presence of such an effect at a short-wave shift of the R_1 line in the luminescence spectra of thin films of $(Y_{0.06}Ga_{0.94})_2O_3$:Cr compared to single crystal samples. Given that, for example, the grain diameters vary from 25 to 170 nm (Fig. 3), this shift is considered as an average result due to the different magnitude of the nephelauxetic effect in crystallites of different sizes.

4. CONCLUSIONS

It has been established that thin films of $(Y_{0.06}Ga_{0.94})_2O_3$:Cr with an average surface roughness of 2.9 nm are formed on υ-SiO_2 substrates after heat treatment in argon, which are formed from nanocrystalline grains with an average diameter of 123 nm.

It is shown that, at low-temperature luminescence of thin $(Y_{0.06}Ga_{0.94})_2O_3$:Cr films, the shape of the luminescence spectrum depends on the energy of the excitation quanta, and the spectrum shows the luminescence of the $(Y_{0.06}Ga_{0.94})_2O_3$ in the form of a broad band with a maximum in the region of 400 nm, the luminescence of defects according to stoichiometry in a band with a maximum in the region of 600 nm and the activator luminescence of Cr^{3+} ions in the region of 690–750 nm, in which an intense R_1 line is distinguished. The maximum of this band was shifted to the high-energy region relative to single crystal samples. The analysis of this shift is based on the fact that at smaller sizes of nanocrystals in thin films relative to single crystals, the influence of surface energy is observed, since the number of elementary cells in nanocrystals decreases and the relative number of elementary cells on the surface of the crystallite increases proportionally. As a result, the volume of the unit cell increases, and the Cr–O distance increases accordingly. The consequence is the weakening of the ligand field and the appearance of a nephelauxetic effect, which leads to a high-energy shift of the R_1 band in the activator luminescence of thin $(Y_{0.06}Ga_{0.94})_2O_3$:Cr^{3+} films at a low temperature of 8.6 K.

ACKNOWLEDGEMENTS

The authors would like to thank Prof. T. M. Demkiv for the measurements of the luminescence spectra.

REFERENCES

1. Z. Galazka, S. Ganschow, A. Fiedler, R. Bertram, D. Klimm, K. Irmscher, R. Schewski, M. Pietsch, M. Albrecht, and M. Bickermann, *J. Cryst. Growth*, **486**: 82 (2018); https://doi.org/10.1016/j.jcrysgro.2018.01.022
2. M. He, Q. Zeng, and L. Ye, *Crystals*, **13**, No. 10: 1434 (2023); https://doi.org/10.3390/cryst13101434
3. V. Vasyltsiv, A. Luchechko, Y. Zhydachevskyy, L. Kostyk, R. Lys, D. Slobodzyan, R. Jakieła, B. Pavlyk and A. Suchocki, *J. Vacuum Science & Technol. A*, **39**, No. 3: 033201 (2021); https://doi.org/10.1116/6.0000859
4. S. Kumar and R. Singh, *phys. status solidi (RRL)*, **7**, No. 10: 781 (2013); https://doi.org/10.1002/pssr.201307253
5. E. Nogales, J. A. García, B. Méndez, and J. Piqueras, *J. Appl. Phys.*, **101**, No. 3: 033517 (2007); https://doi.org/10.1063/1.2434834
6. S. M. Xu, W. Ge, X. Zhang, P. Zhang, and Y. Li, *J. of Luminescence*, **246**, 118831 (2022); https://doi.org/10.1016/j.jlumin.2022.118831
7. R. Suzuki, S. Nakagomi, Y. Kokubun, N. Arai, and S. Ohira, *Appl. Phys. Lett.*, **94**, No. 22: 222102 (2009); https://doi.org/10.1063/1.3147197
8. O. M. Bordun, B. O. Bordun, I. Yo. Kukharskyy, and I. I. Medvid, *J. Appl. Spectrosc.*, **86**, No. 6: 1010 (2020); https://doi.org/10.1007/s10812-020-00932-4
9. D. Guo, Q. Guo, Z. Chen, Z. Wu, P. Li, and W. Tang, *Materials Today Physics*, **11**: 100157 (2019); https://doi.org/10.1016/j.mtphys.2019.100157
10. M. Alonso-Orts, E. Nogales, J. M. San Juan, M. L. Ny, J. Piqueras, and B. Mėndez, *Phys. Rev. Appl.*, **9**: 064004 (2018); http://dx.doi.org/10.1103/PhysRevApplied.9.064004
11. M. Crozzolin, C. Belloni, J. Xu, T. Nakanishi, J. Ueda, S. Tanabe, F. Dallo, E. Balliana, A. Saorin, F. Rizzolio, D. Cristofori, P. Riello, A. Benedetti, and M. Back, *J. Mater. Chem. C*, **12**, No. 29: 10929 (2024); doi:10.1039/D4TC01386G
12. D. M. Esteves, A. L. Rodrigues, L. C. Alves, E. Alves, M. I. Dias, Z. Jia, W. Mu, K. Lorenz, and M. Peres, *Scientific Reports*, **13**: 4882 (2023); https://doi.org/10.1038/s41598-023-31824-0
13. T. Minami, T. Nakatani, and T. Miyata, *J. Vac. Sci. Technol. A*, **18**, No. 4: 1234 (2000); https://doi.org/10.1116/1.582332
14. A. K. Saikumar, Sh. D. Nehate, and K. B. Sundaram, *ECS J. of Solid State Science and Technol.*, **8**, No. 7: Q3064 (2019); https://doi.org/10.1149/2.0141907jss
15. O. M. Bordun, B. O. Bordun, I. I. Medvid, and I. Yo. Kukharskyy, *Acta Physica Polonica A*, **133**, No. 4: 910 (2018); https://doi.org/10.12693/APhysPolA.133.910
16. K. H. Choi and H. C. Kang, *Materials Letters*, **123**: 160 (2014); https://doi.org/10.1016/j.matlet.2014.03.038
17. T. Igarashi, M. Ihara, T. Kusunoki, K. Ohno, T. Isobe, and M. Senna, *Appl. Phys. Lett.*, **76**, No. 12: 1549 (2000); https://doi.org/10.1063/1.126092
18. C. B. Willingham, J. M. Wahl, P. K. Hogan, L. C. Kupferberg, T. Y. Wong, and A. M. De, *Proc. SPIE*, **5078**: 179 (2003); https://doi.org/10.1117/12.500986
19. O. M. Bordun, I. M. Bordun, and S. S. Novosad, *J. Appl. Spectr.*, **62**, No. 6:

1060 (1995); https://doi.org/10.1007/BF02606760
20. E. F. Armendáriz-Alonso, O. Meza, E. G. Villabona-Leal, and Elías Pérez, *J. Sol–Gel Sci. and Technol.*, **111**: 216 (2024); https://doi.org/10.1007/s10971-024-06450-5
21. K. Wasa, M. Kitabatake, and H. Adachi, *Thin Film Materials Technology: — Sputtering of Compound Materials* (William Andrew Inc.: 2004)
22. O. M. Bordun, B. O. Bordun, I. J. Kukharskyy, I. I. Medvid, O. Ya. Mylyo, M. V. Partyka, and D. S. Leonov, *Nanosistemi, Nanomateriali, Nanotehnologii*, **17**, Iss. 1: 123 (2019); https://doi.org/10.15407/nnn.17.01.123
23. https://photonscience.desy.de/facilities/petra_iii/beamlines/p66_superlumi/index_eng.html
24. C. V. Thompson, *Solid State Phys.*, **55**: 269 (2001); https://doi.org/10.1016/S0081-1947(01)80006-0
25. C. V. Thompson, *J. Appl. Phys.*, **58**: 763 (1985); https://doi.org/10.1063/1.336194
26. O. M. Bordun, B. O. Bordun, I. Yo. Kukharskyy, I. I. Medvid, I. I. Polovynko, Zh. Ya. Tsapovska, and D. S. Leonov, *Nanosistemi, Nanomateriali, Nanotehnologii*, **19**, Iss. 1: 159 (2021); https://doi.org/10.15407/nnn.19.01.159
27. O. M. Bordun, I. I. Medvid, I. Yo. Kukharskyy, and B. O. Bordun, *Phys. and Chem. of Solid State*, **17**, No. 1: 53 (2016); https://doi.org/10.15330/pcss.17.1.53-59
28. E. Nogales, B. Méndez, and J. Piqueras, *Appl. Phys. Lett.*, **86**, No. 11: 113112 (2005); https://doi.org/10.1063/1.1883713
29. H. Tang, N. He, Z. Zhu, M. Gu, B. Liu, J. Xu, M. Xu, L. Chen, J. Liu, and X. Ouyang, *Appl. Phys. Lett.*, **115**, No. 11: 071904 (2019); https://doi.org/10.1063/1.5110535
30. O. M. Bordun, B. O. Bordun, I. Yo. Kukharskyy, and I. I. Medvid, *J. Appl. Spectrosc.*, **84**, No. 1: 46 (2017); https://doi.org/10.1007/s10812-017-0425-3
31. O. M. Bordun, V. G. Bihday, and I. Yo. Kukharskyy, *J. Appl. Spectrosc.*, **80**, No. 5: 721 (2013); https://doi.org/10.1007/s10812-013-9832-2
32. J. B. Prasanna Kumar, G. Ramgopal, D. V. Sunitha, B. Daruka Prasad, H. Nagabhushana, Y. S. Vidya, K. S. Anantharaju, S. C. Prashantha, S. C. Sharma, and K. R. Prabhakara, *Luminescence: J. Biol. Chem. Lum.*, **32**, No. 3: 414 (2017); https://doi.org/10.1002/bio.3197
33. O. M. Bordun, B. O. Bordun, I. Yo. Kukharskyy, D. M. Maksymchuk, and I. I. Medvid, *Phys. and Chem. of Solid State*, **24**, No. 3: 490 (2023); https://doi.org/10.15330/pcss.24.3.490-494
34. R. Rao, A. M. Rao, B. Xu, J. Dong, S. Sharma, and M. K. Sunkara, *J. Appl. Phys.*, **98**, No. 9: 094312 (2005); https://doi.org/10.1063/1.2128044
35. B. M. Weckhuysen, P. Van Der Voort, and G. Catana, *Spectroscopy of Transition Metal Ions on Surfaces* (Leuven University Press: 2000).
36. A. Luchechko, V. Vasyltsiv, Ya. Zhydachevskyy, M. Kushlyk, S. Ubizskii, and A. Suchocki, *J. Phys. D: Appl. Phys.*, **53**, No. 35: 354001 (2020); https://doi.org/10.1088/1361-6463/ab8c7d
37. Y. Tokida and S. Adachi, *J. Appl. Phys.*, **112**, No. 6: 063522 (2012); https://doi.org/10.1063/1.4754517
38. C. Remple, L. M. Barmore, J. Jesenovec, J. S. McCloy, and M. D. McCluskey, *J. Vac. Sci. Teshnol. A*, **41**: 022702 (2023);

https://doi.org/10.1116/6.0002340
39. H. Yusa and M. Miyakawa, *J. Appl. Phys.*, **137**, No. 3: 035902 (2025); https://doi.org/10.1063/5.0246260
40. D. Vollath, F. D. Fischer, and D. Holec, *Beilstein J. Nanotechnol.*, **9**: 2265 (2018); https://doi.org/10.3762/bjnano.9.211
41. P. J. Dereń, A. Watras, and D. Stefańska, *Opt. Spectrosc.*, **131**: 795 (2023); https://doi.org/10.1134/S0030400X23070032
42. J. G. Zhang, B. Li, C. T. Xia, J. Xu, Q. Deng, X. D. Xu, F. Wu, W. S. Xu, H. S. Shi, G. Q. Pei, and Y. Q. Wu, *Sci. China Ser. E-Tech. Sci.*, **50**, No. 1: 51 (2007); https://doi.org/10.1007/s11431-007-2026-5
43. C. K. Jørgensen, *The Nephelauxetic Series P. 73–124 Progress in Inorganic Chemistry* (Ed. F. A. Cotton) (New York–London: Interscience Publishers: 1962), vol. **4**.
44. M. G. Brik, S. J. Camardello, A. M. Srivatsava, N. M. Avram, and A. Suchotcki, *ECS J. Solid State. Sci. Technol.*, **5**: R3067 (2016); https://doi.org/10.1149/2.0091601jss

Наносистеми, наноматеріали, нанотехнології
Nanosistemi, Nanomateriali, Nanotehnologii
2025, т. 23, № 2, сс. 449–465
https://doi.org/10.15407/nnn.23.02.0449

© 2025 ІМФ (Інститут металофізики
ім. Г. В. Курдюмова НАН України)
Надруковано в Україні.

PACS numbers: 61.46.Bc, 68.43.Bc, 71.15.Mb, 73.20.Hb, 73.22.Lp, 81.07.Nb, 85.30.De

Smart Nanocomposites of ZnO & ZnS as Potent Semiconductors Through Hydrogen-Bonded Engineering in Transistors

Fatemeh Mollaamin

Department of Biomedical Engineering,
Faculty of Engineering and Architecture,
Kastamonu University,
Kastamonu, Turkey

We employ first-principles calculations to investigate the structural stability and electronic properties of cubic zinc oxide (ZnO) and zinc sulphide (ZnS) heteroclusters adsorbed with H_2O molecule. A comprehensive investigation on H_2O grabbing by ZnO/ZnS heteroclusters is carried out using DFT computations at the CAM–B3LYP–D3/6–311+G(d, p) level of theory. The notable fragile signal intensity close to the parallel edge of the nanocluster sample might be owing to H/OH-binding-induced non-spherical distribution of ZnO or ZnS heterocluster. The hypothesis of the energy absorption phenomenon is confirmed by density distributions of CDD, TDOS/PDOS/OPDOS, and LOL for ZnO/ZnO–H_2O or ZnS/ZnS–H_2O. A vaster jointed area is engaged by an isosurface map for H/OH adsorption on ZnO or ZnS surface towards formation of ZnO–H_2O or ZnS–H_2O complex due to labelling atoms of O1, Zn15, O27 or S27, H29, H30. Therefore, it can be considered that zinc in the functionalized ZnO or ZnS might have more impressive sensitivity for accepting the electrons in the process of H/OH adsorption. It is considerable that, when all surface atoms of ZnO or ZnS are coated by OH and H groups, the semiconducting behaviour is recovered. Our results open up the possibility of tailoring the electronic properties by controlling the surface adsorption sites.

Ми використовуємо розрахунки з перших принципів для дослідження структурної стабільности й електронних властивостей кубічних гетерокластерів оксиду Цинку (ZnO) та сульфіду Цинку (ZnS), адсорбованих із молекулою H_2O. Комплексне дослідження захоплення H_2O гетерокластерами ZnO/ZnS було проведено з використанням DFT-обчислень на теоретичному рівні CAM–B3LYP–D3/6–311+G(d, p). Примітна слабка інтенсивність сиґналу поблизу паралельного краю зразка нанокластера може бути пов'язана з несферичним розподілом гетерокластера ZnO або ZnS, індукованим зв'язуванням H/OH. Ґіпотезу про явище абсорбції енергії було підтверджено розподілами густини CDD, TDOS/PDOS/OPDOS і LOL для

ZnO/ZnO–H_2O або ZnS/ZnS–H_2O. Ширша з'єднана область охоплюється ізоповерхневою мапою для адсорбції H/OH на поверхні ZnO або ZnS задля утворення комплексу ZnO–H_2O або ZnS–H_2O завдяки маркувальним атомам O1, Zn15, O27 або S27, H29, H30. Отже, можна вважати, що Цинк у функціоналізованому ZnO або ZnS може мати вражаючу чутливість щодо прийняття електронів у процесі адсорбції H/OH. Важливо, що, коли всі поверхневі атоми з ZnO або ZnS покриті групами OH і H, напівпровідникова поведінка відновлюється. Наші результати відкривають можливість налаштування електронних властивостей шляхом контролю вузлів поверхневої адсорбції.

Key words: cubic ZnO/ZnS heteroclusters, semiconductor, H/OH adsorption, first-principles calculations.

Ключові слова: кубічні гетерокластери ZnO/ZnS, напівпровідник, адсорбція H/OH, першопринципні розрахунки.

(Received 6 December, 2024)

1. INTRODUCTION

Zinc oxide (ZnO) is a promising semiconductor material for various applications ranging from optoelectronics to biomedicine, attributed to its wide direct band gap, high excitons-binding energy, high mobility, and high quantum efficiency. To improve further the performance of ZnO devices, plasma treatment is a common method for surface modification [1–4]. The luminescence properties of ZnO after plasma treatment are significantly changed, including ultraviolet (UV) luminescence, visible luminescence, and recombination mechanism [5–11].

Optical properties are improved significantly by H plasma, with negligible alteration in thickness. Although no chemical reaction is introduced, emission intensity is enhanced by Ar plasma by eliminating the non-radiative recombination centres. Furthermore, H and Ar plasma also induce strong exciton localization, leading to significant broadening of the UV spectrum [12–15].

However, replicating or applying the reported improvement in plasma treatments for ZnO often proves challenging. This difficulty arises from several factors, including the diverse properties of ZnO samples, which encompass thin films, single crystals and nanostructures grown through various methods. Moreover, the specific effects of plasma treatments using different gases remain unclear, as each type of gas plasma exhibits unique interactions. Consequently, it is crucial to conduct a systematic comparison of the influence of various plasma gases on the optical and electrical properties and to identify accurately the specific defects affected [16–21].

Transparent and superhydrophilic materials are indispensable for their self-cleaning function, which has become an increasingly popular research topic, particularly in photovoltaic (PV) applications. It was reported hydrophilic and superhydrophilic ZnO by varying the morphology for use as a self-cleaning coating for PV applications [22].

The researchers have applied molecular dynamics simulations through a reactive force field for ZnO–H_2O ambient. The force-field parameters were fitted to a dataset of energies, geometries and charges derived from density functional theory calculations. The applied model has provided a good fit to the quantum mechanics reference data for the ZnO–H_2O system that was present in the dataset. The force field has been used to study how H_2O is adsorbed, molecularly or dissociatively, at monolayer coverage on flat and stepped ZnO surfaces, at different temperatures. The results show that structures that promote hydrogen bonding are favoured and that the presence of steps promotes an increased level of hydroxylation in the water monolayers [23].

The cubic form of zinc sulphide (ZnS) is the prototype II–VI semiconductor with smallest lattice constant of $a_0 = 5.4102$ Å at 300 K and the primarily candidate for UV-light emitting devices because of its large band-gap energy around $\cong 3.7$ eV at room temperature [24].

Many research groups have attempted to dope anions and cations into the ZnO or ZnS lattice, which helps to reach various complex applications since its electronic structure and characteristics may be significantly adjusted. The enhanced catalytic properties reveal the synergy between ZnO and ZnS functional nanomaterials, which upgrade the electron–hole pair, resulting in an enhanced catalytic performance under the visible region. Notably, the ZnO-based ZnS nanocomposite was prepared by a wet chemical method without any template. The template method is not sensitive to the preparation conditions, is easy to operate and implement, and controls nanomaterials' structure, morphology, and particle size through the template material. Generally, the outstanding photocatalytic performance of wurtzite ZnO and ZnS semiconductor and their composite under visible light irradiation could be attributed to synergistic effects, when coupled with other metal oxide semiconductor. The present study is a part of our ongoing research to understand the solar energy conversion/harvesting directions. We reported a facile synthesis of ZnS and ZnO nanoparticles and their nanocomposites by the wet chemical method [25–29].

In this work, we analysed the effect of H_2O adsorption on the properties of ZnO or ZnS heterocluster via the density of state, charge distribution, bond orders and HOMO–LUMO orbitals using DFT studies. The optimized ZnO or ZnS is shown in Fig. 1, *a*, *b*,

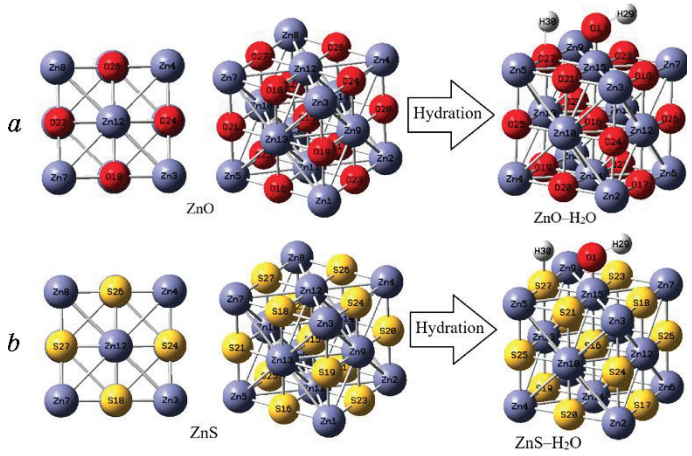

Fig. 1. Characterization of (*a*) ZnO/ZnO–H_2O and (*b*) ZnS/ZnS–H_2O heteroclusters through a labelled ring in clockwise manner including H, O, S, Zn towards H_2O adsorption.

and the Zn and O or S atoms are also numbered to characterize the reaction pathway.

2. THEORY, MATERIALS AND COMPUTATION

The hydration of ZnO or ZnS and formation of ZnO–H_2O or ZnS–H_2O heterocluster was calculated within the framework of first-principles calculation based on density functional theory (DFT) (Fig. 1). The rigid potential energy surface using density functional theory [30–43] was performed due to Gaussian 16 revision C.01 program package [44] and GaussView 6.1 [45]. The coordination input for energy storage on the solar cells has applied 6–311+G(*d*, *p*) and EPR–3 basis sets.

First, we optimized the structural parameters of the nanocluster of ZnO or ZnS and hydrated nanocluster of ZnO–H_2O or ZnS–H_2O for obtaining the highest short-circuit current density. Figure 1 shows the process of H_2O adsorption on nanocluster of ZnO or ZnS which is varied to maximize the absorption in the active region. This is a utility used to calculate ring area and perimeter, since ring area is sometimes involved in wave-function analysis. In this function, it is needed to input the index of the atoms in the ring in clockwise manner, which can conclude the total ring area and total ring perimeter for a tailored ring as 9.4242 Å and 12.2796 $Å^2$ for ZnO (Fig. 1, *a*) and 9.4240 Å and 12.2794 $Å^2$ for ZnS, respectively (Fig. 1, *b*).

3. RESULTS AND DISCUSSION

In this article, the data has evaluated the efficiency of ZnO or ZnS in H_2O medium through energies, geometries and charges derived from density functional theory calculations. The applied model has provided a good fit to the quantum mechanics reference data for the ZnO–H_2O or ZnS–H_2O systems that was present in the dataset. The force field has been used to study how water is adsorbed molecularly at monolayer coverage on ZnO or ZnS surfaces.

The amounts of charge-density differences 'CDD' is measured by considering isolated atoms or noninteracting ones. The mentioned approximation can be the lightest to use because the superposition value may be received from the primary status of the self-consistency cycle in the code that carries out the density functional theory (Fig. 2, *a*, *a*′, *b*, *b*′) [46]. Figure 2, *a*, *b* indicates all Zn, O or S atoms of ZnO or ZnS fluctuating around –9 to –1 Bohr. In Figure

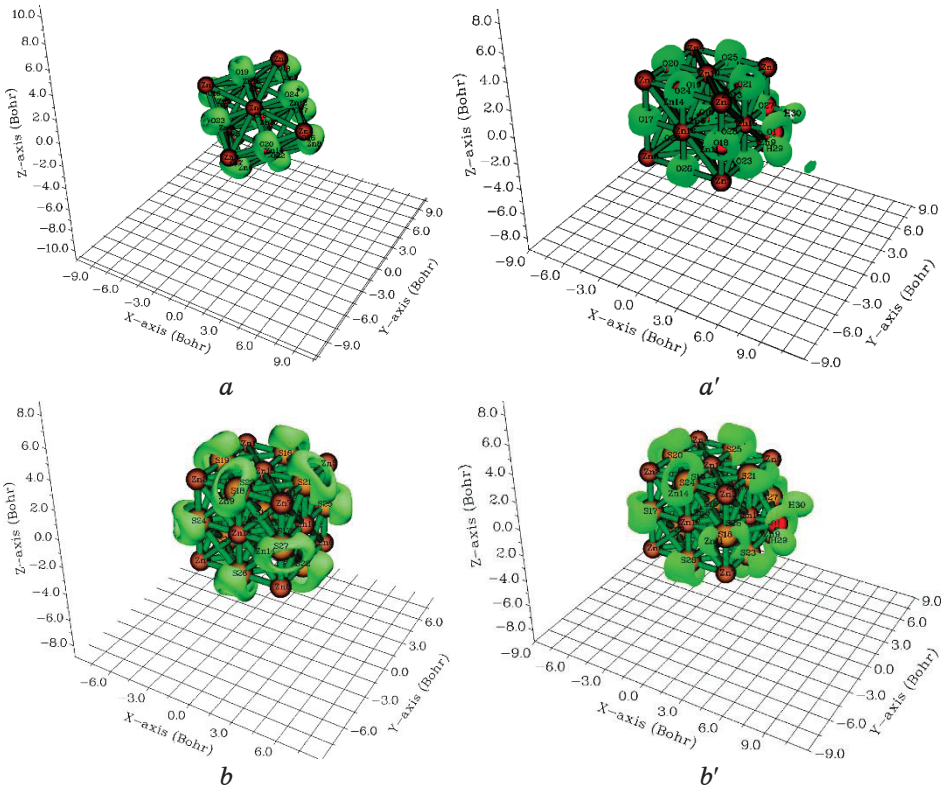

Fig. 2. CDD graphs for heteroclusters of (*a*) ZnO, (*a*′) ZnO–H_2O, (*b*) ZnS, and (*b*′) ZnS–H_2O.

2, a', b', the atom of Zn15, O27 or S27 from ZnO–H_2O or ZnS–H_2O and O1, H29, H30 from H_2O molecule accompanying other Zn, O or S atoms from ZnO–H_2O or ZnS–H_2O have shown the fluctuation around –1 to +1 Bohr and –9 to +1 Bohr, respectively.

Furthermore, atomic charge during H_2O adsorption by ZnO or

TABLE 1. The atomic charge (Q/coulomb) for heteroclusters of ZnO and ZnS through H/OH adsorption and formation of ZnO–H_2O and ZnS–H_2O heteroclusters.

ZnO		ZnO–H_2O		ZnS		ZnS–H_2O	
Atom	Charge	Atom	Charge	Atom	Charge	Atom	Charge
Zn1	0.7141	O1	–0.5958	Zn1	–0.5916	O1	–0.6526
Zn2	0.7139	Zn2	0.6972	Zn2	–0.5915	Zn2	–0.5742
Zn3	0.7135	Zn3	0.7278	Zn3	–0.5915	Zn3	–0.5431
Zn4	0.7141	Zn4	0.7273	Zn4	–0.5914	Zn4	–0.5535
Zn5	0.7141	Zn5	0.5927	Zn5	–0.5914	Zn5	–0.4722
Zn6	0.7135	Zn6	0.6958	Zn6	–0.5913	Zn6	–0.5761
Zn7	0.7140	Zn7	0.7113	Zn7	–0.5913	Zn7	–0.5656
Zn8	0.7140	Zn8	0.7264	Zn8	–0.5912	Zn8	–0.5528
Zn9	1.7451	Zn9	0.5981	Zn9	–0.4176	Zn9	–0.4722
Zn10	1.7450	Zn10	1.7256	Zn10	–0.4179	Zn10	–0.4578
Zn11	1.7471	Zn11	1.7376	Zn11	–0.4175	Zn11	–0.4581
Zn12	1.7471	Zn12	1.8835	Zn12	–0.4176	Zn12	–0.4646
Zn13	1.7461	Zn13	1.9004	Zn13	–0.4175	Zn13	–0.5131
Zn14	1.7460	Zn14	1.6986	Zn14	–0.4176	Zn14	–0.3470
O15	–1.5357	Zn15	1.4867	S15	0.6704	Zn15	–2.6670
O16	–1.2210	O16	–1.5460	S16	0.5475	S16	0.7342
O17	–1.2210	O17	–1.2236	S17	0.5473	S17	0.6123
O18	–1.2210	O18	–1.2143	S18	0.5473	S18	0.7932
O19	–1.2209	O19	–1.2232	S19	0.5475	S19	0.8517
O20	–1.2209	O20	–1.2259	S20	0.5473	S20	0.5726
O21	–1.2209	O21	–1.1381	S21	0.5471	S21	1.1263
O22	–1.2209	O22	–1.2260	S22	0.5469	S22	0.5741
O23	–1.2210	O23	–1.1370	S23	0.5475	S23	1.1166
O24	–1.2210	O24	–1.2155	S24	0.5473	S24	0.5695
O25	–1.2210	O25	–1.2183	S25	0.5471	S25	0.6185
O26	–1.2210	O26	–1.2157	S26	0.5471	S26	0.5693
O27	–1.2210	O27	–1.1850	S27	0.5469	S27	0.2986
		O28	–1.2183			S28	0.6184
		H29	0.2973			H29	0.4588
		H30	0.3764			H30	0.3556

ZnS towards formation of $ZnO–H_2O$ or $ZnS–H_2O$ (Table 1) was discussed. The atomic charge of Zn, O or S, and H/OH adsorbed on ZnO or ZnS have been measured. The values detect that, with adding H_2O, the negative atomic charges of oxygen atoms of O16, O17, O18, O19, O20, O21, O22, O23, O24, O25, O26, O27, O28 in $ZnO–H_2O$ have changed through coating of ZnO with H/OH. In fact, $ZnO–H_2O$ has shown more efficiency than ZnO for admitting the electron from electron donor of O16 to O28 (Table 1 and Fig. 3, *a*).

However, the negative atomic charge of zinc atoms and loss of

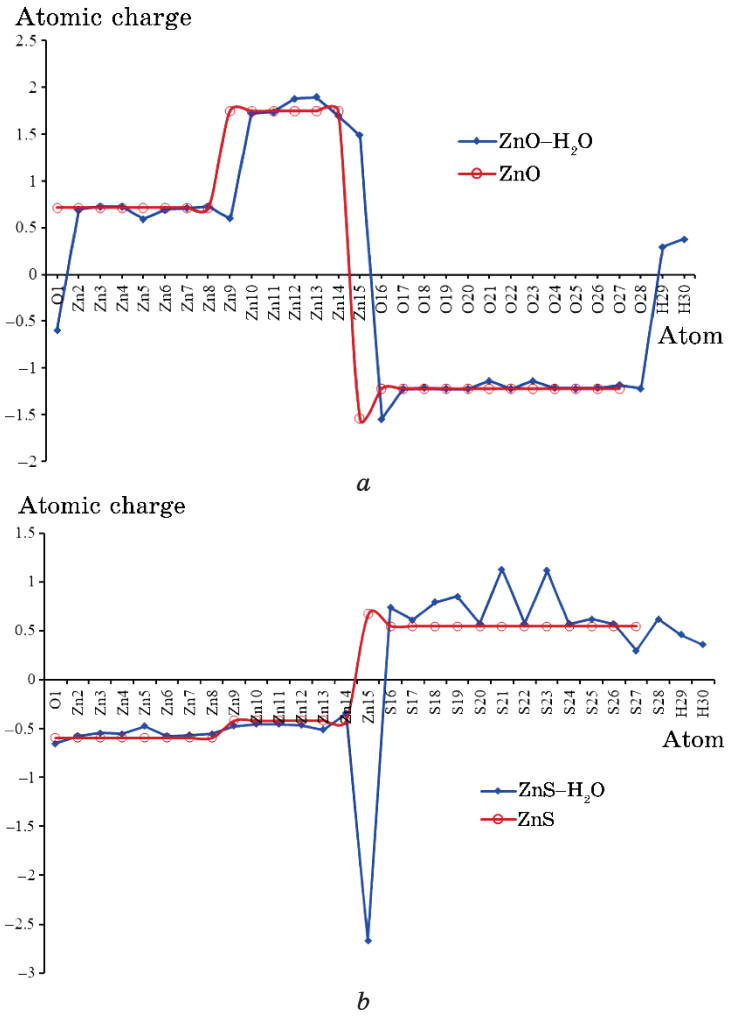

Fig. 3. The fluctuation of atomic charge (*Q*/coulomb) for (*a*) ZnO/$ZnO–H_2O$ and (*b*) ZnS/$ZnS–H_2O$.

negative atomic charge of sulphur in ZnS/ZnS–H_2O have been observed through Table 1 and Fig. 3, *b*. The changes of charge density analysis in the adsorption process have illustrated that ZnO and ZnO–H_2O nanoclusters have shown the 'Bader charge' of –1.747 and –1.900 coulomb, respectively. The differences of charge density for these structures are measured as $\Delta Q_{\text{ads.ZnO–H}_2\text{O}} = -0.153$ coulomb. The changes of charge density analysis in the adsorption process have illustrated that ZnS and ZnS–H_2O nanoclusters have shown the 'Bader charge' of –0.670 and –2.667 coulomb, respectively. The differences of charge density for these structures are measured as $\Delta Q_{\text{ads.ZnS–H}_2\text{O}} = -1.997$coulomb.

To understand better the different adsorption characteristics of ZnO/ZnO–H_2O and ZnS/ZnS–H_2O heteroclusters, total density of states (TDOS) using the Multiwfn program [45] has been measured. This parameter can indicate the existence of important chemical interactions often on the convex side (Fig. 4, *a*, *a*′, *b*, *b*′). In isolated system (such as molecule), the energy levels are discrete, the concept of density of state (DOS) is supposed completely valueless in this situation. Therefore, the original total DOS (TDOS) of isolated system can be written as follows [47]:

$$\text{TDOS}\ (E) = \sum_i \delta\left(E - \int_i\right), \tag{1}$$

$$G(x) = \frac{1}{c\sqrt{2\pi}} e^{-\frac{x^2}{2c^2}}, \text{ where } c = \frac{\text{FWHM}}{2\sqrt{2\ln x}}. \tag{2}$$

Moreover, the curve map of broadened partial DOS (PDOS) and overlap DOS (OPDOS) are valuable for visualizing orbital composition analysis, PDOS function of fragment *A* is defined as

$$\text{PDOS}_A(E) = \sum_i \Xi_{i,A} F\left(E - \int_i\right), \tag{3}$$

where $\Xi_{i,A}$ is the composition of fragment *A* in orbital *i*. The OPDOS between fragment *A* and *B* is defined as

$$\text{OPDOS}_{A,B}\ (E) = \sum_i X^i_{A,B} F\left(E - \in_i\right), \tag{4}$$

where $X^i_{A,B}$ is the composition of total cross term between fragment *A* and *B* in orbital *i*.

In the TDOS map, each discrete vertical line corresponds to a molecular orbital (MO), the dashed line highlights the position of HOMO. The curve is the TDOS simulated based on the distribution of MO energy levels. In the negative part, the region around –0.60 to –0.80 a.u. has obviously larger state density than other regions

for ZnO and ZnO–H_2O nanoclusters (Fig. 4, *a*, *a*′). However, it has been shown a larger state density through pointed peaks for ZnO–H_2O (Fig. 4, *a*′) than ZnO (Fig. 4, *a*) around –0.20 to –0.40 a.u.

It is remarkable that, when all surface atoms of ZnO are coated by OH and H groups, the semiconducting behaviour is recovered. Our results open up the possibility of tailoring the electronic properties by controlling the surface adsorption sites. In the positive

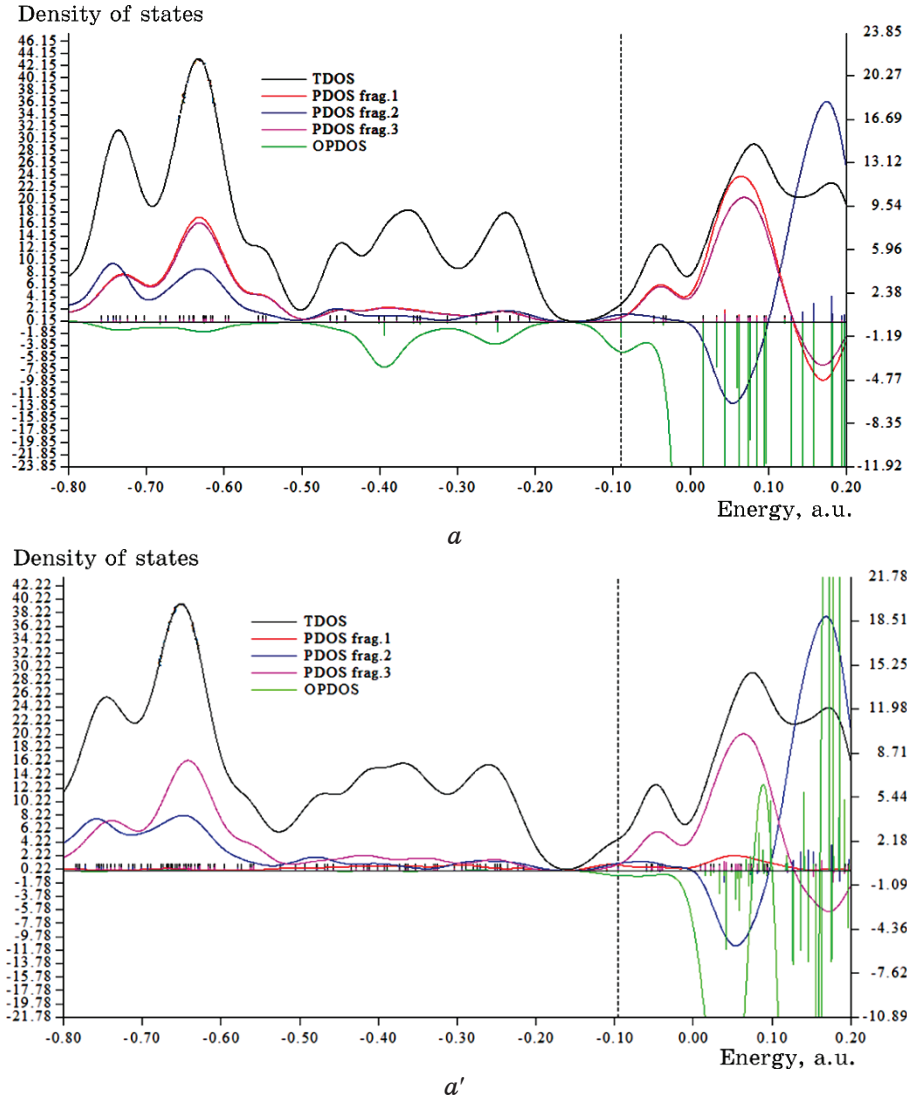

Fig. 4. TDOS/PDOS/OPDOS graphs of heteroclusters of (*a*) ZnO, (*a*′) ZnO–H_2O, (*b*) ZnS, and (*b*′) ZnS–H_2O.

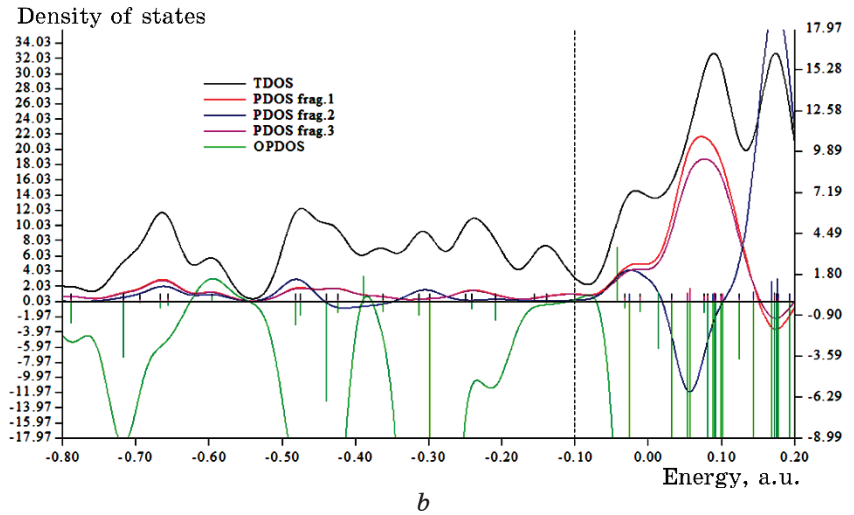

b

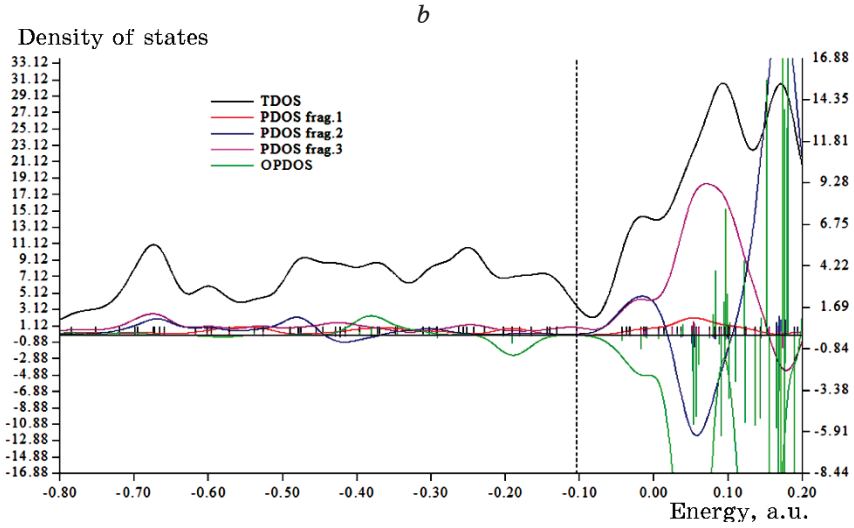

b′

Continuation Fig. 4.

part, the region around 0.1 to 0.2 a.u. has obviously larger state density than other regions for ZnS and ZnS–H_2O nanoclusters (Fig. 4, *b*, *b′*).

Fragment 1 has been defined for Zn1 (Fig. 4, *a*), O1 (Fig. 4, *a′*) and Zn2, Zn4, Zn6, Zn8, Zn10, O16, O19, O22, O24 (Fig. 4, *a*, *a′*) and H30 (Fig. 4, *a′*). Moreover, Fragment 2 has indicated the fluctuation of Zn11, Zn12, Zn13, Zn14, O17, O25, O26, O27 for ZnO and ZnO–H_2O heteroclusters (Fig. 4, *a*, *a′*) and H29 for ZnO–H_2O (Fig. 4, *a′*). Finally, it was considered the fluctuation of O15 (Fig. 4, *a*), Zn15 (Fig. 4, *a′*) and Zn3, Zn5, Zn7, Zn9, O18, O20, O21, O23

for both ZnO and ZnO–H_2O nanoclusters (Fig. 4, *a*, *a*′) through Fragment 3. Moreover, Fragment 1 has been defined for Zn1 (Fig. 4, *b*), O1 (Fig. 4, *b*′) and Zn2, Zn4, Zn6, Zn8, Zn10, S16, S19, S22, S24 (Fig. 4, *b*, *b*′) and H30 (Fig. 4, *b*′). Moreover, Fragment 2 has indicated the fluctuation of Zn11, Zn12, Zn13, Zn14, S17, S25, S26, S27 for ZnS and ZnS–H_2O heteroclusters (Fig. 4, *b*, *b*′) and H29 for ZnS–H_2O (Fig. 4, *b*′). Finally, it was considered the fluctuation of S15 (Fig. 4, *b*), Zn15 (Fig. 4, *b*′) and Zn3, Zn5, Zn7, Zn9, S18, S20, S21, S23 for both ZnS and ZnS–H_2O heteroclusters (Fig. 4, *b*, *b*′) through Fragment 3.

Localized orbital locator (LOL) has similar expression compared to electron localization function (ELF) [48]:

$$\mathrm{LOL}(\mathbf{r}) = \frac{\tau(\mathbf{r})}{1+\tau(\mathbf{r})}, \quad \tau(\mathbf{r}) = \frac{D_0(\mathbf{r})}{\frac{1}{2}\sum_i \eta_i \left|\nabla\varphi_i(\mathbf{r})\right|^2}, \tag{5}$$

$$D_0(\mathbf{r}) = \frac{3}{10}\left(6\pi^2\right)^{2/3}\left[\left(\rho_\alpha(\mathbf{r})\right)^{5/3} + \left(\rho_\beta(\mathbf{r})\right)^{5/3}\right]. \tag{6}$$

Multiwfn [49] also supports the approximate version of LOL defined by Tsirelson and Stash [50], namely, the actual kinetic energy term in LOL is replaced by second-order gradient expansion like ELF, which may demonstrate a broad span of bonding samples. This Tsirelson's version of LOL can be activated by setting 'ELFLOL_type' to 1. For special reason, if 'ELFLOL_type' in settings.ini is changed from 0 to 2, another formalism will be used:

$$\mathrm{LOL}(\mathbf{r}) = \frac{1}{1+\left(\tau(\mathbf{r})\right)^{-2}}. \tag{7}$$

If the parameter 'ELFLOL_cut' in settings.ini is set to x, then, LOL will be zero, where LOL is less than x.

The heteroclusters of ZnO/ZnO–H_2O and ZnS/ZnS–H_2O can be defined by LOL graphs owing to exploring their delocalization/localization characterizations of electrons and chemical bonds (Fig. 5, *a*, *a*′, *b*, *b*′). Covalent zones have high LOL value, the electron depletion zones between valence shell and inner shell are indicated by the blue circles around nuclei (Fig. 5, *a*, *a*′, *b*, *b*′). The counter map of LOL for ZnO/ZnO–H_2O (Fig. 5, *a*, *a*′) and ZnS/ZnS–H_2O (Fig. 5, *b*, *b*′) has shown the localized orbital locator through H/OH adsorption. ZnO–H_2O or ZnS–H_2O heterocluster indicates a larger isosurface map of the localized orbital locator due to labelling atoms of O1, Zn15, O27 or S27, H29, H30. A narrower connected area occupied by an isosurface map means that localized orbital locator is relatively difficult. However, the large counter map

of LOL for ZnO–H_2O or ZnS–H_2O can confirm that ZnO or ZnS can be a promising semiconductor material for various applications.

Moreover, intermolecular orbital overlap integral is important in discussions of intermolecular charge transfer, which can calculate HOMO–HOMO and LUMO–LUMO overlap integrals between the H/OH and heterocluster of ZnO or ZnS. The applied wave-function level is CAM–B3LYP–D3/6–311+G(d, p) that corresponds to HOMO and LUMO, respectively (Table 2).

The amount of 'Mayer bond order' [51] is generally according to empirical bond order for the single bond is near 1.0. 'Mulliken bond order' [52] with a small accord with empirical bond order is not ap-

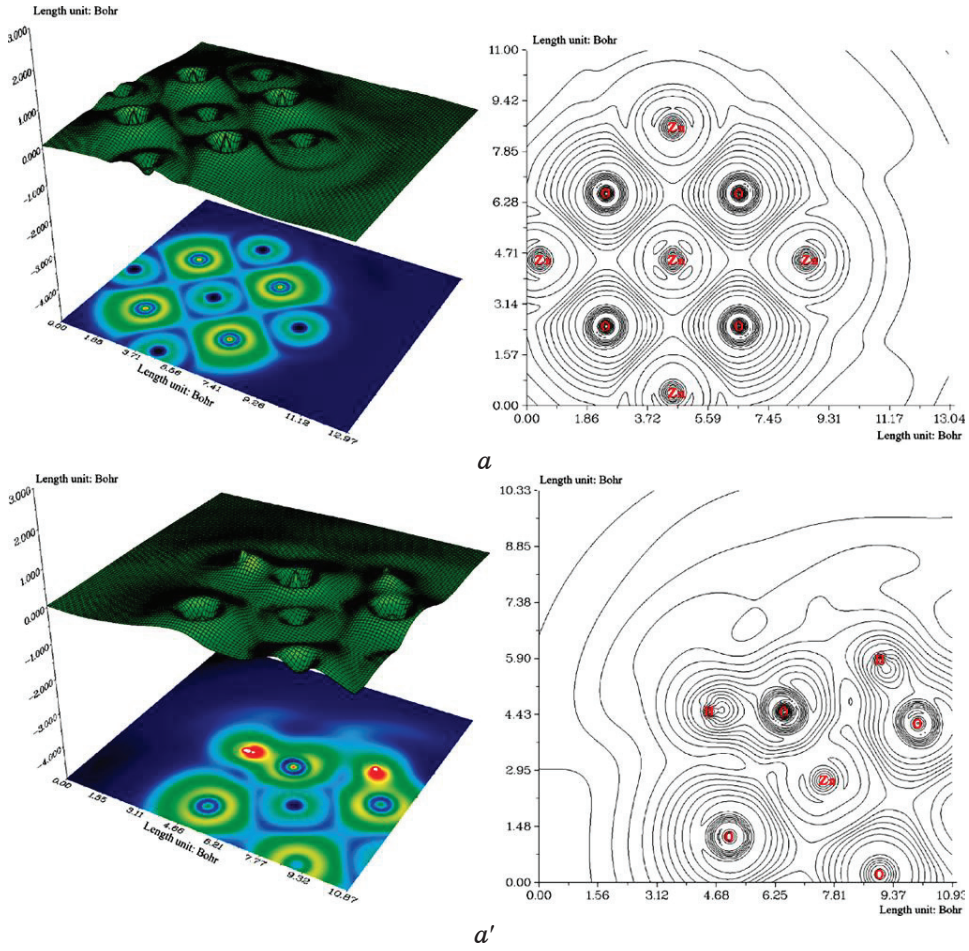

Fig. 5. The graphs of LOL for heteroclusters of (*a*) ZnO, (*a*′) ZnO–H_2O, (*b*) ZnS, and (*b*′) ZnS–H_2O. (Counter line map on the right and shaded surface map with projection in the left.)

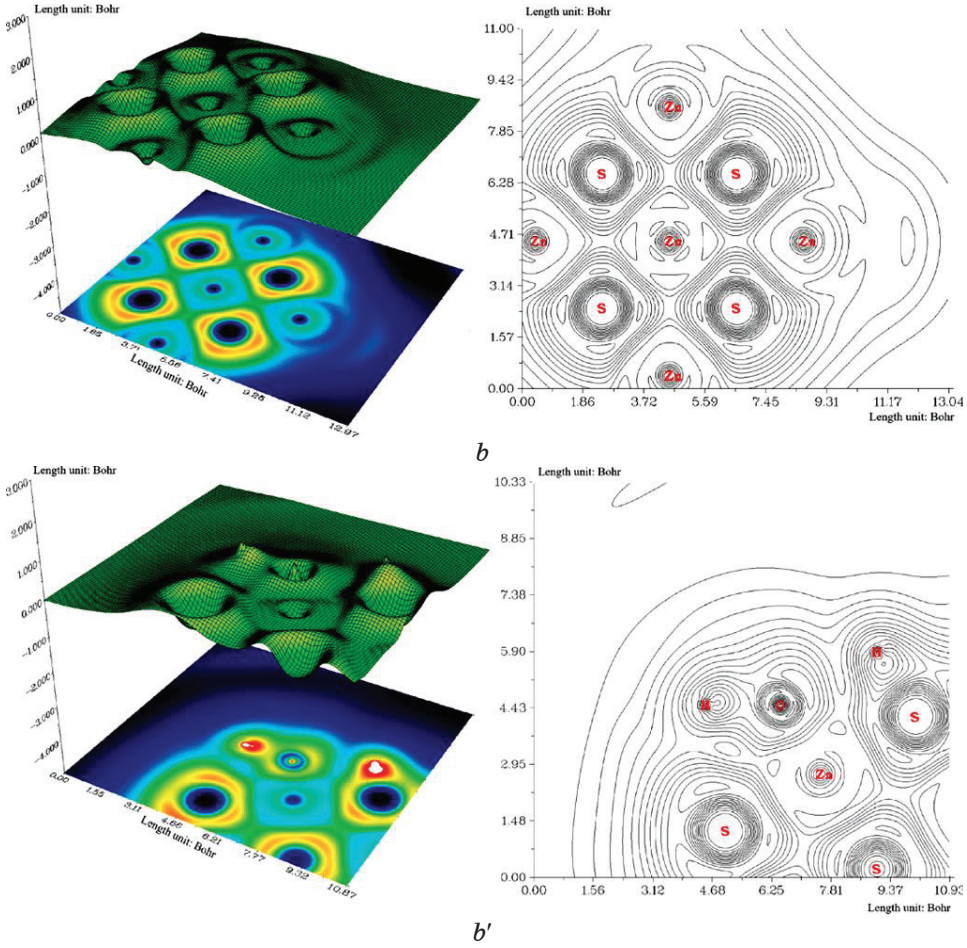

Continuation Fig. 5.

propriate for quantifying bonding strength, for which Mayer bond order always performs better. However, 'Mulliken bond order' is a good qualitative indicator for 'positive amount' of bonding and 'negative amount' of antibonding, which are evacuated and localized, respectively (Table 3).

As it is seen in Table 3, 'Laplacian bond order' [53] has a straight cohesion with bond polarity, bond dissociation energy and bond vibrational frequency. The low value of Laplacian bond order might demonstrate that it is insensitive to the calculation degree applied for producing electron density. Generally, the value of 'Fuzzy bond order' is near Mayer bond order, especially for low-polar bonds, but much more stable with respect to the change in basis-set. Computa-

TABLE 2. LUMO, HOMO, and energy gap (ΔE) for ZnO and ZnS through H/OH adsorption and formation of ZnO–H_2O and ZnS–H_2O heteroclusters.

Heteroclusters	E_{HOMO}, eV	E_{LUMO}, eV	$\Delta E = E_{LUMO} - E_{HOMO}$, eV
ZnO	–2.4280	–1.3056	1.1223
ZnO–H_2O	–2.6110	–1.6053	1.0056
ZnS	–2.7413	–1.1723	1.5690
ZnS–H_2O	–2.7459	–1.1762	1.6696

TABLE 3. The bond orders of Mayer, Wiberg, Mulliken, Laplacian, and Fuzzy types from mixed alpha and beta density matrix for ZnO and ZnS through H/OH adsorption and formation of ZnO–H_2O and ZnS–H_2O heteroclusters.

Bond order	ZnO–H_2O			ZnS–H_2O		
	O1–Zn15	O1–H29	O27–H30	O1–Zn15	O1–H29	S27–H30
Mayer	1.1308	0.6507	0.4783	1.2782	0.6905	0.8056
Wiberg	1.7176	0.6631	0.4490	1.0554	0.6397	0.6436
Mulliken	1.9120	0.1727	0.0573	1.8753	0.1573	0.1864
Laplacian	1.6451	0.2169	0.1505	1.7453	0.2014	0.2491
Fuzzy	1.6561	0.6878	0.4321	1.5246	0.6273	0.6852

tion of 'Fuzzy bond order' demands running 'Becke's DFT' numerical integration, owing to which the calculation value is larger than assessment of 'Mayer bond order' and it can concede more precisely [54].

4. CONCLUSIONS

Considerable attention has recently been given to ZnO or ZnS as a promising multifunctional material with wide-ranging technological applications. Understanding the interaction of water with ZnO or ZnS is important for this material to be used in gas sensing, catalysis and biomedical applications. In summary, H_2O grabbing on the ZnO or ZnS was investigated by first-principles calculations. We have provided ZnO or ZnS heterocluster, and then, the geometrical parameters of H/OH adsorption on the surface of ZnO or ZnS through the absorption status and current charge density were studied. ZnO–H_2O or ZnS–H_2O heterocluster indicates a larger isosurface map of electron delocalization due to labelling atoms of O1, Zn15, O27 or S27, H29, H30. A narrower connected area occupied by an isosurface map means that electron delocalization is relatively difficult. However, the large counter map of LOL for ZnO–H_2O or

$ZnS–H_2O$ can confirm that ZnO or ZnS can be a promising semiconductor material for various applications.

ACKNOWLEDGEMENTS

In successfully completing this paper and its research, the author is grateful to Kastamonu University.

REFERENCES

1. Christopher J. Frederickson, Jae-Young Koh, and Ashley I. Bush, *Nat. Rev. Neurosci.*, 6: 449 (2005); https://doi.org/10.1038/nrn1671
2. Amir Moezzi, Andrew M. McDonagh, and Michael B. Cortie, *Chem. Eng. J.*, **185–186**: 1–22 (2012); https://doi.org/10.1016/j.cej.2012.01.076
3. Jingbin Han, Fengru Fan, Chen Xu, Shisheng Lin, Min Wei, Xue Duan, and Zhong Lin Wang, *Nanotechnology*, **21**, No. 40: 405203 (2010); https://doi.org/10.1088/0957-4484/21/40/405203
4. Zenan Jiang, Saeid Soltanian, Bobak Gholamkhass, Abdullah Aljaafari, and Peyman Servati, *RSC Adv.*, **8**, Iss. 64: 36542 (2018); https://doi.org/10.1039/C8RA07071G
5. J. Čížek, J. Valenta, P. Hruška, O. Melikhova, I. Procházka, M. Novotný, and J. Bulíř, *Appl. Phys. Lett.*, **106**: 251902 (2015); https://doi.org/10.1063/1.4922944
6. Kiyoshi Matsuyama, Kenji Mishima, Takafumi Kato, Keiichi Irie, and Kenichi Mishima, *J. Colloid Interface Sci.*, **367**: 171 (2012); https://doi.org/10.1016/j.jcis.2011.10.003
7. Buguo Wang, Bruce Claflin, Michael Callahan, Z. -Q. Fang, and David Look, *Proc. SPIE*, **8987**: 89871D (2014); https://doi.org/10.1117/12.2042344
8. B. J. Jin, S. Im, and S. Y. Lee, *Thin Solid Films*, **366**: 107 (2000); https://doi.org/10.1016/S0040-6090(00)00746-X
9. C. V. Manzano, D. Alegre, O. Caballero-Calero, B. Alén, and M. S. Martín-González, *J. Appl. Phys.*, **110**: 043538 (2011); https://doi.org/10.1063/1.3622627
10. M. A. Borysiewicz, M. Wzorek, T. Wojciechowski, T. Wojtowicz, E. Kamińska, and A. Piotrowska, *J. Lumin.*, **147**: 367 (2014); https://doi.org/10.1016/j.jlumin.2013.11.076
11. Oscar Marin, Vanessa González, Mónica Tirado, and David Comedi, *Mater. Lett.*, **251**: 41 (2019); https://doi.org/10.1016/j.matlet.2019.05.033
12. Huan-Ming Xiong, Da-Peng Liu, Yong-Yao Xia, and Jie-Sheng Chen, *Chem. Mater.*, **17**: 3062 (2005); https://doi.org/10.1021/cm050556r
13. D. C. Agarwal, U. B. Singh, Srashti Gupta, Rahul Singhal, P. K. Kulriya, Fouran Singh, A. Tripathi, Jitendra Singh, U. S. Joshi, and D. K. Avasthi, *Scientific Reports*, **9**: 6675 (2019); https://doi.org/10.1038/s41598-019-43184-9
14. E. Wolska, J. Kaszewski, P. Kiełbik, J. Grzyb, M. M. Godlewski, and M. Godlewski, *Opt. Mater.*, **36**: 1655 (2014); https://doi.org/10.1016/j.optmat.2013.12.032

15. J.-H. Lim, C.-K. Kang, K.-K. Kim, I.-K. Park, D.-K. Hwang, and S.-J. Park, *Adv. Mater.*, **18**: 2720 (2006); https://doi.org/10.1002/adma.200502633
16. Diana B. Tolubayeva, Lesya V. Gritsenko, Yevgeniya Y. Kedruk, Madi B. Aitzhanov, Renata R. Nemkayeva, and Khabibulla A. Abdullin, *Biosensors*, **13**: 793 (2023); https://doi.org/10.3390/bios13080793
17. Haijie Liu, Yan Zhang, Haihua Zhang, Longcai Wang, Tao Wang, Zhifa Han, Liyong Wu, and Guiyou Liu, *J. Transl. Med.*, **19**: 221 (2021); https://doi.org/10.1186/s12967-021-02892-5
18. Kh. A. Abdullin, M. T. Gabdullin, L. V. Gritsenko, D. V. Ismailov, Zh. K. Kalkozova, S. E. Kumekov, Zh. O. Mukash, A. Yu. Sazonov, and E. I. Terukov, *Semiconductors*, **50**: 1010 (2016); https://doi.org/10.1134/S1063782616080029
19. Shang-Chou Chang, Jhih-Ciang Hu, Huang-Tian Chan, and Chuan-An Hsiao, *Coatings*, **12**: 945 (2022); https://doi.org/10.3390/coatings12070945
20. Shang-Chou Chang, Tsung-Han Li, and Huang-Tian Chan, *Int. J. Electrochem. Sci.*, **16**: 210817 (2021); https://doi.org/10.20964/2021.08.34
21. Cong Zhang, Zongsheng Cao, Guangliang Zhang, Yu Yan, Xin Yang, Jiayuan Chang, Yanfei Song, Yuhang Jia, Peng Pan, Wei Mi, Zhengchun Yang, Jinshi Zhao, and Jun Wei, *Microchem. J.*, **158**: 105237 (2020); https://doi.org/10.1016/j.microc.2020.105237
22. Srijita Nundy, Aritra Ghosh, and Tapas K. Mallick, *ACS Omega*, **5**, No. 2: 1033 (2020); https://doi.org/10.1021/acsomega.9b02758
23. David Raymand, Adri C. T. van Duin, Daniel Spångberg, William A. Goddard III, and Kersti Hermansson, *Surface Science*, **604**, Nos. 9–10: 741 (2010). https://doi.org/10.1016/j.susc.2009.12.012
24. Gang Wang, Baibiao Huang, Zhujie Li, Zaizhu Lou, Zeyan Wang, Ying Dai, and Myung-Hwan Whangbo, *Scientific Reports*, **5**: 8544 (2015); doi:10.1038/srep08544
25. Afaq Ullah Khan, Kamran Tahir, Karma Albalawi, Mona Y. Khalil, Zainab M. Almarhoon, Magdi E. A. Zaki, Salman Latif, Hassan M. A. Hassan, Moamen S. Refat, and Alaa M. Munshi, *Materials Chemistry and Physics*, **291**: 126667 (2022); https://doi.org/10.1016/j.matchemphys.2022.126667
26. Dejan Zagorac, Jelena Zagorac, Milan Pejić, Branko Matović, and Johann Christian Schön, *Nanomaterials*, **12**: 1595 (2022); https://doi.org/10.3390/nano12091595
27. Nicolas Perciani de Moraes, Lucca Gabriel Penida Marins, Marcelo Yuji de Moura Yamanaka, Rebeca Bacani, Robson da Silva Rocha, and Liana Alvares Rodrigues, *J. Photochem. Photobiol. A Chem.*, **418**: 113377 (2021); https://doi.org/10.1016/j.jphotochem.2021.113377
28. Asset Bolatov, Alida Manjovelo, Bilel Chouchene, Lavinia Balan, Thomas Gries, Ghouti Medjahdi, Bolat Uralbekov, and Raphaël Schneider, *Materials*, **17**: 4877 (2024); https://doi.org/10.3390/ma17194877
29. Zhifang Dong, Yan Wu, Natarajan Thirugnanam, and Gonglin Li, *Appl. Surf. Sci.*, **430**: 293 (2018); https://doi.org/10.1016/j.apsusc.2017.07.186
30. P. E. Blöchl, *Phys. Rev. B*, **50**: 17953 (1994); https://doi.org/10.1103/PhysRevB.50.17953
31. J. P. Perdew, K. Burke, and M. Ernzerhof, *Phys. Rev. Lett.*, **77**: 3865 (1996); https://doi.org/10.1103/PhysRevLett.77.3865
32. Paul Ziesche, Stefan Kurth, and John P. Perdew, *Comput. Mater. Sci.*, **11**:

122 (1998); https://doi.org/10.1016/S0927-0256(97)00206-1
33. Marco Arrigoni and Georg K. H. Madsen, *Comput. Mater. Sci.*, 156: 354 (2019); https://doi.org/10.1016/j.commatsci.2018.10.005
34. P. Hohenberg and W. Kohn, *Phys. Rev. B*, 136: B864 (1964); https://doi.org/10.1103/PhysRev.136.B864
35. W. Kohn and L. J. Sham, *Phys. Rev.*, **140**: A1133 (1965); https://doi.org/10.1103/PhysRev.140.A1133
36. Axel D. Becke, *J. Chem. Phys.*, **98**: 5648 (1993); https://doi.org/10.1063/1.464913
37. Chengteh Lee, Weitao Yang, and Robert G. Parr, *Phys Rev B*, **37**: 785 (1988); https://doi.org/10.1103/PhysRevB.37.785
38. K. Kim and K. D. Jordan, *J. Phys. Chem.*, **98**, No. 40: 10089 (1994); https://doi.org/10.1021/j100091a024
39. P. J. Stephens, F. J. Devlin, C. F. Chabalowski, and M. J. Frisch, *J. Phys. Chem.*, **98**, No. 45: 11623 (1994); https://doi.org/10.1021/j100096a001
40. C. J. Cramer, *Essentials of Computational Chemistry: Theories and Models* (Wiley: 2004).
41. Fatemeh Mollaamin and Majid Monajjemi, *Int. J. Quantum Chem.*, **124**: e27348 (2024); https://doi.org/10.1002/qua.27348
42. Fatemeh Mollaamin and Majid Monajjemi, *Molecular Simulation*, **49**, 4: 365 (2023); https://doi.org/10.1080/08927022.2022.2159996
43. S. H. Vosko, L. Wilk, and M. Nusair, *Can. J. Phys.*, **58**, No. 8: 1200 (1980); https://doi.org/10.1139/p80-159
44. M. J. Frisch, G. W. Trucks, H. B. Schlegel, G. E. Scuseria, M. A. Robb et al., *Gaussian 16, Revision C.01* (Wallingford CT: Gaussian, Inc.: 2016).
45. R. Dennington, T. A. Keith, and J. M. Millam, *GaussView 6.0.16* (Semichem Inc.: 2016).
46. Zihan Xu, Chenglong Qin, Yushu Yu, Gang Jiang, and Liang Zhao, *AIP Advances*, **14**: 055114 (2024); https://doi.org/10.1063/5.0208082
47. A. D. Becke and K. E. Edgecombe, *J. Chem. Phys.*, 9: 5397 (1990); https://doi.org/10.1063/1.458517
48. H. L. Schmider and A. D. Becke, *Journal of Molecular Structure: THEOCHEM.*, **527**, Nos. 1–3: 51 (2000); https://doi.org/10.1016/S0166-1280(00)00477-2
49. A. D. Becke and K. E. Edgecombe, *J. Chem. Phys.*, **9**: 5397 (1990); https://doi.org/10.1063/1.458517
50. V. Tsirelson and A. Stash, *Acta Cryst.*, **B58**: 780 (2002); https://doi.org/10.1107/S0108768102012338
51. I. Mayer, *Chemical Physics Letters*, **544**: 83 (2012); https://doi.org/10.1016/j.cplett.2012.07.003
52. F. Mollaamin, M. T. Baei, M. Monajjemi, R. Zhiani, and B. Honarparvar, *Russ. J. Phys. Chem.*, **82**, 2354 (2008); https://doi.org/10.1134/S0036024408130323
53. Tian Lu and Feiwu Chen, *J. Phys. Chem. A*, **117**: No. 14: 3100 (2013); https://doi.org/10.1021/jp4010345
54. Xiyi Wang, Xuefeng Zhang, Witold Pedrycz, Shuang-Hua Yang, and Driss Boutat, *Fractal Fract.*, **8**: 523 (2024); https://doi.org/10.3390/fractalfract8090523

Наносистеми, наноматеріали, нанотехнології
Nanosistemi, Nanomateriali, Nanotehnologii
2025, т. 23, № 2, сс. 467–476
https://doi.org/10.15407/nnn.23.02.0467

© 2025 ІМФ (Інститут металофізики
ім. Г. В. Курдюмова НАН України)
Надруковано в Україні.

PACS numbers: 71.20.Tx, 73.20.Hb, 73.22.-f, 78.20.Bh, 78.66.Tr, 78.67.Sc, 81.05.ub

Електронні властивості нанокомпозитів сквараїнових барвників з одно- та багатостінними вуглецевими нанотрубками: спектроскопія та моделювання

А. М. Гапонов[1], В. С. Максимук[1], О. Л. Павленко[1], О. П. Дмитренко[1], М. П. Куліш[1], А. І. Момот[1], А. П. Науменко[1], Б. О. Ботвиновський[1], П. О. Теселько[2], О. Д. Качковський[3]

[1]*Київський національний університет імені Тараса Шевченка, вул. Володимирська, 60, 01033 Київ, Україна*
[2]*Інститут хімії високомолекулярних сполук НАН України, Харківське шосе, 48, 02160 Київ, Україна*
[3]*Інститут біоорганічної та нафтохімії імені В. П. Кухаря НАН України, вул. Мурманська, 1, 02094 Київ, Україна*

Розглядаються оптичні властивості плівок нанокомпозитів на основі барвників з одно- та багатостінними вуглецевими нанотрубками. Показано, що в залежності від типу нанотрубок має місце трансформація спектрів вбирання порівняно зі спектрами плівки барвників на підкладинках кварцу. На прикладі комплексів фуллеренів C_{70} зі сквараїновими барвниками показано можливість зміни спектрів вбирання залежно від діяметра вуглецевої структури.

The optical properties of nanocomposite films based on dyes with single- and multiwalled nanotubes are considered. As shown, depending on the type of nanotubes, there is a transformation of the absorption spectra compared to the spectra of the dye films on quartz substrates. Model of the complexes based on C_{70} fullerene with squaraine dyes is used to demonstrate the possibility of dependence of the absorption spectra on the diameter of the carbon structure.

Ключові слова: одностінні вуглецеві нанотрубки, багатостінні вуглецеві нанотрубки, фуллерени C_{70}, сквараїнові барвники, плівки, оптична спектроскопія, квантово-хемічні розрахунки.

Key words: single-walled carbon nanotubes, multiwalled carbon nanotubes, C_{70} fullerenes, squaraine dyes, films, optical spectroscopy, quantum-

chemical calculations.

(Отримано 20 жовтня 2024 р.; після доопрацювання — 14 березня 2025 р.)

1. ВСТУП

Комплекси вуглецевих наноструктур (вуглецеві нанотрубки, графен, фуллерени) із сенсибілізаторами-барвниками знаходять все ширші області практичного застосування. Так, вуглецеві наноструктури з барвниками використовуються у створенні хемічних і біологічних сенсорів, зокрема для виявлення токсичних речовин, біомолекул, а також у діягностиці для створення флюоресцентних біомаркерів і контрастних аґентів для візуалізації [1, 2]. Вуглецеві наноструктури в поєднанні з барвниками слугують для створення фотодіод, сонячних елементів завдяки їхній здатності до ефективного вбирання та випромінювання світла. Зокрема, перспективними є розробки систем нанотрубок з барвниками для одночасної фототермічної та фотодинамічної терапії пухлинних захворювань [3]. Нанотрубки під час вбирання енергії електромагнетних хвиль близького інфрачервоного діяпазону можуть перетворювати її у теплову, таким чином приводячи до фототермічного ефекту. Водночас, барвник-фотосенсибілізатор, що знаходиться у комплексі з нанотрубкою, за вбирання випромінення в області фототерапевтичного вікна (600–1200 нм) може ґенерувати синґлетний Оксиґен, що дає змогу цілеспрямовано руйнувати клітини перероджених тканин.

Багато досліджень було присвячено вивченню ефективних характеристик комплексів нанотрубок з барвниками, однак механізми їхньої взаємодії залишаються не до кінця визначеними. Серед таких, як саме, впливає тип нанотрубок, їхній радіюс на властивості самого барвника. Адже відомо, що нерівномірність розподілу заряду на молекулах барвників сприяє процесам аґреґації цих молекул [4]; більше того, впливає як тип підкладинки, поверхня, так і температурні режими осадження [5].

У даній роботі розглянуто зміни спектральних властивостей барвників, осаджених на одно- та багатостінні вуглецеві нанотрубки, які мають різний діяметер, у порівнянні із їхніми спектрами на кварцовій підкладинці та здійснено квантово-хемічні розрахунки взаємодії скваранових барвників із вуглецевими структурами, що мають різну кривину π-спряженої поверхні.

2. МЕТОДИКА ЕКСПЕРИМЕНТУ ТА МОДЕЛЮВАННЯ

Для вивчення спектральних особливостей барвників за нанесення

їх на вуглецеві нанотрубки було обрано водорозчинні, функціоналізовані октадециламіном одностінні вуглецеві нанотрубки діяметром від 2 до 10 нм і довжиною від 0,5 до 2 мкм. Діяметер багатостінних вуглецевих нанотрубок був більшим. Обидва види нанотрубок були спочатку піддані ультразвуковому дисперґуванню у водному розчині. Електронно-мікроскопічні зображення одержаних плівок наведено на рис. 1 у випадку одностінних (ліворуч) і багатостінних нанотрубок (праворуч) — ОСВНТ і БСВНТ відповідно. Видно, що має місце формування субмоношарових плівок. Оскільки багатостінні нанотрубки не були функціоналізованими для розчинення у воді, ступінь їхнього ультразвукового дисперґування сприяв формуванню більш товстих плівок у порівнянні із випадком одностінних нанотрубок.

Під час дисперґування у розчини з нанотрубками було додано скваріновi барвники, розчинені у хлороформі. Концентрації барвників були підібрані таким чином, щоб вже у початковому розчині хлороформу уникнути аґреґації цих молекул, що контролювалося спектроскопією вбирання. Нанесення зразків на кварцові підкладинки відбувалося шляхом занурення останніх у розчини одностінних нанотрубок із барвниками та розчини багатостінних нанотрубок з барвниками (метод Ленґмюра–Блоджетт [6]). Зразки плівок висихали за кімнатної температури.

Для пояснення механізмів взаємодії барвників із нанотрубками було проведено квантово-хемічні розрахунки для модельних випадків зі скваріновим барвником і вуглецевими наноструктура-

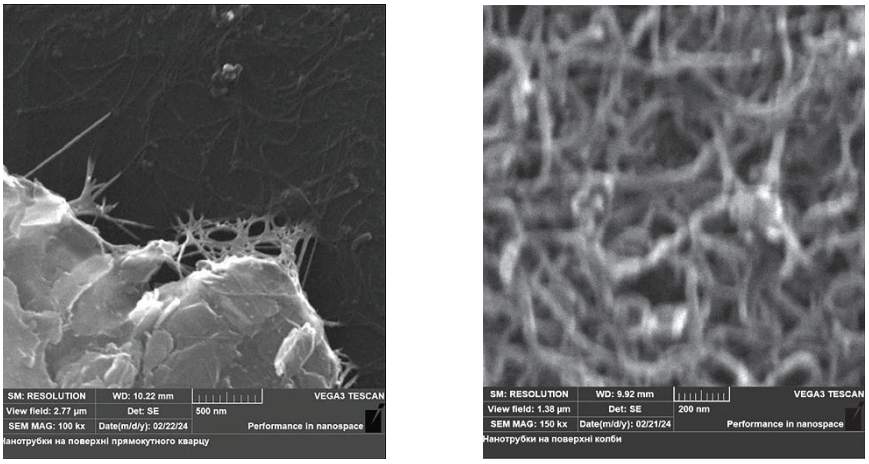

а *б*

Рис. 1. Електронно-мікроскопічне зображення плівок одностінних вуглецевих нанотрубок (*а* — верхня частина зображення) та багатостінних (*б*) вуглецевих нанотрубок.[1]

ми. Для розрахунків будови, розподілу зарядів і електронної структури використовували напівемпіричне наближення AM1 у програмному пакеті Gaussian 09 [7], для розрахунку електронних переходів — метод ZINDO. Розглянемо, чи може впливати кривина вуглецевої наноструктури на оптичні властивості барвників. Оскільки діяметер навіть одностінної нанотрубки перевищує 2 нм, а задавання моделів нанотрубок з більшими діяметрами вимагає окремих підходів, розглянемо як найпростіший модель фуллерена C_{70} як структуру, що має два різні діяметри за рахунок своєї еліпсоїдальної форми: більший діяметер, який складає близько 0,9 нм, та короткий — 0,83 нм [8]. Для комплексів барвник–C_{70} розташуємо барвник для випадків, коли сквараїн знаходиться біля більшого та меншого діяметрів молекули фуллерена C_{70}. Незважаючи на те, що діяметри розглядуваних нанотрубок значно перевищують діяметри молекули C_{70}, даний модель покликаний для розгляду впливу кривини поверхні вуглецевих наноструктур, яка відповідає за густину їхніх електронних станів, на спектральні властивості барвників. До розгляду додамо також графенову площину з даним скваraїновим барвником.

3. РЕЗУЛЬТАТИ Й ОБГОВОРЕННЯ

Як видно з рисунка 2, спектри вбирання скваraїнового барвника,

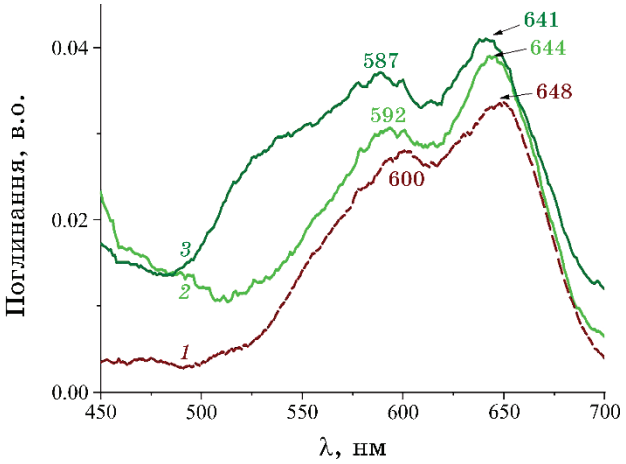

Рис. 2. Нормалізовані спектри вбирання для плівок: *1* — чистий барвник, нанесений на кварцову підкладинку методом спін-коатінґу з хлороформного розчину; *2* — нанокомпозит барвників з ОСВНТ, нанесений на кварцову підкладинку методом Ленґмюра–Блоджетт; *3* — нанокомпозит барвників з БСВНТ, нанесений на кварцову підкладинку також методом Ленґмюра–Блоджетт.[2]

нанесеного на підкладинку із розчину хлороформу методом спінкоатінґу має 2 широкі піки при 648 і 600 нм. Головний пік, що відповідає за π–π-переходи, які роблять головний внесок у спектер вбирання розчинів мономерних барвників, і розташований при 634 нм [9, 10] у випадку плівки зсувається в область більших довжин хвиль на 14 нм, що вказує на *J*-аґреґацію барвників. Більше того, пік істотно розширяється, а пік, який для розчинів мономерів ледь помітний, для плівки зростає за інтенсивністю та також розширяється, маючи максимум при 600 нм.

З додаванням даних барвників до розчину з нанотрубками, нанесенням даних розчинів на підкладинки та випаровуванням розчинників спектер вбирання дещо змінюється; так, довгохвильова смуга зсувається у бік менших довжин хвиль на 4 нм, а короткохвильове плече — на 2 нм. Водночас, інтенсивності обох піків також змінюються: для барвників, що взаємодіють з ОСВНТ, відбувається відносне зростання довгохвильової компоненти вбирання. У випадку багатостінних нанотрубок піки майже зрівнюються за інтенсивністю, причому має місце виникнення додаткового плеча в області 500–550 нм, піки барвників на багатостінних нанотрубках зміщуються на 3–5 нм порівняно зі спектрами барвників у плівці з одностінними вуглецевими нанотрубками.

Очевидно, що процеси *J*- та *H*-аґреґації, які характерні для даних барвників у плівках, визначають різні чинники, такі як тип підкладинок, рельєф поверхні, що впливають на спектри.

Спробуємо оцінити за допомогою квантово-хемічних розрахунків роль впливу вигнутости вуглецевих площин на спектри барвників. На рисунку 3 зображено моделі фуллеренів C_{70}, біля яких розташовано скваражнові барвники, а саме, біля більшого та меншого за діяметром фуллерена, а також комплекс даного барвника з графеновою площиною.

Розрахунки вказують, що в результаті оптимізації комплексу з фуллереном молекула скваражнового барвника розташовується на віддалі у 3,48 Å (для випадку, коли барвник паралельний до меншого діяметра C_{70}, — *L*-локалізація); водночас, скваражнове кільце знаходиться паралельно над п'ятикутником у боковій частині фуллерена C_{70}. У іншому випадку віддаль є більшою і складає 3,58 Å; водночас, скваражнове кільце знаходиться над атомом Карбону, який є вершиною трьох шестикутників. Також спостерігається незначне вигинання площини барвника відносно його початкового стану.

Щодо розподілу заряду, то, згідно з розрахунками, окрема молекула фуллерена C_{70} має 30 атомів Карбону з неґативними значеннями зарядів, а 40 атомів позитивно заряджені. У комплексі зі скваражновим барвником, який містить два електроно-донорні атоми Оксиґену, кількість неґативно заряджених атомів збіль-

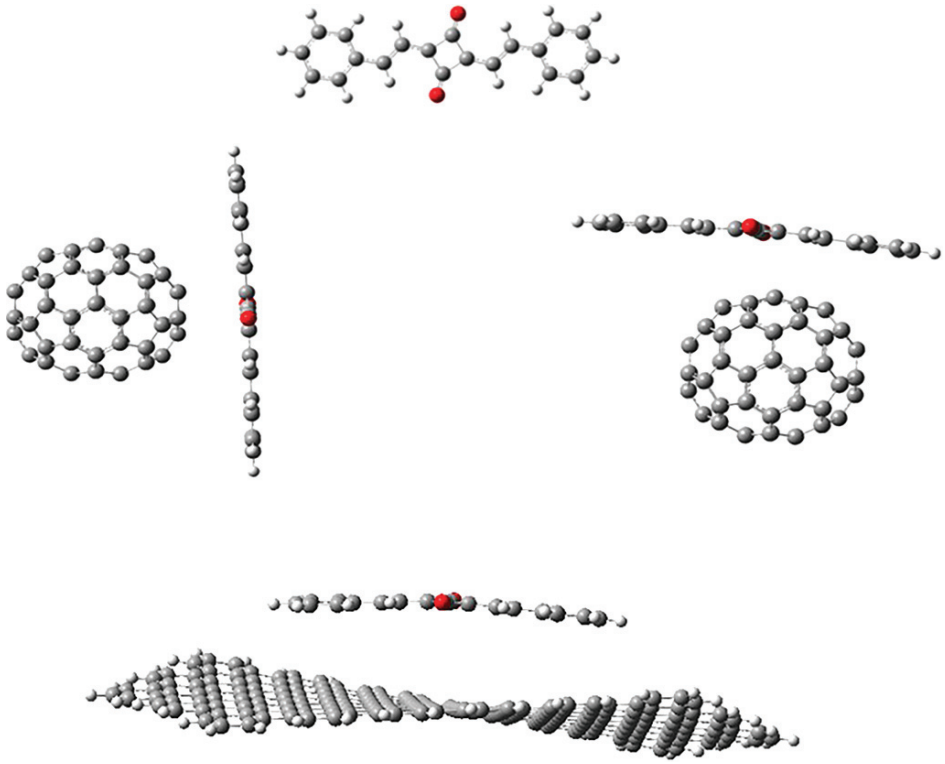

Рис. 3. Оптимізована геометрія скваранового барвника (вгорі), комплексів фуллеренів C_{70} зі скваранновими барвниками у випадку локалізації останніх вздовж меншого (*L*-локалізація, ліворуч) і більшого (*S*-локалізація, праворуч) діяметрів фуллерена C_{70}; оптимізована геометрія скваранового барвника з графеновою площиною (внизу).[3]

шується до 31 для випадку *L*-локалізації, причому додатковий неґативно заряджений атом локалізований у п'ятичленному кільці фуллерена C_{70}, що знаходиться найближче до скваранового фраґмента барвника. У випадку *S* кількість позитивно та неґативно заряджених атомів залишається постійною, як у незалежному фуллерені C_{70}, проте відбувається перерозподіл заряду, що зображено на рис. 4.

Щодо молекули барвника, то її хромофор зазнає істотних змін у розподілі зарядів (рис. 4, *б*). Електроно-донорні атоми Оксиґену, які до взаємодії мали значення неґативного заряду у –0.542 е.о., частково втратили його та набули значення у –0.484 е.о. В межах кінцевих груп, — фенольних кілець, — відбулось альтернування зарядів, на відміну від вихідного стану, де всі Карбонові атоми мали однакові значення величин зарядів. Зміни величин зарядів однакові в обох випадках розташування барвника віднос-

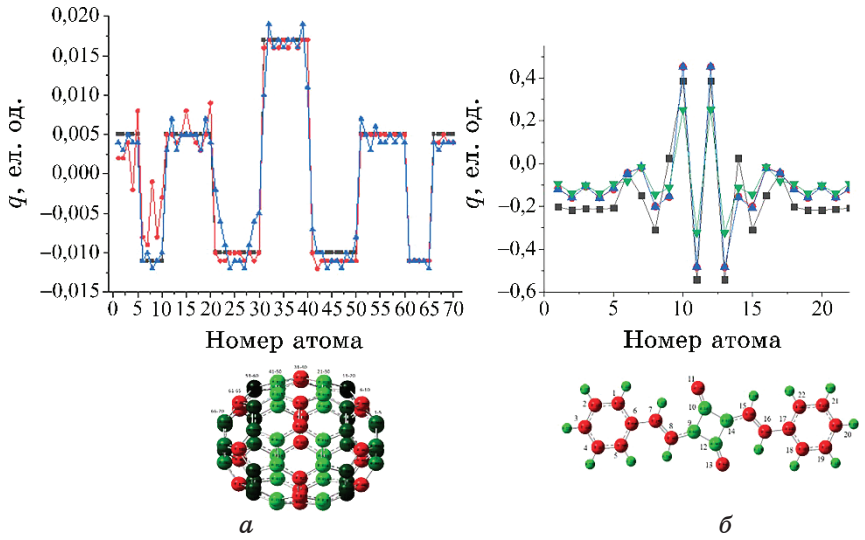

Рис. 4. *а* — розподіл заряду у Карбонових атомів молекули фуллерена C_{70} (чорні квадрати) та на них же у комплексах C_{70} зі скваріновими барвниками: кільця — у випадку *L*-локалізації, трикутники — у випадку *S*-локалізації. *б* — розподіл заряду у Карбонових атомів молекули барвника (чорні квадрати) та них же у комплексах з фуллереном: кільця — у випадку *L*-локалізації, трикутники «вгору» — у випадку *S*-локалізації, трикутники «вниз» — для випадку з графеновою площиною. Нумерацію атомів наведено під графіками.[4]

но фуллерена C_{70}. За взаємодії з графеновою площиною кінцеві групи барвника ведуть себе подібно до випадків з фуллереном, а атоми Оксиґену та сусідні до них атоми втрачають значення зарядів ще більше.

Розглянемо, як впливає зміна розподілу заряду комплексів фуллерена C_{70} із скваріновими барвниками на їхню електронну структуру. Згідно з розрахунками, для комплексів скваріновогo барвника та фуллерена C_{70} має місце пониження HOMO-рівня відносно рівнів окремого барвника в обох випадках розташування. При цьому рівень LUMO для обох варіянтів комплексів локалізований на фуллерені (рис. 5), опускаючись відносно значення LUMO окремого фуллерена.

В цілому щілина комплексів звужується в обох випадках локалізацій барвника відносно рівнів окремого барвника, що корелює з результатами, одержаними в [11]. Проте за розташування барвника паралельно до меншого радіюса має місце більший зсув піку вбирання у червону область, в той час як його розташування паралельно до більшого радіюса дає менший зсув. Тобто барвник, знаходячись біля вуглецевої наноструктури з більшим радіюсом,

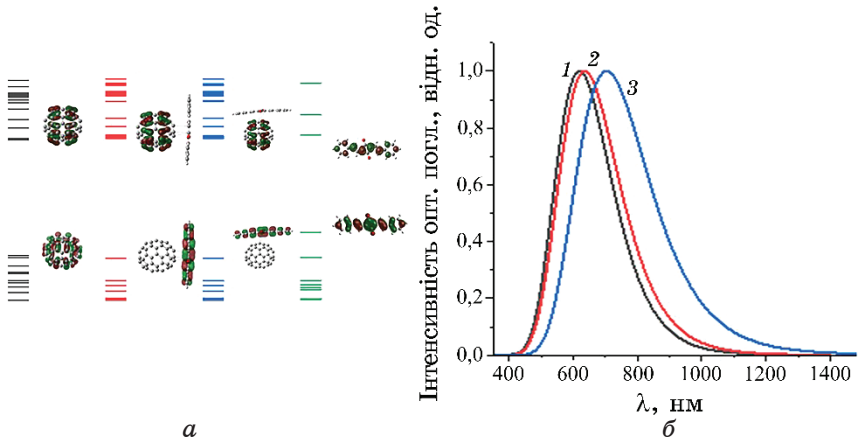

Рис. 5. *а* — форми молекулярних орбіталей в області енергетичної щілини молекули фуллерена C_{70}, скваріїнового барвника та для їхніх комплексів. *б* — розраховані спектри вбирання скваріїнового барвника (*1*) та його комплексів з фуллереном C_{70} для *L*-локалізації (*2*) та *S*-локалізації (*3*).[5]

буде зміщувати пік вбирання менше у порівнянні з випадком, коли вуглецева наноструктура більш вигнута.

Оптимізація досліджуваної системи барвник–графенова площина вказує, що барвник також зазнає змін, що проявляється, окрім розподілу заряду, на електронній структурі, адже величина енергетичної щілини істотно звужується у порівнянні зі щілиною комплексів з фуллереном C_{70}, розмір якої, згідно з розрахунками, складає 3,3 еВ або 376 нм, що може приводити до зсуву максимуму спектрів вбирання в короткохвильову область. Тому моделювання барвника з площиною потребує більш детальних досліджень.

Одержані результати вказують, що радіюс вуглецевої наноструктури впливає на спектри барвника, та це має бути предметом подальших досліджень.

4. ВИСНОВКИ

За взаємодії скваріїнових барвників з нанотрубками різного діяметра, що реалізується шляхом осадження їх з розчинів за методом Ленґмюра–Блоджетт, має місце трансформація максимумів вбирання композитних плівок відносно спектрів вбирання плівки барвників. З формуванням комплексів фуллеренів C_{70}, що мають більший і менший діяметри, а також графенової площини зі скваріїновими барвниками, що містять 2 електроно-донорні ато-

ми Оксиґену, відбувається перерозподіл заряду на хромофорах барвників і молекулах фуллеренів. Такий перерозподіл заряду приводить до змін геометрії барвників і пониження симетрії молекули C_{70}, що супроводжується зміщеннями електронних рівнів C_{70}. А зміни енергетичної щілини мають місце для кожного з випадків комплексів скваraїнового барвника з вуглецевими наночастинками.

ЦИТОВАНА ЛІТЕРАТУРА–REFERENCES

1. Mohd Nurazzi Norizan, Muhammad Harussani Moklis, Siti Zulaikha Ngah Demon, Norhana Abdul Halim, Alinda Samsuri, Imran Syakir Mohamad, Victor Feizal Knight, and Norli Abdullah, *RSC Adv.*, **10**, No. 71: 43704 (2020); https://doi.org/10.1039/D0RA09438B
2. Olushola Sunday Ayanda, Augusta Oluchi Mmuoegbulam, Onyemaechi Okezie, Naseer Inuwa Durumin Iya, Sa'adatu Eri Mohammed, Philip Hegarty James, Abba Bashir Muhammad, Augustine Agorye Unimke, Sabur Ajibola Alim, Sharhabil Musa Yahaya, Ayomipo Ojo, Toyin Olanike Adaramoye, Stella Kemilola Ekundayo, Aminu Abdullahi and Hamza Badamasi, *J. Nanoparticle Res.*, **26**, No. 5: 1 (2024); https://doi.org/10.1007/s11051-024-06006-2
3. Mohammed Faiad Naief, Samar Naser Mohammed, Hadil Jubair Mayouf, and Ahmed Mishaal Mohammed, *J. Organometallic Chem.*, **999**, No. 10: 122819 (2023); https://doi.org/10.1016/j.jorganchem.2023.122819
4. *J-Aggregates* (Ed. T. Kobayashi) (World Scientific: 2012), vol. **2**.
5. V. M. Bordyuh, O. B. Melnichuk, and A. M. Buryachkovsky, *Semiconductor Physics, Quantum Electronics & Optoelectronics*, **16**, No. 1: 91 (2013).
6. X. Li, L. Zhang, X. Wang, I. Shimoyama, X. Sun, W. S. Seo, and H. Dai, *J. Am. Chem. Soc.*, **129**, No. 16: 4890 (2007); https://doi.org/10.1021/ja0713041
7. M. J. Frisch, G. W. Trucks, H. B. Schlegel, G. E. Scuseria, M. A. Robb, J. R. Cheeseman, G. Scalmani, V. Barone, G. A. Petersson, H. Nakatsuji, X. Li, M. Caricato, A. Marenich, J. Bloino, B. G. Janesko, R. Gomperts, B. Mennucci, H. P. Hratchian, J. V. Ortiz, A. F. Izmaylov, J. L. Sonnenberg, D. Williams-Young, F. Ding, F. Lipparini, F. Egidi, J. Goings, B. Peng, A. Petrone, T. Henderson, D. Ranasinghe, V. G. Zakrzewski, J. Gao, N. Rega, G. Zheng, W. Liang, M. Hada, M. Ehara, K. Toyota, R. Fukuda, J. Hasegawa, M. Ishida, T. Nakajima, Y. Honda, O. Kitao, H. Nakai, T. Vreven, K. Throssell, J. A. Montgomery, Jr., J. E. Peralta, F. Ogliaro, M. Bearpark, J. J. Heyd, E. Brothers, K. N. Kudin, V. N. Staroverov, T. Keith, R. Kobayashi, J. Normand, K. Raghavachari, A. Rendell, J. C. Burant, S. S. Iyengar, J. Tomasi, M. Cossi, J. M. Millam, M. Klene, C. Adamo, R. Cammi, J. W. Ochterski, R. L. Martin, K. Morokuma, O. Farkas, J. B. Foresman, and D. J. Fox, *Gaussian 09, Revision A.02* (Wallingford CT: Gaussian, Inc.: 2016).
8. Lilia M. Baldauf, Kamran B. Ghiassi, Marilyn M. Olmstead, and Alan L. Balch, *Nanoscale*, **12**, No. 39: 20356 (2020); https://doi.org/10.1039/D0NR05824F
9. O. L. Pavlenko, V. A. Brusentsov, O. P. Dmytrenko, M. M. Sieryk,

V. A. Sendiuk, M. P. Kulish, and O. D. Kachkovskyi, *Nanosistemi, Nanomateriali, Nanotehnologii*, **15**, Iss. 4: 589 (2017); https://doi.org/10.15407/nnn.15.04.0589

10. A. M. Gaponov, O. L. Pavlenko, O. P. Dmytrenko, M. P. Kulish, T. M. Pinchuk-Rugal, T. O. Busko, and O. D. Kachkovsky, *International Conference 'Nanotechnology and Nanomaterials'* (Ukraine: 2022), p. 339–354; https://doi.org/10.1007/978-3-031-14543-4_24
11. O. Pavlenko, O. Dmytrenko, M. Kulish, A. Gaponov, N. Obernikhina, O. Kachkovsky, and L. Bulavin, *Ukrainian Journal of Physics*, **65**, No. 9: 741 (2020); https://doi.org/10.15407/ujpe65.9.741

[1]*Taras Shevchenko National University of Kyiv,*
60, Volodymyrs'ka, Str.,
UA-01033 Kyiv, Ukraine
[2]*Institute of Macromolecular Chemistry, N.A.S. of Ukraine,*
48, Kharkivs'ke Highway,
UA-02160 Kyiv, Ukraine
[3]*V. P. Kukhar Institute of Bioorganic Chemistry and Petrochemistry, N.A.S. of Ukraine,*
1, Murmans'ka Str.,
UA-02094 Kyiv, Ukraine

[1] **Fig. 1.** Electron microscopic images of films of single-walled carbon nanotubes (*а*—top part of the image) and multi-walled carbon nanotubes (*б*).

[2] **Fig. 2.** Normalized absorption spectra for films: *1*—film of pure dye deposited onto a quartz substrate by spin coating from a chloroform solution; *2*—nanocomposite of dye with SWCNT deposited onto a quartz substrate using the Langmuir–Blodgett method; *3*—dye nanocomposite with MWCNT deposited onto a quartz substrate also using the Langmuir–Blodgett method.

[3] **Fig. 3.** Optimized geometry of squaraine dye (top), fullerene C_{70} complexes with squaraine dyes in cases where the dyes are localized along the smaller diameter (*L*-localization, left) and larger diameter (*S*-localization, right) of fullerene C_{70}; optimized geometry of the squaraine dye with a graphene plane (bottom).

[4] **Fig. 4.** *а*—Charge distribution on the carbon atoms of fullerene C_{70} molecule (black squares) and on it in the complexes with squaraine dyes: circles—*L*-localization, triangles—*S*-localization. *б*—Charge distribution in carbon atoms of the dye molecule (black squares) and in complexes with fullerene: circles correspond to *L*-localization, upward triangles correspond to *S*-localization, downward triangles correspond to the case with a graphene plane. The atom numbering is shown under the graphs.

[5] **Fig. 5.** *а*—Forms of molecular orbitals in the energy gap region for fullerene C_{70}, squaraine dye, and their complexes. *б*—Calculated absorption spectra of squaraine dye (*1*) and its complexes with fullerene C_{70} for *L*-localization (*2*) and *S*-localization (*3*).

Наносистеми, наноматеріали, нанотехнології
Nanosistemi, Nanomateriali, Nanotehnologii
2025, т. 23, № 2, сс. 477–487
https://doi.org/10.15407/nnn.23.02.0477

© 2025 ІМФ (Інститут металофізики
ім. Г. В. Курдюмова НАН України)
Надруковано в Україні.

PACS numbers: 61.80.Ed, 61.80.Fe, 61.80.Hg, 61.80.Jh, 61.82.Rx, 65.80.Ck, 81.05.ue

The Impact of γ, Neutron, Ion, and Electron Irradiation on the Structure and Properties of Graphene

Roman Biliak

Lviv Polytechnic National University,
12, Stepan Bandera Str.,
UA-79013 Lviv, Ukraine

The development of nuclear energy and space industry imposes new requirements on materials and devices based on them. One such requirement is the resistance of materials to radioactive radiation. Therefore, the study of the impact of radiation on the structure and properties of graphene is a key stage in the research of this 'two-dimensional' material. This article examines the influence of γ-radiation, neutron, electron, and ion irradiation on graphene and devices based on it. All types of radiation induce defects in graphene proportionally to the intensity, exposure time, and particles' energy. Studies have shown that devices based on graphene remain functional during irradiation; and further heating and annealing can set off the effect of defects, restoring the characteristics to their initial values. This unique property demonstrates graphene ability to self-heal defects caused by irradiation.

Розвиток термоядерної енергетики та космічної індустрії ставить нові вимоги до матеріялів і приладів, які на них ґрунтуються. Однією з таких вимог є стійкість матеріялів до радіоактивного випромінення. Тому вивчення впливу випромінення на структуру та властивості графену є ключовим етапом у дослідженні цього «двовимірного» матеріялу. У цій статті розглядається вплив γ-випромінення, нейтронного, електронного та йонного опромінювання на графен і прилади, засновані на ньому. Усі види опромінення спричиняють дефекти у графені пропорційно інтенсивності, часу експозиції та енергії частинок. Дослідження показали, що пристрої, засновані на графені, залишаються працездатними під час опромінення, а подальше нагрівання та відпал можуть компенсувати дефекти, повертаючи характеристики до початкових значень. Ця унікальна властивість свідчить про здатність графену самозаліковувати дефекти, що виникли внаслідок опромінення.

Key words: graphene, γ-radiation, neutron irradiation, electron irradiation, ion irradiation, self-healing effect, nuclear fusion.

Ключові слова: графен, γ-випромінення, нейтронне опромінення, електронне опромінення, йонне опромінення, ефект самозаліковування, термоядерна синтеза.

(Received 19 December, 2023; in revised form, 24 January, 2024)

1. INTRODUCTION

As of today, graphene is one of the most actively researched materials worldwide [1]. The interest in this material is driven by its unique properties and two-dimensional structure [2, 3]. One key research direction for graphene is the study of the impact of irradiation on its structure and properties [4]. This issue is particularly relevant due to plans for using graphene-based devices and materials in nuclear reactors, the space industry, and other fields, where the level of radiation exposure is significant, and conventional semiconductor devices cannot withstand such conditions [5–7]. Based on literature sources on the graphene structure, it can be concluded that it interacts weakly with radioactive radiation [8–10].

Thermonuclear fusion requires the use of new materials and sensors for accurate measurement of the magnetic field and plasma control in the reactor, especially in the DEMO reactor. Considering the high neutron flux [11] and temperature conditions that can reach 350°C during the reaction [12], traditional Hall sensors may not cope with this task. For this reason, graphene-based sensors [11] are considered one of the possible alternatives.

Recently, SpaceX successfully launched the 'Fourth Transporter' mission [13], which, in addition to commercial purposes, also included scientific research. Students from the Netherlands and Chile developed devices incorporating graphene elements to study the effects of space travel and space conditions on graphene components. Graphene elements will undergo a series of tests to check their performance and resistance to extreme conditions of the space environment, such as vibrations, radiation, and temperature changes. The obtained data will be used to develop sensors and instruments for navigation and astronomical observations in space [13].

2. IMPACT OF γ-RADIATION

Studying the impact of γ-radiation on graphene and micro- and nanoelectronic devices based on it is crucial due to their potential applications in the space industry and nuclear energy. Ensuring the reliability and long-term operation of such equipment requires understanding how γ-radiation affects various components and devel-

oping devices and materials resistant to this type of radiation.

Y. Zhang and colleagues [14] investigated the influence of γ-radiation on graphene layers. Graphene oxide was first obtained using the improved Hummers method, and then, graphene oxide was exfoliated to obtain graphene oxide. Subsequently, graphene oxide was transformed into graphene using sodium citrate. The prepared graphene underwent heat treatment in a nitrogen atmosphere and was later irradiated with γ-rays from a Co^{60} source at a dose of 100 kGy with an accumulation rate of 2 kGy/h. Gamma irradiation resulted in a reduction in the distance between graphene layers, but it increased the size of the graphite crystal and the number of layers. The authors suggest that this increase was likely caused by cross-linking opened due to gamma irradiation [14].

Other researchers investigated the impact of γ-radiation on graphene-based devices. Xu and colleagues [15] studied the effects of γ-radiation on graphene/Si Schottky diodes. Co^{60} served as the radiation source, and the devices were irradiated without electrical bias. The devices were irradiated up to a dose of 10 kGy at a dose rate of 0.5 Gy/s. The research revealed an increase in reverse current after irradiation. γ-radiation disrupted C=C bonds in graphene and Si–O bonds in SiO_2. Photoelectron spectroscopy showed the formation of defects in the form of unpaired Si bonds. γ-irradiation of graphene/Si Schottky diodes led to the degradation of their electrical characteristics, including a reduction in the Schottky barrier height, resulting in a significant increase in reverse current [15].

Another team of scientists led by Xi [16] investigated the impact of γ-radiation on energy-independent memory using graphene nanodisks (Fig. 1). Co^{60} was also used as the radiation source, and it was found that irradiation caused electron loss through photoemission. Despite significant shifts in the graphene and surrounding oxide conduction zone, data retention after irradiation remained satisfactory. The researchers concluded that γ-radiation affects significantly devices in programmed states, but data retention after irradiation is acceptable, with devices exhibiting good data retention even after irradiation with a dose of 10 kGy [16].

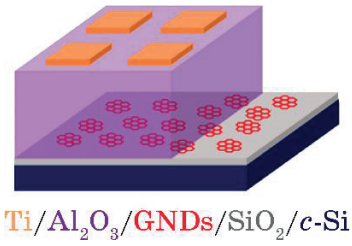

Fig. 1. Scheme of graphene nanodisk memory [16].

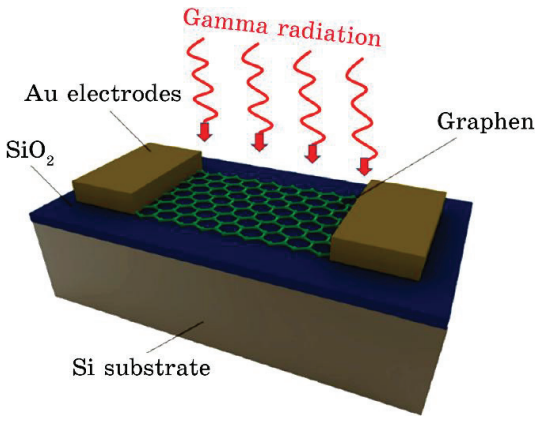

Fig. 2. Schematic representation of the graphene field-effect transistor (GFET) [17].

Similar results were obtained by a team of scientists from the Brookhaven National Laboratory [17] on Long Island, New York, USA. The team studied the impact of γ-quanta on the graphene field-effect transistor (GFET) schematic representation of the transistor shown in Fig. 2. Co^{60} served as the traditional radiation source, and the radiation dose was approximately of 1 kGy/h, similar to previous studies. The study found that transistors exhibit high sensitivity to this type of radiation. γ-radiation resulted in a decrease in electron mobility in graphene and a shift of the Dirac point towards positive *p*-doping.

Raman spectroscopy indicated an increase in the *D*-peak to *G*-peak intensity ratio after γ-irradiation, suggesting an increase in disorder in monolayer graphene [17].

As a result, it can be stated confidently that this type of irradiation affects the physical and electrical properties of graphene. The acquired defects degrade graphene properties, and this type of radiation influences the interactions between graphene and other substances within the device. It is noteworthy that, after such testing, all devices retained their functionality.

3. IMPACT OF NEUTRON IRRADIATION

It is crucial to understand the impact of neutron irradiation on graphene, as this material exhibits higher radiation resistance [18]. This characteristic makes it promising for use in various sensors in the space industry and, particularly, in nuclear energy, including future thermonuclear fusion reactors.

Eapen and colleagues [19] from the University of North Carolina

investigated the effects of neutron irradiation using the PULSTAR reactor with a flux of $2.8 \cdot 10^{-9}$ dpa/s. The irradiation was performed at $\cong 325$ K with an average fast neutron flux of $2 \cdot 10^{12}$ n/(cm^2·s). The Raman spectroscopy results showed an increase in the intensity of the *D*-peak after irradiation, indicating the formation of new defects in graphene. X-ray photoelectron spectroscopy (XPS) results indicated changes in the chemical structure of irradiated graphene samples [19]. Specifically, a high content of sp^3 bonds was noted, likely formed during heating and cooling. These sp^3 bonds may suggest the formation of new chemical bonds and defects in graphene.

In 2019, Bolshakova *et al.* [18] conducted the world's first study on the influence of neutron irradiation on Hall sensors based on monolayer graphene. The study was conducted *in-situ*, meaning information was collected from Hall sensors located in a magnetic field in the operating reactor. The neutron flux in the reactor was of $1.5 \cdot 10^{20}$ n/(m^2·s). Graphene for Hall sensors was grown using the CVD method on a copper foil, and the substrate was made of Al_2O_3. The experiment lasted for 48 hours. After irradiation, the sensitivity of the sensors remained unchanged, indicating that graphene-based sensors are resistant to neutron irradiation.

Another research team led by Semir El-Ahmar [6] also investigated the effects of neutron irradiation on Hall sensors based on graphene passivated with a 100-nm Al_2O_3 layer. They used hydrogen-intercalated graphene grown on a semi-insulating high-purity single-crystal 4*H*-SiC(0001) substrate by the CVD method. Irradiation was performed at the National Centre for Nuclear Research (NCBJ) using the MARIA research nuclear reactor. MARIA is a high-performance device for extracting nuclear energy with a thermal neutron flux up to $2.5 \cdot 10^{14}$ cm^{-2}·s^{-1} and fast neutrons up to $1.0 \cdot 10^{14}$ cm^{-2}·s^{-1}. The samples were irradiated with fast neutrons at a fluence of $\approx 6.6 \cdot 10^{17}$ cm^{-2} for an exposure time of 121 hours. Electrical measurements were taken before and after irradiation, and the temperature during irradiation did not exceed 300°C [6].

Raman spectroscopy revealed a characteristic defect *D*-peak, indicating that the neutron flux penetrates through the Al_2O_3 layer to graphene, creating defects. Hall effect measurements showed that the structure after a nuclear reaction retained the characteristics of graphene, which would not have been the case, if the sheet had undergone intensive chemical bonding with the substrate [6]. This indicates the stability of graphene to neutron irradiation. As a result of the study, scientists found that the defect density was seven orders of magnitude lower than the fluence, suggesting that graphene has a small cross-section for neutrons [6].

Neutron irradiation leads to structural changes in graphene, including the formation of defects and alterations in the chemical

structure. However, Hall sensors in two studies [6, 18] did not lose their functionality, demonstrating the resilience of graphene to neutron irradiation.

4. IMPACT OF ION IRRADIATION

The study of the impact of ion irradiation on graphene is essential, as this type of radiation can be used to create defects in graphene in the form of nanopores [20] and alter its properties. Ion irradiation is also a common technique in the production of semiconductor devices [21]. Ions can be either atoms with unpaired electrons or whole molecules with unpaired charges [22].

A research team led by Kichul Yoon [25] investigated the influence of ion irradiation on graphene using the Zeiss ORION NanoFab ion microscope, operating at a voltage of 25–27 kV and using the helium and neon gas atoms as ions for irradiating CVD-grown graphene. Researchers observed the formation of various types of defects, including single-atom vacancy defects (monovacancies) and Stone–Wales defects (STW).

Xu and the team [24] also studied the impact of low-energy (less than 50 eV) ion irradiation on graphene. Monolayer graphene samples were irradiated with various ions, including boron, nitrogen, and fluorine, with different energies and fluences. Analysis of the samples before and after irradiation was performed using X-ray photoelectron spectroscopy (XPS), X-ray spectroscopy, Raman spectroscopy, and scanning electron microscopy [24]. The research revealed that low-energy ion irradiation can be successfully used to dope graphene with other atoms, but it also introduces damage and defects into the graphene [24]. The level of damage depends on the type of ion and fluence. Boron irradiation caused the least damage among the three types of ions considered, as this atom is the lightest. Nitrogen and fluorine irradiation at high fluences led to significant changes in the structure and properties of graphene, including its transformation into amorphous carbon [24].

Vázquez and the team proposed using this type of irradiation for graphene modification, specifically for creating nanopores, which could further be applied in filtration and sensing devices [21].

Ion irradiation causes serious damage to the two-dimensional structure of graphene, a conclusion supported by other researchers as well [23–26].

5. IMPACT OF ELECTRON IRRADIATION

Scanning electron microscopy and transmission electron microscopy

are crucial tools for studying micro and nanoscale objects, making the investigation of electron irradiation's effects on graphene important due to potential damage to the studied samples. Additionally, this type of radiation can be employed to control graphene properties, such as adding functional groups, altering electronic structure, or manufacturing graphene devices through electron beam lithography (EBL) [27].

I. Childres and colleagues [29] presented data on the impact of electron irradiation on the electrical transport properties of monolayer graphene and the performance of devices based on this material. The irradiation resulted in a decrease in charge carrier mobility in graphene and the appearance of the *D*-peak in Raman spectroscopy, indicating defects induced by irradiation [29].

Studying the impact of electron irradiation on graphene devices revealed two main effects: a reduction in the charge-neutral point (CNP) for substrate-supported graphene and a decrease in graphene mobility with the appearance of the *D*-peak in Raman spectroscopy, suggesting irradiation-induced defects [29].

Similar conclusions were drawn by other researchers, including Yangbo Zhou and colleagues [30], who investigated mechanically exfoliated graphene layers irradiated with electron beams ranging from 1 keV to 30 keV. Irradiation doses were controlled by the beam current (from 0 ± 1 pA at 2 keV to 130 ± 1 pA at 30 keV). The study revealed that electron irradiation can lead to changes in the electrical characteristics of graphene devices, such as increased resistance and reduced charge carrier mobility. The effects of irradiation depended on electron energy and dose, with high-energy electrons and large doses causing significant changes in graphene properties [30].

Electron irradiation can also have a positive impact on the operation of graphene-based devices. Hossain *et al.* [31] investigated the influence of electron irradiation on graphene and $1/f$ noise (flicker noise). The level of $1/f$ noise is an important indicator for assessing material suitability for practical devices in various fields. The authors demonstrated an interesting feature of $1/f$ noise in graphene: it decreases with an increase in the concentration of defects resulting from electron irradiation [31]. They found that bombarding graphene devices with 20 keV electrons can reduce the spectral noise density by an order of magnitude. The authors analyzed this noise reduction using mobility mechanisms and fluctuations in the number of charge carriers. The research results showed that electron irradiation introduces defects into graphene, confirmed by the appearance of disorder peaks in Raman spectroscopy. Interestingly, the noise level in graphene decreases after irradiation, contrary to the behaviour of traditional materials, where irradiation typically

increases noise levels [31]. This noise reduction is explained by decreased mobility caused by defect introduction. In graphene, mobility is limited by long-range Coulomb scattering from charged defects, even at room temperature, unlike traditional materials where phonon scattering typically determines mobility limitations [31].

In conclusion, electron irradiation influences graphene, altering its electronic properties and structure. It is important to use scanning and transmission electron microscopes cautiously for graphene investigation and electron beam lithography (EBL) in the fabrication of graphene devices. Prolonged exposure can lead to a deterioration of graphene device properties; so, optimal conditions should be adhered to for preserving its characteristics.

6. IMPACT OF TEMPERATURE ON GRAPHENE

Understanding how temperature affects graphene and graphene-based devices is crucial for predicting and comprehending whether such devices can operate in high-temperature environments, such as nuclear fusion reactors.

Studies have shown that elevated temperatures can restore the properties of graphene and reduce defects that accumulate in samples during irradiation [6, 14, 24, 30]. The processing temperature in experiments was around 300°C. Performing several annealing cycles proves to be more effective than a single annealing process [6]. These findings indicate that graphene possesses self-healing properties for defects induced by irradiation through annealing.

7. CONCLUSION

Summarizing the obtained results, it is noteworthy that all types of radiation have an impact on the structure of graphene, inducing defects in the material. It is evident that an increase in fluence and particle energy leads to a higher concentration of defects in graphene. An important conclusion is that graphene-based sensors, even in the presence of defects, continue to function effectively, demonstrating the resilience of graphene to radiation. This opens up possibilities for the application of graphene in high-radiation environments where traditional semiconductors may not be efficient.

Radiation exposure also allows for the modification of the graphene structure, creating pores and altering the interactions between graphene and substrates. A significant outcome is the reduction in the $1/f$ noise level upon irradiation, in contrast to the increased noise observed in classical semiconductors. Post-irradiation

material treatment contributes to defect reduction, indicating graphene ability to compensate for them.

It is crucial to conduct more in-situ studies, particularly measuring sensor characteristics during irradiation, rather than solely before and after, to gain a more precise understanding of the impact of radiation on device functionality. Considering the unique properties and radiation resistance of graphene, this material stands out as an excellent candidate for applications in nuclear energy and space exploration.

REFERENCES

1. M. A. Al Faruque, M. Syduzzaman, J. Sarkar, K. Bilisik, and M. Naebe, *Nanomaterials*, **11**, No. 9: 2414 (2021); https://doi.org/10.3390/nano11092414
2. R. Mas-Balleste, C. Gomez-Navarro, J. Gomez-Herrero, and F. Zamora, *2D Nanoscale*, **3**: 20 (2011); https://doi.org/10.1039/C0NR00323A
3. S. E. Taher, J. M. Ashraf, K. Liao, and R. K. Abu Al-Rub, *Graphene and 2D Mater.*, **8**: 161 (2023); https://doi.org/10.1007/s41127-023-00066-2
4. A. Paddubskaya, K. Batrakov, A. Khrushchinsky, S. Kuten, A. Plyushch, A. Stepanov, G. Remnev, V. Shvetsov, M. Baah, Y. Svirko, and P. Kuzhir, *Nanomaterials*, **11**, No. 1: 170 (2021); https://doi.org/10.3390/nano11010170
5. E. Shinn, A. Hübler, D. Lyon, M. Grosse Perdekamp, A. Bezryadin, and A. Belkin, *Complexity*, **18**, No. 3: 24 (2013); https://doi.org/10.1002/cplx.21427
6. S. El-Ahmar, M. Szary, T. Ciuk, R. Prokopowicz, A. Dobrowolski, J. Jagiełło, and M. Ziemba, *Applied Surface Science*, **590**, No. 24: 152992 (2022); http://dx.doi.org/10.1016/j.apsusc.2022.152992
7. T. Scalia, L. Bonventre, and M. L. Terranova, *Nanomaterials (Basel)*, **13**, No. 4: 680 (2023); https://doi.org/10.3390/nano13040680
8. E. V. Gorbar and S. G. Sharapov, *Osnovy Fizyky Grafenu* [Fundamentals of Graphene Physics] (Kyiv: Instytut Teoretychnoi Fizyky im. M. M. Bogoliubova–Kyivskyi Natsionalnyi Universytet imeni Tarasa Shevchenka: 2013) (in Ukrainian).
9. Jamie H. Warner, Franziska Schäffel, Alicja Bachmatiuk, and Mark H. Rümmeli, *Graphene: Fundamentals and Emergent Applications* (Elsevier: 2013); https://doi.org/10.1016/C2011-0-05169-4
10. *Graphene Materials: Structure, Properties and Modifications* (Eds. G. Z. Kyzas and A. C. Mitropoulos) (Rijeka, Croatia: InTech: 2017); http://dx.doi.org/10.5772/intechopen.65151
11. Ivan Ďuran, Slavomír Entler, Ondřej Grover, Inessa Bolshakova, Karel Výborný, Martin Kočan, Tomáš Jirman, George Vayakis, Oleksandr Vasyliev, Maksym Radishevskyi, Zhenxing Wang, and Daniel Neumaier, *Fusion Engineering and Design*, **146**, Pt. B: 2397 (2019); https://doi.org/10.1016/j.fusengdes.2019.03.20
12. W. Biel, R. Albanese, R. Ambrosino, M. Ariola, M. van Berkel, I. Bolshakova, K. J. Brunner, R. Cavazzana, M. Cecconello, S. Conroy,

A. Dinklage, I. Duran, R. Dux, T. Eade, S. Entler, G. Ericsson, E. Fable, D. Farina, L. Figini, C. Finotti, Th. Franke, L. Giacomelli, L. Giannone, W. Gonzalez, A. Hjalmarsson, M. Hron, F. Janky, A. Kallenbach, J. Kogoj, R. König, O. Kudlacek, R. Luís, A. Malaquias, O. Marchuk, G. Marchiori, M. Mattei, F. Maviglia, G. De Masi, D. Mazon, H. Meister, K. Meyer, D. Micheletti, S. Nowak, Ch. Piron, A. Pironti, N. Rispoli, V. Rohde, G. Sergienko, S. El Shawish, M. Siccinio, A. Silva, F. Da Silva, C. Sozzi, M. Tardocchi, M. Z. Tokar, W. Treutterer, and H. Zohm, *Fusion Engineering and Design*, **146**, Pt. A: 465 (2019); https://doi.org/10.1016/j.fusengdes.2018.12.092

13. K. Sowery, *Applied Nanolayers' Graphene is Approaching Sun Synchronous Orbit. Electronic Specifier* (Published Online April 7, 2022); https://www.electronicspecifier.com/industries/industrial/applied-nanolayers-graphene-is-approaching-sun-synchronous-orbit ().
14. Y. Zhang, J. Shi, C. Chen, N. Li, Zh. Xu, L. Liu, L. Zhao, J. Li, and M. Jing, *Physica E: Low-Dimensional Systems and Nanostructures*, **97**, Iss. 3: 151 (2018); http://dx.doi.org/10.1016/j.physe.2017.11.007
15. Y. Xu, J. Bi, K. Xi, and M. Liu, *The Japan Society of Applied Physics*, **12**, No. 6: 061004 (2019); http://dx.doi.org/10.7567/1882-0786/ab1e98
16. K. Xi, J. S. Bi, Y. Hu, B. Li, J. Liu, Y. N. Xu, and M. Liu, *Applied Physics Letters*, **113**, No. 16: 164103 (2018); https://doi.org/10.1063/1.5050054
17. Konstantinos Alexandrou, Amrita Masurkar, Hassan Edrees, James F. Wishart, Yufeng Hao, Nicholas Petrone, James Hone, and Ioannis Kymissis, *Applied Physics Letters*, **109**: 153108 (2016); https://doi.org/10.1063/1.4963782
18. I. A. Bolshakova, Ya. Ya. Kost, M. I. Radishevskyi, F. M. Shurygin, O. V. Vasyliev, Z. Wang, D. Neumaier, M. Otto, M. Bulavin, and S. Kulikov, *Nanomaterials in Biomedical Application and Biosensors (NAP-2019). Springer Proceedings in Physics. Vol. 244* (Eds. A. Pogrebnjak, M. Pogorielov, and R. Viter) (Singapore: Springer: 2020), p. 199–209; https://doi.org/10.1007/978-981-15-3996-1_20
19. J. Eapen, R. Krishna, T. D. Burchell, and K. L. Murty, *Journal of Nuclear Materials*, **2**, No. 1: 43 (2013); http://dx.doi.org/10.1080/21663831.2013.841782
20. Linjie Fan, Jinshun Bi, Kai Xi, Xueqin Yan, Yannan Xu, and Lanlong Ji, *IEEE Sensors Journal*, **21**, No. 14: 16100 (2021); http://dx.doi.org/10.1109/JSEN.2021.3075691
21. H. Vázquez, E. H. Ahlgren, O. Ochedowski, A. A. Leino, R. Mirzayev, R. Kozubek, H. Lebius, M. Karlusic, M. Jaksic, and A. V. Krasheninnikov, *Carbon*, **114**: 511 (2017); http://dx.doi.org/10.1016/j.carbon.2016.12.015
22. A. Kamarou, *Radiation Effects and Damage Formation in Semiconductors due to High-Energy Ion Irradiation* (Published Online Jan. 2006); https://nbn-resolving.org/urn:nbn:de:gbv:27-20070402-150459-6
23. *Mala Hirnycha Entsyklopediia* [Concise Mining Encyclopaedia] (Eds. V. S. Biletskyi) (Donetsk, Ukraine: 2004), vol. **1**, p. 640 (in Ukrainian).
24. Y. Xu, K. Zhang, C. Brüsewitz, X. Wu, and H. C. Hofsass, *AIP Advances*, **3**, No. 7: 072120 (2013); http://dx.doi.org/10.1063/1.4816715
25. K. Yoon, A. Rahnamoun, J. L. Swett, V. Iberi, D. A. Cullen,

I. V. Vlassiouk, A. Belianinov, S. Jesse, X. Sang, O. S. Ovchinnikova, A. J. Rondinone, R. R. Unocic, and A. C. T. van Duin, *ACS Nano*, **10**, No. 9: 8376 (2016); http://dx.doi.org/10.1021/acsnano.6b03036
26. S. Kim, O. Dyck, A. V. Ievlev, I. V. Vlassiouk, S. V. Kalinin, A. Belianinov, S. Jesse, and O. S. Ovchinnikova, *Carbon*, **138**: 277 (2018), https://doi.org/10.1016/j.carbon.2018.06.017
27. M. M. Lucchese, F. Stavale, E. H. Martins Ferreira, C. Vilani, M. V. O. Moutinho, Rodrigo B. Capaz, C. A. Achete, and A. Jorio, *Carbon*, **48**, No. 5: 1592 (2010); http://dx.doi.org/10.1016/j.carbon.2009.12.057
28. D. Teweldebrhan and A. A. Balandin, *Applied Physics Letters*, **94**, No. 1: 013101 (2008); http://dx.doi.org/10.1063/1.3062851
29. Isaac Childres, Luis A. Jauregui, Michael Foxe, Jifa Tian, Romaneh Jalilian, Igor Jovanovic, and Yong P. Chen, *Applied Physics Letters*, **97**, No. 17: 173109 (2010); http://dx.doi.org/10.1063/1.3502610
30. Yangbo Zhou, Jakub Jadwiszczak, Darragh Keane, Ying Chen, Dapeng Yud, and Hongzhou Zhang, *Nanoscale*, **25**: 1 (2017); http://dx.doi.org/10.1039/C7NR03446F
31. Md. Zahid Hossain, Sergey Rumyantsev, Michael S. Shur, and Alexander A. Balandin, *Applied Physics Letters*, **102**: 153512 (2012); http://dx.doi.org/10.1063/1.4802759

Наносистеми, наноматеріали, нанотехнології
Nanosistemi, Nanomateriali, Nanotehnologii
2025, т. 23, № 2, сс. 489–500
https://doi.org/10.15407/nnn.23.02.0489

© 2025 ІМФ (Інститут металофізики
ім. Г. В. Курдюмова НАН України)
Надруковано в Україні.

PACS numbers: 33.20.-t, 78.20.Ci, 78.40.Me, 78.67.Bf, 87.19.xj, 87.53.Bn, 87.64.km

Modification of Optical Spectra and Cytostasis of Doxorubicin and Conium Solutions with High-Energy Electron Irradiation

M. A. Zabolotnyy[1], L. I. Aslamova[1], G. I. Dovbeshko[2], O. P. Gnatyuk[2], V. Yu. Povarchuk[2], D. S. Leonov[3], R. V. Lytvyn[3,7], and M. Yu. Barabash[3–6]

[1]*Taras Shevchenko National University of Kyiv,*
64, Volodymyrs'ka Str.,
UA-01033 Kyiv, Ukraine
[2]*Institute of Physics, N.A.S. of Ukraine,*
46, Nauky Ave.,
UA-03028 Kyiv, Ukraine
[3]*Technical Centre, N.A.S. of Ukraine,*
13, Pokrovs'ka Str.,
UA-04070 Kyiv, Ukraine
[4]*Gas Institute, N.A.S. of Ukraine,*
39, Degtyarivs'ka Str.,
UA-03113 Kyiv, Ukraine
[5]*National Technical University of Ukraine*
'Igor Sikorsky Kyiv Polytechnic Institute',
37, Beresteiskyi Ave.,
UA-03056 Kyiv, Ukraine
[6]*Institute for Applied Control Systems, N.A.S. of Ukraine,*
42, Academician Glushkov Ave.,
UA-03187 Kyiv, Ukraine
[7]*I. M. Frantsevych Institute for Problems of Materials Sciences, N.A.S. of Ukraine,*
3, Omeljan Pritsak Str.,
UA-03142 Kyiv, Ukraine

The characteristics of optical absorption and cytostatic activity under high-energy electron irradiation of a solution of doxorubicin (of anthracycline class) in sodium chloride are studied. The energy of irradiating electrons was of 1 MeV, and the absorbed dose was within 2–90 kGy. As proven, when sodium chloride is irradiated, the absorbed dose affects the optical absorption spectra of samples and leads to an increase in the cytostatic effect of the drug. As shown, the optical spectra and cytostatic activity change with time in a co-ordinated manner. The dissolution of conium (of alkaloid class) in irradiated sodium chloride causes shifts of the maxima of the infrared absorption spectra of conium. A possible rea-

son for the changes in solution properties, when using pre-irradiated sodium chloride, is the conformational rearrangement of the antitumour drug molecules. This effect can be caused by the interaction with bubbstons and their clusters, which are formed under the impact of irradiation.

У роботі досліджено характеристики оптичного вбирання та цитостатичної активности під час опромінення високоенергетичними електронами розчину доксорубіцину (класу антрациклінів) у Натрію хлориді. Енергія електронів опромінення дорівнювала 1 МеВ, а увібрана доза знаходилася у межах 2–90 кГр. Доведено, що за опромінення Натрію хлориду величина увібраної дози впливає на спектри оптичного вбирання зразків і приводить до посилення цитостатичної дії препарату. Показано, що зміни оптичних спектрів і цитостатичної активности відбуваються узгоджено в часі. Розчинення коніуму (хемічного класу алкалоїдів) в опроміненому Натрію хлориді зумовлює зсуви максимумів ІЧ-спектрів увібрання коніуму. Можливою причиною зміни властивостей розчину за використання попередньо опроміненого Натрію хлориду є конформаційна перебудова молекул протипухлинного препарату. Такий ефект може зумовлюватися взаємодією з бабстонами та їхніми кластерами, що виникають під впливом радіяційного опромінення.

Key words: NaCl, doxorubicin, conium, bubbstons, optical absorption, high-energy electrons, radiation dose, cytotoxicity.

Ключові слова: NaCl, доксорубіцин, коніум, бабстони, оптичне вбирання, високоенергетичні електрони, доза опромінення, цитотоксичність.

(Received 25 March, 2025; in revised form, 9 April, 2025)

1. INTRODUCTION

The problem of antimicrobial resistance in 2020 was proclaimed by the World Health Organization as one of the ten global public health threats facing humankind.

It should be noted that the use of anticancer chemotherapy drugs is associated with a number of significant problems. These problems include nonspecific action and high toxicity of anticancer drugs to organs and tissues not affected by the tumour. A serious obstacle to the therapeutic effect of drug therapy is the resistance of malignant tumours to cytostatics [1, 2].

One of the most promising new approaches for modifying water-soluble antitumour drugs has been developed at the Taras Shevchenko National University of Kyiv [3, 4]. It is based on the use of high-energy (of 1 or 2 MeV) electron irradiation of sodium chloride for injections before dissolving antitumour drugs in it.

Studies [5, 6] have shown that the cytostatic activity of doxoru-

bicin and conium increases. The magnitude of the activity increase depends on the antitumour drug concentration, the radiation dose I absorbed by sodium chloride, and the time interval between the irradiation and determination of cytostatic activity. It is important that the above-mentioned drugs are related to different chemical compounds: doxorubicin belongs to the anthracycline class, while conium is an alkaloid.

The aim of the study is to investigate the mechanisms of high-energy electron irradiation effect on the optical spectra and cytostatic activity of doxorubicin and conium solution in sodium chloride pre-irradiated with electrons, and to assess the possibility of modifying existing antitumour drugs.

2. MATERIALS AND EXPERIMENTAL PROCEDURE

The absorption spectra of doxorubicin (Pharmacia Italia SpA, Italy) and conium (*Conium maculatum*, Weleda, Germany) solutions in sodium chloride were studied. Conium contains the alkaloids coniine ($C_8H_{17}N$), N-methylconiine ($C_9H_{19}N$), γ-coniceine ($C_8H_{15}N$), conhydrine ($C_8H_{17}NO$), and pseudoconhydrine ($C_8H_{17}NO$)). Sodium chloride for injections (0.9% NaCl, YURiA-PHARM, Ukraine) was used as a solvent for antitumour drugs.

The solvent was irradiated with electrons with energy of 1 MeV using a resonant linear electron accelerator Argus (pulse duration of 3.3 μs, pulse frequency of 400 Hz). The average current density of the electron beam was of 0.1 μA/cm^2, which corresponded to a flow density of $6.25 \cdot 10^{11}$ cm$^{-2} \cdot$s^{-1}. The absorbed dose I was determined, considering that one gray (Gy) corresponds to a fluence of $4.5 \cdot 10^9$ cm^{-2}. The dose I absorbed by the solvent ranged from 2 to 90 kGy.

The IR absorption spectra were recorded with a Bruker IFS-66 spectrometer; the absorption spectra in the visible and ultraviolet (UV) ranges were recorded with a Shimadzu UV-260 spectrophotometer with a measuring range of 190–900 nm.

The luminescence was recorded with a CaryEclipse spectrofluorometer (Varian) using a 1×1 cm^2 quartz cell.

The cytostatic activity of doxorubicin was determined using Lewis lung carcinoma (LLC) cell line.

All samples for recording IR spectra were formed as KBr tablets. The IR spectra were recorded using a Bruker IFS 66 Fourier-transform IR spectrometer (Germany) in transmission mode. The accuracy of the wave-number determination was 0.2 cm^{-1}, the transmittance was determined with accuracy of 0.1%. The OPUS 5.5 software package was used for the spectra recording and processing.

3. RESULTS AND DISCUSSION

The effect of preliminary electron irradiation of sodium chloride for injections on the optical and cytostatic properties of doxorubicin and conium dissolved in it was studied. The Fourier-transform infrared (FTIR) absorption spectra $A(I, k)$ in the UV range for doxorubicin after its dissolution in sodium chloride for injections, which was pre-irradiated with high-energy electrons, are shown in Figs. 1, 2.

The data shown in Fig. 1 indicate significant changes in the spectra, which was caused by solvent irradiation. In the range of va-

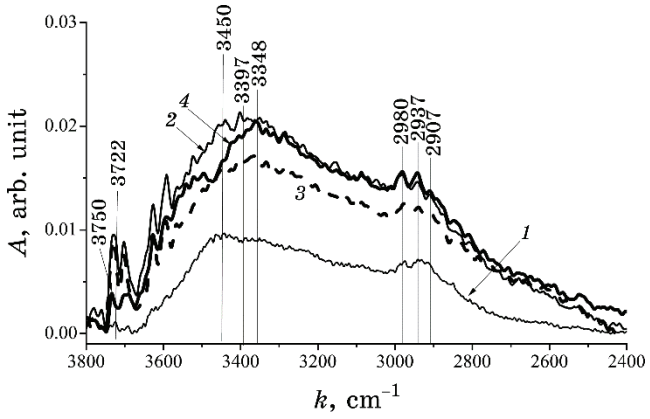

Fig. 1. Absorption spectra for doxorubicin in the range 3800–2400 cm^{-1}: curve *1* (I = 0 kGy), curve *2* (I = 10 kGy), curve *3* (I = 40 kGy), curve *4* (I = 80 kGy).

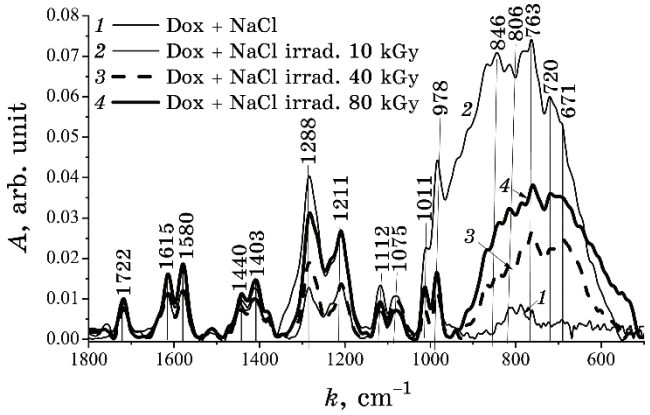

Fig. 2. Absorption spectra for doxorubicin in IR the range: curve *1* (I = 0 kGy), curve *2* (I = 10 kGy), curve *3* (I = 40 kGy), curve *4* (I = 80 kGy).

lence vibrations of OH–NH–CH molecular groups at 3800–2400 cm^{-1}, the intensity of this band increases for all samples with irradiated solvent without exception (curves *2–4*). Besides, a shift of the maximum of this band to higher frequencies is observed compared to the non-irradiated sample (*1*).

Analysis of the spectra in Figs. 1, 2 and the data listed in Table 1 indicates that the position of the absorption maxima corresponds to the values of the corresponding normal vibration of a certain molecular group. A comparison of the positions of the peaks, which correspond to vibrations of the same groups of atoms of unirradiated sodium chloride and solution samples irradiated with different doses, showed that some absorption maxima shifted, split and sometimes vanished. These effects can be associated with specific interactions between molecular groups, bubbstons and free radicals that appeared after irradiation.

The complete vanishing of a maxima compared to the control

TABLE 1. Maximums of IR absorption spectra of doxorubicin with saline irradiated by 1-MeV electrons with different doses.

Wave-number, cm^{-1}			
Dox + NaCl	Dox + NaCl (irrad. 10 kGy)	Dox + NaCl (irrad. 40 kGy)	Dox + NaCl (irrad. 80 kGy)
671.374	—	—	671.374
720.436	720.436	—	720.436
763.186	763.186	759.225	763.186
806.824	806.824	806.824	806.824
—	846.113	846.113	846.113
978.772	978.772	978.772	978.772
1011.502	1011.502	1011.502	1011.502
1075.962	1075.962	1075.962	1075.962
1288.453	—	—	1282.387
1403.152	1403.152	1403.152	1403.152
1572.995	1580.123	1575.697	1575.697
1615.075	1615.075	1615.075	1615.075
2925.531	2937.000	—	2925.531
—	2980.385	2980.385	2980.385
—	–	—	3348.112
—	3450.845	3450.845	3450.845
—	3600.645	—	3600.645
—	3625.685	3625.685	3625.685
3693.217	3700.760	3700.760	3700.760
3722.331	3722.331	3722.331	3722.331
—	3750.509	3750.509	3750.509

sample occurs due to changes in the conformational characteristics of molecules belonging to those molecular groups whose vibrations have corresponding frequencies (Table 1). Since vibrations are active in the IR spectrum only when they lead to a change in the dipole moment of a molecule, those molecular groups, whose maxima vanish after irradiation, do not affect the total dipole moment of the molecule because they oscillate near the centre of symmetry.

This conclusion correlates with the findings of the analysis of the spectra in the range 500–1000 cm^{-1}, in which the deformation vibrations of hydrogen bonds contribute. A significant increase in the absorption intensity is also observed, which is the largest in the spectrum *2*. At the same time, no significant shifts of bands are observed in the range corresponding to vibrations of C=O double bonds and deformation vibrations of CH.

The increase in the intensity of the bands along with high-frequency shifts can indicate an increase in the number of hydrogen bond groups in the case of valence vibrations. The distortion of the planar shape of the doxorubicin molecule due to the free rotation of its parts around single bonds can lead to a change in the positions of the maximums of the absorption bands with a frequency shift to the low-frequency range of the spectrum. These effects can be caused by nonspecific interactions between the molecular groups of doxorubicin and the radiolysis products of the solvent water. This conclusion is confirmed by the data presented in Fig. 3, which shows the effect of irradiation by value $\Delta A(I,k)/A(0,k)$, where $\Delta A(I, k) = A(I, k) - A(0, k)$ ($A(0, k) = A(I = 0$ kGy)) in the FTIR spectra of doxorubicin solution.

The curves *1*, *2*, and *3* in Fig. 3 are given by functions

$$\frac{\Delta A(I = 10, \text{kGy})}{A(0,k)}, \quad \frac{\Delta A(I = 40, \text{kGy})}{A(0,k)}, \text{ and } \frac{\Delta A(I = 80, \text{kGy})}{A(0,k)},$$

respectively. According to the spectra in Fig. 3, $A(I, k_{1,2})/A(0, k_{1,2}) > 7$ for all used values of I and wave-numbers $k_1 = 668.94$ cm^{-1} and $k_2 = 900.60$ cm^{-1}. This behaviour of $A(I, k)$ may indicate the invariance of the power centres responsible for the absorption of waves with wave-numbers k_1, k_2, and their coagulation under the influence of irradiation with high-energy electrons.

The dependence of the optical absorption spectra of doxorubicin solution in the UV and visible range on the absorbed dose was investigated (see Fig. 4).

The time interval between the irradiation of the samples and the measurements shown in Fig. 4 did not exceed ten days. During this time, no changes in each of the spectra were observed for all I under study. The absorption value of doxorubicin solution in the visible range (Fig. 4) does not monotonically depend on I that is consis-

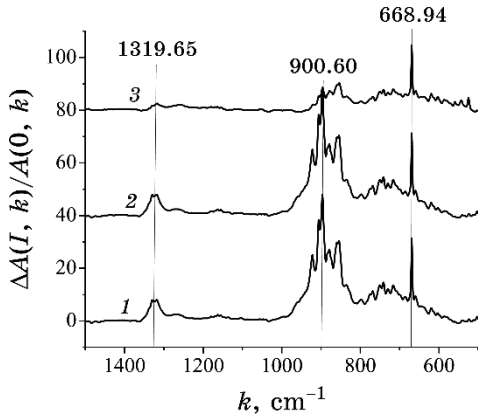

Fig. 3. Ratio of difference in absorbances of irradiated and non-irradiated doxorubicin solution to absorbance of non-irradiated doxorubicin.

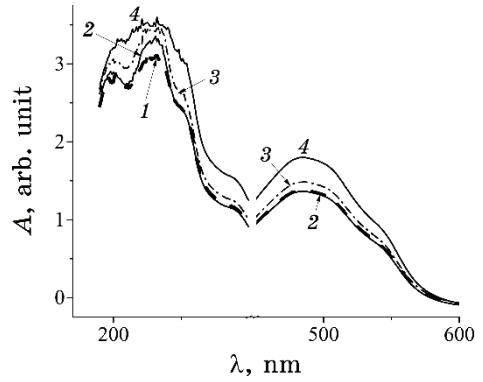

Fig. 4. Optical absorption spectra of doxorubicin solution in the UV and visible range: curve *1*—I = 0 kGy, curve *2*—I = 10 kGy, curve *3*—I = 40 kGy, curve *4*—I = 80 kGy.

tent with the data obtained for the infrared range (Figs. 1, 2). The optical spectra recorded within ten days after solvent irradiation were analyzed using the OriginLab software package. The experimental spectra were approximated by linear combinations of Lorentzian functions (Fig. 5).

The dose dependence of the position of the maxima of the absorption spectra in the UV and visible range, recorded immediately after solvent irradiation and preparation of doxorubicin solutions, is presented in Table 2.

The results of the analysis of the obtained spectra indicate shifting of the maxima (Table 1) and dramatic changes in their intensities, depending on the solvent irradiation dose.

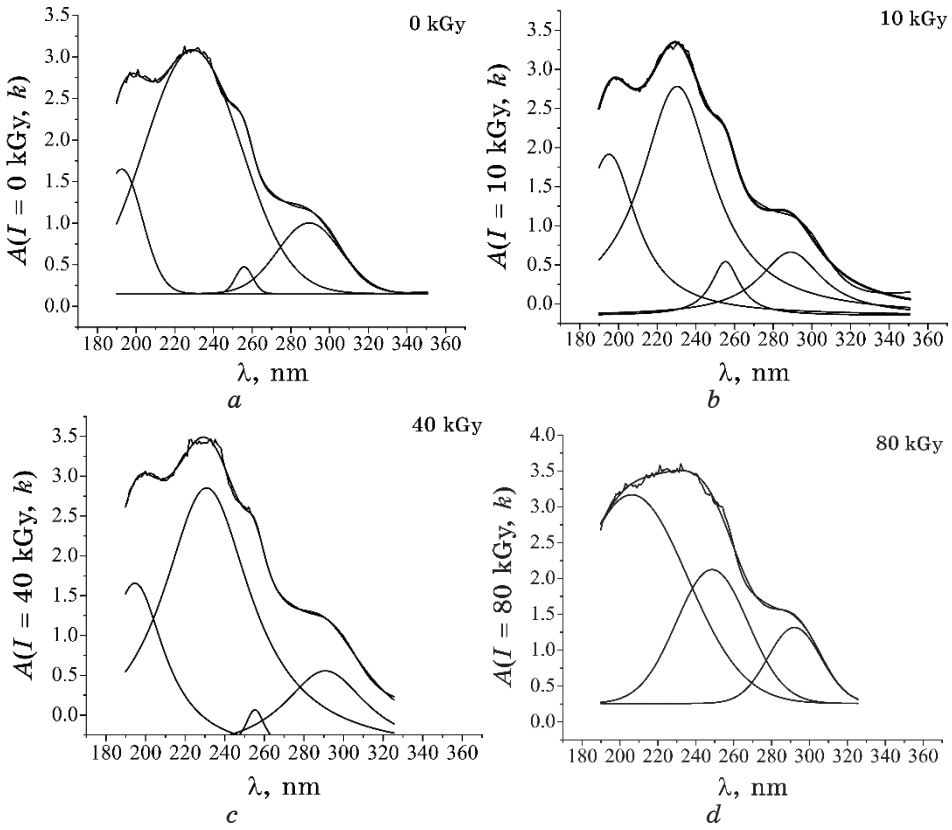

Fig. 5. Approximation of absorption spectra of doxorubicin solution in sodium chloride in the UV range by linear combinations of Lorentzian functions: (*a*) $I = 0$ kGy, (*b*) $I = 10$ kGy, (*c*) $I = 40$ kGy, (*d*) $I = 80$ kGy.

TABLE 2. Position of maxima of absorption spectra in the UV and visible range as a function of dose in optical absorption spectra.

λ/*I*, kGy	irrad. 0 kGy	irrad. 10 kGy	irrad. 40 kGy	irrad. 80 kGy
λ, nm	192.57	195.10	194.59	206.20
λ, nm	229.32	230.31	230.83	248.51
λ, nm	255.81	255.34	255.27	—
λ, nm	289.45	290.06	290.79	292,04
λ, nm	471.44	474.53	474.71	474.34
λ, nm	509.07	510.72	510.81	510.13

The effect of irradiating solvent on an alkaloid drug (conium) was also studied in order to compare it with an anthracycline drug

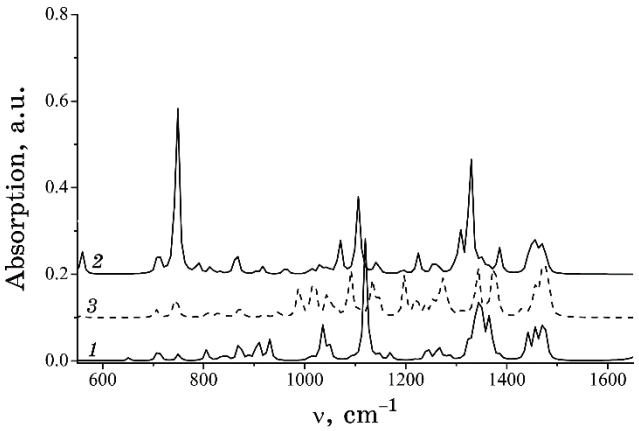

Fig. 6. Dependence of normalized absorption of conium on wave number for 0.9% NaCl solution non-irradiated (curve *1*) and irradiated with different doses of absorbed electron radiation: *2*—5 kGy, *3*—10 kGy.

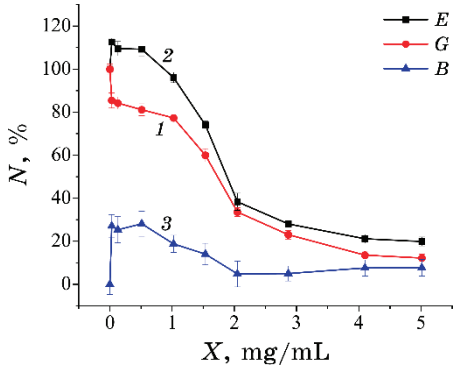

Fig. 7. Cytostatic effect of doxorubicin dissolved in irradiated and non-irradiated sodium chloride solvent.

(doxorubicin).

The addition of solvent (Fig. 6) irradiated with different doses of electron radiation affected the position of the maxima of the conium absorption bands: 1120 cm^{-1} line (curve *1*) shifted to 1106 cm^{-1} (curve *2*), then, to 1089 cm^{-1} (curve *3*). This shift of the absorption lines of conium in the vibrational range of the IR spectrum indicates a change of conformational state caused by the interaction with bubbstons (their clusters) present in the irradiated solvent.

The cytostasis of doxorubicin dissolved in sodium chloride irradiated with high-energy electrons in comparison to a non-irradiated solvent was studied. Figure 7 shows the numbers of live LLC cells in percentage (*N*) after 24-h incubation of doxorubicin solution for

different concentrations (X).

In Figure 7, curve *1* shows the percentage of live LLC cells after incubation of doxorubicin dissolved in irradiated ($I = 40$ kGy) sodium chloride for different concentrations of doxorubicin; curve *2* shows the percentage of live cells for the non-irradiated solvent; curve *3* shows difference of curves *2* and *1*. The dependences in Fig. 7 show the effect of the irradiated solvent depending on the doxorubicin concentration.

A possible reason for the changes in the spectra of doxorubicin solution, when using a pre-irradiated solvent, is the conformational rearrangements in the antitumour drug molecules caused by the interaction with bubbstons and their clusters under the radiation exposure. The space distribution of the electric field of single bubbstons was studied in Refs. [6–8], but the formation of bubbston clusters has not been fully investigated. On the one hand, solving this problem is complicated due to the nonlinear nature of the equations describing the electric field of the double electric layer of a bubbston; on the other hand, it is due to the lack of information about the polarization, deformation, and forces of individual bubbstons and their clusters. When bubbstons coagulate, their spherical symmetry is broken; the fractal dimension of coagulants depends on the mechanisms of cluster growth [7].

Usually, the electric potential distribution $\varphi(k)$ in the vicinity of a single spherically symmetric bubbston is determined using the Poisson–Boltzmann equation [9] and information on the distribution of counter-ions (n_0) and density $\rho(r)$ around the inner positively charged surface of the air–liquid interface [10].

In the case of spherical symmetry of the nanoparticle and zero total charge of the nanoparticle and the adjacent layer of singly-charge counter-ions with a concentration of n_0, the corresponding equations are [10, 11] as follow:

$$Q_0 + 4\pi \int_{R_0}^{\infty} \rho(r) r^2 dr = 0\,, \quad \frac{1}{r^2}\frac{\partial}{\partial r}\left(r^2 \frac{\partial \phi(r)}{\partial r}\right) = -\frac{\rho(r)}{\varepsilon\varepsilon_0} = \frac{2en_0}{\varepsilon\varepsilon_0}\sinh\left(\gamma\phi(r)\right), \quad (1)$$

where R_0 is the radius of the bubbston air bubble, ε_0 is the vacuum permittivity, ε is the dielectric constant, T is the ambient temperature, k_B is the Boltzmann constant, and $\gamma = e/(k_B T)$.

At low values of electrical energy,

$$\frac{e\phi(r)}{k_B T} << 1\,, \quad (2)$$

the Debye radius (R_D) is supposed to be $R_D = \sqrt{\dfrac{\varepsilon\varepsilon_0 k_B T}{2e^2 n_0}}$. Therefore, the R_D decreases with increasing n_0 caused by irradiation.

Using the Maple 2019 software, Eqs. (1) were solved numerically

for $n_0 = 10^{21}$, $3 \cdot 10^{21}$, 10^{22} m^{-3}. The parameter R_D was estimated by the co-ordinate of the point r_0, at which the derivative $\phi(r)/r = r_0$ differs from the tangent of the angle at the point R_0. This analysis showed that the space dimensions of bubbstons decrease, when sodium chloride is irradiated with electrons, causing changes in the distribution of ponderomotive forces near a bubbston.

4. SUMMARY

The mechanisms of antitumour drug modification of doxorubicin and conium solutions in sodium chloride for injections, irradiated with high-energy electrons, are investigated. Modifications of existing antitumour drugs without adding foreign nanoparticles are developed. It should be noted that doxorubicin belongs to the chemical class of anthracyclines, and conium belongs to the class of alkaloids.

It is shown that the absorption spectra of doxorubicin solution in the infrared range are characterized by a non-monotonic dependence of the ratio of intensities of high- and low-frequency maxima on the absorbed dose. This behaviour is caused by the coagulation (clustering) of bubbstons, which can occur at high bubbston concentrations (at high doses of absorbed radiation).

The radiation dose absorbed by sodium chloride affects the spectral dependence of the absorption of doxorubicin dissolved in it (in the visible range). In the range 175–250 nm, the absorbance decreases, however, in the range 250–600 nm, it increases as compared to the absorbance of doxorubicin solution prepared with non-irradiated solvent. The value of the absorption difference modulus in the visible range of the spectrum increases monotonically with increasing absorbed radiation dose, which does not coincide with the behaviour in the infrared range. This is associated with the dependence of molecular absorption processes on the frequency of electromagnetic radiation.

It is shown that the addition of an irradiated solvent affects the positions of the maximums of the conium absorption bands. The absorption line at 1120 cm^{-1} shifts to 1106 cm^{-1}, and then, to 1089 cm^{-1}. This shift of conium absorption lines in the vibrational range of the IR spectrum can indicate changes in its conformational state caused by interaction with bubbstons (or their clusters) present in the irradiated solvent. The effect of irradiation ($I = 2$ kGy, 5 kGy) on the IR spectra of the conium solution was observed over the course of two weeks.

The study of the doxorubicin pharmacological activity performed using the Lewis lung carcinoma cell line proved that pre-irradiation of sodium chloride with high-energy electrons before dissolving

doxorubicin increased the cytotoxic/cytostatic effect of the drug. This effect was most pronounced at relatively low concentrations.

The optical effects of doxorubicin dissolved in pre-irradiated sodium chloride decreases significantly after two–four months; the higher the radiation dose, the slower the relaxation processes proceed. The forces of interaction of bubbstons during their clustering depend on their mutual orientation and are non-central.

REFERENCES

1. L. Aslamova, M. Zabolotnyy, G. Dovbeshko, G. Solyanik, O. Gnatyuk, and M. Tsapko, *Proceedings of International Conference 'Medical Physics 2023' (9–11 November 2023, Kaunas, Lithuania)*, p. 149–152.
2. Dharmendra Kumar, *Journal of Nanomedicine Research*, **7**, Iss, 4: 262 (2018); doi:10.15406/jnmr.2018.07.00197
3. M. A. Zabolotnyy, M. P. Kulish, O. P. Dmytrenko, G. I. Solyanyk, Yu. I. Prylutskyi, M. A. Drapikovskyi, M. O. Kuzmenko, N. A. Poluyan, and V. A. Kiyashko, *Method of Modification of Water-Soluble Anticancer Drugs Using Radiation Exposure* (Patent for the Invention of Ukraine No. 116, 227; Registered on 26.02.2018).
4. Rashmi Bangarh, Reena V. Saini, Adesh K. Saini, Tejveer Singh, Hemant Joshi, Seema Ramniwas, Moyad Shahwan, and Hardeep Singh Tuli, *Cancer Pathogenesis and Therapy*, **3**, Iss. 2: 120 (2025); https://doi.org/10.1016/j.cpt.2024.07.002
5. L. Aslamova, M. Zabolotnyy, G. Dovbeshko, and G. Solyanik, *Proceedings of 15th International Conference 'Medical Physics in the Baltic States 2021' (4–6 November 2021, Kaunas, Lithuania)*, p. 70–73.
6. M. A. Zabolotnyy, N. A. Poluyan, G. I. Dovbeshko, Yu. M. Kondratzky, M. P. Kulish, A. I. Momot, and O. P. Dmytrenko, *Nanosistemi, Nanomateriali, Nanotehnologii*, **12**, Iss, 4: 651 (2014) (in Ukrainian); https://www.imp.kiev.ua/nanosys/media/pdf/2014/4/nano_vol12_iss4_p0651p0664_2014.pdf
7. Dominik Kosior, Agata Wiertel-Pochopien, Przemyslaw B. Kowalczuk, and Jan Zawala, *Minerals*, **13**, Iss. 9: 1130 (2023); https://doi.org/10.3390/min13091130
8. M. A. Zabolotnyy, L. I. Aslsmova, G. I. Dovbeshko, O. P. Gnatyuk, G. I. Solyanyk, V. P. Dankevych, D. S. Leonov, M. Yu. Barabash, and V. A. Chernyak, *Nanosistemi, Nanomateriali, Nanotehnologii*, **22**, Iss. 2: 481 (2024) (in Ukrainian); https://doi.org/10.15407/nnn.22.02.481
9. C. G. Gray and P. J. Stiles, *European Journal of Physics*, **39**, No. 5: 053002 (2018); doi:10.1088/1361-6404/aaca5a
10. M. A. Zabolotnyy, L. I. Aslamova, G. I. Dovbeshko, O. P. Gnatyuk, V. B. Neimash, V.Yu. Povarchuk, V. E. Orel, D. L. Kolesnyk, L. M. Kirkilevska, and G. I. Solyanyk, *Nuclear Physics and Atomic Energy*, **23**: 131 (2022); https://doi.org/10.15407/jnpae2022.02.131
11. A. I. Momot, A. G. Zagorodny, and I. S. Orel, *Phys. Rev. E*, **95**, No. 1: 013212 (2017); https://doi.org/10.1103/PhysRevE.95.013212

Наносистеми, наноматеріали, нанотехнології
Nanosistemi, Nanomateriali, Nanotehnologii
2025, т. 23, № 2, сс. 501–514
https://doi.org/10.15407/nnn.23.02.0501

© 2025 ІМФ (Інститут металофізики
ім. Г. В. Курдюмова НАН України)
Надруковано в Україні.

PACS numbers: 81.05.U-, 81.05.Zx, 83.60.Np, 83.80.Mc, 85.40.Ls, 87.50.C-, 87.85.jf

EMI Shielding with Textile Fabrics: An Unadorned Review

N. V. Krishna Prasad[1] and N. Madhavi[2]

[1]*Department of Physics, G.S.S,*
GITAM University,
Bengaluru, India
[2]*Govt. College (Autonomous),*
Department of Statistics,
Rajhamundry, India

Electromagnetic radiation emitted from various sources need to be shielded. Especially, in case of human beings, this is of prime significance. EMI shielding can be done using various shields with more and more flexibility through stretchable, bendable, and droppable shields. In view of human health and its importance, lot of emphasis has been laid in developing textile fabrics, which can exhibit shielding properties along with mechanical strength, based on textile structure and material. The required characteristics such as electric and magnetic properties in normal textile fabrics are not up to the mark. Hence, these properties are to be added. This can be achieved by coating the layer, conductive yarn or magnetic fibre integration, *etc*. Based on the previous work done, an attempt was made to review the various materials and their use for this very purpose. This mainly includes fabrics with metal coating, MXene coating, carbon coating, *etc*. It is observed that high conductivity and effective EMI shielding make MXenes to be in the forefront in EMI shielded fabrics, while other coatings (magnetic and conductive) will be the next choice.

Електромагнетне випромінення, що випромінюється різними джерелами, потребує екранування. Це має першочергове значення, особливо для людей. Екранування від електромагнетних перешкод може бути здійснене за допомогою різних екранів з більшою гнучкістю завдяки розтяжним, гнучким і скидальним екранам. З огляду на важливість здоров'я людини, велику увагу приділяють розробці текстильних тканин, які можуть проявляти екранувальні властивості разом з механічною міцністю, залежно від структури текстилю та матеріялу. Потрібні характеристики, такі як електричні та магнетні властивості, у звичайних текстильних тканин не відповідають вимогам. Тому ці властивості необхідно додати. Цього можна досягти шляхом нанесення покриття, провідної нитки або інтеґрації магнетного волокна тощо. На основі по-

передньої роботи було зроблено спробу переглянути різні матеріяли та використання їх саме для цієї мети. Це головним чином включає тканини з металевим покриттям, покриттям максенами, вуглецевим покриттям тощо. Помічено, що висока провідність й ефективне екранування від електромагнетних перешкод висувають максени на передній план у тканинах, що екранують від електромагнетних перешкод, тоді як інші покриття (магнетні та провідні) будуть наступним вибором.

Key words: textile fabrics, EMI shielding, shielding effectiveness.

Ключові слова: текстильні тканини, екранування електромагнетних перешкод, ефективність екранування.

(Received 28 December, 2023; in revised form, 23 July, 2024)

1. INTRODUCTION

EMI (Electromagnetic Interference) is a phenomenon that takes place, when an electromagnetic field disturbs the operation of an electronic device close to it. Various EMI-shielding materials protect devices and human beings from this radiation by reflecting or absorbing it [1, 2]. In spite of huge increase in usage of electronic devices, shielding of human as well as equipment from EM waves is of prime importance. Since life without technology is not possible, electromagnetic irradiance even though dangerous for devices and human beings needs to be used in daily life. Many devices like switches, regulators, and circuit boards are likely to become defective due to EMI. These radiations also effect human cells and capable of altering DNA. Human cells subjected to EM radiation might lead to cancer. In addition, exposure to EM radiation leads to fatigue, stress and many other diseases. Earlier reports indicated biological impacts of EM radiation from various home appliances like TV, oven, *etc*. It was reported that exposure to microwaves impacts bone marrow and liver tissues [3, 4].

Figure 1 shows some of the non-cancerous effects of low frequency in the human beings.

Recent focus on developing EMI-shielding devices was towards usage of textile fabrics. Since textile fabrics are thin, lightweight, and flexible, they are preferred especially in view of cyber security. Reflection by conductive materials that lead to secondary electromagnetic radiation can be minimized through absorption [5, 6]. This mechanism in EMI shielding is widely used in medical electrical equipment. Generally, shielding materials are tested between 10^4–10^{12} Hz for computers, motors, and power lines [7, 8], while as other experiments like magnetic resonance tomography are tested for low frequencies [9, 10]. Various frequency ranges in a shielding

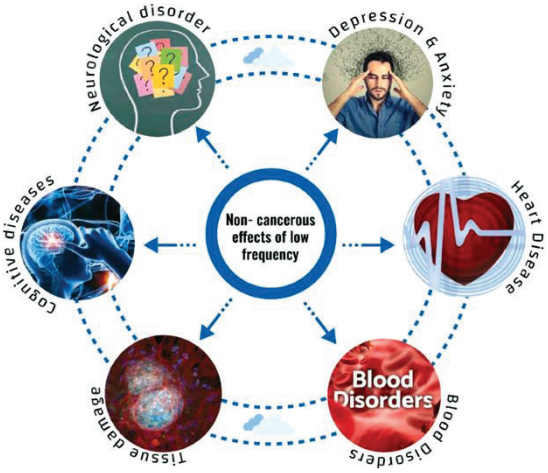

Fig. 1. Non-cancerous effects of low frequency in the human beings [4].

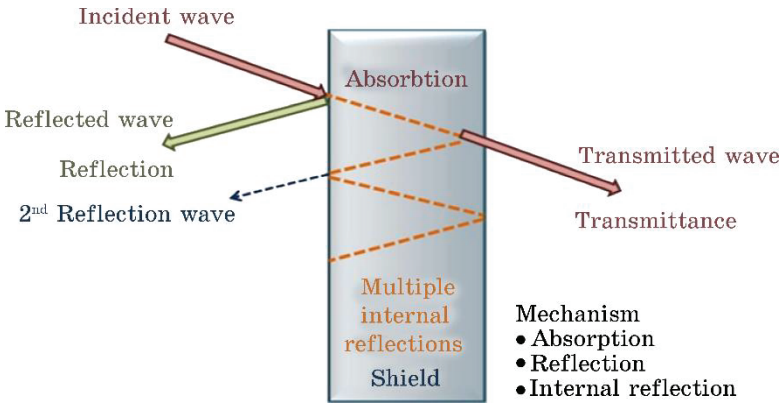

Fig. 2. Schematic representation of the EMI-shielding mechanism [4].

material demand various physical properties [11].

Figure 2 shows the mechanism of EMI shielding.

The effectiveness of shielding (SE) is given by:

$$SE = 20 \log T^{-1} \text{ or as } SE = 10 \log \left(\frac{P_0}{P_t} \right), \tag{1}$$

$$SE = SE_R + SE_A + SE_M, \tag{2}$$

where SE is a parameter comprises of shielding due to reflection (SE_R), absorption (SE_A), and multiple reflections (SE_M) inside the shielding material. T represents the transmission coefficient, P_0 and

P_t represent powers without and with shielding [12, 13]. Textile-based EMI shielding has gained more significance in recent times due to advent of novel materials such as MXenes. It is reported that EMI shielding depends on reflection and absorption inside the shielding fabric [12]. The thickness, porosity, conductivity, dielectric and magnetic properties influence shielding properties in textiles. If the thickness of the fabric is very small, multiple reflections need to be considered [14].

In general, electrical conductivity and thickness of a material determine high-frequency properties, while low-frequency properties are determined by magnetic properties [15–24]. Different methods are reported, while probing EMI shielding in materials. These include free space, shielded box, shielded room and coaxial transmission-line methods [25]. Coaxial transmission method is used between 10 kHz to 1 GHz. Free space method is preferred, if large distance exists between antenna and the device. Shielded-box method was confined to approximately 500 MHz with low reproducibility. Shielded room method uses an anechoic chamber, which is unsuitable for specimens in small size [26]. Various materials are used in EMI-shielding materials and some of them are discussed in the next subsequent sections.

2. ROLE OF MXenes IN EMI SHIELDING

Many techniques in preparation of EMI shielded fabrics are based on fibres, metal coating, and carbon coating. However, MXenes and their use in preparation of conductive coatings were widely reported. MXenes are 2*D* layered materials with nitrides [27]. Even though their preparation [28–30] is not mentioned in this review; sixty plus MXenes with different chemical composition and properties were reported [31].

2.1. MXene Coating

2*D* nature of MXenes makes them significant as coatings on textile fabrics. Electromagnetic interference shielding in combination with solar water evaporation as well as photothermal conversion was reported [32]. SiO_2 nanoparticles and PFOTES along with MXene were combined to yield shield effectiveness of 36 dB. Similarly, MXene textiles of bark shape demonstrated high effectiveness, good Joule heating and piezoresistive sensing [33]. It is reported that bark shape enhanced EMI-shielding effectiveness. Similarly efficient fabric shield with good electrical conductivity and low resistance with MXene loaded on cotton fabric that can be used as strain sensor to

detect human motion was reported [34]. Basalt fibre fabrics are used as EMI shields [35]. Combination of Mxene with polymer network results in a textile fabric EMI shielding [36]. Samples without Mxene have almost zero EMI shielding in *X*-band [37]. Polyethylene terephthalate textiles applied with Ppy-modified Mxene sheets are coated with silicon. This yields 1000-S/m electrical conductivity and shielding efficiency of 90 dB [38]. Mxene combined with Pani nanowires on carbon-fibre fabric with PDMS coating reported a conductivity of 325 S/m and 35-dB effectiveness [39]. In a similar way, 3-dimensional nanoflower structure gives an effectiveness of 52 dB efficiency in *X*-band [40]; Mxene with metal reported 54 dB in *X*-band [41]; MXene with carbon-based conductive materials reported about 43 dB shielding [42].

2.2. MXene Fibres

Apart from MXenes, another possibility is to use MXene fibres. MXene fibres can be used as core in a coaxially spun fibre [43]. MXene fibres are reported to exhibit a shielding effectiveness of 27 to 33 dB for single layer with conductivity of 10^5 S/m. If 3 layers are considered, *SE* was up to 100 dB. Coaxial spinning of MXene core and aramid nanofibre shell has an efficiency of 83 dB [44]. Similarly, MXene fibres designed from MXene–glutaraldehyde (GA) solution with thermal drawing yield *SE* of 50–60 dB in *X*-band [45]. In continuation, short MXene fibres, which produce MXene nonwoven, yielded *SE* of 75 dB in *X*-band [46]. Similarly, a combination of reduced graphene oxide (*r*GO) and MXene to form a core shell aerogel reported to have *SE* value up to 83 dB, which could sustain 83% even after four months [47].

3. ROLE OF METALS IN EMI SHIELDING

Majority of the metals exhibits very high conductivity. However, low conductivity was seen in case of thin films and transition metals [48, 49]. Based on the magnetic properties, metals are used as coating to produce EMI shielding.

3.1. Metal Coatings & Metal Wires

Fabrics coated with metal (smart textiles) are used as strain sensors to detect human motion [50], as electrodes in ECG [51], textile batteries [52], textile solar cells [53], *etc*. In the same way, it was reported that EMI-shielding properties can be added to textile fabrics by metal coating. In this context, copper-coated polyester nonwoven

was of importance [54]. As shown in Fig. 2, thick layer of copper was formed on the fibre, which reported a shielding effectiveness of 42 dB to 63 dB between 30 MHz to 1.5 GHz, depending on the coating thickness. In multilayer systems, 90 dB can be attained with three to five layers of copper-coated nonwoven fabrics.

Figure 3 shows a copper-coated PES fabric.

By using the above material, 30 to 55 dB can be attained between 0.5 GHz–1.5 GHz in a PES nonwoven fabric. This uses electroless plating of copper [55]. Apart from copper, silver is often selected to get high conductivity in coating. An oxidized-cellulose textile surface exhibited 47 dB and 69 dB for single and triple layers [56].

Combination of silver nanowires with Fe_3O_4 nanoparticles produced *SE* of 60 dB for single fabric layer and 100 dB for three fabric layers in *X*-band [58]. Silver nanowires combined with CNTs reached more than 51 dB EMI shielding [59]. A PES woven fabric,

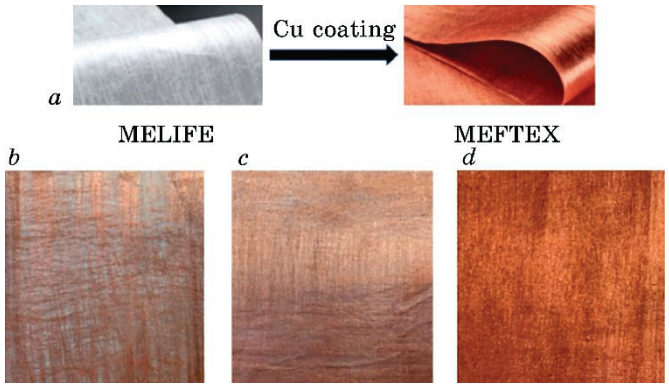

Fig 3. Copper-coated PES fabric [54].

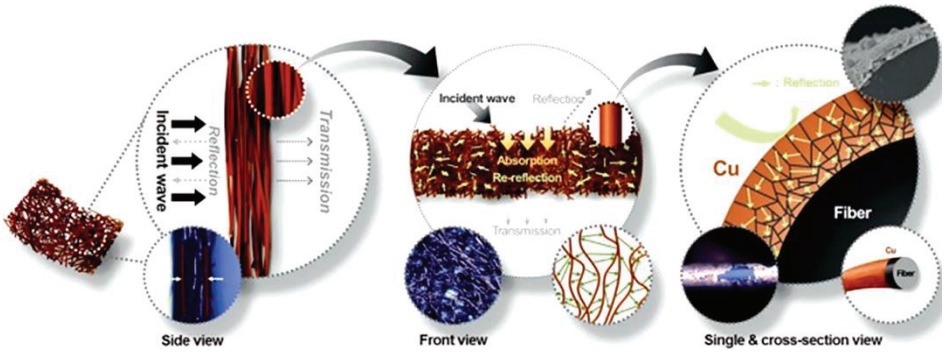

Fig. 4. EMI-shielding mechanism in copper-based activated carbon fibres [57].

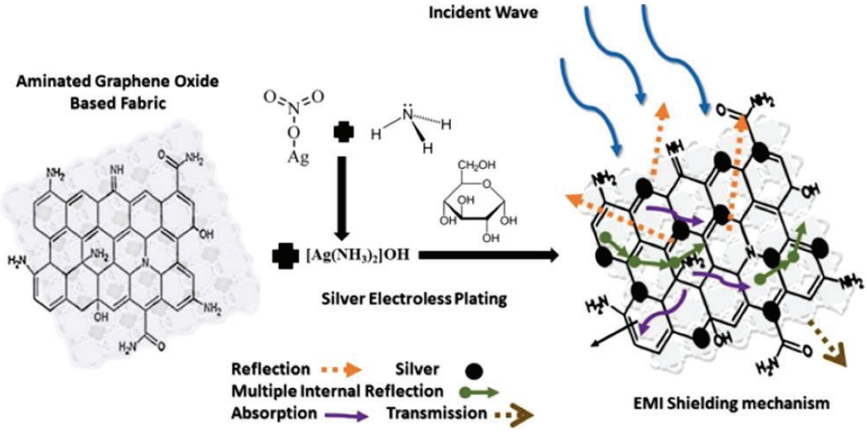

Fig. 5. Mechanism of Ag/aminated GO-based cotton fabrics [63].

when dipped in $Ni(CH_3CO_2)_2$ solution along with hydrazine hydrate, formed nickel nanoparticles on the surface of the fabric giving rise to 32-dB effectiveness. This is due to the ferromagnetic and conductive nature of nickel [60]. Keeping the mechanical, thermal, and chemical stability in view, various researchers opted for embedding of metal nanoparticles in polymeric coatings. A textile fabric immersed in PVB–ethanol solution embedded with silver nanowires yield an effectiveness of 59 dB between 5–18 GHz [61]. Silver nanowires with polyurethane layer exhibit *SE* of 64 dB that reduced by 11% after 20 washing cycles and to 18% after 5000 cycles. This fabric can be used as for various applications, where washing of fabric is essential [62].

Apart from these regular metals in nanoform, liquid metals are proposed. This include In, Pb, Ga, Bi, Sn, *etc.* with low melting points. A combination of liquid metal and PDMS coating yielded 73-dB efficiency [64, 65].

Apart from coating of textiles, metal wires can be inserted. Instead of polyamide filament yarns coated with silver, yarns with stainless-steel fibres are being used in smart textiles [66–69]. Since stainless-steel fibres exhibit magnetic properties, they are suitable for EMI shielding [70]. In place of stainless-steel yarns, self-spun yarns, which include stainless-steel wires, are widely used for EMI-shielding textile fabrics. A ring-spun composite yarn from stainless steel and polyester fibre reached EMI-shielding effectiveness of 31–35 dB in the range of 8.2–18.0 GHz [71–73]. A wrap yarn with same combination has *SE* around 5–28 dB for various wrapping densities in the frequency range of 4–8 GHz [74]. However, metal coatings are reported to have higher shielding effectiveness as compared to metal-wire approach [75, 76].

4. ROLE OF CARBON IN EMI SHIELDING

Designing of textile fabrics with carbon coating or carbon fibres was one of the techniques investigated. Carbon coated textiles are used in batteries, sensors [77], and electronic textiles [78–80]. Carbon has various forms like quantum dots, graphene, CNTs, carbon black and graphite [81]. Based on their dimension, carbon can have different conductivities [82]. Based on these conditions, they are well suited for EMI-shielding applications.

4.1. Carbon Coatings, Carbon Fibres, and Filaments

Carbon coatings with CNTs (carbon nanotubes) on fabrics enhance their EMI-shielding effectiveness. 1*D*-shape high anisotropic conductivity of carbon nanotubes influence EMI-shielding properties. Usage of CNTs along cotton fibres has *SE* of 21.5 dB in *X*-band and 20.8 dB in Ku-band [83].

By adding graphene, *SE* was enhanced [4]. EMI-shielding effectiveness was increased to 55 dB by adding ZnO nanoparticles and *r*GO in a textile coating [85] as desired in most of the shielding applications. Apart from copper, silver nanowires in combination with graphene reached *SE* of 72 dB at 8.2 GHz [90]. Usage of *r*GO sheets with silver nanoparticle coating on a fabric reach *SE* of 27 dB in *X*-band [86]. Combination of CNTs with nickel ferrite ($NiFe_2O_4$) coating on a textile fabric reached *SE* of 84 dB in *X*-band with enhanced structural stability and thermal conductivity [87]. Apart from carbon material and metal fillers' combination, conductive polymers are also used. It is reported that PANI polymerized on CNT improved distribution of CNT on cotton fabrics [88]. Usage of recycled carbon fibres reached *SE* of around 30–70 dB. In a similar way, 73 dB of *SE* with carbon fibre/TPU composite was reported [89].

These are some of the materials and methods reviewed in prepa-

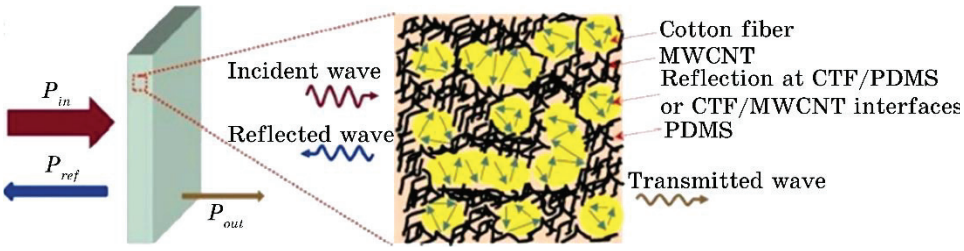

Fig. 6. EMI-shielding mechanism for PDMS/MWCNT-based cotton fabric [84].

ration of fabric textiles, which exhibit EMI shielding. Majority of the assessments were carried out in *X*-band, and a shielding effectiveness of about 30–90 dB was reported. The samples are of thickness below 1 mm. These values correlate with *SE* values of electro spun nanofibre mats [13]. Based on various factors, EMI-shielding fabrics, macroscopic textiles, and nanofibrous mats can be used in variety of applications.

5. CONCLUSIONS AND FUTURE PERSPECTIVES

Smart textiles and research in their area is widely enhancing in view of their EMI-shielding properties. Required physical properties, which include electrical and magnetic conductivity, may be added to regular fabrics by coating with conductive polymers, carbon- or metal-based coatings as well as MXenes. Apart from this, developing of yarns using metal wires or carbon fibres to produce EMI-shielding textile fabrics is of significance. In this review, some of the developments in this area of research were presented. In many cases, 30-dB to 100-dB EMI-shielding effectiveness based on various coatings was observed. Various approaches may be used to obtain high EMI-shielding effectiveness not limited to *X*-band, but also in other frequency ranges.

Future research is mainly focused on investigating more and more materials to dig their inherent properties and tailor them to act as a durable EMI shield. Emphasis should be laid on polymers

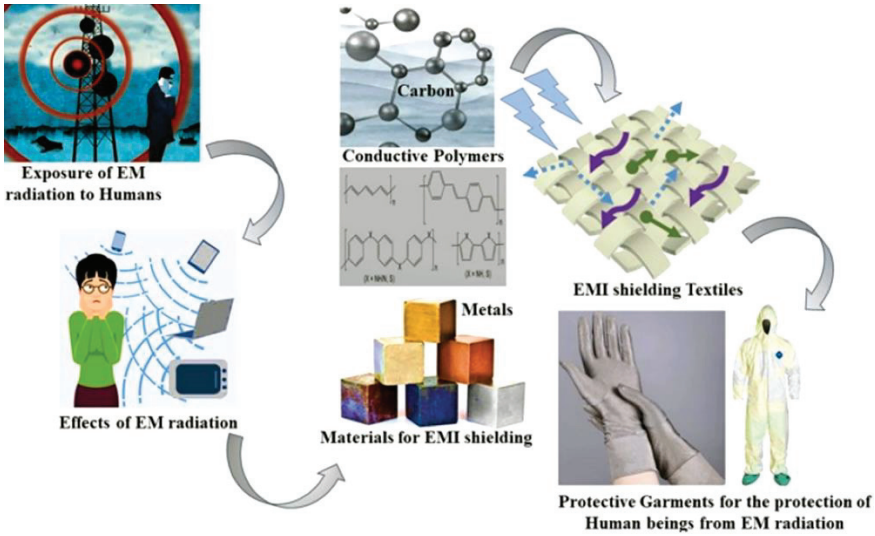

Fig. 7. Schematic representation of future perspectives [4].

and natural chemicals, which suit for EMI shielding. This would be economical and environment friendly. Fabrics should be reusable and could withstand various conditions like stress and strain. Since the effectiveness is reported to decrease with multiple washes, self-cleaning techniques need to be envisaged. In view of the significant potential for development of EMI-shielding fabrics at various work places with different conditions, emphasis need to be towards development of durable, flexible, and lightweight textiles for EMI-shielding applications.

REFERENCES

1. H. Wang, S. N. Li, M. Y. Liu, and Y. Zhou, *Macromol. Mater. Eng.*, **306**: 2100032 (2021); https://doi.org/10.1002/mame.202100032
2. M. Y. Peng and F. X. Qin, *J. Appl. Phys.*, **30**: 225108 (2021); https://doi.org/10.1063/5.0075019
3. Francis Francis, *IEEE Proceeding* (1997), p. 289–293.
4. Saba Akram, Munir Ashraf, Amjed Javid, Hafiz Affan Abid, Sheraz Ahmad, Yasir Nawab, Abher Rasheed, Zhebin Xue, and Anum Nosheen, *Synthetic Metals*, **294**: 117305 (2023); https://doi.org/10.1016/j.synthmet.2023.117305
5. H. T. Guan and D. D. L. Chung, *J. Mater. Sci.*, **56**: 8037 (2021); doi:10.1007/s10853-021-05808-2
6. M. W. Dai, Y. H. Zhai, and Y. Zhang, *Chem. Eng. J.*, **421**: 127749 (2021); https://doi.org/10.1016/j.cej.2020.127749
7. Jan Mocha, Dariusz Wyjcik, and Maciej Surma, *Proc. SPIE,* **1071507**: 1 (2018); doi:10.1117/12.2317672
8. J. H. Wu and D. D. L. Chung, *Carbon*, **40**: 445 (2002); doi:10.1016/S0008-6223(01)00133-6
9. J. S. Roh, Y. S. Chi, and T. J. Kang, *Text. Res. J.*, **78**: 825 (2008); https://doi.org/10.1177/152808371878331
10. S. Ren, S. Guo, X. Liu, and Q. Liu, *IEEE Trans. Magn.*, **52**, No. 10: 9401907 (2016); doi:10.1109/TMAG.2016.2575803
11. T. Blachowicz, A. Ehrmann, M. Malczyk, A. Stasiak, R. Osadnik, R. Paluch, M. Koruszc, J. Pawlyata, K. Lis, and K. Lehrich, *ICECCME Proc.* (2021), p. 1–8; doi:10.1109/ICECCME52200.2021.9591034
12. Y. Y. Yao, S. H. Jin, H. M. Zou, L. J. Li, X. L. Ma, G. Lv, F. Gao, X. J. Lv, and Q. H. Shu, *J. Mater. Sci.*, **56**, No. 11: 6549 (2021); doi:10.1007/s10853-020-05635-x
13. Y. P. Duan, S. H. Liu, and H. T. Guan, *Sci. Technol. Adv. Mater.*, **6**: No. 5: 513 (2005); doi:10.1016/j.stam.2005.01.002
14. R. R. Liang, W. J. Cheng, H. Xiao, M. W. Shi, Z. H. Tang, and N. A. Wang, *Text. Res. J.*, **88**, No. 9: 973 (2018); doi:10.1177/0040517517693980
15. D. D. L. Chung, *Carbon*, **39**: 279 (2001); http://doi.org.S0008-6223(00)00184-6
16. D. Knittel and E. Schollmeyer, *Synthetic Met.*, **159**: 14 (2009); https://doi.org/10.1016/j.synthmet.2009.03.021

17. R. Kacprzyk, *Fibres Text. East. Eur.*, **19**, No. 01: 84 (2011).
18. J. T. Meding, K. Tuvshinbayar, C. Dopke, and F. Tamoue, *Commun. Dev. Assem. Text. Prod.*, **2**: 1 (2021); doi:10.25367/cdatp.2021.2.p49-60
19. A. Schwarz-Pfeiffer, M. Obermann, and M. O. Weber, *IOP Conf. Ser. Mater. Sci. Eng.*, **141**: 01 (2016); doi:10.1088/1757-899X/141/1/012008
20. E. Pakdel, J. F. Wang, S. Kashi, L. Sun, and X. G. Wang, *Adv. Coll. Interf. Sci.*, **277**: 102116 (2020); doi:10.1016/j.cis.2020.102116
21. G. Ehrmann, T. Blachowicz, S. V. Homburg, and A. Ehrmann, *Bioengineering*, **09**: 02 (2022); doi:10.3390/bioengineering9020084
22. V. Schneider, A. Reinholdt, U. Kreibig, T. Weirich, G. Guntherodt, B. Beschoten, A. Tillmanns, H. Krenn, K. Rumpf, and P. Granitzer, *Z. Phys. Chem.*, **220**: 02 (2006); https://doi.org/10.1524/zpch.2006.220.2.173
23. T. Blachowicz, A. Tillmanns, M. Fraune, B. Beschoten, and G. Guntherodt, *Phys. Rev. B*, **75**: 054425 (2007); doi:10.3390/coatings11020122
24. A. Regtmeier, J. Meyer, N. Mill, M. Peter, A. Weddemann, J. Mattay, and A. Hutten, *J. Magn. Magn. Mater.*, **326**: 112 (2013); doi:10.1016/j.jmmm.2012.08.048
25. Liyan Wang, Xiangting Dong, Guangqing Gai, Li Zhao, Shuzhi Xu, and Xinfu Xiao, *J. Nanopart. Res.*, **17**: Article No. 91 (2015); doi:10.1007/s11051-015-2910-z
26. S. Geetha, K. K. S. Kumar, C. R. K. Rao, M. Vijayan, and D. C. Trivedi, *J. Appl. Polym. Sci.*, **112**: 2073 (2009); https://doi.org/10.1002/app.29812
27. M. Naguib, V. N. Mochalin, M. W. Barsoum, and Y. Gogotsi, *Adv. Mater.*, **26**: 7 (2014); doi:10.1002/adma.201304138
28. M. W. Barsoum, *Prog. Solid State Chem.*, **28**: 1 (2000); https://doi.org/10.1016/S0079-6786(00)00006-6
29. A. Sinha, Dhanjai, H. M. Zhao, Y. J. Huang, X. B. Lu, J. P. Chen, and R. Jain, *TrAC Trends Anal. Chem.*, **105**: 424 (2018); doi:10.1016/j.trac.2018.05.021
30. C. Zhang, L. McKeon, M. P. Kremer, S. H. Park, O. Ronan, A. Seral-Ascasco, S. Barwich, C. O. Coileáin, N. McEvoy, H. C. Nerl, B. Anasori, J. N. Coleman, Y. Gogotsi, and V. Nicolosi, *Nat. Commun.*, **10**: 1795 (2019); doi:10.1038/s41467-019-09398-1
31. M. Naguib, O. Mashtalir, J. Carle, V. Presser, J. Lu, L. Hultman, Y. Gogotsi, and M. W. Barsoum, *ACS Nano*, **6**: 2 (2012); doi:10.1021/nn204153h
32. E. Li, Y. M. Pan, C. F. Wang, C. T. Liu, C. Y. Shen, C. F. Pan, and X. H. Liu, *ACS Appl. Mater. Interfaces*, **13**: 24 (2021); doi:10.1021/acsami.1c07976
33. X. H. Zheng, P. Wang, X. S. Zhang, Q. L. Hu, Z. Q. Wang, W. Q. Nie, L. H. Zou, C. L. Li, and X. Han, *Compos. A: Appl. Sci. Manuf.*, **152**: 7 (2022); doi:10.1016/j.compositesa.2021.106700
34. X. S. Zhang, X. F. Wang, Z. W. Lei, L. L. Wang, M. W. Tian, S. F. Zhu, H. Xiao, X. N. Tang, and L. J. Qu, *ACS Appl. Mater. Interfaces*, **12**: 12 (2020); doi:10.1021/acsami.0c01182
35. J. Yu, Z. L. Cui, Y. J. Lu, J. L. Zhao, Y. Zhang, G. Q. Fan, S. Y. Liu, Y. B. He, Y. H. Yu, and D. M. Qi, *Compos. B: Eng.*, **224**: 109193 (2021); doi:10.1016/j.compositesb.2021.109193
36. D. J. Yao, Z. H. Tang, Z. H. Liang, L. Zhang, Q. J. Sun, J. M. Fan,

G. K. Zhong, Q. X. Liu, Y. P. Jiang, X. G. Tang, V. A. L. Roy, and J. Ouyang, *J. Coll. Interface Sci. A*, **630**: 23 (2023); doi:10.1016/j.jcis.2022.09.003
37. S. Uzun, M. K. Han, C. J. Strobel, K. Hantanasirisakul, A. Goad, G. Dion, and Y. Gogotsi, *Carbon*, **174**: 382 (2021); doi:10.1016/j.carbon.2020.12.021
38. Q. W. Wang, H. B. Zhang, J. Liu, S. Zhao, X. Xie, L. X. Liu, R. Yang, N. Koratkar, and Z. Z. Yu, *Adv. Funct. Mater.*, **29**: 07 (2019); doi:10.1002/adfm.201806819
39. J. Li, Y. X. Li, L. Y. Yang, and S. G. Yin, *Adv. Mater. Interfaces*, **9**: 10 (2022); doi:10.1002/admi.202102266
40. L. X. Liu, W. Chen, H. B. Zhang, Q. W. Wang, F. L. Guan, and Z. Z. Yu, *Adv. Funct. Mater.*, **29**: 44 (2019); doi:10.1002/adfm.201905197
41. D. B. Zhang, R. Yin, Y. J. Zheng, Q. M. Li, H. Liu, C. T. Liu, and C. Y. Shen, *Chem. Eng. J.*, **12**: 42 (2022); https://doi.org/10.1021/acsami.0c15134
42. L. X. Liu, W. Chen, H. B. Zhang, Y. Zhang, P. P. Tang, D. Y. Li, Z. M. Deng, L. X, and Z. Z. Yu, *Chem. Eng. J.*, **430**: 02 (2022); doi:10.1016/j.cej.2021.133074
43. L. X. Liu, W. Chen, H. B. Zhang, L. X. Ye, Z. G. Wang, Y. Zhang, P. Min, and Z. Z. Yu, *Nano-Micro Lett.*, **14**: 01 (2022); doi:10.1007/s40820-022-00853-1
44. T. Z. Zhou, Y. Yu, B. He, Z. Wang, T. Xiong, Z. X. Wang, Y. T. Liu, J. W. Xin, M. Qi, H. Zhang, X. Zhou, L. Gao, Q. Cheng, and L. Wei, *Nat. Commun.*, **13**: 01 (2022); doi:10.1038/s41467-022-32361-6
45. J. H. Xiong, H. W. Zheng, R. J. Ding, P. Y. Li, Z. L. Liu, X. Zhao, F. H. Xue, Z. Chen, Q. Yan, Q. Y. Peng, and X. He, *Mater. Des.*, **223**: 111207 (2022); https://doi.org/10.1016/j.matdes.2022.111207
46. X. H. Zheng, J. H. Tang, P. Wang, Z. Wang, L. Zou, and C. Li, *J. Coll. Interface Sci.*, **628**: 994 (2922); doi:10.2139/ssrn.4136044
47. N. F. Mott, *Proc. R. Soc. A*, **153**: 699 (1936); https://doi.org/10.1098/rspa.1936.0031
48. N. Laman and D. Grischkowsky, *Appl. Phys. Lett.*, **93**: 05 (2008); doi:10.1063/1.2968308
49. J. L. Wang, C. H. Lu, and K. Zhang, *Energy Environ. Mater.*, **03**: 01 (2020); doi:10.1002/eem2.12041
50. D. Pani, A. Achilli, and A. Bonfiglio, *Adv. Mater. Technol.*, **03**: 10 (2018); doi:10.1002/admt.201800008
51. Z. N. Wang, H. X. Wang, S. Ji, H. Wang, D. J. L. Brett, and R. F. Wang, *J. Alloy. Comp.*, **814**: 151789 (2020); doi:10.1016/J.JALLCOM.2019.151789
52. A. Ehrmann and T. Blachowicz, *AIMS Mater. Sci. B*, **06**: 02 (2019); doi:10.3934/matersci.2019.2.234
53. S. Hu, D. Wang, A. P. Periyasamy, D. Kremenakova, J. Militky, and M. Tunak, *Polymers*, **13**: 23 (2021); doi:10.3390/polym13234176
54. T. Blachowicz, D. Wojcik, M. Surma, M. Magnuski, G. Ehrmann, and A. Ehrmann, *Fibers,* **11**: 29 (2023): doi:10.3390/fib11030029
55. S. Hu, D. Wang, Y. Kyosev, D. Kremenakova, and J. Militky, *Polym. Test.*, **114**: 107706 (2022); doi:10.1016/j.polymertesting.2022.107706
56. S. W. Hong, S. S. Yoo, J. Y. Lee, and P. J. Yoo, *J. Mater. Chem. C*, **8**: 40 (2020); doi:10.1039/D0TC02483J

57. J. Lee, Y. Liu, Y. Liu, S.-J. Park, M. Park, and H. Y. Kim, *J. Mater. Chem. C*, **5**: 31 (2017); doi:10.1039/C7TC02074K
58. J. Y. Zong, X. J. Zhou, Y. F. Hu, T. B. Yang, D. X. Yan, H. Lin, J. Lei, and Z. M. Li, *Comp. B: Eng.*, **225**: 109299 (2021); doi:10.1016/j.compositesb.2021.109299
59. L. C. Jia, G. Q. Zhang, L. Xu, W. J. Sun, G. J. Zhong, J. Lei, D. X. Yan, and Z. M. Li, *ACS Appl. Mater. Interfaces*, **11**: 1 (2019); doi:10.1021/acsami.8b18459
60. B. Moazzenchi and M. Montazer, *Colloids Surf. A: Physicochem. Eng. Asp.*, **571**: 110 (2019); doi:10.1016/j.colsurfa.2019.03.065
61. J. C. Liu, S. Lin, K. Huang, C. Jia, Q. M. Wang, Z. W. Li, J. N. Song, Z. L. Liu, H. Y. Wang, and M. Lei, *NPJ Flex. Electron.*, **4**: 10 (2020); doi:10.1038/s41528-020-0074-0
62. L. C. Jia, K. Q. Ding, R. J. Ma, H. L. Wang, W. J. Sun, D. X. Yan, B. Li, and Z. M. Li, *Adv. Mater. Technol.*, **04**: 1800503 (2019); doi:10.1002/admt.201800503
63. S. Akram, A. Javid, and M. Ashraf, *Mater. Sci. Eng. B*, **288**: 116159 (2023); doi:10.1016/j.mseb.2022.116159
64. T. Daeneke, K. Khoshmanesh, N. Mahmood, I. A. de Castro, D. Esrafilzadeh, S. J. Barrow, M. D. Dickey, and K. Kalantar-zadeh, *Chem. Soc. Rev.*, **47**: 4073 (2018); doi:10.1039/C7CS00043J
65. Li-Chuan Jia, Xian-Xiang Jia, Wen-Jin Sun, Yun-Peng Zhang, Ling Xu, Ding-Xiang Yan, Hai-Jun Su, and Zhong-Ming Li, *ACS Appl. Mater. Interfaces*, **12**: 47 (2020); doi:10.1021/acsami.0c14397
66. G. Ehrmann and A. Ehrmann, *Encyclopedia,* **01**: 01 (2021); doi:10.3390/encyclopedia1010013
67. O. Atalay, F. Kalaoglu, and S. K. Bahadir, *J. Eng. Fibers Fabr.*, **14**: 01 (2019); doi:10.1177/1558925019856603
68. A. B. Nigusse, D. A. Mengistie, B. Malengier, G. B. Tseghai, and L. Van Langenhove, *Sensors*, **21**: 12 (2021); doi:10.3390/s21124174
69. T. Blachowicz and G. Ehrmann, *Sensors*, **21**: 18 (2021); doi:10.3390/s21186042
70. A. A. Simegnaw, B. Malengier, M. G. Tadesse, and L. van Langenhove, *Materials*, **15**: 8 (2022); doi:10.3390/ma15082892
71. S. J. He, Z. Liu, and H. Y. Wang, *Text. Res. J.*, **93**: 03 (2022); doi:10.1177/0040517522112257
72. V. Rubeziene, A. Abraitiene, J. B. Guzaitiene, S. V. Zuravliova, A. Sankauskaite, Z. Kancleris, P. Ragulis, and G. Slekas, *J. Text. Inst.*, **109**: 03 (2018); doi:10.1080/00405000.2017.1347229
73. E. Mikinka and M. Siwak, *Mater. Today Commun.*, **32**: 2 (2022); doi:10.1016/j.mtcomm.2022.104039
74. K. K. Gupta, S. M. Abbas, and A. C. Abhyankar, *J. Text. Inst.*, **113**: 1862 (2022); doi:10.1080/00405000.2021.1954427
75. J. Krishnasamy, A. Ramasamy, A. Das, and A. Basu, *J. Thermoplast. Comp. Mater.*, **32**: 03 (2018); doi:10.1177/0892705718759389
76. Y. Gao, C. Xie, and Z. J. Zheng, *Adv. Energy Mater.*, **11**: 03 (2021); doi:10.1002/aenm.202002838
77. M. S. Sadi, J. J. Pan, A. C. Xu, D. S. Cheng, G. M. Cai, and X. Wang, *Cellulose*, **26**: 05 (2019); doi:10.1007/s10570-019-02628-1

78. A. Lund, N. M. vander Velden, N. K. Persson, M. M. Hamedi, C. Muller, *Mater. Sci. Eng. R: Rep.*, **126**: 1 (2018); doi:10.1016/j.mser.2018.03.001
79. S. Muller, D. Wieschollek, I. J. Juhasz, E. S. Hellkamp, and A. Ehrmann, *Optik*, **198**: 163243 (2019); doi:10.1016/j.ijleo.2019.163243
80. C. Y. Wang, K. L. Xia, H. M. Wang, X. P. Liang, Z. Yin, and Y. Y. Zhang, *Adv. Mater.*, **31**: 1801072 (2019); doi:10.1002/adma.201801072
81. A. Alaghmandfard, O. Sedighi, N. T. Rezaei, A. A. Abedini, A. M. Khachatourian, M. S. Toprak, and A. Seifalian, *Mater. Sci. Eng. C*, **120**: 111756 (2021); doi:10.1016/j.msec.2020.111756
82. S. K. Tiwari, S. Sahoo, N. Wang, and A. Huczko, *J. Sci. Adv. Mater. Devices*, **05**: 01(2020); doi:10.1016/j.jsamd.2020.01.006
83. B. M. Li, O. Yildiz, A. C. Mills, T. J. Flewwellin, P. D. Bradford, and J. S. Jur, C*arbon*, **168**: 673 (2020); doi:10.1016/j.carbon.2020.06.057
84. J. S. Hu, J. S. Yu, Y. Li, X. Q. Liao, X. W. Yan, and L. Li, *Nanomaterials*, **10**: 04 (2020); https://doi.org/10.3390/nano10040664
85. P. Schal, I. J. Juhasz, N. Grimmelsmann, and A. Ehrmann, *J. Coat. Technol. Res.*, **15**: 04 (2018); doi:10.1007/s11998-017-0024-5
86. Y. C. Li, X. R. Huang, L. J. Zeng, R. F. Li, H. F. Tian, X. W. Fu, Y. Wang, and W. H. Zhong, *J. Mater. Sci.*, **54**: 12 (2019); doi:10.1007/s10853-018-3006-9
87. Jie Li, Yan-Jun Tan, Yi-Fu Chen, Hong Wu, Shaoyun Guo, and Ming Wang, *Appl. Surf. Sci.*, **466**: 657 (2019); doi:10.1016/j.apsusc.2018.10.079
88. C. T. Lan, M. Guo, C. L. Li, Y. P. Qiu, Y. Ma, and J. Q. Sun, *ACS Appl. Mater. Interfaces*, **12**: 7477 (2020); doi:10.1021/acsami.9b21698
89. S. Gupta, C. Chang, A. K. Anbalagan, C. H. Lee, and N. H. Tai, *Compos. Sci. Technol.*, **188**: 107994 (2020); doi:10.1016/j.compscitech.2020.107994

Наносистеми, наноматеріали, нанотехнології
Nanosistemi, Nanomateriali, Nanotehnologii
2025, т. 23, № 2, сс. 515–521
https://doi.org/10.15407/nnn.23.02.0515

© 2025 ІМФ (Інститут металофізики
ім. Г. В. Курдюмова НАН України)
Надруковано в Україні.

PACS numbers: 07.60.Rd, 78.20.Ci, 78.40.Fy, 78.67.Bf, 79.20.Eb, 81.16.Mk, 82.70.Dd

Study of Characteristics of Semiconductor GaAs Nanoparticles Prepared by Laser Ablation Method

Atyaf S. Al Rawas[1], Enas G. Yonis[1], and A. J. Jarjees Alsoofy[2]

[1]*College of the Dentistry,*
Department of the Basic Science,
Mosul University,
Mosul, Iraq
[2]*College of Science,*
Department of Physics,
Mosul University,
Mosul, Iraq

Gallium arsenide GaAs nanoparticles are prepared in water using laser ablation method. The optical properties and energy gap of the colloidal solution are investigated using UV-visible spectrometer; the absorption peaks are observed between 200 and 300 nm wavelength, and the energy gap is calculated of about 1.86 eV. Zeta potential value is of about –22.18 mV that gives the impression of acceptable stability of the colloidal solution.

Наночастинки арсеніду Ґалію GaAs було одержані у воді методом лазерної абляції. Оптичні властивості й енергетичну заборонену зону колоїдного розчину було досліджено за допомогою УФ-оптичного спектрометра; піки вбирання було спостережено в діяпазоні довжин хвиль від 200 до 300 нм, а енергетичну заборонену зону було розраховано приблизно у 1,86 еВ. Значення дзета-потенціялу становило приблизно –22,18 мВ, що створює враження прийнятної стабільности колоїдного розчину.

Key words: gallium arsenide GaAs, laser ablation, zeta potential, optical properties of GaAs.

Ключові слова: арсенід Ґалію GaAs, лазерна абляція, дзета-потенціял, оптичні властивості GaAs.

(Received 12 February, 2024; in revised form, 27 February, 2024)

1. INTRODUCTION

Studying the optical properties of the semiconductors gives a clear indication to determine the nature of the use of a substance semiconductor, and to understand the mechanism of electronic transfers between energy bands by measuring the absorption of radiation by the semiconductor and its transmittance. All semiconducting materials share an important and distinctive feature in a scheme of absorption, which is the increase in absorbance when the absorbed radiation energy becomes equal to the gap energy and this point has been called the fundamental absorption edge [1].

Progress in solid-state physics has been characterized by a shift in dealing with large crystals to dealing with small crystals that are characterized by the length of at least one of their dimensions being within the range (100–1 nm). The change in dimensions affects the properties of the electron in the semiconductor, such as the Broglie wavelength and the wave behaviour of the particle; particles behave wave-like. In addition, the decrease in the size of the crystals leads to a greater separation of the energy levels and an increase in the effective energy gap, which leads to the appearance new physical properties due to quantum effects such as quantum Hall effects, quantum conductance oscillations [2, 3].

Nanotechnology is any technology that is accomplished on a nanometer scale and has many applications. Nanotechnology includes the production and application of physical, chemical, and life (biological) systems on a scale that extends from a single atom or molecules to dimensions of a fraction of a micron, as well as the integration of the resulting nanostructures into systems [4].

The process of manufacturing materials on the nanoscale can be done in two ways, the first is self-assembly, or called a bottom-up approach, in which nanomaterial are built atom by atom (atom-by-atom), the second method is called top-down approach, in which materials are sculpted to obtain their nanosize [5, 6].

The concept of the assembly method was derived from natural biological processes where molecules combine to form a more complex compound with nanoscopic dimensions. In this method, the secondary units assemble and organize into a final structure characterized by the lowest possible free energy, and this process is directed according to the properties of the secondary units. The nanostructure or microstructure can be obtained from one or more building components. For example, the superlattice resulting from the assembly of magnetic and semiconducting nanoparticles, in which the nanocrystal contains two construction components and is characterized by specifications, which differ from the properties of separate universes, as seen in Fig. 1 [3, 7].

2. EXPERIMENTAL METHOD

Laser ablation method has been used to prepare GaAs nanoparticles. The nanoparticles have been extracted from GaAs plate immersed in water and using Nd:YAG laser with 1064-nm wavelength, 1.32 J/cm^2, 8-cm lens' length and 5-min. ablation time.

The extracted GaAs nanoparticles were predicated in the water as shown in Fig. 2.

The water colour was changed to a light brown colloidal solution of GaAs nanoparticles as shown in Fig. 3.

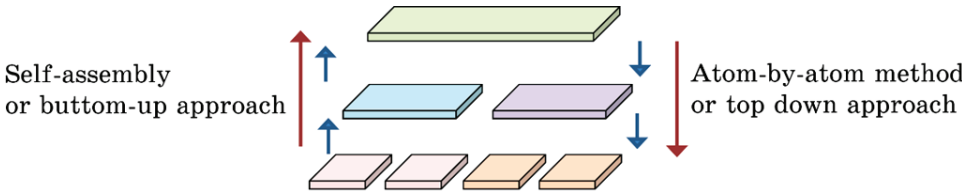

Fig. 1. Manufacturing materials on the nanoscale methods.

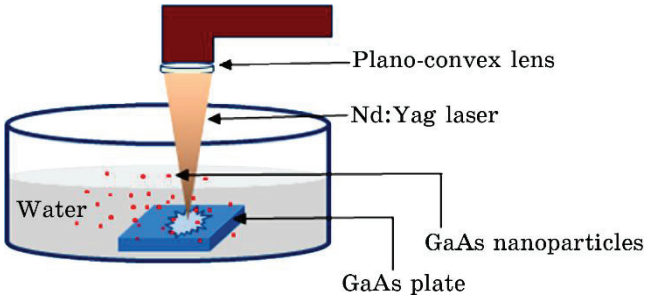

Fig. 2. Laser ablation method.

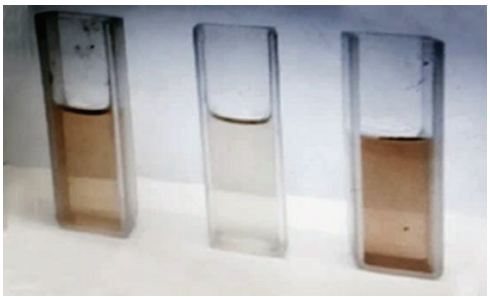

Fig. 3. Light brown colloidal solution of GaAs nanoparticles.

3. RESULTS AND DISCUSSION

The transmittance of GaAs has been examined using UV-visible spectroscopy.

The transmittance of the particles increases with wavelength and stabilizes approximately between 60% and 75% over the wavelength range 800–1000 nm (Fig. 4). The absorbance and reflectance spectrums are determined using Ref. [8] as follow:

$$A = \ln(1/T), \tag{1}$$

$$R + A + T = 1. \tag{2}$$

The absorbance show several peaks within the range 200–300 nm, which belong to the GaAs nanoparticles [9]. The reflectance also varied with wavelength as shown in Fig. 4, *c*.

The optical constants n, k, and absorption coefficient have been deduced from the optical properties using Eqs. (3), (4) and (5), respectively, and showed a clear variation with wavelength as shown in Fig. 5 [10–12]:

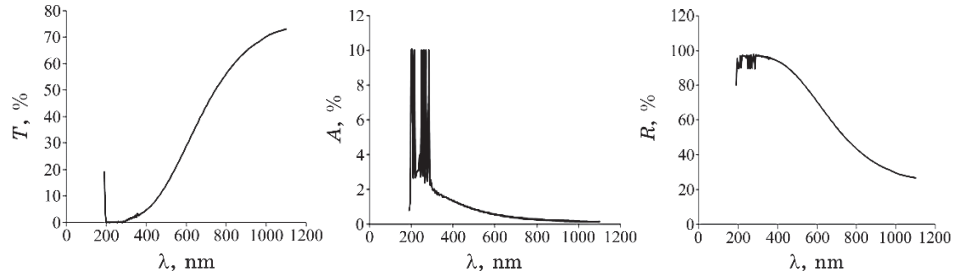

Fig. 4. Transmittance, absorbance, and reflectance of GaAs nanoparticles *versus* wavelength.

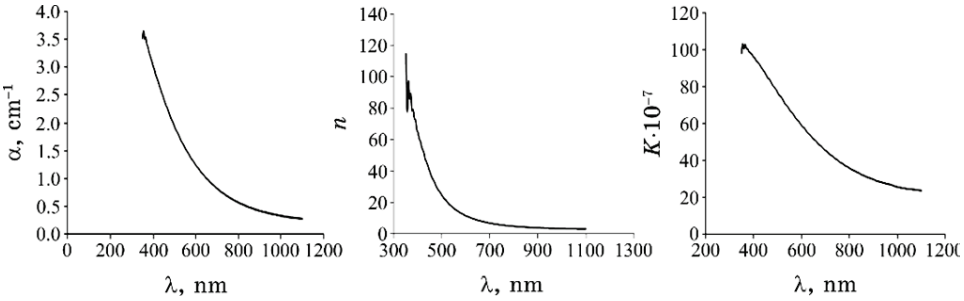

Fig. 5. Absorption coefficient, refractive index, and extinction coefficient of GaAs nanoparticles *versus* wavelength.

$$n_0 = (1+R)/(1-R) + \sqrt{4R/(1-R)^2 - k_0^2}\,, \tag{3}$$

$$k_0 = \alpha\lambda/(4\pi)\,, \tag{4}$$

$$\alpha = 2.303A/t. \tag{5}$$

where α is the absorption coefficient, A is the absorbance and t is the film thickness.

The energy gap of GaAs nanoparticles was also investigated by drawing the relation between the square of the absorption coefficient multiplied by the energy $(\alpha h\nu)^2$ [$(\text{eV/cm})^2$] and the photon energy E [eV], where the tangent to the curve showed that the energy gap of the GaAs nanoparticles of about 1.86 eV (Fig. 6).

One of the most important properties of colloidal solutions is stability, and this property is measured by examining the zeta potential. The stability of the colloidal solutions increases with the increases in the zeta potential. Figure 7 shows that the zeta potential value is of around –22.01 mV that reflects acceptable stability for

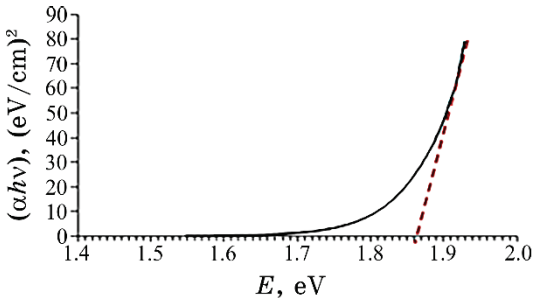

Fig. 6. The energy gap of GaAs nanoparticles *versus* wavelength.

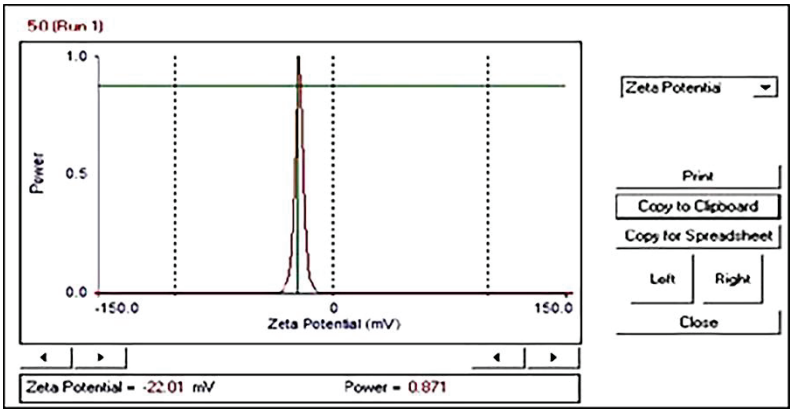

Fig. 7. Zeta potential of GaAs nanoparticles.

the colloidal solution of GaAs nanoparticles [13].

4. CONCLUSION

Gallium arsenide GaAs nanoparticles have been prepared in water using Laser ablation method, the transmittance of the particles show good transmittance of about 60–75% over the wavelength range 800–1000 nm. The absorbance, reflectance, refractive index and extinction coefficient were varied with wavelength. The energy gap was calculated of about 1.86 eV; finally, the zeta potential value was of –22.18 mV.

ACKNOWLEDGMENT

We extend our sincere thanks to the College of Dentistry and the University of Mosul for their continued support in completing the research.

REFERENCES

1. J. Kleperis, J. Zubkans, and A. R. Lusis, *Optical Organic and Semiconductor Inorganic Materials*, **2968**: 186 (1997); https://doi.org/10.1117/12.266832
2. S. Bayda, M. Adeel, T. Tuccinardi, M. Cordani, and F. Rizzolio, *Molecules*, **25**, Iss. 1: 112 (2020); https://doi.org/10.3390/molecules25010112
3. D. Sundaram, V. Yang, and R. A. Yetter, *Progress in Energy and Combustion Science*, **61**: 293 (2017); https://doi.org/10.1016/j.pecs.2017.02.002
4. J. Zhang, M. Terrones, C. R. Park, R. Mukherjee, M. Monthioux, N. Koratkar, and A. Bianco, *Carbon*, **98**, Iss. 70: 708 (2016); https://doi.org/10.1016/j.carbon.2015.11.060
5. P. A. Patil, S. Dalvi, V. Dhaygude, and S. D. Shete, *Indo Global Journal of Pharmaceutical Sciences*, **12**: 183 (2022); https://doi.org/10.35652/IGJPS.2022.12022
6. M. Kichu, T. Malewska, K. Akter, I. Imchen, D. Harrington, J. Kohen, and J. F. Jamie, *Journal of Ethnopharmacology*, **166**: 5 (2015); https://doi.org/10.1016/j.jep.2015.02.053
7. A. Ramazan and H. Misak, *Journal of Nano Education*, **3**, Iss. 1–2: 13 (2011); https://doi.org/10.1166/jne.2011.1012
8. L. M. Abduljabbar, *Iraqi Journal of Laser*, **13**: 29 (2014); https://doi.org/10.31900/ijl.v13iA.71
9. T. Sharifi, D. Dorranian, and M. J. Torkamany, *Journal of Experimental Nanoscience*, **8**, Iss. 6: 808 (2013); https://doi.org/10.1080/17458080.2011.608729
10. K. Satoh, Y. Kakehi, A. Okamoto, S. Murakami, K. Moriwaki, and T. Yotsuya, *Thin Solid Films*, **516**, Iss. 17: 5814 (2008); https://doi.org/10.1016/j.tsf.2007.10.055
11. T. Amakali, L. S. Daniel, V. Uahengo, N. Y. Dzade, and N. H. de Leeuw,

Crystals, **10**: 132 (2020); https://doi.org/10.3390/cryst10020132
12. R. H. AL-Saqa and I. K. Jassim, *Digest Journal of Nanomaterials & Biostructures*, **18**, No. 1: 165 (2022); https://doi.org/10.15251/DJNB.2023.181.165
13. S. Ajith, F. Almomani, A. Elhissi, and G. Husseini, *Helyion*, **20**, Iss. 9: 1 (2023); https://doi.org/10.1016/j.heliyon.2023.e21227

Наносистеми, наноматеріали, нанотехнології
Nanosistemi, Nanomateriali, Nanotehnologii
2025, т. 23, № 2, сс. 523–538
https://doi.org/10.15407/nnn.23.02.0523

© 2025 ІМФ (Інститут металофізики
ім. Г. В. Курдюмова НАН України)
Надруковано в Україні.

PACS numbers: 61.05.cp, 61.46.Df, 68.37.Hk, 78.30.Hv, 78.67.Bf, 81.07.Dc, 81.40.Ef

Synthesis and Characterization of CuO Nanoparticles: Effect of Rapid Thermal Annealing

Kenza Almi, Said Lakel, Maria Nor Elyakin Boumezrag, and Hanna Touhami

Laboratory of Metallic and Semiconducting Materials,
University of Biskra,
Biskra, Algeria

This work is a comparative study of the effect of two different annealing methods on the copper-oxide (CuO) nanoparticles' properties. These later are synthesized using the direct precipitation method. Rapid thermal annealing (RTA) and slow thermal annealing (STA) are two methods of annealing tested. The prepared samples are annealed in air at various temperatures of 300, 400, 500°C for 1 hour. Then, they are characterized by employing scanning electron microscopy (SEM), x-ray diffraction (XRD), UV–visible and Fourier Transform Infrared (FT-IR) spectroscopies. The main results revealed an increase in the grain size with both methods as the annealing temperature increases. It reaches 30.93 nm with RTA and 26.75 nm with STA at 500°C. XRD spectra show, in the case of RTA at 500°C, a significant decrease in the intense picks corresponding to the (002) and (111) orientations. This result indicates that, beyond 400°C, one hour of RTA is not suitable for enhancing CuO-nanoparticles' crystallinity compared to STA. The optical analysis demonstrates that the energy of the optical band gap in STA is higher than that in RTA. It reaches 2.88 eV at 500°C using RTA that is close to the gap value for CuO in the range of 1.8–2.8 eV. FT-IR results show, for both methods, the presence of characteristic peaks of the Cu–O bonds in the monoclinic CuO structure without any trace to Cu_2O structure. Nevertheless, samples subject to RTA for one hour are more susceptible to absorbing species of C=O bond than those subject to STA. Hence, RTA at 500°C is far from producing CuO nanoparticles with preferred characteristics. It needs further research to examine higher-temperature annealing with controlling annealing time.

Ця робота є порівняльним дослідженням впливу двох різних методів відпалювання на властивості наночастинок оксиду Купруму (CuO). Пізніше їх було синтезовано методом прямого осадження. Було протестовано два методи відпалювання: швидке термічне відпалювання (ШТВ) та повільне термічне відпалювання (ПТВ). Підготовлені зразки відпалюва-

ли на повітрі за різних температур у 300, 400, 500°C упродовж 1 години. Потім їх характеризували за допомогою сканувальної електронної мікроскопії (SEM), рентґенівської дифракції (XRD), УФ-оптичної спектроскопії та інфрачервоної спектроскопії з Фур'є-перетвором (FT-IR). Основні результати показали збільшення розміру зерен за обома методами з підвищенням температури відпалу. Він сягає 30,93 нм із ШТВ і 26,75 нм із ПТВ за 500°C. Рентґенівські дифракційні спектри показали у випадку ШТВ за 500°C значне зменшення інтенсивних піків, що відповідають орієнтаціям (002) й (111). Цей результат показав, що понад 400°C одна година ШТВ не підходить для підвищення кристалічности наночастинок CuO порівняно з ПТВ. Оптична аналіза показала, що енергія оптичної забороненої зони за ПТВ вища, ніж за ШТВ. Вона сягає 2,88 еВ за 500°C з використанням ШТВ, що близько до значення забороненої зони CuO в діяпазоні 1,8–2,8 еВ. Результати FT-IR показали для обох методів наявність характерних піків від зв'язків Cu–O у моноклінній структурі CuO без будь-яких слідів структури Cu_2O. Тим не менш, зразки, піддані ШТВ протягом однієї години, більш схильні до поглинання частинок зі зв'язками C=O, ніж зразки, піддані ПТВ. Отже, ШТВ за 500°C є далеким від утворення наночастинок CuO з бажаними характеристиками. Є потреба у подальших досліджень для вивчення відпалу за вищої температури з контролем часу відпалювання.

Key words: annealing methods, copper oxide, nanoparticles, nanoparticles' synthesis methods, rapid thermal annealing.

Ключові слова: методи відпалювання, оксид Купруму, наночастинки, методи синтези наночастинок, швидке термічне відпалювання.

(Received 24 December, 2023; in revised form, 27 December, 2023)

1. INTRODUCTION

Nanoparticles are particles of matter, whose properties are quite different from those of the corresponding bulk material [1]. Their properties depend on their size, shape, and morphology [2–4]. Thus, the main advantage of nanomaterials is that they can be used to improve current materials or create new ones having exceptional properties.

Copper oxide in its nanostructure attracts considerable attention because of its outstanding properties. It is non-toxic, its constituents are available in abundance, it is a good solar absorber [5], a good electrical conductor [6], and it is stable at high pressure and temperature [7]. The enhancement in these properties can be influenced by the morphology of its nanostructures, which in turn depends on the process of synthesis [3, 6, 8, 9].

The thermal annealing process is an important step in synthesizing nanostructures of a metal oxide including copper oxide. There

are two techniques of thermal annealing, which are slow thermal annealing (STA) and rapid thermal annealing (RTA). The influence of these kinds of annealing on the physical properties of copper oxide in the form of thin-film nanostructure is the most commonly studied by researchers [10–15]. This may be due to the diverse applications possible of this kind of nanostructure [6, 16, 17]. Some of them confirmed the efficient impact of STA in an optimum annealing-temperature range of 200–650°C on structural and electrical properties of thin copper-oxide films [10–12, 18–22], and others demonstrated that RTA is an effective and efficient technique to enhance the structural properties in a high annealing-temperature range from 400°C to 800°C for a tuning time corresponding to each temperature [13–15, 23].

Nevertheless, several studies showed the effective implementation of copper oxide in form of nanoparticle structure to produce materials for environment, energy [24–33], and therapeutics [34–38]; annealing process in operation represents an important step in synthesising copper oxide [39, 40]. There are only a few reports studied the effects of annealing temperature in the case of copper-oxide nanoparticles [24, 40, 41]. Yet, in all previous research, the annealing process was performed in different conditions, which are specific to each experimental work, and they in turn may influence the obtained results. No study was conducted so far that reported the results of the effect of the rapid and slow thermal annealing processes performed under the same experimental conditions to conclude the efficiency of one annealing method relative to the other.

Therefore, this work aims to examine the efficient effect of rapid annealing on the physical properties of copper-oxide nanoparticles compared to the slow annealing process.

2. MATERIALS AND METHODS

2.1. CuO-Nanoparticles' Synthesis

CuO nanoparticles were synthesized using the sol–gel method through the following process. 2 g of $CuSO_4 \cdot 5H_2O$ is dissolved in 20 ml of distilled water. On the other hand, 8 g of NaOH has been dissolved in 200 ml of the same solvent. Each solution is stirred separately for a few minutes at room temperature to obtain two homogenous solutions of 0.4 mol/l and 1 mol/l, respectively. Sodium hydroxide solution is completely added to the first solution of cupric sulphate and then stirred for one hour on a heating plate set at 100°C. The solution is then left to cool at room temperature; then, it is filtered to get a black powder. This later is carefully collected and dried in an oven for an hour at 100°C to evaporate all residual

solvents on the substrate surface. After that, it was milled using a ceramic mortar. Thus, copper-oxide nanoparticles are obtained.

2.2. Specimen Preparation

After synthesizing CuO nanoparticles, they were divided into two portions. From the first portion, three fractions were prepared to undergo a rapid heat annealing at 300°C, 400°C, and 500°C for one hour. In the same way, three other fractions were prepared from the second portion, but this time to undergo a slow heat annealing at the same temperatures and during the same time. In both annealing processes, a Nabertherm GmbH annealing furnace was used. It is an electrically heated furnace that heats from 30 to 3000°C.

In STA, the sample is heated gradually in the oven from room temperature to the target temperature with a heating rate of 2°C per minute. Once the set temperature is reached, heating maintains it constant for one hour; then, it automatically stops heating allowing gradual cooling of the sample. Whereas in the case of the RTA, the sample is heated directly at the desired temperature for one hour; then, it is immediately removed from the oven and cooled at room temperature. To do so, the sample is put in a special glass tube, which is brought in through a hole drilled in the back of the oven made to evacuate the vapour produced during heating.

After heat treatment, different specimens were subdivided into small amounts to be characterized.

2.3. Specimen Characterization

To determine the nanoparticles' size and shape, a morphological study was conducted using a scanning electron microscope of TESCAN-VEG03 type. Magnification of 5 μm has been used. Structural properties were studied using Rigaku Mini Flax 600 x-ray diffractometer (CuK_α radiation, $\lambda = 1.54056$ Å); x-ray diffraction patterns were set between $2\theta = 20°$ and 80° with a step of 0.5° per minute. In this intention, infrared spectrophotometry (FT-IR-8400S) was used as well. Optical properties were analyzed employing a UV–visible spectrophotometer (Perkin Elmer-Lambda 25); the spectral range was measured between 200 and 800 nm.

3. RESULTS AND DISCUSSION

3.1. Morphological Analysis

SEM images of the surface morphology of the prepared CuO

nanoparticles are presented in Fig. 1. They show that most CuO nanoparticles have a sheet-like shape. The same result was found in the literature using the same synthesizing method [41]. Actually, sheet average particle size varies in a broad range in this structure; so, it is not practical for easy to measure the particle size of our samples. Nevertheless, SEM results reveal some distinctions between the morphology of the RTA and STA samples annealed at different temperatures. RTA images at different temperatures show an inhomogeneous distribution of the nanoparticles with large conglomerates compared to STA samples [10]. This could be justified by the grain growth mechanism correlated to rapid thermal annealing [42, 43]. The fast ramping to the target temperature triggers the nucleation process within the short time; a higher temperature generates high pressure, which promotes the mutual diffusion of small and intermediate grains during annealing, resulting in larger agglomerates [10, 44].

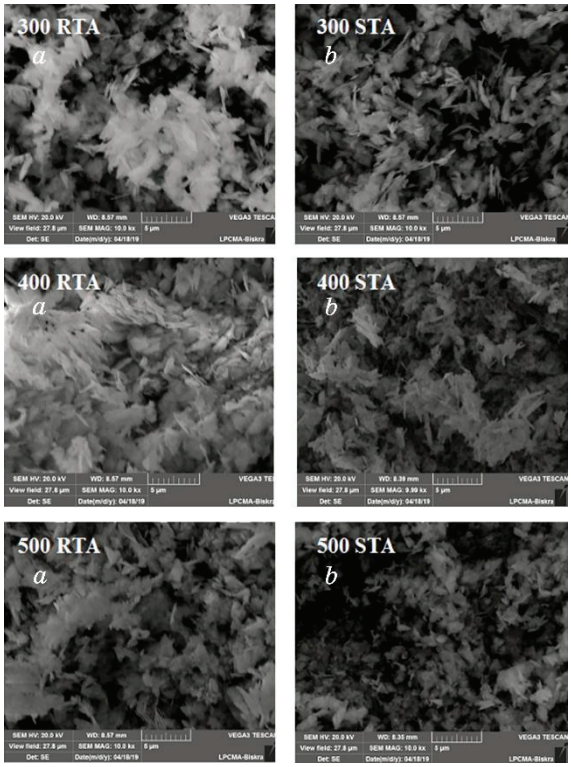

Fig. 1. SEM images of the CuO nanoparticles synthesized using (*a*) RTA and (*b*) STA at 300°C, 400°C, and 500°C for one hour of annealing.

3.2. Structural Analysis

The x-ray diffractograms of the prepared CuO nanoparticles are presented in Fig. 2. The results show that the peaks in all obtained XRD spectra are well matched with the monoclinic phase of CuO crystals (JCPDS card No. 080-1268). All samples exhibit the same preferential orientations, (111) and (002), which agree with research on copper-oxide nanoparticles [8, 9]. X-ray diffractograms' analysis demonstrates that, in both methods, the diffracted intensity of the most intense peaks increases with the increase of the temperature except for the case of RTA at 500°C, where it decreases significantly as depicted in Fig. 3, *a*, *b*. It is also noticeable that STA peaks are more intense than RTA peaks at all positions and almost at all the studied annealing temperatures (Fig. 2).

Further, Table 1 indicates that the crystallite size calculated in both techniques of annealing increases with the increase of the temperature, but it takes higher values in RTA cases.

To explain those observations, it is necessary to return to the factors associated with both peak intensity and crystallite size. Thermal treatment increases the crystalline nature, which leads to an increase in the number of grains orientated in a particular direction. By increasing the annealing temperature, many different grains of the same orientation coalesce together and form a large

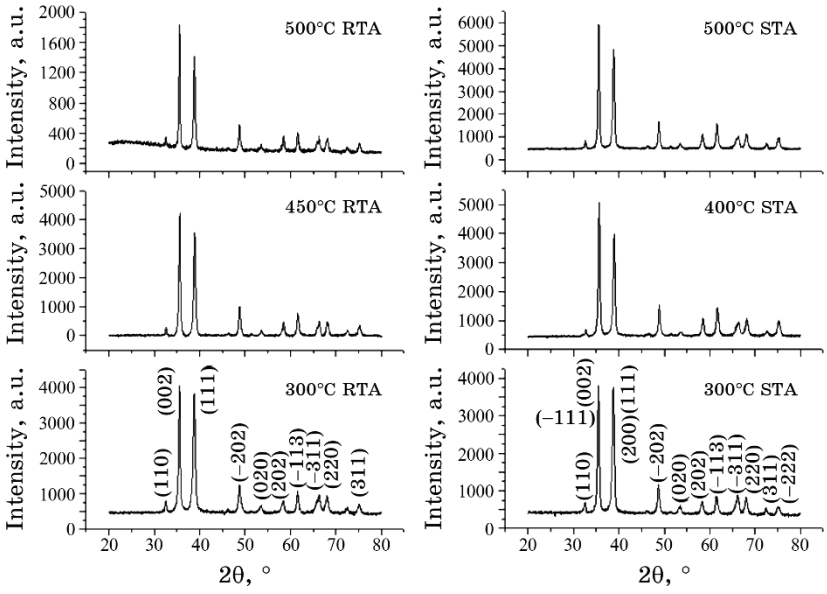

Fig. 2. XRD patterns of CuO nanoparticles prepared with RTA and STA at 300°C, 400°C, 500°C for one hour of annealing.

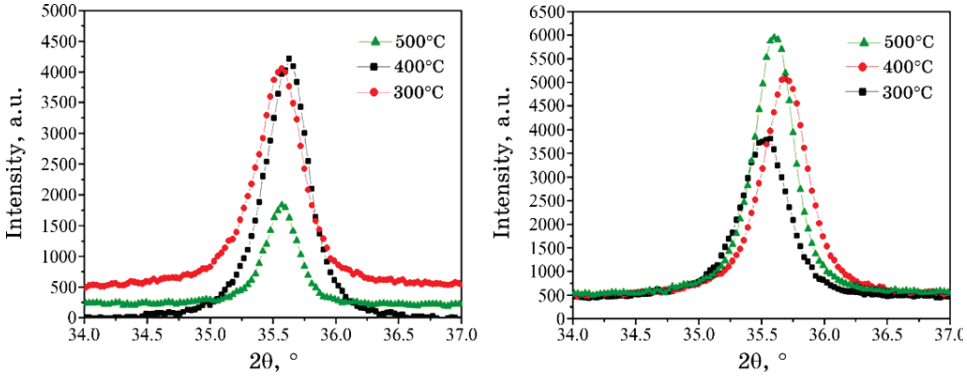

Fig. 3. The predominant peak corresponding to the (002) orientation as a function of annealing temperature and method: (*a*) RTA case; (*b*) STA case.

TABLE 1. Structural properties of CuO nanoparticles annealed following two methods.

Annealing method	STA			RTA		
Annealing temperature T, °C	300	400	500	300	400	500
Crystallite size D, nm	22.28	23.48	26.75	22.36	24.22	30.93
Strain $\varepsilon \cdot 10^{-2}$, %	0.146	0.141	0.120	0.139	0.133	0,099
Dislocation density $\delta \cdot 10^{-2}$, nm^{-2}	0.201	0.181	0.139	0,200	0.170	0.104

grain having a certain orientation. Therefore, the diffracted intensity is supposed to be increased as the crystallite size increases as in the case with STA samples. In contrast, RTA spectrum measured at 500°C revealed a significant decrease in the intensity even though the crystallite size increased at that temperature. This proves that texture may change during grain growth and affects the kinetics in the process of rapid annealing [45].

This could be justified by the fact that the rapid annealing process at high temperature (above 400°C) for one hour can favour the crystallization process, but, at the same time, may produce microcracks in the growing grains after sudden cooling from high temperature to room temperature [46, 47]. These microcracks can scatter x-rays in different directions, thereby changing the texture and reducing the peak intensity in a particular direction as indicated in Fig. 3, *a*, as it can be attributed to the grain recrystallization in contrast to recovery behaviour, which occurs in the case of RTA at relatively high temperatures [46, 47]. Recrystallization results in the formation of new grain orientations that explains the reduction of the peak intensity, and the recovery occurs during the incubation

period for recrystallization [47] that, on the other hand, explains why the grain size did not decrease. Peak intensity can increase again, when the recrystallization is completed, and this depends on both the annealing time and temperature [45–49].

For this reason, further study is required to be conducted about the effect of rapid thermal-annealing time and temperature.

The high intensity of STA peaks compared to RTA peaks may be explained by the difference in the crystal structure factor of the samples. It is known that the diffracted intensity in a particular direction is proportional to the square of the structure factor modulus. This latter reflects the total scattering from each crystal plane and depends on the distribution of atoms in the crystal structure. In other words, it is related to both the crystal structure and composition. Therefore, the peak intensity is affected by the thermal perturbation of the atoms and, more generally, by the disorder. Atoms, which have undergone rapid heating, are perturbed and susceptible to disorders more than those undergone slow heating. The latter has time to return to its equilibrium state; this leads to a low state of disorder and high diffracted intensity.

In addition, Figure 3 shows that, by increasing temperature, curves shift towards increasing θ in both methods, especially, in the STA method; this means that the nanoparticles have undergone compressive stress. This can be explained by the merging process induced by increasing thermal annealing, and this, in turn, enlarges the grain size [10, 42].

The crystalline size increases from 19.99 to 31.47 nm for temperatures from 350 to 550°C. This can be explained by the merging process induced by thermal annealing.

Table displays the calculated values of compressive stress and dislocation density (δ), where δ is determined, based on the crystallite size (D), using the formula [50]

$$\delta = D^{-2}, \tag{1}$$

whereas the microstrain values were determined using the following formula [50]:

$$\varepsilon = \frac{\beta \cos \theta}{4}. \tag{2}$$

As illustrated in Table, the dislocation density and the compressive stress values decrease as the temperature increases in both techniques of annealing. The decrease is slightly higher in RTA than in STA. The increase in the temperature stimulates the kinetics and the interactions of the dislocations. This leads to an increase in the migration and annihilation of the dislocation and, conse-

quently, to a decrease in their density.

However, rapid thermal annealing enhances the concentration of the vacancies in the lattice arrangement, which, in turn, increases the velocity of dislocation glide motion. Therefore, the dislocation density is reduced more effectively in rapid thermal annealing than in slow thermal annealing. This behaviour can also be attributed to the grain boundary effects. It is known that dislocation density, stress, and grain-boundary size are interrelated [51]. Grain boundaries contribute to the strain-hardening phenomenon in metals. They block the continued movement of dislocations in the metal during straining. As more dislocations become blocked, the metal becomes more difficult to deform. That is probably what happened in the case of the RTA, in which crystallite size takes higher values than those in STA, thereby, higher values of boundary size and lower values of stress.

3.3. Optical Analysis

The optical band-gap energy (E_g) for CuO nanoparticles was estimated employing the absorption spectrum fitting method (ASF) [52]. In this method, the optical band gap can be calculated using only the absorbance spectrum without any need for thickness. It is based on the following equation [52]:

$$A = B_1\lambda\left(\frac{1}{\lambda} - \frac{1}{\lambda_g}\right)^m + B_2, \tag{3}$$

where A is the absorbance, λ is the wavelength, B_1 and B_2 are independent on λ, m takes the value of $1/2$ for the best fitting.

Thus, the value of the band gap is obtained from $1/\lambda_g$, where E_g is equal to $1240°/\lambda_g$. The value of λ_g can be determined by extrapolating the straight line of $(A/\lambda)^2$ *versus* $1/\lambda$ curves, shown in Fig. 4, at $(A/\lambda)^2 = 0$. Table 2 displays the variation in the optical gap as a function of the annealing temperature. It can be noticed that the optical gap decreased by increasing the annealing temperature in the two cases of the annealing method.

However, the RTA method yielded lower values of the energy gap, especially, at 500°C (Fig. 5). This may be justified by the fact that the increase in particle size decreases the optical gap according to the potential-well quantum theory, *i.e.*, the quantum confinement in nanometer particle-size materials. This result confirms what is mentioned above (Fig. 1): the particle size for RTA is larger than the particle size for STA.

On the other hand, to understand better the effect of two types

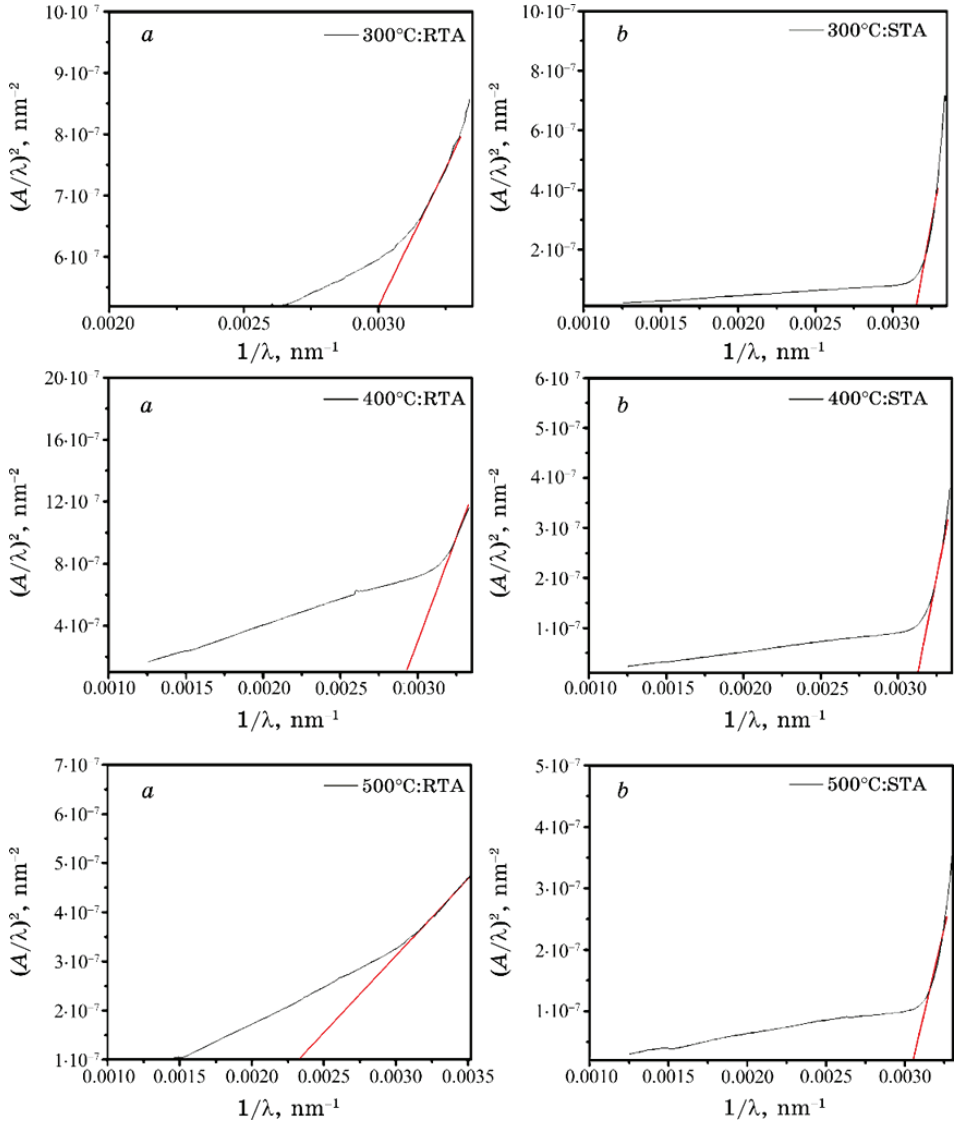

Fig. 4. ASF diagrams for samples prepared using (*a*) RTA and (*b*) STA annealing methods at 300°C, 400°C, 500°C for one hour of annealing.

of annealing processes on the structure of copper oxide, an infrared absorption bands analysis was done.

FT-IR spectra of all the samples are presented in Fig. 6. All samples' spectra show a wide band located at around 3440 cm^{-1} that corresponds to the O–H-group stretching of a water molecule adsorbed on the oxide surface [53], and an intense peak located at

TABLE 2. Energy-gap values calculated using two methods of annealing at different temperatures.

Annealing temperature T, °C	300	400	500
RTA: E_g, eV	3.72	3.63	2.88
STA: E_g, eV	3.91	3.87	3.79

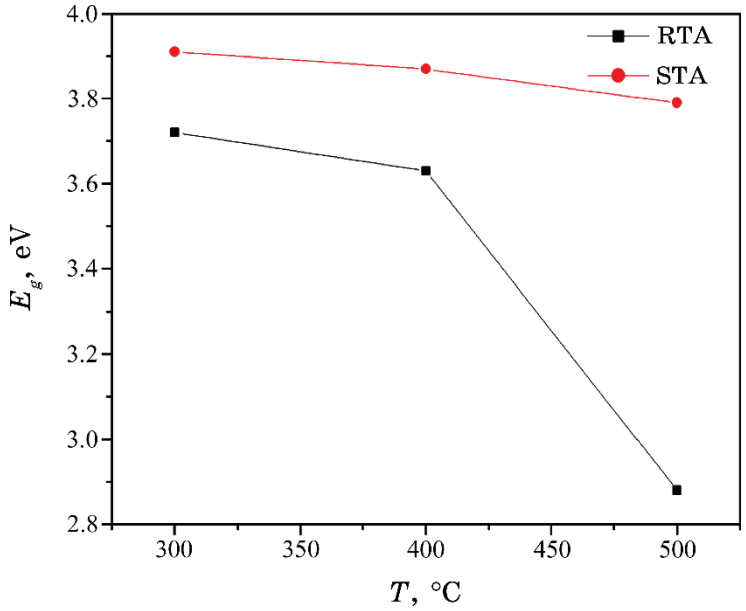

Fig. 5. Optical band-gap energy of the prepared CuO nanoparticles as a function of annealing temperature following two methods: RTA and STA for one hour of annealing.

1384 cm^{-1}, which is attributed to the stretching vibration of C=O group indicating the presence of absorbed species in the surface of nanoparticles [53, 54]. Another intense peak at around 613 cm^{-1} is attributed to the Cu–OH-vibration bands [54]; but the most intense absorption bands are located at around 494 cm^{-1} and 504 m^{-1}; it is assigned to the stretching vibrations of Cu–O indicating the formation of copper oxide [55].

It is noticed that, by increasing the annealing temperature, Cu–O-bond concentration increased and Cu–OH-bond concentration decreased, especially, in the case of RTA. However, the decrease of O–H- and C=O-bonds' concentrations is noticed in the case of STA, particularly, at 500°C, where the O–H group disappears. This means that 500°C is not sufficient to remove all residues and impurities in RTA more than in STA.

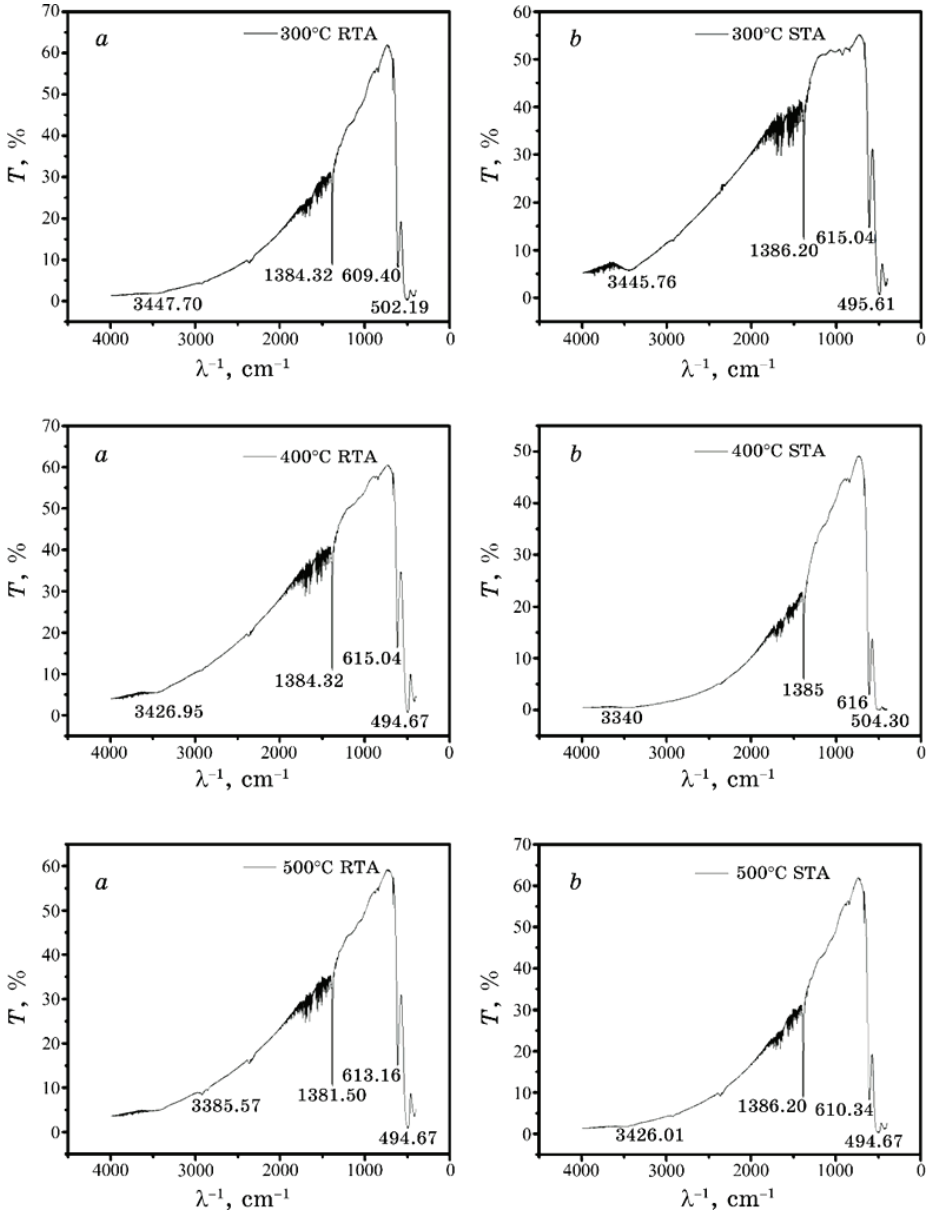

Fig. 6. FT-IR spectra of CuO nanoparticles prepared following: (*a*) RTA and (*b*) STA at 300°C, 400°C, 500°C for one hour.

No FT-IR peak of Cu_2O exists in all synthesized samples.

Both method of annealing did not affect the crystal phase of CuO nanoparticles, but affect only the crystal quality. The same result

was found in literature [41, 56].

4. CONCLUSIONS

In summary, this work reports the results of the effect of rapid and slow temperature annealing on the structural and optical properties of copper oxide nanoparticles. RTA and STA effects were studied for the first time under the same working conditions in the case of copper-oxide nanoparticles using the direct precipitation method. The objective of the work is to provide the literature with data about the effect of rapid thermal annealing on copper-oxide nanoparticles' properties and to examine the efficiency of this method of annealing compared to slow thermal annealing in enhancing CuO-nanoparticles' properties. The results showed that samples in both methods have a sheet-like shape at different tested temperatures. They reveal a change in the texture of samples, which underwent rapid thermal annealing at 500°C for 1 hour. Compared to STA, RTA at 500°C is not sufficient to remove all residues and impurities, but it has recorded relatively the lowest value of band-gap energy. Thus, rapid thermal annealing at 500°C resulted in improved optical properties of CuO nanoparticles, whereas STA resulted in improved crystalline nature of CuO nanoparticles.

We need to increase further annealing temperature and shorten the annealing time at the target temperature to study the effect of RTA on improving the crystallinity of copper-oxide nanoparticles.

REFERENCES

1. Ibrahim Khan, Khalid Saeed, and Idrees Khan, *Arabian Journal of Chemistry*, **12**, No. 7: 908 (2019); https://doi.10.1016/j.arabjc.2017.05.011
2. S. Rehman, A. Mumtaz, and S. K. Hasanain, *Journal of Nanoparticle Research*, **13**: 2497 (2011); http://dx.doi.org/10.1007/s11051-010-0143-8
3. S. Neeleshwar, C. L. Chen, C. B. Tsai, Y. Y. Chen, C. C. Chen, S. G. Shyu, and M. S. Seehra, *Physical Review B*, **71**, Iss. 20: 201307 (2005); https://doi.10.1103/PhysRevB.71.201307
4. S. Anandan, G. J. Lee, and J. J. Wu, *Ultrasonics Sonochemistry*, **19**, Iss. 3: 682 (2012); https://doi.10.1016/j.ultsonch.2011.08.009
5. Y. P. Sukhorukov, B. A. Gizhevskii, E. V. Mostovshchikova, A. Ye. Yermakov, S. N. Tugushev, and E. A. Kozlov, *Technical Physics Letters*, **32**: 132 (2006); https://doi.10.1134/S1063785006020131
6. H. Zhang and M. Zhang, *Materials Chemistry and Physics*, **108**, Iss. 2–3: 184 (2008); https://doi.org/10.1016/j.matchemphys.2007.10005
7. H. S. Devi and T. D. Singh, *Advances in Electronics and Electrical Engineering*, **4**, Iss. 1: 83 (2014).
8. J. Zhu, D. Li, H. Chen, X. Yang, L. Lu, and X. Wang, *Materials Letters*, **58**, Iss. 26: 3324 (2004); https://doi.org/10.1016/j.matlet.2004.06.031

9. P. Mallick and S. Sahu, *Nanoscience and Nanotechnology*, **2**, Iss. 3: 71 (2012); https://doi.org/10.5923/j.nn.20120203.05
10. N. Touka, D. Tabli, K. Badari et al., *Journal of Optoelectronics and Advanced Materials*, **21**, Iss. 12: 698 (2019).
11. N. A. Raship, M. Z. Sahdan, F. Adriyanto, M. F. Nurfazliana, and A. S. Bakri, *AIP Conference Proceedings*, **1788**, Iss. 1: 030121 (2017); https://doi.org/10.1063/1.4968374
12. N. Serin, T. Serin, Ş. Horzum, and Y. Çelik, *Semiconductor Science and Technology*, **20**, Iss. 5: 398 (2005); https://doi.org/10.1088/02681242/20/5/012
13. S. Masudy-Panah, R. S. Moakhar, C. S. Chua, A. Kushwaha, T. I. Wong, and G. K. Dalapati, *RSC Advances*, **6**, Iss. 35: 29383 (2016); https://doi.org/10.1039/C6RA03383K
14. R. Gottesman, A. Song, I. Levine, M. Krause, A. N. Islam, D. Abou-Ras, T. Dittrich, R. van de Krol, and A. Chemseddine, *Advanced Functional Materials*, **30**, Iss. 21: 1910832 (2020); https://doi.org/10.1002/adfm.201910832
15. K. Bergum, H. N. Riise, S. Gorantla, P. F. Lindberg, I. J. T. Jensen, A. E. Gunnæs, A. Galeckas, S. Diplas, B. G. Svensson, and E. Monakhov, *Journal of Physics: Condensed Matter*, **30**, Iss. 7: 075702 (2018); doi:10.1088/1361-648X/aaa5f4
16. R. B. Vasiliev, M. N. Rumyantseva, N. V. Yakovlev, and A. M. Gaskov, *Sensors and Actuators B: Chemical*, **50**, Iss. 3: 186 (1998); https://doi.10.1016/S0925-4005(98)00235-4
17. T. Ishihara, M. Higuchi, T. Takagi, M. Ito, H. Nishiguchi, and Y. Takita, *Journal of Materials Chemistry*, **8**, Iss. 9: 2037 (1998); https://doi.10.1039/A801595C
18. Sylvester Lekoo Mammah, Fidelix Ekeoma Opara, Valentine Benjamin Omubo-Pepple, Joseph Effiom-Edem Ntibi, Sabastine Chukwuemeka Ezugwu, and Fabian Ifeanyichukwu Ezema, *Natural Science*, **5**, Iss. 3: 389 (2013); https://doi.10.4236/ns.2013.53052
19. H. Hashim, S. F. A. Samat, S. S. Shariffudin, and P. S. M. Saad, *IOP Conference Series: Materials Science and Engineering*, **340**, Iss. 1: 012008 (2018); https://doi.10.1088/1757899X/340/1/012008
20. D. Wojcieszak, A. Obstarczyk, E. Mańkowska, M. Mazur, D. Kaczmarek, K. Zakrzewska, P. Mazur, and J. Domaradzki, *Materials Research Bulletin*, **147**: 111646 (2022); https://doi.10.1016/j.materresbull.2021.111646
21. N. Al Armouzi, Gh. El Hallani, A. Liba, M. Zekraoui, H. S. Hilal, N. Kouider, and M. Mabrouki, *Materials Research Express*, **6**, Iss. 11: 116405 (2019); https://doi.10.1088/2053-1591/ab44f3
22. U. Akgul, K. Yildiz, and Y. Atici, *The European Physical Journal Plus*, **131**, Iss. 89: 1 (2016); doi:10.1140/epjp/i2016160893
23. G. Martínez-Saucedo, G. Torres-Delgado, J. Márquez-Marín, O. Zelaya-Ángel, and R. Castanedo-Pérez, *Journal of Alloys and Compounds*, **859**: 157790 (2021); doi:101016/jjallcom2020157790
24. L. Xiong, H. Xiao, S. Chen, Z. Chen, X. Yi, S. Wen, G. Zheng, Y. Ding, and H. Yu, *RSC Advances*, **4**, Iss. 107: 62115 (2014); https://doi.org/10.1039/C4RA12406E
25. Dongjing Liu, Weiguo Zhou, and Jiang Wu, *The Canadian Journal of*

Chemical Engineering, **94**, Iss. 12: 2276 (2016); https://doi.org/10.1002/cjce.22613
26. A. Maini and M. A. Shah, *International Journal of Ceramic Engineering & Science*, **3**, Iss. 4: 192 (2021); https://doi.org/10.1002/ces210097
27. M. B. Gawande, A. Goswami, F. X. Felpin, T. Asefa, X. Huang, R. Silva, X. Zou, R. Zboril, and R. S. Varma, *Chemical Reviews*, **116**, Iss. 6: 3722 (2016); https://doi.org/10.1021/acs.chemrev5b00482
28. Dongjing Liu, Weiguo Zhou, and Jiang Wu, *The Canadian Journal of Chemical Engineering*, **94**, Iss. 12: 2276 (2016); https://doi.org/10.1002/cjce.22613
29. G. Eranna, B. C. Joshi, D. P. Runthala, and R. P. Gupta, *Critical Reviews in Solid State and Materials Sciences*, **29**, Iss. 3–4: 111 (2004); https://doi.org/10.1080/10408430490888977
30. P. Gao, Y. Chen, H. Lv, X. Li, Y. Wang, and Q. Zhang, *International Journal of Hydrogen Energy*, **34**, Iss. 7: 3065 (2009); https://doi.org/10.1016/j.ijhydene200812.050
31. T. I. Arbuzova, B. A. Gizhevskii, S. V. Naumov, A. V. Korolev, V. L. Arbuzov, K. V. Shal'nov, and A. P. Druzhkov, *Journal of Magnetism and Magnetic Materials*, **258**: 342 (2003); https://doi.org/10.1016/S0304-8853(02)01052-1
32. X. P. Gao, J. L. Bao, G. L. Pan, H. Y. Zhu, P. X. Huang, F. Wu, and D. Y. Song, *The Journal of Physical Chemistry B*, **108**, Iss. 18: 5547 (2004); https://doi.org/10.1021/jp037075k
33. P. P. C. Udani, P. V. D. S. Gunawardana, H. C. Lee, and D. H. Kim, *International Journal of Hydrogen Energy*, **34**, Iss. 18: 7648 (2009); https://doi.org/10.1016/j.ijhydene.2009.07035
34. A. Toolabia, M. R. Zareb, A. Rahmanic, E. Hoseinzadehd, M. Sarkhoshe, and M. Zaref, *J. Basic. Appl. Sci. Res.*, **3**, Iss. 2: 221 (2013).
35. S. Jadhav, S. Gaikwad, M. Nimse, and A. Rajbhoj, *Journal of Cluster Science*, **22**: 121 (2011); https://doi.org/101007/s1087601103497
36. A. Rahim, Z. U. Rehman, S. Mir, N. Muhammad, F. Rehman, M. H. Nawaz, M. Yaqub, S. A. Siddiqi, and A. A. Chaudhry, *Journal of Molecular Liquids*, **248**: 425 (2017); https://doi.org/10.1016/j.molliq 2017.10.087
37. D. Rehana, D. Mahendiran, R. S. Kumar, and A. K. Rahima, *Biomedicine & Pharmacotherapy*, **89**: 1067 (2017); https://doi.org/10.1016/j.biopha2017.02.101
38. Sunday Adewale Akintelu, Aderonke Similoluwa Folorunso, Femi Adekunle Folorunso, and Abel Kolawole Oyebamiji, *Heliyon*, **6**, Iss. 7: e04508 (2020); doi:10.1016/j.heliyon.2020.e04508
39. Y. Unutulmazsoy, C. Cancellieri, L. Lin, and L. P. H. Jeurgens, *Applied Surface Science*, **588**: 152896 (2022); https://doi.org/10.1016/j.apsusc.2022.152896
40. T. T. Ha, B. T. Cong, P. N. Hai, N. Hoang, H. V. Chinh, B. T. Huong, N. T. Linh, B. T. Son, T. T. Q. Hoa, and T. N. Viet, *VNU Journal of Science: Mathematics-Physics*, **38**, Iss. 2: 4642 (2022); doi:10.25073/2588-1124/vnumap4642
41. V. U. Siddiqui, A. Ansari, I. Khan, M. K. Akram, and W. A. Siddiqi, *Materials Research Express*, **6**, Iss. 11: 115095 (2019); doi:10.1088/2053-1591/ab4ace

42. S. N. Khan, S. Ge, E. Gu, S. K. Karunakaran, W. Yang, R. Hong, Y. Mai, X. Lin, and G. Yang, *Advanced Materials Interfaces*, **8**, Iss. 18: 2100971 (2021); doi:10.1002/admi.202100971
43. Roland Mainz, B. C. Walker, S. S. Schmidt, O. Zander, A. Weber, H. Rodriguez-Alvarez, J. Just, M. Klaus, R. Agrawal, and T. Unold, *Physical Chemistry Chemical Physics*, **15**, Iss. 41: 18281 (2013); https://doi.org/10.1039/C3CP53373E
44. A. A. Baqer, K. A. Matori, N. M. Al-Hada, A. H. Shaari, H. M. Kamari, E. Saion, J. L. Y. Chyi, and C. Azurahanim Abdullah, *Results in Physics*, **9**: 471 (2018); https://doi.101016/j.rinp2018.02.079
45. A. Rollett, F. J. Humphreys, G. S. Rohrer, and G. H. Hatherly, *Recrystallization and Related Annealing Phenomena* (Burlington: Elsevier Science: 2004), 658 p.
46, Y. C. Lee, S. Y. Hu, W. Water, K. K. Tiong, Z. C. Feng, Y. T. Chen, J. C. Huang, J. W. Lee, C. C. Huang, J. L. Shen, and Mou-Hong Cheng, *Journal of Luminescence*, **129**, Iss. 2: 148 (2009); doi:10.1016/j.jlumin.2008.09.003
47. M. K. Puchert, P. Y. Timbrell, and R. N. Lamb, *Journal of Vacuum Science & Technology A: Vacuum, Surfaces, and Films*, **14**, Iss. 4: 2220 (1996); doi:10.1116/1580050
48. P. Cotterill and P. R. Mould, *Recrystallization and Grain Growth in Metals* (London: Surrey Univ. Press: 1976), 409 p.
49. P. R. Rios, F. Siciliano Jr., H. R. Z. Sandim, R. L. Plaut, and A. F. Padilha, *Materials Research*, **8**: 225 (2005); doi:10.1590/S1516-14392005000300002
50. L. Zhou, S. Wang, H. Ma, S. Ma, D. Xu, and Y. Guo, *Chemical Engineering Research and Design*, **98**: 36 (2015); doi:10.1016/j.cherd.2015.04.004
51. D. Z. Voyiadjis, D. Faghihi, and Y. Zhang, *International Journal of Solids and Structures*, **51**, Iss. 10: 1872 (2014); doi:10.1016/j.ijsolstr.2014.01.020
52. N. Ghobadi, *International Nano Letters*, **3**, Iss. 1: 2 (2013); https://doi.10.1186/2228-5326-3-2
53. J. M. Aguirre, A. Gutiérrez, and O. Giraldo, *Journal of the Brazilian Chemical Society*, **22**: 546 (2011); doi:10.1590/S0103-50532011000300019
54. C. Henrist, K. Traina, C. Hubert, G. Toussaint, A. Rulmont, and R. Cloots, *Journal of Crystal Growth*, **254**, Iss. 1–2: 176 (2003); doi:10.1016/S0022-0248(03)01145-X
55. J. Liu, X. Huang, Y. Li, K. M. Sulieman, X. He, and F. Sun, *Journal of Materials Chemistry*, **16**, Iss. 45: 4427 (2006); https://doi.10.1039/C6DT04500
56. F. A. Akgul, G. Akgul, N. Yildirim, H. E. Unalan, and R. Turan, *Materials Chemistry and Physics*, **147**, Iss. 3: 987 (2014); doi:10.1016/j.matchemphys 2014.06.047

Наносистеми, наноматеріали, нанотехнології
Nanosistemi, Nanomateriali, Nanotehnologii
2025, т. 23, № 2, сс. 539–546
https://doi.org/10.15407/nnn.23.02.0539

© 2025 ІМФ (Інститут металофізики
ім. Г. В. Курдюмова НАН України)
Надруковано в Україні.

PACS numbers: 68.37.Hk, 68.37.Ps, 78.30.Jw, 78.67.Bf, 81.07.Nb, 81.16.Fg, 82.35.Cd

Study of the Effect of Adding Aniline on the Polymerization of Pyrrole Aldehyde (Shape and Size of the Resulting Nanoparticles and Film Properties)

Marwa AlKheder, Ahmad Al-Hamdan, and Taymaa AlAwad

Faculty of Science,
Al Furat University,
Deir-ez-Zor, Syria

Conducting polymers are important materials with important applications. Most of their applications depend on the shape of the particles and often on their thin films. In this paper, a new copolymer is synthesized from aniline and formylpyrrole in acidic solution. The polymer is described using infrared spectroscopy, and the presence of hexagonal rings in its structure is confirmed. In the scanning electron microscopy (SEM) images, a change in the shape of the particles is observed to become fibres instead of balls in poly(2-formylpyrrole) (PFPy) that confirms the effect of the presence of aniline as a reactant. Thin films are fabricated by anchoring onto glass films of different thicknesses. The surface of the film appears rough and contains many peaks, whose heights range between 10 and 30 nanometers, and the dimensions of its particles match the SEM images.

Провідні полімери є важливими матеріялами з важливими застосуваннями. Більшість їх застосувань залежить від форми частинок і часто від їхніх тонких плівок. У цій статті синтезовано новий кополімер з аніліну та формілпіролу в кислотному розчині. Полімер описано за допомогою інфрачервоної спектроскопії та підтверджено наявність гексагональних кілець у його структурі. На зображеннях сканувальної електронної мікроскопії (СЕМ) спостерігається зміна форми частинок, які перетворюються на волокна замість кульок у полі(2-формілпіролі), що підтверджує вплив присутности аніліну як реаґенту. Тонкі плівки виготовлено шляхом закріплення на скляних плівках різної товщини. Поверхня плівки виглядає шерсткою та містить багато піків, висота яких варіюється від 10 до 30 нанометрів, а розміри її частинок відповідають зображенням СЕМ.

Key words: aniline, 2-formylpyrrole, thin films, polymerization, conducting polymers.

Ключові слова: анілін, 2-формілпірол, тонкі плівки, полімеризація, провідні полімери.

(Received 9 December, 2023)

1. INTRODUCTION

Conducting polymers were discovered in the middle of the last century [1], and have been developed over the past years to obtain materials with unique properties [2]. Conducting polymers are used in the manufacture of sensors and biosensors [3] and electronic applications [4, 5], rechargeable batteries [6], enzyme-immobilization matrices [7], light-emitting diodes [8], optical displays [9], as membranes [10] (in addition to their uses in chemical analysis and others [11]). Thin films are the basis for most applications of sensors, modified electrodes [12], and electrochemical drug release systems all rely on conducting polymer films [13].

Poly(2-formylpyrrole) was prepared by the action of strong acids on the monomer [14]. The resulting polymer particles depend on the method of synthesis and the conditions applied. All the references, which mentioned the preparation of polyformyl, had spherical particles, which agglomerated and formed clusters [14]. Spherical particles are of different sizes and rough surfaces [15]. The particles form thin films easily, and the films have good mechanical properties and good chemical stability [16]. The thickness of polyformylpyrrole thin films can be easily controlled regardless of the supporting substrate [17]. The shape and size of the particles make up the film material greatly affect its properties and, thus, its applications [18].

In this work, we present a method for modifying polyformylpyrrole with a small amount of aniline to improve the linking of polymeric chains and change the shape of the particles and the properties of their thin films.

2. EXPERIMENTAL

2.1. Materials and Measurements

Aniline >98% sigma, Pyrrole-2-carboxaldehyde 98% sigma, Hydrochloric acid 35.5% sigma, Ethanol 99% sigma: polymer was characterized with surface morphologies examined with SEM, EDX and XPS (TESCAN model MIRA3), FT-IR (JASCO FT/IR model M4100) spectrophotometer between 4000 and 400 cm^{-1}, and AFM (Nanosurf model: eseyscan2).

2.2. Polymer Synthesis

2-Formylpyrrole (20 mmol) was dissolved in 25 ml of alcohol (5% hydrochloric acid prepared by adding the appropriate amount of concentrated 35% hydrochloric acid to the alcohol). Then, aniline is added in a varying percentage each time to the reaction medium. The mixture is stirred, and a bright yellow precipitate is formed.

Then, it soon begins to dissolve and the solution becomes darker and darker until a very soft dark green precipitate is formed. After a period of 48 hours, the precipitate is separated with the sediment and washed well several times with distilled water and then alcohol.

2.3. Films Fabrication

Films fabricated by anchoring method with glass plates were immersed in the reaction medium (four sheets in each experiment) and removed successively for different times. The films were gently washed with distilled water and alcohol, then, dried with gentle air without touching the film and prepared for later study. Table 1 shows a list of the experiments carried out and the weight yield of the reaction. The thicknesses of thin films were calculated from the optical absorption spectrum [17].

3. RESULTS AND DISCUSSION; POLYMER CHARACTERIZATION

Scanning Electron Microscope Images (SEM). SEM images provide important information about the physical size, shape, surface nature, and accumulation method of nanoparticles in a descriptive manner. Figure 1 shows SEM images of the prepared samples. We note that the polymer has particles in the form of fibres with sharp irregular angles. The fibre sizes are for diameter: 95, 75, 123, 156 nm and for length: 800, 1200, 1500, 1800 nm for the percentage of aniline of 2, 5, 10, 15%, respectively. In comparison with the SEM images of the same polymer prepared in the absence of aniline, we notice a significant difference in the shape and size of the prepared particles, as the prepared particles appear spherical in shape, while they are in the form of fibres and rods, if they are prepared in the presence of aniline.

FT-IR Spectrum. Figure 2 shows the FT-IR spectrum of the resulting polymers. In the IR spectrum, a broad peak around 3500 cm^{-1} is due to the stretching of the [O–H] bond, and this band obscures completely any peak of the primary or secondary amine. A weak peak at 1730 cm^{-1} is due to stretching of the unreacted carbonyl group at the end of the polymer chain. The peaks at 1585, 1490,

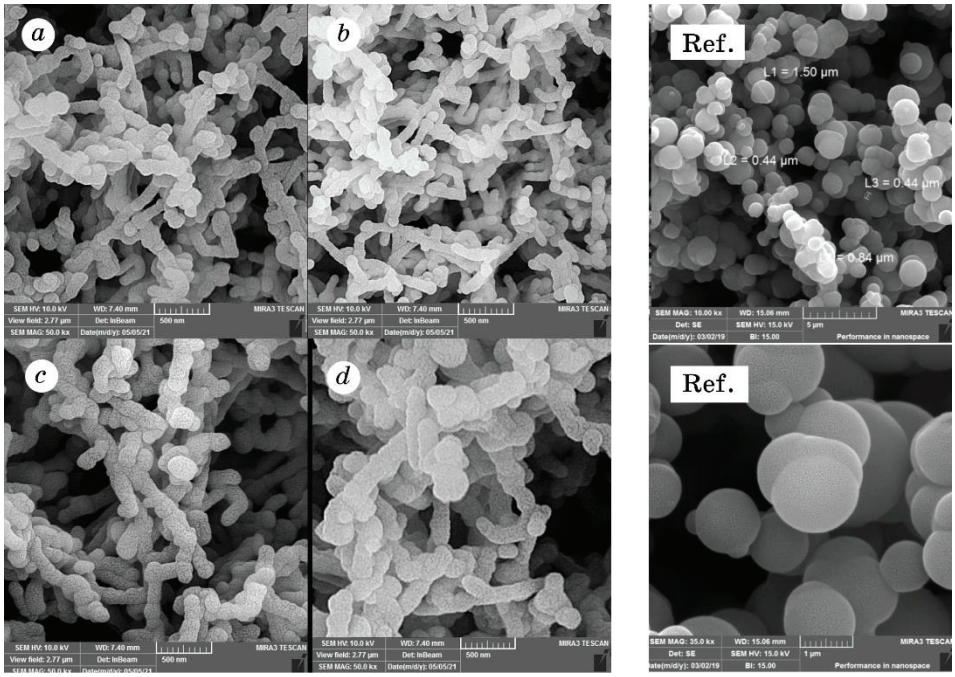

Fig. 1. SEM images of the polymer with percentage of aniline: (*a*) 2%; (*b*) 5%; (*c*) 10%; (*d*) 15%; and (Ref.)—reference [14].

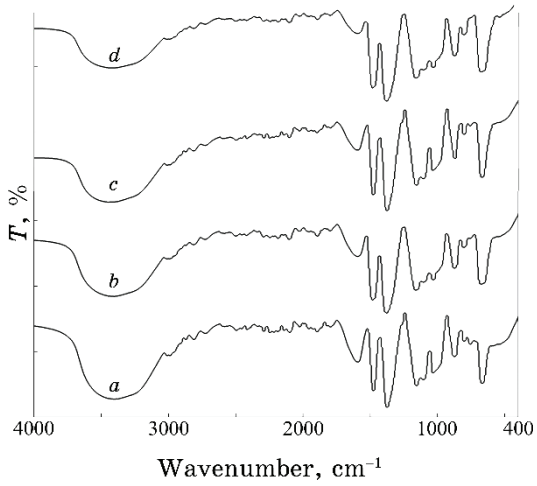

Fig. 2. The FT-IR spectrum of the resulting polymers.

1290 and 1160 cm^{-1} mostly belong to the hexagonal rings that confirms the inclusion of aniline within the polymer chains.

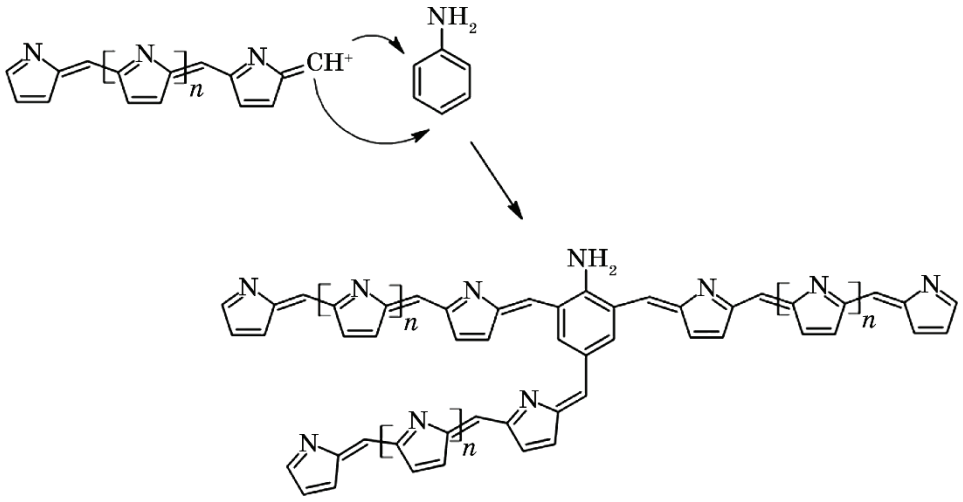

Fig. 3. Proposed linking scheme for polymeric chain.

An increase in the percentage of aniline in the reaction solution corresponds to an increase in the intensity of signals returning to the hexagonal rings compared to others.

During the experiment, a yellow precipitate formed at the beginning of the experiment and then dissolved again later. The precipitate is Schiff's base, which dissociates in acidic media into the aldehyde and amine. The presence of the active aromatic ring in aniline during the reaction makes it vulnerable to electrophilic attack by the electrophile formed during the polymerization reaction, and this helps to link the polymeric chains and form random branched chains. Figure 3 shows the proposed linking scheme for polymeric chains.

On the other hand, the presence of the amine in the acidic environment gives aryl ammonium salts, which may play the role of an electrophile that attacks the active aromatic rings (both aniline and pyrrole) in the presence of an oxidizer (here, the aldehyde plays the role of the oxidizer), which gives possibilities for different binding to the polymer structure as is published in Ref. [19].

Figure 4 shows the proposed possibilities for the structure of polymers formed during the reaction. The polymer formed is a mixture of all possibilities, and one cannot be preferred over the other.

Thin Films. Five thin films with different thicknesses were fabricated during the reactions for different reaction times. Table shows the reaction times and film thicknesses. The thickness of the films increases with increasing reaction time in an unsteady manner, and this is consistent with that researchers have found in previous studies [17]. The thickness of the first films (with different durations)

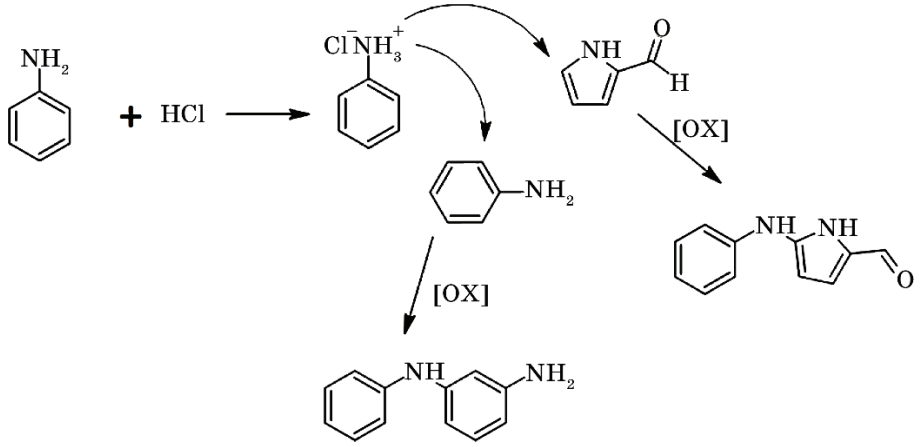

Fig. 4. The proposed possibilities for the structure of polymers formed during the reaction.

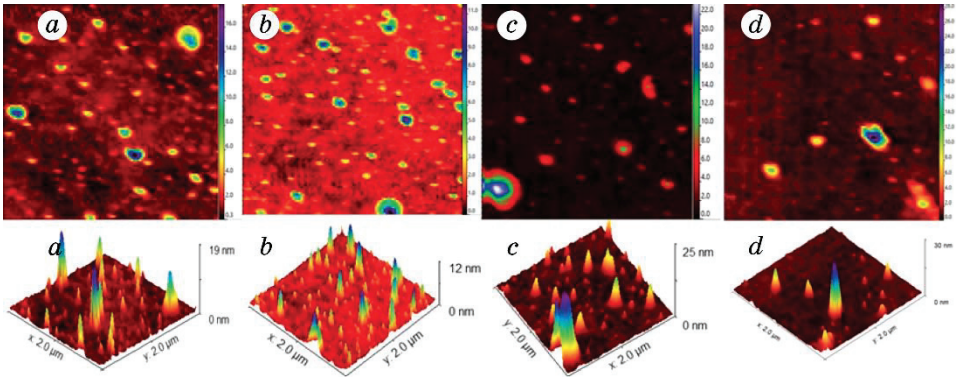

Fig. 5. AFM images of thin films on glass (3*D* image and topography at 6 h).

also increases with the decrease in the percentage of aniline due to the consumption of part of the aldehyde in the form of Schiff's base at the beginning of the reaction. In addition, the movement of the precipitate, when the reaction is triggered, reduces the stability of the molecules attached to the surface of the substrate during the beginning of the reaction. For long times (> 2 h), the films thickness are increase with increasing percentage of aniline. It is believed that this is due to the activity of the aniline ring in the reaction.

Figure 5 shows AFM images of thin films on glass. The surface of the film appears rough and contains many peaks, whose heights range between 10 and 30 nanometers, and the dimensions of its particles match the SEM images.

4. CONCLUSIONS

Adding aniline to the 2-formylpyrrole, polymerization reaction affects the shape and size of the polymer particles, giving rod-shaped particles of different sizes instead of balls. Aniline causes changes in the positioning and shape of the particles, which make up the prepared thin films. Aniline enters the polymer chain in two ways. The first one is by linking the chains as a result of the electrophilic addition to the aromatic ring, and the second one is as a result of the formation of an alkyl ammonium that plays the role of an electrophile in the presence of the aldehyde as an oxidant. This leads to the formation of a random copolymer of aniline and 2-formylpyrrole.

HIGHLIGHTER

1) Changing the shape of the polyformylpyrrole particles by adding a small amount of aniline.
2) Formation of a random copolymer of aniline and 2-formylpyrrole with properties different from the base polymer.
3) Thin films of different thicknesses are easily fabricated using the anchoring method.

REFERENCES

1. R. Kumar, S. Singh, and B. C. Yadav, *IARJSET*, **2**, Iss 11: 2394 (2015).
2. Y. P. Zhang, S. H. Lee, K. R. Reddy, A. I. Gopalan, and K. P. Lee, *Journal of Applied Polymer Science*, **104**, Iss. 4: 2743 (2007); https://doi.org/10.1002/app.25938
3. Sandra C. Hernandez, Debangshu Chaudhuri, Wilfred Chen, Nosang V. Myung, and Ashok Mulchandani, *Inter Science*, **19**, Iss. 19–20: 2125 (2007); doi:10.1002/elan.200703933
4. J. C. Zhang, X. Zheng, M. Chen, X. Y. Yang, and W. L. Cao, *Express Polymer Letters*, **5**, Iss. 5: 401 (2011); https://doi.org/10.3144/expresspolymlett.2011.39
5. A. Rudge, J. Davey, I. Raistrick, S. Gottesfeld, and J. P. Ferraris, *Journal of Power Sources*, **47**, Iss. 1–2: 89 (1994); https://doi.org/10.1016/0378-7753(94)80053-7
6. L. Duan, J. Lu, W. Liu, P. Huang, W. Wang, and Z. Liu, *Colloids and Surfaces A: Physicochemical and Engineering Aspects*, **414**, Iss. 2012: 98 (2012); https://doi.org/10.1016/j.colsurfa.2012.08.033
7. Gülay Bayramoğlu, Meral Karakişla, Begum Altıntaş, Ayşegül U. Metin, Mehmet Saçak, and M. Yakup Arica, *Process Biochemistry*, **44**, Iss. 8: 880 (2009); https://doi.org/10.1016/j.procbio.2009.04.011
8. T. Kasa and F. Gebrewold, *Advances in Physics: Theories and Applications*, **62**, Iss. 2017: 28 (2017).

9. A. Mirsakiyeva, PhD Thesis (Stockholm, Sweden: KTH Royal Institute of Technology: 2017).
10. Hammou Gherras, Ahmed Yahiaoui, Aicha Hachemaoui, Abdelkader Belfedal, Abdelkader Dehbi and Abdel-Hamid I. Mourad, *Journal of Semiconductors*, **39**, Iss. 10: 102001 (2018); https://doi.org/10.1088/1674-4926/39/10/102001
11. G. H. Shim and S. H. Foulger, *Photonics and Nanostructures — Fundamentals and Applications*, **10**, Iss. 4: 440 (2012); https://doi.org/10.1016/j.photonics.2011.12.001
12. G. A. Edwards, *Chemically Modified Electrodes*, **1**, Iss. 1: 295 (2007); https://doi.org/10.1016/B978-044451958-0.50021-5
13. Akira Baba, Rigoberto C. Advincula, and Wolfgang Knoll, *Studies in Interface Science*, **1**, Iss. 1: 55 (2001); https://doi.org/10.1016/s1383-7303(01)80016-8
14. Ahmad Al-Hamdan, Ahmad Al-Falah, Fawaz Al-Deri, and Ibrahim Al-Ghoraibi, *Nanosistemi, Nanomateriali, Nanotehnologii*, **20**, Iss. 1: 195 (2022); https://doi.org/10.15407/nnn.20.01.195
15. Ahmad Al-Hamdan, Ahmad Al-Falah, Fawaz Al-Deri, and Marwa Al-Kheder, *Nanosistemi, Nanomateriali, Nanotehnologii*, **19**, Iss. 4: 913 (2021); https://doi.org/10.15407/nnn.19.04.913
16. Ahmad Al-Hamdan, Ahmad Al-Falah, and Fawaz Al-Deri, *Int. J. Thin Films Sci. Tec.*, **10**, Iss. 2: 101 (2021); https://doi.org/10.18576/ijtfst/100205
17. Ahmad Al-Hamdan, Ahmad Al-Falah, and Fawaz Al-Deri, *Int. J. Thin Films Sci. Tec.*, **11**, Iss. 2: 153 (2022); http://dx.doi.org/10.18576/ijtfst/110201
18. Ugur Ulusoy, *Minerals*, **13**, Iss. 1: 91 (2023); https://doi.org/10.3390/min13010091
19. A. Al-Hamdan, A. Al-Falah, F. Al-Deri, and M. Al-Kheder, *Polym. Sci. Ser. B*, **63**, No. 3: 191 (2021); https://doi.org/10.1134/S1560090421030015

Наносистеми, наноматеріали, нанотехнології
Nanosistemi, Nanomateriali, Nanotehnologii
2025, т. 23, № 2, сс. 547–558
https://doi.org/10.15407/nnn.23.02.0547

© 2025 ІМФ (Інститут металофізики
ім. Г. В. Курдюмова НАН України)
Надруковано в Україні.

PACS numbers: 78.20.Ci, 78.40.Me, 78.67.Sc, 81.07.Pr, 82.35.Np, 85.60.Dw

Synthesis and Improved Optical Properties of PVA–In_2O_3–Fe_2O_3 Nanostructures to Use in Optical Fields

Noor Hayder, Majeed Ali Habeeb, and Noor A. Sami

College of Education for Pure Sciences,
Department of Physics,
University of Babylon,
Hillah, Iraq

The PVA–In_2O_3–Fe_2O_3 nanocomposites are fabricated by the casting method. Solar cells, transistors, and electronic gate units are just a few examples of the many nanoelectronic–optical systems, which can benefit from these nanocomposites. Nanocomposites including polyvinyl alcohol (PVA), indium oxide (In_2O_3), and iron oxide (Fe_2O_3) have their optical characteristics studied. The nanocomposites have significant ultraviolet (UV) light absorption properties. Moreover, the transmittance diminishes, when the In_2O_3–Fe_2O_3-nanoparticles' increase. By raising the weight percent ratio of In_2O_3–Fe_2O_3 nanosize components to 6 percent, we found that polyvinyl-alcohol average energy gap (E_g) decreases that makes it suitable for photonics applications. A number of optical characteristics are evaluated, such as the extinction coefficient (k), absorption coefficient (α), refractive index (n), optical conductivity, the real component (ε_1) and imaginary component (ε_2) of the dielectric constant.

Нанокомпозити ПВС–In_2O_3–Fe_2O_3 виготовлено методом лиття. Сонячні елементи, транзистори й електронні затвори — це лише кілька прикладів багатьох наноелектронно-оптичних систем, які можуть отримати користь від цих нанокомпозитів. Досліджено оптичні характеристики нанокомпозитів, що містять полівініловий спирт (ПВС), оксид Індію (In_2O_3) й оксид Феруму (Fe_2O_3). Нанокомпозити мають істотні властивості щодо вбирання ультрафіолетового (УФ) світла. Крім того, коефіцієнт пропускання зменшується зі збільшенням кількости наночастинок In_2O_3–Fe_2O_3. Збільшивши вагове співвідношення нанорозмірних компонентів In_2O_3–Fe_2O_3 до 6 відсотків, ми виявили, що середня ширина забороненої зони полівінілового спирту (E_g) зменшується, що робить його придатним для застосування у фотоніці. Оцінено низку оптичних характеристик, таких як коефіцієнт екстинкції (k), коефіцієнт вбирання (α), показник заломлення (n), оптична провідність, дійсна складова (ε_1) та уявна складова (ε_2) діелектричної проникности.

Key words: polyvinyl alcohol, indium oxide, iron oxide, optical properties.

Ключові слова: полівініловий спирт, оксид Індію, оксид Феруму, оптичні властивості.

(Received 22 December, 2023)

1. INTRODUCTION

The optical properties of polymers play a crucial role in various applications such as electrical transitions, insulation covers, optical filters, greenhouses, and selective surfaces. However, the primary objective of boosting the optical properties of these polymers is accomplished by improving reflection, interference, antireflection, and polarization phenomena [1, 2]. Polymers have become the preferred choice over traditional silica-based optical materials, because they are easier to process, less expensive, and can be produced in larger quantities [3, 4]. Polymers can have their characteristics enhanced and controlled by adding the right dopant. Some key points about optical properties of the intermixture composed of several metal salts interacting with PVA are shown, which are determined by refractive index and the light absorption coefficient [5, 6]. There are myriad uses for polymers. The polymeric properties such as piezoelectric, optical, semiconductor and electro-optical ones have enabled more recent developments in stretchable electronics [7]. Dopant–polymer optical properties are very sensitive with respect to electronic nature of electrolytes. For good optical properties of produced materials, it is necessary to have command over electronic mechanisms [8, 9].

2. EXPERIMENTAL PROCEDURE

The samples were fabricated using polyvinyl alcohol (PVA), indium oxide (In_2O_3), and iron oxide (Fe_2O_3). The nanoparticles composed of In_2O_3–Fe_2O_3 were incorporated into a polymer PVA by the casting method at various weight percentages: 0, 2, 4, and 6 wt.%. To create a more uniform solution, 40 ml of distilled water was used to dissolve polyvinyl alcohol (PVA). The solution was then stirred using a magnetic stirrer at a temperature of 70°C for duration of 30 minutes. The UV/1800/Shimadzu spectrophotometer is utilized for the precise measurement of the optical characteristics of PVA–In_2O_3–Fe_2O_3 nanocomposites within the wavelength range of 200 to 1100 nm.

Absorbance is the quotient of the intensity of light absorbed by a material (I_A) and the intensity of incoming light (I_0) [10, 11]:

$$A = I_A/I_0. \tag{1}$$

The transmittance (T) is defined as the ratio of the intensity of the transmitting rays (I_T) passing through the film to the intensity of the incident rays (I_0), which fall on it [12, 13]:

$$T = I_T/I_0. \tag{2}$$

Absorption coefficient (α) is defined as the ability of a material to absorb the light of a given wavelength [14, 15]:

$$\alpha = 2.303A/t, \tag{3}$$

where A is the absorption of the material, t—the sample thickness in cm. The coefficient α for this transition type is given by [16, 17]

$$\alpha h\nu = B\left(h\nu - E_g^{opt}\right)^r, \tag{4}$$

where E_g^{opt} is energy gap between direct transitions.

The refractive index (n) is given by [18, 19]

$$n = \sqrt{4R - \frac{k^2}{(R-1)^2}} - \frac{R+1}{R-1}. \tag{5}$$

The below equation can be employed to obtain the extinction coefficient (k) [20]:

$$k = \alpha\lambda/(4\pi). \tag{6}$$

The formulas for the real (ε_1) and imaginary (ε_2) components of the dielectric constant may be used to separate it [21, 22]:

$$\varepsilon_1 = n^2 - k^2, \tag{7}$$

$$\varepsilon_2 = 2nk. \tag{8}$$

The optical conductivity (σ) is determined *via* the equation given by Ref. [23]:

$$\sigma_{opt} = \alpha nc/(4\pi). \tag{9}$$

3. RESULTS AND DISCUSSION

Figure 1 shows the absorption spectra for PVA–In_2O_3–Fe_2O_3 nanocomposites *versus* wavelength. In the visible/near infrared spec-

trum, films often have low absorption values. This explains, why objects absorb light of longer wavelengths because few photon interacts with atoms well and transmit less energy. Therefore, since the photon interacts with matter depending on its frequency and, thus, the wavelength, there will be an increasing in absorbance as the wavelength decreases. That means that these unbound electrons will simply absorb the falling light. This leads to an increase in absorbance with increasing weight percentages of In_2O_3–Fe_2O_3 nanoparticles [24, 25].

Optical transmittance spectra at different incident-light wave-

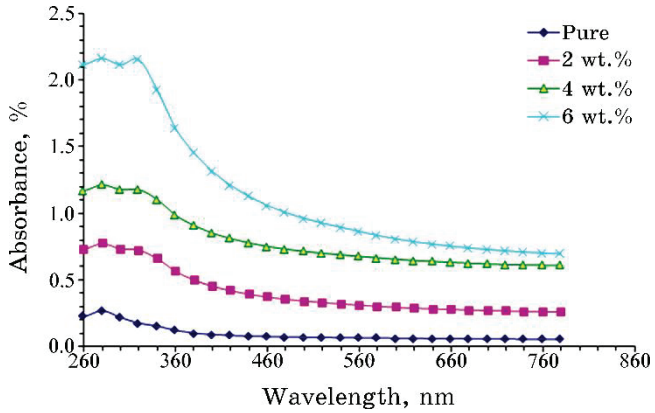

Fig. 1. The relationship between the wavelength and changes in the absorbance of PVA–In_2O_3–Fe_2O_3 nanocomposites.

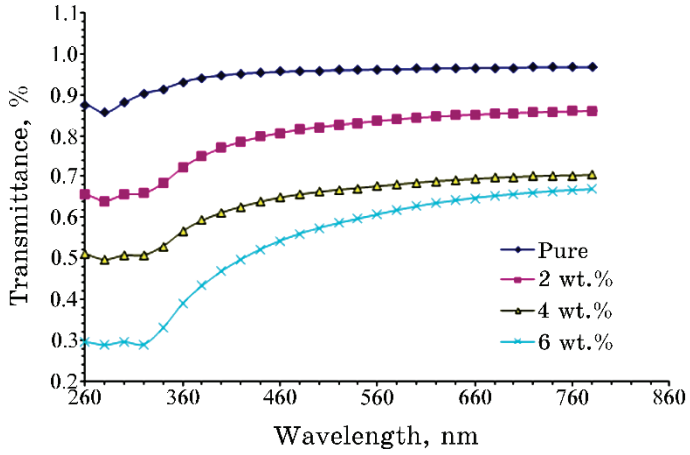

Fig. 2. The PVA–In_2O_3–Fe_2O_3-nanocomposites' transmission changes depending on the wavelength.

lengths are shown in Fig. 2 as a function of increasing the concentration of In_2O_3–Fe_2O_3 in PVA films. Transmittance drops with increasing concentration of In_2O_3–Fe_2O_3 nanoparticles, as seen in this graph. The addition of In_2O_3–Fe_2O_3, which possesses electron-accepting electromagnetic energy, has the capability to enhance the excited states of electrons [26, 27]. It also conforms to that previously was determined in other studies [28, 29].

The absorbance coefficient *versus* wavelength is drawn in Fig. 3 for PVA–In_2O_3–Fe_2O_3 nanocomposites. The low absorption coefficient at long wavelengths and low energy level 1–3 eV is revealed in Fig. 3. The probability of an incident-photon exciting an electron from the value band to the conductivity band because $h\nu$ is lower than E_g is rather small. However, if the incident-photons' energy is higher than prohibited energy gap of the material, a good absorption at high energies occurs since the electron hops to the conduction band from valence band [30]. The absorption value gives away, if it is the direct electron transition or no. Therefore, with α values more than 10^4 cm^{-1} at high energies, direct electron transition means that both the electrons and photons retain the same amount of energy and the momentum. At low energies, when the absorption coefficient is small $\alpha < 10^4$ cm^{-1}, indirect electron transition is expected, whereby phonons preserve electrons' momenta [31].

In Figure 4, we can see, how the square root of the absorption edge $h\nu$ relates to the photon energy. To calculate the size of the energy gap for an approved indirect transition by following a straight line from the peak, all the way is down the x-axis, where the square root of the product of Planck's constant and frequency is zero. A smaller energy gap is seen for higher concentrations of

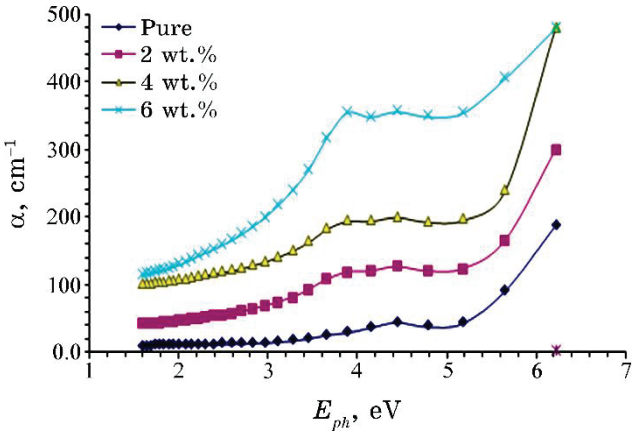

Fig. 3. The absorption coefficient of PVA–In_2O_3–Fe_2O_3 nanocomposites will change as a function of photon energy.

In_2O_3–Fe_2O_3 nanoparticles. The growth of the localized levels inside the forbidden energy gap is the corresponding reason.

The transition occurs in a two-stage process, when the amount of In_2O_3–Fe_2O_3 increases. With a rise in the amount of In_2O_3–Fe_2O_3 nanoparticles, the electron moves from a valence band passing through its local levels until it reaches the conduction band. The reason for such observation lies in the nature of these materials: since they are heterogeneous (for example, electrical conductivity depends on the degree of concentration), the density of localized states rises with the increase of In_2O_3–Fe_2O_3-nanoparticles' concen-

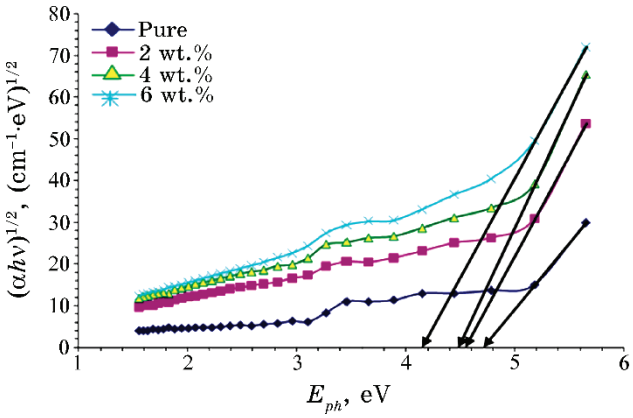

Fig. 4. The correlation between the square root of ($\alpha h\nu$) and the energy of the photons for nanocomposites consisting of PVA–In_2O_3–Fe_2O_3.

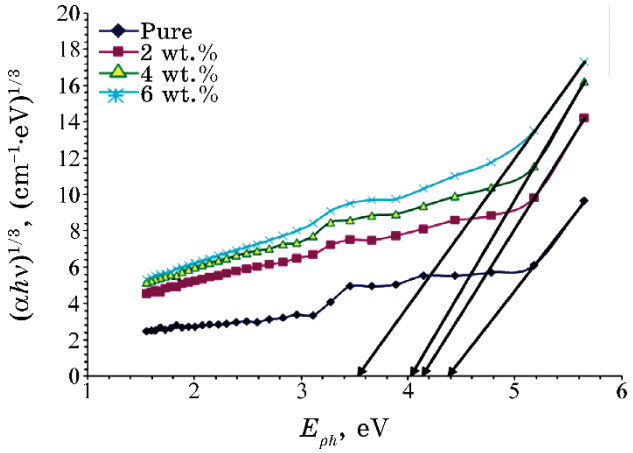

Fig. 5. The correlation between the cubic root of ($\alpha h\nu$) and the energy of photons for PVA–In_2O_3–Fe_2O_3 nanocomposites.

tration. This is that other researchers have already shown [32, 33].

Forbidden energy-gap transitions also use the same procedure to obtain them. Figure 5 depicts the forbidden transition of the indirect energy gap of PVA–In_2O_3–Fe_2O_3 nanocomposites.

Figure 6 shows the connection between refractive index and wavelength. There is a significant increment observed in the refractive index with an increase in nanocomposite density. The low transmittance in the UV region gives a higher value for the refractive index. They have high transmittance, which makes them transparent; hence, they are low in the visible zone [34, 35].

Figure 7 shows the variation of (k) for PVA–In_2O_3–Fe_2O_3 nanocomposites with wavelengths. Observed (k) values suggest that it decreases with increasing concentration of In_2O_3–Fe_2O_3 nanoparticles in a solution. The absorption coefficient increases with the percentage of In_2O_3–Fe_2O_3 nanoparticles, thus, resulting in an increase. Consequently, the structure of the host polymer will be altered by the atoms of the In_2O_3–Fe_2O_3 nanoparticles [36, 37].

The equations (7) and (8) were used to determine the real and imaginary components of the dielectric constants for the nanocomposites consisting of PVA–In_2O_3–Fe_2O_3. Figure 8 illustrates the correlation between the variable ε_1 and the wavelength. Reducing the k value results in the noticeable influence of n on the ε_1 value, as seen in this figure. The actual dielectric constant increases as the concentration of In_2O_3–Fe_2O_3-nanoparticles' increases. Figure 9 illustrates the correlation between the variable ε_2 and the wavelength. The absorption coefficient, denoted as k, governs the relationship between k and α, ultimately determining the value of k. This value of k influences subsequently [38–40].

The optical conductivity (σ_{opt}) may be calculated using Eq. (9). Nanocomposites made of PVA–In_2O_3–Fe_2O_3 show wavelength-

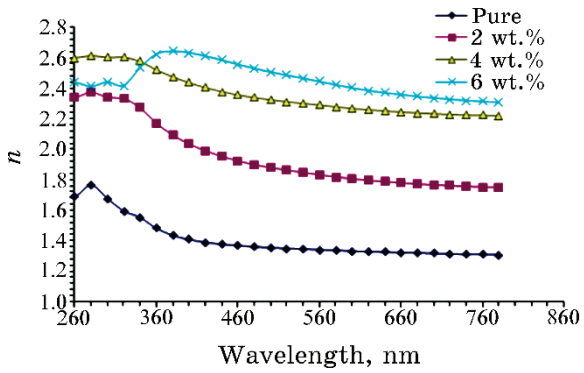

Fig. 6. Relationship between the refractive index and wavelength for PVA–In_2O_3–Fe_2O_3 nanocomposites.

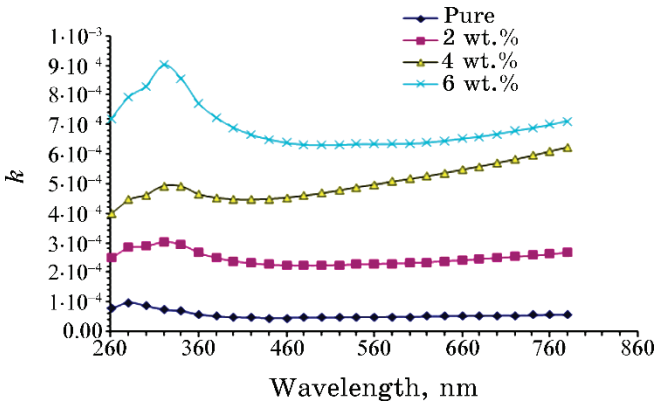

Fig. 7. The relationship between the extinction coefficient and wavelength for the nanocomposites PVA–In_2O_3–Fe_2O_3.

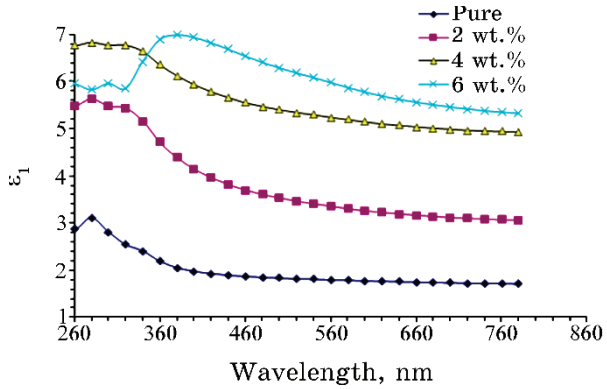

Fig. 8. Relationship between the wavelength and the real part of the dielectric constant of nanocomposite consisting of PVA, In_2O_3, and Fe_2O_3.

dependent changes in optical conductivity (Fig. 10). Improving optical conductivity may be achieved by increasing the iron oxide to iron trioxide weight ratio in PVA polymer to 6 weight percents. Elevated electron mobility is the result of expanding the band gap to include additional energy levels [41, 42]. Therefore, electrons can go from the valence band to the newly formed energy levels and, then, into the conduction band. So, the band gap narrows and conductivity grows [43].

4. CONCLUSIONS

Through the casting approach, nanoparticles of In_2O_3–Fe_2O_3 were

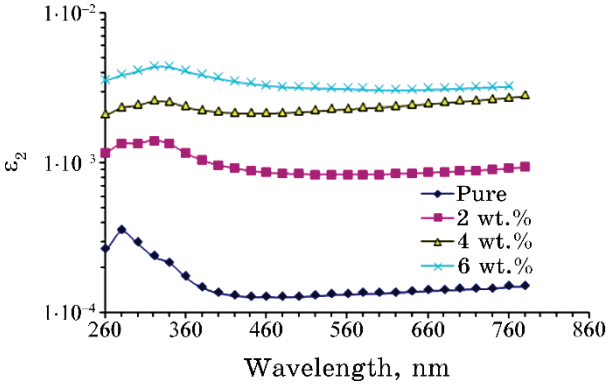

Fig. 9. The variation of imaginary part of the dielectric constant of PVA–In_2O_3–Fe_2O_3 nanocomposites with wavelength.

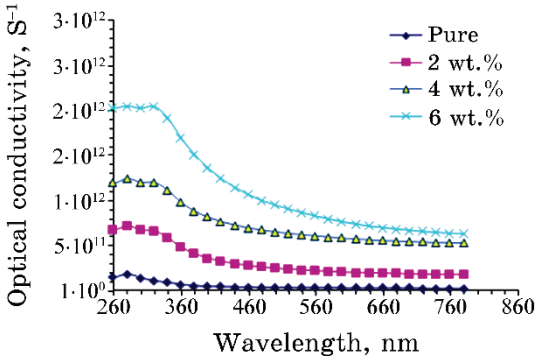

Fig. 10. The variation of optical conductivity of PVA–In_2O_3–Fe_2O_3 nanocomposites with wavelength.

integrated into polyvinyl alcohol (PVA), resulting in the development of cost-effective optoelectronic nanocomposites. The percentage of In_2O_3–Fe_2O_3 nanoparticles in PVA–In_2O_2–Fe_2O_3 nanocomposites determines how much light the composites absorb. At 6 weight percent (wt.%) of In_2O_3–Fe_2O_3 nanoparticles, the energy gap of PVA for permitted indirect transitions dropped from 4.75 eV to 4.15 eV and, for prohibited indirect transitions, from 4.4 eV to 3.55 eV.

Optoelectronics is one of numerous optical areas and nanoscale technologies, which will benefit greatly from this finding. These enhancements are closely related to the variables of extinction coefficient, absorption coefficient, optical conductivity, refractive index, imaginary and real dielectric constants, and concentrations of In_2O_3–Fe_2O_3 nanoparticles. Happening more often, nanocomposites made of PVA–In_2O_3–Fe_2O_3 show outstanding optical properties,

which increase their prospective applications in electric and opto-electronic fields, according to these results.

REFERENCES

1. M. Hdidar, S. Chouikhi, A. Fattoum, M. Arous, and A. Kallel, *Journal of Alloys and Compounds*, **750**: 375 (2018); https://doi.org/10.1016/j.jallcom.2018.03.272
2. S. M. Mahdi and M. A. Habeeb, *Optical and Quantum Electronics,* **54**, Iss. 12: 854 (2022); https://doi.org/10.1007/s11082-022-04267-6
3. V. M. Mohan, P. B. Bhargav, V. Raja, A. K. Sharma, and V. V. R. Narasimha Rao, *Soft Mater.*, **5**, No. 1: 33 (2007); https://doi.org/10.1080/15394450701405291
4. M. A. Habeeb and Z. S. Jaber, *East European Journal of Physics*, **4**: 176 (2022); doi:10.26565/2312-4334-2022-4-18
5. M. A. Habeeb, *European Journal of Scientific Research*, **57**, No. 3: 478 (2011).
6. Q. M. Jebur, A. Hashim, and M. A. Habeeb, *Egyptian Journal of Chemistry*, **63**: 719 (2020); https://dx.doi.org/10.21608/ejchem.2019.14847.1900
7. R. Tintu, K. Saurav, K. Sulakshna, V. P. N. Nampoori, P. Radhakrishnan, and S. Thomas, *J. Nano Oxide Glas.*, **2**, No. 4: 167 (2010).
8. A. H. Hadi and M. A. Habeeb, *Journal of Mechanical Engineering Research and Developments*, **44**, No. 3: 265 (2021); https://jmerd.net/03-2021-265-274
9. N. Hayder, M. A. Habeeb, and A. Hashim, *Egyptian Journal of Chemistry*, **63**: 577 (2020); doi:10.21608/ejchem.2019.14646.1887
10. S. M. Mahdi and M. A. Habeeb, *Polymer Bulletin*, **80**, No. 12: 12741 (2023); https://doi.org/10.1007/s00289-023-04676-x
11. M. A. Habeeb, A. Hashim, and N. Hayder, *Egyptian Journal of Chemistry*, **63**: 709 (2020); https://dx.doi.org/10.21608/ejchem.2019.13333.1832
12. A. Hashim, M. A. Habeeb, and Q. M. Jebur, *Egyptian Journal of Chemistry*, **63**: 735 (2020); https://dx.doi.org/10.21608/ejchem.2019.14849.1901
13. S. M. Mahdi and M. A. Habeeb, *Physics and Chemistry of Solid State*, **23**, No. 4: 785 (2022); doi:10.15330/pcss.23.4.785-792
14. Nawras Karim Al-Sharifi and Majeed Ali Habeeb, *Silicon*, **15**: 4979 (2023); https://doi.org/10.1007/s12633-023-02418-2
15. M. A. Habeeb and W. S. Mahdi, *International Journal of Emerging Trends in Engineering Research*, **7**, No. 9: 247 (2019); doi:10.30534/ijeter/2019/06792019
16. M. A. Habeeb and R. S. Abdul Hamza, *Journal of Bionanoscience*, **12**, No. 3: 328 (2018); https://doi.org/10.1166/jbns.2018.1535
17. A. Hashim, A. J. Kadham Algidsawi, H. Ahmed, A. Hadi, and M. A. Habeeb, *Nanosistemi, Nanomateriali, Nanotehnologii*, **19**, Iss. 2: 353 (2021); https://doi.org/10.15407/nnn.19.02.353
18. M. A. Habeeb, A. Hashim, and N. Hayder, *Egyptian Journal of Chemistry*, **63**: 697 (2020); https://dx.doi.org/10.21608/ejchem.2019.12439.1774
19. M. A. Habeeb and W. K. Kadhim, *Journal of Engineering and Applied Sciences*, **9**, No. 4: 109 (2014); doi:10.36478/jeasci.2014.109.113

20. Alaa Abass Mohammed and Majeed Ali Habeeb, *Silicon*, **15**: 5163 (2023); https://doi.org/10.1007/s12633-023-02426-2
21. M. A. Habeeb, *Journal of Engineering and Applied Sciences*, **9**, No. 4: 102 (2014); doi:10.36478/jeasci.2014.102.108
22. A. Hashim, A. J. Kadham, A. Hadi, and M. A. Habeeb, *Nanosistemi, Nanomateriali, Nanotehnologii*, **19**, Iss. 2: 327 (2021); https://doi.org/10.15407/nnn.19.02.327
23. S. M. Mahdi and M. A. Habeeb, *Digest Journal of Nanomaterials and Biostructures*, **17**, No. 3: 941(2022); https://doi.org/10.15251/DJNB.2022.173.941
24. A. Hashim, A. J. Kadham Algidsawi, H. Ahmed, A. Hadi, and M. A. Habeeb, *Nanosistemi, Nanomateriali, Nanotehnologii*, **19**, Iss. 1: 91 (2021); https://doi.org/10.15407/nnn.19.01.091
25. A. H. Hadi and M. A. Habeeb, *Journal of Physics: Conference Series*, **1973**, No. 1: 012063 (2021); doi:10.1088/1742-6596/1973/1/012063
26. Q. M. Jebur, A. Hashim, and M. A. Habeeb, *Egyptian Journal of Chemistry*, **63**, No. 2: 611 (2020); https://dx.doi.org/10.21608/ejchem.2019.10197.1669
27. Bahaa Hussien Rabee and Idrees Oreibi, *Bulletin of Electrical Engineering and Informatics*, **7**, No. 4: 538 (2018); https://doi.org/10.11591/eei.v7i4.924
28. M. A. Habeeb and A. H. Mohammed, *Optical and Quantum Electronics*, **55**, Iss. 9: 791 (2023); https://doi.org/10.1007/s11082-023-05061-8
29. M. H. Dwech, M. A. Habeeb, and A. H. Mohammed, *Ukr. J. Phys.*, **67**, No. 10: 757 (2022); https://doi.org/10.15407/ujpe67.10.757
30. R. S. Abdul Hamza and M. A. Habeeb, *Optical and Quantum Electronics*, **55**, Iss. 8: 705 (2023); https://doi.org/10.1007/s11082-023-04995-3
31. A. J. Kadham Algidsawi, A. Hashim, A. Hadi, M. A. Habeeb, and H. H. Abed, *Physics and Chemistry of Solid State*, **23**, No. 2: 353 (2022); https://doi.org/10.15330/pcss.23.2.353-360
32. M. A. Habeeb and W. H. Rahdi, *Optical and Quantum Electronics*, **55**, Iss. 4: 334 (2023); https://doi.org/10.1007/s11082-023-04639-6
33. H. N. Chandrakala, B. Ramaraj, Shivakumaraiah, G. M. Madhu, and Siddaramaiah, *Journal of Alloys and Compounds*, **551**: 531 (2013); https://doi.org/10.1016/j.jallcom.2012.10.188
34. A. Hashim and M. A. Habeeb, *Journal of Bionanoscience*, **12**, No. 5: 660 (2018); https://doi.org/10.1166/jbns.2018.1578
35. S. M. Mahdi and M. A. Habeeb, *AIMS Materials Science*, **10**, No. 2: 288 (2023); doi:10.3934/matersci.2023015
36. O. E. Gouda, S. F. Mahmoud, A. A. El-Gendy, and A. S. Haiba, *Indonesian Journal of Electrical Engineering*, **12**, No. 12: 7987 (2014).
37. A. A. Mohammed and M. A. Habeeb, *East European Journal of Physics*, **2**: 157 (2023); doi:10.26565/2312-4334-2023-2-15
38. A. J. K. Algidsawi, A. Hashim, A. Hadi, and M. A. Habeeb, *Semiconductor Physics, Quantum Electronics and Optoelectronics*, **24**, No. 4: 472 (2021); https://doi.org/10.15407/spqeo24.04.472
39. N. Tran, A. Mir, D. Mallik, A. Sinha, S. Nayar, and T. J. Webster, *Int. J. Nanomedicine*, **5**: 277 (2010).
40. Z. S. Jaber, M. A. Habeeb, and W. H. Radi, *East European Journal of Phys-*

ics, **2**: 228 (2023); doi:10.26565/2312-4334-2023-2-25
41. M. A. Habeeb and R. S. A. Hamza, *Indonesian Journal of Electrical Engineering and Informatics*, **6**, No. 4: 428 (2018); doi:10.11591/ijeei.v6i1.511
42. N. K. Al-Sharifi and M. A. Habeeb, *East European Journal of Physics*, **2**: 341 (2023); doi:10.26565/2312-4334-2023-2-40
43. Madalina Elena Grigore, Elena Ramona Biscu, Alina Maria Holban, Monica Cartelle Gestal, and Alexandru Mihai Grumezescu, *Pharmaceuticals*, **9**, No. 4: 75 (2016); https://doi.org/10.3390/ph9040075

Наносистеми, наноматеріали, нанотехнології
Nanosistemi, Nanomateriali, Nanotehnologii
2025, т. 23, № 2, сс. 559–568
https://doi.org/10.15407/nnn.23.02.0559

© 2025 ІМФ (Інститут металофізики
ім. Г. В. Курдюмова НАН України)
Надруковано в Україні.

PACS numbers: 72.80.Tm, 77.22.Ch, 77.22.Gm, 81.07.Pr, 82.35.Np

Fabrication and Tailored Dielectric Characteristics of ZrO_2–Sb_2O_3-Nanoparticles-Doped PVA for Electronics Applications

Ahmed Hashim[1] and Farhan Lafta Rashid[2]

[1]*College of Education for Pure Sciences,*
Department of Physics,
University of Babylon,
Hillah, Iraq
[2]*College of Engineering,*
Petroleum Engineering Department,
University of Kerbala,
Kerbala, Iraq

Polymer-nanocomposites' films have numerous applications in various fields due to their few cost, lightweight, and good chemical and physical properties. The current study aims to investigate of dielectric properties of PVA–ZrO_2–Sb_2O_3 nanocomposites at frequency range from 100 Hz to 5 MHz. The results demonstrate that the dielectric constant, dielectric loss, and A.C. electrical conductivity of PVA are increased with increasing the ZrO_2–Sb_2O_3-nanoparticles' content. The dielectric constant and dielectric loss of PVA–ZrO_2–Sb_2O_3 nanocomposites are reduced, while the A.C. electrical conductivity is increased with rising frequency. The obtained results exhibited that the PVA–ZrO_2–Sb_2O_3 nanocomposites can be considered as promising nanomaterials to apply various electronics applications.

Полімерні нанокомпозитні плівки мають численні застосування в різних галузях завдяки своїй низькій вартості, легкій вазі та добрим хемічним і фізичним властивостям. Метою цього дослідження є вивчення діелектричних властивостей нанокомпозитів ПВС–ZrO_2–Sb_2O_3 в діапазоні частот від 100 Гц до 5 МГц. Результати показали, що діелектрична проникність, діелектричні втрати та змінна електропровідність полівінілового спирту збільшувалися зі збільшенням вмісту наночастинок ZrO_2–Sb_2O_3. Діелектрична проникність і діелектричні втрати нанокомпозитів ПВС–ZrO_2–Sb_2O_3 зменшувалися, тоді як змінна електропровідність збільшувалася зі зростанням частоти. Одержані результати показали, що нанокомпозити ПВС–ZrO_2–Sb_2O_3 можна розглядати як перспективні наноматеріяли для застосування в різних електронних пристроях.

Key words: PVA, ZrO_2–Sb_2O_3, nanocomposites, dielectric properties, electronics applications.

Ключові слова: полівініловий спирт, ZrO_2–Sb_2O_3, нанокомпозити, діелектричні властивості, застосування в електроніці.

(Received 3 September, 2023)

1. INTRODUCTION

Polymeric materials are used instead of traditional materials because they are cheap, light, and have the proper physical and chemical properties. The performance properties of polymer composites are superior to those of individual polymers. It is simple to modify the microstructural, electrical, mechanical, and other properties of polymers by adding nanofillers into the polymer matrices in varying amounts. Modified polymer composites are significantly affected by the size, shape, concentration, and interfacial contact with nanoparticles (NPs). The strength of the bonds between polymer and nanoparticles is an important consideration for composite material performance [1].

Inorganic particles embedded in the polymer matrix have been found to increase the density, mechanical, magnetic, redox, electronic, and thermal properties of the material. These properties depend on the shape, size, adhesion of particle–matrix interfaces, and filler content in the polymer matrix of the nanocomposites (NCs). Metal oxide nanoparticles have been found to be effective for potential applications in photocatalysis [2].

The surface of the nanoscale metal oxides provides vacancies' orbitals to interact with the host polymers that leads to charge transfer between them. The characteristics of individual polymeric nanocomposites are affected by the structure of the components, the content and shape of the nanometal oxides, the morphology of the composites, in addition to the nature of interactions at the interfaces between components in the NCs. Therefore, the improvement of such properties and interfacial interactions between polymers and nanometal oxides acquire a role in decorated the optoelectrical properties of polymeric nanocomposites.

In this article, the authors have focused on the effect and role of different nanometal oxides in the modification of the optical and electrical properties of host polymers to be suitable for optoelectronic and industrial applications [3].

ZrO_2 is a technologically important material due to its superior hardness, high refractive index, optical transparency, chemical stability, photothermal stability, high thermal-expansion coefficient,

low thermal conductivity, high thermomechanical resistance, and high corrosion resistance. These unique properties of ZrO_2 have led to their widespread applications in the fields of optical, structural materials, solid-state electrolytes, gas-sensing, thermal barriers coatings, corrosion-resistant materials, catalysts [4].

Antimony oxide (Sb_2O_3) has a wide band gap of 3.4 eV that is widely used in various applications as catalyst, flame retardant, optoelectronic and photoelectric devices. The photocatalytic activity of pure Sb_2O_3 is low due to high band gap ($E_g = 3.4$ eV) [5].

A polar organic polymer such as polyvinyl alcohol (PVA) has received a lot of interest in recent years due to its highly transparent, mechanical flexibility, affordable, non-toxic, high-biocompatibility, and good storage properties as well as strong chemical and thermal stabilities [6]. The nanoparticles-doped polymers comprised of great applications for a variety of fields like optical, optoelectronics, and electronics approaches [7–31].

The current work aims to investigate of dielectric properties for PVA–ZrO_2–Sb_2O_3 nanocomposites to use in different electronics applications.

2. MATERIALS AND METHODS

The nanocomposites films of PVA doped with ZrO_2–Sb_2O_3 nanoparticles were fabricated *via* dissolving of 0.5 gm PVA in 30 ml of distilled water by using magnetic stirrer to mix the polymer for 1 hour to obtain solution that is more homogeneous. The ZrO_2 and Sb_2O_3 nanoparticles were added to PVA with different contents of 2.2%, 4.4% and 6.6% at constant ratio 1:1. The casting process was used to prepare the PVA–ZrO_2–Sb_2O_3-nanocomposites' films. The dielectric properties of PVA–ZrO_2–Sb_2O_3-nanocomposites' films were tested at frequency ranged between 100 Hz and $5 \cdot 10^6$ Hz using LCR meter type (HIOKI 3532-50 LCR HI TESTER).

The dielectric constant (ε') is given by [32]

$$\varepsilon' = C_p/C_0, \tag{1}$$

where C_p is the matter capacitance, C_0 is the vacuum capacitance.

Dielectric loss (ε'') is determined by [33]

$$\varepsilon'' = \varepsilon' D, \tag{2}$$

where D is the dispersion factor.

The A.C. electrical conductivity is found by [34]

$$\sigma_{A.C.} = 2\pi f \varepsilon' D \varepsilon_0. \tag{3}$$

3. RESULTS AND DISCUSSION

The variation of dielectric constant and dielectric loss for PVA–ZrO_2–Sb_2O_3 nanocomposites with frequency and ZrO_2–Sb_2O_3-NPs' content are shown in Figs. 1–4.

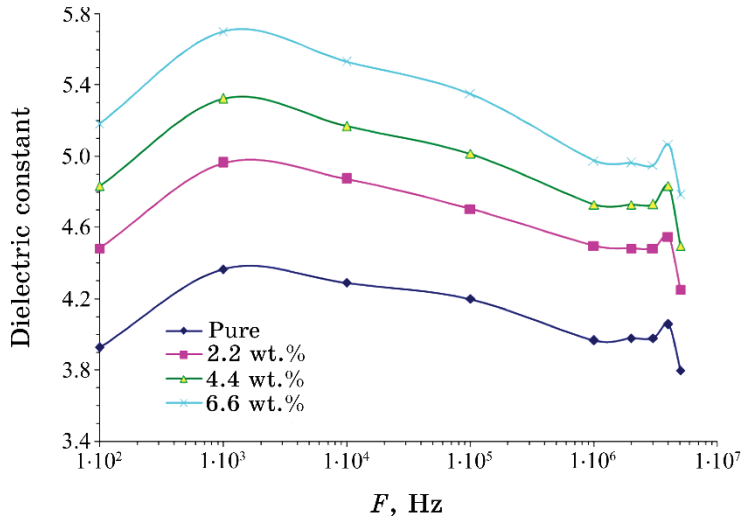

Fig. 1. Variation of dielectric constant for PVA–ZrO_2–Sb_2O_3 nanocomposites with frequency.

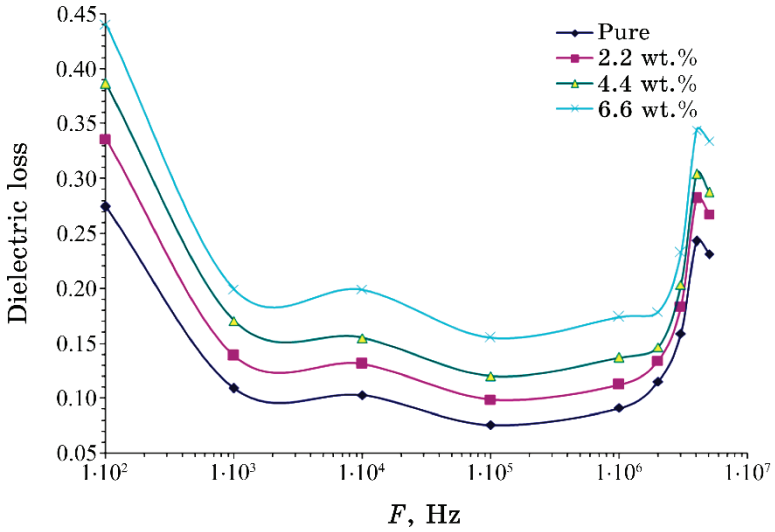

Fig. 2. Behaviour of dielectric loss for PVA–ZrO_2–Sb_2O_3 nanocomposites with frequency.

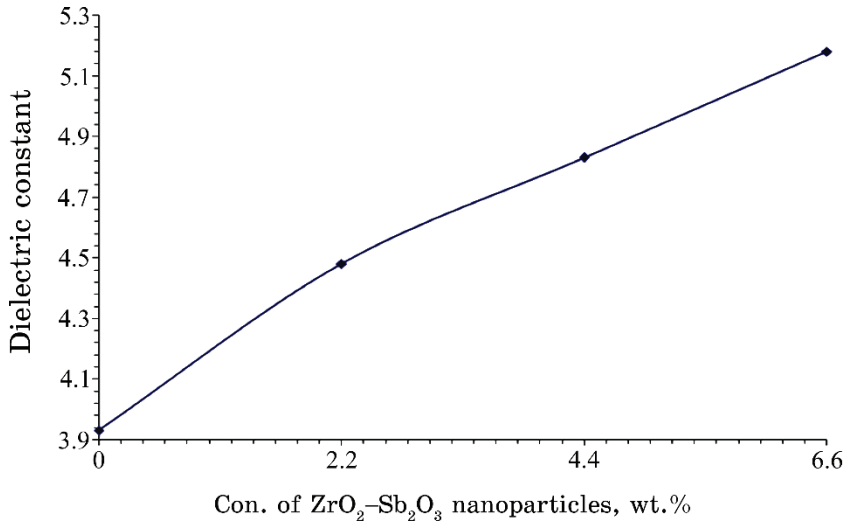

Fig. 3. Dielectric constant variation for PVA with ZrO_2–Sb_2O_3-NPs' content.

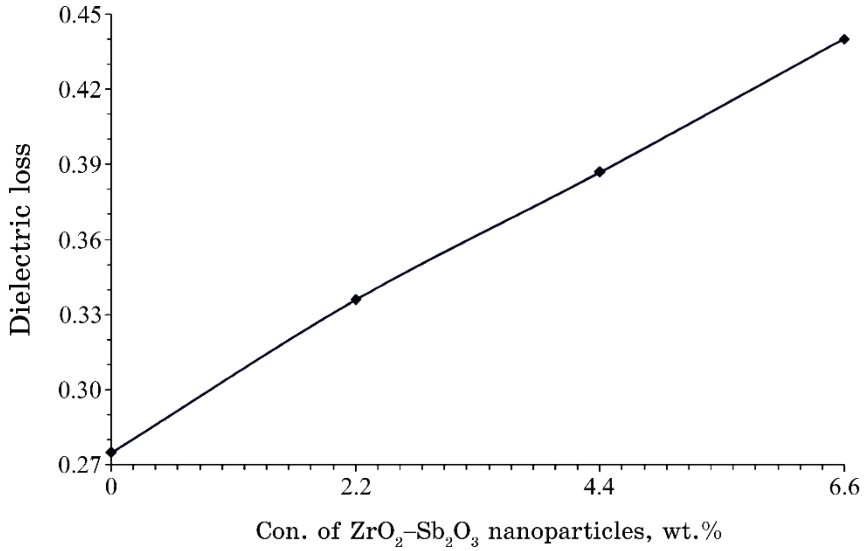

Fig. 4. Behaviour of dielectric loss for PVA with ZrO_2–Sb_2O_3-NPs' content.

The dielectric constant and dielectric loss of PVA increase with increasing ZrO_2–Sb_2O_3-NPs' content; this is due to increase in the number of charges' carriers. The elevated values of dielectric constant and dielectric loss at low frequencies were assigned to the availability of enough time for the dipoles to interact with the

fields before it changes, while dielectric constant and dielectric loss values' decrease at high frequencies relate to the short time available to them [35–45].

Figures 5 and 6 illustrate behaviour of A.C. electrical conductivity for PVA–ZrO_2–Sb_2O_3 nanocomposites with frequency and ZrO_2–

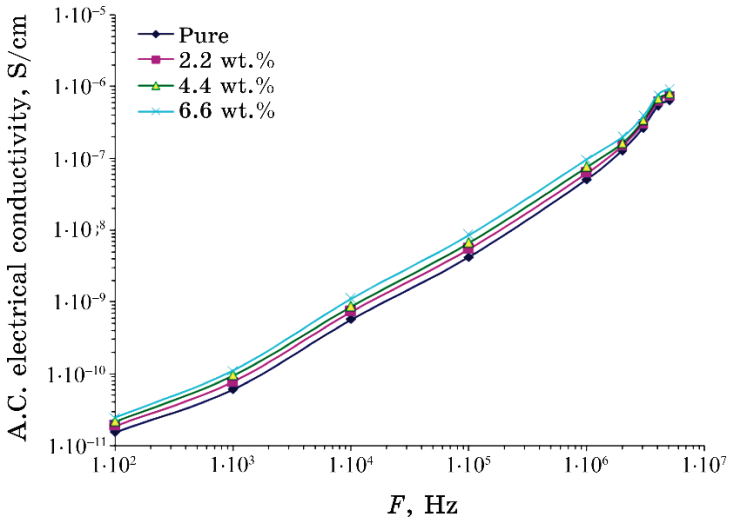

Fig. 5. Behaviour of A.C. electrical conductivity for PVA–ZrO_2–Sb_2O_3 nanocomposites with frequency.

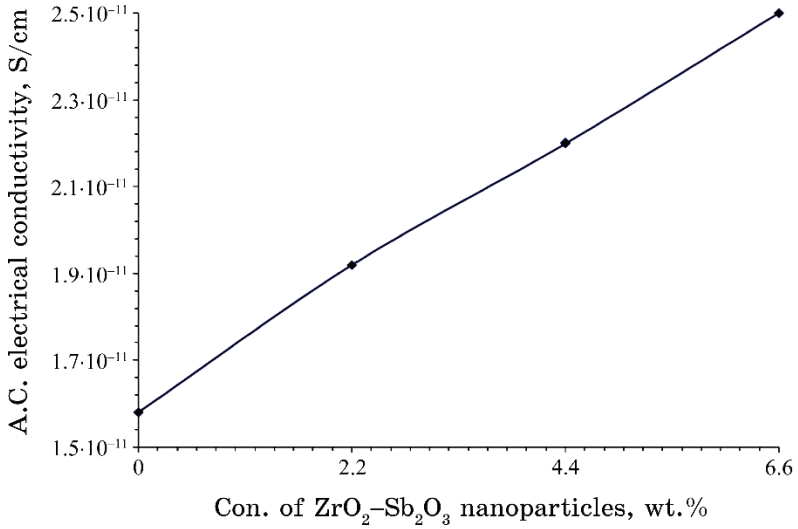

Fig. 6. Performance of A.C. electrical conductivity for PVA with ZrO_2–Sb_2O_3-NPs' content.

Sb_2O_3-NPs' content, respectively. The A.C. conductivity rises with increasing ZrO_2–Sb_2O_3-NPs' content. In all samples, the conductivity increases with frequency. The bonds are designed to switch at high frequencies, resulting in a dielectric transition with vulnerable trustworthy polar functional groups, which causes physiological adaptations within the polymer structure *via* the formation of charge transfer complexes, implying increased electrical conductivity of the films.

The rise of A.C. electrical conductivity with nanoparticles' content can be related to increase of charge-carriers' numbers [46–58].

4. CONCLUSIONS

The present work included investigation of dielectric properties for PVA–ZrO_2–Sb_2O_3 nanocomposites to employ in various electronics fields. The results showed that the dielectric constant, dielectric loss, and A.C electrical conductivity of PVA are increased with increasing the ZrO_2–Sb_2O_3-NPs' content. The dielectric constant and dielectric loss of PVA–ZrO_2–Sb_2O_3 nanocomposites are reduced, while the A.C. electrical conductivity is increased with rising frequency. Finally, the obtained results displayed that the PVA–ZrO_2–Sb_2O_3 nanocomposites can be suitable for various electronics applications.

REFERENCES

1. A. M. Ismail and F. G. El Desouky, *Scientific Reports*, **13**: 1 (2023); https://doi.org/10.1038/s41598-023-32090-w
2. N. Rouabah, R. Nazir, Y. Djaballah, A. Mir, I. Ameur, and O. Beldjebli, *Iranian Journal of Catalysis*, **13**, No. 1: 23 (2023); doi:10.30495/IJC.2023.1970800.1968
3. M. Q. A. Al-Gunaid, G. H. Maheshwarappa, S. B. Shivanna, M. A. H. Dhaif-Allah, W. A. Ahmed, and F. H. Al-Ostoot, *European Journal of Chemistry*, **14**, No. 3: 1 (2023).
4. D. Hirani, K. Shah, and B. S. Chakrabarty, *International Journal of Scientific & Technology Research*, **8**, Iss. 12: 4001 (2019).
5. B. R. Kumar and B. Hymavathi, *Adv. Nat. Sci.: Nanosci. Nanotechnol.*, **9**: 1 (2018); https://doi.org/10.1088/2043-6254/aadc6b
6. Alaa M. Abd-Elnaiem, M. Rashad, T. A. Hanafy, and N. M. Shaalan, *Journal of Inorganic and Organometallic Polymers and Materials*, **33**: 2429 (2023); https://doi.org/10.1007/s10904-023-02616-w
7. Angham Hazim, Hayder M. Abduljalil, and Ahmed Hashim, *Trans. Electr. Electron. Mater.*, **21**: 48 (2020); https://doi.org/10.1007/s42341-019-00148-0
8. A. F. Kadhim and A. Hashim, *Opt. Quant. Electron.*, **55**: 432 (2023); https://doi.org/10.1007/s11082-023-04699-8
9. H. Ahmed and A. Hashim, *Silicon*, **14**: 6637 (2022);

https://doi.org/10.1007/s12633-021-01449-x
10. H. Ahmed and A. Hashim, *Silicon*, **13**: 4331 (2020); https://doi.org/10.1007/s12633-020-00723-8
11. Hind Ahmed and Ahmed Hashim, *Transactions on Electrical and Electronic Materials*, **22**: 335 (2021); https://doi.org/10.1007/s42341-020-00244-6
12. Wissam Obeis Obaid and Ahmed Hashim, *Silicon*, **14**: 11199 (2022); https://doi.org/10.1007/s12633-022-01854-w
13. O. B. Fadil and A. Hashim, *Silicon*, **14**: 9845 (2022); https://doi.org/10.1007/s12633-022-01728-1
14. Hind Ahmed and Ahmed Hashim, *Silicon*, **15**: 2339 (2023); https://doi.org/10.1007/s12633-022-02173-w
15. H. B. Hassan, H. M. Abduljalil, and Ahmed Hashim, *Nanosistemi, Nanomateriali, Nanotehnologii*, **20**, Iss. 4: 941 (2022); https://doi.org/10.15407/nnn.20.04.941
16. H. A. Jawad and Ahmed Hashim, *Nanosistemi, Nanomateriali, Nanotehnologii*, **20**, Iss. 4: 963 (2022); https://doi.org/10.15407/nnn.20.04.963
17. N. AH. Al-Aaraji, Ahmed Hashim, A. Hadi, and H. M. Abduljalil, *Silicon*, **14**: 10037 (2022); https://doi.org/10.1007/s12633-022-01730-7
18. H. Ahmed and A. Hashim, *Opt. Quant. Electron.*, **55**: 1 (2023); https://doi.org/10.1007/s11082-022-04273-8
19. Hind Ahmed and Ahmed Hashim, *Opt. Quant. Electron.*, **55**: 280 (2023); https://doi.org/10.1007/s11082-022-04528-4
20. Ghaith Ahmed and Ahmed Hashim, *Silicon*, **15**: 3977 (2023); https://doi.org/10.1007/s12633-023-02322-9
21. Mohanad H. Meteab, Ahmed Hashim, and Bahaa H. Rabee, *Opt. Quant. Electron.*, **55**: 187 (2023); https://doi.org/10.1007/s11082-022-04447-4
22. Batool Mohammed, Hind Ahmed, and Ahmed Hashim, *Nanosistemi, Nanomateriali, Nanotehnologii*, **21**, Iss. 1: 113 (2023); https://doi.org/10.15407/nnn.21.01.113
23. A. Hashim, *Nanosistemi, Nanomateriali, Nanotehnologii*, **19**, Iss. 3: 647 (2021); https://doi.org/10.15407/nnn.19.03.647
24. Angham Hazim, Ahmed Hashim, and Hayder M. Abduljalil, *Nanosistemi, Nanomateriali, Nanotehnologii*, **18**, No. 4: 983 (2020); https://doi.org/10.15407/nnn.18.04.983
25. Ahmed Hashim and Zinah Sattar Hamad, *Nanosistemi, Nanomateriali, Nanotehnologii*, **18**, No. 4: 969 (2020); https://doi.org/10.15407/nnn.18.04.969
26. A. Hazim, A. Hashim, and H. M. Abduljalil, *Egypt. J. Chem.*, **64**, No. 1: 359 (2021); doi:10.21608/EJCHEM.2019.18513.2144
27. H. Ahmed and A. Hashim, *Journal of Molecular Modeling*, **26**: 1 (2020); doi:10.1007/s00894-020-04479-1
28. H. Ahmed and A. Hashim, *Silicon*, **14**: 4907 (2022); https://doi.org/10.1007/s12633-021-01258-2
29. A. Hashim, *Opt. Quant. Electron.*, **53**: 1 (2021); https://doi.org/10.1007/s11082-021-03100-w
30. H. Ahmed and A. Hashim, *Trans. Electr. Electron. Mater.*, **23**: 237 (2022); https://doi.org/10.1007/s42341-021-00340-1
31. Hind Ahmed and Ahmed Hashim, *Silicon*, **14**: 7025 (2021); https://doi.org/10.1007/s12633-021-01465-x

32. A. H. Selçuk, E. Orhan, S. Bilge Ocak, A.B. Selçuk, and U. Gökmen, *Materials Science–Poland*, **35**, Iss. 4: 885 (2017); doi:10.1515/msp-2017-0108
33. T. A. Abdel-Baset and A. Hassen, *Physica B*, **499**: 24 (2016); http://dx.doi.org/10.1016/j.physb.2016.07.002
34. C. S. Rani and N. J. John, *Int. J. of Innovative Techno. and Exploring Eng.*, **8**, Iss. 11: 1285 (2019).
35. D. Hassan and A. H. Ah-Yasari, *Bulletin of Electrical Engineering and Informatics*, **8**, Iss. 1: 52 (2019); doi:10.11591/eei.v8i1.1019
36. D. Hassan and A. Hashim, *Bulletin of Electrical Engineering and Informatics*, **7**, Iss. 4: 547 (2018); doi:10.11591/eei.v7i4.969
37. Ahmed Hashim, M. H. Abbas, Noor Al-Huda Al-Aaraji, and Aseel Hadi, *J. Inorg. Organomet. Polym.*, **33**: 1 (2023); https://doi.org/10.1007/s10904-022-02485-9
38. A. Hashim, M. H. Abbas, N. AH. Al-Aaraji, and A. Hadi, *Silicon*, **15**: 1283 (2023); https://doi.org/10.1007/s12633-022-02104-9
39. Mohanad H. Meteab, Ahmed Hashim, and Bahaa H. Rabee, *Silicon*, **15**: 1609 (2023); https://doi.org/10.1007/s12633-022-02114-7
40. Z. S. Hamad and A. Hashim, *Nanosistemi, Nanomateriali, Nanotehnologii*, **20**, Iss. 1: 159 (2022); https://doi.org/10.15407/nnn.20.01.159
41. A. Hashim and Z. S. Hamad, *Nanosistemi, Nanomateriali, Nanotehnologii*, **20**, Iss. 1: 165 (2022); https://doi.org/10.15407/nnn.20.01.165
42. A. Hashim and A. Jassim, *Nanosistemi, Nanomateriali, Nanotehnologii*, **20**, Iss. 1: 177 (2022); https://doi.org/10.15407/nnn.20.01.177
43. A. Hashim and Z. S. Hamad, *Nanosistemi, Nanomateriali, Nanotehnologii*, **20**, Iss. 2: 507(2022); https://doi.org/10.15407/nnn.20.02.507
44. B. Mohammed, H. Ahmed, and A. Hashim, *Journal of Physics: Conference Series*, **1879**: 1 (2021); doi:10.1088/1742-6596/1879/3/032110
45. N. Algethami, A. Rajeh, H. M. Ragab, A. E. Tarabiah, and F. Gami, *J. Mater. Sci.: Mater. Electron*, **33**: 10645 (2022); https://doi.org/10.1007/s10854-022-08048-5
46. I. R. Agool, F. S. Mohammed, and A. Hashim, *Advances in Environmental Biology*, **9**, No. 11: 1 (2015).
47. B. H. Rabee and A. Hashim, *European Journal of Scientific Research*, **60**, No. 2: 247 (2011).
48. N. Al-Huda Al-Aaraji, A. Hashim, A. Hadi, and H. M. Abduljalil, *Silicon*, **14**: 4699 (2022); https://doi.org/10.1007/s12633-021-01265-3
49. M. H. Meteab, A. Hashim, and B. H. Rabee, *Silicon*, **15**: 251 (2023); https://doi.org/10.1007/s12633-022-02020-y
50. Ahmed Hashim, Aseel Hadi, Noor Al-Huda Al-Aaraji, and Farhan Lafta Rashid, *Silicon*, **15**: 5725 (2023); https://doi.org/10.1007/s12633-023-02471-x
51. Arshad Fadhil Kadhim and Ahmed Hashim, *Silicon*, **15**: 4613 (2023); https://doi.org/10.1007/s12633-023-02381-y
52. Haitham Ahmed Jawad and Ahmed Hashim, *Nanosistemi, Nanomateriali, Nanotehnologii*, **21**, Iss. 1: 133 (2023); https://doi.org/10.15407/nnn.21.01.133
53. B. Hussien, A. K. Algidsawi, and A. Hashim, *Australian Journal of Basic and Applied Sciences*, **5**, No. 7: 933 (2011).
54. M. A. Habbeb, A. Hashim, and Abdul-Raheem K. AbidAli, *European Journal of Scientific Research*, **61**, No. 3: 367 (2011).

55. A. Hashim, A. Hadi, and M. H. Abbas, *Opt. Quant. Electron.*, **55**: 642 (2023); https://doi.org/10.1007/s11082-023-04929-z
56. A. Hashim, A. Hadi, and M. H. Abbas, *Silicon*, **15**: 6431 (2023); https://doi.org/10.1007/s12633-023-02529-w
57. K. Parangusan, V. Subramaniam, A. B. Ganesan, P. S. Venkatesh, and D. Ponnamma, *J. Mater. Sci.: Mater. Electron.*, **34**: 1 (2023); https://doi.org/10.1007/s10854-023-10478-8
58. Huda Abdul Jalil Hussien, and Ahmed Hashim, *J. Inorg. Organomet. Polym.*, **33**: 2331 (2023); https://doi.org/10.1007/s10904-023-02688-8

Наносистеми, наноматеріали, нанотехнології
Nanosistemi, Nanomateriali, Nanotehnologii
2025, т. 23, № 2, сс. 569–578
https://doi.org/10.15407/nnn.23.02.0569

© 2025 ІМФ (Інститут металофізики
ім. Г. В. Курдюмова НАН України)
Надруковано в Україні.

PACS numbers: 72.80.Tm, 77.22.Ch, 77.22.Gm, 77.84.Lf, 81.07.Pr, 82.35.Np

Influence of CuO–SiO_2-Nanoparticles' Addition on Dielectric Characteristics of PVA for Nanodielectric Applications

Rehab Shather Abdul Hamza[1], Majeed Ali Habeeb[1], and Idrees Oreibi[2]

[1]*College of Education for Pure Sciences,*
Department of Physics,
University of Babylon,
Hillah, Iraq
[2]*Directorate of Education Babylon,*
Ministry of Education,
Babylon, Iraq

The nanocomposites consisting of polyvinyl alcohol (PVA), copper oxide (CuO), and silicon dioxide (SiO_2) are produced using the solution cast method. The samples are consisted of PVA serving as the organic host matrix, together with different amounts of nanosize CuO and SiO_2 ranging from 0 to 6 wt.%. This study investigates the electrical properties of nanocomposites (NCs), namely, PVA–CuO–SiO_2. An inquiry is carried out to examine the electrical properties of NCs throughout the frequency range of 100 to $5{\cdot}10^6$ Hz under standard temperature settings. The experimental findings indicate the reduction in the dielectric constant (ε') and loss (ε'') of the PVA–CuO–SiO_2 NCs with increasing frequency. The electrical conductivity $\sigma_{A.C.}$ of an alternating current (A.C.) increases with higher frequencies. The ε', ε'', and $\sigma_{A.C.}$ of pure PVA increase with the increasing concentration of the CuO–SiO_2 nanoparticles (NPs). The definitive results demonstrated that the PVA–CuO–SiO_2 nanostructures have promising potential for various electrical and electronic nanodevices.

Нанокомпозити, що складаються з полівінілового спирту (ПВС), оксиду Купруму (CuO) та діоксиду Силіцію (SiO_2), було одержано методом лиття з розчину. Зразки складалися з ПВС, який служив органічною матрицею-хазяїном, разом із різною кількістю нанорозмірних CuO та SiO_2 від 0 до 6 ваг.%. У цьому дослідженні вивчено електричні властивості нанокомпозитів (НК), а саме, ПВС–CuO–SiO_2. Було проведено дослідження з метою вивчення електричних властивостей НК у всьому діяпазоні частот від 100 до $5{\cdot}10^6$ Гц за стандартних температурних умов. Експериментальні результати показали пониження діелектричної проникности (ε') та втрат (ε'') НК ПВС–CuO–SiO_2 зі збільшенням частоти. Електропровідність $\sigma_{A.C.}$ змінного струму збільшується за вищих час-

тот. Значення ε', ε'' і $\sigma_{A.C.}$ чистого ПВС збільшуються зі збільшенням концентрації наночастинок $CuO–SiO_2$. Остаточні результати продемонстрували, що наноструктури ПВС–$CuO–SiO_2$ мають багатообіцяючий потенціял для різних електричних та електронних нанопристроїв.

Key words: nanocomposites, PVA, $CuO–SiO_2$ nanoparticles, electrical properties.

Ключові слова: нанокомпозити, полівініловий спирт, наночастинки $CuO–SiO_2$, електричні властивості.

(Received 3 December, 2023)

1. INTRODUCTION

Nanotechnology is a recently emerged scientific field that explores the distinct characteristics of materials at the nanoscale scale, which vary dramatically from those shown by the same materials at higher particle sizes [1, 2]. It has revolutionized multiple domains, with medicine being the most significant beneficiary. Notably, nanotechnology relies on principles of biology, pharmacy, engineering, physics, and chemistry. Therefore, researchers must possess a comprehensive foundation encompassing all these disciplines. Nanotechnology has revolutionized several aspects of our lives. Examining the management of several illnesses has instilled significant optimism for the potential remedy of various formerly untreatable conditions. Nanotechnology has great potential for revolutionizing medical practices by enabling precise diagnostics and highly efficient treatments for life-threatening illnesses like cancer. These advancements will be realized over the next decade via nanomedicine [3, 4].

Polymer nanocomposites (NCs) have gained substantial attention from both academia and industry in recent decades and have emerged as essential materials for developing cutting-edge applications, particularly in the field of electrical engineering [5, 6]. Polyvinyl alcohol (PVA) is well recognized as a very important polymer and is extensively used in several crucial applications and industries. Examples of these applications and businesses include electrochromics, fuel cells, biomedical domains, and sensors. Polyvinyl alcohol (PVA) has distinct characteristics compared to other polymers, such as exceptional mechanical robustness, resistance to corrosion, and favourable thermal stability [7, 8].

Polyvinyl alcohol (PVA) is a hydrophilic artificial polymer that is a granular powder with no smell, transparent appearance, lack of taste, and white or cream hue. Due to its water-solubility, PVA may produce hydroxyl organic components. Two prominent features of

PVA are its susceptibility to biological degradation and its biocompatibility. Polyvinyl alcohol (PVA) has exceptional tensile strength and durability, along with a remarkable ability to resist the permeation of oxygen and odours. The visual propagation of light is exceptional. Additionally, it has exceptional attributes in terms of form, mixing, and adherence [9, 10].

Silicon dioxide, also known as silica, is a compound consisting of silicon and oxygen. Its chemical formula is SiO_2, and it is mostly found in nature as quartz. All types of silica have the same chemical makeup but vary in atomic arrangement [11, 12].

The SiO_2 particles operate as a solid plasticizer, enhancing the composite polymer dimensional stability and chemical and mechanical properties [13]. Moreover, SiO_2 is an amorphous, non-toxic material with several potential applications. Silica is a solid substance that lacks odour and comprises silicon (Si) and oxygen atoms (O_2). Silica (SiO_2) particles go airborne and aggregate to create non-combustible particulate matter [14, 15].

CuO nanoparticles (NPs) have been utilized to improve the characteristics of polymer films, regardless of whether they are derived from petroleum or biological sources. This is attributed to their ability to enhance the mechanical properties of polymers, relatively low toxicity, thermal stability, and high surface area to volume ratio [16]. Copper oxide is a metallic substance with semiconductor properties and unique optical, electrical, and magnetic attributes. It has found applications in several domains, such as near-infrared filters, sensors, catalysis, producing supercapacitors, magnetic storage media, and semiconductors [17, 18].

The electrical properties of pure PVA were improved by including the copper oxide (CuO) and silicon dioxide (SiO_2) nanoparticles (NPs) in this work. The study results show a substantial improvement in the aspects mentioned above.

2. MATERIALS AND METHODS

The casting approach was used to manufacture nanocomposite films by adding polyvinyl alcohol (PVA), copper oxide (CuO), and silicon dioxide (SiO_2) nanoparticles. The experimental protocol included the dissolution of pure polyvinyl alcohol (PVA) in 40 ml of distilled water for 45 minutes. A magnetic stirrer was used to agitate the mixture at 50°C, enhancing the solution uniformity and homogeneity throughout this procedure. The polymer was modified by adding copper oxide (CuO) and silicon dioxide (SiO_2) nanoparticles at varying weight percentages 0%, 2%, 4%, and 6%. Following four days of air-drying the solution at room temperature, the outcome was the achievement of polymer nanocomposite formation. The PVA–

$CuO–SiO_2$ NCs were obtained from the Petri dish and used for measurement. The dielectric properties of NCs were assessed using the LCR meter/HIOKI/3532/50/LCR-HI-TESTER with a frequency range from 100 Hz to 5 MHz.

To get the value of the dielectric constant (ε'), the following formula might be used [19, 20]:

$$\varepsilon' = C_p/C_0, \tag{1}$$

where C_p, C_0 are signifying capacitance and vacuum capacitor.

Dielectric loss (ε'') is given by [21, 22]:

$$\varepsilon'' = \varepsilon' D; \tag{2}$$

here, the displacement (D) is used.

The A.C. electrical conductivity is calculated as follows [23, 24]:

$$\sigma_{\text{A.C.}} = \omega\varepsilon_0\varepsilon'', \tag{3}$$

where ω is angular frequency.

3. RESULTS AND DISCUSSION

Figure 1 illustrates the variations in the dielectric properties of nanocomposites made up of polyvinyl alcohol (PVA), copper oxide (CuO), and silicon dioxide (SiO_2), referred to as $PVA–CuO–SiO_2$ nanocomposites, as a function of frequency. The results suggest that the ε' negatively correlates with the frequency (f) in all samples. At low frequencies, the insulating materials' dipoles align with the applied electric field, causing charge accumulation. This accumulation leads to increased polarization and, consequently, an increase in the ε'. At higher frequencies, the dipoles cannot align quickly enough with the direction of the applied electric field; this results in a reduction in polarization and, therefore, a drop in the ε' value. This characteristic has many applications, including communication antennas and microwave components [25, 26].

Figure 2 depicts the dielectric loss of nanocomposites made up of polyvinyl alcohol (PVA), copper oxide (CuO), and silicon dioxide (SiO_2), which varies with frequency. The graph data demonstrates a negative correlation between frequency and dielectric loss, indicating that as frequency increases, dielectric loss decreases. This behaviour is attributed to mobile charges inside the polymer backbone. The occurrence arises from diminishing the impact of space charge polarization as the frequency increases. The dielectric loss of $PVA–CuO–SiO_2$ NCs increases with more electrons, especially, at

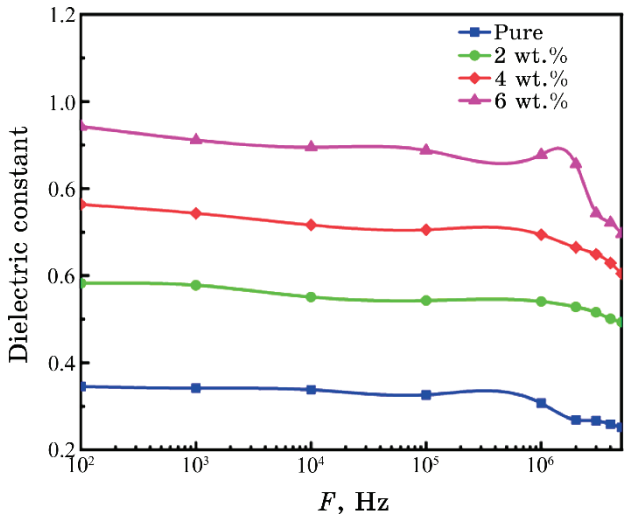

Fig. 1. Behaviour of ε′ with a frequency for the PVA–CuO–SiO_2 NCs.

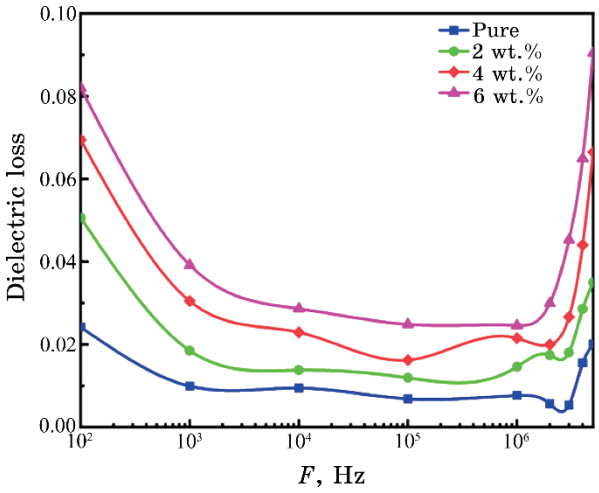

Fig. 2. Behaviour of ε″ with a frequency for the PVA–CuO–SiO_2 NCs.

intermediate frequencies, but decreases as the frequency increases [27–30].

Figures 3 and 4 depict the relationship between the levels of nanoparticles and the dielectric properties, including the dielectric constant and dielectric loss, in nanocomposites made of polyvinyl alcohol (PVA), copper oxide (CuO), and silicon dioxide (SiO_2).

The data demonstrates the relationship between the concentration of CuO–SiO_2 nanoparticles and the simultaneous rise in ε′ and ε″.

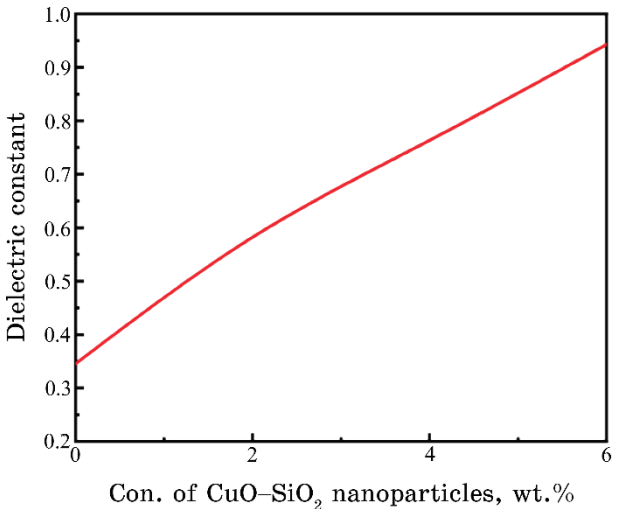

Fig. 3. Influence of $CuO–SiO_2$ NPs' content on the ε′ of PVA–$CuO–SiO_2$ NCs at 100 Hz.

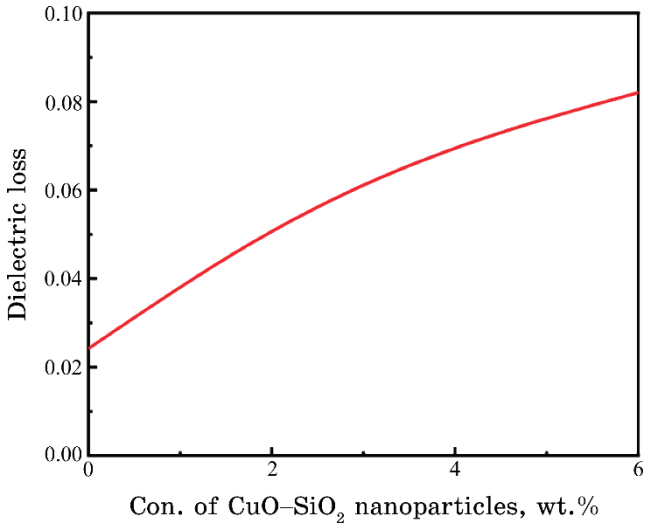

Fig. 4. Influence of $CuO–SiO_2$ NPs' content on the ε″ of PVA–$CuO–SiO_2$ NCs at 100 Hz.

The observed phenomena may be explained by interfacial polarization inside the nanocomposites when an electric field is applied [31, 32]. This polarization increases charge carriers, resulting in a higher dielectric constant and dielectric loss. This behaviour is consistent with the discoveries made by other researchers [33–36].

Figures 5 and 6 depict the correlation between the frequency (f) and the concentration of $CuO–SiO_2$ nanoparticles in the PVA–$CuO–SiO_2$ nanocomposites, especially, in connection to the performance of A.C. electrical conductivity. The graph demonstrates a direct relationship between the A.C. electrical conductivity and the electric

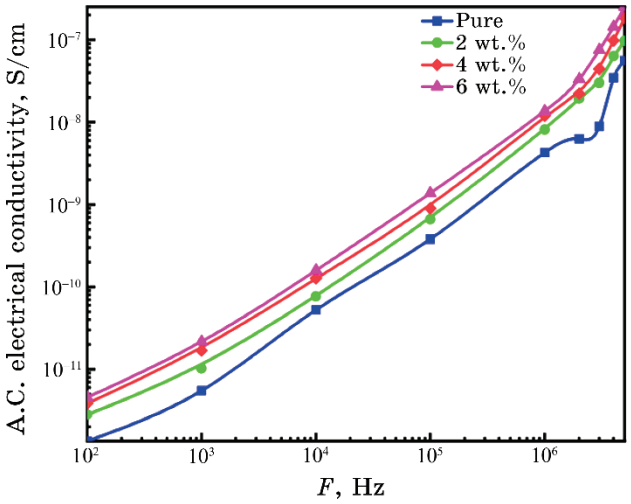

Fig. 5. Variation of conductivity for PVA–$CuO–SiO_2$ NCs with frequency f.

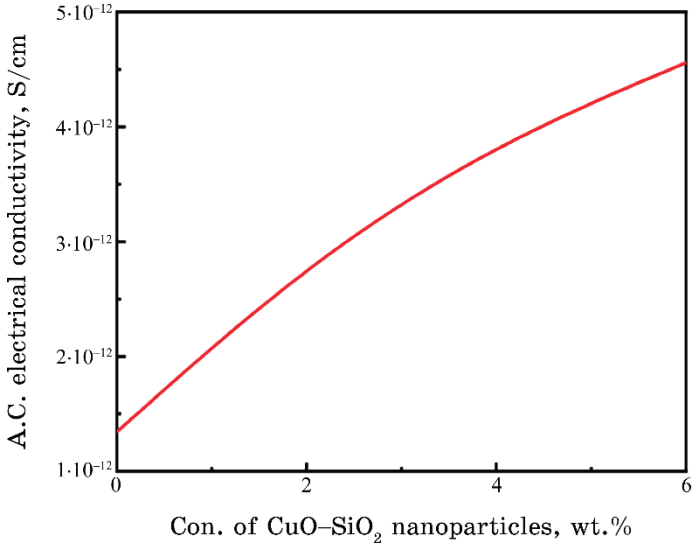

Fig. 6. Variation of electrical conductivity for PVA–$CuO–SiO_2$ NCs with $CuO–SiO_2$ NPs' contents.

TABLE. Dielectric constant, dielectric loss, and A.C. electrical conductivity values at 100 Hz for PVA–CuO–SiO_2 nanocomposites.

Content of CuO–SiO_2 NPs, wt.%	Dielectric constant	Dielectric loss	A.C. electrical conductivity, S/cm
0	0.34	0.024	$1.34 \cdot 10^{-12}$
2	0.58	0.050	$2.81 \cdot 10^{-12}$
4	0.76	0.069	$3.86 \cdot 10^{-12}$
6	0.94	0.082	$4.55 \cdot 10^{-12}$

field frequency in all nanocomposite samples. This phenomenon may be ascribed to the migration of ions inside the clusters and the movement of electrically charged particles [37–39]. At lower frequencies, there is a higher accumulation of charge at the interface between the electrode and electrolyte, leading to a decrease in the number of ions that can move and, therefore, a drop in electrical conductivity. The conductivity increases directly to the concentration of CuO–SiO_2 nanoparticles. The rise in electric charge results from the creation of fully saturated nanoparticles.

Table displays the dielectric constant, dielectric loss, and A.C. electrical conductivity values of PVA–CuO–SiO_2 nanocomposites at a frequency of 100 Hz [40–42].

4. CONCLUSION

The present investigation entails the fabrication of nanostructured films comprising PVA–CuO–SiO_2 by the solution casting technique. An inquiry has been carried out to examine the electrical properties of nanostructures consisting of PVA–CuO–SiO_2. The dielectric properties of PVA–CuO–SiO_2 nanocomposites indicate that ε', ε'', and $\sigma_{A.C.}$ of pure PVA increase, when the concentration of CuO–SiO_2 nanoparticles increases. In addition, the ε' increased from 0.34 to 0.94 at a frequency of 100 Hz, whereas the ε'' increased from 0.024 to 0.082 at the same frequency. The ε' and ε'' drop in magnitude as the frequency increases, but the A.C. electrical conductivity experiences an increase. The dielectric properties of the PVA–CuO–SiO_2 nanostructures render them highly appropriate for a wide range of flexible nanoelectronics applications, owing to their cost-effectiveness, high energy-storage capacity, and low loss.

REFERENCES

1. S. Rajendran, M. Sivakumar, and R. Subadevi, *Materials Letters*, **58**, No. 5: 641 (2004); https://doi.org/10.1016/S0167-577X(03)00585-8

2. S. M. Mahdi and M. A. Habeeb, *Optical and Quantum Electronics,* **54**, Iss. 12: 854 (2022); https://doi.org/10.1007/s11082-022-04267-6
3. V. M. Mohan, P. B. Bhargav, V. Raja, A. K. Sharma, and V. V. R. Narasimha Rao, *Soft Mater.*, **5**, No. 1: 33 (2007); https://doi.org/10.1080/15394450701405291
4. M. A. Habeeb and Z. S. Jaber, *East European Journal of Physics*, **4**: 176 (2022); doi:10.26565/2312-4334-2022-4-18
5. M. A. Habeeb, *European Journal of Scientific Research*, **57**, No. 3: 478 (2011).
6. Q. M. Jebur, A. Hashim, and M. A. Habeeb, *Egyptian Journal of Chemistry*, **63**: 719 (2020); https://dx.doi.org/10.21608/ejchem.2019.14847.1900
7. R. Tintu, K. Saurav, K. Sulakshna, V. P. N. Nampoori, P. Radhakrishnan, and S. Thomas, *J. Nano Oxide Glas.*, **2**, No. 4: 167 (2010).
8. A. H. Hadi and M. A. Habeeb, *Journal of Mechanical Engineering Research and Developments*, **44**, No. 3: 265 (2021); https://jmerd.net/03-2021-265-274/
9. N. Hayder, M. A. Habeeb, and A. Hashim, *Egyptian Journal of Chemistry*, **63**: 577 (2020); doi:10.21608/ejchem.2019.14646.1887
10. S. M. Mahdi and M. A. Habeeb, *Polymer Bulletin*, **80**, No. 12: 12741 (2023); https://doi.org/10.1007/s00289-023-04676-x
11. M. A. Habeeb, A. Hashim, and N. Hayder, *Egyptian Journal of Chemistry*, **63**: 709 (2020); https://dx.doi.org/10.21608/ejchem.2019.13333.1832
12. A. Hashim, M. A. Habeeb, and Q. M. Jebur, *Egyptian Journal of Chemistry*, **63**: 735 (2020); https://dx.doi.org/10.21608/ejchem.2019.14849.1901
13. S. M. Mahdi and M. A. Habeeb, *Physics and Chemistry of Solid State*, **23**, No. 4: 785 (2022); doi:10.15330/pcss.23.4.785-792
14. Madalina Elena Grigore, Elena Ramona Biscu, Alina Maria Holban, Monica Cartelle Gestal, and Alexandru Mihai Grumezescu, *Pharmaceuticals*, **9**, No. 4: 75 (2016); https://doi.org/10.3390/ph9040075
15. M. A. Habeeb and W. S. Mahdi, *International Journal of Emerging Trends in Engineering Research*, **7**, No. 9: 247 (2019); doi:10.30534/ijeter/2019/06792019
16. M. A. Habeeb and R. S. Abdul Hamza, *Journal of Bionanoscience*, **12**, No. 3: 328 (2018); https://doi.org/10.1166/jbns.2018.1535
17. A. Hashim, A. J. Kadham Algidsawi, H. Ahmed, A. Hadi, and M. A. Habeeb, *Nanosistemi, Nanomateriali, Nanotehnologii*, **19**, Iss. 2: 353 (2021); https://doi.org/10.15407/nnn.19.02.353
18. M. A. Habeeb, A. Hashim, and N. Hayder, *Egyptian Journal of Chemistry*, **63**: 697 (2020); https://dx.doi.org/10.21608/ejchem.2019.12439.1774
19. M. A. Habeeb and W. K. Kadhim, *Journal of Engineering and Applied Sciences*, **9**, No. 4: 109 (2014); doi:10.36478/jeasci.2014.109.113
20. M. Hdidar, S. Chouikhi, A. Fattoum, M. Arous, and A. Kallel, *Journal of Alloys and Compounds*, **750**: 375 (2018); https://doi.org/10.1016/j.jallcom.2018.03.272
21. M. A. Habeeb, *Journal of Engineering and Applied Sciences*, **9**, No. 4: 102 (2014); doi:10.36478/jeasci.2014.102.108
22. A. Hashim, A. J. Kadham, A. Hadi, and M. A. Habeeb, *Nanosistemi, Nanomateriali, Nanotehnologii*, **19**, Iss. 2: 327 (2021); https://doi.org/10.15407/nnn.19.02.327

23. S. M. Mahdi and M. A. Habeeb, *Digest Journal of Nanomaterials and Biostructures*, **17**, No. 3: 941 (2022); https://doi.org/10.15251/DJNB.2022.173.941
24. A. Hashim, A. J. Kadham Algidsawi, H. Ahmed, A. Hadi, and M. A. Habeeb, *Nanosistemi, Nanomateriali, Nanotehnologii*, **19**, Iss. 1: 91 (2021); https://doi.org/10.15407/nnn.19.01.091
25. A. H. Hadi and M. A. Habeeb, *Journal of Physics: Conference Series*, **1973**, Iss. 1: 012063 (2021); doi:10.1088/1742-6596/1973/1/012063
26. Q. M. Jebur, A. Hashim, and M. A. Habeeb, *Egyptian Journal of Chemistry*, **63**, No. 2: 611 (2020); https://dx.doi.org/10.21608/ejchem.2019.10197.1669
27. Bahaa Hussien Rabee and Idrees Oreibi, *Bulletin of Electrical Engineering and Informatics*, **7**, No. 4: 538 (2018); https://doi.org/10.11591/eei.v7i4.924
28. M. A. Habeeb and A. H. Mohammed, *Optical and Quantum Electronics*, **55**, Iss. 9: 791 (2023); https://doi.org/10.1007/s11082-023-05061-8
29. M. H. Dwech, M. A. Habeeb, and A. H. Mohammed, *Ukr. J. Phys.*, **67**, No. 10: 757 (2022); https://doi.org/10.15407/ujpe67.10.757
30. R. S. Abdul Hamza and M. A. Habeeb, *Optical and Quantum Electronics*, **55**, Iss. 8: 705 (2023); https://doi.org/10.1007/s11082-023-04995-3
31. A. J. Kadham Algidsawi, A. Hashim, A. Hadi, M. A. Habeeb, and H. H. Abed, *Physics and Chemistry of Solid State*, **23**, No. 2: 353 (2022); https://doi.org/10.15330/pcss.23.2.353-360
32. M. A. Habeeb and W. H. Rahdi, *Optical and Quantum Electronics*, **55**, Iss. 4: 334 (2023); https://doi.org/10.1007/s11082-023-04639-6
33. H. N. Chandrakala, B. Ramaraj, Shivakumaraiah, G. M. Madhu, and Siddaramaiah, *Journal of Alloys and Compounds*, **551**: 531 (2013); https://doi.org/10.1016/j.jallcom.2012.10.188
34. A. Hashim and M. A. Habeeb, *Journal of Bionanoscience*, **12**, No. 5: 660 (2018); https://doi.org/10.1166/jbns.2018.1578
35. S. M. Mahdi and M. A. Habeeb, *AIMS Materials Science*, **10**, No. 2: 288 (2023); doi:10.3934/matersci.2023015
36. O. E. Gouda, S. F. Mahmoud, A. A. El-Gendy, and A. S. Haiba, *Indonesian Journal of Electrical Engineering*, **12**, No. 12: 7987 (2014); https://doi.org/10.11591/telkomnika.v12i12.6675
37. A. A. Mohammed and M. A. Habeeb, *East European Journal of Physics*, **2**: 157 (2023); doi:10.26565/2312-4334-2023-2-15
38. N. K. Al-Sharifi and M. A. Habeeb, *East European Journal of Physics*, **2**: 341 (2023); doi:10.26565/2312-4334-2023-2-40
39. N. Tran, A. Mir, D. Mallik, A. Sinha, S. Nayar, and T. J. Webster, *Int. J. Nanomedicine,* **5**: 277 (2010).
40. Z. S. Jaber, M. A. Habeeb, and W. H. Radi, *East European Journal of Physics*, **2**: 228 (2023); doi:10.26565/2312-4334-2023-2-25
41. M. A. Habeeb and R. S. A. Hamza, *Indonesian Journal of Electrical Engineering and Informatics*, **6**, No. 4: 428 (2018); doi:10.11591/ijeei.v6i1.511
42. A. J. K. Algidsawi, A. Hashim, A. Hadi, and M. A. Habeeb, *Semiconductor Physics, Quantum Electronics and Optoelectronics*, **24**, No. 4: 472 (2021); https://doi.org/10.15407/spqeo24.04.472

Наносистеми, наноматеріали, нанотехнології
Nanosistemi, Nanomateriali, Nanotehnologii
2025, т. 23, № 2, сс. 579–590
https://doi.org/10.15407/nnn.23.02.0579

© 2025 ІМФ (Інститут металофізики
ім. Г. В. Курдюмова НАН України)
Надруковано в Україні.

PACS numbers: 61.05.cp, 61.25.hp, 81.40.Jj, 82.35.Np, 87.19.xb, 87.53.-j, 87.85.Rs

Структура, механічні та бактерицидні властивості гідроґелевих композитів ПВС–ПЕҐ–TiO_2, зшитих електронним опроміненням

І. О. Ситник[1,2], В. Л. Демченко[2], В. Б. Долгошей[1], М. В. Юрженко[2,3], В. Б. Неймаш[4], Г. Є. Монастирський[1], Н. П. Рибальченко[5]

[1]*Національний технічний університет України «Київський політехнічний інститут імені Ігоря Сікорського», Берестейський проспект, 37, 03056 Київ, Україна*
[2]*Інститут електрозварювання ім. Є. О. Патона НАН України, вул. Казимира Малевича, 11, 03150 Київ, Україна*
[3]*Інститут хімії високомолекулярних сполук НАН України, Харківське шосе, 48, 02160 Київ, Україна*
[4]*Інститут фізики НАН України, просп. Науки, 46, 03028 Київ, Україна*
[5]*Інститут мікробіології і вірусології ім. Д. К. Заболотного НАН України, вул. Академіка Заболотного, 154, 03143 Київ, Україна*

В роботі описано процес синтези гідроґелевих матеріялів на основі полівінілового спирту (ПВС) і поліетиленгліколю (ПЕҐ), наповнених частинками діоксиду Титану в концентраціях 1%, 0,1% і 0,01% мас. Розподіл за розмірами частинок діоксиду Титану було одержано методом динамічного розсіювання світла. Для одержання даних про структуру одержаних матеріялів до і після опромінення електронами використовувалася ширококутова рентґенографія, за результатами якої було виявлено можливий взаємочин між частинками діоксиду Титану та полімерною матрицею. Випробування на розрив показали пониження міцности на розрив і деформацію щодо розриву гідроґелю зі зростанням концентрації діоксиду Титану. Гідроґелі ПВС–ПЕҐ–TiO_2 не проявили антимікробної дії до референтних штамів *Staphylococcus aureus* і *Escherichia coli*.

The paper describes the synthesis process of hydrogel materials based on polyvinyl alcohol (PVA) and polyethylene glycol (PEG) filled with tita-

nium-dioxide particles in concentrations of 1%, 0.1%, and 0.01% mass. The size distribution of titanium dioxide particles is obtained by the method of dynamic light scattering. To obtain data on the structure of the obtained materials before and after electron irradiation, wide-angle radiography is used, the results of which reveal a possible interplay between the titanium-dioxide particles and the polymer matrix. Tensile tests show a decrease in the tensile strength and strain to break of the hydrogel with increasing titanium-dioxide concentration. PVA–PEG–TiO_2 hydrogels do not show antimicrobial activity against reference strains of *Staphylococcus aureus* and *Escherichia coli.*

Ключові слова: гідроґель, ПВС–ПЕҐ, TiO_2, електронне опромінення, механічна міцність, бактерицидна активність.

Key words: hydrogel, PVA–PEG, TiO_2, electron irradiation, mechanical strength, bactericidal activity.

(Отримано 18 квітня 2024 р.)

1. ВСТУП

Полімерні композитні матеріяли здатні задовольняти більшість сучасних вимог до матеріялів, які мали б комплекс необхідних функціональних властивостей [1].

Наповнення полімерів дисперсними наповнювачами дає змогу одержувати матеріяли з певними функціональними характеристиками [2, 3].

Гідроґелі — це об'ємні гідрофільні полімерні мережі, здатні вбирати велику кількість води чи то біологічних рідин, що робить їх особливо корисними в медицині та фармацевтиці. Їхня схожість з живими тканинами краща будь-якого іншого виду синтетичних біоматеріялів, що пояснюється їхнім високим вбиранням води та м'якою консистенцією, близькою до консистенції природніх тканин, тим самим забезпечуючи їхню високу біосумісність [4].

Використання гідроґелів для створення пов'язок є сучасною альтернативою традиційним марлевим пов'язкам для лікування ран [5]. Ефективні пов'язки мають бути нетоксичними, підтримувати вологість у місці рани, захищати рану від подальших пошкоджень і сприяти загоєнню. Гідроґелі можуть містити до 96% води, чим підтримують вологе середовище, ідеальне для загоєння рани, можуть вбирати певну кількість ранового ексудату й особливо ефективні для зневоднених або некротичних ран [6]. Листові гідроґелі легко видалити, не пошкоджуючи ложе рани завдяки вологій поверхні між раною та пов'язкою; вони охолоджують рану та сприяють полегшенню болю [7].

Потребу в гідроґелях для медичних застосувань зумовлено їхніми властивостями, такими як гідрофільність і біосумісність. Вони є дуже затребуваними для лікування ран; тому важливо розробити методики найбільш ефективного виробництва гідроґелів медичного призначення з урахуванням доступности сировини та лікувальних властивостей матеріялу.

У цій роботі для синтези гідроґелю використовується полімерний композит ПВС–ПЕҐ із включеннями частинок TiO_2 з метою надання антибактеріяльних властивостей одержаним гідроґелевим матеріялам. ПВС є синтетичним полімером, який використовується з початку 1930-х років у широкому діяпазоні промислових, медичних і харчових застосувань. Різні властивості, такі як в'язкість, температура топлення, показник заломлення, змінюються залежно від молекулярної маси та відсотка гідролізи [8]. ПВС часто використовується у поєднанні з іншими полімерами [9]. Поліетиленґліколь (ПЕҐ) розчиняється у воді, етанолі, ацетонітрилі, бензолі та дихлорметані, є універсальним простим поліефіром, який широко використовується в різних галузях, включаючи медицину [10].

Зшивання гідратованої полімерної системи ПВС–ПЕҐ і результівні механічні властивості досягнуто за допомогою йонізувального випромінення, яке спричиняє радіолізу води й утворення вільних радикалів, таких як радикали OH, H і гідратовані електрони: $H_2O \rightarrow {}^{n}OH$, H^{n}, e^{-}_{aq}, H^{+}, H_2O_2, H_2 [11–14].

Гідроксильні радикали, поміж інших реакційноздатних форм, відіграють найважливішу роль, відриваючи Гідроґен від полімерних ланцюгів з утворенням макрорадикалів, сприяючи перехресному зшиванню макромолекул полімеру [11, 12].

Наночастинки TiO_2 є одними з найбільш вивчених для антимікробних застосувань завдяки їхній бактерицидній активності та безпеці [15]. Крім цього, діоксид Титану вирізняється високою хемічною стабільністю, супергідрофільністю, біосумісністю та відносно дешевому виробництву [16].

Також TiO_2 служить фотокаталізатором і напівпровідником із забороненою зоною у 3,2 еВ, який є як у аморфній (нефотоактивній), так і у трьох природніх кристалічних формах: анатазі, рутилі та брукіті, причому анатаз є більш фотоактивним і, отже, ліпшим для фотокаталітичних застосувань [16].

Отже, діоксид Титану є перспективним наповнювачем для гідроґелевих композитних матеріялів завдяки його фотокаталітичним і антибактеріяльним властивостям. Високий попит на гідроґелеві перев'язувальні матеріяли вимагає подальших досліджень таких матеріялів і методів виробництва їх.

Метою даної роботи є дослідження особливостей структурної організації, механічних і бактерицидних властивостей гідроґеле-

вих композитів ПВС–ПЕҐ–TiO_2, зшитих електронним опроміненням.

2. СИНТЕЗА

Процедура синтези включає розчинення 4,8 г полівінілового спирту (ПВС 17-99) у 28,6 мл води та 0,6 г поліетиленґліколю (ПЕҐ-6000) у 3,95 мл води за температур у 95°C і 20°C відповідно з подальшим перемішуванням. До розчину ПВС додавали розчин ПЕҐ і змішували впродовж 10 хвилин, утворюючи однорідну суміш обох компонентів.

Далі діоксид Титану (Sigma-Aldrich) з середнім діяметром частинок у 265 нм додавали в різних пропорціях (1%, 0,1% і 0,01% мас.) до суміші ПВС–ПЕҐ разом з 2 мл води. Магнетним перемішуванням було досягнуто однорідність розчину ПВС–ПЕҐ–TiO_2.

Сформовані таким чином ґелі поміщались у zip-пакети та зберігалися за температур у 4°C впродовж 4 днів. Охолоджені ґелі було опромінено електронами з енергією у 4 МеВ із дозою опромінення у 33 кГр.

3. МЕТОДИ ДОСЛІДЖЕНЬ

3.1. Метод динамічного розсіювання світла

Для одержання графіка розподілу частинок діоксиду Титану за розмірами застосовано метод динамічного розсіювання світла (DLS) з використанням аналізатора частинок LiteSizer 500. У цьому методі використовується явище хаотичного теплового руху частинок у рідині, де швидкість руху частинок обернено пропорційна їхнім розмірам. Розсіяння світла на зразку детектується й фіксується багато разів. Порівнюючи записи в різні моменти часу можна визначити швидкість руху частинок. Одержана інформація уможливлює одержати розподіл частинок за розмірами та середнє значення розміру.

Для визначення розмірів частинок TiO_2 0,1 г діоксиду Титану додали до 1,5 мл води, результівну суміш заливали в одноразову кювету, яку поміщали в прилад LiteSizer 500. Температура проведення досліджень складала 25°C.

3.2. Метод ширококутової рентґенографії

Дослідження кристалічної структури TiO_2 й структурної організації зразків на основі полівінілового спирту проводилися методом ширококутової рентґенографії на дифрактометрі XRD-7000

виробництва Shimadzu. Його рентґенооптична схема використовує метод Дебая–Шеррера на проходження первинного пучка електронів через досліджуваний зразок із застосуванням CuK_α-випромінення ($\lambda = 1.54$ Å) і графітового монохроматора.

Відносний рівень кристалічности аморфно-кристалічного полімеру визначався за формулою

$$X_{\text{кр}} = \frac{Q_{\text{кр}}}{Q_{\text{кр}} + Q_{\text{ам}}} \cdot 100;$$

тут $Q_{\text{кр}}$, $Q_{\text{ам}}$ — площа графіку під дифракційними максимумами для кристалічної й аморфної структури полімеру відповідно, $Q_{\text{кр}} + Q_{\text{ам}}$ — площа всього графіку аморфно-кристалічної структури в інтервалі кутів розсіяння ($2\Theta_1$–$2\Theta_2$).

Дослідження було проведено методом автоматичного покрокового сканування в режимі з $U = 30$ кВ, $I = 30$ мА у інтервалі кутів розсіяння (2Θ) від 3 до 50 ґрадусів і часом експозиції у 5 с. Температура проведення досліджень складала $T = 20 \pm 2$°C.

3.3. Випробування на механічну міцність

Міряння міцности та видовження до розриву зразків з концентраціями у 1%, 0,1% і 0,01% мас. TiO_2 проводили на розривній машині Shimadzu AGS-X 10kN Tensile Tester. Розміри прямокутніх зразків складали 50×8,5×5,8 мм, швидкість розтягу — 5 мм/хв. Для поліпшення зчеплення зразків з тиґлями між зразком і поверхнями тиґлів поміщали тонкий шар паперу, призначений для вбирання надлишкової вологи.

3.4. Антимікробна активність зразків щодо референтних штамів

Оцінка бактерицидної активности зразків проводили щодо референтних штамів умовно-патогенних мікроорганізмів, — грампозитивних *Staphylococcus aureus* ATCC 25923 і грам-неґативних *Escherichia coli* ATCC 25922, — методом дифузії в агар на твердому поживному середовищі Luria–Bertani (LB). Поживне середовище LB у чашках Петрі засівали $0{,}100 \pm 0{,}001$ мл інокулята тест-культур мікроорганізмів *Staphylococcus aureus*, *Escherichia coli* з розрахунку $2{,}5 \pm 0{,}1 \cdot 10^5$ КУО/мл. Зразки, наповнені TiO_2, які мали форму дисків діяметром $d = 10 \pm 0{,}5$ мм поміщали на поверхню поживного середовища, засіяного тест-мікроорганізмами. Чашки зі зразками інкубували 24 год. за температури $T = 37{,}0 \pm 0{,}1$°C. Антимікробну активність оцінювали за наявністю чіткої зони затримки росту навколо диска полімерного зразка. Зразок без напо-

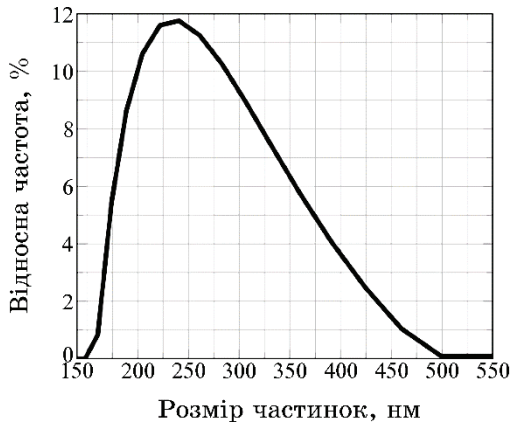

Рис. 1. Залежність відносної частоти частинок TiO_2 від їхнього діяметра.[1]

внювача був використаний як контрольний. Експеримент був повторений тричі.

4. ОБГОВОРЕННЯ ТА РЕЗУЛЬТАТИ

4.1. Розмір частинок

Застосовуючи метод динамічного розсіювання світла (DLS) було проведено аналізу розміру та розподілу частинок. На рисунку 1 представлено залежність відносної частоти розподілу частинок TiO_2 за кількістю від їхнього діяметра.

Середній діяметер частинок TiO_2 склав 265 нм. Частинки мали розміри в діяпазоні від 150 нм до 540 нм, а індекс полідисперсности, який є мірою неоднорідности вибірки за розмірами, складає 9%.

4.2. Ширококутова рентґенографія

Дослідження структури одержаних зразків показали, що чистий полівініловий спирт має напівкристалічну структуру. Це демонструють дифракційні піки із $2\theta_m \cong 11{,}2°$, 19,5°, 23,0°, 40,8°, що відповідають кристалографічним площинам з Міллеровими індексами (100), (101), (200), (201), як показано на рис. 2.

Під час аналізи ширококутових рентґенівських дифрактограм досліджуваних зразків було встановлено, що додавання поліетиленґліколю з молекулярною масою 6000 до складу полівінілового спирту не змінює його структурних особливостей (рис. 3), зокрема кутове положення та співвідношення інтенсивностей основних

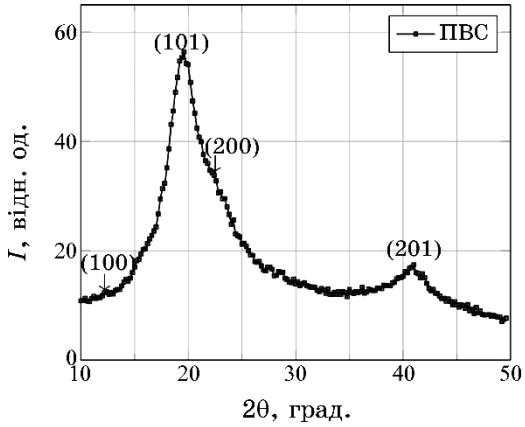

Рис. 2. Рентґенограма полівінілового спирту.[2]

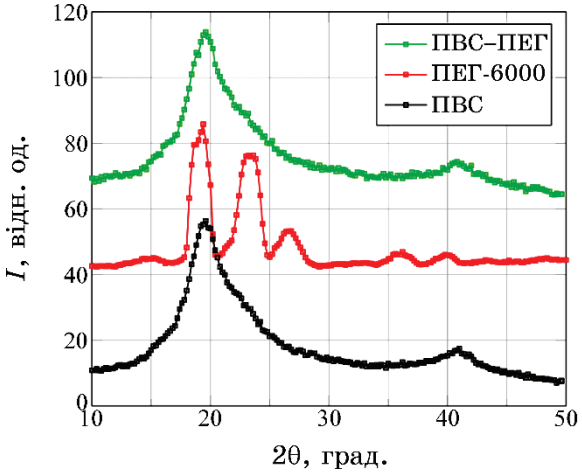

Рис. 3. Рентґенівські дифрактограми полівінілового спирту, поліетиленґліколю 6000 та композиту полівініловий спирт–поліетиленґліколь 6000.[3]

дифракційних піків залишаються незмінними. Це також підтверджується майже ідентичним рівнем кристалічности ПВС та його суміші з поліетиленґліколем 6000. Кристалічність полівінілового спирту та його суміші з поліетиленґліколем 6000 становить приблизно 46% і 47% відповідно. Варто зазначити, що кристалічність самого поліетиленґліколю 6000 дорівнює близько 88%.

Аналіза рентґенівських дифрактограм вихідного зразка ПВС–ПЕҐ–6000 і зразка, що був опромінений електронами (див. рис. 4), виявила, що опромінення зразка з дозою у

33 кГр приводить до більш вираженого дифракційного піку із $2\theta_m \cong 23{,}0°$, що відповідає кристалографічним площинам (101).

Крім цього, опромінення зразка ПВС–ПЕҐ-6000 швидкими електронами спричиняє збільшення ступеня його кристалічности з 47% до 53%.

Дослідження вихідного порошку TiO_2 методом ширококутової рентґенографії виявили кристалічну структуру анатазу з харак-

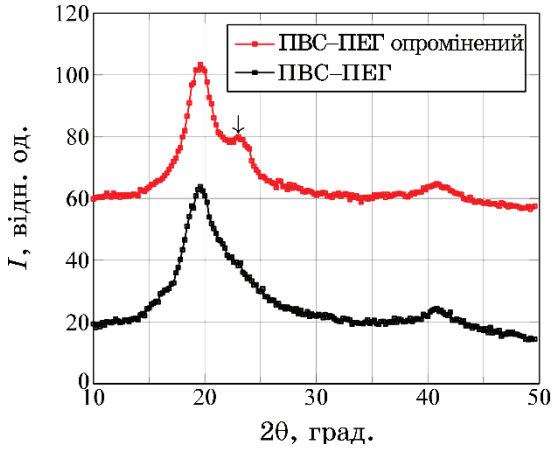

Рис. 4. Ширококутові рентґенівські дифрактограми вихідного зразка полівініловий спирт–поліетиленґліколь 6000 і опроміненого електронами з дозою у 33 кГр.[4]

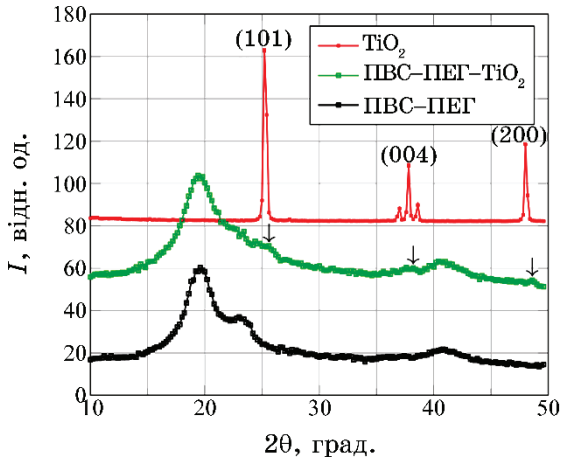

Рис. 5. Ширококутові рентґенівські дифрактограми порошку TiO_2 та зразків опромінених електронами (33 кГр) ПВС–ПЕҐ і ПВС–ПЕҐ–1% мас. TiO_2.[5]

терними піками (101), (004) і (200), які спостерігаються на дифрактограмі (рис. 5).

Дифрактограма зразка ПВС–ПЕҐ, що містить 1% мас. TiO_2, також показала піки, що відповідають TiO_2. Однак ці піки продемонстрували невеликий зсув кутового положення порівняно з вихідним порошком TiO_2 (на рис. 5 вказано стрілкою). Це свідчить про можливий взаємочин між полімерною матрицею ПВС–ПЕҐ і частинками TiO_2.

4.3. Випробування на розрив

Аналіза механічних характеристик гідроґелю дає змогу оцінити міцність матеріялу на розрив та виміряти його подовження до розриву.

На рисунку 6 представлено залежність між напруженням і відносною деформацією для зразків полівінілового спирту з поліетиленґліколем (ПВС–ПЕҐ), опромінених електронами, що містять різні концентрації діоксиду Титану.

Результати експерименту дали змогу встановити показники міцности на розрив і максимальне подовження до розриву. Ці значення було внесено в табл.

Результати дослідження свідчать про пониження як міцности на розрив, так і максимального подовження зі збільшенням концентрації TiO_2.

Найбільш ймовірно, що частинки TiO_2 слугують дефектами у полімерній матриці, неґативно впливаючи на механічні властивості, аналогічно до порожнин.

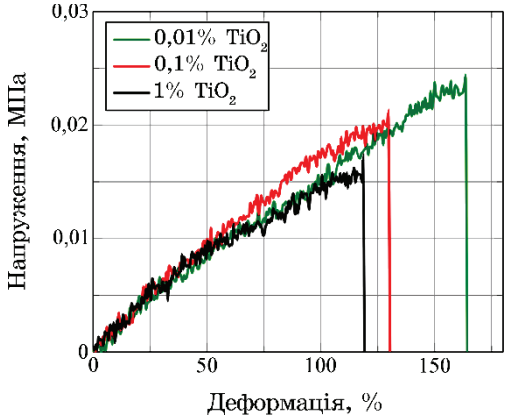

Рис. 6. Криві напруження–деформації для зразків з різними концентраціями TiO_2.[6]

ТАБЛИЦЯ. Значення деформації та механічного напруження для зразків гідроґелю з концентраціями у 0,01%, 0,1%, 1% мас. TiO_2, опроміненого електронами з дозою у 33 кГр.[7]

0,01% TiO_2	0,1% TiO_2	1% TiO_2
≅ 164%	≅ 131%	≅ 120%
23,2 ± 0,5 кПа	20,2 ± 0,4 кПа	16,2 ± 0,5 кПа

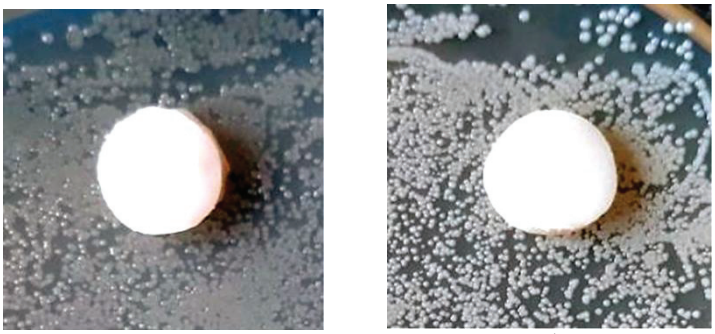

а *б*

Рис. 7. Дослідження бактерицидної дії зразків із вмістом 1% мас. TiO_2: *а — Escherichia coli*, *б — Staphylococcus aureus*.[8]

4.4. Бактерицидна дія

Було проведено перевірку антибактеріяльних властивостей гідроґелевих композитів ПВС–ПЕҐ, що були наповнені частинками оксиду Титану з середнім розміром у 265 нм.

На рисунку 7 зображено гідроґелеві зразки із вмістом 1% мас. TiO_2, розташовані в чашках Петрі, що були засіяні тестовими культурами *Escherichia coli* і *Staphylococcus aureus*.

Відсутність областей без явного росту бактерій вказує на відсутність антимікробної активности зразків. Це може свідчити про те, що розмір використаних частинок TiO_2 є занадто великим, щоб ефективно пригнічувати ріст мікроорганізмів.

5. ВИСНОВКИ

В результаті проведених досліджень визначено середній діяметер частинок TiO_2 гідроґелевих зразків, який становить 265 нм.

Структурні дослідження зразків показали, що з додаванням діоксиду Титану до полімерної матриці ПВС–ПЕҐ спостерігається незначне зміщення кутового положення дифракційних максимумів, які відповідають кристалічній структурі TiO_2. Це може свід-

чити про взаємочин діоксиду Титану з полімерною матрицею ПВС–ПЕҐ.

Дослідження механічних властивостей гідроґелевих матеріялів показали, що зі зростанням концентрації TiO_2 у полімерній матриці відбувається зменшення значень міцности на розрив і видовження до розриву зразків.

Дослідження антибактеріяльних властивостей зразка ПВС–ПЕҐ–1% мас. TiO_2 показали відсутність бактерицидної дії, що, ймовірно, пов'язане з великим розміром частинок.

ФІНАНСУВАННЯ

Роботу виконано за фінансової підтримки ґранту Національного фонду досліджень України «Розробка біополімерних нанокомпозитних матеріялів для стимуляції регенерації живих тканин та загоєння ран» (ідентифікатор заявки 2023.05/0009).

ЦИТОВАНА ЛІТЕРАТУРА–REFERENCES

1. P. D. Stukhlyak, M. M. Mytnyk, and V. O. Orlov, *Materials Science*, **37**, No. 1: 80 (2001); https://doi.org/10.1023/A:1012338422984
2. V. Demchenko, N. Rybalchenko, S. Zahorodnia, K. Naumenko, S. Riabov, S. Kobylinskyi, A. Vashchuk, Ye. Mamunya, M. Iurzhenko, O. Demchenko, G. Adamus, and M. Kowalczuk, *ACS Applied Bio Materials*, **5**: 2576 (2022); https://doi.org/10.1021/acsabm.2c00034
3. V. Demchenko, Ye. Mamunya, S. Kobylinskyi, S. Riabov, K. Naumenko, S. Zahorodnia, O. Povnitsa, N. Rybalchenko, M. Iurzhenko, G. Adamus, and M. Kowalczuk, *Molecules*, **27**: 3769 (2022); https://doi.org/10.3390/molecules27123769
4. N. A. Peppas, P. Bures, W. Leobandung, and H. Ichikawa, *European Journal of Pharmaceutics and Biopharmaceutics*, **50**, No. 1: 27 (2000); https://doi.org/10.1016/S0939-6411(00)00090-4
5. Vanessa Jones and Joseph E. Grey, *BMJ*, **332**, No. 7544: 777 (2006); https://doi.org/10.1136/bmj.332.7544.777
6. Patrick S. Murphy and Gregory R. D. Evans, *Plastic Surgery International*, **2012**: 190436 (2012); https://doi.org/10.1155/2012/190436
7. Ted S. Stashak, Ellis Farstvedt, and Ashlee Othic, *Clinical Techniques in Equine Practice*, **3**, No. 2: 148 (2004); https://doi.org/10.1053/j.ctep.2004.08.006
8. C. C. DeMerlis and D. R. Schoneker, *Food and Chemical Toxicology*, **41**, No. 3: 319 (2003); https://doi.org/10.1016/S0278-6915(02)00258-2
9. P. D. Stukhlyak and K. M. Moroz, *Materials Science*, **46**, No. 4: 455 (2011); https://doi.org/10.1007/s11003-011-9312-x
10. Payam Zarrintaj, Mohammad Reza Saeb, Seyed Hassan Jafari, and Masoud Mozafari, *Compatibilization of Polymer Blends. Micro and Nano Scale Phase Morphologies, Interphase Characterization and Properties* (Elsevier: 2020), Ch. 18, p. 511–537; https://doi.org/10.1016/B978-0-12-816006-0.00018-9

11. H. D. Kupianskyi, I. V. Olkhovyk, and V. B. Neimash, *XV Vseukrainska Naukovo-Praktychna Konferentsiya Studentiv, Aspirantiv ta Molodykh Vchenykh 'Teoretychni i Prykladni Problemy Fizyky, Matematyky ta Informatyky'* (Kyiv: VPI VPK 'POLITEKhNIKA': 2017), p. 35–38; https://ela.kpi.ua/handle/123456789/20459
12. J. M. Rosiak, and P. Ulański, *Radiation Physics and Chemistry*, **55**, No. 2: 139 (1999); https://doi.org/10.1016/S0969-806X(98)00319-3
13. P. Ulański, I. Janik, and J. M. Rosiak, *Radiation Physics and Chemistry*, **52**, No. 1: 289 (1998); https://doi.org/10.1016/S0969-806X(98)00155-8
14. V. B. Neimash, H. D. Kupianskyi, I. V. Olkhovyk, V. Yu. Povarchuk, and I. S. Roguts'kyi, *Ukrainian Journal of Physics*, **62**, No. 5: 402 (2018); https://doi.org/10.15407/ujpe62.05.0402
15. T. Verdier, M. Coutand, A. Bertron, and C. Roques, *Coatings*, **4**, No. 3: 670 (2014); https://doi.org/10.3390/coatings4030670
16. Sarah Glass, Betsy Trinklein, Bernd Abel, and Agnes Schulze, *Frontiers in Chemistry*, **6**: Article 340 (2018); https://doi.org/10.3389/fchem.2018.00340

[1]*National Technical University of Ukraine 'Igor Sikorsky Kyiv Polytechnic Institute', 37, Beresteiskyi Ave., 37, UA-03056 Kyiv, Ukraine*
[2]*E. O. Paton Institute of Electric Welding, N.A.S. of Ukraine, 11, Kazimir Malevich Str., UA-03150 Kyiv, Ukraine*
[3]*Institute of Chemistry of High Molecular Compounds, N.A.S. of Ukraine, 48 Kharkivske Shose, UA-02160 Kyiv, Ukraine*
[4]*Institute of Physics, N.A.S. of Ukraine, 46, Nauky Ave., UA-03028 Kyiv, Ukraine*
[5]*D. K. Zabolotny Institute of Microbiology and Virology, N.A.S. of Ukraine, 154, Academician Zabolotny Str., UA-03143 Kyiv, Ukraine*

[1] **Fig. 1.** Dependence of the relative frequency of TiO_2 particles on their diameter.
[2] **Fig. 2.** Wide-angle x-ray diffraction pattern of polyvinyl alcohol.
[3] **Fig. 3.** Wide-angle x-ray diffraction patterns of polyvinyl alcohol, polyethylene glycol 6000 and the polyvinyl alcohol–polyethylene glycol 6000 composite.
[4] **Fig. 4.** Wide-angle x-ray diffraction patterns of the original sample polyvinyl alcohol–polyethylene glycol 6000 and irradiated with electrons with a dose of 33 kGy.
[5] **Fig. 5.** Wide-angle x-ray diffraction patterns of TiO_2 powder and electron-irradiated (33 kGy) samples of PVA–PEG and PVA–PEG–1 wt.% TiO_2.
[6] **Fig. 6.** Stress–strain curves for samples with different TiO_2 concentrations.
[7] **TABLE.** Values of strain and mechanical stress for hydrogel samples with concentrations of 0.01%, 0.1%, 1% wt. TiO_2 irradiated with electrons with a dose of 33 kGy.
[8] **Fig. 7.** Study of the bactericidal action of samples containing 1% wt. TiO_2: *a*—*Escherichia coli*, *б*—*Staphylococcus aureus*.

Наносистеми, наноматеріали, нанотехнології
Nanosistemi, Nanomateriali, Nanotehnologii
2025, т. 23, № 2, сс. 591–602
https://doi.org/10.15407/nnn.23.02.0591

© 2025 ІМФ (Інститут металофізики
ім. Г. В. Курдюмова НАН України)
Надруковано в Україні.

PACS numbers: 62.23.Pq, 62.25.Mn, 68.37.Hk, 78.30.Jw, 81.70.Bt, 81.70.Pg, 83.80.Tc

Study of Nano-Titanium-Dioxide Effect on Mechanical, Thermal, and Morphological Properties of Polypropylene–Low-Density Polyethylene Blend

Abeer Adnan Abd[1] and Zainab S. Al-Khafaji[2,3]

[1]*Polymer Department,*
College of Materials Engineering,
Babylon University,
Hillah, Babil, Iraq
[2]*Department of Civil Engineering,*
Faculty of Engineering and Built Environment,
Universiti Kebangsaan Malaysia,
43600 UKM Bangi, Selangor, Malaysia
[3]*Imam Ja'afar Al-Sadiq University,*
Qahira, Baghdad, Iraq

The study is aimed to improve the mechanical and thermal properties of a low-density polypropylene–polyethylene blend mixed at 80–20 wt.%. Titanium dioxide is added at different percent ratios: 0, 2, 4, 6, 8 wt.%. Particle sizes and melt processing of the low-density polyethylene–polypropylene blending play a significant role in thermoplastic arrangements. The composite material is prepared using the composite by the melt mixing technique in a screw extruder. The results show that the mechanical properties are improved, when TiO_2 particles are added at an average particle size of 0.201. The tensile strength and hardness increase with the increase in filler content. The tensile modulus increases due to the higher surface area of the filler. The bending strength decreases due to the decrease in elasticity and the increase in tensile strength. The impact strength decreases by 2% and then increases. FT-IR results show the physical bonds between the filler particles and the blend. DSC-test results indicate two glass transition temperatures, making the blend immiscible. SEM results show that ethylene–propylene–diene monomer (EPDM) rubber (as a type of synthetic thermoset elastomeric copolymers produced from a terpolymer of ethylene, propylene and a diene monomer) coupling agents enhance the adhesion between the titanium dioxide and the blended composite.

Метою дослідження було поліпшення механічних і термічних властивостей суміші поліетилену низької густини та поліпропілену, замішаної з вмістом 80–20 мас.%. Діоксид Титану додавали в різних відсоткових співвідношеннях: 0, 2, 4, 6, 8 мас.%. Розміри частинок та оброблення ро-

зтопу суміші поліетилену низької густини та поліпропілену відіграють значну роль у термопластичних композиціях. Композитний матеріял був виготовлений з використанням композиту методом змішування розтопу в шнековому екструдері. Результати показують, що механічні властивості поліпшилися із додаванням частинок TiO_2 із середнім розміром частинок 0,201. Міцність на розрив і твердість зростають зі збільшенням вмісту наповнювача. Модуль пружности збільшується завдяки більшій площі поверхні наповнювача. Міцність на вигин зменшується через зменшення еластичности та збільшення міцности на розрив. Ударна в'язкість зменшується на 2%, а потім зростає. Результати ІЧ-спектроскопії з Фур'є-перетвором проявили фізичні зв'язки між частинками наповнювача та сумішшю. Результати ДСК-тестів показали дві температури склування, що робить суміш незмішуваною. Результати СЕМ показали, що сполучна речовина «синтетичний каучук на основі сополімеру етилену, пропілену з добавкою дієнового мономера» (СКЕПТ) підсилює адгезію між діоксидом Титану та змішаним композитом.

Key words: titanium dioxide, polypropylene, polyethylene, blend, EPDM.

Ключові слова: діоксид Титану, поліпропілен, поліетилен, суміш, СКЕПТ.

(Received 4 February, 2024; in revised form, 22 March, 2024)

1. INTRODUCTION

In recent years, a significant focus has been on the study and development of composites, which incorporate nanoparticles [1–3]. These nanocomposites have garnered significant interest due to their impressive enhancements in various characteristics, such as mechanical strength, optical clarity, and thermal conductivity [4, 5]. In addition, they have shown great potential for a wide range of applications. Nevertheless, a significant hurdle in polymer nanocomposite technology is inhibiting particle aggregation [6–8]. Surface modification can help overcome this issue by improving the interfacial interaction between the polymer matrix and inorganic particles, which, in turn, can enhance the general properties of nanocomposites [9–13].

Polyethylene (PE) and polypropylene (PP) were developed recently due to low cost, good mechanical properties, lightweight, and desirable applications. PE in two kinds, of low and high density, may be added to PP to develop mechanical PP properties [14]. The blend of PP and PE is used because PP and PE have similar characteristics, such as reasonable wear and mechanical, thermal, electrical, and chemical resistance, used in pipes. PE has more moisture and depredation resistance than PP; therefore, it was blended with it [15, 16]. The characteristics of the PP–PE blend are refined by several additives, which are mixed

with them, like adding nanofillers, which improve the properties such as TiO_2, CaO, Al_2O_3, ZrO_2, and SiO_2 have [17].

Inorganic particles like clay, silica, $CaCO_3$, layered silicate nanoparticles, and titanium dioxide (TiO_2) have garnered significant attention as inorganic materials for inorganic–organic nanocomposites. One material that stands out is TiO_2, which has significant potential in various applications, such as photocatalytic activity and photoelectric conversion in solar cells. In addition, TiO_2 nanoparticles also exhibit antibacterial properties, help prevent odours, and have a self-cleaning mechanism [18, 19]. The numerous benefits of TiO_2 make it a highly desirable inorganic component for creating nanocomposite materials. These materials offer exceptional mechanical properties, low density, and protection against the UV and thermal degradation, critical in regions with intense sunlight, high temperatures, and humidity, including Vietnam's tropical climate. Various polymers can be effectively combined with TiO_2 nanoparticles through different processing techniques, including sol–gel or polymerization in solution. These polymers include poly(methyl methacrylate), epoxy, polyethersulphonate, poly(ethylene terephthalate), and polystyrene [20].

By adding small amounts of nanoparticles, polymer nanocomposites improve the mechanical properties, heat resistance, thermal resistance, degradation, and elastic modulus. Besides, other characteristics like melt processing, polymer crystallization, and electrical and thermal conductivities can be modified [21]. Nanofillers like SiO_2, TiO_2, Al_2O_3, and ZrO_2 reinforce the polymers by embedding them in the polymer matrix. TiO_2 is very important due to particular characteristics like low density, thermal degradation, hydrophilic and photocatalytic degradation, and a large surface ratio, which makes them aggregate easily; therefore, styrene ethylene butylene styrene (SEBS) can be used as a coupling agent [22].

SEBS showed good attributes, as found by Sajad and Farmarz's desperation of titania nanoparticles in the matrix, and increased the samples' thermal stability. Another coupling agent used with ethylene and propylene is PDEM (propylene diethylene monomer) to prevent filler agglomeration [23].

The current work aims to enhance the mechanical, thermal, and morphology properties of polypropylene–low-density polyethylene blend by preventing filler agglomeration in nanocomposite material by using EPDM coupling agents.

2. EXPERIMENTAL WORK

The polypropylene purchased from Sabic Company is produced in Saudi Arabia, and the low-density polyethylene purchased from

Amber Kabir Petrochemical Company is made in Iran. The polypropylene and polyethylene pellets were mixed with TiO nanofiller with PDEM as coupling agent, then, put in the twin-screw extruder with a speed of 35 cycles/min at 170°C to mix, then, roll through the roller to get the sheet of 5-mm thickness. The samples are then cut into the required shapes.

3. RESULTS AND DISCUSSION

3.1. Mechanical Properties Tests Results and Discussion

The tensile strength test results (stress–strain curve for the composite) are represented in Fig. 2. The results show that the tensile strength increases, when titanium oxide increases due to high sur-

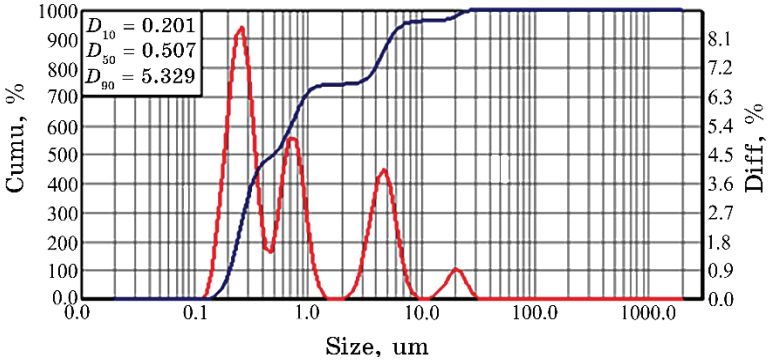

Diam, um	Percent
0.100	0.00
0.200	9.48
0.500	49.80
1.000	71.67
2.000	74.30
5.000	88.15
10.000	96.09
20.000	98.02
45.000	100.00
75.000	100.00

Fig. 1. LBZA average particle size of titanium dioxide.

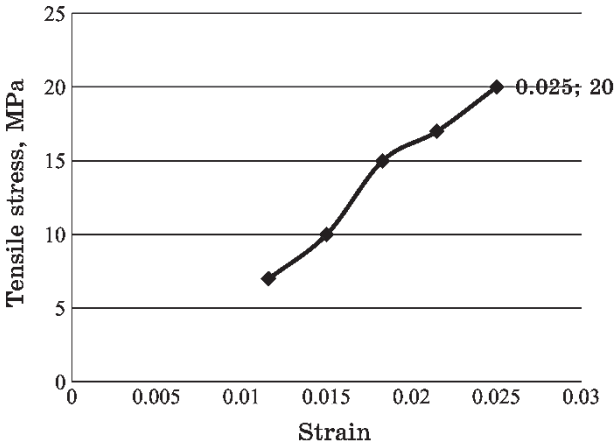

Fig. 2. Tensile strength *versus* strain.

face activity between the filler and the coupling agent PDEM and polypropylene and polyethylene that is due to reduction in interfacial tension, stabilization of morphology, enhancements adhesion between faces in the solid state facilitating the stress transfer, hence improving the mechanical properties of the product.

The tensile strength modulus increases, when the titanium dioxide percentage increases, as shown in Fig. 3, due to the maximum surface area, aspect ratio, and loading, which all will increase the modulus. Through active sites or coupling agents, fillers with strong chain attachments resist the chain extension most.

The hardness increases to 6% of titanium dioxide. Then, it decreases, as shown in Fig. 4, because titanium dioxide has higher hardness than the polypropylene–polyethylene blend and has a high

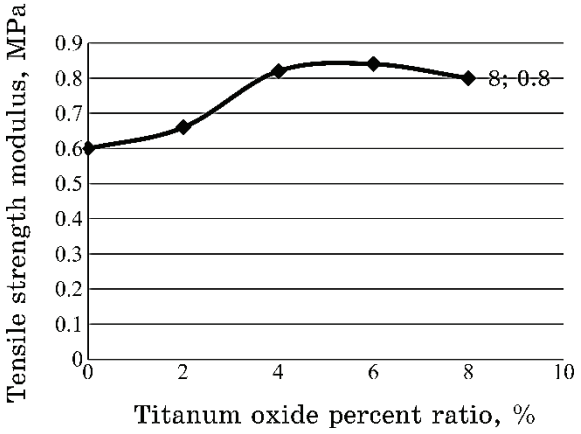

Fig. 3. Tensile modulus *versus* titanium oxide content.

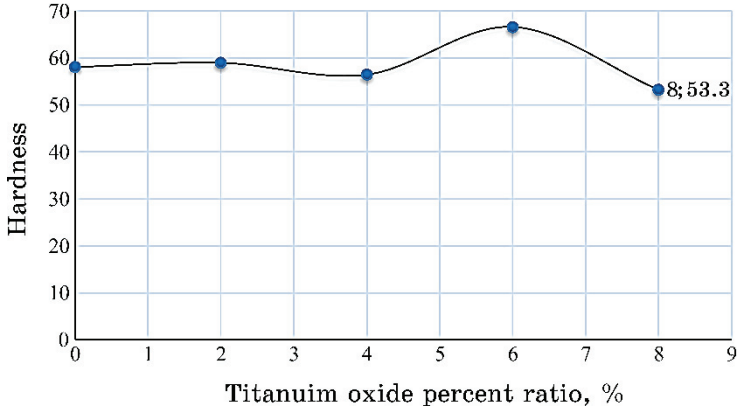

Fig. 4. The total percent hardness *versus* titanium oxide content.

surface area due to the small particle size of the filler. The reason behind the hardness increases is that the density increases. The different shapes of particles, which are irregular, including pentagonal and rectangular shapes, and have high surface area, aspect ratio, and high loading; therefore, the surface area increases.

The flexural strength test was used with the machine at the 2-mm/min speed applied at 3 points. A load was applied at the central axis until fracture occurred. The bending strength decreases, when filler content increases (Fig. 5) due to the high modulus-strength increase of blend material and the elasticity decrease, and it has a brittle fracture. When the filler content is increased, the distance between polymer chains is increased, hindering the movements of chains.

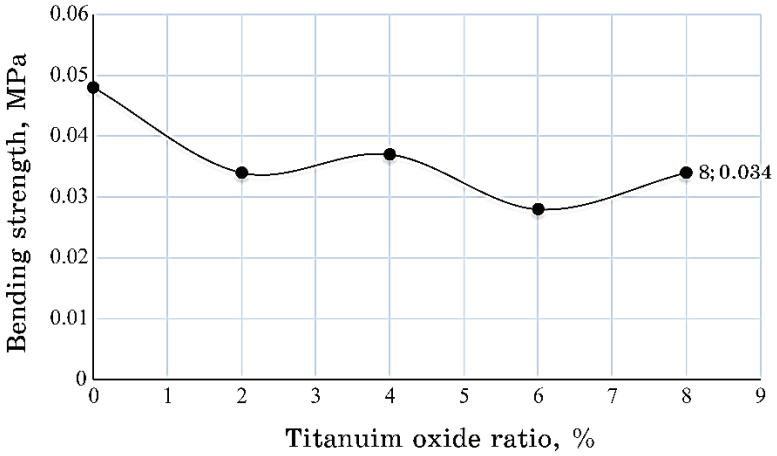

Fig. 5. Bending strength *versus* titanium oxide content.

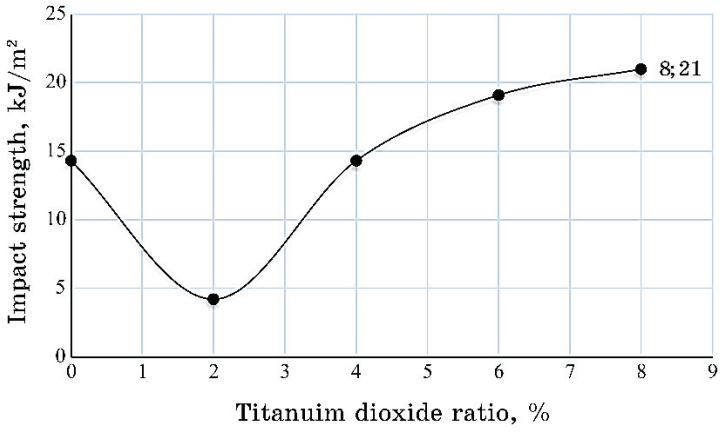

Fig. 6. Impact strength *versus* titanium dioxide ratio content.

The impact strength decreases to 2%, as shown in Fig. 6, because the elasticity decrease is related to PP having a methyl group, which is rigid and attached to a carbon atom of the polymer main chain, limiting the spin of the chain, producing a stronger but less flexible material; then, the impact strength increases; due to the high surface area of filler and high hardness, also titanium dioxide has high surface activity with higher content.

3.2. DSC-Test Results and Discussion

The thermal properties were indicated by the DSC test for the samples. As shown in Figure 7, there are two T_g, 125.59°C and 155.82°C; so, it is an immiscible blend. The glass transition temperature T_g is decreased for the sample 2 and, then, increased in other samples due to the filler-particles' (TiO_2) substantial spaces in the structure performance as strengthening filler between chains due to small average particle size (D50:0.507) and making van der Waals bonds, as shown in Figs. 7–11.

3.3. FT-IR Results and Discussion

As shown in Figure 12, there is a physical attraction between titanium-dioxide particles and the PE–PP blend.

In sample 1, there is no titanium dioxide. Titanium dioxide was

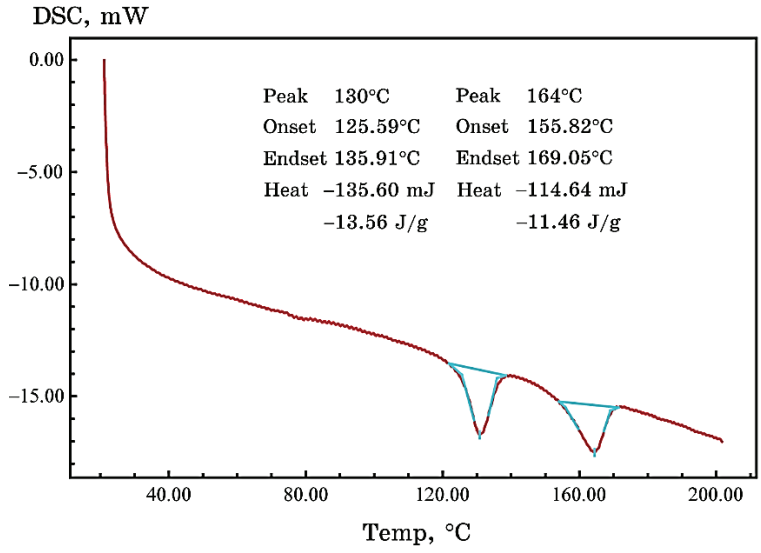

Fig. 7. The DSC test for sample 1.

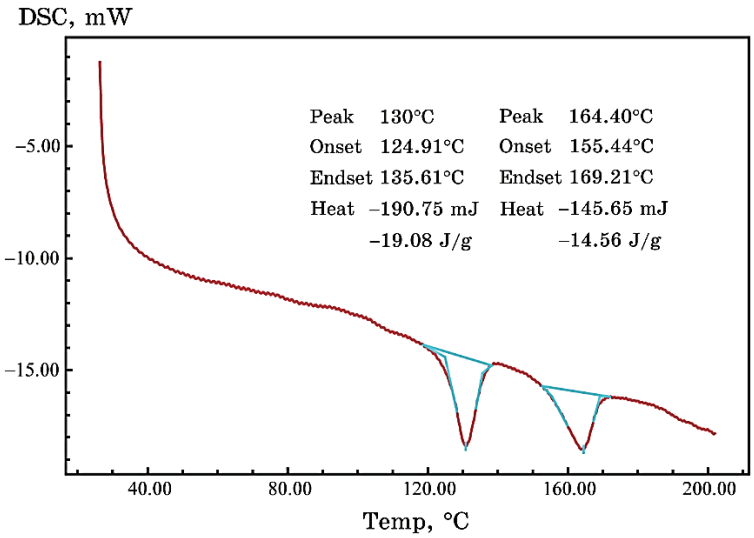

Fig. 8. The DSC test for sample 2.

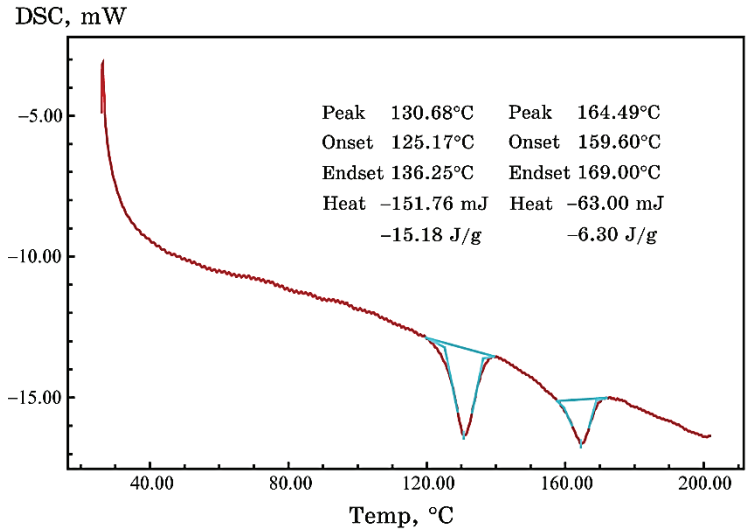

Fig. 9. The DSC test for sample 3.

added in other samples at different ratios 2, 4, 6, 8%. The transparency intensity increases, when the titanium-dioxide filler content increases, because titanium-dioxide particles far apart the distance between chains, and the light can pass through the chains.

Then, the transparency intensity decreases because the content of filler particles increases, and the distance between chains increases.

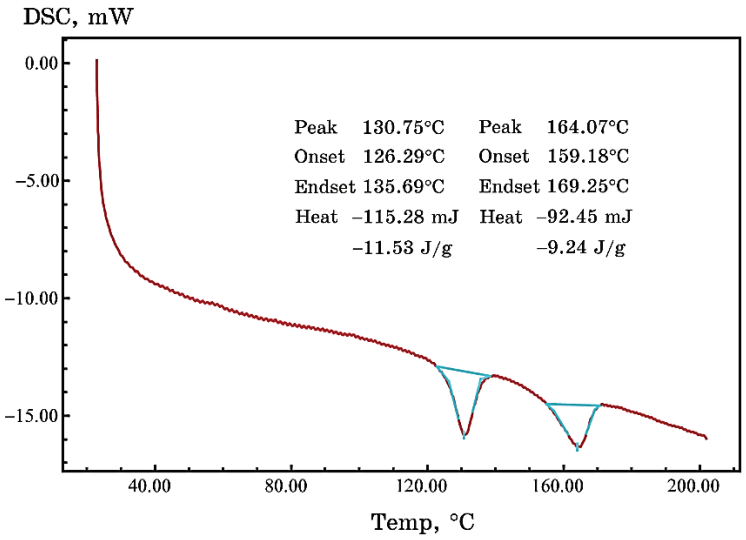

Fig. 10. The DSC test for sample 4.

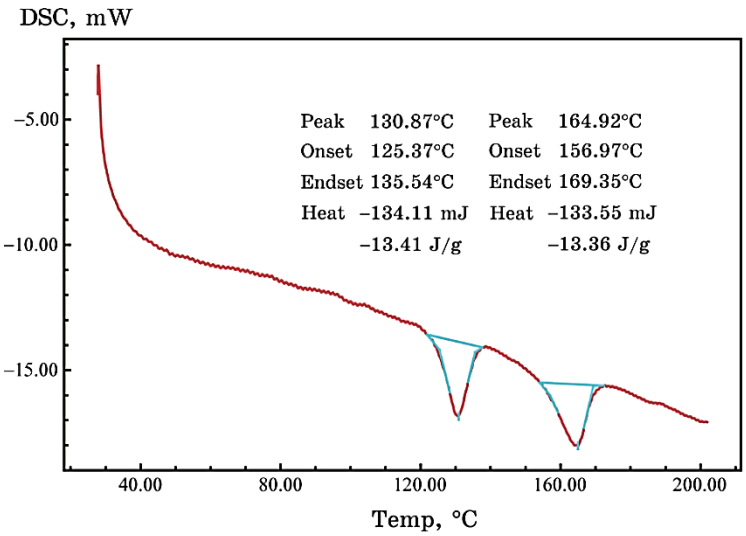

Fig. 11. The DSC test for sample 5.

The light cannot pass through the chains. There is vibration in the range of 466–700 cm^{-1} due to the single bond between the titanium and oxygen atoms, Ti–O, and often present in the stretching of the titanium-dioxide molecule.

The bond at 1410 cm^{-1} and 1375 cm^{-1} occurred due to the symmetric bending of the $-CH_3$ group and the scissoring of an extended

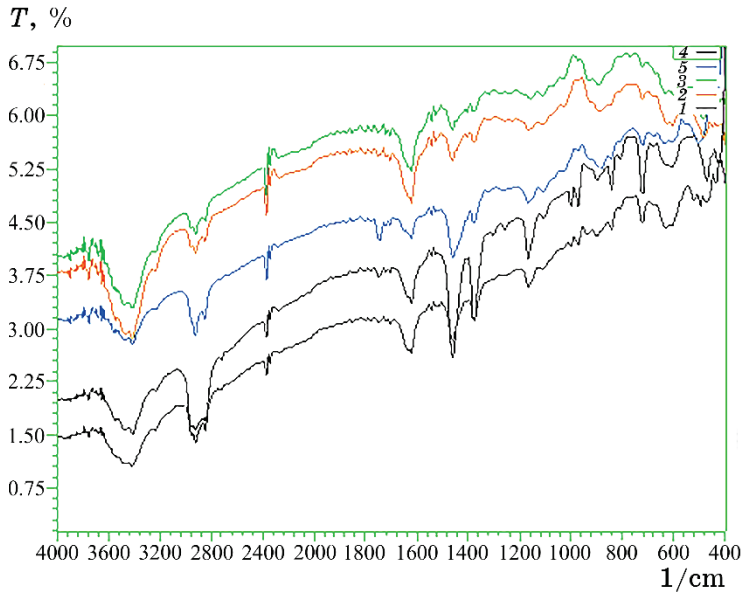

Fig. 12. Transparency *versus* the wavelength for the samples.

chain alkyl group. In addition, the peak at 1462 cm^{-1} is attributed to the vibrational changes occurring in the C–H bond.

3.4. SEM Results and Discussion

The morphology of the specimens shown in Fig. 13 in sample 1 is a pure blend containing 70–20% of PP–PE blend without titanium dioxide, as shown in Fig. 13. There are little delaminations of the PP–PE blend and immiscible blend. In sample 2, there is more delamination and white colour in most of the reigns than in sample 1 due to TiO_2 addition. The homogenous structure appears in the sample 3. As shown in the sample 3, there is no delamination due to good adhesion between TiO_2 particles and the blend, because the EPDM coupling agent enhances the adhesion. As shown in samples 3, 4, the filler particles were distributed evenly due to good adhesion, when the titanium-dioxide filler increased. There is no evidence of agglomeration of filler particles in the samples. In the sample 5, there are separation between titanium-dioxide particles, as shown in white dots, and delamination due to the high fraction of filler content.

4. CONCLUSIONS

1. The tensile stress is improved at 5 wt.% titanium-dioxide con-

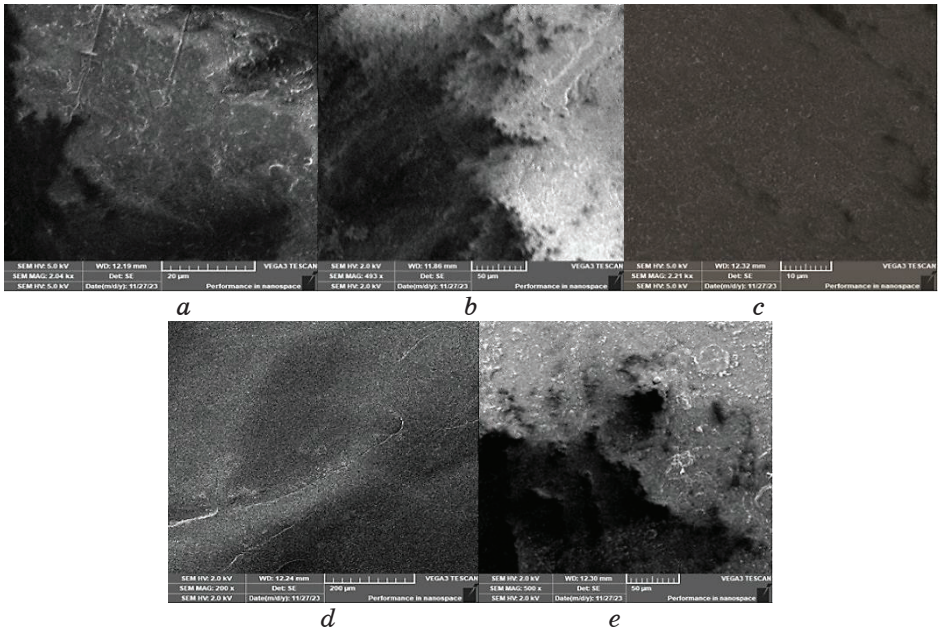

Fig. 13. SEM for the samples (*a*—sample 1 (0% TiO_2); *b*—sample 2 (2% TiO_2); *c*—sample 3 (4% TiO_2); *d*—sample 4 (6% TiO_2); *f*—sample 5 (8% TiO_2).

tent, when compared with neat blend samples.

2. The tensile strength modulus is improved at 5 wt.% titanium-dioxide content.
3. The bending strength has a minimum value of 4%, in which the elasticity is decreased to the minimum value, and the tensile modulus is increased to the maximum value.
4. SEM tests reveal the enhanced morphology in samples 3 and 4 due to the EPDM coupling agent, which enhances the adhesion.
5. The titanium-dioxide particles increase the temperature of the nanocomposites' glass transition. DSC results indicate that the blend is immiscible.

REFERENCES

1. N. S. Radhi and Z. S. Al-Khafaji, *Proc. 6th International Scientific Conference on Nanotechnology, Advanced Materials and Its Applications (May 13–14, 2018, Iraq)*, p. 1–9.
2. S. Sattar, Y. Alaiwi, N. S. Radhi, Z. Al-Khafaji, O. Al-Hashimi, H. Alzahrani, and Z. M. Yaseen, *J. King Saud Univ. Sci.*, **35**, No. 8: 102861 (2023); doi.org/10.1016/j.jksus.2023.102861
3. N. M. Dawood, N. S. Radhi, and Z. S. Al-Khafaji, *Mater. Sci. Forum*, **1002**, No. 1: 33 (2020); doi.org/10.4028/www.scientific.net/MSF.1002.33

4. N. S. Radhi, H. H. Jamal Al-Deen, R. Safaa Hadi, N. Al-Ghaban, and Z. S. Al-Khafaji, *J. Nanostruct.*, **14**, No. 1: 1 (2024); https://jns.kashanu.ac.ir/article_113861.html
5. A. J. Salman, Z. F. Jawad, R. J. Ghayyib, F. A. Kareem, and Z. Al-Khafaji, *Energies*, **15**, No. 18: 6808 (2022); https://doi.org/10.3390/en15186808
6. H. A. Sallal, M. H. Mahboba, M. S. Radhi, A. Hanif, Z. S. Al-Khafaji, S. Ahmad, and Z. M. Yaseen, *J. King Saud Univ. Sci.*, **36**, No. 2: 103061 (2024); https://doi.org/10.1016/j.jksus.2023.103061
7. A. M. Humad, A. J. Dakhil, S. A. Al-Mashhadi, Z. Al-Khafaji, Z. A. Mohammed, and S. F. Jabr, *Res. Eng. Struct. Mater.*, **10**, No. 1: 1 (2024); http://dx.doi.org/10.17515/resm2023.43me0806rs
8. I. A. U. Kadhim, H. A. Sallal, and Z. S. Al-Khafaji, *ES Mater. Manuf.*, **21**, No. 1: 828 (2023); https://dx.doi.org/10.30919/esmm5f828
9. A. H. Jasim, N. S. Radhi, N. E. Kareem, Z. S. Al-Khafaji, and M. Falah, *Open Eng.*, **13**, No. 1: 20220472 (2023); https://doi.org/10.1515/eng-2022-0472
10. N. S. Radhi, A. H. Jasim, Z. S. Al-Khafaji, and M. Falah, *Nanosistemi, Nanomateriali, Nanotehnologii*, **21**, Iss. 4: 769 (2023); https://doi.org/10.15407/nnn.21.04.769
11. N. D. Fahad, N. S. Radhi, Z. S. Al-Khafaji, and A. A. Diwan, *Heliyon*, **9**, No. 3: 14103 (2023); https://doi.org/10.1016/j.heliyon.2023.e14103
12. S. Sattar, Y. Alaiwi, N. S. Radhi, and Z. Al-Khafaji, *Acad. J. Manuf. Eng.*, **21**, No. 4: 86 (2023); https://ajme.ro/current_issue.php
13. E. Mohammed and Z. Al-Khafaji, *Acad. J. Manuf. Eng.*, **21**, No. 3: 1 (2023); https://ajme.ro/content.php?vol=21&year=2023&issue=3&offset=0
14. M. Awang and W. R. Wan Mohd, *IOP Conf. Ser.: Mater. Sci. Eng.*, **342**, Iss. 1: 012046 (2018); DOI:10.1088/1757-899X/342/1/012046
15. C. Rosales, C. Bernal, and V. Pettarin, *Polym. Test.*, **90**, No. 1: 106598 (2020); https://doi.org/10.1016/j.polymertesting.2020.106598
16. J. A. Vallejo-Montesinos, J. A. L. Martínez, J. A. Montejano-Carrizales, E. Perez, J. A. B. Pérez, A. A. Almendárez-Camarillo, and J. A. Gonzalez-Calderon, *Mech. Mater. Sci. Eng.*, **8**, No. 1: 1 (2017); doi:10.2412/mmse.96.48.950
17. O. Kaymakci and N. Uyanik, *Mater. Plast.*, **57**: 309 (2020); https://doi.org/10.37358/Mat.Plast.1964
18. B. Al-Zubaidy, N. S. Radhi, and Z. S. Al-Khafaji, *Int. J. Mech. Eng. Technol.*, **10**, No. 1: 776 (2019); https://cdnx.uobabylon.edu.iq/research/repository1_publication14452_28_816.pdf
19. S. A. Hamza and N. S. Radhi, *Acad. J. Manuf. Eng.*, **21**, No. 1: 65 (2023); https://ajme.ro/content.php?vol=21&year=2023&issue=1&offset=0
20. H. A. Sallal, M. S. Radhi, M. H. Mahboba, and Z. Al-Khafaji, *Egypt. J. Chem.*, **55**, No. 6: 197 (2023); doi:10.21608/EJCHEM.2022.154630.6684
21. B. M. Rudresh, B. N. Ravikumar, and D. Madhu, *Indian J. Adv. Chem. Sci.*, **4**, No. 1: 68 (2016); https://ijacskros.com/artcles/IJACS-M174.pdf
22. H. Jones, J. McClements, D. Ray, C. S. Hindle, M. Kalloudis, and V. Koutsos, *Polym.*, **15**, No. 21: 4200 (2023); https://doi.org/10.3390/polym15214200
23. S. Daneshpayeh, F. Ashenai Ghasemi, and I. Ghasemi, *Teh. Glas.*, **13**, No. 3: 165 (2019); https://doi.org/10.31803/tg-20190312191013

Наносистеми, наноматеріали, нанотехнології
Nanosistemi, Nanomateriali, Nanotehnologii
2025, т. 23, № 2, сс. 603–610
https://doi.org/10.15407/nnn.23.02.0603

© 2025 ІМФ (Інститут металофізики
ім. Г. В. Курдюмова НАН України)
Надруковано в Україні.

PACS numbers: 06.60.Vz, 61.72.Mm, 62.20.fk, 62.23.St, 68.37.Lp, 81.20.Hy, 83.50.Uv

Study of Copper Microstructure after ECAP and Rolling

A. T. Turdaliev[1], A. S. Yerzhanov[2], and B. B. Makhmutov[2]

[1]*International Transport and Humanitarian University,*
Zhetisu 1, Microdistrict 32,
KZ-050063 Almaty, Kazakhstan
[2]*Karaganda Industrial University,*
30, Republic Ave.,
KZ-101400 Temirtau, Kazakhstan

In this article, the evolution of copper grade microstructure after equal-channel angular pressing (ECAP) and rolling is investigated. There is a relatively equiaxed ultrafine-grained structure formed after rolling after 10 passes of ECAP transformed into a lamellar structure with smaller grain-boundary spacing. After 10 passes of ECAP, the grain-boundary spacing is 180 nm, and it is reduced to 110 nm after rolling. Microstructure grinding during rolling almost does not occur. There is an increase in the share of large-angle boundary by 20% compared to the states after 10 passes of ECAP.

У цій статті досліджується еволюція мікроструктури мідних сортів після рівноканального кутового пресування (РККП) та вальцювання. Спостерігається відносно рівноосьова ультрадрібнозерниста структура, що утворюється після вальцювання, яка після 10 проходів РККП перетворюється на пластинчасту структуру з меншою віддаллю між межами зерен. Після 10 проходів РККП віддаль між межами зерен становить 180 нм, а після вальцювання вона зменшується до 110 нм. Подрібнення мікроструктури під час вальцювання майже не відбувається. Спостерігається збільшення частки великокутової межі на 20% порівняно зі станом після 10 проходів РККП.

Key words: microstructure, severe plastic deformation, pressing, rolling.

Ключові слова: мікроструктура, інтенсивна пластична деформація, пресування, вальцювання.

(Received 25 February, 2024; in revised form, 26 February, 2024)

1. INTRODUCTION

Nowadays, copper and copper alloys are widely used in industry due to their excellent physical and chemical properties. They make a great contribution to modern life: in magnetic circuits, power and communication cables, and other electrical devices. Recent achievements in the electronics industry have drawn the attention of many researchers to the development of copper-based alloys. Such alloys should have high strength and good electrical conductivity. However, high strength and good electrical conductivity are the two opposite conditions of all alloys.

Much works have been done in adding alloying elements (such as Cr, Ag, Zr, Nb and Co) to pure copper die. Such conventional hardening methods lead to various types of defects (*e.g.*, dislocations, hardening particles, point defects) in the copper die, which increase the scattering of conduction electrons and increase the electrical resistivity. Studies by K. X. Wei *et al*. [1] and C. Zhu *et al*. [2] have shown that the addition of Mg to copper-based alloys yields favourable results, and a reduction in production costs is achieved when Cu–Mg alloy contact wires are used.

Traditional metal forming techniques, including rolling and drawing, are commonly used to manufacture copper wires. High tensile strength (> 500 MPa) and good conductivity ($> 60\%$ IACS) are the most important properties required for wires [2]. Cold working improves the microstructure and increases the strength of alloys.

A high dislocation density is required to transform a coarse-grained material into an ultrafine-grained material, and a high stress shall be applied to increase the dislocation density [3–6]. At the same time, grain boundaries are reorganized to form an ultrafine-grained (UFG) or nanostructures. Conventional metal processing methods, such as extrusion or rolling, are limited in their ability to produce nanostructures for two important reasons. First, a limit to the amount of stress can be applied using these methods. Secondly, the stresses applied in conventional processes are insufficient to form nanostructures due to the low machinability of metal alloys under ambient conditions and low temperatures. As a result of these limitations, alternative machining methods based on the application of extreme deformation are needed. That means that very high stresses are applied at low temperatures without changing cross-sectional dimensions.

A new process of extreme plastic deformation, equal channel angular pressing (ECAP), can be used to obtain nanostructures with high strength and good electrical conductivity [7–11]. ECAP process has proven to be an efficient method for grinding metal grains

and composites and has the advantage of being scalable for the production of large volume samples. Although ECAP is an effective processing tool for laboratory research, it is labour-intensive and not easy to use in industrial conditions [12, 13].

In copper, high structure grinding and growth of mechanical properties are achieved during ECAP. Similar changes are observed when other metals are treated with ECAP, as well as with other methods of severe plastic deformation (SPD) [14–18]. Further microstructure grinding is only possible when followed by another strain method. Therefore, combinations of ECAP and other metal forming techniques began to be used later on [19–22]. The most widespread is the combination of ECAP with subsequent rolling. It allows obtaining sheet semi-finished products with ground structure and increased strength properties, which can be used in industry.

From the presented literature data, it can be concluded that copper is significantly hardened after SPD due to the grinding of its microstructure, and additional rolling after ECAP will further grind the microstructure and prepare the work piece for further use.

Therefore, the purpose of this work is to study the peculiarities of nanostructures formation in copper using ECAP and rolling.

2. EXPERIMENTAL METHODS

M2 grade copper was used for the study and was supplied as a bar with a diameter of 25 mm and a length of 120 mm. M2 grade copper contained 99.7% Cu.

A tooling with a channel-crossing angle of 90° was used to perform the ECAP. The speed of movable die was 5 mm/sec. Pressing was carried out at room temperature using the Vs route for 10 cycles. The rolling direction after ECAP was perpendicular to the extrusion direction during pressing. At the same time, before rolling, the samples, which had a cylinder shape after pressing, were milled to obtain two parallel flat surfaces 15 mm apart. Rolling was carried out with compression rates per pass of 5–10%. The final thickness of samples after rolling was equal to 1.5 mm, *i.e.*, the total compression was of 90%, which corresponds to the degree of true deformation of 2.7.

Optical microscope, transmission electron microscope and EBSD analysis were used to analyze the microstructure of the samples. Samples for metallographic analysis were thinned on a Tenupol-5 device using the electrolyte composition: 250 ml of H_3PO_4, 250 ml of ethyl alcohol, and 500 ml of distilled water. EBSD measurements were performed on a JOEL field emission electron microscope (at 20 kV) using the Oxford software package.

3. RESULTS AND DISCUSSION

The microstructure of the initial bar consisted of large grains of 120 μm. Twins were observed in the body of many grains (Fig. 1, *a*). After 10 passes, clear thin boundaries appeared in the structure with presumably high-angle disorientation. The shape of grains has become more regular. The structure consisted of both fairly equiaxed grains and grains elongated in the shear direction. The grain size was of 350 nm (Fig. 1, *b*). A large number of twins were also observed in the structure.

EBSD analysis showed that the structure became much more equiaxed after 10 cycles. However, even after such a number of ECAP cycles, the structure remained extremely heterogeneous as small submicron grains were adjacent to areas consisting predominantly of subgrains. In general, no significant differences in microstructure in different planes were found, except for metallographic texture.

Metallographic analysis showed that the microstructure after rolling is significantly different from the obtained microstructure after ECAP (Fig. 1, *c*). A distinct fine-grained lamellar microstructure is observed. Lamellar boundaries parallel to the rolling plane are straight and clear. Many lamellae are internally divided into individual fragments by transverse boundaries, often thick and eroded. In the rolling plane the structure is characterized by sufficient equiaxiality, most grains are irregularly shaped; their boundaries are thick and indistinct.

EBSD confirms the data of metallographic analysis and shows that the majority of lamellar boundaries acquire high-angle disorientation with increasing number of cycles, and the structure becomes quite homogeneous. However, the transverse boundaries within the lamellae retain predominantly low-angle disorientation.

In our case, the Vs route carried out pressing, so, the shear direction in each subsequent pressing cycle was different. In such a

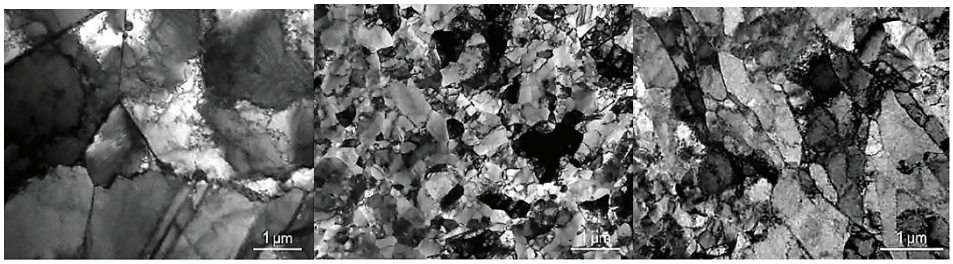

a *b* *c*

Fig. 1. Graphs of microhardness distribution along the bar section.

case, the newly formed shear bands are likely to intersect the bands formed during the previous cycle. Therefore, a rather equiaxed structure can occur at the intersection of shear zones that are perpendicular to each other (since the sample has been rotated at 90°C). The number of such intersections increases with each new pass and the volume fraction of equiaxed structures increases. In addition, the temperature of shear zone is probably much higher than the temperature of material volume. Therefore, the dynamic processes of return and recrystallization are more active and the fraction of large-angle boundary increases.

Figure 2, *a* shows the dependence of the large-angle boundary spacing (LABs) on the number of passes in different planes of the sample. Since after 1–2 passes the structure contains only a small number of grains whose size can be measured, the results of such measurements are very unreliable, so, they are not given at all. After 4 cycles, the average distance between large-angle boundaries was about 1 μm, whereas, after 10 cycles, it decreased to 700 nm. The distance between low-angle boundaries (SABs) as a function of the number of cycles varies similarly to the grain size, decreasing after the first two passes and then remaining almost constant at approximately 400 nm (Fig. 2, *b*).

In general, the obtained data on copper microstructure after ECAP coincide quite well with the known literature data. Thus, the transformation of elongated subgrains with predominantly low-angle boundaries formed after the first pass into a fairly equiaxed grain-subgrain structure with increasing number of passes was observed in the paper [9].

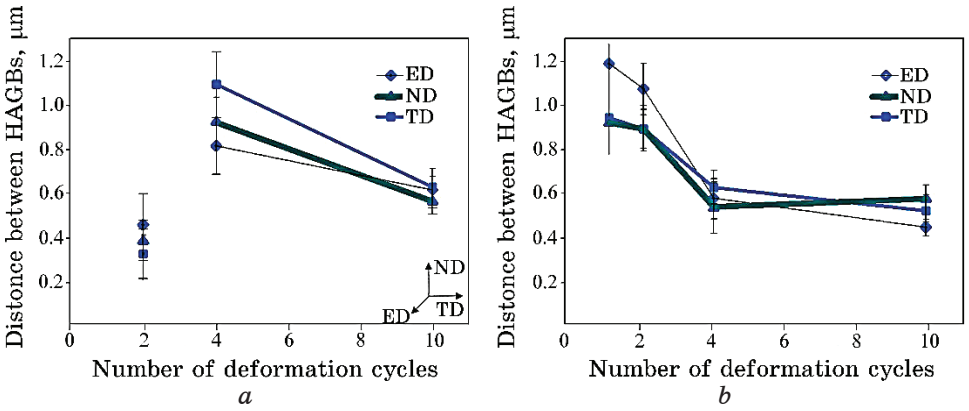

Fig. 2. Distances between boundaries after ECAP according to EBSD analysis: *a*—distance between large-angle boundaries; *b*—distance between low-angle boundaries.

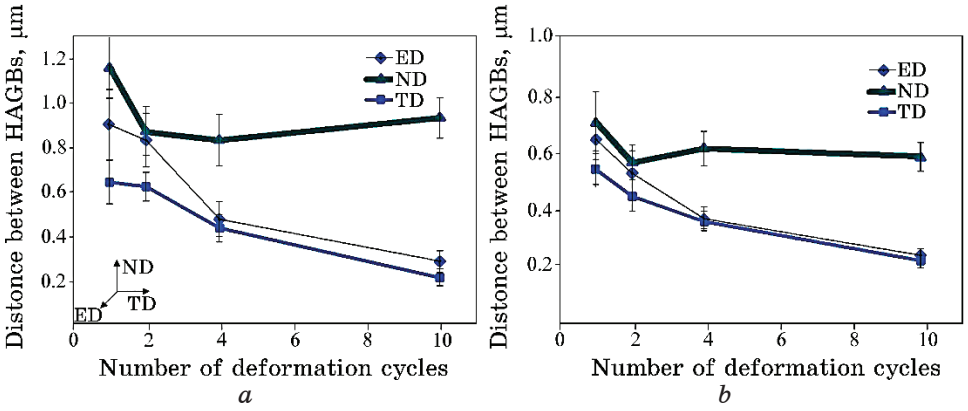

Fig. 3. Distances between boundaries after ECAP according and rolling to EBSD analysis: *a*—distance between large-angle boundaries; *b*—distance between low-angle boundaries.

The numerical values obtained from EBSD analysis after rolling show a significant difference between the microstructure in the rolling plane and in other planes. Thus, in the ED and TD planes, the distances between large-angle boundaries and low-angle boundaries decrease monotonically enough with increasing number of ECAP cycles, reaching values of 200–300 nm after 10 passes (Fig. 3). In the rolling plane, the distances between the boundaries almost do not change with the change in the number of passes, and are about 1000 nm for large-angle boundaries, and about 600 nm for low-angle boundaries. In the rolling plane, the portion of large-angle boundaries is basically unchanged after the first 4 cycles, amounting to 25–30%, and it increases to 45% after 10 cycles. In the ED and TD planes, in all cases except for 1 pass of ECAP, the portion of large-angle boundaries was almost the same and much higher than in the rolling plane. Large-angle boundaries portion increased by 20% after rolling compared to the values after ECAP.

4. CONCLUSION

The following conclusions can be drawn from the results obtained. Morphologically, the microstructure after ECAP does not differ from the typical microstructure formed in cubic metals during cold straining. The elongated microstructure becomes equiaxed after 10 straining cycles and the large-angle boundaries portion increases. Transverse grain size almost does not decrease with increasing number of passes. Rolling leads to a further reduction in the size of the structural components, at least in the RD and TD planes.

The conducted studies have shown that rolling after ECAP leads to extremely serious changes in microstructure. Instead of a relatively equiaxed structure, a lamellar structure is formed typical of cold-rolled b.c.c. metals.

REFERENCES

1. K. X. Wei, W. Wei, W. Wang, F, Du, and Q. B. Alexandrov, *Mater. Sci. Eng. A*, **528**: 1478 (2011); https://doi.org/10.1016/j.msea.2010.10.059
2. C. Zhu, A. Ma, J. Jiang, X. Li, D. Song, D. Yang, Y. Yuan, and J. Chen, *J. Alloys Compd.*, **582**: 135–140 (2014); https://doi.org/10.1016/j.jallcom.2013.08.007
3. I. E. Volokitina, *Prog. Phys. Met.*, **24**: No. 3: 593 (2023); https://doi.org/10.15407/ufm.24.03.593
4. A. Bychkov and A. Kolesnikov, *Metallography, Microstructure, and Analysis*, **12**, No. 3: 564 (2023); https://doi.org/10.1007/s13632-023-00966-y
5. I. E. Volokitina, A. V. Volokitin, M. A. Latypova, V. V. Chigirinsky, and A. S. Kolesnikov, *Prog. Phys. Met.*, **24**, No. 1: 132 (2023); https://doi.org/10.15407/ufm.24.01.132
6. Nurlan Zhangabay, Islambek Baidilla, Askhat Tagybayev, Ulanbator Suleimenov, Zhangeldi Kurganbekov, Medetbek Kambarov, Alexandr Kolesnikov, Gulnaz Ibraimbayeva, Khassen Abshenov, Irina Volokitina, Bakhytzhan Nsanbayev, Yermek Anarbayev, and Pavel Kozlov, *Case Stud. Constr. Mater.*, **18**: e02161 (2023); https://doi.org/10.1016/j.cscm.2023.e02161
7. Krzysztof Muszka, Lukasz Madej, and Janusz Majta, *Mater. Sci. Eng. A*, **574**: 68 (2013); https://doi.org/10.1016/j.msea.2013.03.024
8. A. V. Volokitin, I. E. Volokitina, and E. A. Panin, *Prog. Phys. Met*, **23**: No. 3: 411 (2022); https://doi.org/10.15407/ufm.23.04.684
9. V. D. Sitdikov, I. V. Alexandrov, M. M. Ganiev, E. I. Fakhretdinova, and G. I. Raab, *Rev. Adv. Mater. Sci.*, 41–44 (2015).
10. E. P. Orlova, G. G. Kurapov, and A. Turdaliev, *J. Chem. Technol. Metall.*, **51**: 451 (2016).
11. T. H. Fang, W. L. Li, N. R. Tao, and K. Lu, *Science*, **331**: 1587 (2011) https://doi.org/10.1126/science.1200177
12. M. Murugesan, D. Won, and J. Johnson, *Materials*, **12**: 609 (2019); https://doi.org/10.3390/ma12040609
13. C. Z. Duan and L. C. Zhang, *Materials Science and Engineering A*, **532**: 111 (2012); https://doi.org/10.1016/j.msea.2011.10.071
14. I. Volokitina, *J. Chem. Technol. Metall*, **57**: 631 (2022).
15. A. Denissova, T. Fedorova, D. Lawrinuk, A. Kolesnikov, A. Yerzhanov, Y. Kuatbay, and Y. Liseitsev, *Case Stud. Constr. Mater.*, **18**: e02346 (2023); https://doi.org/10.3390/ma15072584
16. I. Volokitina, A. Volokitin, and D. Kuis, *J. Chem. Technol. Metall.*, **56**: 643 (2021).
17. A. V. Polyakov, I. P. Semenova, and G. I. Raab, *Adv. Mater. Sci.*, **31**: 78 (2012).
18. M. O. Kurin, O. O. Horbachov, A. V. Onopchenko, and T. V. Loza, *Metallofiz. Noveishie Tekhnol.*, **44**, No. 6: 785 (2022).

https://doi.org/10.15407/mfint.44.06.0785
19. B. Sapargaliyeva, A. Agabekova, G. Ulyeva, A. Yerzhanov, and P. Kozlov, *Case Stud. Constr. Mater.*, **18**: e02162 (2023); https://doi.org/10.1016/j.cscm.2023.e02162
20. E. Panin, T. Fedorova, D. Lawrinuk, A. Kolesnikov, A. Yerzhanov, Z. Gelmanova, and Y. Liseitsev, *Case Stud. Constr. Mater*, **19**: e02609 (2023); https://doi.org/10.1016/j.cscm.2023.e02609
21. Sergey Lezhnev, Evgeniy Panin, and Irina Volokitina, *Advanced Materials Research*, **814**: 68 (2013); https://doi.org/10.4028/www.scientific.net/AMR.814.68
22. A. Naizabekov and E. Panin, *Journal of Materials Engineering and Performance*, **28**, No. 3: 1762 (2019); https://doi.org/10.1007/s11665-019-3880-6

Наносистеми, наноматеріали, нанотехнології
Nanosistemi, Nanomateriali, Nanotehnologii
2025, т. 23, № 2, сс. 611–618
https://doi.org/10.15407/nnn.23.02.0611

© 2025 ІМФ (Інститут металофізики
ім. Г. В. Курдюмова НАН України)
Надруковано в Україні.

PACS numbers: 62.20.Qp, 62.23.Hj, 68.37.Hk, 68.37.Lp, 81.20.Hy, 81.40.Jj, 83.50.Uv

Investigation of Properties' Change of Copper Wire in the Process of Twisting and Subsequent Drawing

A. V. Volokitin, I. E. Volokitina, and T. D. Fedorova

Karaganda Industrial University,
30, Republic Ave.,
101400 Temirtau, Kazakhstan

In this paper, the change in the mechanical properties of copper wire in the process of deformation in a new way is studied. This new method consists in combining two technologies in one line, namely, traditional drawing and twisting in an equal-channel stepped matrix. The twisting of the work piece occurs precisely in an equal-channel stepped matrix due to its rotation around the work piece axis that allows achieving the twisting in the entire volume of the work piece, followed by calibration of the cross-section due to the passage of the die channel. A physical experiment has shown the possibility of obtaining increased mechanical properties in copper wire by obtaining the nanostructure in the surface layer. In this regard, the use of an improved drawing method, combining torsion methods, which implement a simple shear scheme and the classical drawing process through a die, allows expanding the limits of the use of traditional structural materials.

У цій роботі досліджено зміну механічних властивостей мідного дроту в процесі деформування новим способом. Цей новий метод полягає в поєднанні двох технологій в одній лінії: традиційного волочіння та скручування у рівноканальній ступінчастій матриці. Скручування заготівки відбувається саме в рівноканальній ступінчастій матриці завдяки її обертанню навколо осі заготівки, що дає змогу досягти скручування у всьому об'ємі заготівки з подальшим калібруванням поперечного перерізу за рахунок проходження каналу матриці. Фізичний експеримент показав можливість одержання підвищених механічних властивостей мідного дроту шляхом одержання наноструктури у поверхневому шарі. Тому використання вдосконаленого методу волочіння, що поєднує методи кручення, якими реалізується проста схема зсуву, та класичний процес волочіння через матрицю, уможливлює розширити межі використання традиційних конструкційних матеріялів.

Key words: copper wire, drawing, twisting, microstructure, mechanical

properties.

Ключові слова: мідний дріт, волочіння, скручування, мікроструктура, механічні властивості.

(Received 24 June, 2024; in revised form, 26 June, 2024)

1. INTRODUCTION

Over the past few years, articles on the application of severe plastic deformation (SPD) methods have been the most widely read and cited. This is due to the fact that SPD is successfully used to produce submicron granular structures, and in some cases nanoscale crystallites, in a wide range of alloys [1–7]. However, despite the large number of SPD methods, the creation of deformation nanostructuring technologies for industrial use and, in particular, for the production of mass products, including wire, is a complex scientific and technical problem, the solution of which requires the development of continuous SPD schemes that ensure the production of ultrafine-grained and nanostructures in long metal semi-finished products. Such new technologies can be based on the well-known metal drawing process.

Traditionally, most metals and alloys for structural purposes are characterized by a homogeneous microstructure, where the average grain sizes in different parts are more or less uniform. According to the classical Hall–Petch ratio [8], a homogeneous polycrystalline metal can be strengthened by reducing the average grain size, since an increase in the volume fraction of grain boundaries will further hinder the movement of dislocations. However, a reduction in grain size will inevitably lead to a decrease in the ductility and deformability of the material due to the limited mobility of dislocations, thereby creating a dilemma known as the 'strength–ductility compromise', which limits the use of many metallic materials. However, in recent years, metals with a gradient nanostructure have become a new class of structural materials with a promising potential to overcome the compromise between strength and ductility. In such materials, nanostructures smaller than 1000 nm are formed in the surface layer, thereby, improving their mechanical properties [9–11].

Therefore, the development and development of new processes for obtaining high-strength materials with improved strength properties is an urgent and important issue for the development of production. In this regard, the use of an improved drawing method, combining torsion methods, which implement a simple shear scheme and the classical drawing process through a die, allows expanding

the limits of the use of traditional structural materials.

The purpose of this work is to study changes in the mechanical properties of copper wire during deformation in a new way, which consists in twisting the wire in an equal-channel step matrix and traditional drawing.

2. EXPERIMENTAL METHODS

To implement the combined technology for the deformation of copper wire, an industrial drum drawing mill B-1/550M was used. The deformation was carried out at room temperature using the Vs route (the rotation of the wire after each deformation cycle was carried out at 90°). The number of passes was 3. The reduction in the diameter of the wire after each deformation cycle was 0.5 mm. So, after 3 deformation passes, we got a wire with a diameter of 5.0 mm.

The technology of the twisting process in an equal-channel step matrix with subsequent drawing has no significant differences from classical drawing (Fig. 1). At the first stage, the wire is sharpened on the cutting machine to the required diameter. Next, the wire is passed through a lubricated chamber, in which a rotation mechanism is installed. The wire passes through the hole of the matrix bandage, and then through the hole of the die. The front end of the wire is fixed in the pliers of the drawing drum. Next, two segments of an equal-channel stepped matrix are installed around the wire and are inserted into the bandage according to the wedge principle. At this stage, all preparatory operations are completed. After that,

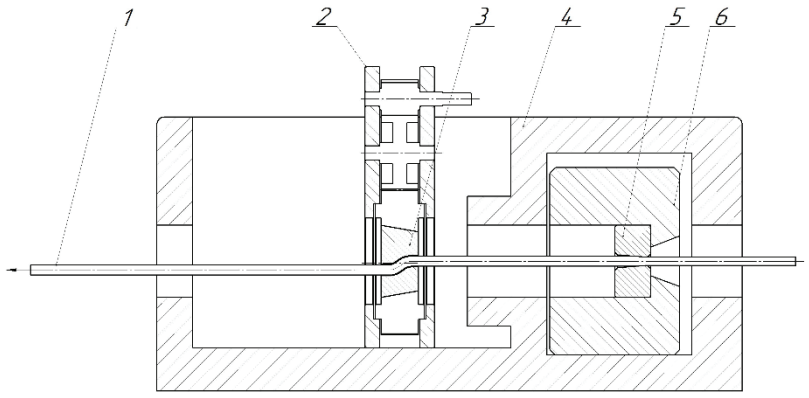

Fig. 1. Diagram of the combined wire deformation process: *1*—wire; *2*—frame; *3*—drawing block; *4*—drive gear; *5*—intermediate gear; *6*—bandage; *7*—equal-channel stepped matrix; *8*—fiber holder; *9*—die.

the mill is started with the output to the planned drawing speed and the mechanism that rotates the equal-channel step matrix is set in motion in parallel.

Metallographic analysis was carried out on a transmission electron microscope JEM 2100. Objects for TEM were prepared by jet polishing on a Tenupol-3 device at room temperature and a voltage of 25 V in a 7%-solution of H_3PO_4 in distilled water.

The effectiveness of hardening after deformation was evaluated by measuring microhardness in accordance with GOST 9450-76 with an interval of 1 mm, as shown in Fig. 2, using the Vickers method. The indenter was a diamond tip in the form of a four-sided pyramid with a square base. The load was of 0.5 N.

Tensile tests were carried out using the Instron 5982 electromechanical measuring machine. The tests were carried out in accordance with GOST 10446-80 'Wire. Tensile testing method' and GOST 1497-2000 'Metals. The method of tensile testing'. These standards establish methods for testing static tensile strength at a temperature of 20°C of wire made of metals and their alloys with a diameter or maximum cross-sectional size not exceeding 16 mm of circular cross-section. As test samples, wire segments with an initial estimated working length of 26 ± 0.1 mm and a diameter of 5 mm, limited with an error of up to 1%, were used. To recalculate the elongation with the reference of the rupture site to the middle of the calculated length, marks were scratched along the entire working length of the sample at regular intervals. The full length of the sample included sections for fixing it in the clamps of the bursting machine. The strain rate was of $0.56 \cdot 10^{-3}$ s^{-1}, which corresponds to a stretching rate of 0.5 mm/min. After the tensile tests, a fractographic analysis of the surface of the destroyed samples was carried out using scanning electron microscopy (SEM). Due to the large depth of focus, SEM gives an apparent volume and thereby facilitates the interpretation of the fracture topography.

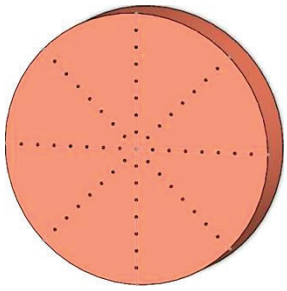

Fig. 2. Hardness measurement point diagrams.

3. RESULTS AND DISCUSSION

Figure 3 shows photos of the microstructure obtained using TEM. The first image was obtained at a distance of ≈0.2 mm from the surface of the wire (surface layer) (Fig. 3, *a*). As shown, the grain boundaries are fibrous and curved, which is usually characteristic of a large number of defects, the average grain size is 500 nm. This approach to the formation of the nanostructure of the wire surface layer is created due to friction and torsion during twisting in an equal-channel stepped matrix and is based on the use of the strain-rate intensity coefficient, which controls the thickness of the layer of intense plastic deformation. As a result, a layer of nanofine-deformed grains is created in the wire with generated at the material-tool contact. The following TEM image was obtained at a distance of ≈2 mm from the wire surface (middle layer) (Fig. 3, *b*). A bimodal structure has been formed here, which consists of small grains with high-angle boundaries and large grains with a developed substructure. The average grain size is 2 microns. Inside the grains, a thin structure is formed in the form of clusters of dislocations and cells. Large grains were most likely formed by the mechanism of diffusion-free recrystallization, since, if dynamic recrystallization had occurred, the grains would not have had distortions of the crystal lattice and would not contain defects. In addition, the last image was obtained from the central part of the wire. The structure is a cellular dislocation structure of deformation origin with an average grain size of 4 microns (Fig. 3, *c*). They are observed as large grains with a small number of subboundaries, as well as grains containing a large number of subboundaries.

Figure 4 shows the stress–strain curves and mechanical properties of the samples obtained during stretching. The tensile strength of deformed copper wire compared to undeformed increases from

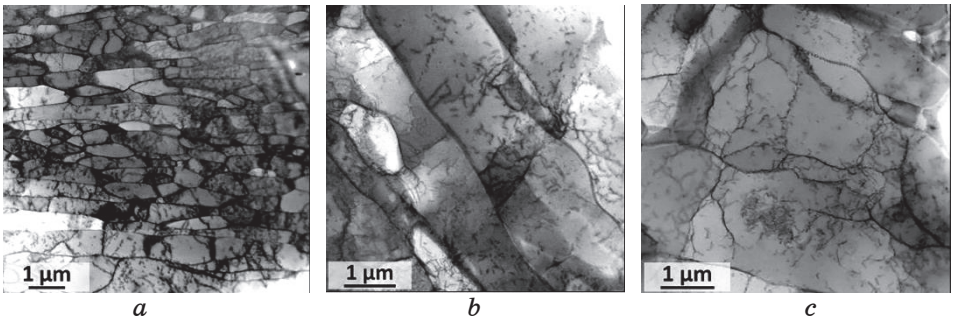

Fig. 3. Microstructure of deformed copper wire (cross section): *a*—surface layer; *b*—middle layer; *c*—central part.

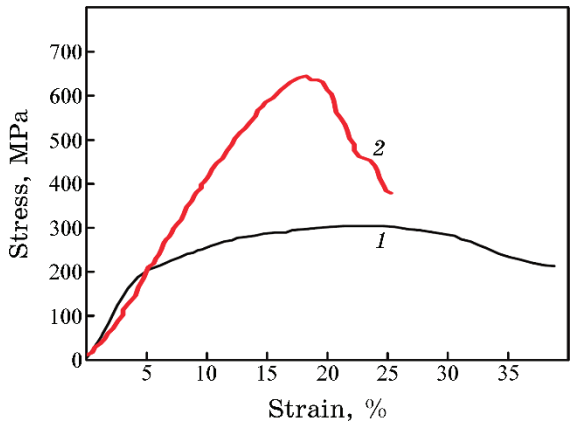

Fig. 4. Stretching curves of copper wire: *1*—before deformation; *2*—after 3 deformation cycles.

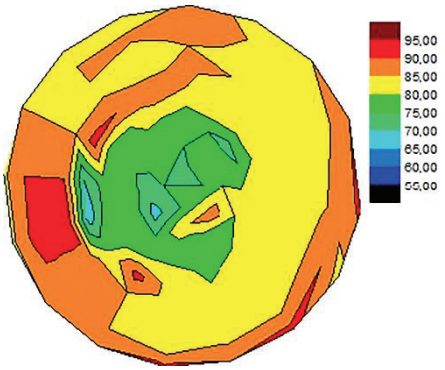

Fig. 5. Hardness distribution map in copper wire in cross section.

302 to 635 MPa, and the yield strength increases from 196 to 406 MPa—an increase of almost 100%. The elongation decreased from 42% to 27%. The obtained results of plastic properties are superior to some existing SPD methods of wire [12–15].

Figure 5 demonstrates a map of the hardness distribution of the sample, which shows that the hardness values of the surface layers are higher. The central regions have lower hardness values. This hardness distribution confirms the presence of a gradient microstructure.

A more accurate measurement of microhardness was carried out by Vickers hardness test randomly. Thus, the average value of microhardness in the surface layers was of 216 MPa, in the middle layers microhardness value was of 174 MPa, and 155 MPa in the centre of the wire. Such a spread of microhardness can be explained

by the formation of a gradient structure and the hardening of grain boundaries due to an increase in the density of dislocations.

Fractographic analysis of copper wire after stretching showed that the fracture has a mixed viscous character. The destruction zone of the wire surface layer has elongated pits and micropores; there are no cut zones. This indicates viscous destruction, since the main feature of such destruction is high-energy intensity, and slow crack development, resulting in a large number of pits. The middle part of the wire occupies the periphery of the fracture and consists of ridges of separation, the microrelief is stepped and traces of viscous stratification are visible. In the central part of the copper wire, together with large sections of the quasi-cut, areas with the formation of a shallow relief are observed.

4. CONCLUSION

Metallographic analysis showed the presence of a gradient structure in the copper wire after deformation by a new method. A nanostructure with a grain size of ≈ 500 nm was obtained in the surface layer, which increases to 4 microns towards the centre of the wire. The micromechanical tests carried out to determine the microhardness confirmed the presence of a gradient microstructure in the copper wire. Tensile tests showed not only a 2-fold increase in the strength properties of the wire, but not a strong decrease in plastic properties. Fractographic analysis of the destroyed wire samples showed the presence of a viscous fracture, which also indicates good plastic properties.

ACKNOWLEDGMENT

This research has been/was/is funded by the Science Committee of the Ministry of Science and Higher Education of the Republic of Kazakhstan (Grant No. AP19676903).

REFERENCES

1. I. E. Volokitina, *Progress in Physics of Metals*, **24**, No. 3: 593 (2023); https://doi.org/10.15407/ufm.24.03.593
2. A. Bychkov and A. Kolesnikov, *Metallography, Microstructure, and Analysis*, **12**, No. 3: 564 (2023); https://doi.org/10.1007/s13632-023-00966-y
3. M. A. Latypova, V. V. Chigirinsky, and A. S. Kolesnikov, *Progress in Physics of Metals*, **24**, No. 1: 132 (2023); https://doi.org/10.15407/ufm.24.01.132
4. A. Denissova, T. Fedorova, D. Lawrinuk, A. Kolesnikov, A. Yerzhanov, Y. Kuatbay, and Y. Liseitsev, *Case Stud. Constr. Mater.*, **18**: e02346 (2023);

https://doi.org/10.3390/ma15072584
5. M. Ved, N. Sakhnenko, I. Yermolenko, and G. Yar-Mukhamedova, *Chemico-Technological Journal*, **8**: 147 (2021); https://doi.org/10.18321/ectj697
6. A. V. Volokitin, I. E. Volokitina, and E. A. Panin, *Progress in Physics of Metals*, **23**: No. 3: 411 (2022); https://doi.org/10.15407/ufm.23.04.684
7. I. Volokitina, A. Volokitin, and D. Kuis, *J. Chem. Technol. Metall.*, **56**: 643–647 (2021).
8. M. Murugesan, D. Won, and J. Johnson, *Materials*, **12**: 609 (2019); https://doi.org/10.3390/ma12040609
9. I. E. Volokitina, A. V. Volokitin, E. Panin, T. Fedorova, D. Lawrinuk, A. Kolesnikov, A. Yerzhanov, Z. Gelmanova, and Y. Liseitsev, *Case Stud. Constr. Mater.*, **19**: e02609 (2023); https://doi.org/10.1016/j.cscm.2023.e02609
10. M. Latypova, V. Chigirinsky, and A. Kolesnikov, *Progress in Physics of Metals*, **24**, No. 1: 132 (2023); https://doi.org/10.15407/ufm.24.01.132
11. I. E. Volokitina, *Metal Science and Heat Treatment*, **63**, Nos. 3–4: 163 (2021).
12. L. David, *Journal of The Minerals*, **59**: 21 (2021); https://doi.org/10.1007/s11837-007-0111-7
13. B. Sapargaliyeva, A. Agabekova, G. Ulyeva, A. Yerzhanov, and P. Kozlov, *Case Stud. Constr. Mater.*, **18**: e02162 (2023); https://doi.org/10.1016/j.cscm.2023.e02162
14. G. I. Raab, D. V. Gunderov, L. N. Shafigullin, Yu. M. Podrezov, M. I. Danylenko, N. K. Tsenev, R. N. Bakhtizin, G. N. Aleshin, and A. G. Raab, *Materials Physics and Mechanics*, **3**, No. 24: 242 (2015).
15. I. E. Volokitina and A. V. Volokitin, *Physics of Metals and Metallography*, **119**, No. 9: 917 (2018).

Наукове видання

НАНОСИСТЕМИ, НАНОМАТЕРІАЛИ, НАНОТЕХНОЛОГІЇ

ЗБІРНИК НАУКОВИХ ПРАЦЬ

ТОМ 23

випуск 2

(2025)

Підписано до друку 26.06.2025. Формат 70×100/16.
Папір офсетний. Друк різографічний.
Ум. друк. арк. 26,81. Обл.-вид. арк. 24,67.
Наклад 55 прим. Зам. № 2

Поліграфічно-розмножувальна дільниця РВВ ІМФ ім. Г. В. Курдюмова НАН України
бульв. Акад. Вернадського, 36; 03142 Київ, Україна

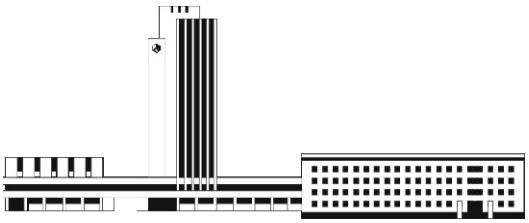

НАЦІОНАЛЬНА АКАДЕМІЯ НАУК УКРАЇНИ

Засновник: Інститут металофізики ім. Г. В. Курдюмова НАН України
Видавець: Інститут металофізики ім. Г. В. Курдюмова НАН України

Передплатний індекс 94919 ISSN 1816-5230

Інформація про передплату на збірник наукових праць
«НАНОСИСТЕМИ, НАНОМАТЕРІАЛИ, НАНОТЕХНОЛОГІЇ»

Редакція щоквартального збірника наукових праць «НАНОСИСТЕМИ, НАНОМАТЕРІАЛИ, НАНОТЕХНОЛОГІЇ» (CODEN: NNNAAT; ISSN (Print): 1816-5230, ISSN (Online): 2617-3794) повідомляє читачів про передплату (що починається з поточного кварталу випуску). Цей збірник входить за індексом **94919** до «Каталогу видань України». Рекомендуємо оформити передплату:
1) через ТОВ **«ПресЦентр Київ»** / LLC **'PresCentr Kyiv'** / (01019 Київ, Україна, а/с 185; тел. / факс: +380 44 5361180 / +380 44 5361175; e-mails: podpiska1@prescentr.kiev.ua, market7@prescentr.kiev.ua, ksl1@prescentr.kiev.ua) чи то через Internet:
Наносистеми, наноматеріали, нанотехнології (prescentr.kiev.ua) (Product Code: 14724);
2) через передплатну аґенцію «Меркурій» / Subscription agency 'Mercury' (49000 Дніпро, Слобожанський проспект, буд. 10, корп. 2, кв. 51; 03056 Київ, вул. Вадима Гетьмана, буд. 27, оф. 74; тел.: +380 93 3935740 / +380 44 2210557; e-mails: podpiska@mercury.net.ua, l.podbereznaja.mercury@gmail.com);
3) безпосереднім перерахуванням від **390 грн.** за один примірник випуску до **1560 грн.** за один том (4 випуски у рік):
«ОТРИМУВАЧУ»: Інститут металофізики ім. Г. В. Курдюмова НАН України
на розрахунковий рахунок № UA058201720313291001201001901 в банку ГУДКСУ в м. Києві
Код банку: 820172
Код єдиного державного реєстру підприємств і організацій України (ЄДРПОУ): 05417331
Для «ПОСТАЧАЛЬНИКА» — Інституту металофізики ім. Г. В. Курдюмова НАН України
Свідоцтво платника податку на додану вартість (ПДВ) № 36283185, індивідуальний податковий номер (ІПН) 054173326066
Код призначення платежу: 25010100
ПРИЗНАЧЕННЯ ПЛАТЕЖУ: за збірник «Наносистеми, наноматеріали, нанотехнології» для РВВ ІМФ НАНУ
ПІДСТАВА: передоплата 100%

INFORMATION FOR FOREIGN SUBSCRIBERS

Editorial Board of a Quarterly Collected Scientific Transactions 'Nanosistemi, Nanomateriali, Nanotehnologii' (CODEN: NNNAAT; ISSN (Print): 1816-5230, ISSN (Online): 2617-3794) advertises the subscription on an annual basis. Orders should be placed through one of the methods described below. Besides 1) the subscription *via* the LLC **'PresCentr Kyiv'** / **«ПресЦентр Київ»** (with address: UA-01019 Kyiv, Ukraine, P.B. 185; tel. / fax: +380 44 5361180 / +380 44 5361175; e-mails: podpiska1@prescentr.kiev.ua, market7@prescentr.kiev.ua, ksl1@prescentr.kiev.ua) or *via* Internet:
Наносистеми, наноматеріали, нанотехнології (prescentr.kiev.ua) (Product Code: 14724),
as well as besides 2) the subscription *via* Subscription agency 'Mercury' / «Меркурій» (with juridical address: UA-49000 Dnipro, Slobozhansky Ave., Bldg. 10/2, apt. 51; postal address in Kyiv: UA-03056 Kyiv, Vadym Hetman Str., Bldg. 27, off. 74; tel.: +380 93 3935740 / +380 44 2210557, e-mails: podpiska@mercury.net.ua, l.podbereznaja.mercury@gmail.com),
3) the Editorial Board will take orders sent directly to the Editorial Board. To obtain our collected scientific transactions, the persons and institutions interested in this title should made the definite payment sent, according to the order, to the account of the Publisher—G. V. Kurdyumov Institute for Metal Physics of the N.A.S. of Ukraine.
The periodical frequency is 4 issues per year. The annual subscription rate for 'Nanosistemi, Nanomateriali, Nanotehnologii' is **160 USD** (or **148 EUR**), including airmail postage, packing and handling charges. All other-currency payments should be made using the current conversion rate set by the Publisher (subscribers should contact the Editorial Board).
Subscription is valid after obtaining by the Editorial Board of banker's order. Banker's order should be sent to the address:
G. V. Kurdyumov Institute for Metal Physics, N.A.S. of Ukraine,
currency account No. UA603223130000025308000000067, MFO 322313,
in the Kyiv's Branch of JSC 'The State Export-Import Bank of Ukraine' (Public Joint Stock Company 'Ukreximbank') (11^{b} Bulvarno-Kudryavska Str., UA-04053 Kyiv, Ukraine)
simultaneously with written notice providing the Editorial Board with a copy of banker's order for subscription and detailed address for mailing.
Prepayment is 100%.
Address of the Editorial Board: G. V. Kurdyumov Institute for Metal Physics, N.A.S. of Ukraine, 36 Academician Vernadsky Blvd., UA-03142 Kyiv, Ukraine.
E-mail: tatar@imp.kiev.ua (with subject beginning by word 'NNN')
Fax: +380 44 4242561. Phone: +380 44 4241221, +380 44 4249042.
After receiving of banker's order, the Editorial Board will send the guarantee letter to the subscriber's address for mailing the journal for a corresponding term.
The Editorial Board of this journal hopes for effective co-operation with its present and future readers and requests to promote the maximum information about its contents to persons and organizations concerned.

© Інститут металофізики ім. Г. В. Курдюмова НАН України (Київ), 2025

Індекс 94919